

Landslides in the Nepal Himalaya: a
quantitative assessment of
spatiotemporal characteristics,
susceptibility, and landscape
preconditioning

by

Joshua Nathan Jones

A thesis submitted in partial fulfilment of the degree of

DOCTOR OF PHILOSOPHY

University of East Anglia, School of Environmental Sciences

June 2021



This copy of the thesis has been supplied on condition that anyone who consults it is understood to recognise that its copyright rests with the author and that use of any information derived therefrom must be in accordance with current UK Copyright Law. In addition, any quotation or extract must include full attribution.

Abstract

Mountainous regions such as the Himalaya are severely affected by landslides. Strategies to manage landslide hazard often rely on statistical landslide susceptibility models that forecast the locations of future landslides. Susceptibility models are typically space and/or time independent. However, recent observations suggest that several processes (i.e., earthquake preconditioning, path dependency) are capable of imparting transient controls on landslide occurrence that invalidate the assumption of time-independence. Consequently, it is vital to improve understanding of processes that influence landsliding through space and time, and to assess how these affect typical landslide susceptibility approaches.

Therefore, this thesis aims to quantify the spatiotemporal characteristics, distributions, and preconditioning of monsoon-triggered landslides in the Nepal Himalaya, and how these factors influence regression-based susceptibility modelling. This aim is achieved by developing a 30-year inventory of ~12,900 monsoon-triggered landslides, which is used to: 1) assess the overall characteristics and distributions of monsoon-triggered landslides; 2) systematically quantify spatiotemporal variations in landslide processes and distributions, and how this influences landslide susceptibility modelling; 3) determine empirical relationships between monsoon-strength and landsliding to determine how earthquake preconditioning and cloud-outburst storms transiently perturb landslide rates in Nepal, and 4) recommend a best-practice framework for modelling landslide susceptibility in regions impacted by spatiotemporally varying landslide processes.

Spatiotemporal variations in landslide occurrence are found to relate to permafrost degradation, path dependency, earthquake-preconditioning, and the occurrences of storms. Such variation significantly compromises the applicability and accuracy of regression-based susceptibility models, with models developed from specific regions or time slices incapable of consistently predicting other landslide data. However, susceptibility models developed using 6–8 years of landslide data offered consistently reliable prediction. Overall, it is recommended that typical space-time independent regression-based susceptibility models are avoided in dynamic mountainous regions unless developed with 6-8 years of multi-temporal landslide data and/or specific knowledge of any spatiotemporally varying landslide processes.

Access Condition and Agreement

Each deposit in UEA Digital Repository is protected by copyright and other intellectual property rights, and duplication or sale of all or part of any of the Data Collections is not permitted, except that material may be duplicated by you for your research use or for educational purposes in electronic or print form. You must obtain permission from the copyright holder, usually the author, for any other use. Exceptions only apply where a deposit may be explicitly provided under a stated licence, such as a Creative Commons licence or Open Government licence.

Electronic or print copies may not be offered, whether for sale or otherwise to anyone, unless explicitly stated under a Creative Commons or Open Government license. Unauthorised reproduction, editing or reformatting for resale purposes is explicitly prohibited (except where approved by the copyright holder themselves) and UEA reserves the right to take immediate 'take down' action on behalf of the copyright and/or rights holder if this Access condition of the UEA Digital Repository is breached. Any material in this database has been supplied on the understanding that it is copyright material and that no quotation from the material may be published without proper acknowledgement.

List of contents

Chapter 1 Introduction, aims and study region.....	24
1.1 Motivation.....	24
1.2 Research problems	24
1.2.1 Spatial applicability	25
1.2.2 Temporal applicability.....	26
1.2.2.1 Path dependency.....	27
1.2.2.2 Earthquake preconditioning.....	27
1.2.3 Lack of long-term landslide data.....	29
1.3 Aims and objectives	29
1.4 Study region.....	32
1.4.1 Why Nepal?.....	32
1.4.2 Tectonic, geological, and geomorphological setting.....	34
1.4.2.1 Tethyan Himalaya.....	35
1.4.2.2 Greater Himalaya.....	36
1.4.2.3 Lesser Himalaya	37
1.4.2.4 Sub Himalaya.....	38
1.4.3 Landslide setting	38
1.4.3.1 Landslide predisposing factors.....	40
1.4.3.2 Precipitation-triggered landslides	44
1.4.3.3 Coseismic landslides	46
1.4.3.4 Current status of landslide hazard management in Nepal.....	48
1.5 Conclusion	49
Chapter 2 Landslide inventory development, analysis, and susceptibility modelling	51

2.1 Introduction.....	51
2.2 Methods: landslide inventory development	52
2.2.1 Inventory type	53
2.2.2 Study region and inventory scale	53
2.2.3 Landslide mapping procedure	53
2.2.3.1 Imagery acquisition	55
2.2.3.2 Imagery processing.....	57
2.2.3.3 Landslide mapping	59
2.3 Methods: obtaining triggering and predisposing factor data.....	65
2.3.1 Trigger event data collection.....	65
2.3.1.1 PERSIANN-CDR.....	68
2.3.2 Predisposing factor data collection	69
2.3.2.1 Topographic data	71
2.3.2.2 Hydrological data.....	71
2.3.2.3 Regional geology data	73
2.3.2.4 Landcover data	74
2.3.2.5 Permafrost data	74
2.3.2.6 Distance to roads.....	75
2.3.2.7 Issues with temporal variation	75
2.4 Methods: analysis of inventory characteristics and distributions	76
2.4.1 Landslide path dependency	77
2.4.2 Landslide geometry	78
2.4.2.1 Aspect Ratio (AR).....	79
2.4.2.2 Roundness	80
2.4.3 Landslide size.....	81

2.4.4 Landslide spatial distributions	83
2.4.4.1 Predisposing factor frequency analysis	83
2.4.4.2 Anselin Local Moran's I	85
2.5 Methods: susceptibility modelling.....	86
2.5.1 Principles of landslide susceptibility modelling.....	87
2.5.2 Principles of Binary Logistic Regression (BLR) modelling.....	88
2.5.3 The LASSO.....	89
2.5.4 Model implementation within glmnet.....	90
2.5.5 AUROC validation	92
2.5.6 Susceptibility map production	93
2.6 Results: inventory analysis and susceptibility modelling.....	93
2.6.1 Landslide path dependency	93
2.6.2 Landslide geometry	93
2.6.2.1 Aspect Ratio (AR)	93
2.6.2.2 Roundness	94
2.6.3 Landslide size.....	96
2.6.4 Landslide spatial distributions	99
2.6.4.1 Predisposing factor analysis.....	99
2.6.4.2 Anselin Local Moran's I	109
2.6.5 BLR susceptibility modelling.....	111
2.6.5.1 Regression coefficients and LASSO selection	111
2.6.5.2 Model validation	113
2.6.5.3 Regional susceptibility map	113
2.7 Discussion and conclusions	115
2.7.1 Path dependency.....	115

2.7.2 Influences of topographic factors on landslide distributions and morphology	118
2.7.2.1 Spatial distributions.....	118
2.7.2.2 Landslide geometry	121
2.7.2.3 Landslide size	123
2.7.3 Influences of lithology on landslide distributions and morphology	127
2.7.4 Influences of distance to roads and land use	130
2.7.5 Landslide susceptibility	131
2.7.5.1 Regression coefficients and AUROC.....	131
2.7.5.2 Data and methodological limitations	132
2.7.6 Conclusions.....	135
Chapter 3 Spatial heterogeneity in landslide processes: insights from field data and BLR susceptibility modelling	137
3.1 Introduction.....	137
3.2 Study region.....	139
3.2.1 Langtang Valley.....	139
3.2.2 Arniko Highway.....	141
3.3 Methods	142
3.3.1 Field methodologies	142
3.3.1.1 Landslide mapping	142
3.3.1.2 Lithological mapping	143
3.3.1.3 Structural mapping.....	144
3.3.1.4 Landslide susceptibility mapping	144
3.4 Results	145
3.4.1 Lithological units	145
3.4.1.1 Langtang Unit 1.....	145

3.4.1.2	Langtang Unit 2.....	146
3.4.1.3	Langtang Unit 3.....	146
3.4.1.4	Langtang Unit 4.....	150
3.4.1.5	Arniko phyllite	150
3.4.1.6	Arniko quartzite	150
3.4.1.7	Arniko schist.....	150
3.4.1.8	Arniko dolomite.....	150
3.4.2	Landslide inventory mapping	154
3.4.3	Qualitative descriptions of landslide types and processes	157
3.4.3.1	Rockfalls.....	157
3.4.3.2	Rotational slides and slumps	159
3.4.3.3	Shallow translational slides.....	159
3.4.3.4	Debris flows.....	161
3.4.3.5	Debris avalanche (Langtang Avalanche)	163
3.4.3.6	Relict alluvial fans	164
3.4.4	Structural data	165
3.4.5	BLR analysis and susceptibility modelling	169
3.4.5.1	BLR coefficient and LASSO results.....	169
3.4.5.2	Susceptibility modelling and AUROC validation results.....	172
3.5	Discussion	175
3.5.1	Insights from field data: impacts of leucogranite and bedrock discontinuities.....	175
3.5.2	Spatial heterogeneity in landslide controls	179
3.5.3	Impacts of spatial heterogeneity on landslide susceptibility modelling	185

3.5.4 Impacts of landslide type on landslide susceptibility modelling and hazard management	186
3.6 Conclusions	188
Chapter 4 Temporal variations in landslide processes and distributions: implications for landslide susceptibility modelling	190
4.1 Introduction.....	190
4.2 Data and methods	192
4.2.1 Path dependency.....	192
4.2.1.1 The overlap index	192
4.2.1.2 Unaffected area.....	193
4.2.1.3 Number of overlaps.....	194
4.2.2 K-S and Chi-2 analysis.....	194
4.2.3 BLR modelling.....	197
4.2.4 AUROC model validation	199
4.3 Results 201	
4.3.1 Path dependency.....	201
4.3.1.1 The overlap index	201
4.3.1.2 Unaffected area.....	201
4.3.1.3 Number of overlaps.....	203
4.3.2 K-S and Chi-2 analysis.....	203
4.3.3 BLR modelling.....	205
4.3.4 AUROC validation	210
4.4 Discussion	211
4.4.1 Data limitations and assumptions.....	211
4.4.2 Landslide path dependency	217
4.4.3 Landslide spatial distributions	220

6.2.1 Limitations: spatial and temporal heterogeneity	269
6.2.2 Potential solutions	270
6.2.3 Proposed framework for optimum susceptibility modelling.....	279
6.2.4 Implications for Nepal.....	281
6.2.5 Wider implications and considerations.....	282
6.3 Final conclusions	283
Appendices.....	286
Appendix A. Decision tree outlining process for deciding whether a bare earth feature visible in satellite imagery should be mapped as a rainfall-triggered landslide.....	286
Appendix B. Examples of road tip and other anthropogenic features often visible in the Landsat imagery,.....	287
Appendix C. Author version of paper published in the Quarterly Journal of Engineering Geology and Hydrogeology.....	287
Appendix D. Regional coseismic model regression coefficients and LASSO selection percentages.....	305
Appendix E. Land use and geology regression coefficients and LASSO selection percentages for the 12 BLR models developed in Chapter 4.	306
Appendix F. Correlations between SASMI and landslide volume.	308
Appendix G. Non-best-fit correlations between proxies of ASM-strength and landslide volume.	309
Appendix H. Non-best-fit correlations between proxies of ASM-strength and landslide volume.	311
Appendix I. Non-best-fit correlations between proxies of ASM-strength and landslide volume.	313
Appendix J. Correlations between 2015 percentage change in landsliding and 'PGA-excess topography' at excess topography thresholds of 25°, 30°, 35° and 40°.	315
Appendix K. Correlations between 2015 percentage change in landsliding and 'PGA-excess topography' at excess topography thresholds of 25°, 30°, 35° and 40°.	316
Appendix L. Correlations between 2015 percentage change in landsliding and 'PGA-excess topography' at PGA thresholds of > 0.1g.....	317

Appendix M. Correlations between 2015 percentage change in landsliding and ‘PGA-excess topography’ at PGA thresholds of > 0.2g.....	318
Appendix N. Correlations between 1989 percentage change in landsliding and ‘PGA-excess topography’ at an excess topography threshold of 45°.	319
References.....	320

List of figures

Figure 1.1. Location of the study region.	33
Figure 1.2. Nepal tectonic units and elevation profile, after DeCelles et al. (2004)..	35
Figure 1.3. Schematic diagrams of the typical landslide types found in Nepal (USGS 2004a).....	39
Figure 1.4. Jure landslide example: a) photograph showing the landslide scar and upper deposits taken in April 2018. b) aerial view of the landslide from 0.3 m ESRI/Maxar imagery. c) approximate location of the Jure landslide within Nepal.	46
Figure 1.5. Locations of the Gorkha 2015 coseismic landslides mapped by Roback et al. (2018).	48
Figure 2.1. Generalised workflow for landslide mapping procedure used in this thesis.....	56
Figure 2.2. Example false colour RGB pre- and post-monsoon season Landsat satellite imagery used to map landslides. a) pre-imagery. b) post-imagery. c) resulting mapped landslides.	61
Figure 2.3. Examples of fresh and reactivated landslides in false RGB Landsat satellite imagery. a) and d) show pre-monsoon season imagery with pre-existing landslides. b) and e) show post-monsoon season imagery with a clear fresh failure and several reactivated or remobilised failures respectively. c) and f) show the new features from b) and e) delineated as yellow polygons.	64
Figure 2.4. Locations of all 12,838 mapped landslide polygons in the ASM-inventory. Insets show smaller scale view of delineated polygons in two subregions.	65

Figure 2.5. PERSIANN-CDR precipitation data examples for a) peak monthly monsoon period (May – September) rainfall from 2002, and b) mean total monthly rainfall for the period 1988 – 2018.....70

Figure 2.6. Landslide predisposing factor datasets for a) elevation, b) hillslope angle, c) aspect, d) planform curvature, e) profile curvature, f) local relief, g) excess topography, h) distance to channels, i) near channel ksn, j) near channel SSP, k) bedrock geology, l) land use, m) PFI and n) distance to roads.....73

Figure 2.7. Examples of landslide path dependency types.....78

Figure 2.8. Examples of landslide Aspect Ratio (AR) types, where AR1 has $L/W = < 2$, AR2 has $L/W = 2 - 4$, and AR3 has $L/W > 4$80

Figure 2.9. Number of landslides in each tectonic unit (a), and of each path dependent type (b) and AR type (c).94

Figure 2.10. Proportions of all landslides, landslides in each tectonic unit, and landslides of each path dependent type that are of geometric type a) AR1, b) AR2, and c) AR3.....95

Figure 2.11. Mean roundness of all landslides, landslides in each tectonic unit, and of landslides of each path dependent and AR type.95

Figure 2.12. Three-parameter inverse-gamma distributions fitted to the probability density functions of landslide area for a) all landslides, b) AR1 landslides, c) AR2 landslides, d) AR3 landslides, e) spatially associated (partial) landslides, and f) spatially unassociated landslides. Note that a p-value > 0.01 indicates that the three-parameter inverse-gamma distribution provide a good fit to the actual data, whilst the D-value gives the maximum distance between the actual data and the fitted distribution.97

Figure 2.13. Relationship between AR and log-area for the entire ASM-inventory. Top shows raw data, bottom with those data binned into boxplots.....98

Figure 2.14. Three-parameter inverse-gamma distributions fitted to the probability density functions of landslide area for a) all landslides, and landslides in b) the Greater Himalaya, c) the Lesser Himalaya, and d) the Sub Himalaya. Note that a p-

value > 0.01 indicates that the three-parameter inverse-gamma distribution provide a good fit to the actual data, whilst the D-value gives the maximum distance between the actual data and the fitted distribution.	99
Figure 2.15. Frequency analysis showing the proportions of all landslides, various landslide subsets, and the study region at bins of aspect (a – c) and hillslope angle (d – f).....	101
Figure 2.16. Frequency analysis showing the proportions of all landslides, various landslide subsets, and the study region at bins of planform curvature (a – c) and profile curvature (d – f).....	102
Figure 2.17. Frequency analysis showing the proportions of all landslides, various landslide subsets, and the study region at bins of elevation (a – c) and excess topography (d – f).....	103
Figure 2.18. Frequency analysis showing the proportions of all landslides, various landslide subsets, and the study region at bins of local relief (a – c) and distance to channels (d – f).....	104
Figure 2.19. Frequency analysis showing the proportions of all landslides, various landslide subsets, and the study region at bins of ksn (a – c) and distance to roads (d – f).....	106
Figure 2.20. Frequency analysis showing the proportions of all landslides, various landslide subsets, and the study region at bins of PFI (a – c) and land use (d – f).107	
Figure 2.21. Frequency analysis showing the proportions of all landslides, various landslide subsets, and the study region at each geology category (a – c).....	108
Figure 2.22. Anselin Local Moran’s I analysis for a) AR, b) roundness, c) area, d) elevation, e) local relief, f) excess topography, g) slope, and h) aspect.	110
Figure 2.23. Anselin Local Moran’s I analysis for a) planform curvature, b) profile curvature, c) distance to roads, d) distance to channels, e) near channel Specific Stream Power (SSP), and f) near channel ksn.	111

Figure 2.24. a) Self-validated Receiver Operator Curves (ROCs) and associated average AUC values for the 50 trained models. b) independent 10-fold cross validated AUROCs.....	114
Figure 2.25. Final susceptibility maps derived from the average regression coefficients of all factors selected by the LASSO in at least 50% of the 50 trained models for a) the entire study region, b) Kathmandu and Bhaktapur and c) Langtang Valley.....	114
Figure 2.26. Proportion of a) the entire study region, b) Kathmandu and Bhaktapur and c) Langtang Valley that fall within 0.1 probability bins of observing a landslide.	116
Figure 2.27. Correlation between local relief and AR across the entire ASM-inventory.	123
Figure 2.28. Correlation between the log of landslide area and a) elevation, b) excess topography, c) local relief, d) average total monsoon rainfall, e) annual total monsoonal rainfall, and f) annual peak monthly rainfall.	126
Figure 2.29. Three-parameter inverse-gamma distributions fitted to the probability density functions of landslide area for landslides that occurred within a) sandstone and conglomerate, b) schist, c) phyllite, d) granites and gneisses, and e) dolomites. Note that a p-value > 0.01 indicates that the three-parameter inverse-gamma distribution provide a good fit to the actual data, whilst the D-value gives the maximum distance between the actual data and the fitted distribution.....	129
Figure 2.30. Correlations between rock Uniaxial Compressive Strength (UCS) and a) average landslide size, b) power-law exponent, and c) power-law rollover value.	130
Figure 3.1. a) regional locations of Langtang Valley (red outline), the Arniko Highway (blue outline), Kathmandu, the Gorkha earthquake epicentre, the Main Central Thrust (MCT), Main Boundary Thrust (MBT), Main Frontal Thrust (MFT) and the South Tibetan Detachment (SDT). b) The known geology, main towns, and trekking routes within Langtang. c) The known geology, main towns, and main road	

within the Arniko region. All geology data are from maps provided by the Nepal Government Department of Mines and Geology.....	140
Figure 3.2. Photo panel depicting Langtang Unit 1. a) platy mineral texture and small garnet minerals. b) elongated plagioclase orientated parallel to foliation. c) mylonitic fabric. d) typical appearance of an outcrop.....	147
Figure 3.3. Photo panel depicting Langtang Unit 2. a) mineralogy dominated by muscovite, biotite, and quartz, with subordinate tourmaline. b) mylonitic fabric and leucogranite intrusions. c) high proportions of biotite and muscovite with occasional garnets within leucogranite intrusions. d) typical appearance of an outcrop / landslide scar.	148
Figure 3.4. Photo panel depicting Langtang Unit 3. Leucogranites dominated by a) muscovite, b) tourmaline, c) garnet and d) epidote, were common. This unit was often found intruded into unit 4 (e) and in bedrock across the eastern portions of the valley (f).	149
Figure 3.5. Photo panel depicting Langtang Unit 4. a – c) fine grained nature of this unit, b – c) leucogranite intrusions into this unit. d) typical appearance of an outcrop.	151
Figure 3.6. Photo panel depicting Arniko phyllite. a) muscovite-plagioclase rich mineralogy. b) typical outcrop. c) quartz vein intrusions. d) well foliated and fissile composition.	152
Figure 3.7. Photo panel depicting Arniko quartzite. a) crystalline, quartz rich composition. b) typical appearance of an outcrop.	152
Figure 3.8. Photo panel depicting Arniko schist. a – b) fine grained and well-banded biotite and muscovite rich mineralogy.	153
Figure 3.9. Photo panel depicting Arniko dolomite. a – c) fine grained calcareous mineralogy. c) biotite and muscovite veins. d) typical appearance of an outcrop.	153
Figure 3.10. a) Summary of landslide and lithology collected in the field across Langtang and subsequently defined geological unit boundaries. The location of the main trekking paths and positions of the Langtang Lirung west glacier and ablation	

zones are also shown. b) (next page) Summary of field landslide and lithology data collected across the Arniko region.....	155
Figure 3.11. Three-parameter inverse-gamma distributions fitted to the probability density functions of landslide area for landslides in, a) Langtang, and b) Arniko. Following the approach of Marc et al. (2019), the two largest events were removed from the Langtang case as they were > 2 times greater than the third largest event. Note that a p-value > 0.01 indicates that the three-parameter inverse-gamma distribution provide a good fit to the actual data, whilst the D-value gives the maximum distance between the actual data and the fitted distribution.....	156
Figure 3.12. Photo panel depicting typical rockfalls observed across both regions. a – b) larger-sale rockfalls. c – d) control of bedrock discontinuity geometry on block development and failure. e) monsoon triggered rockfall beneath a terrace deposit. f) leucogranite intrusions into the bedrock of a rockfall scar.	158
Figure 3.13. Photo panel depicting typical rotational slides and slumps in Langtang (a – b) and Arniko (c).....	160
Figure 3.14. a) Shallow translational slides observed in the upper reaches of Langtang Valley. B) small translational failure at the toe of a hillside in the Arniko region.	161
Figure 3.15. Photo panel depicting debris flows observed across both regions. a – c) large debris flows in Arniko with multiple source zones. d) debris flow levee channels observed in Langtang.....	162
Figure 3.16 . a) The bedrock scar and deposition zone of the Langtang avalanche. b – c) the intersection between trekking paths and the avalanche debris in October 2018. Trekking path highlighted with red-dashed line.	164
Figure 3.17. Relic alluvial fan incised by a more recent debris flow in Langtang Valley.	165
Figure 3.18 . a) All discontinuity data collected in the Arniko region. b) Set 1 data. c) Set 2 data. d) Set 3 data. e) fault data.	166
Figure 3.19. a) All discontinuity data collected in Langtang. b) Main set data. c) Sub-set data. d) fault data.	167

Figure 3.20. The mean conjugate planes and principal stress axes for a) Arniko and b) Langtang	168
Figure 3.21. a – p) BLR coefficients and LASSO selection percentages for all independent predisposing factor variables included within the BLR modelling...	170
Figure 3.22. Final susceptibility maps developed from the average regression coefficients from the 50 models developed for, a) Arniko, and b) Langtang.	173
Figure 3.23. ROCs and AUC values for a) the self-validated (success rate) of the Arniko models. b) the self-validated (success rate) of the Langtang models. c) independent 10-fold validated success of the Arniko models. d) independent 10-fold validated success of the Langtang models. e) 10-fold validated success of using the Arniko models to hindcast the Langtang landslides. f) 10-fold validated success of using the Langtang models to hindcast the Arniko landslides.	174
Figure 3.24. Photo panel depicting the extensive leucogranite intrusions observed within Langtang Valley. Photos taken during October 2018.	176
Figure 3.25. The proportion of landslides and the study regions within aspect bins for a) Arniko and b) Langtang. Rose diagrams of landslide aspect data for c) Arniko and d) Langtang.	178
Figure 3.26. a) The percentage of landslides across each 200 m elevation bin across Langtang as well as the percentage of each elevation bin that is covered by different degrees of permanent snow/ice and permafrost, with permafrost defined by the Permafrost Index (PFI) of Gruber, (2012). PERMA100 = PFI of 1 – 0.75, PERMA75 = PFI of 0.5 – 0.75, PERMA25 = PFI of 0 – 0.25, and PERMA0 = no permafrost. This also shows the estimated lower limits of glaciation during the LGM and 1970s, as well as elevation ranges characterised by anomalous increases and decreases in landslide occurrence. b) the same permafrost, permanent snow/ice, and glacial extent data as in a), but with mean excess topography per elevation bin.....	182
Figure 3.27. ROCs and AUC values for a) the self-validated (success rate) of the coseismic model. b) independent 10-fold validated success of the coseismic model. c	

– d) 10-fold validated success of using the coseismic model to hindcast the Langtang and Arniko data only	187
Figure 4.1. Workflow methodology for, a) comparing landslide distributions in different time slices using K-S and Chi-2 statistics. b) developing and validating landslide susceptibility models using the BLR-LASSO approach. c) developing and validating landslide susceptibility models using the BLR-LASSO approach for increasingly long pseudohistorical (multi-seasonal) landslide inventories.	196
Figure 4.2. a) Raw overlap Index vs time between time slices for the ASM-inventory. b) The same data as in a) but displayed as boxplots binned every three years.....	202
Figure 4.3. The Theoretically Unaffected Area (TUA) and Actually Unaffected Area (AUA) through time for the ASM-inventory and Roback et al. (2018) coseismic inventory.	202
Figure 4.4. The area of landslides at different degrees of overlap for the ASM-inventory.	203
Figure 4.5. For each predisposing factor of interest, the percentage of the 435 K-S or Chi-2 tests that showed similarity between two years and different alpha significance values.....	204
Figure 4.6. a – m) For each predisposing factor from Fig. 4.5 with > 20% overall similarity, the percentage of the 29 tests per year that showed similarity to at least one other year at different alpha significant values.....	205
Figure 4.7. a – n) Results of Binary Logistic Regression (BLR) modelling for each predisposing factor. Blue circles show the average regression coefficient calculated from the 50-models run per year. Error bars show +/- 1 SD. Bars show the percentage of the 50 models run for each year in which that control factor was selected by the LASSO (Least Absolute Shrinkage and Selection Operator). Red line shows the 0-line of the regression coefficient axis. Positive coefficients indicate that a factor is making landslides more likely, whilst a negative coefficient indicates that a factor is making landslides less likely.....	207

Figure 4.8. AUROC validation results quantifying how accurately the BLR susceptibility models trained on one year’s landslide and control factor data could forecast/hindcast the landslide occurrences from another year. All results were obtained via 10-fold cross validation, whereby 10-models trained on one year were used to forecast/hindcast 10 random subsets of data from another year, thus giving 100 results per validation from which the averages and standard deviations on this plot were calculated..... 211

Figure 4.9. AUROC values obtained from predicting (or hindcasting) the landslide occurrence in the years 2014 – 2018 using models developed using 1993 and 2002 plus increasingly more seasons of landslide data (i.e. increasingly long pseudo-historical landslide inventories. Grey-dashed lines show +/- 1 standard error. 212

Figure 4.10. The percentage of the Chi-2 tests per year that showed similarity to at least one other year at different alpha values for the MODIS land use data..... 217

Figure 4.11. Proportion of the study region, all landslide data and landslide data per time slice that fall within given bins of a) slope, b) local relief and c) excess topography..... 221

Figure 5.1. Correlation between time slice length (where variation is due to varying number of non-monsoon days between October and April) and number of mapped features..... 241

Figure 5.2. Relationship between total rainfall in the non-monsoon months included in each mapping interval and the deviations from the normal in the normalised rate (Figure 5.4b). 241

Figure 5.3. a – d) Empirical relationships between measures of landslide volume (m^3/km^2) and PERSIANN-CDR total MJJAS precipitation for a) total “New + RR” volume, b) total “New Only” volume, c) scar “New + RR” volume and d) scar “New Only” volume. e – h) Empirical relationships between measures of landslide volume (m^3/km^2) and APHRODITE total MJJAS precipitation > 25 mm for e) total “New + RR” volume, f) total “New Only” volume, g) scar “New + RR” volume and h) scar “New Only” volume. 246

Figure 5.4. ASM strength-normalised rate of landsliding from 1988 - 2018 for a) the normalisation using PERSIANN-CDR data and total MJJAS precipitation, and b) the normalisation using APHRODITE data and total MJJAS precipitation > 25 mm. The occurrences of historical $M_w > 6.0$ earthquakes are shown, as are monthly grid-averaged PERSIANN-CDR (a) and APHRODITE (b) precipitation totals 248

Figure 5.5. Three-parameter inverse-gamma distributions fitted to the probability density functions of landslide area for landslides that occurred in a) all years, b) the pre-2015 non-perturbed years, c) 1989, d) 1993, e) 1995, f) 2002, g) 2015, and h) post-2015). 249

Figure 5.6. Number of daily cells per monsoon season that observed Z-score anomalies greater than 12, 14 and 16. For reference, the normalised rates and associated +/-1 SD (red lines) from Fig. 5.4b are also shown. 251

Figure 5.7. The locations and IDs of the 84 APHRODITE rainfall grid cells across the study region. Maximum Z-scores from the 2004 monsoon seasons are shown alongside the 2004 landsliding. Also shown is the extent of the 2002 extreme rainfall, the landsliding from 2002 and the extent of permafrost across the study region.. 252

Figure 5.8. Correlations between maximum summed PGA and excess monsoon-triggered 2015 landsliding for a) PGA in the 2015 main shock and largest aftershock. b) the summed PGA from a) plus the PGA from 2011. c) the summed PGA from b) plus the PGA from 1988. d) the summed PGA from c) plus the PGA from 1934. e – f) show the same correlations as a – d) but this time with summed PGAs multiplied by excess topography above a threshold angle of 45°. The linear best-fits are shown with +/- 1 standard error in each case..... 259

Figure 5.9. Map showing the 2015 ASM-landsliding and the epicentres of the 2015 Gorkha earthquake main shock, Gorkha earthquake largest aftershock, 2011 Sikkim earthquake, 1988 Bihar earthquake, and 1934 Bihar earthquake. The PGA distributions of the 2015 Gorkha earthquake main shock, the 2011 Sikkim earthquake, and the 1988 Bihar earthquake are also shown. 260

Figure 6.1. Proposed decision-making framework for selecting the optimum susceptibility modelling method given your landslide data availability and resource capabilities..... 280

List of tables

Table 2.1. Typical landslide inventory scales, and their appropriate applications and study region sizes, as defined by Fell et al. (2008).54

Table 2.2. Summary of total number and number of reactivated/remobilised landslides mapped in each inventory time slices, and the satellite products used to map each time slice.58

Table 2.3. Summary of global gauge-based precipitation products, from Sun et al. (2018), see Sun et al. (2018) for references.....67

Table 2.4. Summary of global satellite-derived precipitation products, from Sun et al. (2018), see Sun et al. (2018) for references.....67

Table 2.5. Summary of bin classifications for all predisposing factors of interest....84

Table 2.6. Summary size statistics and power-law parameters for the entire ASM-inventory and various inventory subsets.....98

Table 2.7. Summary of LASSO selection percentages, mean regression coefficients and coefficient standard deviations (SD) for the 50 trained models developed using the entire ASM-inventory..... 112

Table 2.8. Summary of rock type UCS and associated landslide size statistics. 128

Table 2.9. Summary of published susceptibility models developed within the study region used for this thesis. 133

Table 3.1. Rock-strength estimate descriptions of Hack and Huisman (2002)..... 144

Table 3.2. Summary size statistics for the Langtang and Arniko field-remote sensing landslide inventories. *Note, in the Langtang case, the two largest events, both of which were >2* the size of the third largest, were removed from the analysis following the method of Marc et al. (2019), see Chapter 5 (section 5.2.2.1)..... 157

Table 5.1. Summary volume statistics and satellite information for all mapped monsoon seasons within the ASM-inventory.	234
------------------------------------------------------------------------------------------------------------------------------	-----

List of equations

Equation 2.1. Specific Steam Power.....	71
Equation 2.2. Roundness.....	81
Equation 2.3. Theoretical Circular Perimeter.	81
Equation 2.4. Probability density function of landslide area.	81
Equation 2.5. Three-parameter inverse-gamma distribution.	81
Equation 2.6. Binary regression equation.	88
Equation 2.7. Log-odds function.....	88
Equation 2.8. Rearranged binary logistic regression equation.	88
Equation 4.1. The overlap index.....	192
Equation 4.2. Actually unaffected area (AUA).....	193
Equation 4.3. Theoretically unaffected area (TUA).....	193
Equation 5.1. Derivation of ‘K’ constant required for estimating landslide widths.	233
Equation 5.2. Estimation of landslide width using the ‘K’ constant.....	233
Equation 5.3. Estimation of landslide scar areas.....	233
Equation 5.4. Landslide area-volume relationship.....	233

Acknowledgements

This thesis is the product of almost four years of research and would not have been possible without a number of institutions and individuals. Firstly, it is imperative to note that this work was supported by the Natural Environment Research Council and EnvEast DTP [grant number NE/L002582/1], the University of Plymouth, and AECOM.

Secondly, I would like to extend a massive thanks to my supervisory team: Dr Sarah Boulton, Dr Georgina Bennet, Dr Martin Stokes, Dr Michael Whitworth, and Dr Mark Cooker. To Mark, who though joined the team late, provided indispensable advice regarding the thesis-writing and submission process. To Mike, whose expertise in the field and geomorphological mapping training was key to the successful fieldtrips, and who went out of his way to ensure I had a good experience on my AECOM engineering geology placement. To Martin, whose “out-of-the-box” thinking led to a number of interesting and unexpected results / outputs, and whose diligent and in-depth commenting on my work massively helped me improve my narrative construction and writing style (one day I’ll stop writing ridiculously long sentences!). To Georgie, whose landslide and geohazard expertise, encouragement, and support was invaluable throughout. And finally, to Sarah, who as well as doing all of the above, provided unparalleled guidance, help and assistance throughout all aspects of the project. It is no understatement to say that this thesis would not have been possible without your input and insight, so again, I would like to extend my deepest thanks.

I would also like to express my gratitude to my wider ‘academic support network’ of fellow PhD students from Plymouth, UEA and beyond, including but certainly not limited to: Jesse Zondervan, Kilan Eichenseer, Wycliff Tupiti, Symeon Makris, Ben Clarke, James Fulton, and James Christie. Being able to “talk-science”, vent-frustrations, and socialise with you all was a great highlight of my PhD experience. I am also incredible grateful to the various people who have provided me with technical support and in-field assistant throughout this project. To Shaun Lewin, whose GIS-wizardry and problem solving was unparalleled. And to Tim Webster, Benedetta Dini, and Crpa Ngmia, whose knowledge, support, and assistance in collecting field-data and navigating the Nepal Himalaya was invaluable. I would also like to acknowledge the work and effort of Storm Roberts, the first student I have had the privilege to help supervise, and whose MGeol thesis paved the way for some of the analysis in Chapter 4. And last, but certainly not least, I would like to say a sincere thanks to my parents, sisters, and wider family, whose unwavering support has been unmatched.

Chapter 1 Introduction, aims and study region

1.1 Motivation

A landslide can be defined as any downslope movement of earth material (Varnes 1958). Landslides are a globally occurring natural hazard that pose significant threats to life and sustainable development (Petley 2012). According to the Centre for Research on the Epidemiology of Disasters (CRED), landslides account for 17% of all fatalities due to natural hazards (Sassa & Canuti 2009), with an estimated 56,000 landslide fatalities between 2004 and 2016 (Froude & Petley 2018). These human losses are concentrated in Asia, particularly in countries along the Himalaya Arc (Petley 2012), with India, Nepal and China experiencing the highest proportions of reported landslide fatalities (Kirschbaum *et al.* 2010). The economic impact of landslides is also severe, with global losses due to landslides of ~\$20 billion per year (Klose *et al.* 2016). This cost accounts for ~10% of the 2020 total global losses due to natural hazards (Munich RE 2021), with the highest losses focused in developed countries such as Japan, Italy and Canada (Sidle & Ochiai 2006). Furthermore, there is growing evidence to show that landslide occurrences and impacts are increasing owing to rapid global development and climate change (Crozier 2010; Huggel *et al.* 2012; Gariano & Guzzetti 2016; McAdoo *et al.* 2018), highlighting the current and future need to manage and mitigate landslide impacts.

1.2 Research problems

Effective landslide management and mitigation requires the zonation of landslide hazard, vulnerability, and risk. Such zonation typically involves the development of landslide susceptibility models, which forecast the likely geographic locations of future landslides (Guzzetti *et al.* 2006). Landslide susceptibility models can be developed using two main approaches: 1. physically based techniques (e.g. Goetz *et*

al. 2011; Park *et al.* 2019; Wang *et al.* 2019), which quantify landslide susceptibility using empirical equations, or 2. statistical approaches (e.g. Baeza & Corominas 2001; Lee *et al.* 2008; Aditian *et al.* 2018; Reichenbach *et al.* 2018), which quantify landslide susceptibility based on the locations of previous landslides. However, as physically based techniques typically require vast quantities of empirical data, statistical approaches are often the only viable method to assess landslide susceptibility across regional to global scales, or in data-scarce locations. Statistical landslide susceptibility modelling is thus very common (Reichenbach *et al.* 2018), and a fundamental component of many forms of landslide hazard analysis, risk assessment, land use planning and early warning systems (e.g. Fell *et al.* 2008; van Westen *et al.* 2008; Palau *et al.* 2020).

As outlined by Pourghasemi *et al.* (2018) and Reichenbach *et al.* (2018), the most commonly used statistical approach is logistic regression, which is a classification algorithm used to predict binary outcomes (e.g. landslide presence and absence) based on a given set of independent covariates (e.g. landslide predisposing factors such as elevation, slope angle, geology etc., see section 1.4.3) (Lombardo *et al.* 2020). As such, there is a clear need to ensure that regression-based modelling is conducted as accurately and reliably as possible, and to challenge any methodological assumptions or limitations that this approach uses. Indeed, despite the pervasiveness and importance of regression-type modelling, as outlined in the following sections, there are several fundamental limitations and areas of uncertainty surrounding their use.

1.2.1 Spatial applicability

Regression-based landslide susceptibility models are commonly applied across a range of spatial scales (Cascini 2008), from individual slope units (e.g. Alvioli *et al.* 2016; Amato *et al.* 2019) to catchments (e.g. Romer & Ferentinou 2016) to nations (e.g. Trigila *et al.* 2013) and even globally (e.g. Lin *et al.* 2017). When conducting regression-based susceptibility modelling, regardless of the scale, the method requires that each independent covariate (landslide predisposing factor) is assigned a single coefficient. This implicitly assumes that the influences of landslide

predisposing factors are spatially homogenous, with coefficient values that reflect the average predisposing factor influence across the entire study region, despite the fact that landslide occurrence is often heterogeneous (e.g. Van Westen *et al.* 1999; Chalkias *et al.* 2014, 2020). In the case of slope units, catchments and other local scale study region sizes, the assumption of spatial homogeneity in landslide predisposing factor weightings is likely valid, as landslide-landscape interactions would not be expected to change significantly through space. As such, regression-based models developed at these scales should be localised enough to provide accurate results (e.g. Pradhan 2010; Romer & Ferentinou 2016). However, when study regions are large (e.g., > 100 – 1000 km²), this is almost certainly not the case, with significant expected heterogeneity in landscape-landslide processes (Yang *et al.* 2019a, b). As such, typical regression-based susceptibility methods applied at regional scales may be unreliable and inaccurate at the local scale (e.g. Bueechi *et al.* 2019), where the variability between landslide occurrence and landslide predisposing factors differs from the regional average (Yang *et al.* 2019b). Dealing with this problem is challenging (see Chapter 6), but one solution could be to use geographically weighted (i.e. more spatially dependent) regression (Wheeler & Páez 2010), whereby predisposing factor coefficients are taken as variables related to spatial location (e.g. Erener & Düzgün 2010, 2012; Chalkias *et al.* 2014, 2020; Feuillet *et al.* 2014). However, these approaches require significant landslide data at all locations, and as this data condition is rarely met, studies are often forced to rely on regional scale models that cannot necessarily reflect local scale spatial variability (Yang *et al.* 2019b). This raises the question of how accurately such regional scale susceptibility models can be used as prediction tools for local scale regions and for other geographic regions, and thus how appropriate it is to undertake regional scale susceptibility modelling without considering spatial heterogeneity.

1.2.2 Temporal applicability

Most regression-based statistical landslide susceptibility approaches utilize the principals of uniformitarianism, with an assumption that, for a given region and trigger type, the spatial distributions of past landslides will be sufficiently similar to those of future landslides so as to facilitate basic prediction (Aleotti & Chowdhury,

1999). However, it is well described that climatic, tectonic and anthropogenic drivers, all of which can influence landslide susceptibility, can vary significantly over long (> 1000 year) timescales (e.g. Molnar & England 1990; Kirchner *et al.* 2001; Rahaman *et al.* 2009; Syvitski & Kettner 2011; Larsen & Montgomery 2012; Bennett *et al.* 2016), thus invalidating the assumption of long-term landslide time independency (Lombardo *et al.* 2020). Furthermore, there is now growing evidence to suggest that landslide occurrence cannot be assumed to be stationary over short (e.g. annual to decadal) time periods. The following sections describe two processes that potentially challenge short-term time-independent regression-based landslide susceptibility modelling: path dependency and earthquake preconditioning.

1.2.2.1 Path dependency

Path dependency describes how pre-existing landslides can impart a time-dependent legacy effect that controls the occurrence and size of new landslides (Samia *et al.* 2017b; Temme *et al.* 2020). Specifically, this legacy effect causes new landslides to have an increased likelihood of occurring within or overlapping the boundary of a pre-existing landslide, with overlapping landslides having larger average areas and roundness than landslides that do not occur across pre-existing landslides (Samia *et al.* 2017b). Furthermore, it has now been shown that the inclusion of time-dependent path dependency in landslide susceptibility models can significantly improve model performance (Samia *et al.* 2018; 2020). However, the wider applicability of using path dependency in landslide susceptibility modelling remains uncertain, as path dependency is yet to be rigorously tested in regions outside of Italy. As such, quantifying whether landslides exhibit path dependent behaviour in other geomorphic regions should be considered a vital area of future research with important implications for landslide susceptibility modelling (Samia *et al.* 2017b).

1.2.2.2 Earthquake preconditioning

Earthquake preconditioning describes how landscape damage induced by large magnitude ($\sim M_w$ 6.0) earthquakes can transiently increase rates of subsequent landslide occurrence. This concept was first introduced by Parker *et al.* (2015), who observed that landslide rates in New Zealand were elevated in regions affected by

earlier earthquakes. Specifically, they found that the probability of 1968 M_w 7.1 Inangahua earthquake coseismic landslides was highest in the regions that were coincident with areas of high shaking during the 1929 M_w 7.7 Buller earthquake. Parker *et al.*, (2015) suggest that this decadal scale increase in landside occurrence was caused by the non-linear accumulation of brittle hillslope damage over multiple episodes of seismicity. Such brittle damage can accumulate at the near-surface via the cracking and dilation of hillslope mass, as well as through seismically induced cyclical changes in hillslope stress distributions (Petley *et al.* 2005; Bagde & Petroš 2009; Clarke & Burbank 2011; Nara *et al.* 2011).

Furthermore, earthquake preconditioning has also been observed over annual timescales. For example, the 1999 M_w 7.6 ChiChi earthquake caused a 60% decrease in the rainfall intensity required to trigger landslides in the subsequent 1 – 7 years (Lin *et al.* 2008; Chen & Hawkins 2009). This transient change caused a factor of ten increase in rainfall-triggered landslide occurrence immediately after the earthquake, under otherwise uniform conditions, that decreased to pre-earthquake levels over the following 5 – 7 years (Hovius *et al.* 2011; Marc *et al.* 2015). Similarly, the 2008 M_w 7.9 Wenchuan earthquake temporarily caused the antecedent rainfall thresholds for landslide initiation to fall from 300 mm to 100 mm (Tan 1996; Tang *et al.* 2015; Zhang & Zhang 2017). Earthquake preconditioning has also been tentatively observed following the 2005 M_w 7.6 Kashmir (Pakistan) earthquake (Zhang & Zhang 2017), the 2004 M_w 6.6 Niigata (Japan) earthquake, and the 2008 M_w 6.8 Iwate (Japan) earthquake (Marc *et al.* 2015). Most recently, a study by Marc *et al.* (2019) attempted to quantify earthquake preconditioning in the Nepal Himalaya following the 2015 M_w 7.8 Gorkha earthquake. They found that post-earthquake rates of monsoon-triggered landslides during the 2015 monsoon season were increased by a factor of 4 – 8. However, in the absence of a longer-term empirical relationship between monsoonal strength and landsliding, they were unable to fully quantify the timescale of this preconditioning, as it was unclear whether the landside rates in 2016 – 2018 were elevated beyond that expected from the monsoon strength (Marc *et al.* 2019). Furthermore, Nepal is known to have been impacted by several other large magnitude earthquakes in the past century, with notable $> M_w$ 6.0 events in 1934,

1988 and 2011, and it remains unclear whether these events induced any long-term damage similar to that observed in New Zealand.

Overall, the earthquake preconditioning concept suggests that landslide occurrence is a product of time-dependent factors relating to historic damage accumulation, as well as time-independent predisposing factors relating to geomorphology, climate and human activity (Parker *et al.* 2015). However, a detailed understanding of the magnitudes and timescales of this process remain uncertain and poorly quantified outside of New Zealand, Taiwan and China, thus representing a clear knowledge gap with potentially important implications for the time-independent assumptions of landslide susceptibility in other seismogenic regions.

1.2.3 Lack of long-term landslide data

A common problem when investigating both path dependency and earthquake preconditioning is that large-scale, long-term landslide datasets are required to fully quantify these processes. For example, the path dependency characteristics quantified by Samia *et al.* (2017) in Italy were derived from a 60-year multi-seasonal inventory across a 78.9 km² region. Similarly, the earthquake preconditioning results for Taiwan involved a landslide dataset spanning several decades, with the shorter (sub-decadal) landslide inventory used by Marc *et al.* (2019) for Nepal not sufficiently long to fully isolate earthquake landslide impacts from monsoonal impacts. Furthermore, few, if any, studies have systematically quantified how landslide spatial distributions vary through time. As highlighted by Samia *et al.* (2017), this is likely because long-term landslide data are uncommon and time-consuming to develop (Brenning 2005; Reichenbach *et al.* 2018). This lack of long-term landslide datasets highlights that there is a clear and pressing need for more long-term, multi-temporal landslide inventories to be published to facilitate new research into the temporal nature of landslide characteristics, distributions, and processes.

1.3 Aims and objectives

The aim of this thesis is to quantify the spatiotemporal characteristics, preconditioning and susceptibility of monsoon-triggered landslides in Nepal.

Specifically, this thesis will investigate how spatial and temporal changes in landslide characteristics, distributions, and preconditioning impacts logistic regression-type susceptibility approaches. The reason for using the logistic regression approach is that as this method is the most commonly used in the landslide susceptibility literature, it is particularly vital to assess and understand the limitations of this approach, and challenge the spatial and temporal assumptions that this methodology employs. Indeed, throughout this thesis, a variety of commonly used methods in the landslide literature are applied in order to assess their appropriateness and to allow for robust and unbiased comparison between this work and other studies. This aim will largely be achieved via the development and analysis of a new long-term, multi-temporal landslide inventory of Asia Summer Monsoon (ASM)-triggered landslides in central-eastern Nepal. This will involve consideration of the following objectives:

1) To develop a 30-year inventory of monsoon-triggered landslides across central-eastern Nepal. (Chapter 2). As well as being used throughout the thesis, this inventory will be made public to provide an important resource for local hazard managers and the wider geohazards/geoscience community.

2) To assess the overall (space and time independent) geometries, spatial associations, sizes, spatial distributions, and susceptibility of ASM-triggered landslides in Nepal (Chapter 2). This will be achieved using spatial statistics and Binary Logistic Regression (BLR)-based susceptibility modelling. Specific questions to be answered here include: what are the geometries, sizes, and overall spatial distributions of these landslides? How do these events compare to other rainfall-triggered and coseismic inventories for Nepal? What insights do these analyses provide into landslide processes in the Himalaya and other similar geomorphic regions?

The results from 1) and 2) are based solely on remotely sensed data with limited consideration of potential heterogeneity across space and time. As such, objectives 3) – 5) expand upon the results of 2) using additional field data and further analysis to investigate whether the characteristics and susceptibility of ASM-triggered

landslides in Nepal are influenced by any spatially and/or temporally dependent processes.

3) To use additional field data from two sub-regions with distinctly different landscapes (Langtang Valley and the Arniko Highway) to provide further insight into how landslide characteristics, processes and distributions vary through space (Chapter 3). These field data will be used alongside a previously published regional inventory of coseismic landslides (Roback *et al.* 2018) to assess how spatial heterogeneity impacts BLR-type landslide susceptibility modelling. This will answer questions such as: how well can susceptibility models developed from one region be used to forecast or hindcast the other; how well do regional models forecast or hindcast local regions; and thus, is it appropriate to undertake regional scale susceptibility modelling without considering spatial heterogeneity?

Furthermore, as outlined in section 1.4.3, knowing what types of landslide have been used to train a susceptibility model is vital for ensuring that any model outputs are used appropriately and effectively for hazard management. As such, Chapter 3 also provides detailed field-based qualitative descriptions of the types of landslide included in both the remotely sensed and field derived landslide inventories used throughout this thesis before discussing the implications of this for the use and interpretation of the developed landslide susceptibility maps.

4) To quantify how ASM-triggered landslide processes and occurrence varies through time (Chapter 4). Specific questions to answer here include: is landslide path dependency occurring in Nepal and, if so, what are the characteristics of this process? Do ASM-triggered landslide spatial distributions vary significantly through time, particularly in response to extreme events? What are the impacts of any observed temporal variation on the forecasting (or hindcasting) power of BLR susceptibility modelling? Finally, if BLR modelling is impacted by temporal heterogeneity, can the choice of landslide data used to train a model (i.e., event vs historical inventories) influence the accuracy and consistency of susceptibility modelling?

5) To investigate how the rates and drivers of landsliding in the Himalaya vary through time (Chapter 5). Specifically, by quantifying an empirical relationship

between ASM-strength and landsliding, the relative landslide impacts of the ASM, extreme rainfall, and earthquake preconditioning can be isolated and quantified. This should allow identification of whether earthquake preconditioning is occurring in the Himalaya and, if so, provide novel insight into its timescales, magnitudes, and causes.

6) To discuss the overall results and implications of 1) – 5), alongside further literature, in the context of the applicability of regression type landslide susceptibility models (Chapter 6). Specifically, this will consider how spatial and temporal heterogeneity impacts the use of logistic regression-type models, outline potential solutions to reducing these impacts, and provide a framework to aid practitioners in optimising their approach to landslide susceptibility in regions impacted by spatially and temporally heterogeneous processes.

Completion of these objectives will provide novel information on landslide processes in mountainous terrain and allow for a detailed evaluation of the major spatial and temporal limitations of regression-based susceptibility modelling approaches. As well as facilitating the improvement and advancement of landslide susceptibility modelling in a country that (as described in section 1.4) is severely impacted by landslides, this research will provide insight and practical suggestions to aid the wider application and development of landslide susceptibility models in dynamic mountainous regions.

1.4 Study region

The study region for this thesis is a ~45,000 km² portion of the central-eastern Nepal Himalaya (Fig. 1.1). The following sections outline why this region has been selected, followed by descriptions of its tectonic, geological, geomorphological and landslide setting.

1.4.1 Why Nepal?

There are a number of reasons for selecting Nepal as the study area. First, Nepal is severely impacted by landslides from a socio-economic perspective, with ~78 fatalities per year (Petley *et al.* 2007) and landslide induced economic losses of ~\$12

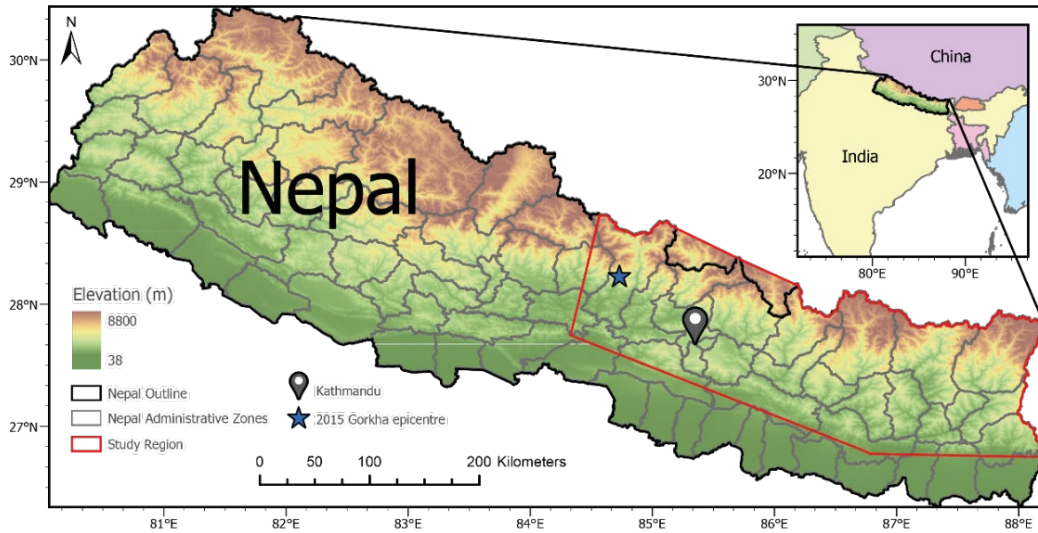


Figure 1.1. Location of the study region.

million between 1971 and 2017 (Adhikari & Adhikary 2019; Shrestha 2019). As such, an increased understanding of landslide processes and susceptibility in Nepal has the potential to translate into policy and management strategies with highly tangible benefits to local communities. Second, for the reasons outlined in section 1.4.3, landslides in Nepal are extremely pervasive, with multiple landslide trigger events occurring annually, including the Asia Summer Monsoon (ASM), storms, floods and earthquakes (e.g. Dhital 2003; Cook *et al.* 2018; Roback *et al.* 2018; Marc *et al.* 2019). It is thus an ideal location for a project with aims and objectives that relate to a number of different processes. Indeed, a major objective of this project is to develop a long-time series of multi-temporal landslide data. Nepal facilitates the development of such an inventory, as it is annually impacted by the ASM from May to September.

The specific region of central-eastern Nepal was selected for much of the same reasoning as for selecting Nepal as a country. This region encompassed areas known to have been impacted by specific events such as the Gorkha earthquake (Martha *et al.* 2017; Roback *et al.* 2018), earlier earthquakes in 1934, 1988 and 2011 (USGS 2018b, a, d), outburst storms in 1993 and 2002 (Dhital 2003; Petley *et al.* 2007), and is well documented to be significantly affected by the Asia Summer Monsoon (Marc *et al.* 2019). Indeed, specific catchments within this study region such as the Bhote

Kosi have widely reported landslide impacts and vulnerabilities (e.g. Regmi *et al.* 2017; Tanoli *et al.* 2017), making this a region that is particularly in need of an improved understanding of landslide hazard and process. Furthermore, central-eastern Nepal has a higher population and infrastructure density than western and far-western Nepal, so has a generally higher vulnerability to landsliding and a need for improved landslide hazard management and mitigation.

Finally, it should be noted that a small portion of China was initially included in the study region (Fig 1.1). This was included to obtain a greater coverage of the Greater and Tethyan Himalayas (see section 1.4.1), as most of Nepal occurs within the Lesser and Sub Himalayas. However, as discussed in Chapter 2, no landslides ended up being mapped in this region due to cloud and snow cover, so the Chinese portion of the study region is often not included in later figures and/or analysis.

Consequently, it is a good region for conducting analysis that requires long-term landslide data, such as characterising path dependency and quantifying temporal variations in landslide spatial distributions. Third, as described below, the selected study region is highly spatially heterogeneous in terms of its geology and geomorphology, making it ideal for investigating how landslide processes vary across diverse landscapes. Fourth, the seismogenic nature of Nepal make it well-placed to study earthquake preconditioning over multiple timescales, which is a key aspect of this project. Indeed, Nepal has been impacted by four large magnitude ($> M_w$ 6.0) earthquakes over the past century, with events in 1934, 1988, 2011 and 2015 (USGS 2018a, b, c, d) Finally, as described in section 1.2.2, the Himalaya is a region that remains understudied in relation to key processes such as path dependency and earthquake preconditioning, so quantifying the characteristics of these processes in this region will provide novel results that should further our understanding of how these processes vary in different geological settings.

1.4.2 Tectonic, geological, and geomorphological setting

The Nepal Himalaya can be subdivided into four main tectonic units: the Tethyan Himalaya; the Greater Himalaya; the Lesser Himalaya, and the Sub Himalaya (Fig 1.2). These units formed as a direct result of the Tibet-Himalaya orogeny that

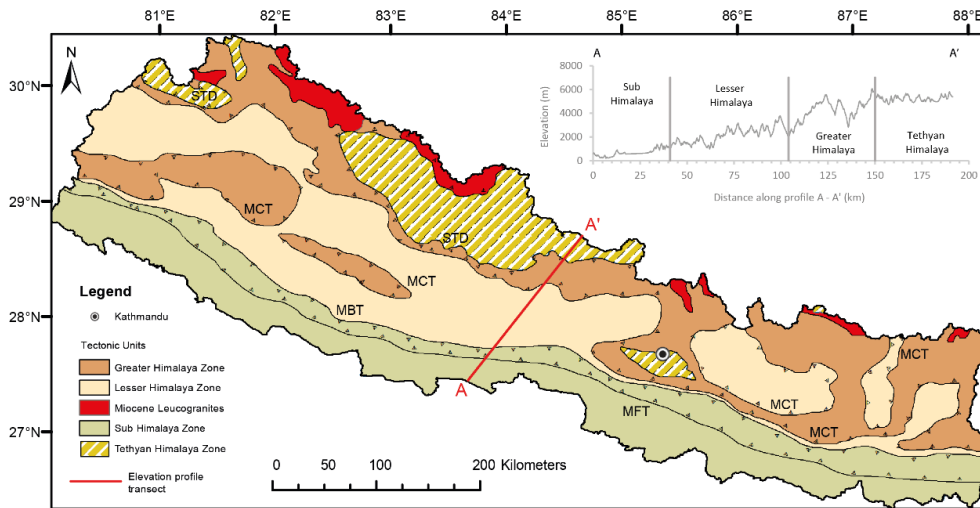


Figure 1.2. Nepal tectonic units and elevation profile, after DeCelles *et al.* (2004).

initiated at 40 – 65 Ma when the Indian plate began to collide with the Eurasian plate (Yin & Harrison 2000; Yin 2006; Najman *et al.* 2010; Leech *et al.* 2005). These units are lithologically and geomorphologically distinct, which as described in section 1.4.3, leads to the occurrence of a variety of landslide predisposing factors.

1.4.2.1 Tethyan Himalaya

The Tethyan Himalaya is a 50 – 25 Ma fold-thrust belt composed of Proterozoic (~1804 Ma) to late Eocene (~40 Ma) siliciclastic and carbonate rocks and widespread outcrops of Cambrian granitic core complexes (DeCelles *et al.* 1998; Liu & Einsele 1999). These rocks compose the main Tethyan Himalaya Sequence (THS) (DeCelles *et al.* 1998), which has a combined stratigraphic thickness of ~ 10 km and an along-Himalaya-strike width of ~ 200 km (Robinson *et al.* 2001). The Tethyan Himalaya is bound by the Indus-Yarlung suture zone to the north, which marks the initial collision of India and Tibet, and the South Tibetan Detachment system (STD) to the south. The STD is a system of low angle north-dipping normal faults that are thought to be associated with the northward gravitational collapse of the THS along a 15 - 30° dipping lithological interface (Burg & Chen 1984; DeCelles *et al.* 1998). The STD places the late Cambrian to Lower Ordovician high-grade rocks of the THS above the lower-grade rocks of the Greater Himalayan Complex (GHC) (Royden & Burchfiel 1987). The STD is thought to have been active between 23-18 Ma (Hodges

et al. 1996), although it may have been dynamic as early as 15-13 Ma (Godin *et al.* 2001), and is now a series of low-angle north-dipping faults.

Topographically, the Tethyan Himalaya extend northward from the high peaks of the Himalaya, with average elevations of 5000 m (Lavé & Avouac 2001) and average hillslope angles of 30 – 35°. Due to these high elevations, much of the Tethyan Himalaya are impacted by glacial and paraglacial processes, with diverse landforms such as active glaciers, moraines, alluvial fans, braided rivers, rock avalanches, debris-flows, and sediment-mantled slopes. The processes of glacial erosion and moraine / lake formation have largely obscured the geomorphic record of river incision, with the main rivers transecting the Tethyan Himalaya cutting narrow and steep N-S gorges (Lavé & Avouac 2001).

1.4.2.2 Greater Himalaya

The Greater Himalaya is composed of low to high-grade Neoproterozoic (~1800 Ma) to Ordovician (~480 Ma) rocks that form an almost continuous belt along the strike of the Himalaya (Parrish & Hodges 1996; DeCelles *et al.* 2000). These rocks include low-grade Precambrian to Palaeozoic paragneiss, orthogneiss, amphibolite, schist, marble and metavolcanic protoliths (DeCelles *et al.* 1998; Robinson *et al.* 2001). These rocks are often referred to as the Greater Himalayan Complex (GHC) and also include outcrops of Miocene leucogranites in the upper portion of the sequence (Searle *et al.* 1997). The Greater Himalaya is bound by the STD to the north and the Main Central Thrust (MCT) to the south. The MCT was the main accommodator of plate convergence from the early - middle Miocene (20 – 25 Ma) to the late Miocene (12-10 Ma) (LeFort 1975; Coleman 1998; Godin *et al.* 2001). However, it is widely accepted that the MCT briefly reactivated from 5 - 3 Ma, causing further folding (Schelling & Arita 1991; Catlos *et al.* 2001; Takagi *et al.* 2003; Vannay *et al.* 2004). The MCT currently exists as a 2 – 10 km deep shear zone (MacFarlane *et al.* 1992) with a flat – ramp – flat geometry dipping at 30 – 60° north (Decelles *et al.* 2001). The MCT has displaced the Greater Himalaya southward relative to India, juxtaposing the GHC against the sequences of the Lesser Himalaya.

Geomorphologically, the Greater Himalaya extend from the northern boundary of the Mahabharat Mountains to the southern boundary of the Tibetan plateau. The elevations south of the Mahabharat Mountains initially decrease to 2000 m, before increasing in a step-wise manner to peak elevations that exceed 7000 m (Lavé & Avouac 2001). This higher region is characterised by a dense network of steeply incised valleys and ridges, with average hillslope angles of $\sim 35^\circ$. There is a general absence of preserved terrace levels in the Greater Himalaya, and a lack of space for terraces to form, which is consistent with the expected high incision rates (Lavé & Avouac 2001). Furthermore, hillslopes in this region are considered to be near the critical slopes angles for mass movement, with a topography that largely evolves via bedrock landsliding driven by fluvial incision (Burbank *et al.* 2012).

1.4.2.3 Lesser Himalaya

The Lesser Himalayan Zone (LHZ) is composed of Proterozoic (~ 1870 Ma) to Palaeocene (~ 68 Ma) metasedimentary, metavolcanic and sedimentary rocks (Frank *et al.* 1995; Upreti 1999). The LHZ sequences can be subdivided into two main portions. The lower portion is composed of Proterozoic to Permian low-grade metasedimentary, metavolcanic and sedimentary rocks that form a large hinterland dipping duplex, and the upper portion is composed of Permian to Palaeocene metasedimentary and sedimentary rocks (DeCelles *et al.* 1998). This sequence has a total stratigraphic thickness of ~ 10 km, and is bounded by the MCT to the north and the Main Boundary Thrust (MBT) to the south (Robinson *et al.* 2001). The MCT places Precambrian – Cambrian medium-grade metasedimentary, metaplutonic, and metavolcanic rocks over the upper portion of the LHZ. The MBT began to accommodate convergence in 12 – 10 Ma, and juxtaposes the metasedimentary rocks of the Lesser Himalaya in the northern hanging wall against the unmetamorphosed Neogene foreland basin deposits of the Sub Himalaya in the footwall (Yin 2006).

Topographically, the Lesser Himalaya range from the northern boundary of the Siwalik Hills to the northern boundary of the Mahabharat Mountains. This encapsulates an elevation range of 1000 – 3500 m, with average elevations within the Mahabharat Mountains of 2500 – 3500 m (Lavé & Avouac 2001). The Lesser

Himalaya have prominent fill terraces that were deposited during the late Pleistocene and subsequently incised (Lavé & Avouac 2001).

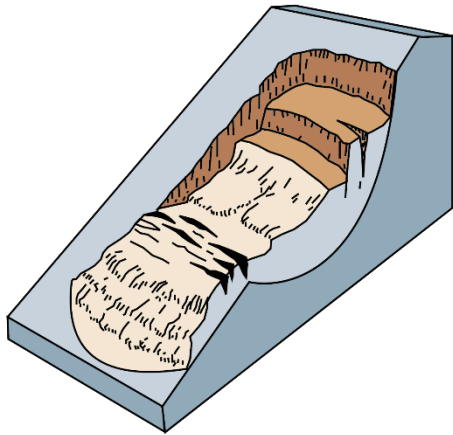
1.4.2.4 Sub Himalaya

The Sub Himalaya can be divided into the Siwalik Hills and the plains of the active Indo-Gangetic Himalayan foreland basin. The Sub Himalaya are bound by the MBT to the north and the Main Frontal Thrust to the south (MFT). The MFT began accommodating convergence in the Late Pliocene, with continued uplift throughout the Neogene and Quaternary resulting in significant erosion and deposition of Himalayan sediments onto the Himalayan foreland basin (Yin 2006). This formed the Siwalik Group, a geological unit composed of Neogene sediments that have a stratigraphic thickness of 3.5 – 5.5 km (Robinson *et al.* 2001) and are currently being uplifted by the active MFT at $\sim 6.9 \pm$ mm/yr (Wesnousky *et al.*, 1999; Avouac, 2003). This uplift is juxtaposing the Siwalik Group against the overlying Quaternary sediments of the active Himalayan foreland basin, which have been eroded from the Himalayan orogeny and Indian Peninsula highlands (DeCelles *et al.* 1998; Yin 2006).

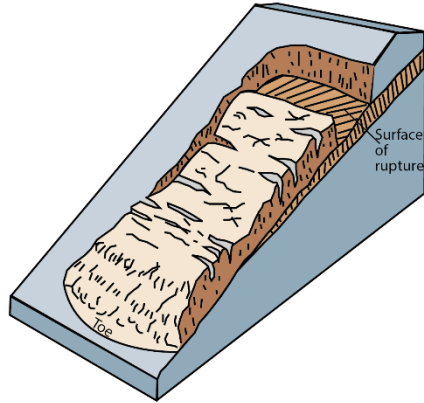
The geomorphology of the Sub Himalaya is highly dichotomous, with the lowlands of the Indo-Gangetic Plain having elevations of just 0 – 50 m, and the Siwalik Hills having elevations of 500 – 1000 m. The morphology of the Siwalik hills is dominated by rows of gentle hills separated by narrow elongated piggyback basins (Lavé & Avouac 2001). Fluvial terraces are pervasive across the Sub Himalaya. In the Indo-Gangetic plains, aggrading alluvial systems are generally not incising into the bedrock, however, along the MFT, incision is more intense as rivers compensate for active thrusting and faulting (Lavé & Avouac 2001).

1.4.3 Landslide setting

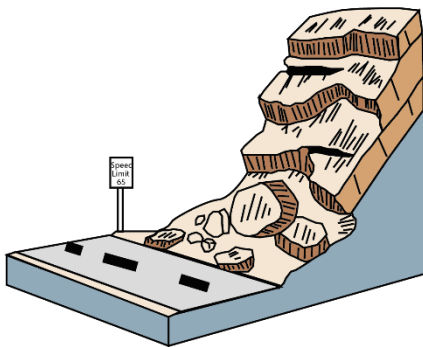
Landslides occur due to the interplay between predisposing (or controlling) factors that condition landscape susceptibility to failure, and the trigger events that actually initiate failure. Landslides in Nepal vary greatly in type and scale, from entire hillslope-scale failures, to minor rock falls and slumps, to debris flows and avalanches (Fig. 1.3) (Shroder & Bishop 1998; Jones *et al.* 2020). This heterogeneity in landslide type and characteristics is a direct result of the varying predisposing factors and



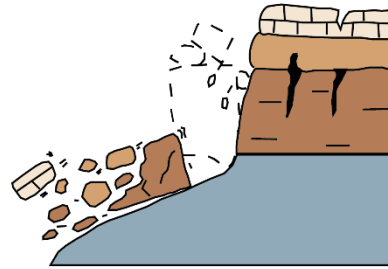
a) Rotational slide



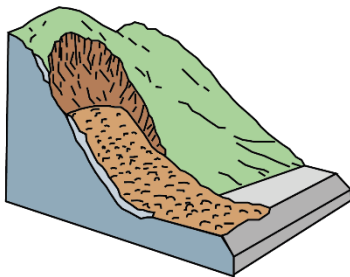
b) Translational slide



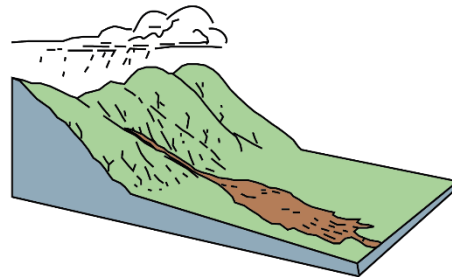
c) Rockfall



d) Topple



e) Debris avalanche



e) Debris flow

Figure 1.3. Schematic diagrams of the typical landslide types found in Nepal (USGS 2004a).

trigger events that occur across the region. In the context of landslide susceptibility modelling and associated hazard management, understanding landslide type is vital for a number of reasons. First, if the final purpose of a susceptibility model/map is to inform hazard management, then knowing what types of landslide were used to train a susceptibility model is a fundamental requirement. For example, if a given susceptibility model identifies a region of very high landslide susceptibility, then hazard managers may decide to install some form of mitigation strategy in that region. However, the appropriate mitigation strategy will depend strongly on the type of landslide that the region is susceptible too (i.e., what landslide types the model was trained on). For example, the hazard management response to a model trained on predominantly debris flow type landslides would likely be very different to the response to a model trained on predominantly rockfall type landslides, so it is vital that all susceptibility models have clear information on landslide type. Second, from a geomorphological-understanding perspective, to correctly interpret the physical meanings of susceptibility model outputs (e.g., regression coefficients) it is necessary to have the context of landslide type. For example, certain topographic, geological, or land use characteristics may be predisposed to rockfalls (e.g., steep cliffs, hard bedrock, no vegetation), whilst other landscape characteristics may favour the development of flows or slides. As such, subsequent chapters describe and discuss not just the characteristics and distributions of the various landslide inventories produced and used across this thesis, but also provide qualitative descriptions of the types of landslides observed across the study region (see Chapter 3). To provide appropriate context for these descriptions and results, the following section describes the main predisposing and triggering factors that are likely to be influencing landslide occurrence and type in Nepal.

1.4.3.1 Landslide predisposing factors

As outlined in section 1.4.2, the study region is heterogeneous in terms of its geology and geomorphology. Consequently, this section will outline some of the key predisposing factors that may be impacting landslides across the study region, and that are analysed in later chapters (e.g. Chapter 2, sections 2.3.2, 2.4.4, and 2.6.4).

Landscape topography can have major impacts on slope stability, with factors such as elevation, hillslope angle and local relief commonly found to influence landslide susceptibility (Reichenbach *et al.* 2018). Indeed, elevation is known to have a strong influence on orographic precipitation, with precipitation rates observed to increase with altitude, thus causing higher elevation hillslopes to become saturated more quickly relative to lower elevation hillslopes (Carrara *et al.* 1978; Gallart & Clotet 1988; Bai *et al.* 2014). Likewise, local relief, which is the variation in height over a local area (e.g. the difference in height between the highest and lowest points within a given locality), can control both orographic precipitation and set the limits on maximum potential landslide runout and size (Valagussa *et al.* 2019; Medwedeff *et al.* 2020). Hillslope angle can also affect slope stability by controlling the rates and directivity of overland flow, groundwater flow, percolation and saturation (Sidle & Bogaard 2016), whilst also influencing downslope material-transport processes (Roering *et al.* 1999). Furthermore, the distributions of hillslope angles in active mountain regions suggests that landscapes have a critical threshold gradient at which the likelihood of hillslope failure increases rapidly due to limitations in material strength (Korup *et al.* 2007). This defines the concept of excess topography, which is a measure of rock volume above a landscapes critical threshold angle (Blöthe *et al.* 2015), and thus a potential predisposing factor for describing portions of a landscape with enhanced slope instability. As described in section 1.4.2, the different tectonic units that comprise the study region vary significantly in terms of these topographic factors, so understanding how the influences of these factors vary across the study region will be a key focus of subsequent analysis (e.g. Chapter 2, section 2.7.2).

Other topographical controlling factors likely to be affecting landslides in the study region are hillslope curvature, which is the second derivative of hillslope surface, and hillslope aspect, which is the orientation of a hillslope surface. Hillslope curvature can be considered in both profile and planform, where profile classifies curvature parallel to the direction of steepest descent, and planform classifies curvature perpendicular to the direction of steepest descent. Curvatures can be defined as slope transitions that are concave, convex, or planar in form. Curvature influences hillslope stability through its control on flow velocities draining across a landscape

surface (Kayastha 2012). A concave hillslope in both directions causes the downslope focusing and convergence of surface and groundwater flows, resulting in an increase in pore water pressure that creates conditions sensitive to failure (Chang *et al.* 2007). Similarly, concave curvatures will focus the transport of material, potentially causing greater accumulations of loose unconsolidated material that is more readily induced to fail (Ohlmacher 2007).

The influence of hillslope aspect on slope stability is predominantly due to its control on the variable exposure of hillslopes to sunlight (and thus temperature), wind and precipitation (Rech *et al.* 2001). This variable exposure controls the relative intensity of rock breakdown via physical and chemical weathering, and thus the availability of loose unconsolidated material (McFadden *et al.* 2005; Meunier *et al.* 2008; Parker *et al.* 2017). This impact on material properties will also affect vegetation cover and land use, which as described later, will potentially affect soil strength and infiltration rates (Wieczorek 1996). Furthermore, due to the directivity of rainfall, hillslope aspect also controls which hillslopes get most rainfall during a given storm, thus affecting subsurface moisture content and retention rates (Baeza & Corominas 2001). Hillslope aspect also impacts the triggering of coseismic landslides, as seismic directivity causes wave amplification on hillslopes oriented perpendicularly to the fault plane (Tibaldi *et al.* 1995). Similarly, oblique seismic waves crossing hillslope ridges can be asymmetrically amplified, causing hillslopes oriented away from the direction of seismic wave propagation to be more greatly affected (Meunier *et al.* 2008).

Another major landslide controlling factor is bedrock geology, which controls fundamental hillslope strength. Generally, less indurated sedimentary rocks, such as those in the Sub-Himalaya, are more susceptible to failure relative to highly indurated igneous and metamorphic rocks such as those found in the Greater and Tethyan Himalaya (Keefer 2002). This is because less indurated rocks will be more fractured and porous, and thus allow greater rates of infiltration and permeation. Similarly, structural features such as active and dormant faults allow increased infiltration of groundwater, which can lead to weakening through geochemical alteration (Warr & Cox 2001). Active fault structures can also increase susceptibility

to landsliding through the reduction in rock-strength caused by past earthquakes (Brune 2001; Kellogg 2001).

Hydrological factors can also play an important role in predisposing hillslope stability. For example, stream networks with high Specific Stream Power (SSP) or normalised steepness index (see Chapter 2, section 2.3.2.2 for details on these factors), such as the channels in the Greater and Lesser Himalaya, will have higher rates of incision and erosions. As such, landslides will have a higher percentage likelihood of occurring in these locations due to fluvial undercutting of hillslopes that increases shear stresses and removes lateral support (Korup 2004).

Another key set of landslide controlling factors are anthropogenic factors such as land use change and road building, both of which can increase landscape susceptibility to landsliding by disturbing the fragile hillslope equilibrium often reached by long-term natural processes (Zhang & Liu 2010). For example, the steepening, heightening, loading or undercutting of hillslopes, all of which occur during road construction, can reduce the shear strength and increase the shear stresses acting on a hillslope (Alexander 1992). This is likely a major problem in Nepal, which has observed significant increases in road construction over the past few decades (McAdoo *et al.* 2018). Likewise, anthropogenic activities relating to land use, agriculture, and drainage can also influence landslide occurrence (Glade 2003). For example, poorly designed and managed drainage, irrigation and cultivation systems can increase infiltration rates and reduce soil cohesion, thus increasing pore water pressures whilst reducing regolith shear strength (Alexander 1992). Irrigation systems have also been observed to cause liquefaction-induced slope failure during earthquakes (e.g. Watkinson & Hall 2019). Another major land use related process that influences landsliding is deforestation. The roots of larger vegetation types can reinforce hillslopes, whilst deep-rooted transpiration can increase stability through the removal of water and subsequent reduction in pore water pressure (Sidle & Bogaard 2016). As with road construction, these issues relating to irrigation and cultivation are likely to be an issue across Nepal, with the country experiencing a widespread and continued rise in the area of land dedicated to cropland (Paudel *et al.* 2016).

Finally, as the study region includes hillslopes at high elevations, the presence of permanent, transient, or degrading permafrost could also predispose landscapes to failure. For example, the presence of permafrost can increase hillslope shear strength via ice-bonding between fractures (Mccoll 2012). Conversely, degrading permafrost can reduce shear strength through the removal of ice-bonding and frost-cracking processes (Matsuoka & Murton 2008), and has been linked to several landslide events in other regions (e.g. Fischer *et al.* 2012; Hilger *et al.* 2018).

1.4.3.2 Precipitation-triggered landslides

Precipitation is the most common trigger of landslides in Nepal (Upreti & Dhital 1996). The main precipitation event to impact the study region is the Asia Summer Monsoon (ASM), though less frequent, but higher magnitude, cloud outburst storms have also been recorded (Dhital 2003; Petley *et al.* 2007). Indeed, annual rainfall in Nepal ranges from 1500 – 2500 mm/yr (Chalise & Khanal 2001), of which over 80% falls during the monsoonal months of May/June – September (Dahal & Hasegawa 2008). However, the monsoonal precipitation is spatially heterogeneous, with average precipitation rates of up to 160 mm in northwest Nepal compared with up to 5500 mm in parts of central Nepal (Dahal & Hasegawa 2008). The Nepal monsoon season is particularly prone to causing landslides, as much of the total rainfall is deposited during short, intense periods. For example, up to 10% of the total yearly monsoonal rainfall has been observed to fall in a single day, whilst 50% has been observed to fall within periods as short as 10 days (Alford 1992). Furthermore, rainfall in the Himalaya is strongly controlled by orographic effects. Consequently, northern central Nepal, where the topography is extreme and elevations rise rapidly, has the highest mean values of annual and 24-hour rainfall (Dahal & Hasegawa 2008).

Despite the pervasiveness of precipitation-triggered landslides, there has been relatively little research into rainfall thresholds for Nepal. One of the earliest studies was by Caine & Mool (1982) in the Kolpu Khola catchment of central Nepal. They found that the daily rainfall threshold required for failure was 100 mm and that landslide frequencies at this threshold increased into the monsoon season,

presumably due to higher groundwater levels and saturation. Further research was completed by Dahal *et al.* (2006) who found that debris flows and slides were triggered when the 24 hr cumulative rainfall exceeded 260 mm, but that shallower flows could be triggered by cumulative rainfall as low as 230 mm over the same time period. Similarly, Khanal & Watanabe (2005) found that landslides in the Syangja district of western Nepal occurred when daily rainfall exceeded 230 mm. Gabet *et al.* (2004) found that, for the Khudi catchment of central Nepal (Annapurna Range), cumulative rainfall must exceed 528 mm, plus a minimum daily rainfall of at least 9 mm. More recently, Dahal & Hasegawa (2008) attempted to calculate the empirical relationships between rainfall intensity, duration and landsliding using 193 landslide events that occurred between 1951 and 2006. They found that for durations < 10 hours, rainfall intensity of 12 mm/hr is necessary to trigger landslides, whilst an average of < 2 mm/hr is sufficient if durations exceed 100 hours. Furthermore, they found that intensities of < 1 mm/hr can trigger landslides if maintained for over a month, which is common during the monsoon season.

Precipitation-triggered landslides in the study region tend to be small (< 1000 m²), shallow (0.5 – 2 m thick) rock falls and slides (e.g. Fig. 1.3 a – c; USGS 2004) (Thapa & Dhital 2000; Khanal & Watanabe 2005). These smaller failures are typically caused by abrupt increases in pore water pressure along the soil-bedrock contact due to short duration, high intensity rainfall. However, larger landslides can also be triggered by rainfall. For example, multiple debris flows (e.g. Fig. 1.3f) were reported following a severe outburst storm in 1993 (Thapa & Dhital 2000; Dhital 2003). Likewise, larger landslides caused by progressive failure across multiple rainfall cycles are also observed. An example of such a large-scale progressive failure is the 2014 Jure landslide that occurred along the Arniko Highway, ~80 km east of Kathmandu (Fig. 1.4). This was one of the single most deadly landslides in Nepal's history, causing 156 fatalities and destroying dozens of buildings (Van Der Geest & Schindler 2016). This landslide also dammed the Sunkoshi River, which was breached 37 days later, causing severe flooding to areas more than 30 km downstream (Shrestha & Nakagawa 2016). The Jure landslide occurred on the 2nd August (mid monsoon season), with a total width of 900 m wide, a height of 1500, a

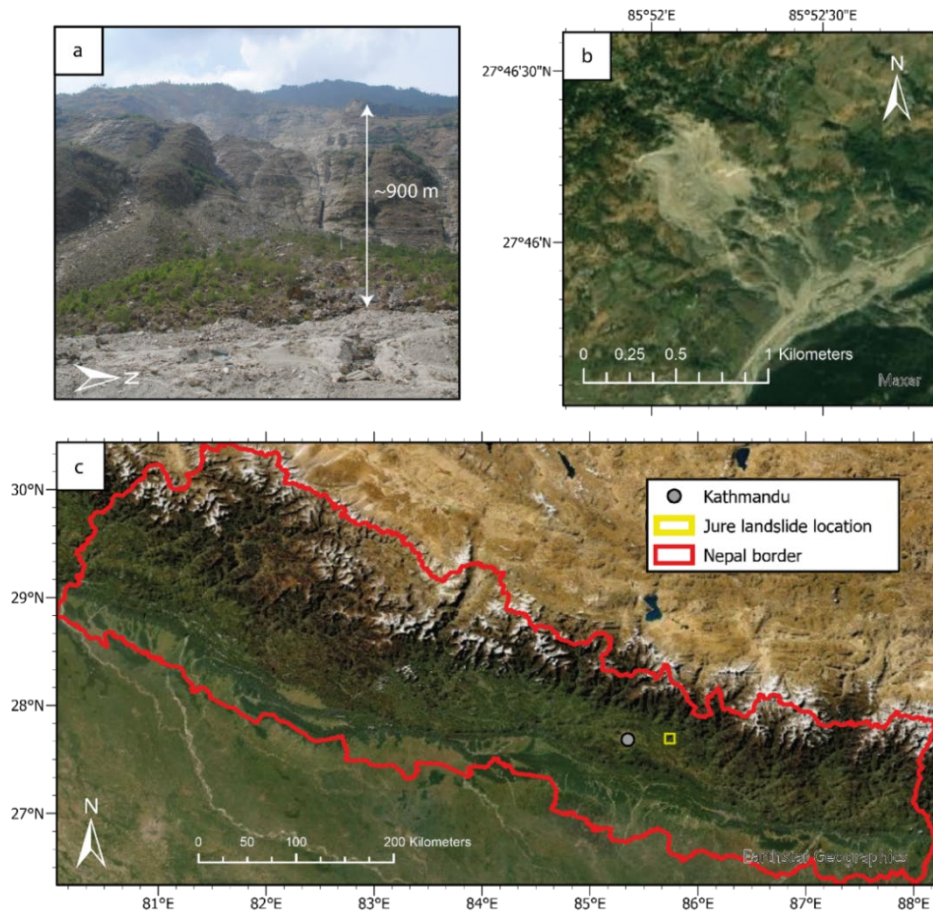


Figure 1.4. Jure landslide example: a) photograph showing the landslide scar and upper deposits taken in April 2018. b) aerial view of the landslide from 0.3 m ESRI/Maxar imagery. c) approximate location of the Jure landslide within Nepal.

maximum depth of 200 m and a volume of $\sim 6 \times 10^6 \text{ m}^3$ (Yagi *et al.* 2020) (Fig. 1.4b). However, despite failing catastrophically in 2014 following several days of rainfall totalling 140 mm, this event was not just attributable to the 2014 monsoon season, but a result of progressive slope deformation since 2004 (Yagi *et al.* 2020).

1.4.3.3 Coseismic landslides

Coseismic landslides in the study region are also common owing to Nepal's seismogenic setting. As outlined in section 1.4.2, Nepal is located across a region that is actively accommodating the convergence between the Indian and Eurasian plates. As such, large magnitude, shallow and deep-seated, strike-slip and megathrust earthquakes are common (Mukul *et al.* 2014; Elliott *et al.* 2016). Such large magnitude earthquakes are well described to be major triggers of landslides, as strong

ground motion accelerations alter hillslope equilibrium and cause landscape shear strengths to be temporarily exceeded (Newmark 1965; Von Specht *et al.* 2019). Indeed, landslide densities have also been shown to broadly scale with peak ground acceleration (PGA). For example, Hovius *et al.* (2011) and Meunier *et al.* (2008) found that landslides triggered by the Northridge, Chi Chi, Chuetsu and Iwate-Miyagi earthquakes correlate with changes in PGA. Similarly Dai *et al.* (2011) found that for the 2008 Wenchuan earthquake, landslide point density values increased with PGA, reaching a maximum at 1.0 – 1.2 g, whilst landslide area density values reached a peak at 0.8 – 1.0 g.

The most recent example of a major landslide-triggering earthquake in the study region was the April 2015 M_w 7.8 Gorkha earthquake that triggered 24,915 landslides covering a total area of over 87 km² with an estimated total volume of 0.12 – 1.1 km³ (Roback *et al.* 2018) (Fig. 1.5). Of these landslides, ~75% were rockfalls or topples (e.g. Fig. 1.3 c – d) with areas < 1000 m² (Tiwari *et al.* 2017), though some debris flows and debris avalanches were also reported (e.g. Fig. 1.3 e – f) (Jones *et al.* 2020). In terms of the overall sizes of the Gorkha coseismic landslides, as described in Chapter 2 (section 2.4.3), landslide area-frequency distributions can be described using power-law scaling exponents (e.g. Guzzetti *et al.* 2002; Malamud *et al.* 2004). The Gorkha coseismic landslides had a power-law scaling exponent of approximately -2.5 (Roback *et al.* 2018), a value that is slightly higher than the exponents calculated for similar earthquake events such as Northridge, California (-2.39), Chi Chi, Taiwan (-2.3) and Wenchuan, China (-2.19) (Frattoni & Crosta 2013). This suggests that the Gorkha earthquake triggered relatively few large area landslides, a suggestion that is corroborated by field observations (Collins & Jibson 2015; Roback *et al.* 2018). As expected, the largest failures were typically found to occur within the fault rupture zone where PGA was greatest (Tiwari *et al.* 2017).

The controls on the spatial distributions of the Gorkha coseismic landslides have also been comprehensively assessed (e.g. Martha *et al.* 2017; Roback *et al.* 2018). Landslide densities were found to increase from E-W, most likely as a result of fault rupture directivity, and from the Lesser to Greater Himalaya, most likely due to the greater pervasiveness of steep slopes and higher mean annual rainfall. Coseismic

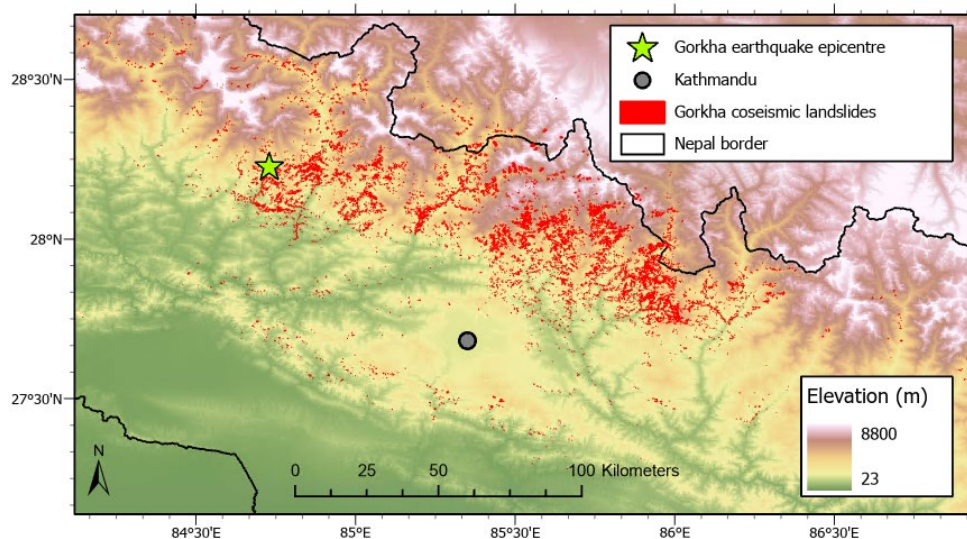


Figure 1.5. Locations of the Gorkha 2015 coseismic landslides mapped by Roback *et al.* (2018).

landslide densities were also generally greatest within crystalline bedrock sequences, though there are no clear reported relationships with any individual lithological units. Overall, the analysis by Roback *et al.* (2018) suggests that there was no single clear control on landslide occurrence, but that it was instead a combination of proximity to the deepest part of the fault rupture, steep slopes ($> 40^\circ$) and high mean annual precipitation (> 1500 mm). The 2015 coseismic landslides were also found to have very high levels of river channel connectivity, with over 50% of landslide debris deposited directly into stream channels. Connectivity was found to be highest for larger landslides in the Higher Himalaya, whilst the largest area failures were found to have the longest runout distances.

1.4.3.4 Current status of landslide hazard management in Nepal

Before 2015, landslide hazard management in Nepal was largely undertaken according to the relatively outdated Natural Disaster Relief Act (1982) and the 2009 National strategy for Disaster Risk Management (Gaire *et al.* 2015). This saw landslide risk being managed across a multitude of technical departments and government ministries, with little communication with local governments, insufficient resources and expertise (e.g., lacking updated susceptibility maps), and

thus a very ad hoc, reactive, approach to landslide hazard management (Oven *et al.* 2021).

Since 2015, the Nepal Government initiated a more proactive approach to landslide hazard, with the Department of Geology and Mines undertaking detailed geohazard assessments across 455 locations in 15 districts using technical support from the United Nations Office for Project Services (UNOPS) and the National Reconstruction Authority (Oven *et al.* 2021). This assessment classified local regions into three groups, Category 1 (safe), Category 2 (at risk) and Category 3 (unsafe), for the purposes of post-earthquake reconstruction and preparedness planning. However, this classification has been criticised as being too 'static' and not properly considering the evolving nature of landslide hazard (Kincey *et al.* 2021; Oven *et al.* 2021). It also remains unclear the degree to which landslide susceptibility maps are being used across the country. During a visit to Nepal in April 2018, the Department of Geology and Mines was visited to see what susceptibility resources they had available. It was evident that they had very few maps available, with those that were available seemingly based on outdated landslide inventories. This suggests that the various literature publications on updated landslide susceptibility across Nepal have not permeated through to use within the relevant government ministries. One reason for this could be due to limited technical resources and capacity. It was unclear during our visit exactly what technical resources were available to the relevant stakeholders, or whether they had the expertise to develop the types of susceptibility model typically presented in the literature. Overall, it is therefore evident that improved susceptibility maps (particularly those that are not time independent) could be used to assist current strategies used to implement landslide management planning and preparedness, though with the caveat that undertaking this could be limited by technical resources and capacity.

1.5 Conclusion

Overall, this thesis aims to investigate the spatiotemporal characteristics, preconditioning and susceptibility of monsoon-triggered landslides in Nepal. Chapter 2 will describe the methodologies used to obtain the ASM-triggered

landslide inventory and other predisposing factor data used throughout this thesis before presenting an overall analysis of the inventory characteristics, distributions, and susceptibility. Chapter 3 will then use additional field data and a comprehensive coseismic inventory to consider some of the spatial issues associated with landslide processes, with a focus on the comparison between landslide occurrences in the two distinctly different geomorphological regions of Langtang Valley and the Arniko Highway. Chapter 4 will quantify the characteristics of landslide path dependency, the temporal variation in ASM-triggered landslide spatial distributions, and the implications of this variation for logistic regression-based landslide susceptibility modelling. Chapter 5 will then consider how ASM-triggered landslide rates in Nepal have changed through time, with a focus on the characteristics and causes of earthquake preconditioning. Finally, Chapter 6 will summarise the overall conclusions from this thesis before discussing these in the context of landslide susceptibility modelling and recommending a framework for best practice when conducting susceptibility modelling in regions with spatiotemporally varying landslide processes.

Chapter 2 Landslide inventory development, analysis, and susceptibility modelling

2.1 Introduction

The overall aim of this thesis is to provide insight into the spatiotemporal characteristics, preconditioning and susceptibility of landslide occurrences in active mountainous regions. Landslide occurrences are typically caused by complex interactions between a trigger event, such as an earthquake or rainfall, and predisposing factors that control latent hillslope stability (Reichenbach *et al.* 2018; see Chapter 1, section 1.4.3). Any investigation into landslide occurrence thus requires data on past landslides and the triggering and predisposing factors that influenced those landslides. The rarity of long-term landslide data often limits efforts to better understand landslide occurrences (e.g. Chapter 1, section 1.2.3). However, thanks to a growing archive of freely available satellite imagery, developing long-term landslide inventories is becoming ever more feasible. A central objective of this thesis is to develop a 30-year multi-seasonal inventory of Asia Summer Monsoon (ASM)-triggered landslides across the central-eastern Nepal Himalaya. From this point forward, this inventory will be referred to as the “ASM-inventory”. The ASM-inventory will be one of the primary outputs of this project and is the dataset on which the analyses in this and all subsequent chapters are based.

The aim of this chapter is to describe the key methodologies used to develop and analyse the ASM-inventory and to present a preliminary analysis of the inventory characteristics and susceptibility. Since many of the methodologies presented in this chapter are also used in subsequent chapters, this chapter will be referenced throughout the thesis.

The specific objectives of this chapter are as follows:

1. To describe the methodologies used to develop the ASM-inventory.

2. To describe the methodologies used to obtain triggering and predisposing factor data.
3. To outline the main methodologies used to analyse and assess the overall ASM-inventory characteristics and distributions. This includes the methodologies used to assess landslide spatial associations, geometry, size, and spatial distributions.
4. To outline the general methodologies used in Chapters 2, 3 and 4 for developing Binary Logistic Regression (BLR)-based landslide susceptibility models.
5. To present the results from the methodologies outlined in objectives 3) and 4) as applied to the entire ASM-inventory. Specifically, this will quantify the overall (largely space and time independent) geometries, spatial associations, sizes, spatial distributions, and susceptibility of the landslides within the ASM-inventory.
6. Finally, this chapter will discuss the results of objective 5) within the context of the wider literature, with a focus on the processes controlling monsoon-triggered landslide characteristics in Nepal and how these compare to coseismic landslides across the same region. The landslide susceptibility model developed here will also be compared to published models already developed for the region before discussing the potential limitations of typical susceptibility approaches and how these will be investigated in subsequent chapters.

2.2 Methods: landslide inventory development

A landslide inventory is a database that typically contains information on landslide location, size, trigger event, type and state (Reichenbach *et al.* 2018). Where the trigger event is the process that initiated landslide movement and state is the current activity level (e.g., stable, active, reactivated) of a landslide that has already occurred. The following sections outline the methodologies used to develop the ASM-triggered landslide inventory used throughout this thesis.

2.2.1 Inventory type

There are three main types of landslide inventory: event, seasonal and historical (Guzzetti *et al.* 2012). An event inventory contains landslide data from a single discrete triggering event such as a typhoon or earthquake (e.g. Roback *et al.* 2018). A seasonal inventory contains all landslides that have occurred within a defined time interval such as a monsoon season (e.g. Fiorucci *et al.* 2011), and a historic inventory contains all landslides visible in a given region, likely associated with a range of unidentified or undated triggering events (e.g. Jaiswal *et al.* 2011; Martha *et al.* 2012). The former two inventory types can be considered as ‘multi-temporal’ if they include information on multiple events or seasons. In this thesis, the aim was to develop a long-term (30-year) multi-seasonal inventory of landslides triggered in 29 separate Asia Summer Monsoon seasons.

2.2.2 Study region and inventory scale

Landslide inventories are commonly developed over a wide range of study region sizes and spatial scales (Guzzetti *et al.* 2012). The appropriate spatial scale is determined by the size of the study area and the application for which mapping is being undertaken (Table 2.1; Fell *et al.* 2008). In this thesis, the aim was to develop an inventory over a large (~45,000 km²) region of central-eastern Nepal (see Fig. 1.1) for the purpose of assessing landslide characteristics, distributions, and susceptibility. This required that the ASM-inventory was developed at the moderate-to large-scale (Table 2.1). Moderate-scale landslide inventories are typically developed using optical satellite or aerial imagery with a spatial resolution of at least 30 x 30 m (e.g. Duman *et al.*, 2005). Such moderate-scale inventories are unlikely to have been fully corroborated with detailed fieldwork, and will likely not include information on the smallest landslides.

2.2.3 Landslide mapping procedure

Landslide inventories are developed via the mapping of landslides. Landslides can be mapped using both field and remote sensing methods. Field mapping of landslides involves going into the field and physically recording all landslides evident in the landscape (e.g. Jones *et al.* 2020). Remote sensing methodologies involve mapping

Scale	Application	Typical study area size
Small (< 1:100,000)	Preliminary assessments of landslide hazard for informing broad policy / general public.	> 10,000 km ²
Medium (1:25,000 – 1:100,000)	Landslide susceptibility, vulnerability, risk zoning for regional development purposes. Assessing large-medium size and regional level landslide processes, characteristics and distributions.	1000 – 10,000 km ²
Large (> 1:25,000)	Landslide susceptibility, vulnerability, risk zoning for local development purposes. Risk zoning for major engineering projects and for site-specific projects. Detailed investigations into smaller, hillslope specific landslide processes, characteristics and distributions	10 – 1000 km ²

Table 2.1. Typical landslide inventory scales, and their appropriate applications and study region sizes, as defined by Fell et al. (2008).

landslides visible in remotely sourced data such as aerial photographs, surface morphology models or optical satellite imagery (Reichenbach *et al.* 2018). It is a common misconception that field mapping is more accurate than remote mapping (Guzzetti *et al.* 2012). In reality, field mapping is often hampered by local perspective (i.e. not being able to fully see large or complex landslides from the ground) and cover by vegetation or human activity that makes landslide boundaries difficult to trace (e.g. Santangelo *et al.* 2010). Consequently, field mapping is usually only employed to conduct detailed investigations of single landslides or groups of landslides that have important anthropogenic implications (e.g. Jones *et al.* 2020), to validate limited portions of remotely-developed inventories (e.g. Rabby & Li 2019), or to map regions where remote imagery is unavailable or of poor quality (e.g. Van Den Eeckhaut *et al.* 2007b). Fieldwork can also be expensive, time consuming and logistically challenging, particularly in high-mountain regions with extreme terrain. As outlined previously, this ASM-inventory was intended to be a multi-temporal inventory of landslides triggered during 29 separate monsoon-seasons and mapped across a large 45,000 km² region at a moderate resolution of at least 30 x 30 m. These spatial and temporal resolution requirements limited the methodologies that could be employed to map the landslides. The study region size, extremity of the terrain, and lack of temporal information made field mapping inappropriate. Furthermore, there are very few remote sensing products that cover central-eastern Nepal at the required spatial and temporal scales. For example, whilst aerial photography does cover Kathmandu valley across multiple time periods, the majority of the country is

only covered by a single aerial photograph survey from the 1990s. Furthermore, there is no available high-resolution LiDAR data to allow accurate mapping from surface morphology. Consequently, the only viable method of developing the ASM-inventory was with satellite data, and the only freely available satellite product to cover central-eastern Nepal at a minimum of 30 x 30 m spatial resolution across a 30-year period was Landsat (Woodcock *et al.* 2008).

The Landsat satellite programme is a joint NASA/USGS project that freely provides the longest continuously acquired space-based archive of the Earth's surface (Woodcock *et al.* 2008). Landsat satellites 1/2/3 cover the period of 1972 to 1983. These satellites had a maximum temporal resolution of 18 days and a maximum spatial resolution of 40 m, but were found to have intermittent spatial coverage over Nepal. Landsat satellites 4/5 cover the period 1982 – 2011, have a maximum temporal resolution of 16 days and a maximum spatial resolution of 30 m. In Nepal, they provide good spatial coverage from 1987, making them ideal for mapping medium-large landslides since 1988. Landsat 7 was launched in 1999. It has 30 m multispectral bands, a 15 m panchromatic band and a temporal resolution of 16 days. However, in 2003, this satellite suffered a Scan Line Corrector (SCL) failure that reduced the data coverage of each image by 22 - 35% (Alexandridis *et al.* 2013), rendering the imagery less effective for accurate landslide mapping after 2003. Landsat 8 was launched in 2013. Like Landsat 7, this also had 30 m multispectral bands, a 15 m panchromatic band and a temporal resolution of 16 days.

As such, the ASM-inventory was mapped exclusively with Landsat 4/5/7/8 imagery, which allowed the mapping of landslides from 1988 to 2018. Figure 2.1 shows a schematic of the general workflow used to map the landslides that form the ASM-inventory. This workflow is divided into three sections: imagery acquisition, imagery processing and landslide mapping, as described in the following sections.

2.2.3.1 Imagery acquisition

To map landslides in a given time slice (monsoon season), it is necessary to have imagery taken both before and after that time slice. The two images can then be compared to identify any new landslide features that have occurred in that time-

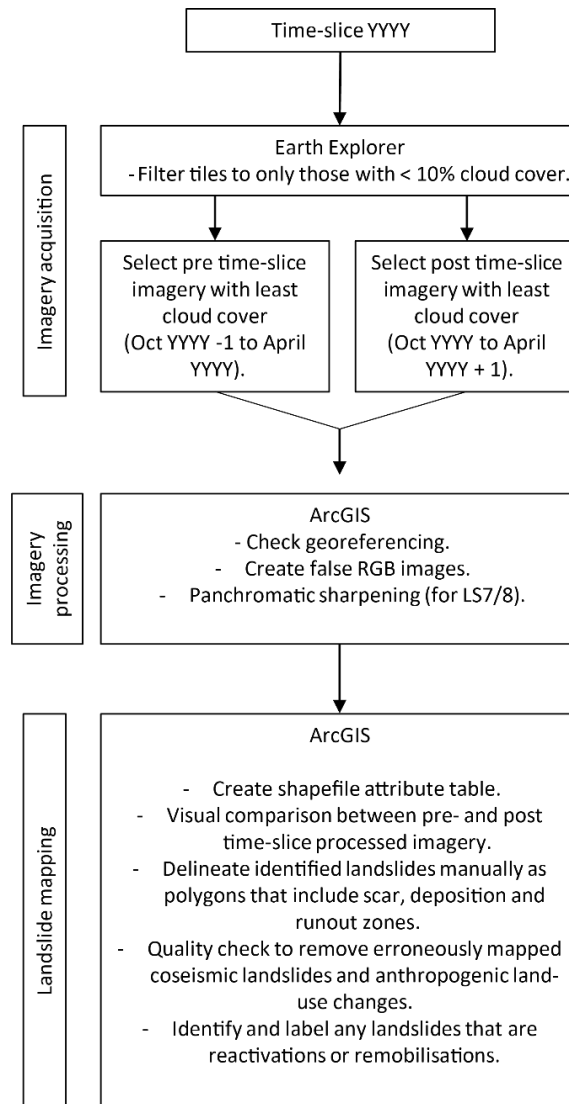


Figure 2.1. Generalised workflow for landslide mapping procedure used in this thesis.

period (i.e. any landslides that are visible in the post imagery that were not visible in the pre imagery). In this case, the ASM-inventory includes a separate time slice for every monsoon-season between 1988 and 2018, excluding 2011 and 2012 which could not be mapped due to the Landsat 7 scan-line errors. As the Nepal monsoon season runs from ~ May to September, pre- and post-season imagery needed to be obtained in the October – April period preceding and following each monsoon season. Landsat imagery from the required time periods were obtained for the entire study region from the USGS Earth Explorer platform (<https://earthexplorer.usgs.gov/>). This platform allows the user to define a required period and study region extent, as well as to filter out imagery with high cloud cover.

The study region (see Fig. 1.1) encompassed four Landsat tiles, so four pairs of images were required to fully map each monsoon season. For optimal mapping, images with < 10% cloud cover were required. Unfortunately, the nature of Nepal's climate meant that this severely limited the available imagery. Ideally, pre- and post-images would have been obtained as close to the start/end of a monsoon-season as possible to ensure that each time slice was the same length. However, owing to the high levels of cloud cover, pre- and post-imagery for a given monsoon season could have been dated any time between the April and October before/after that season. This meant that the pairs of images for each monsoon period will have encompassed the target monsoon season plus a varying number of non-monsoon months either side. This was an unavoidable limitation of the available satellite data, and the potential impacts of this have been fully evaluated for all analysis where this may affect the results (e.g. Chapter 5, section 5.2.2.1). Another consequence of the limited available imagery is that the post-imagery used to map one time slice typically had to be used as the pre-imagery for the next time slice. As such, the ASM-inventory is continuous across the 30-years mapped.

In total, ~144 Landsat satellite images were obtained from Earth Explorer. Table 2.2 outlines which Landsat satellites were used to map each monsoon-season, whilst Data File 1 (available [here](#)) is a polygon shapefile of the inventory that includes the specific dates of the pre- and post-images used to map each individual landslide.

2.2.3.2 Imagery processing

The landslides that occurred within each given period were mapped by identifying landslides that were visible in the post imagery, but not the pre imagery. When landslides occur, they typically change the landcover of a landscape, thus modifying the optical properties of the land surface (Guzzetti *et al.* 2012). The differences in spectral signals produced by different land covers can be captured by passive (optical) sensors, thus providing imagery from which landslides can be identified and mapped. Optical satellites such as Landsat are typically multispectral, i.e. they capture reflectance values at several specific bands of the spectral range, including blue, green, red, and near infrared light. These different bands can be combined in

different combinations to create false colour composite images such as NDVI that enhance different parts of the visible or infrared spectrum relative to others. This is particularly useful in landslide mapping as it can allow bare-earth reflectivity to be enhanced relative to vegetation reflectivity, thus “highlighting” landslides and other

Year	Total number mapped events	Number reactivated/remobilised events	Satellites used
1988	551	98	Landsat 4/5
1989	361	55	Landsat 4/5
1990	282	75	Landsat 4/5
1991	185	43	Landsat 4/5
1992	206	54	Landsat 4/5
1993	688	66	Landsat 4/5
1994	239	36	Landsat 4/5
1995	329	46	Landsat 4/5
1996	349	106	Landsat 4/5
1997	248	45	Landsat 4/5
1998	270	58	Landsat 4/5
1999	369	57	Landsat 4/5
2000	474	106	Landsat 7
2001	570	132	Landsat 7
2002	1334	275	Landsat 7
2003	296	43	Landsat 7
2004	563	97	Landsat 4/5
2005	149	33	Landsat 4/5
2006	197	37	Landsat 4/5
2007	211	39	Landsat 4/5
2008	216	44	Landsat 4/5
2009	175	39	Landsat 4/5
2010	310	73	Landsat 4/5
2013	423	64	Landsat 8
2014	498	114	Landsat 8
2015	1318	358	Landsat 8
2016	882	296	Landsat 8
2017	744	186	Landsat 8
2018	401	85	Landsat 8
TOTAL	12838	2760	

Table 2.2. Summary of total number and number of reactivated/remobilised landslides mapped in each inventory time slices, and the satellite products used to map each time slice.

bare-earth features that have appeared within the landscape between two images. Optical satellites such as Landsat 7/8 also include panchromatic sensors that combine the information from the three visible bands (blue, green, red) instead of partitioning them into different spectra. As panchromatic sensors collect more solar radiation per pixel, they typically have higher resolutions than their multispectral counterparts. This is useful, as panchromatic and multispectral bands can be combined using pan-sharpening techniques, whereby the separate blue, green and red multispectral bands are merged with the higher resolution panchromatic band in order to produce a colour composite with the spatial and spectral properties of both input types.

As such, for all acquired imagery, false colour RGB images were compiled with the red band set to the Near Infrared multispectral band, and the green and blue bands kept to the green and blue multispectral bands. This band combination was used because it strongly highlighted the reflectivity difference between vegetated areas and bare earth. In addition, for the Landsat 7 and 8 imagery, the ArcGIS image analysis pan-sharpening tools were used to enhance the 30 m multispectral bands with the 15 m panchromatic bands to produce 15 m resolution colour composites.

2.2.3.3 Landslide mapping

Once all of the necessary imagery was acquired and processed, landslide mapping was conducted manually within the ArcGIS platform. Manual landslide mapping involves using expert knowledge to delineate landslides based on the reflectivity and morphology of features within the imagery. This approach is relatively time consuming and potentially subjective in that it is always influenced by the experience of the mapper, but is advantageous in that all landslides are individually checked. Manual mapping was chosen over automatic or semi-automatic mapping because whilst AI (Artificial Intelligence) landslide mapping algorithms are ever improving, ensuring that they do not include erroneous or inaccurate landslide polygons remains challenging (e.g. Yagi *et al.*, 2009). Indeed, Valagussa *et al.* (2019) estimated that 30% of an automatically produced landslide inventory for the Iwate-Miyagi Nairiku, Japan, earthquake event were unreliable. Furthermore, automatic landslide

mapping methods regularly suffer from the problem of amalgamation, where the runout of several landslides have become contiguous, and thus the algorithm maps them as one polygon, rather than several (e.g. Marc & Hovius, 2015). As such, it was decided that more accurate mapping would be achieved with a manual approach.

To generate the inventory, a polygon feature dataset was first created for each time slice (monsoon season) within the inventory. For each time slice, landslides were then identified by direct visual comparison of the pre- and post-imagery (e.g., Figs. 2.2a – c), delineated as polygons, and stored in the feature dataset for that time slice. Identifying which features in the imagery were landslides required several layers of decision making. These are outlined below and shown visually in a decision tree in Appendix A.

The first step in identifying a landslide is to locate new, fresh, bare-earth features that appear between the pre- and post-imagery, i.e., to find the locations where earth material has been disturbed. Typically, in the Himalayas, this will be visible as a change from vegetation to fresh bare-earth, or from weathered bare-earth to fresh bare-earth. As outlined in the previous section, the satellite imagery were processed to enhance the visibility of bare-earth relative to vegetation. As such, it was fundamentally easiest to see fresh bare-earth features that had replaced vegetation. Consequently, it is possible that some fresh bare-earth features that occurred over weathered bare earth or other material such as snow may have been missed. Indeed, very few landslides were observed in the most northern parts of the study region where there were high amounts of permanent snow and ice. This suggests that either far fewer landslides occur in snow and ice (e.g., due to processes such as frost bonding or glacial buttressing; see Chapter 3) or that the landslides that did occur in these regions were simply very difficult to observe (e.g., because movement beneath the snow does not fully dislodge the snow on the ground, surface). It should therefore be noted that landslides in snow-covered regions may have been missed, and therefore that subsequent susceptibility analyses may underestimate landslide susceptibility on these snow-covered regions.

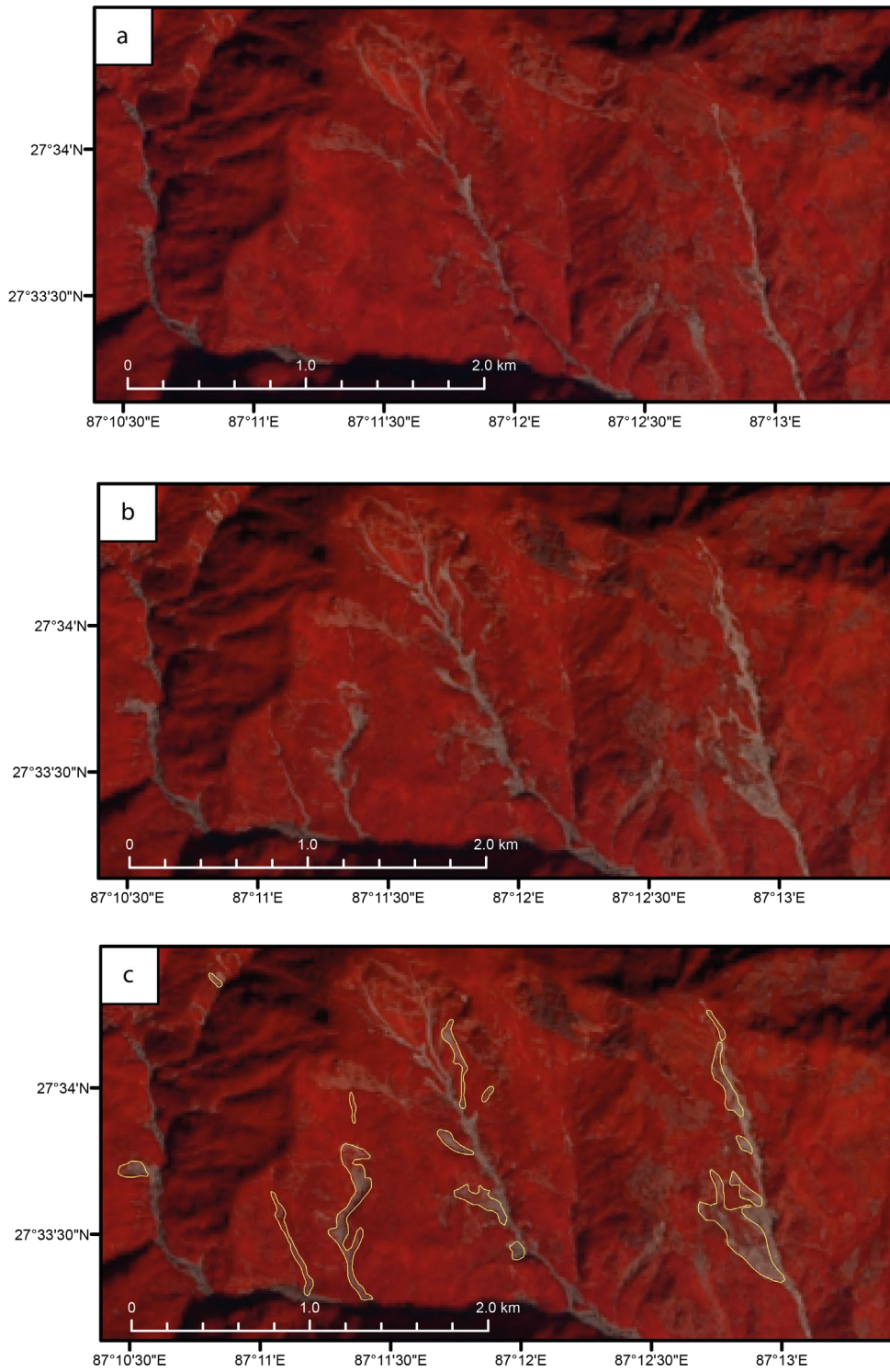


Figure 2.2. Example false colour RGB pre- and post-monsoon season Landsat satellite imagery used to map landslides. a) pre-imagery. b) post-imagery. c) resulting mapped landslides.

Once bare-earth features had been located, it was necessary to decide which features were rainfall-triggered landslides and which were features due to other processes (e.g., coseismic landslides or anthropogenic features). Before outlining how rainfall-triggered landslides and other processes were distinguished, it should be noted that all features composed of less than ~6 pixels were discounted for being too small to confirm what that feature likely was.

To avoid erroneously mapping coseismic landslides, all time slices known to have experienced earthquakes $> M_w$ 6.0 were identified. Between 1988 and 2018, three $> M_w$ 6.0 earthquakes occurred within or near the study region. The 1988 M_w 6.6 Bihar earthquake, the 2011 M_w 6.6 Sikkim earthquake and the 2015 M_w 7.8 Gorkha earthquake. As the 2011 and 2012 monsoon-seasons were un-mappable (due to the Landsat 7 scanline errors) there were no time slices that corresponded to the Sikkim earthquake. However, the 12/08/1988 Bihar earthquake occurred within the 1988 monsoon-season time slice, and the 25/04/2015 Gorkha earthquake and associated aftershocks (including the M_w 7.3 event on the 12/05/2015) occurred within the 2015 monsoon-season time slice. To avoid erroneously mapping coseismic events in 2015, the comprehensive inventory of coseismic landslides published by Roback *et al.* (2018) was used. Any new landslides visible in the 2015 time slice imagery that were not included in the Roback inventory were assumed to have been triggered by the subsequent monsoon. Avoiding erroneous mapping of coseismic events was more challenging in 1988 as there are no published coseismic inventories for this event. This earthquake occurred to the south of the study region in the Terai region, where the topography is flat and generally less prone to landsliding. As quantified by Densmore & Hovius (2000), coseismic landslides are typically triggered near ridgelines, high on hillslopes, whereas rainfall-triggered landslides are more likely than coseismic landslides to occur at lower hillslope positions. As such, for the 1988 time slice, the portion of the study region that observed > 0.1 g isoseismals during the 1988 earthquake, as defined by the USGS (USGS 2018a), was extracted. Then, within that region, the slope-position of observed new landslides was used to determine whether they were coseismic or monsoon-triggered, i.e., ridgeline-initiating landslides were interpreted to be coseismic, and all others were interpreted

to be monsoon-triggered. Furthermore, in some select cases, local knowledge was used to distinguish between earthquake and rainfall-triggered landslides. For example, in the Arniko and Langtang regions where fieldwork was conducted (see Chapter 3), local people often remembered when a given landslide occurred and were able to confirm whether or not it had been triggered by the Gorkha earthquake. To avoid erroneously mapping anthropogenic features such as cut-and-fill occurrences, road-associated mass-wasting, and deforestation, landslide shape and position were assessed. For shape, landslides typically have a longer downslope axis and shorter width axis. They also tend to have source zones, narrower runout zones, and then splayed or fan-shaped deposition zones. In contrast, anthropogenic features such as deforestations and areas of cut-and-fill tend to be more cuboid in shape and occur on flatter ground or stepped terraces (e.g., Appendix B). As such, features that were cuboid and/or occurring on flatter terrace areas were assumed to be anthropogenic and so not mapped. In terms of road-associated mass-wasting, a common construction practice in Nepal is to tip material excavated for road-construction onto hillslopes. These road-tips can look very similar to landslides, but typically occur simultaneously with the occurrence of a new road or track (e.g. Appendix B). As such, any features splaying or connected to a new road were also discounted from the inventory.

Once a feature had been identified as a rainfall-triggered landslide, the final landslide polygon boundary was drawn to include the combined scar and runout zones, as these were indistinguishable at the spatial resolution of the imagery. In addition, all identified landslides were classified as being spatially independent of any previous failures (e.g., Fig. 2.3a - c), or as being reactivated or remobilised, with the latter being defined in cases where a landslide appeared to intersect or initiate from the boundary of a pre-existing landslide scar (e.g. Fig 2.3d - f). Unfortunately, the resolution of the imagery made it challenging to distinguish between reactivations (i.e., the failure of new material that initiates from or intersects with the scar of a previous landslide) and remobilisations (i.e., the movement of material that had already failed or been disturbed by a previous landslide), so the two were grouped together. Finally, where

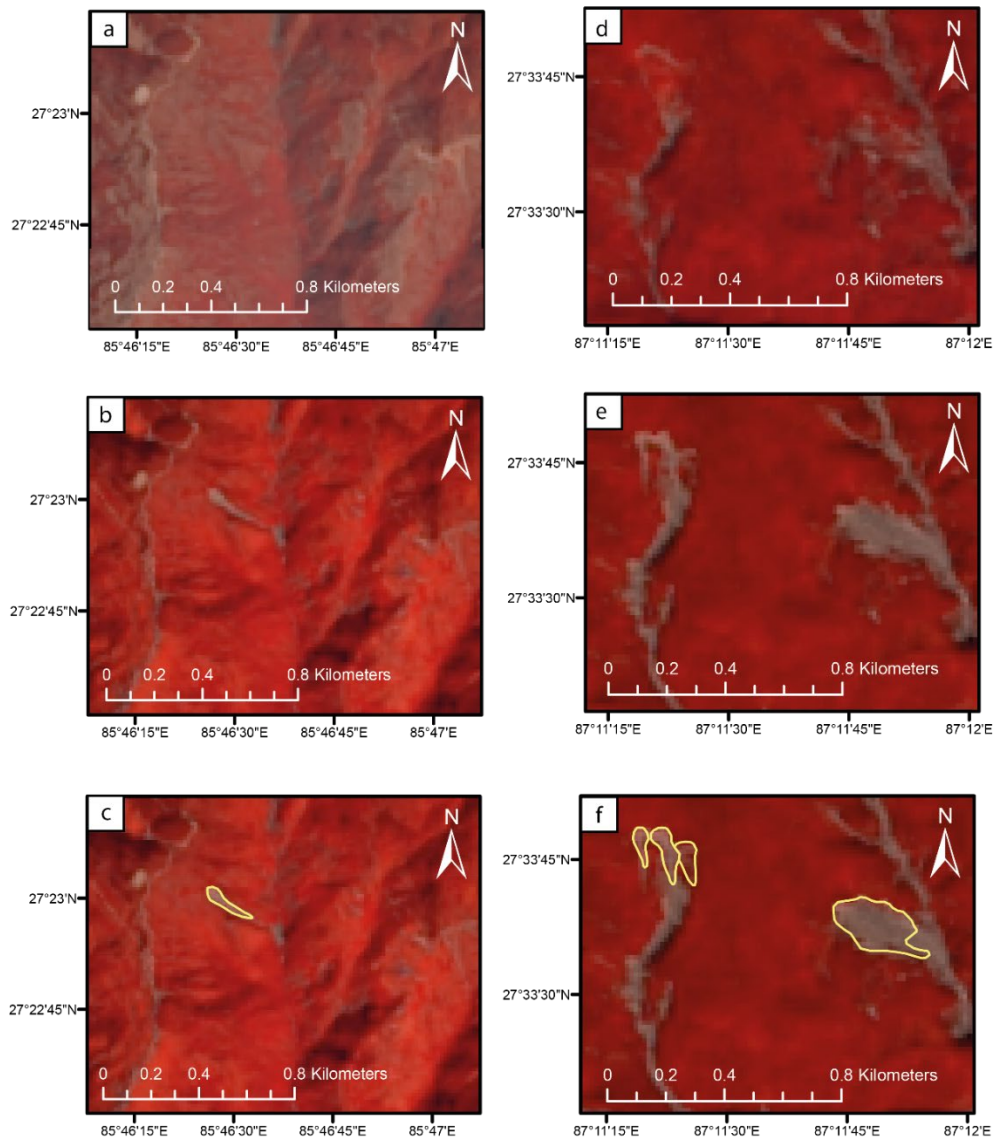


Figure 2.3. Examples of fresh and reactivated landslides in false RGB Landsat satellite imagery. a) and d) show pre-monsoon season imagery with pre-existing landslides. b) and e) show post-monsoon season imagery with a clear fresh failure and several reactivated or remobilised failures respectively. c) and f) show the new features from b) and e) delineated as yellow polygons.

possible (i.e. where imagery resolution and landslide size allowed), care was taken to avoid amalgamating collocated landslides. This was achieved by assessing whether a given bare-earth feature had multiple distinct higher source zones, and then splitting a given amalgamation between those source zones.

In total, 12,838 monsoon-triggered landslides were initially mapped across 29 monsoon-season time slices between 1988 and 2018, excluding 2011 and 2012 (Fig.

2.4; Table 2.2). As mentioned above, Data File 1 (available [here](#)) is a freely available polygon shapefile that includes the locations, satellite information, and basic geometries (perimeters and areas) of all 12,838 landslides in the inventory.

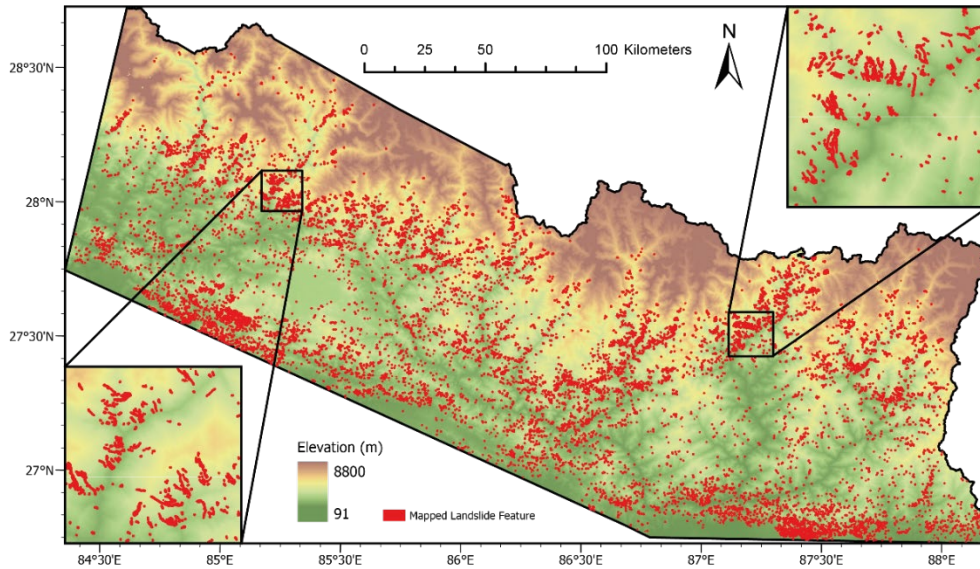


Figure 2.4. Locations of all 12,838 mapped landslide polygons in the ASM-inventory. Insets show smaller scale view of delineated polygons in two subregions.

2.3 Methods: obtaining triggering and predisposing factor data

To understand the spatial and temporal controls on landslide occurrence, it is necessary to obtain data for the event(s) that triggered those landslides and for those factors likely to have predisposed the landscape to failure. The following sections outline the methods and properties of the main triggering and predisposing data used throughout this thesis.

2.3.1 Trigger event data collection

The ASM-inventory includes landslides that are assumed to have been triggered during the monsoon-season. This is assumed because even though each time slice of the inventory includes some non-monsoon months, over 90% of rainfall-triggered landslides in Nepal are known to occur during the monsoon season (May –

September) (Petley *et al.* 2007; Stanley *et al.* 2020) when Nepal experiences >80% of its yearly rainfall (Dahal & Hasegawa 2008). As such, information on monsoon season precipitation for the study region from 1988 – 2018 were required.

There are two main sources of precipitation data: gauge-based instruments and satellites. The main advantage of gauge-based instruments is that these measure accumulated rainfall directly at the Earth's surface (Kidd 2001). It is estimated that there are a total of 150,000 - 250,000 rain gauge instruments across the globe, although many of these have not operated continuously or concurrently (Strangeways 2006; Kidd *et al.* 2017). These instrument data have been used to develop multiple global precipitation products, as shown in Table 2.3 (Sun *et al.* 2018).

Perhaps the most comprehensive of these instrument-derived datasets is that established by the Global Precipitation Climatology Centre (GPCC), who obtain primary data from National Meteorological Agencies (NMAs) as well as from the global networks of the Climate Research Unit (CRU; 11,800 stations), the Food and Agricultural Organisation (FAO; 13,500 stations) and the National Centres for Environmental Information (GHCN2 and GHVN daily; 34,800 stations) (Sun *et al.* 2018). In total, the GPCC product integrates over 85,000 stations worldwide, with full coverage from 1901 at a spatial resolution of 0.5° by 0.5° (Rudolph *et al.* 2011). However, the major drawback of instrument derived datasets such as GPCC is that they are dependent on the spatial distributions of the instrumentation, which can be highly irregular (Sun *et al.* 2018). For example, in Nepal, the GPCC full dataset uses just 280 gauges across the entire country (Müller & Thompson 2013). Furthermore, gauge instruments, particularly those in extreme rural areas, frequently get damaged and can have large sources of error from wind, evaporation, site location and instrument error (Michelson 2004). As such, it was decided that purely gauge-based rainfall products were not sufficiently accurate for use in this project.

The main advantage of satellite-derived precipitation datasets is that they provide global, homogenous precipitation measurements (Sun *et al.* 2018). There are multiple methods that are used to derive precipitation data from different satellite

Data set	Resolution	Frequency	Coverage	Period	Source	Reference
CRU	0.5° x 0.5°	Monthly	Global land	1901 - 2015	The CRU of the University of East Anglia	(Harris et al., 2014; New et al., 2000)
GHCN-M	5° x 5°	Monthly	Global land	1900 - present	National Climatic Data Centre	(Peterson & Vose, 1997)
GPCC	0.5° x 0.5° 1.0° x 1.0°	Monthly	Global land	1901 - 2013	GPCC	(Rudolf et al., 2009)
GPCC-daily	2.5° x 2.5° 1.0° x 1.0°	Daily	Global land	1988 - 2013	GPCC	(Schamm et al., 2014)
PRECL	0.5° x 0.5° 1.0° x 1.0° 2.5° x 2.5°	Monthly	Global land	1948 - 2012 (0.5°) 1948 - present	NCEP / NOAA	(Chen et al., 2002)
UDEL	0.5° x 0.5°	Monthly	Global land	1900 - 2014	University of Delaware	(Willmott & Matsuura, 1995)
CPC-Global	0.5° x 0.5°	Daily	Global land	1979 - 2005	CPC	(Xie et al., 2010)

Table 2.3. Summary of global gauge-based precipitation products, from Sun et al. (2018), see Sun et al. (2018) for references.

Data set	Adjusted	Res.	Freq.	Coverage	Period	Data source	Algorithm	Reference
GPCP	GPCC, GHCN	2.5°	Monthly	Global	1979 - present	GPI, OPI, SSM/I scattering, SSM/I emission, TOVS		(Adler et al., 2003)
GPCP 1dd	GPCC, GHCN	1.0°	Daily	Global	1996 - present	SSM/I-TMPI, TOVS		(Huffman & Bolvin, 2013)
GPCP_PEN_v2.2	GPCC, GHCN	2.5°	5-daily	Global	1979 - 2014	OPI, SSM/I, GPI, MSU		(Xie et al., 2003)
CMAP	GPCC, GHCN	2.5°	Monthly	Global	1979 - present	GPI, OPI, SSM/I scattering, SSM/I emission, MSU, NCEP-NCAR		(Xie et al., 2003; Xie & Arkin, 1997)
CPC-Global	GTS, COOP, NMAs	0.5°	Daily	Global land	2006 - present	GTS, COOP, NMAs		(Xie et al., 2010)
TRMM 3B43	GPCC	0.25°	Monthly	50°S - 50°N	1998 - present	TMI, TRMM, Combined Instrument, SSM/I, SSMIS, AMSR-E, AMSU-B, MHS, GEO-IR	Probability matching	(Huffman et al., 2007)
TRMM 3B42	x	0.25°	3 hr / daily	50°S - 50°N	1998 - present	TMI, TRMM, Combined Instrument, SSM/I, SSMIS, AMSR-E, AMSU-B, MHS, GEO-IR	Probability matching	(Huffman et al., 2007)
GSMaP	x	0.1°	1 hr / daily	60°S - 60°N	2002 - 2012	TMI, AMSR-E, AMSR-E, SSM/I, multifunctional transport satellites (MTSAT), METEOSAT-7/8, GOES 11/12	Kalman filter model	(Ushio et al., 2009)
PERSIANN-CCS	x	0.04°	30 min / 3, 6 hr	60°S - 60°N	2003 - present	Meteosat, GOES, GMS, SSM/I polar, near polar precipitation radar, TMI, AMSR	Artificial Neural Networks	(Sorooshian et al., 2000)
PERSIANN-CDR	GPCP	0.25°	3, 6hr/daily	60°S - 60°N	1983 - present	GOES 8, GOES 10, GMS-5, Metsat-6 and Metsat-7, TRMM, NOAA 15, 16, 17, DMSP F13, F14, F15	Artificial Neural Networks	(Ashouri et al., 2015)
CMORPH	x	0.25° / 8 km	30 min / 3 hr / daily	60°S - 60°N	2002 - present	TMI, SSM/I, AMSR-E, AMSU-B, Meteosat, GOES, MTSAT	Propagation & Morphing	(Joyce et al., 2004)
GPM	x	0.1°	30 min / 3 hr / daily	60°S - 60°N	2015 - present	GMI, AMSR-2, SSMIS, Madaras, MHS, Advanced Technology Microwave Sounder	IMERG	(Hou et al., 2008, 2014)
MSWEP	CPC, GPCC	0.1° / 0.5°	3 hr / daily	Global	1979 - present	CPC, GPCC, CMORPH, GSMaP-MVK, TMPA ERA-Interim, JRA-55		(Beck et al., 2017)

Table 2.4. Summary of global satellite-derived precipitation products, from Sun et al. (2018), see Sun et al. (2018) for references.

sensors (see Sun *et al.*, (2018) and the references therein for more details), resulting in various satellite-derived precipitation products that are available for use. However, few of these have the spatial ($< 0.25^\circ$ by 0.25°) and temporal (1988 – 2018) resolutions required for this project (Table 2.4; Sun *et al.*, 2018). As can be seen from Table 2.4, one of the few freely available products to meet this specification was the PERSIANN-CDR product.

2.3.1.1 PERSIANN-CDR

The PERSIANN Climate Data Record (CDR) has a spatial resolution of 0.25° by 0.25° , temporal resolutions of 3 hours, 6 hours, 1 day and 1 month, covers latitudes 60° S – 60° N, and covers the period 1983 – present (Ashouri *et al.* 2015). This record was developed by applying the PERSIANN algorithm on GridSat-B1 IR satellite data. This algorithm was trained using hourly stage IV precipitation data from the National Centres for Environmental Prediction (NCEP) and then adjusted using the Global Precipitation Climatology Project (GPCP) monthly gauge and satellite-based dataset (Ashouri *et al.* 2015). The PERSIANN-CDR product is now a widely used product that has been well evaluated in the literature (e.g. Nguyen *et al.* 2020 and references therein). Indeed, PERSIANN-CDR was found to perform excellently when evaluated against 1400 ground-stations at capturing the spatial and temporal patterns of rainfall in the monsoon-regions of eastern China (Miao *et al.* 2015), and outperformed the TMPA (TRMM Multi-satellite Precipitation Analysis) dataset in its ability to capture the overall characteristics of Hurricane Katrina (Nguyen *et al.* 2020). Furthermore, the PERSIANN-CDR product was found to have lower monthly mean variance when compared to other satellite derived products, showing particularly small variance with the GPCP1DD product (Huffman *et al.* 2001; Gehne *et al.* 2016). Similarly, despite being slightly outperformed by other products, the PERSIANN-CDR dataset was capable of capturing inter-annual monsoon precipitation in Pakistan, with high (0.8) R^2 values when compared to in-situ data (Ullah *et al.* 2019). However, it should be noted that the PERSIANN-CDR product has some limitations. First, it is reported to have a tendency to under-predict values of extreme precipitation (Miao *et al.* 2015). Second, as with all satellite derived products, it remains unclear how well orographic effects are captured (Adam *et al.*

2006). However, a benefit of the PERSIANN-CDR product is that it is designed specifically for use in longer-term studies (Ashouri *et al.* 2015) and is considered one of the most temporally homogenous products. As such, unlike other satellite products whose methodologies could introduce temporal variance, any errors in the PERSIANN-CDR product introduced by orographic effects should be more systematic through time, which is important for a long-term study such as this.

Monthly PERSIANN-CDR data were acquired from the Centre for Hydrometeorology and Remote Sensing (CHRS) data portal: <https://chrsdata.eng.uci.edu/> (Nguyen *et al.* 2019). The study region was composed of 85 PERSIANN-CDR grids that intersected the mapping area. For each grid, standard GIS raster tools were used to calculate the total, peak (e.g. Fig. 2.5a) and mean (Fig. 2.5b) monthly precipitation totals across the study region for each monsoon season.

2.3.2 Predisposing factor data collection

To understand landslide occurrence, it is also necessary to obtain data for predisposing factors that may influence latent slope stability. As outlined in Chapter 1 (section 1.4.3.1), there are a number of predisposing factors that might be expected to control landslide occurrence across the study region. Specifically, this thesis considers the 14 factors described in Chapter 1, section 1.4.3.1. These are: elevation, hillslope angle, aspect, planform and profile curvature, local relief, excess topography, Specific Stream Power (SSP), channel normalised steepness index (k_{sn}), distance to channels, distance to roads, bedrock geology, land use and Permafrost Index (PFI). These 14 factors were selected for several reasons. First, they are all factors with commonly observed and geomorphically explainable controls on landsliding (Reichenbach *et al.* 2018). As such, using these factors allow the controls and distributions of the landslides in the ASM-inventory to be robustly compared to landslide data from other regions and studies, and allows a thorough assessment of the wider usefulness of including these factors in susceptibility modelling in Nepal. Second, these were all factors for which sufficient data were obtainable. Indeed, as outlined by Reichenbach *et al.* (2018), there are some two dozen predisposing factor

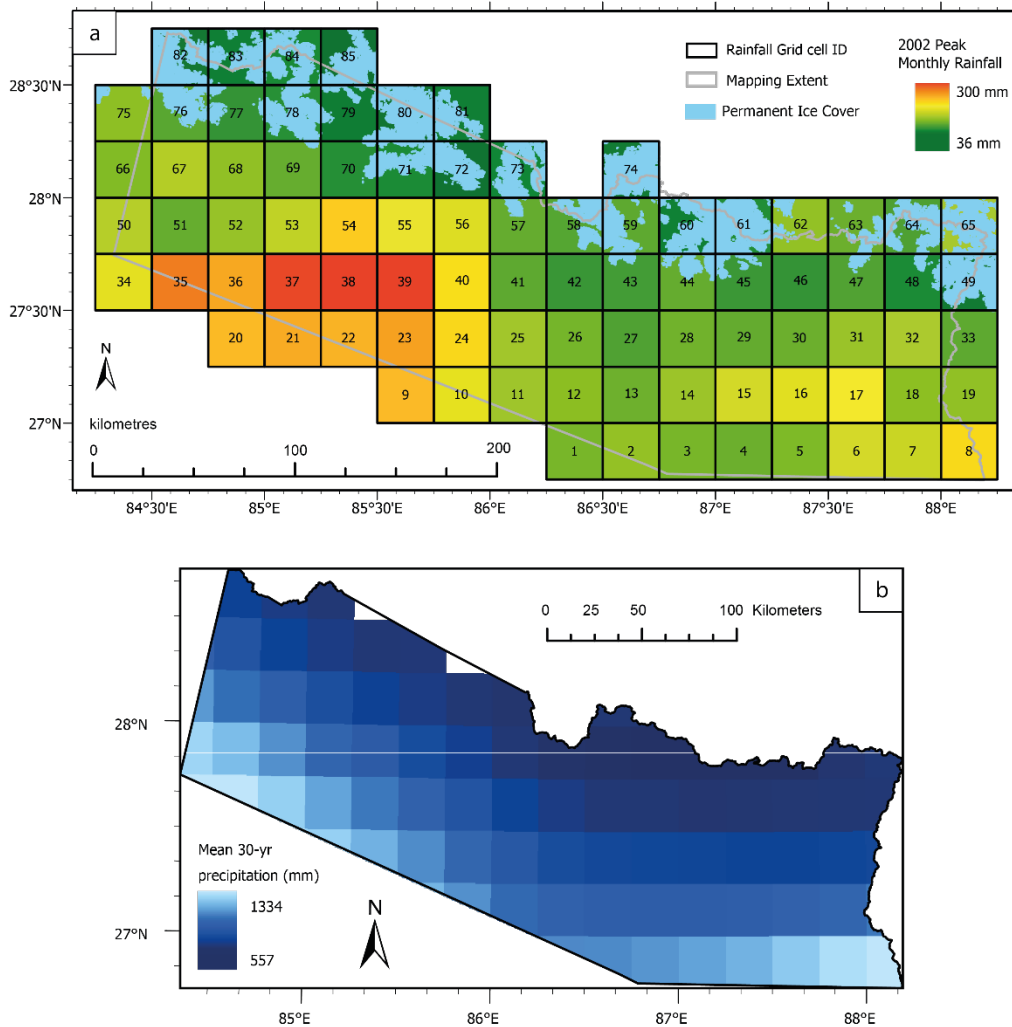


Figure 2.5. PERSIANN-CDR precipitation data examples for a) peak monthly monsoon period (May – September) rainfall from 2002, and b) mean total monthly rainfall for the period 1988 – 2018.

classes used within the literature for susceptibility modelling. However, not all of these could be included in this case due to a lack of data. For example, geotechnical and geo-structural factors relating to soil characteristics, hydrogeological parameters, and structural geology (e.g., fault locations, discontinuity densities and geometries) are commonly used in the literature, but could not be used in this case as these data do not exist across Nepal. The following sections will now describe the relevant data collection methodologies for each of the factors used in this study.

2.3.2.1 Topographic data

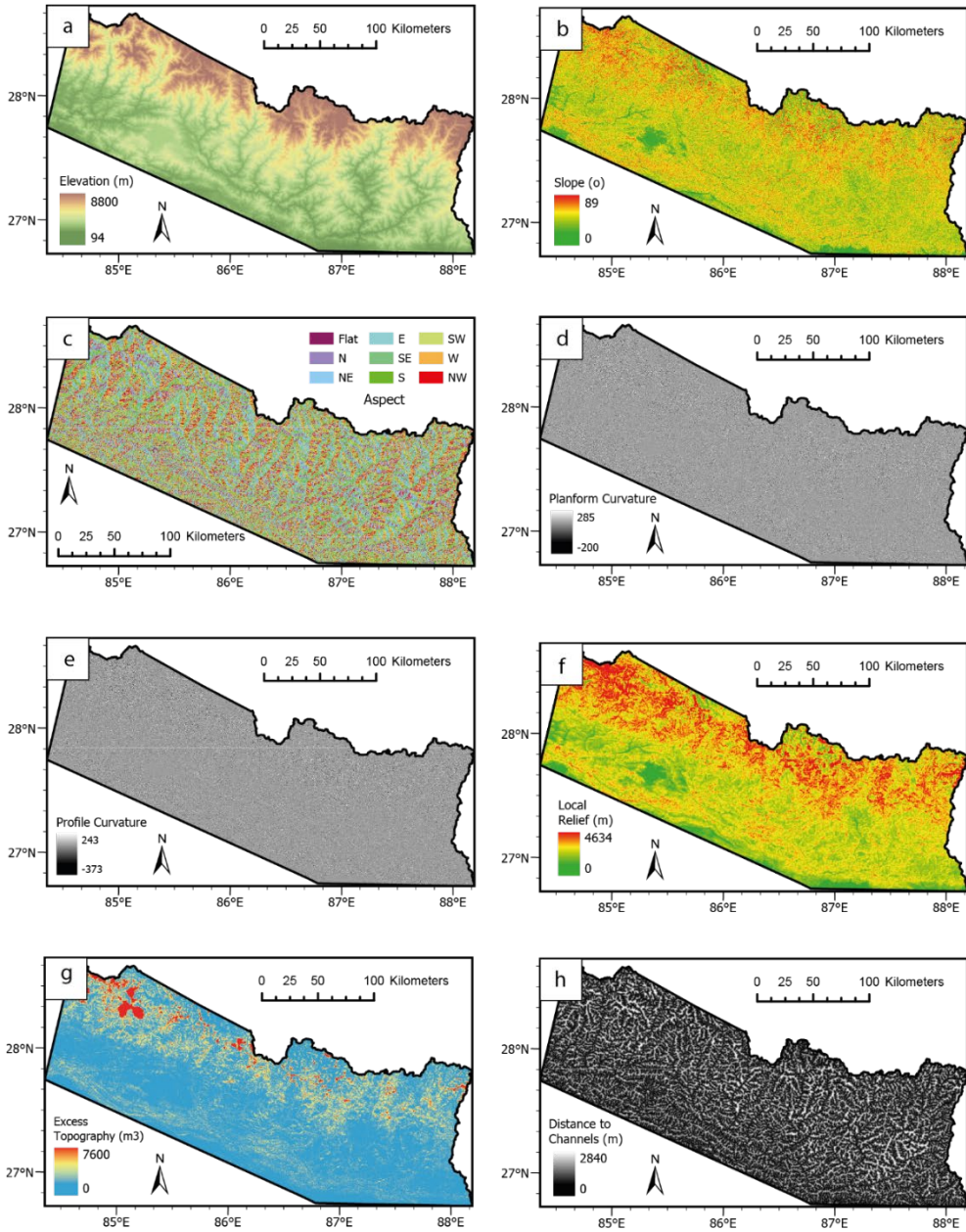
Topographic factors including elevation, local relief, hillslope angle, curvature, aspect, and excess topography were obtained from the ALOS World 3D – 30 m (AW3D30) version 2.1 global Digital Surface Model (DSM). This is a freely available DSM developed by the Japan Aerospace Exploration Agency (JAXA) that has a horizontal resolution of 1x1 arc seconds (approx. 30 x 30 m mesh) and a target height accuracy of 5 m. The relevant tiles were downloaded, mosaicked, and cropped to the extent of the study region using standard ArcGIS tools (Fig. 2.6a). Rasters of slope, aspect, planform and profile curvature, and local relief were then derived from the cropped DEM using the ArcGIS spatial toolbox (Figs. 2.6b - f). Local relief defines the relative elevation change within a local area. This was calculated using standard ArcGIS tools, whereby for each cell in the study region the difference between the highest and lowest elevations within a 1 km radius was obtained. Excess topography, which is a measure of the total volume of rock mass above a specified threshold hillslope angle (Blöthe *et al.* 2015), was extracted from the DSM for threshold angles of 20 - 45° using the “excesstopography” function in the Matlab TopoToolbox (Schwanghart & Scherler 2014) (Fig. 2.6g).

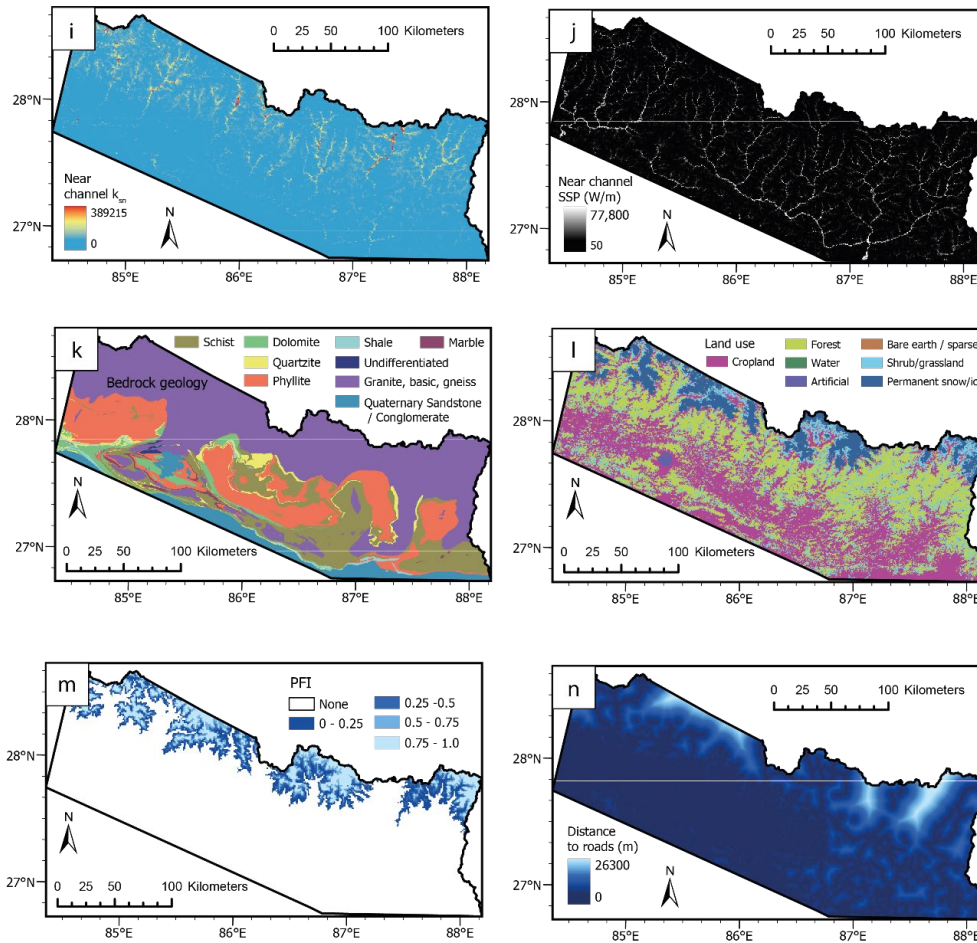
2.3.2.2 Hydrological data

The ALOS DSM was also used to derive three hydrological factors; distance to river channels, near channel k_{sn} , and near channel Specific Stream Power (SSP). First, the TopoToolbox “STREAMobj” function was used to extract the stream channel network across the study region for a threshold upstream area of 1 km². Euclidean distances to these channels, with a 30 m buffer, were then extracted for every landslide and cell within the study region using standard ArcGIS distance tools (Fig. 2.6h). Second, the normalised steepness index (k_{sn}) for those channels was extracted using the TopoToolbox “ k_{sn} ” function (Fig. 2.6i). Finally, the Specific Stream Power of those channels (Fig. 2.6j), which is total stream power per unit channel width, was calculated using Equation 2.1:

$$\Omega = \frac{\rho g Q S}{w}$$

Equation 2.1. Specific Steam Power





Where ρ is the density of water (1000 kg/m^3), g is acceleration due to gravity (9.81 m/s^2), S is the energy gradient, or channel slope (derived from the DSM using standard ArcGIS tools in units of m/m), Q is channel discharge (derived from the DSM using standard hydrological ArcGIS tools in units of m^3/s), and W is channel width (calculated as a function of discharge according to the scaling relationships of Craddock *et al.* (2007) in units of m).

2.3.2.3 Regional geology data

Like many developing countries with extreme, highly inaccessible terrain, Nepal lacks any high-resolution geological data. The Nepal Department of Mines and

Geology hold 1:250,000 regional scale maps of the main lithologies mapped across the country. These maps were digitised to a raster file from high-resolution scans using ArcGIS georeferencing and topology tools (Fig. 2.6k).

2.3.2.4 Landcover data

Nepal does not have accurate field-validated landcover maps. As such, data on landcover across Nepal had to be acquired from a global satellite data product. The product selected was the ESA-GlobCover 2009 dataset, which was developed using data from the 300 m MERIS sensor on board the ENVISAT satellite. The 2009 Landcover product, released on 21/12/2010, was created using automatic and regionally tuned classifications of the global MERIS FR (MEdium Resolution Imaging Spectrometer Full Resolution) mosaics acquired throughout 2009. In total, 22 landcover classes are identified following the definitions of the United Nations (UN) Land Cover Classification System (LCCS) (Bontemps *et al.* 2011). However, in this thesis, the initial 22 landcover classes are simplified into 7 broad classes (Fig. 2.6l). The original map projection of this product is a Plate-Carrée WGS84 ellipsoid, and has an estimated overall accuracy of 73% (Defourny *et al.* 2009).

2.3.2.5 Permafrost data

Permafrost is defined as sub-surface material with a temperature of $\leq 0^{\circ}\text{C}$ for at least two consecutive years (ACGR, 1988). As outlined in Chapter 1 (sections 1.4.2 and 1.4.3), permafrost is pervasive in the Greater and Tethyan Himalaya, and potentially capable of influencing landslide occurrence. However, field-validated permafrost data are extremely sparse, so models of permafrost extent are difficult to calibrate and validate (Gruber 2012). As such, this project makes use of a global model developed by Gruber (2012), which estimates permafrost extent via a global permafrost zonation index (Fig. 2.6m). This permafrost zonation index, which has a spatial resolution of 500 x 500 m, has values between 0.01 and 1, where a value of 1 suggests that permafrost will be present under all conditions, and a value of 0.01 suggests that permafrost will be present under ideal meteorological conditions only. This index is quantified as a function of Mean Annual Air Temperature (MAAT) combined with the stochastically modelled influences of snow cover, solar radiation,

subsurface properties, and vegetation. The MAAT data are based on the CRU (Climate Research Unit) TS 2.0 product (Mitchell *et al.* 2003), whilst topographic data used are from SRTM30. It is important to note that this model should not be considered as a representation of reliable ground truth, though it does compare favourably with the older, and still widely used, International Permafrost Association (IPA) map (Heginbottom & Dubreuil 1993; Brown *et al.* 1997). It also gives a much more consistent zonation and consideration of error, as it includes a ‘fringe area’ that maps the maximum plausible extension of the permafrost region.

2.3.2.6 Distance to roads

Road data across the study region were obtained from the Open Street Map (Humanitarian Data Exchange 2020). All primary, secondary and trunk roads were extracted from this dataset, and the Euclidean distances to these roads, with a 30 m buffer, calculated using standard ArcGIS distance tools for every landside and cell within the study region (Fig. 2.6n).

2.3.2.7 Issues with temporal variation

Of the factors described above, most can be considered as stationary through time. For example, geology and other topographical factors are unlikely to have changed considerably with respect to the data resolution across the 30-year time period. However, three of the factors (land use, PFI and distance to roads) will have observed some temporal variation. Unfortunately, in all of these cases, annual data for those factors did not exist for the entire mapped period, and self-compilation of these data was considered outside of the scope of this thesis. As such, when interpreting any results pertaining to these factors, it is important to consider that these factors will be most accurate in the years close to when the data were obtained (2009 for land use, 2012 for PFI and 2017 for road distance), and may be inaccurate in the years significantly before or after.

In the case of PFI, any temporal changes are unlikely to have had a significant impact on the PFI classifications. It is estimated that the lower limit of permafrost extent (LLP) shifted no more than 100 - 300 m between 1973 and 1991, before remaining relatively stable until at least 2004 (Fukui *et al.* 2007). Furthermore, the current rate

of change of permafrost extent is estimated to be $\sim 1.3 - 2.6$ m / year, with a maximum expected potential increase in the LLP of 188 m between 2009 and 2039 (Chauhan & Thakuri, 2017). These studies show that whilst permafrost extent is likely changing in response to climate change, the rate of change is small relative to the 500 x 500 m resolution of the PFI data used here, with even the maximum expected changes for the next 20 years below the resolution of the dataset.

Similarly, whilst the land use of the study region has changed across the past 30-years, much of this change has been an increase in urban development (Paudel *et al.* 2016) where landslides do not tend to occur, with less change observed in the higher mountains where most landslides do occur. Furthermore, even if there have been changes in the land use within the higher Himalaya, unless these changes are occurring over extensive regional scales, they would not change the overall designations of this 300 x 300 m dataset. Finally, for distance to major roads, it is true that road locations will have changed throughout the 30-year period considered here, with road building initiatives increasing road density, particularly the density of small informal rural roads, across Nepal (McAduo *et al.* 2018). However, as outlined in section 2.3.3.6, the “distance to roads” factor was based solely on the positions of large trunk, primary and secondary roads in 2017. These larger roads were used exclusively as these types of infrastructure were more likely to have existed for the entirety of the mapped period. For example, construction of the Arniko highway trunk road began in 1961 (Murton 2017; Ao *et al.* 2020). However, it is still possible that some of the primary and secondary roads included in the dataset did not exist in the early part of the time period. As such, the distance to roads metric can only be confidently considered as a topographic metric of “distance to road position in 2017”.

2.4 Methods: analysis of inventory characteristics and distributions

The following sections describe the methodologies used to assess the characteristics and distributions of the ASM-inventory in terms of landslide path dependency, geometry, size, and spatial distributions. Note, Data File 2 is a point inventory (.txt file; available [here](#)) showing all of the key information extracted using the subsequent

methodologies for each of the individual 12838 landslides in the inventory. The methodologies for size and spatial distribution analysis are used again in subsequent chapters.

2.4.1 Landslide path dependency

Landslide path dependency is a concept introduced by Samia *et al.* (2017a, b) that describes how existing landslides can have a legacy effect that influences the locations of future landslides (Samia *et al.* 2020). Specifically, it describes how future landslides have a transiently increased likelihood of occurring within or across an existing landslide. Such path dependent landslides, termed here as spatially associated landslides, are also expected to have different geometric, size, and spatial characteristics to non-path dependent, or spatially unassociated, landslides (Samia *et al.* 2017b). This study considers both aspects of path dependency. In Chapter 4, which considers the temporal aspects of landslide occurrence, the metrics proposed by Samia *et al.* (2017b) (see Chapter 4, section 4.2.1) are used to quantify whether the landslides in the ASM-inventory are actually influenced by path dependency (i.e. whether new landslides overlap with existing landslides more than would be expected if their distributions were random). However, this chapter considers whether spatially associated landslides have different geometric, size, and spatial distributions compared to spatially unassociated landslides. To do this, landslides in the inventory are classified into three types: 1) spatially associated (within), which are those landslides that occur fully inside a previous landslide; 2) spatially associated (partial), which are those landslides that occur partially within (i.e. cross the boundary of) a previous landslide, and 3) spatially unassociated, which are those that occur completely outside of a previous landslide (e.g. Fig. 2.7a - c). These types were defined using the ArcGIS “Select by Location” tool, which identifies all landslides that were fully within or intersecting a landslide polygon from a previous time slice within the last 30 years. All landslides not occurring within or intersecting a previous landslide were classified as being spatially unassociated. Finally, it should be noted that path dependency determination has previously been shown to be dependent on the spatial and temporal resolution of the landslide data used to assess it. For example, Roberts *et al.* (2021) find that the rates and magnitudes of path dependency

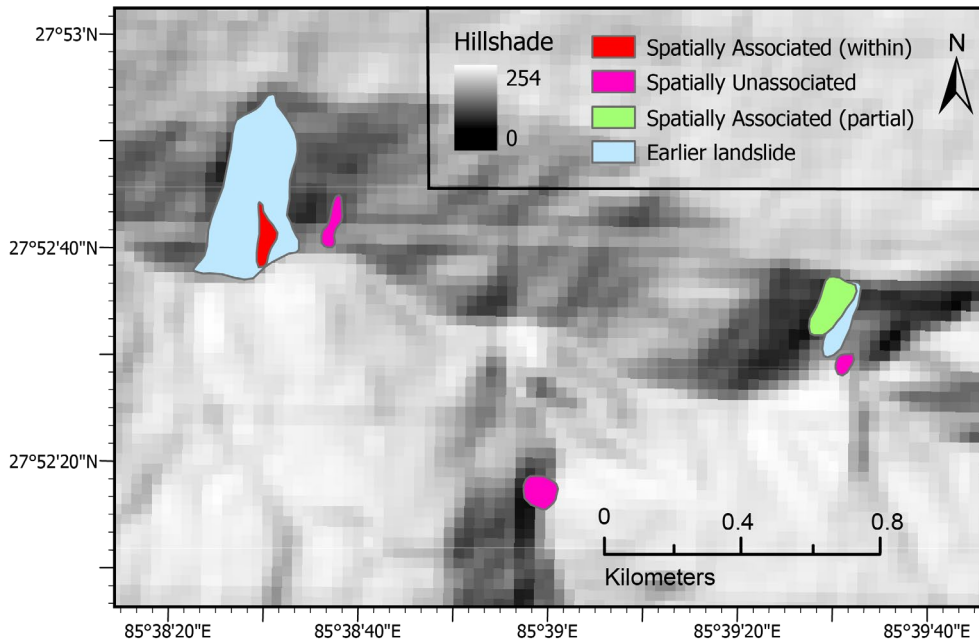


Figure 2.7. Examples of landslide path dependency types.

metrics are sensitive to inventory length, study region size and the size/type of landslides mapped. As such, all path dependency results presented and discussed throughout this thesis should be considered in the context of the characteristics and spatial and temporal resolutions of the ASM-inventory (i.e., annual 30-year temporal resolution, 15-30 m spatial resolution, 45,000 km² study, and inclusion of only recent rainfall-triggered landslides without larger scale relict failures).

2.4.2 Landslide geometry

Landslide geometries and shapes are known to vary significantly between trigger-types, landslide types and geomorphic settings (e.g., Taylor *et al.* 2018) and across landslides of different path dependency types (e.g., Samia *et al.* 2017b). Here, landslides geometries within the ASM-inventory are quantified according to two metrics: Aspect Ratios (AR) and roundness. In essence, both metrics allow a basic quantification of landslide shape, which as outlined in the section below can provide useful insight into landslide type in the absence of field validated landslide observations. The aspect ratio essentially defines the degree of landslide elongation, i.e., whether a landslide is round (ratio of 1) or tending towards “long and thin” (a high aspect ratio). Similarly, as outlined in the sections below, roundness is a basic

measure of landslide shape that defines how close to perfectly round a landslide is (e.g., Samia *et al.* 2017b). It should also be noted that other methods do exist for quantifying landslide shape. For example, Taylor *et al.* (2018) present an updated methodology for assessing landslide shape using various assumptions of landslide ellipticity. However, the method used by Taylor *et al.* (2018) is more time-consuming to undertake and, as it is a newer methodology, has been less commonly applied to other landslide datasets. Consequently, as the geometric analysis forms only a minor part of this project, it was decided that the more time-efficient and commonly used AR and roundness methods were more appropriate, as these allow a quick and unbiased comparison of our data to other data sets in the literature. However, given the extensive nature of the ASM-inventory, it is acknowledged that assessing the geometries using other methods such as that presented by Taylor *et al.* (2018) would be an interesting area of future study.

2.4.2.1 Aspect Ratio (AR)

In the literature, 2-D landslide shape is commonly described by the landslide aspect ratio (length/width) (e.g., Parise & Jibson 2000; Tian *et al.* 2017, 2020; Roback *et al.* 2018, Taylor *et al.*, 2018). To obtain landslide lengths and widths, the ArcGIS Pro Minimum Bounding Geometry tool was used to fit convex hulls (the smallest convex polygon that encloses a given feature) to each landslide polygon. The widths (shortest distance between two vertices of the convex hull) and lengths (longest distance between two vertices of the convex hull) were then extracted, and the ARs calculated. Then, following the example of Tian *et al.* (2020) each landslide was classified into one of three geomorphic types: AR1 ($L/W \leq 2$), AR2 ($2 < L/W \leq 4$) and AR3 ($L/W > 4$) (e.g., Fig. 2.8a - c). Type AR1 represents isometric landslides with short run-outs, likely dominated by slumps and rotational slides, whilst Type AR2 represents more longitudinal landslides with moderate run-outs, likely dominated by translational slides and soil slips (Parise & Jibson 2000). Type AR3 represents elongated long-runout landslides that are likely dominated by flows. It should be noted that this method always assumes that the longest axis is downslope, and thus that the AR can never be less than one. Consequently, this method does not account for “short-fat”

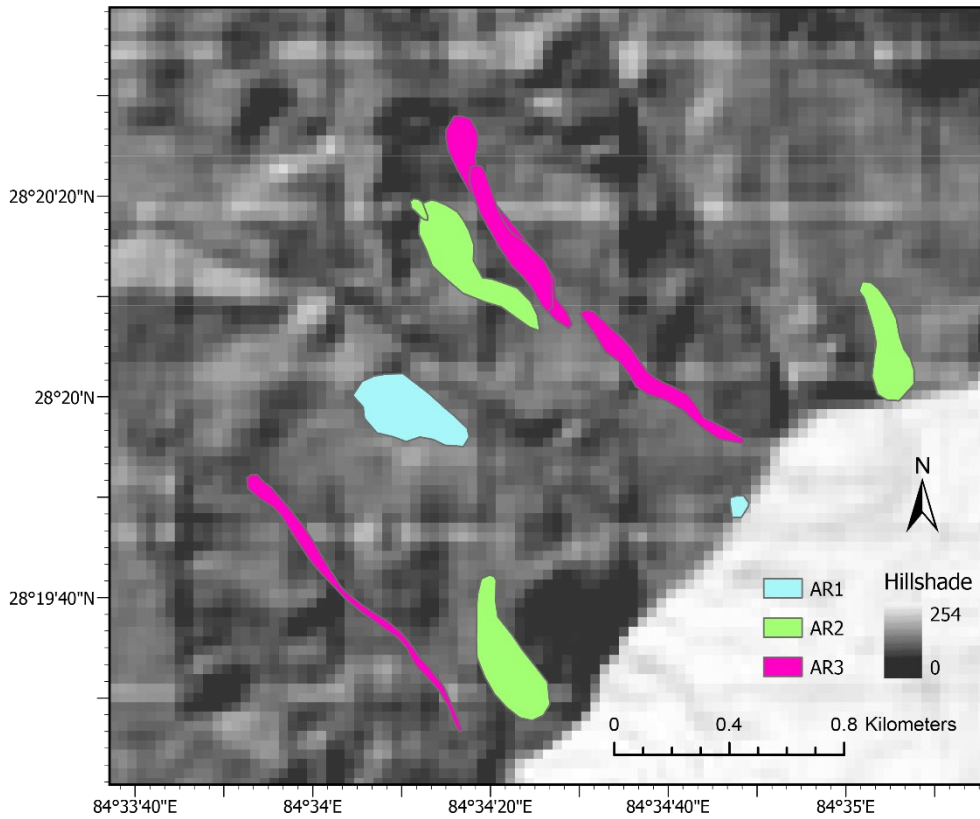


Figure 2.8. Examples of landslide Aspect Ratio (AR) types, where AR1 has $L/W < 2$, AR2 has $L/W = 2 - 4$, and AR3 has $L/W > 4$.

landslides which have a long-axis perpendicular to the slope. However, by comparing how the orientation of the long-axis compares to the aspect of the hillslope on which it occurs, it is possible to assess how many of such “short-fat” landslides are in the inventory. It is found that 99.4% of the landslides have a long-axis orientated within 75° of the hillslope aspect, and of the 0.6% that do not, only 37 landslides had an $AR > 2$, i.e., had a long-axis significantly longer than the short-axis and not orientated downslope. As such, this methodology sufficiently accounts for the vast majority of landslides.

2.4.2.2 Roundness

Roundness is a basic measure of shape introduced by Samia *et al.* (2017b) that quantifies important differences between landslide geometries without making assumptions about underlying landslide shape. Samia *et al.* (2017b) define roundness as:

$$\text{Roundness} = \frac{\text{theoretical circular perimeter}}{\text{actually measured perimeter}}$$

Equation 2.2. Roundness.

Where, the theoretical circular perimeter is the perimeter a landslide would have had if it was perfectly round with the same area (A_L):

$$\text{Theoretical circular perimeter} = 2\pi \sqrt{\left(\frac{A_L}{\pi}\right)}$$

Equation 2.3. Theoretical Circular Perimeter.

A value of one would indicate that a landslide was perfectly round, whereas values approaching zero represents increasingly elongate, or long-runout, landslides. Roundness values were calculated using Equations 2.2 and 2.3 from the areas and perimeters obtained for each landslide using standard GIS geometry tools.

2.4.3 Landslide size

Landslide size distributions are typically characterised according to the probability density function of landslide areas $p(A_L)$ (Malamud *et al.* 2004b):

$$p(A_L) = \frac{1}{N_{LT}} \frac{\partial N_L}{\partial A_L}$$

Equation 2.4. Probability density function of landslide area.

Where N_{LT} is the total number of landslides in the inventory, A_L is landslide area, and δN_L is the number of landslides with areas between A_L and $A_L + \delta A_L$. Landslide area probability density functions typically exhibit power-law decay with exponential roll-over at smaller landslide areas that can be modelled by a three-parameter inverse-gamma distribution, as defined by:

$$pdf(A_L|\alpha, \eta, \lambda) = \left[\frac{\lambda^{2\alpha}}{\Gamma(\alpha)}\right] \left[\left(\frac{1}{x + \eta^2}\right)^{(\alpha+1)}\right] \exp\left[-\frac{\lambda^2}{x + \eta^2}\right]$$

Equation 2.5. Three-parameter inverse-gamma distribution.

Where α controls the exponent of the three-parameter inverse-gamma power law (i.e., the steepness of the right tail of the power-law), η controls the steepness, or bend, of the left-side tail of the distribution, and λ controls the position of the rollover (Malamud *et al.* 2004a, b; Taylor *et al.* 2018). The position of the rollover, which represents the size of the most frequent landslides, is typically used as a way

of comparing the completeness of different inventories as it indicates the landslide area below which the three-parameter inverse-gamma distribution decay observed for medium and larger landslides no longer applies. The exponent of the three-parameter inverse-gamma distribution describes the rate at which the probability of getting proportionally larger landslides decreases. A larger exponent indicates that the probability of getting larger events is decreasing quickly, and thus that proportionally larger landslides are contributing less to each inventory. Conversely, a smaller exponent indicates that the probability of getting larger events is decreasing more slowly, and thus that larger landslides are contributing more to each inventory (Van Den Eeckhaut *et al.* 2007a; Borgomeo *et al.* 2014). Finally, η can be physically understood as describing the likelihood of getting smaller landslides, with a higher value of η equating to a 'heavier tail' (i.e., the left-hand tail dies off more slowly), where the likelihood of getting smaller landslides is decreasing more slowly (Taylor *et al.* 2018).

Here, the LANDSTAT/LAMPRE software (version 10; Rossi & Malamud 2014) is used to fit the three-parameter inverse-gamma distribution (Malamud *et al.* 2004a; Equation 2.5) to the probability density functions of the entire ASM-inventory, as well as to eight subsets of the inventory. These subsets were types AR1, AR2, AR3, spatially associated (partial) and spatially unassociated, as well as for landslides subdivided by the tectonic unit in which they occurred; the Sub-Himalaya, Lesser Himalaya, Greater Himalaya and Tethyan Himalaya. This software uses Maximum Likelihood Estimation (MLE) to optimise the parameters of the probability density function and a bootstrapped (here with 1000 simulations) Kolmogorov-Smirnov (K-S) test to estimate parameter uncertainty and overall goodness of fit of the inventory data to the fitted distribution. This goodness of fit is given by the p- and D-values of each case. If the p-value is > 0.01 , then the null hypothesis that the actual data can be well fitted with a three-parameter inverse-gamma distribution cannot be rejected, whilst the D-value represents that largest distance between the actual data and the fitted three-parameter inverse gamma distribution. This approach was found to require approximately 200 landslides in a given dataset to obtain a robust fit.

2.4.4 Landslide spatial distributions

Quantifying the controls and characteristics of landslide spatial distributions is a vital component of landslide susceptibility, hazard, and risk analysis. In this section, two methods are used to investigate landslide spatial distributions. First, frequency analysis is used to quantify how individual predisposing factors are controlling landslide occurrence. Second, Anselin Local Moran's I analysis is used to identify any significant spatial clusters of landslides occurring at high or low attribute values across the study region.

2.4.4.1 Predisposing factor frequency analysis

As outlined in Chapter 1 (section 1.4.3.1), it is expected that various predisposing factors will influence landslide occurrence. The aim of predisposing factor frequency analysis is to better understand how individual predisposing factors might be controlling landslide occurrence. This is achieved by first dividing each predisposing factor into bins (e.g., slope could be divided into 18 five-degree bins from 0 – 5° to 85 – 90°), and then calculating the frequency and proportion of the study region and landslides that fall within each bin. If a predisposing factor has no influence on landslide occurrence, then the proportions of landslides and study region in each bin should be equal. Conversely, if a predisposing factor does have an influence on landslide occurrence, then there should be some disparity between the proportions of landslides and the study region in each bin. If a bin has a high proportion of the total landslides, then if a landslide was picked from the inventory at random, that landslide would have a higher percentage chance of having occurred within that bin.

To do this, the control factor rasters from section 2.3.2 were divided into the bins shown in Table 2.5 using the ArcGIS reclassify tool. The counts from the attribute tables of these rasters were then used to obtain the proportion of the study region that fell within each bin of each predisposing factor. A single predisposing factor value was then assigned to each landslide, where the assigned value corresponded to the highest point along each landslide crest, i.e., where it is assumed that landslide failure initiated (Lombardo & Mai 2018). The highest point of each landslide polygon was extracted using standard ArcGIS zonal statistic and raster calculator tools, and

the predisposing factor values at each of those points were extracted to the inventory attribute table using the Extract Multi Values to Points tool. The proportion of landslides in each bin of each control factor were then calculated from the attribute table. The bin-proportions for specific geometric, path dependent and tectonic

Factor	Bin	Code	Factor	Bin	Code	Factor	Bin	Code
Aspect	FLAT	1	Elevation (m)	0 - 400	1	Near channel k_{sc}	0 - 500	1
	N	2		400 - 800	2		500 - 1000	2
	NE	3		800 - 1200	3		1000 - 1500	3
	E	4		1200 - 1600	4		1500 - 2000	4
	SE	5		1600 - 2000	5		2000 - 2500	5
	S	6		2000 - 2400	6		2500 - 3000	6
	SW	7		2400 - 2800	7		3000 - 3500	7
	W	8		2800 - 3200	8		3500 - 4000	8
	NW	9		3200 - 3600	9		4000 - 4500	9
	N	10		3600 - 4000	10		4500 - 5000	10
Average annual precipitation (1988 - 2018) (mm)	500 - 600	1	4000 - 4400	11	5000 - 5500	11		
	600 - 700	2	4400 - 4800	12	5500 - 6000	12		
	700 - 800	3	4800 - 5200	13	6000 - 6500	13		
	800 - 900	4	5200 - 5600	14	6500 - 7000	14		
	900 - 1000	5	5600 - 6000	15	7000 - 7500	15		
	1000 - 1100	6	6000 - 6400	16	> 7500	16		
	1100 - 1200	7	6400 - 6800	17	0	1		
	1200 - 1300	8	6800 - 7200	18	Permafrost Index (PFI)	0.25	2	
	1300 - 1400	9	7200 - 7600	19	0.5	3		
Distance to channels (m)	0 - 100	1	7600 - 8000	20	0.75	4		
	100 - 200	2	8000 - 8400	21	1	5		
	200 - 300	3	8400 - 8800	22	0 - 5	5		
	300 - 400	4	Excess topography (m ³)	0 - 50	1	5 - 10	10	
	400 - 500	5		50 - 100	2	10 - 15	15	
	500 - 600	6		100 - 150	3	15 - 20	20	
	600 - 700	7		150 - 200	4	20 - 25	25	
	700 - 800	8		200 - 250	5	25 - 30	30	
	800 - 900	9		250 - 300	6	30 - 35	35	
	900 - 1000	10		300 - 350	7	35 - 40	40	
	1000 - 1100	11		350 - 400	8	40 - 45	45	
	1100 - 1200	12		400 - 450	9	45 - 50	50	
	1200 - 1300	13		450 - 500	10	50 - 55	55	
	1300 - 1400	14		500 - 550	11	55 - 60	60	
	1400 - 1500	15		550 - 600	12	60 - 65	65	
	> 1500	16		600 - 650	13	65 - 70	70	
Distance to roads (m)	0 - 500	1		650 - 700	14	70 - 75	75	
	500 - 1000	2		700 - 750	15	75 - 80	80	
	1000 - 1500	3		> 750	16	80 - 85	85	
	1500 - 2000	4	Local Relief (m)	0 - 200	1	85 - 90	90	
	2000 - 2500	5		200 - 400	2	Geology	Dolomites	1
	2500 - 3000	6		400 - 600	3		Granite/gneisses	2
	3000 - 3500	7		600 - 800	4		Phyllites	3
	3500 - 4000	8		800 - 1000	5		Quaternary SS / cong	4
	4000 - 4500	9		1000 - 1200	6		Marbles	5
	4500 - 5000	10		1200 - 1400	7		Schists	6
	5000 - 5500	11		1400 - 1600	8		Quartzites	7
	5500 - 6000	12		1600 - 1800	9		Shales	8
	6000 - 6500	13		1800 - 2000	10		Undifferentiated	9
	6500 - 7000	14		2000 - 2200	11	Landuse	Cropland	1
	7000 - 7500	15		2200 - 2400	12		Forest	2
	7500 - 8000	16		2400 - 2600	13		Shrub/grass	3
Profile curvature	Lat Concave	1		2600 - 2800	14		Barc / sparse	4
	Lat Convex	2		>2800	15		Water	5
Planform curvature	Up Convex	1					Snow/ice	6
	Up Concave	2	Artificial		7			

Table 2.5. Summary of bin classifications for all predisposing factors of interest.

subsets of the landslide inventory were also calculated to assess if there were any differences in control factor influence across landslide types. Finally, the proportions of the study region and landslide subsets were plotted together, and any significant controls identified.

2.4.4.2 Anselin Local Moran's I

The frequency analysis quantifies the average influence across the entire dataset of different predisposing factors on landslide distributions. Consequently, it does not give any indication of whether there are any spatial structures to landslide distributions. For example, is the influence of a predisposing factor homogenous across the study region? Or are landslides occurring at different values of a given predisposing factor depending on their location?

The Anselin Local Moran's I statistic answers these questions by identifying whether landslide values for a given attribute are part of statistically significant clusters of high or low values, or are spatial outliers. This allows quantification of whether landslides are clustering with respect to high or low values of a given attribute, and, if so, where those high or low clusters are occurring. This tool can also be used to investigate clustering of landslide characteristics such as area, AR or roundness, thus providing vital insight into the potential coincidence between the spatial structures of landslide characteristics and landslide predisposing factors.

This analysis was undertaken using the ArcGIS Pro Cluster and Outlier Analysis (Anselin Local Moran's I) spatial statistics tool. For each attribute of interest (a landslide characteristic or predisposing factor), this tool calculates for each landslide the local Moran's I value by comparing the attribute value at each landslide point to the attribute values of its neighbours. A positive Moran's I value with a significant p-value indicates that the attribute value of that landslide is part of a high-high or low-low cluster (i.e. a cluster of landslides which all have either high or low values of a given attribute). Conversely, a negative Moran's I value with a significant p-value indicates that the attribute value of that landslide is a spatial outlier, i.e., a landslide with a high value of a given attribute surrounded by landslides with a low value of a given attribute, or vice versa. If a Moran's I value does not have a significant p-value,

it indicates that the spatial distribution of the landslide attribute value relative to its neighbours is consistent with what would be expected from a random distribution. To ensure that the critical p-value thresholds are robust, a False Discovery Rate (FDR) correction was applied, which is designed to reduce the likelihood that false clusters are identified and has been confirmed by empirical data to be the optimal approach for correcting for spatial dependence (Caldas de Castro & Singer 2006). The obtained p-values are obtained using a number of permutations, where, for each permutation, the Moran's I value for each feature is calculated based on a random distribution of neighbourhood attribute values around that feature. The p-value is then obtained based on the probability that the actual Moran's I value could be observed in the random distributions. Increasing the number of permutations increases the precision of the p-value. In this case, the maximum of 9999 permutations was used.

2.5 Methods: susceptibility modelling

Landslide susceptibility models are a fundamental component of landslide hazard management and mitigation strategies that are used to forecast the likely geographic locations of future landslides (Guzzetti *et al.* 2006). In this thesis, logistic regression-based susceptibility models are developed for the entire ASM-inventory in this chapter, a coseismic landslide inventory in chapter 3, and to various spatial and temporal subsets of these inventories in chapters 3 and 4. As outlined in the introduction and throughout this thesis, Binary Logistic Regression (BLR) methods are the most commonly used in the literature for assessing landslide susceptibility. As such, it is particularly important to assess and challenge commonly held assumptions associated with this methodology.

This section gives an overview of the main principles of landslide susceptibility modelling, before describing the methodology used here to develop logistic regression-based susceptibility models implemented alongside a LASSO (Least Absolute Shrinkage and Selection Operator) for variable selection.

2.5.1 Principles of landslide susceptibility modelling

The purpose of landslide susceptibility modelling is to forecast where landslides are likely to occur based on the local landscape conditions (Guzzetti *et al.* 2005; Reichenbach *et al.* 2018). As outlined in Chapter 1 (section 1.2), landslide susceptibility models can be developed using physically based techniques (e.g., Goetz *et al.* 2011; Park *et al.* 2019; Wang *et al.* 2019) or statistical approaches (e.g., Baeza & Corominas 2001; Lee *et al.* 2008; Aditian *et al.* 2018; Reichenbach *et al.* 2018). However, as physically based techniques require vast quantities of empirical geotechnical data, statistical approaches are often the only viable method to assess landslide susceptibility across regional to global scales or in data-scarce locations. Most statistical landslide susceptibility approaches utilise the principals of uniformitarianism, whereby it is assumed that, for a given region and trigger type, the spatial distributions of past landslides will be sufficiently similar to those of future landslides so as to facilitate basic prediction (Aleotti & Chowdhury 1999). Typically, statistical susceptibility models are trained using past landslide data contained within either event, seasonal or historical inventories (Guzzetti *et al.* 2012a; see section 2.2.1). Landslide susceptibility models can be applied across a range of spatial scales (Cascini 2008), from slope units (e.g., Alvioli *et al.* 2016; Amato *et al.* 2019) to catchments (e.g., Conforti *et al.* 2012; Romer & Ferentinou 2016) to nations (e.g., Sabatakakis *et al.* 2013; Thi Ngo *et al.* 2020) and even globally (e.g., Lin *et al.* 2017; Stanley & Kirschbaum 2017).

There are many methods that can be used to develop statistical landslide susceptibility modelling, including classical statistics, machine learning, neural networks and decision analysis (Reichenbach *et al.* 2018). A comprehensive review of the landslide susceptibility literature by Reichenbach *et al.* (2018) found that most common approaches were classical statistics, specifically logistic regression modelling. As such, Binary Logistic Regression (BLR) methods are used throughout this thesis to model landslide susceptibility. The principles and methodologies of the BLR approach are outlined in the following sections.

2.5.2 Principles of Binary Logistic Regression (BLR) modelling

Regression analysis aims to predict the relationship between a dependent response variable (Y) and a given set of independent (or predictor) variables (X). Logistic regression is a specific classification algorithm used when predicting a binary outcome. In this case, the binary outcome is that the response variable (Y), has two possible outcomes, landslide presence, or absence. In logistic regression, the probability that Y takes a value of one (π) (i.e. in this case that a landslide is present) can be calculated from Equation 2.6:

$$\varphi(\pi) = \beta_0 + \beta_1 x_1 \dots + \beta_i x_i$$

Equation 2.6. Binary regression equation.

Where φ is the link function that relates the linear predictors on the right hand side of Equation 2.6 to π , the probability that Y takes a value of one (Lombardo & Mai 2018). In BLR, this link function (Equation 2.7) is the logit, or log-odds, function where:

$$\varphi(\pi) = \log_b \left(\frac{\pi}{1-\pi} \right)$$

Equation 2.7. Log-odds function.

Substitution of Equation 2.7 into Equation 2.6 and rearrangement for π gives equation 2.8:

$$\pi = \frac{1}{1 + b^{-(\beta_0 + \beta_1 x_1 + \dots + \beta_i x_i)}}$$

Equation 2.8. Rearranged binary logistic regression equation.

Where, b is the base of the logarithm, β_0 is the y-intercept, or the log-odds of obtaining Y = 1 when all predictors are zero. β_i are the regression coefficients of each independent predictor, x_i . When the regression coefficients, β_i , are negative, the predictor x_i has a negative effect on the probability of Y = 1 (i.e. make landslide occurrence less likely), whilst positive regression coefficients have a positive effect on the probability of Y = 1.

2.5.3 The LASSO

A major consideration when developing BLR models is the number of independent variables (the $\beta_0 \dots \beta_i$ portion of Equation 2.8) to include within the model. In the context of landslide susceptibility, all independent variables should have a physical reason for why they would be expected to influence landslide occurrence. However, as outlined by Reichenbach *et al.* (2018), there are over 596 named independent variables that have been used in the literature. There is often a tendency to assume that the more independent variables used the better the resulting model. However, whilst adding more variables can increase model fit, doing so can lead to overfitting, whereby a developed model is too complex and specific to a single dataset, and thus loses its generalizability and ability to predict other datasets.

A common approach to independent variable selection is to rely fully on user expertise (e.g. Aditian *et al.* 2018), often with a user-defined iterative stepwise method of factor inclusion and exclusion. This approach is often acceptable, but could be problematic if the user is unaware of some local conditions or transient landscape change. As such, a more objective approach is to use automatic selection procedures (e.g. Brenning 2005; Carrara *et al.* 2008; Costanzo *et al.* 2012), such as the LASSO (Least Absolute Shrinkage and Selection Operator) (e.g. Lombardo & Mai 2018), to derive the optimal combination of factors for a given landside dataset.

Here, BLR models are implemented alongside a LASSO for covariate selection using the *glmnet* package within the statistical software, R. The LASSO is based on an algorithm that uses cyclical coordinate descent (Friedman *et al.* 2010) to optimise the objective function using 10-fold cross-validated penalised maximum likelihoods (Hastie & Qian 2014). This achieves automatic factor selection by cycling through different combinations of zero and non-zero set factors until convergence on an optimal solution that balances model fit and number of selected variables (Friedman *et al.* 2010). In other words, the algorithm cycles through multiple different combinations of independent variables (landslide predisposing factors) by systematically setting some factors to zero, until it converges on the optimum solution (Friedman *et al.* 2010). In these models, the optimal solution is the

maximum obtained self-validated model success rate minus one standard error. The success rate is obtained from the Area Under Receiver Operator Curve (AUROC; see section 2.5.5) of each model, i.e. the success of each model at classifying the data used to train that model. As the maximum success rate will by definition always include all inputted variables, by taking the model configuration at the maximum success rate minus one standard error, the algorithm balances model fit and number of selected variables. The advantage of this methodology is that as well as getting results on factor coefficients, the model provides information about which factors were deemed by the model to be most significant in predicting landslide occurrence, all whilst avoiding overfitting. The following section now describes the specific methodology used to implement the BLR-LASSO model.

2.5.4 Model implementation within glmnet

Before running the BLR-LASSO model within glmnet, all landslide and predisposing factor data require processing. First, the study region is divided into a grid of cells, which at a 30 x 30 m resolution produces a grid of $\sim 5 \times 10^7$ cells for the entire study region. All grid-cells are then assigned a value of one if they include a landslide (landslide presence) and a value of zero if not (landslide absence).

All predisposing factor datasets to be included in the model must then be resampled to the same resolution as the grid used to divide the study region. Then, each grid-cell can be assigned a value for every predisposing factor of interest, such that every cell across the study region now has a landslide presence/absence value and a corresponding value for every control factor. The landslide presence cells then need to be split into two groups, with 70% of the presence cells randomly assigned to a training group, and 30% to a testing group. The training group can be used to develop the model, whilst the testing group can be used to validate model fit.

As the entire study region included a very large number of cells, it was computationally expensive to run every single cell through the model at once. As such, 50 smaller, balanced training and testing subsets of the main grid were extracted, where each subset included all of either the training or testing presence cells plus an equal number of randomly selected landslide absence cells. Each of these

subsets included information on landslide presence or absence, plus the associated values of 17 control factors. Of these 17 factors, two are categorical (geology and land use) and the rest are continuous.

To ensure the final regression coefficients calculated for each factor were objectively comparable, the continuous factors were then rescaled using zero-mean unit variance (e.g. Lombardo & Mai 2018). Furthermore, with so many factors, it was possible that some would be collinear. This is potentially problematic, as significant collinearity between factors can introduce error and instability into regression models (Zuur *et al.* 2010). As such, before inputting the training subsets into the glmnet model, collinearity between all factors in all 50 training subsets was tested for using the Variance Inflation Factor (VIF) functions of Zuur *et al.* (2010). The VIF is a common measure of multi-collinearity in a set of regression variables that is equal to the ratio of the variance in a multi-variable model to the variance of a model that only includes a single independent variable. VIF's can be calculated for each individual variable and a VIF > 5 suggests that the associated independent variable is highly collinear with at least one other variable in the model. Here, for each dataset, the VIF's for each independent control factor were calculated. Then, if any factors had VIFs > 5, the factor with the highest VIF was removed and the VIFs were recalculated for the remaining factors. This was repeated until all factors had VIFs < 5. In this case, the total rainfall factor was found to be highly collinear with peak rainfall, average rainfall, and elevation. Once total rainfall was removed, all other factors had VIFs < 5. It should be noted at this point that the term "independent variable" is statistical language to describe any variable that is being used to understand or model the target dependent variable. As such, as highlighted by the VIF analysis, the term "independent variable" does not preclude physical links existing between the different independent variables. However, any potential physical linkages between independent variables are only problematic for logistic regression type models if their effects on landslides are linear and highly correlated, hence why only those independent variables showing high VIF values are removed.

Finally, before running the glmnet model, the two categorical factors were coerced into dummy variables (i.e. presence / absence for each sub-category). Then, each of

the 50 processed training subsets were run through the glmnet model, where each model run used the 10-fold cross-validated LASSO for factor selection. In this case, the LASSO was programmed to obtain the maximum self-validated AUROC value (see section 2.5.5) minus one standard error. The resulting factor selections and associated regression coefficients were then averaged across all 50 models to get final estimates and uncertainties of factor selection and regression coefficients.

2.5.5 AUROC validation

AUROC (Area Under Receiver Operator Curve) validation was used to validate the results of the trained models. The ROC (Receiver Operating Curve) is a probability curve obtained by plotting the TPR (True Positive Rate) against the FPR (False Positive Rate). The TPR, which is commonly referred to as 'sensitivity', is in this case the proportion of landslide presences that were correctly classified as landslide presences, whilst the FPR, which is commonly referred to as '1 - specificity', is the proportion of landslide absences that were incorrectly classified as landslide presences. The area under the ROC (the AUROC value) indicates the degree to which a binary model correctly predicted the observed classes, in this case landslide presences and absences. An AUROC value of one indicates that a model was 100% accurate, whilst an AUROC value of 0.5 is equivalent to the result of a random predictor with no classification capacity. A value < 0.5 indicates that a model is actively reciprocating the classification, i.e. in this case would be predicting landslide absences as presences and vice versa. Typically, a model with an AUROC value of 0.7 - 0.75 is considered good, whilst a model with an AUROC value > 0.8 is considered very good.

Here, 10-fold cross-validation is used to estimate the overall accuracy of the trained models, whereby 100 cross validations between the 50 trained models and 50 testing datasets are undertaken. This was done using the 'pred' function in R, which, for a given pair of trained models and testing datasets, uses the regression coefficients from the trained model to forecast or hindcast the probabilities from the testing dataset. The AUROC can then be calculated by comparing the predicted probabilities for the testing dataset with the actual occurrences of landslides within

that dataset. Using 10-fold cross-validation, this gives 100 ROC curves and associated AUROC values per set of 50 models.

2.5.6 Susceptibility map production

Once all 50 training models for a given situation had been run and validated, a full susceptibility map of the region was produced from the average regression coefficients of all factors selected at least 50% of the time across all 50 trained models. To do this, the ArcGIS raster calculator was used to create zero-mean normalised rasters of each continuous factor. The raster calculator was then used to calculate probability values for each cell across the study region using Equation 2.8, where the β_i coefficients were the average regression coefficients across all 50-models for the factors selected >50% of the time, and x_i were the zero-mean normalised rasters of each corresponding factor.

2.6 Results: inventory analysis and susceptibility modelling

The following sections describe the overall characteristics and distributions of all landslides within the ASM-inventory using the methodologies presented in sections 2.4 and 2.5. Note that of the 12,838 landslides in the ASM-inventory, 13% (1725) occurred in the sub-Himalaya, 45% (5800) in the Lesser Himalaya, 40% (5133) in the Greater Himalaya and < 2% (179) in the Tethyan Himalaya (Fig 2.9a).

2.6.1 Landslide path dependency

Of the 12,838 landslides in the ASM-inventory, 86% (10,977) of landslides were spatially unassociated, 14% (1816) were spatially associated (partial) and 0.35% (45) were spatially associated (within) (Fig. 2.9b). The varying characteristics and distributions of these types are described across the following sections.

2.6.2 Landslide geometry

2.6.2.1 Aspect Ratio (AR)

Across all 12,838 landslides, AR values range between 1.1 – 15.4, with 45% (5808) of landslides of type AR1 ($AR \leq 2$), 44% (5591) of type AR2 ($2 < AR \leq 4$), and 11% (1439) of type AR3 ($AR > 4$) (Fig. 2.9c).

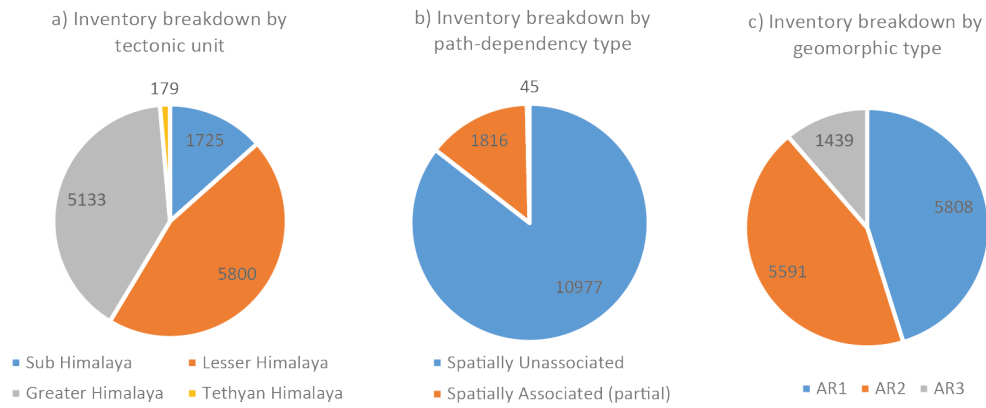


Figure 2.9. Number of landslides in each tectonic unit (a), and of each path dependent type (b) and AR type (c).

The variation in AR type across the different path dependent and tectonic subsets of the inventory was also quantified (Fig. 2.10). For all path dependent subsets, type AR3 (long runout) landslides are least common. However, whilst the proportions of types AR1 and AR2 are broadly the same for the spatially unassociated and spatially associated (within) subsets, if picked at random from the inventory, a landslide of type AR2 has a 7% higher likelihood than type AR1 of being spatially associated (partial). For the tectonic unit subsets, there is a systematic decrease in the proportion of AR1 type landslides in the Sub to Lesser to the Greater Himalaya, with a corresponding increase in types AR2 and AR3.

2.6.2.2 Roundness

The mean roundness values for most subsets ranges between 0.77 and 0.83, with an average of 0.8 across the entire dataset (Fig. 2.11). The spatially associated (partial) landslides had lower roundness values than the spatially unassociated and spatially associated (within) types (0.77 compared to 0.8). For the tectonic units, mean roundness systematically decreases from the Sub to Lesser to Greater Himalaya, whilst the Tethyan Himalaya have a roundness similar to that in the Sub Himalaya. For roundness by AR type, mean roundness values are 0.89 for AR1, 0.76 for AR2 and 0.52 for AR3. This is unsurprising given that the AR and roundness are both metrics that quantify degree of elongation or ellipticity.

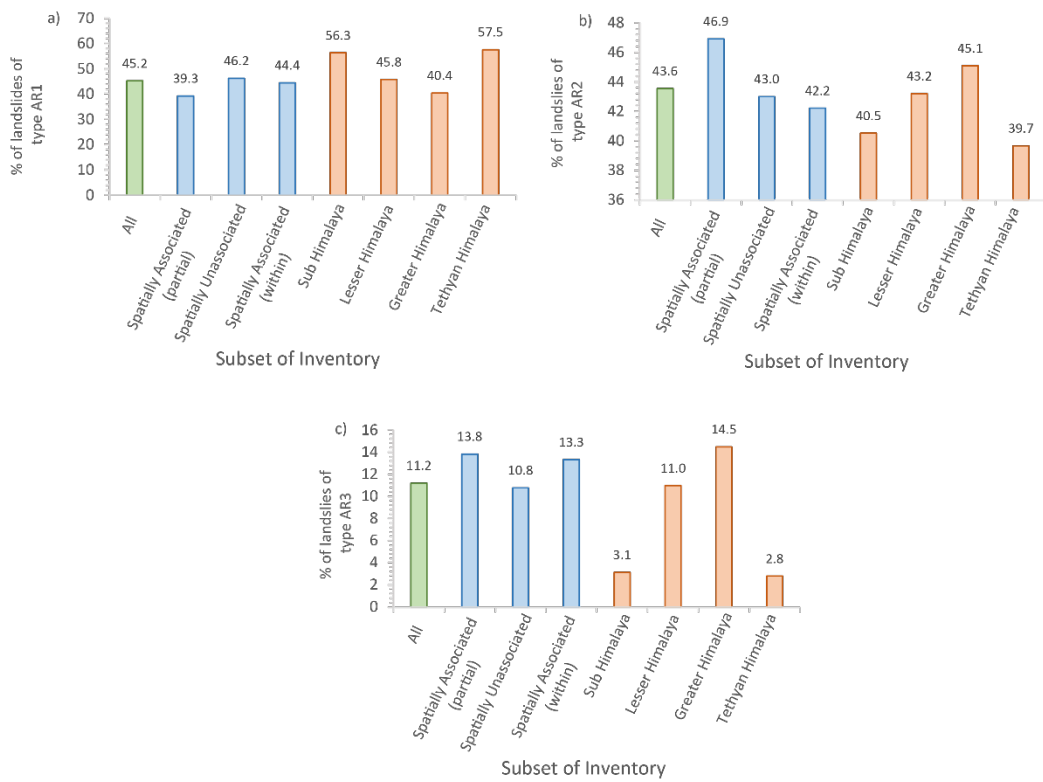


Figure 2.10. Proportions of all landslides, landslides in each tectonic unit, and landslides of each path dependent type that are of geometric type a) AR1, b) AR2, and c) AR3.

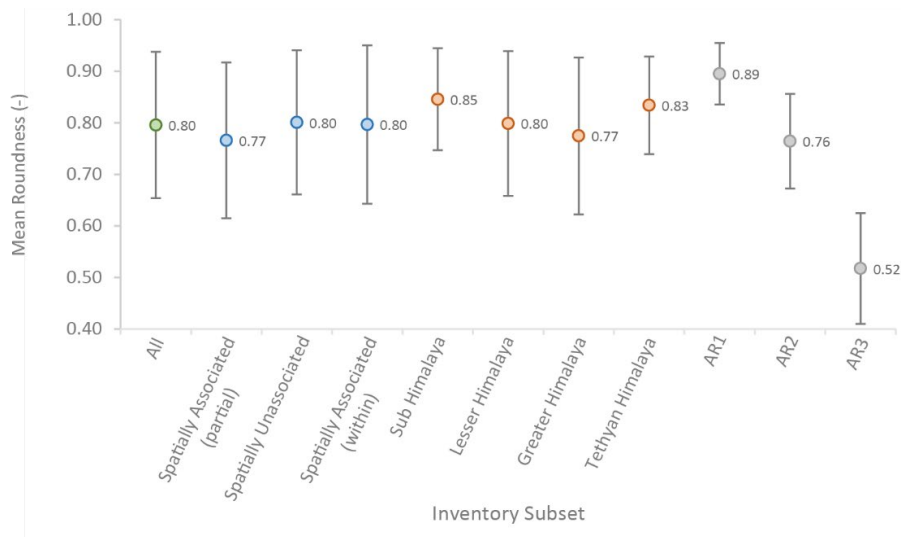


Figure 2.11. Mean roundness of all landslides, landslides in each tectonic unit, and of landslides of each path dependent and AR type.

2.6.3 Landslide size

Overall, the modal landslide area (as given by the rollover) for the entire inventory is 3000 m², with a maximum landslide area of ~685,000 m², and a power-law exponent (α) of 1.79 (Fig 2.12a; Table 2.6).

For the geomorphic types, AR1 landslides have the smallest modal landslide areas (rollovers) of ~2800 m², whilst AR3 have the largest modal areas of ~8300 m², (Fig 2.12; Table 2.6). This suggests that on average the AR3 type landslides are larger than less elliptically shaped landslides. This observation is corroborated by Fig. 2.13, where box plots of the relationship between AR and log-area show a general increase in mean AR as log-area increases. The exponent values for AR1 and AR3 are 2.18 and 2.19, respectively. These exponents are larger than for the overall ASM-inventory, suggesting that the largest landslides are overall contributing less to these distributions than to the entire dataset. The AR2 subset has similar characteristics to the overall inventory, suggesting that this group are generally the most representative of the average observed across the study region.

For the path dependency groups, the spatially associated (partial) landslides have a lower three-parameter inverse-gamma power law exponent (1.62) than spatially unassociated landslides (1.83). This suggests that proportionally larger landslides contribute more to the size distribution of the spatially associated (partial) landslides than for spatially unassociated landslides.

Within the geomorphic units, the Sub Himalaya have a three-parameter inverse-gamma power law exponent of 2.13 compared to 1.79 and 1.82 for the Lesser and Greater Himalaya respectively (Fig 2.14), suggesting that proportionally larger landslides are contributing more to the distributions of the latter. Note, the three-parameter inverse gamma distribution could not be fitted to the spatially associated (within) and Tethyan Himalaya subsets as both had too few landslides (45 and 179 respectively) to obtain significant results. Similarly, it should be noted that caution should be taken when interpreting the three-parameter inverse-gamma power law results for those cases with relatively few landslide cases (e.g., Fig 2.12 e). It is well described that the under-sampling of landslides can affect the characteristics of fitted

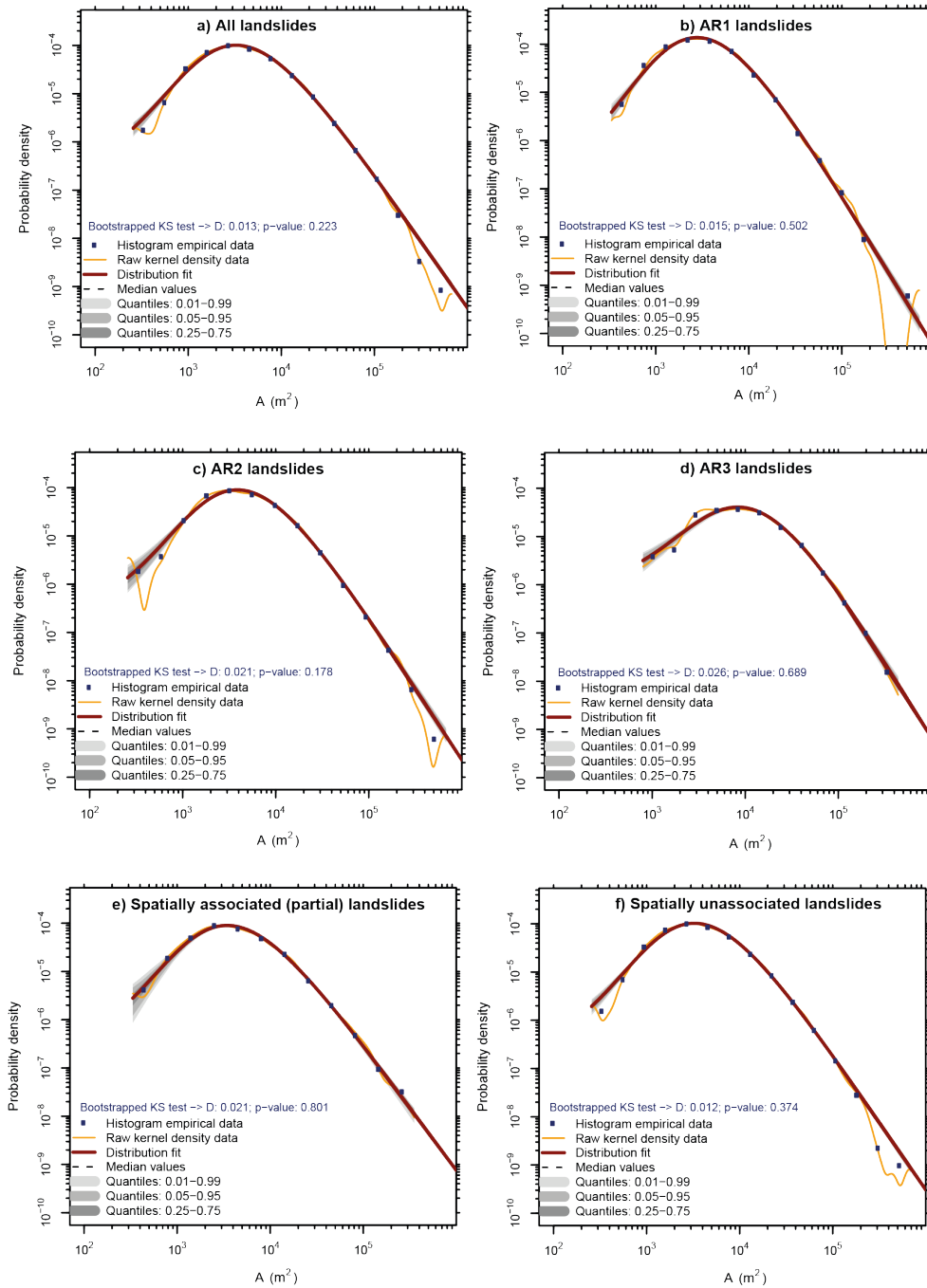


Figure 2.12. Three-parameter inverse-gamma distributions fitted to the probability density functions of landslide area for a) all landslides, b) AR1 landslides, c) AR2 landslides, d) AR3 landslides, e) spatially associated (partial) landslides, and f) spatially unassociated landslides. Note that a p -value > 0.01 indicates that the three-parameter inverse-gamma distribution provide a good fit to the actual data, whilst the D -value gives the maximum distance between the actual data and the fitted distribution.

	All	AR1	AR2	AR3	Partial	Outside	Sub Himalayas	Lesser Himalayas
n	12838	5808	5591	1439	1816	10977	1725	5800
Maximum area (m²)	684783	684783	680500	443661	354290	684783	212401	684783
α	1.79 +/- 0.032	2.18 +/- 0.062	1.99 +/- 0.057	2.17 +/- 0.13	1.62 +/- 0.074	1.83 +/- 0.036	2.13 +/- 0.11	1.79 +/- 0.047
η	29 +/- 0.89	26.8 +/- 1.21	32.8 +/- 1.49	57.2 +/- 4.17	29.3 +/- 2.41	29.1 +/- 0.97	26.2 +/- 2.04	25.9 +/- 1.36
λ	107 +/- 1.58	105 +/- 2.39	121 +/- 2.84	192 +/- 9.41	106 +/- 4.02	108 +/- 1.73	98 +/- 4.12	104 +/- 2.23
Rollover	3266	2764	3866	8346	3444	3256	2376	3213
p-value	0.223	0.502	0.178	0.689	0.801	0.374	0.145	0.916

Table 2.6. Summary size statistics and power-law parameters for the entire ASM-inventory and various inventory subsets.

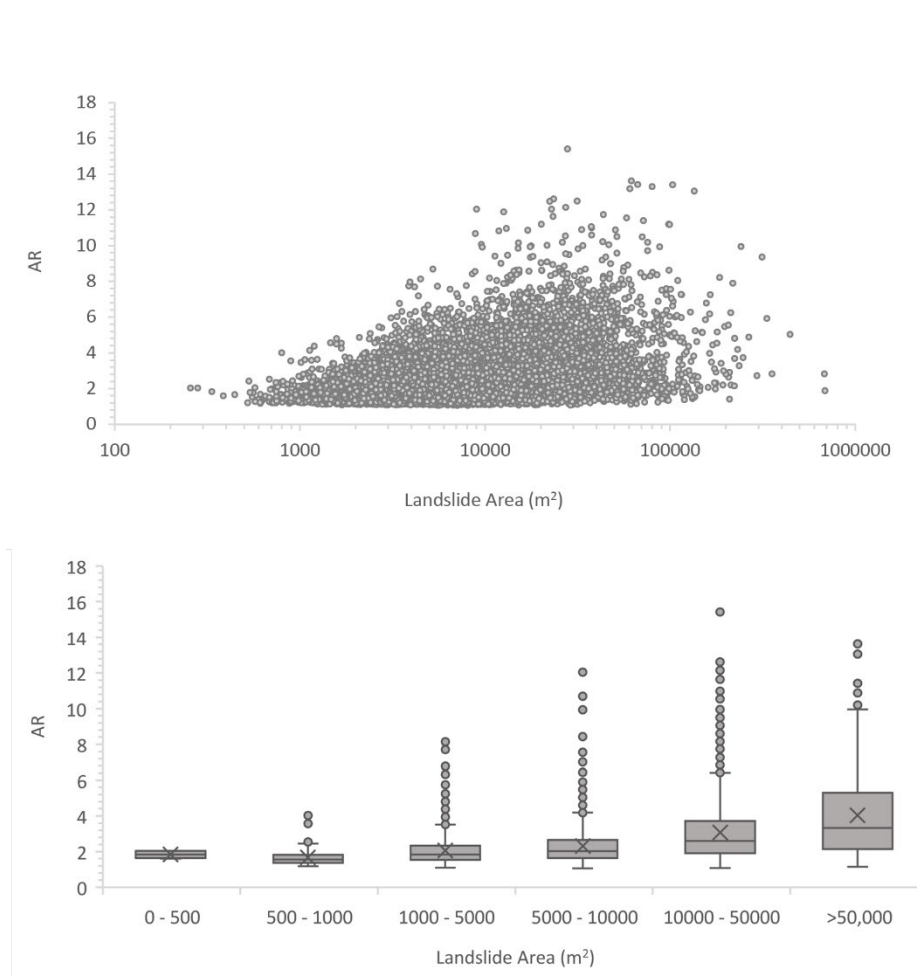


Figure 2.13. Relationship between AR and log-area for the entire ASM-inventory. Top shows raw data, bottom with those data binned into boxplots.

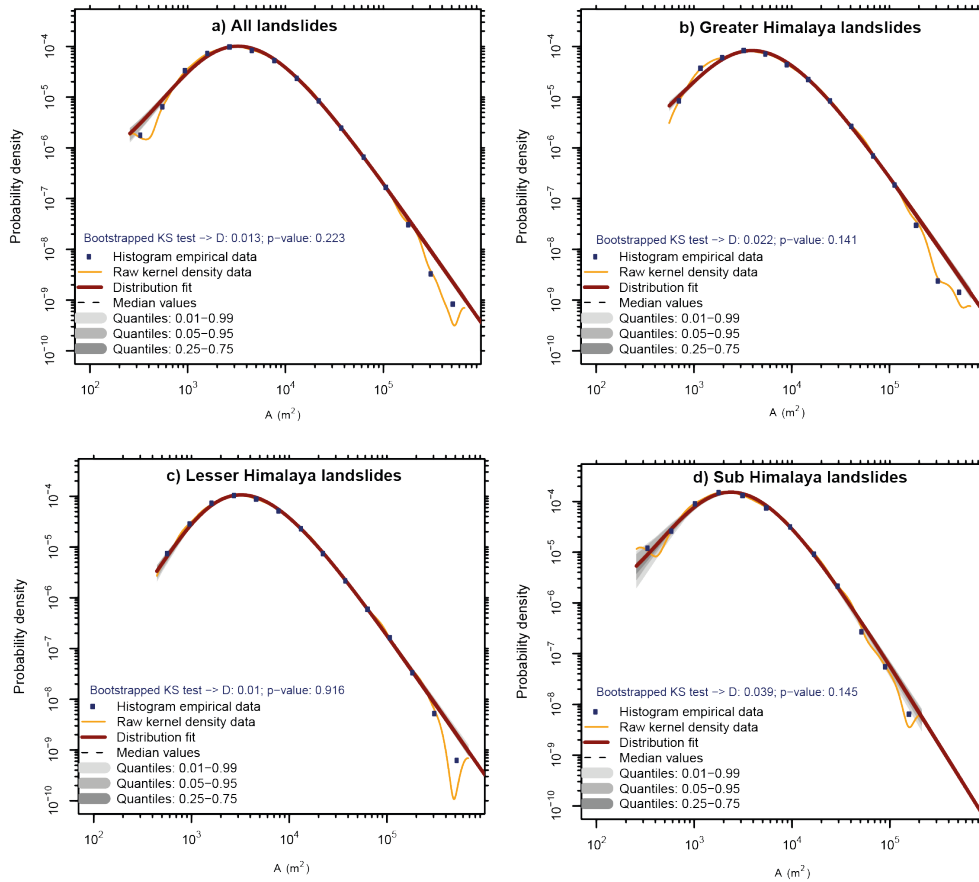


Figure 2.14. Three-parameter inverse-gamma distributions fitted to the probability density functions of landslide area for a) all landslides, and landslides in b) the Greater Himalaya, c) the Lesser Himalaya, and d) the Sub Himalaya. Note that a p -value > 0.01 indicates that the three-parameter inverse-gamma distribution provide a good fit to the actual data, whilst the D -value gives the maximum distance between the actual data and the fitted distribution.

power-law distributions (Stark & Hovius 2001), so the results from the cases with fewer landslides will be inherently more uncertain than those with a large number of landslides.

2.6.4 Landslide spatial distributions

2.6.4.1 Predisposing factor analysis

Figures 2.15 – 2.21, show the proportions of the study region, the entire ASM-inventory, and various subsets of the inventory that fall within each predisposing factor bin. If there is a high proportion of landslides in a given bin, it suggests that a landslide picked at random from the inventory has a higher percentage likelihood of

being within that bin, and vice versa. This section considers some key predisposing factors, describing the most significant observed influences on landslide occurrence. For the topographical control factors investigated, aspect, hillslope angle and curvature had very consistent influences on landslide occurrence across all subsets, with all landslide types having a high percentage likelihood of having occurred on SE and S-facing aspects (Fig. 2.15a – c), slope angles of 35 – 55° (Fig. 2.15d – f) and convex curvatures (Fig. 2.16a – f). The other topographical control factors investigated were elevation (Fig. 2.17a – c), excess topography (Fig. 2.17d – f) and local relief (Fig. 2.18a – c). If you were to pick a landslide at random from the inventory, most landslide subsets had high percentage likelihoods of having occurred at elevations of 400 – 2400 m, excess topographies of 50 – 100 m³, and local reliefs of 400 – 800 m, but low percentage likelihoods of having occurred at elevations > 3800 m, excess topographies < 50 m³ and local reliefs < 400 m. The main subset to deviate from this behaviour were landslides of type AR3, which if picked at random, had a ~10 - 20% likelihood of having occurred at elevations of 2400 – 3600 m (Fig. 2.17a), excess topographies of 50 – 300 m³ (Fig. 2.17d) and local reliefs of 600 – 1000 m (Fig. 2.18a). The landslide subsets for the Tethyan and Sub Himalaya also showed some deviation across these factors (Figs 2.17c, 2.17f and 2.18c), but this is unsurprising given that these tectonic regions are partially defined by their topography.

Two hydrological factors were also considered: distance to channels and near channel k_{sn} (Figs. 2.18d – f; 2.19a – c). For most landslide subsets, if a landslide was picked at random from the inventory, it would have a higher percentage likelihood of having occurred at 100 – 400 m from a channel, though landslides in subset AR3 had a higher percentage likelihood of having occurred at 400 – 1200 m (Fig. 2.18d). Furthermore, the landslides in most subsets had only a 5 – 15% likelihood of having occurred near channels with k_{sn} values < 500, but a 25 – 50% likelihood of having occurred near channels with higher k_{sn} values of 500 – 1000. Again, the main exception to this was subset AR3, landslides within which had only a 15% likelihood of having occurred near channels with k_{sn} < 1000, but a 25% likelihood of having occurred where near channel k_{sn} is 1500 – 2500 (Fig. 2.19a). In contrast, landslides in the Sub and Tethyan Himalaya subsets had higher, 25 – 40% likelihoods of occurring

near channels with lower k_{sn} values of 0 – 1000, but just 10 – 15% likelihoods of occurring near channels with k_{sn} values of 1000 – 2500 (Fig. 2.18c, 2.19c).

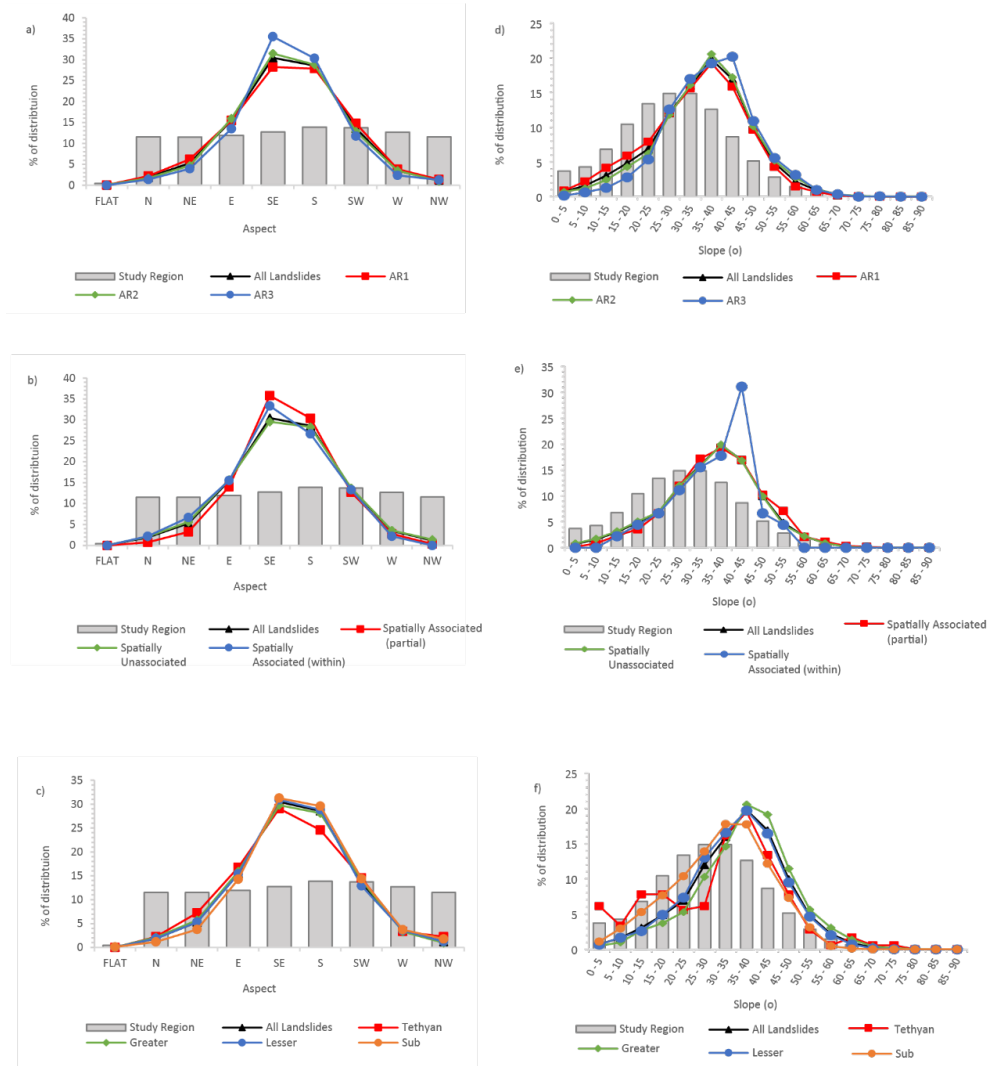


Figure 2.15. Frequency analysis showing the proportions of all landslides, various landslide subsets, and the study region at bins of aspect (a – c) and hillslope angle (d – f).

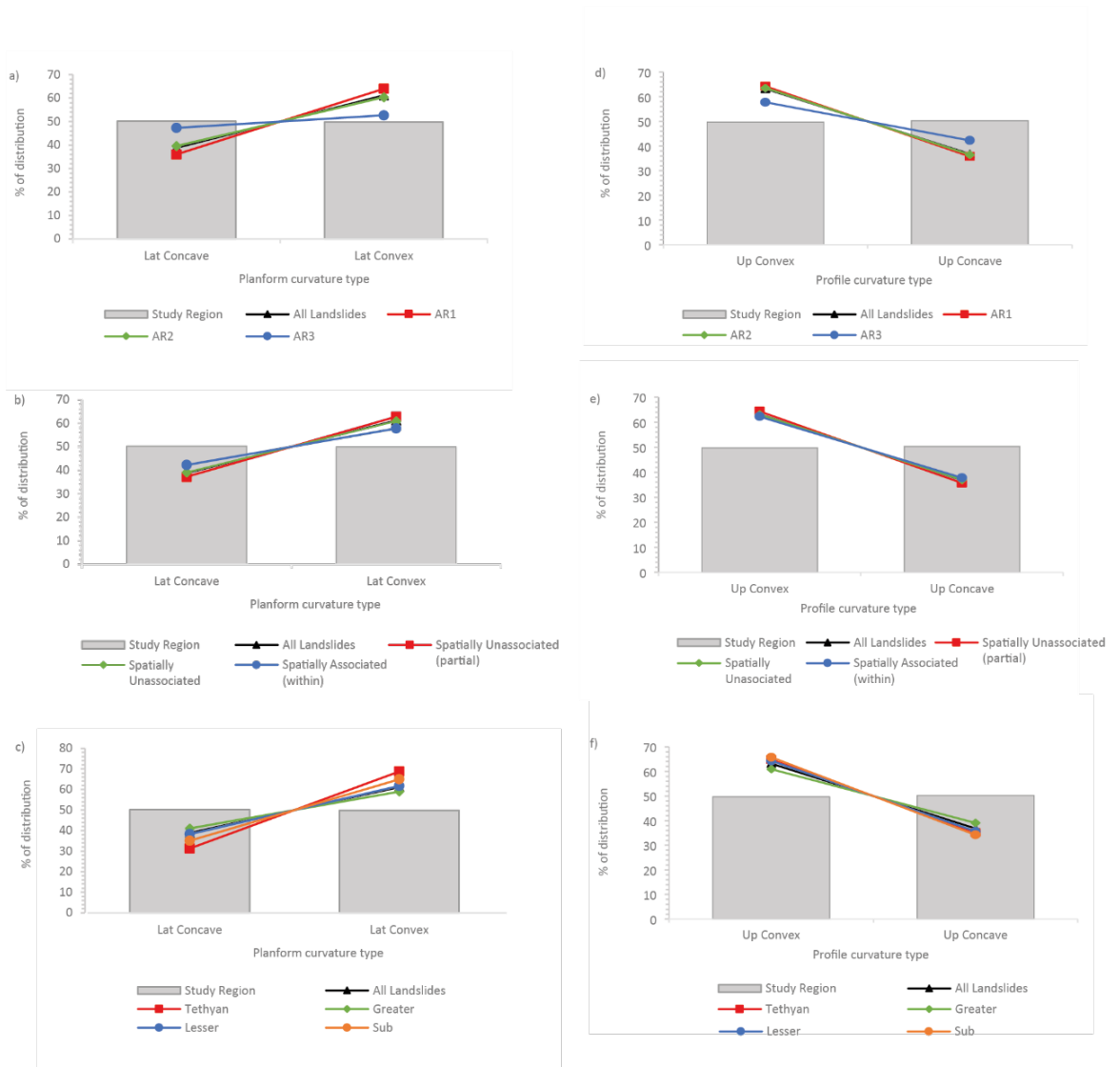


Figure 2.16. Frequency analysis showing the proportions of all landslides, various landslide subsets, and the study region at bins of planform curvature (a – c) and profile curvature (d

– f).

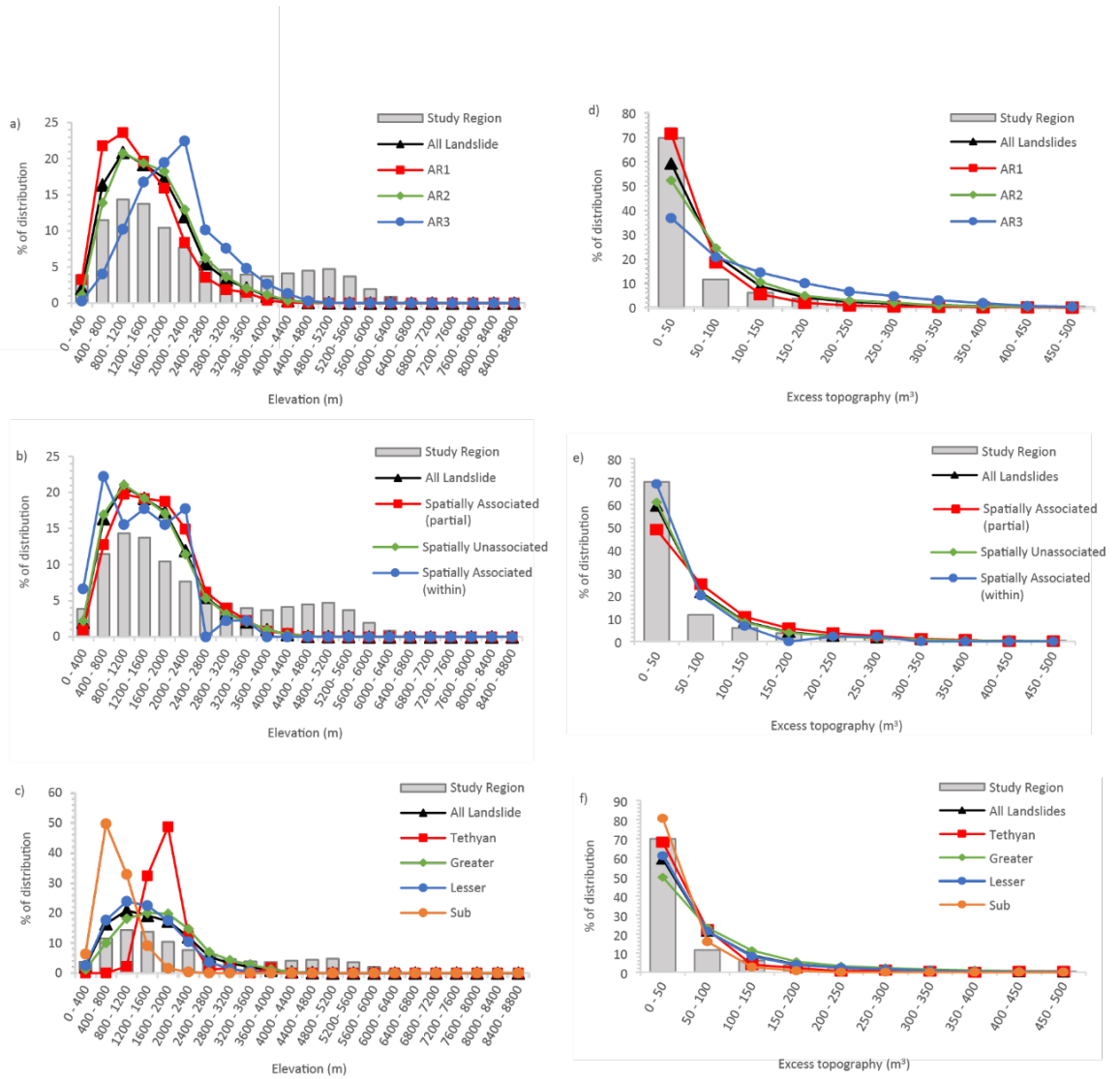


Figure 2.17. Frequency analysis showing the proportions of all landslides, various landslide subsets, and the study region at bins of elevation (a – c) and excess topography (d – f).

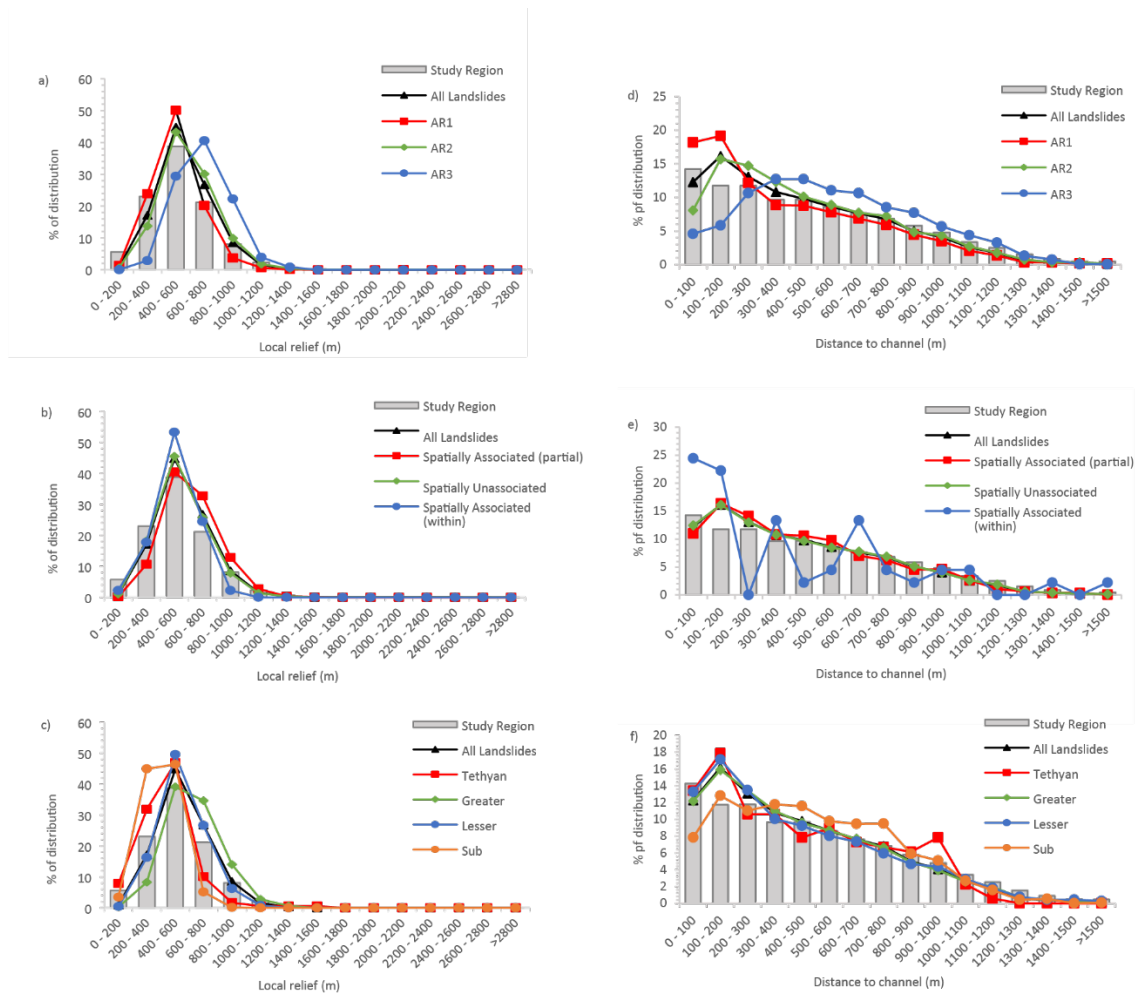


Figure 2.18. Frequency analysis showing the proportions of all landslides, various landslide subsets, and the study region at bins of local relief (a – c) and distance to channels (d – f).

The final predisposing factors considered were distance to roads, PFI extent, land use and geology (Figs. 2.19d – f, 2.20a – c, 2.20d – f and 2.21a – c). With the exception of the Tethyan Himalaya subset, the influence of distance to roads on landslides was consistent across all subsets, with a randomly selected landslide from all subsets having a 30 – 50% likelihood of having occurred within 500 m of a road (Fig. 2.19d – f). The influence of permafrost is similarly consistent, with landslides in all subsets having ~0% likelihoods of occurring within any degree of permafrost (Fig. 2.20a – c). In terms of land use (Fig. 2.20d – f), across most subsets, a randomly picked landslide would have a 5 – 15% likelihood of having occurred within irrigated croplands, a 20 – 50% of having occurred within rain-fed cropland, and almost a 0%

chance of having occurred where there is permanent snow/ice. Most of the geometric subsets follow this pattern, though landslides of type AR3 had 5 – 10% higher likelihoods than the landslides in the other subsets of occurring in forest and grass/shrub land (Fig. 2.20d). Likewise, whilst most of the path dependent subsets follow the average, the spatially associated (within) landslides were ~15% more likely than landslides in the other subsets to have occurred in grass/shrub land (Fig 2.20e). There is also significant variation in landslide-land use distributions across different tectonic units (Fig. 2.20f), with landslides in the Sub Himalaya having a much higher (~50%) likelihood of having occurred in irrigated croplands than landslides in the other tectonic units. Conversely, landslides in the Greater Himalaya were 20 – 25% more likely than landslides in the other units to have occurred in grass/shrub land and sparsely vegetated regions.

Finally, in terms of geology, in most subsets a landslide picked at random had a 25-35% likelihood of having occurred in regions dominated by granites/gneisses, phyllites, or quaternary sandstones/conglomerates, but a less than 20% likelihood of having occurred in any other geological unit. Again, landslides of type AR3 were an exception, with these landslides having a 50% likelihood of having occurred in granites/gneisses. Unsurprisingly, landslides within the different tectonic groups also varied with geology (Fig. 2.21a – c), with landslides in the Sub Himalaya having a ~55% likelihood of having occurred in Quaternary units, which is approximately 30 – 40% higher than the likelihoods of the landslides in other tectonic units occurring across this geology. Furthermore, landslides in the Greater Himalaya had a 60% likelihood of having occurred in granite/gneisses, whilst landslides in the Lesser and Tethyan Himalaya had a 40-50% likelihood of having occurred in phyllite.

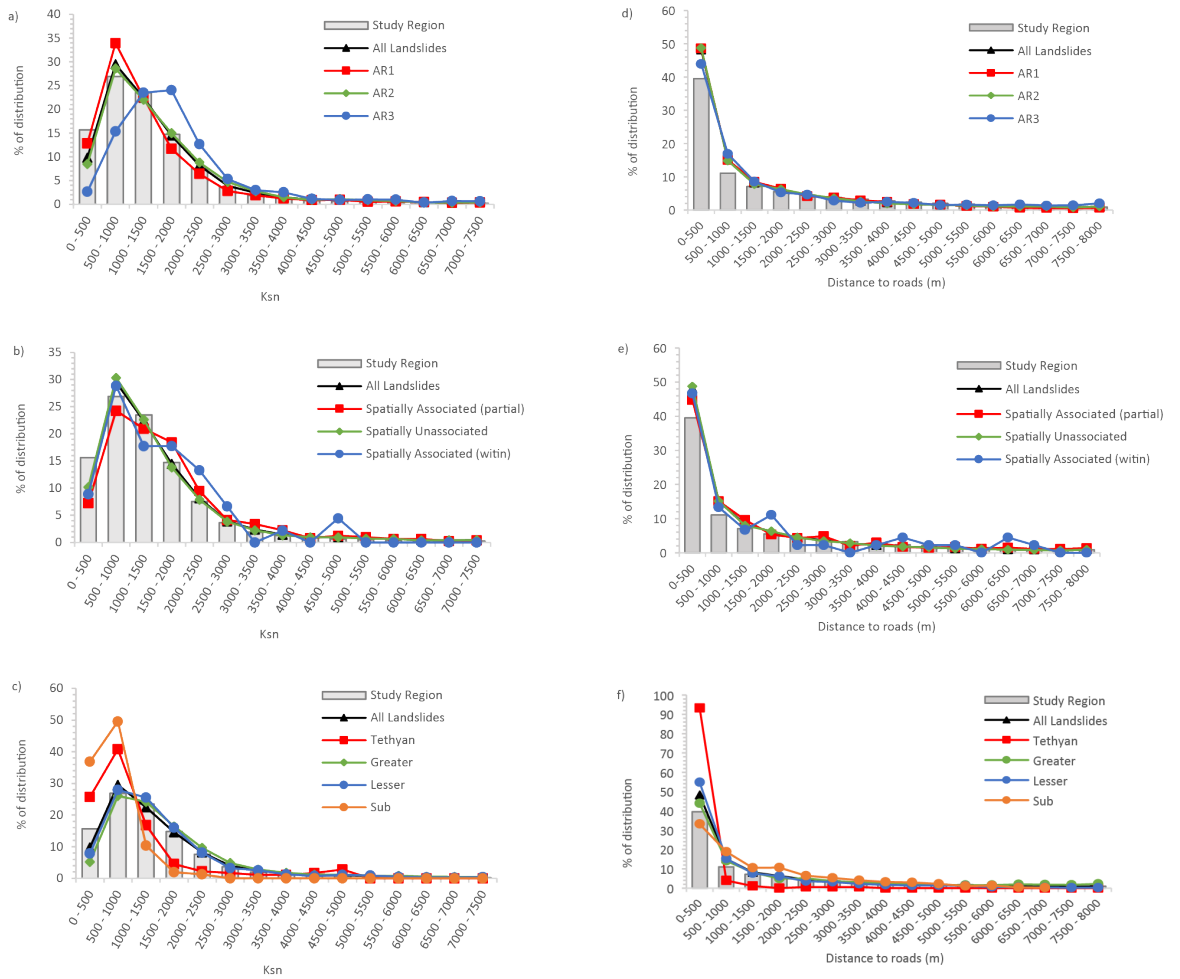


Figure 2.19. Frequency analysis showing the proportions of all landslides, various landslide subsets, and the study region at bins of ksn (a – c) and distance to roads (d – f).

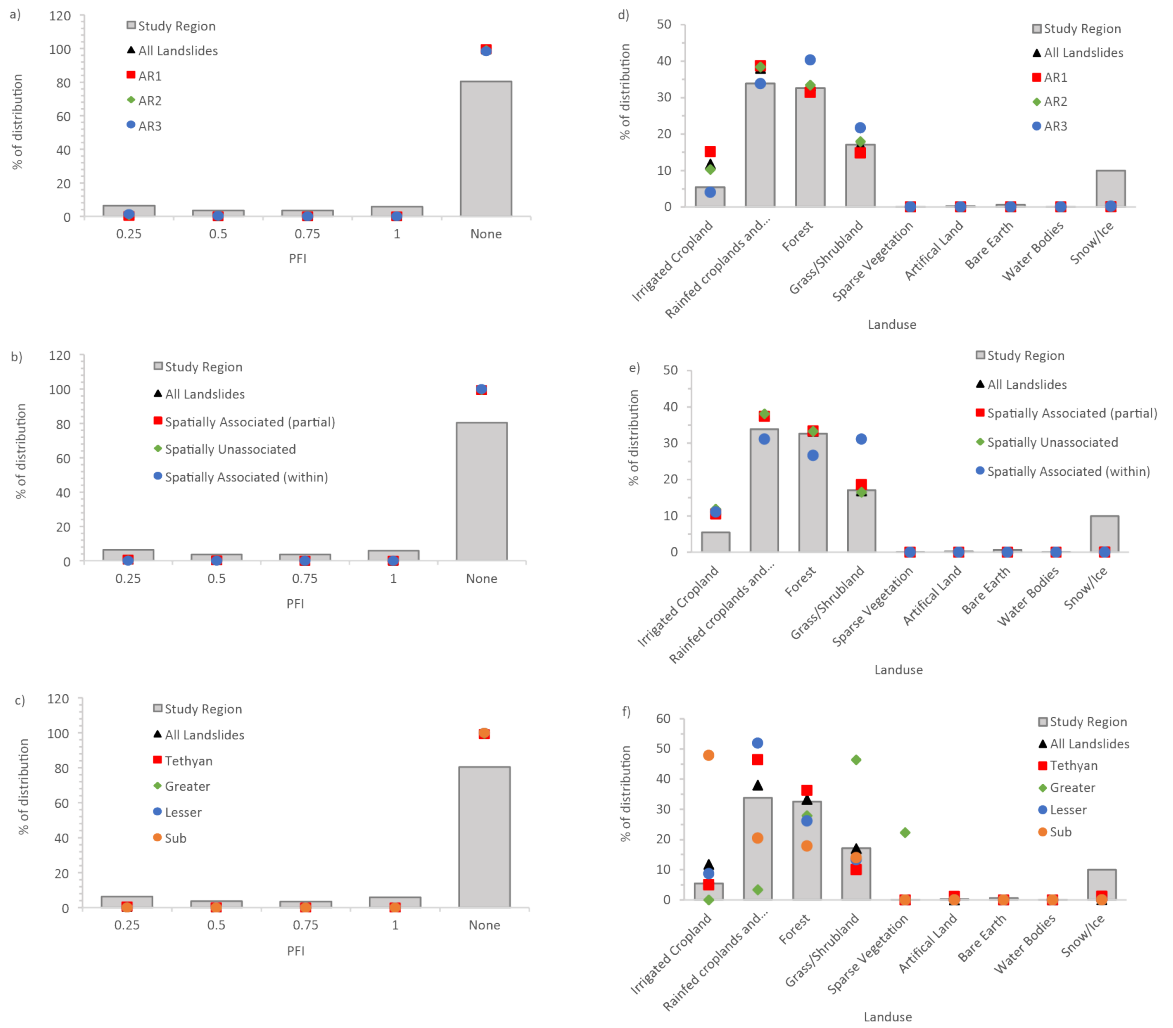


Figure 2.20. Frequency analysis showing the proportions of all landslides, various landslide subsets, and the study region at bins of PFI (a – c) and land use (d – f).

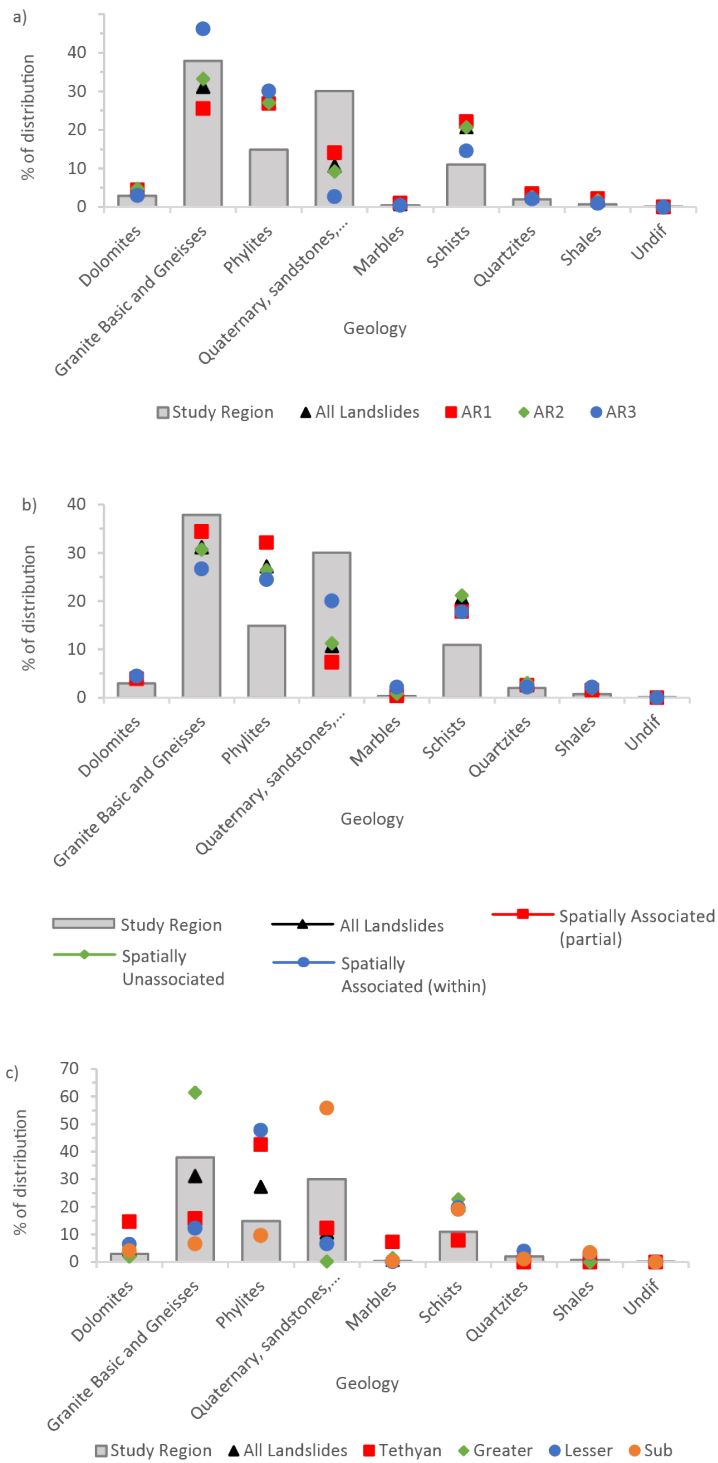


Figure 2.21. Frequency analysis showing the proportions of all landslides, various landslide subsets, and the study region at each geology category (a – c).

2.6.4.2 Anselin Local Moran's I

Figures 2.22 and 2.23 show the results of the Moran's I analysis for the following landslide characteristics and controls: landslide area, landslide roundness, landslide aspect ratio, slope, elevation, aspect, planform curvature, profile curvature, distance to channels and roads, excess topography, local relief, near channel SSP and near channel k_{sn} . Of these, aspect (Fig. 2.22h), planform curvature (Fig. 2.23a) and profile curvature (Fig. 2.23b) show no spatial structure, suggesting that the controls of these factors on landslide occurrence are homogenous across the study region.

As expected, landslide AR and roundness appear well correlated, with both showing a distinct north-south divide between the occurrence of high-high and low-low clusters (Figs 2.22a - b). In both cases, more elongated and lower roundness landslides cluster in the north, whilst less elongate, lower-runout, landslides cluster in the south. However, there are a significant number of high-low and low-high outliers in the Lesser Himalaya to the south, suggesting that the potential for occasional long-runout landslides in this area still exists. A north-south divide in the clustering of landslides is also observed with landslide area (Fig. 2.22c), elevation (Fig. 2.22d), local relief (Fig. 2.22e), excess topography (Fig. 2.22f), and near channel k_{sn} (Fig. 2.23f). In all of these cases, landslides cluster at high values in the north and low values in the south. The exception to this is a "high-high" cluster of landslides with larger areas to the SW of Kathmandu. Conversely, landslide slope values (Fig. 2.22g) show greater heterogeneity, with clusters of landslides at high slopes distributed across the Greater Himalaya and in the western Lesser Himalaya, and clusters of landslides at lower slopes located across the Kathmandu basin and in the central-eastern Lesser Himalaya. Of the remaining factors: distance to roads shows a distinct change east to west (Fig. 2.23c), with significant clusters of landslides occurring at low distances to roads in the west and clusters at high distances in the east. For distance to channels and near channel SSP (Fig. 2.23d - e), there is less overall spatial homogeneity in clustering compared to most of the other factors, with a slight tendency for landslides clusters with high distances to channels and low SSP in the south.

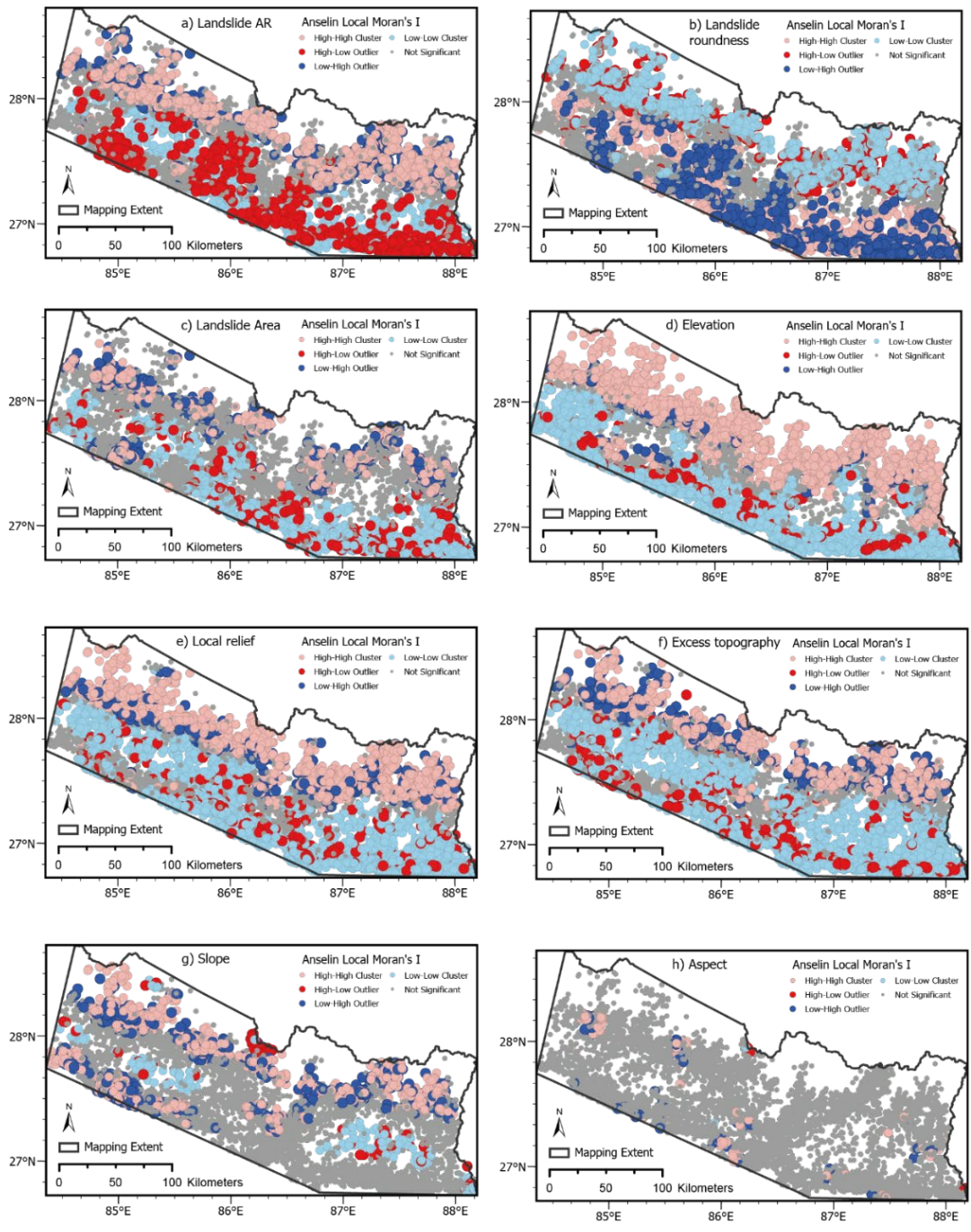


Figure 2.22. Anselin Local Moran's I analysis for a) AR, b) roundness, c) area, d) elevation, e) local relief, f) excess topography, g) slope, and h) aspect.

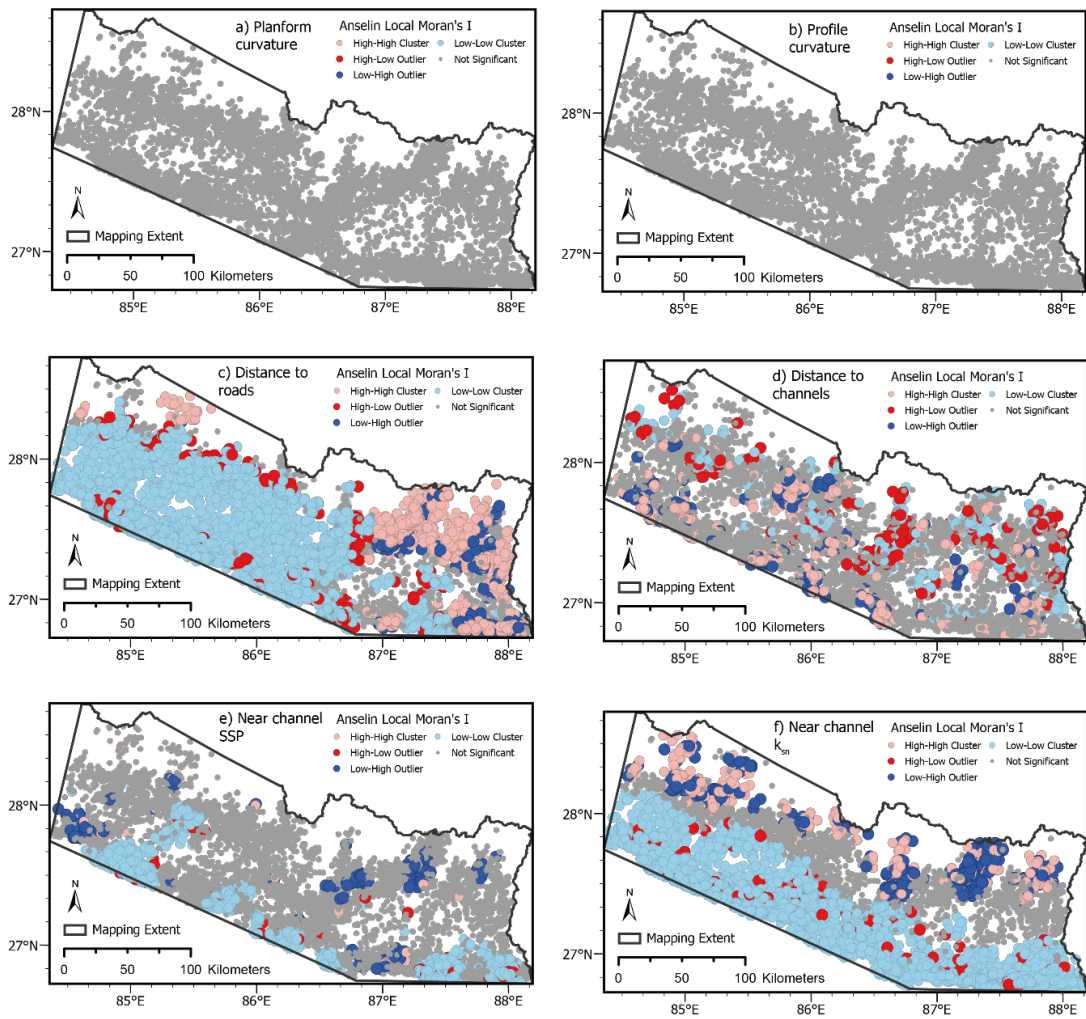


Figure 2.23. Anselin Local Moran's I analysis for a) planform curvature, b) profile curvature, c) distance to roads, d) distance to channels, e) near channel Specific Stream Power (SSP), and f) near channel k_{sn} .

2.6.5 BLR susceptibility modelling

2.6.5.1 Regression coefficients and LASSO selection

Table 2.7 shows the results of the BLR modelling undertaken using the entire ASM-inventory, displaying the percentage of times the LASSO selected each factor across the 50 trained models, as well as the means and standard deviations of the regression coefficients assigned to each factor across those models. The results are ranked according to the magnitudes of the factor regression coefficients, with all factors selected by $> 50\%$ of the trained models highlighted (Table 2.7). The most dominant factors for predicting landslide occurrence are permanent snow/ice and elevation,

Factor	% times selected by LASSO	Mean regression coefficient	SD of regression coefficient
Intercept	100	0.862	0.215
Water	4	-0.832	0.093
Permanent snow and ice	96	-0.782	0.224
Elevation	96	-0.776	0.030
Near channel SSP	4	-0.621	0.022
PFI	100	-0.591	0.145
Slope	96	0.487	0.016
Excess topography	4	0.407	0.012
Local relief	96	0.401	0.037
Quaternary sandstone and conglomerates	96	0.306	0.054
Undifferentiated bedrock	44	-0.289	0.221
Phyllite	6	0.203	0.174
Distance to roads	18	-0.181	0.321
Profile curvature	100	-0.141	0.130
Artificial ground	10	-0.123	0.058
Bare and sparse earth	14	-0.105	0.064
Marble	8	0.088	0.067
Quartzite	42	-0.071	0.046
Shale	38	0.067	0.049
Aspect	100	-0.049	0.017
Cropland	84	0.041	0.029
Dolomite	6	-0.040	0.024
Forest	64	-0.039	0.026
Planform curvature	98	0.036	0.047
Schist	2	-0.027	-
Mean 30-year precipitation	78	0.026	0.013
Near channel k_{sn}	26	0.014	0.013
Shrub and grassland	2	0.005	-
Distance to channels	12	-0.007	0.005
Granites and gneiss	0	-	-

Table 2.7. Summary of LASSO selection percentages, mean regression coefficients and coefficient standard deviations (SD) for the 50 trained models developed using the entire ASM-inventory.

both of which were selected by the LASSOs in 96% of models and had regression coefficients with magnitudes > 0.7 . Both factors had negative coefficients, indicating that the presence of snow/ice and increasing elevations make landslides less likely. The next most important factors were PFI and slope, both of which were selected by the LASSO in $> 96\%$ of the models and had regression coefficients with magnitudes of ~ 0.5 . The regression coefficient for PFI was negative, suggesting that as PFI

increases, landslide occurrence decreases; whilst slope was positive, suggesting that as slope increases likelihood of landslide occurrence increases. Local relief and the presence of Quaternary sandstone/conglomerate also had significant influences on landslide occurrence, being selected by the LASSO in 96% of models with regression coefficients > 0.3 . Both coefficients were positive, indicating that the presence of Quaternary sands/conglomerates and increasing local relief both made landslides more likely. The final factor to have a significant influence on landslide occurrence was profile curvature which was selected 100% of the time and had a coefficient of magnitude 0.14. This coefficient was negative indicating that as curvature got more concave landslides got less likely. Of the other factors included in the model, aspect, cropland, forest, planform curvature and mean precipitation were all selected by the LASSO in $> 50\%$ of the models, but had regression coefficients with magnitudes < 0.1 . All other factors were selected in $< 50\%$ of models by the LASSO, suggesting their influence was limited or inconsistent.

2.6.5.2 Model validation

AUROC validation was used to assess the success rate and predictive power of the 50 trained models. Figure 2.24a shows the initial success rate AUROC results, i.e., the success of each model at classifying the data used to train that model. Figure 2.24b shows the results of the 10-fold cross validation, whereby 100 validations between the trained models and independent testing datasets were undertaken to assess the overall predictive power of this set of models. In both cases, AUROC results were highly consistent, with an average success rate of 0.767 (± 0.0037) across the 50 models, and an average predictive power of 0.769 (± 0.0036) across the 100 independently validated cases.

2.6.5.3 Regional susceptibility map

Figure 2.25 shows the final susceptibility results when the average regression coefficients of all factors selected by the LASSO in $> 50\%$ of the 50 models are applied to every cell across the study region. Figure 2.25a shows the entire study region, whilst insets b) and c) show two sub-regions, Kathmandu/Bhaktapur and Langtang Valley in more detail. Generally, susceptibility is highest across the Lesser Himalaya

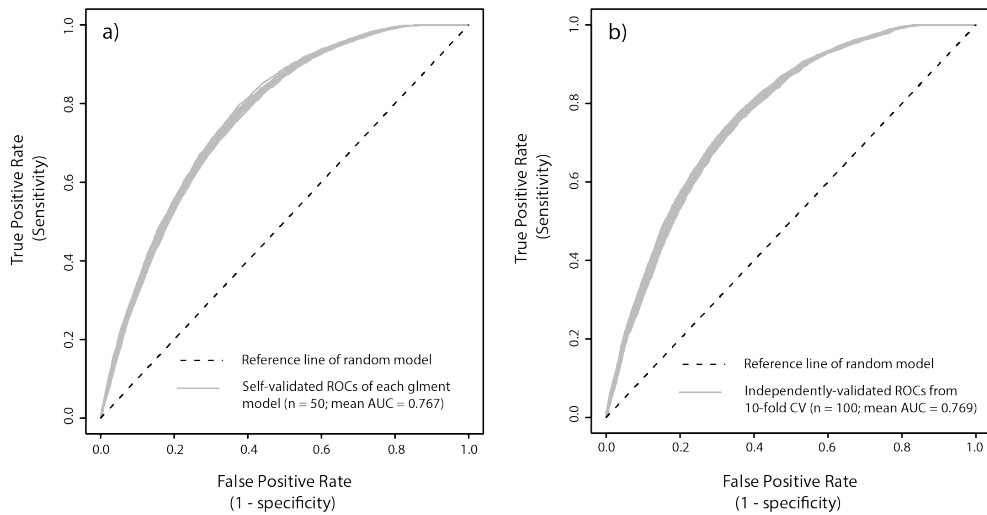


Figure 2.24. a) Self-validated Receiver Operator Curves (ROCs) and associated average AUC values for the 50 trained models. b) independent 10-fold cross validated AUROCs.

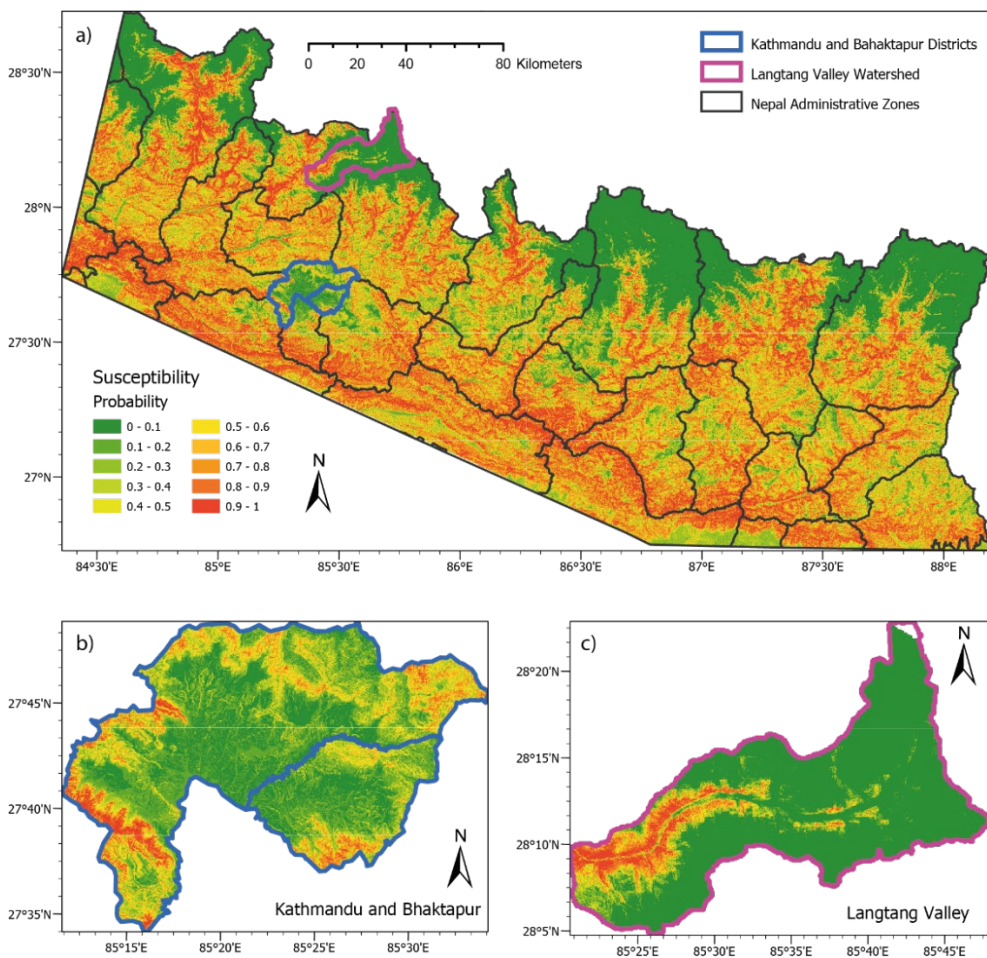


Figure 2.25. Final susceptibility maps derived from the average regression coefficients of all factors selected by the LASSO in at least 50% of the 50 trained models for a) the entire study region, b) Kathmandu and Bhaktapur and c) Langtang Valley.

and the main corridors of the Greater Himalaya to the north, with lower susceptibility values concentrated in the Kathmandu Basin (e.g., Fig. 2.25b) and in the highest elevation portions of the Tethyan Himalaya (e.g. Fig. 2.25c). Figure 2.26a – c shows the proportion of the study region and the selected sub regions that fall within 0.1 probability bins of getting a landslide. Across the entire region and the Kathmandu basin, ~18% of the region is at a probability of 0 – 0.1, with the percentage of the study region then increasing steadily from 5% at the 0.2 – 0.4 probability bin to 10 - 12% the 0.8 – 1 probability bin. The Langtang catchment is skewed by the fact that over 70% of the catchment (which is largely covered in permanent snow/ice and permafrost) is in the 0 – 0.1 probability category. However, 12% of the region still has a probability > 0.5 of experiencing a landslide.

2.7 Discussion and conclusions

The following sections discuss the characteristics of the ASM-inventory within the context of the wider literature, with a focus on the processes controlling monsoon-triggered landslide distributions and morphology. It then compares the results of the landslide susceptibility model produced here to others developed for this region, before discussing the potential limitations of typical landslide susceptibility approaches and how these will be investigated further in subsequent chapters.

2.7.1 Path dependency

Landslide path dependency describes the spatial associations of new landslides with previous landslides. For the entire ASM-inventory, 86% are spatially unassociated with previous landslides, 14% are spatially associated (partial), i.e., intersecting with a previous landslide, and less than 1% are spatially associated (within), i.e., occurring fully inside a previous landslide. These path dependency results differ to those found for a > 60 year multi-temporal inventory in Umbria, Italy, where 19% of landslides were spatially associated (partial), 9% were spatially associated (within) and 72% spatially unassociated (Samia *et al.* 2017b). This is likely a direct result of differences between the ASM-inventory and the Umbria inventory used by Samia *et al.* (2017b). The Umbria inventory included large-scale relict landslides, whereas the ASM-inventory only included recent (< 30-year-old) monsoon-triggered landslides,

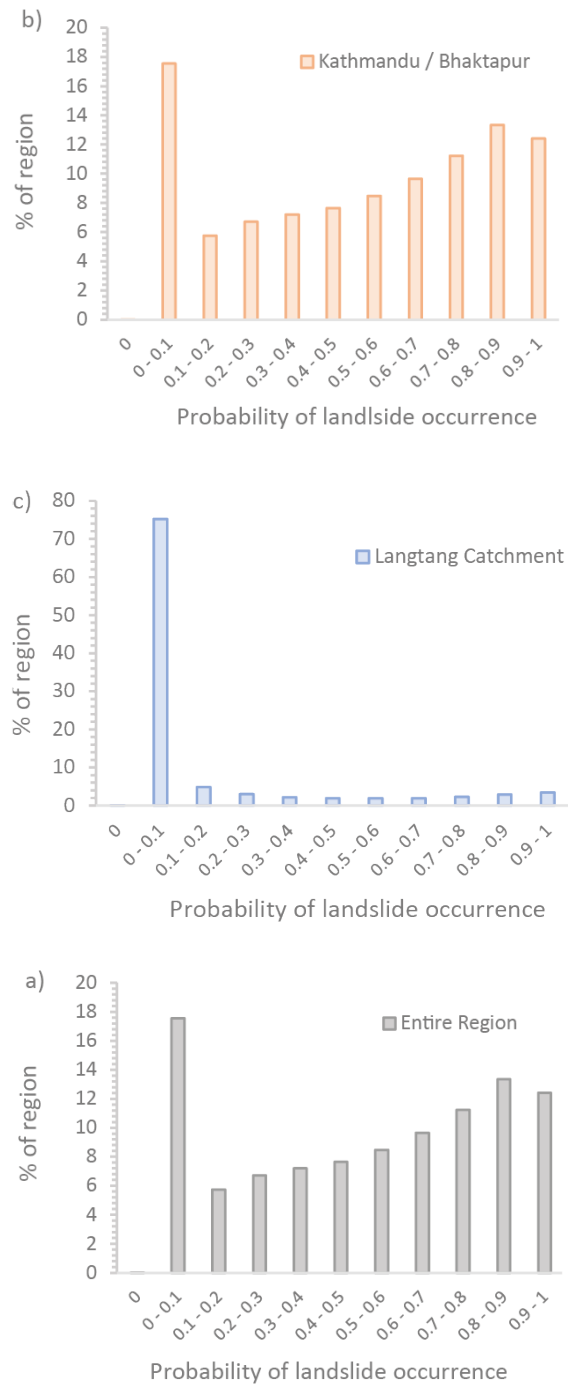


Figure 2.26. Proportion of a) the entire study region, b) Kathmandu and Bhaktapur and c) Langtang Valley that fall within 0.1 probability bins of observing a landslide.

without inclusion of larger relict features. Had such relict features been included in the ASM-inventory, the number of events classified as being within a previous failure would likely have increased significantly, as it is well described that large relict landslides in the Himalaya are both pervasive and capable of inducing landscape

instability (Dunning *et al.* 2009; Hasegawa *et al.* 2009; Marc *et al.* 2019; Dini *et al.* 2020).

The different path dependent classes differ in terms of both their geometries and size, with spatially associated landslides being less round and of larger average size than spatially unassociated landslides (Figs. 2.11; Table 2.6), though with spatially unassociated landslides having a greater maximum landslide size. Furthermore, the exponent of inverse power law decay for the area-frequency distribution of spatially associated landslides is smaller than for spatially unassociated landslides (1.62 compared to 1.83; Table 2.6), suggesting that larger landslides are contributing more to the size distributions of the former. These results show some similarity to that observed by Samia *et al.* (2017b), who also found that spatially unassociated landslides had higher roundness (0.83 compared to 0.78) and higher inverse power law exponents (1.32 compared to 1.28) than spatially associated landslides, whilst spatially associated landslides had larger average sizes. These observations are likely explained by the morphological and structural changes induced within a landscape by previous landslides. Old landslide scars are typically composed of poorly consolidated material with boundaries that have weaker mechanical properties and higher infiltration rates than undisturbed portions of the landscape. As such, spatially associated landslides that reactivate new material near an old landslide scar or remobilise unconsolidated material from within an old landslide scar may have the potential to travel faster and further, thus leading to lower roundness and larger average landslide areas (Samia *et al.* 2017b). However, as suggested by the results presented here (Table 2.6), spatially associated landslides may also be limited in their maximum potential size, with spatially unassociated landslides having greater potential for much larger failures. This could be because previous landslides have already contributed to the partial re-equilibration of the landscape, thus reducing the overall volume of a hillslope that is above the hillslopes threshold angle (i.e. the portion of the terrain with most potential to be a source of landslide material; Loye *et al.* 2009) and so making large future hillslope-scale landslides less likely.

2.7.2 Influences of topographic factors on landslide distributions and morphology

The main topographic predisposing factors considered in this chapter are hillslope aspect, slope angle, curvature, elevation, local relief, excess topography, and distance to channels. The following sections discuss the key influences of these factors on the spatial distributions, geometries, and sizes of monsoon-triggered landslides in Nepal.

2.7.2.1 Spatial distributions

With respect to hillslope aspect, a randomly selected monsoon-triggered landslide had a 30-35% likelihood of having occurred on SE and S facing slopes, compared to < 5% for having occurred on flat, N, NW, W and NW hillslopes. (Fig. 2.15a – c). Similarly, 56% of monsoon-triggered landslides and 60% of coseismic landslides in the Upper Bhote Koshi occurred on S and SE facing slopes (Tanoli *et al.* 2017), whilst across Nepal the 2015 Gorkha coseismic landslides occurred preferentially at SE to W facing hillslopes (Gnyawali & Adhikari 2017). The influence of hillslope aspect on landsliding is predominantly due to its control on variable hillslope exposure to sunlight (and thus temperature), wind and precipitation (Rech *et al.* 2001). In Nepal, the monsoonal rains typically travel S/SE to N/NW across the country. Consequently, slopes facing S/SE are more exposed to precipitation as weather systems typically deposit proportionally more water on hillslopes facing the direction in which they are travelling (Baeza & Corominas 2001). Furthermore, as with the entire northern hemisphere, south-facing slopes in Nepal are exposed to more sunlight. The exposure of hillslopes to rain and sunlight is known to increase slope instability via physical and chemical weathering, and thus modulate the availability of loose unconsolidated material (McFadden *et al.* 2005; Meunier *et al.* 2008; Parker *et al.* 2017). It is thus unsurprising that rainfall-triggered landslides in Nepal are more likely to have occurred at S/SE aspects.

For slope angle, a randomly selected monsoon-triggered landslide had a high likelihood of having occurred where hillslope gradients are 35 – 55° (Fig. 2.15d – f). Tanoli *et al.* (2017) also found that 76% of monsoon-triggered landslides in the Upper Bhote Kosi occurred at slopes of 20 – 50°. Conversely, the 2015 Gorkha

coseismic landslides clustered at higher slope angles of 40 – 80° (Gnyawali & Adhikari 2017; Martha *et al.* 2017; Tanoli *et al.* 2017; Roback *et al.* 2018). Slopes can have several influences on landscape stability. First, slope angle is a dominant control on both the rates and directivity of overland flow, groundwater flow, percolation and saturation (Sidle & Bogaard 2016). Slope angle also influences downslope material-transport, with material flux predominantly controlled by frictional and gravitational forces, both of which are gradient dependent (Roering *et al.* 1999). Second, hillslopes have a critical threshold gradient, controlled by the local geology, at which the likelihood of hillslope failure increases rapidly due to limitations in material strength (Korup *et al.* 2007). For many rock types, static frictional strengths begin to be exceeded at ~30°, so as gradients increase above this, so do hillslope shear stresses and thus hillslope instability (Gnyawali & Adhikari 2017). This process can also explain the observation of landslide distributions with excess topography, which measures the volume of rock mass above a hillslopes critical threshold angle (Blöthe *et al.* 2015). In this case, the likelihood that a randomly selected monsoon-triggered landslide occurred at excess topographies < 50 m³ is ~10% less likely than would be expected given the distribution of excess topography across the study region, and up to 10% more likely where excess topographies are 50 – 100 m³ (Fig. 2.17d – f). Regions with high slope angles and excess topographies are also more likely to have exposed, un-vegetated, and thus weaker bedrock, with higher propensity for failure. Indeed, Martha *et al.* (2017) observed that in 2015, coseismic rockfalls and slides were common on exposed geomorphic escarpments of un-vegetated crystalline rock. A randomly selected ASM-inventory landslide had a ~60% likelihood to have occurred where hillslopes are laterally or upwardly convex (Figs. 2.16a – f). These results are somewhat in contrast to the observations of Tanoli *et al.* (2017), who found that monsoon-triggered landslides were equally likely to occur on concave and convex hillslopes. However, the results here are similar to the observations made by Regmi *et al.* (2014) for monsoon-triggered landslides in the Lesser Himalaya and for Gorkha 2015 coseismic landslides, both of which were also more likely at convex surfaces (Gnyawali & Adhikari 2017). The propensity of landslides to occur at convex topography is somewhat unusual, as it is generally considered that concave surfaces

are more susceptible to rainfall triggered landslides as they concentrate flow and cause increased pore pressures (Ohlmacher 2007). However, the instability of convex slopes could be due to the processes relating to excess topography described above, as such topographic excesses are likely to be convex in nature.

For elevation, a randomly selected ASM-inventory landslide had a 15 – 25% likelihood of having occurred at elevations of 400 – 2400 m (Fig. 2.17a – c). Similarly, Tanoli *et al.* (2017) found that 91% of monsoon-triggered landslides occurred at elevations of 1000 – 2500 m, though the 2015 coseismic landslides were most likely at higher elevations of 1500 – 3500 m (Tanoli *et al.* 2017; Roback *et al.* 2018). For both monsoon-triggered landslides and coseismic landslides, occurrence decreases rapidly at elevations > 4,000 m (Roback *et al.* 2018). The control of elevation potentially relates to glaciation and the presence of snow/ice, with landslide having an almost 0% likelihood of having occurred where there is permanent permafrost, snow, and ice (Figs. 2.20a –f). This is likely because persistent permafrost prevents bedrock cracking (e.g. Hales & Roering 2005), whilst glaciers protect and buttress hillslopes, thus preventing failure (Wegmann *et al.* 1998). It is only when permafrost and glaciers begin to melt, and thus a landscape shifts from being glaciated to periglacial, that landscapes become landslide prone (e.g., Schiermeier 2003; Gruber *et al.* 2004; Gruber & Haeberli 2007). The role of elevation-controlled permafrost, snow, and ice, as well as the differences between periglacial and fluvial landscapes, is discussed in detail throughout Chapter 3.

For local relief, a randomly selected ASM-inventory landslide had a <25% likelihood of having occurred at reliefs < 400 m, but 30-55% likelihoods of having occurred at reliefs of 400 - 1000 m (Fig. 2.19a – c). Conversely, the 2015 coseismic landslides occurred most frequently at higher reliefs of ~ 2000 m, with a decrease in occurrence where reliefs exceeded 3000 – 4000 m (Roback *et al.* 2018). Local relief has a strong influence on orographic precipitation, with precipitation rates during a given rainfall event expected to increase with altitude, thus causing higher elevation hillslopes to become saturated more quickly relative to lower elevation hillslopes (Carrara *et al.* 1978; Gallart & Clotet 1988; Bai *et al.* 2014). This could explain why less landsliding is observed at reliefs < 400 m, but more up to 1000 m.

A randomly selected ASM-inventory landslide had a 5-15% likelihood of having occurred within 100 m of a channel, which was 5 – 10% less likely than would have been expected given the distributions of stream distances across the study region (Fig. 2.18d – f). However, they had 5 – 20% likelihoods of having occurred 100 – 200 m from a channel, which was 5 – 15% more than would have been expected given the landscape distribution of stream distances. In contrast, coseismic landslides were reportedly ~4% more likely at distances greater than 200 m from channels (Tanoli *et al.* 2017), again highlighting that coseismic landslides tend to occur at higher slope positions (Densmore & Hovius 2000; Meunier *et al.* 2008). The tendency of monsoon-triggered landsliding to occur nearer to channels, i.e. closer to the hillslope toe, is unsurprising, as these portions of the hillslope are likely to have greatest upward- and outward-directed positive pore pressures (Densmore & Hovius 2000). Indeed, Meunier *et al.* (2008) found that 47% of landslides triggered by the 1996 typhoon Herb, Taiwan, occurred in the lower quarters of hillslopes. Furthermore, stream channels can induce landsliding via undercutting and erosion of a hillslope toe. Typically, the most erosive portion of a landscape will be located downstream of knickpoints, where a knickpoint refers to a portion of a stream channel with a statistically significant change in channel steepness caused by the interaction between local uplift and incision (Kirby and Whipple, 2001, 2012). In other words, knickpoints identify landscape transitions from a gentler geomorphology to one that is characterised by high rates of incision and erosion. As such, landslides may be expected to occur nearest to streams with high channel steepness (k_{sn}), as these are the channels that incise most rapidly and thus cause adjacent hillslopes to have increased shear stresses through the removal of lateral support (Korup 2004). This expectation is partially corroborated by the results presented in this Chapter, which suggest that, relative to the landscape k_{sn} distributions, monsoon-triggered landslides have the lowest likelihoods of occurrences at the lowest k_{sn} values and the highest likelihoods of occurrences at moderate k_{sn} values (Fig. 2.19a – c).

2.7.2.2 Landslide geometry

Landslides in the ASM-inventory were classified according to two geometrics: the Aspect Ratio (AR) and roundness. The mean roundness of all landslides in the ASM-

inventory was 0.8, whilst AR values ranged from 1.1 – 15.4 with a mean of 2.53. These values compare favourably to other landslide inventories analysed in the literature. For example, Samia *et al.* (2017b) found that landslides in Umbria, Italy had mean roundness values of 0.78 – 0.83, whilst Taylor *et al.* (2018) found AR values of 1.2 – 13.9 (mean = 2.4) for rainfall-triggered landslides in Guatemala and 1.3 – 15.1 (mean = 2.9) for coseismic landslides in Northridge. Similarly, Tian *et al.* (2017, 2020) found AR ranges for coseismic landslides associated with the 2013 Minxian earthquake China, and the 2015 Gorkha earthquake, Nepal, to be 0.3 – 8.0 (mean = 2.11) and 0.3 – 15.44 (mean = 3.2), respectively.

Across the entire ASM-inventory, 45% of landslides had ARs < 1.0 (AR1), 44% had ARs of 2 – 4 (AR2) and 11% had ARs > 4 (AR3). This is in contrast to the 2015 Gorkha coseismic landslides, where for landslides < 10,000 m², 27% were AR1 and 26% AR3, and for landslides > 10,000 m², 16% were AR1 and 37% AR3 (Tian *et al.* 2020). In other words, for both size groups, the Gorkha coseismic inventory had fewer isometric landslides and more elongate landslides. This was similar to the observed geometries of the Minxian coseismic landslides, of which 18% had ARs < 1.2, 63% had ARs of 1.2 – 3.0 and 19% had ARs > 3 (Tian *et al.*, 2020).

This AR analysis shows that coseismic landslides are typically more elongated than monsoon-triggered landslides. This observation is likely explained by the influences of topography on landslide morphology. It is well described that coseismic landslides typically occur nearer ridgelines (Densmore & Hovius 2000; Meunier *et al.* 2008), where there are longer distances from landslide initiation position to the hillslope toe, and thus more potential for long-runout distances. Conversely, rainfall triggered landslides tend to initiate at lower hillslope positions, where distances from landslide initiation to the hillslope toe are shorter. This suggests that local relief plays an important role in controlling landslide geometry. This suggestion is supported by the Moran's I analysis, which shows a clear north-south distinction between clustering of landslides with high and low AR values (Fig. 2.22a). This clustering in AR values is coincident with a similar change in clustering of landslides with respect to elevation, local relief, and excess topography (Fig. 2.22d - f). The elongated landslides of type AR3 are also observed to have higher likelihoods of occurrence further from

channels and at higher elevations, excess topographies, and local reliefs (Figs. 2.17 – 2.18). Furthermore, there is found to be an overall positive correlation between landslide values of local relief and AR (Fig. 2.27). These results corroborate the findings of Roback *et al.* (2018) who found that the runout distance and mobility of the 2015 Gorkha coseismic events were largely controlled by hillslope length. Overall, this suggests that landslide geometry is strongly influenced by topography, with local relief controlling the potential for long-runout landslide events. However, it should also be noted that the roundness values will be influenced by the detail and accuracy to which landslide perimeters were mapped. For example, small but complex non-round landslides may appear round in low-resolution imagery due to a lack of pixels composing each feature. As relatively low resolution (15 – 30 m) imagery was used in this case, this issue may be a potential source of uncertainty that will likely impact the smallest landslides the most.

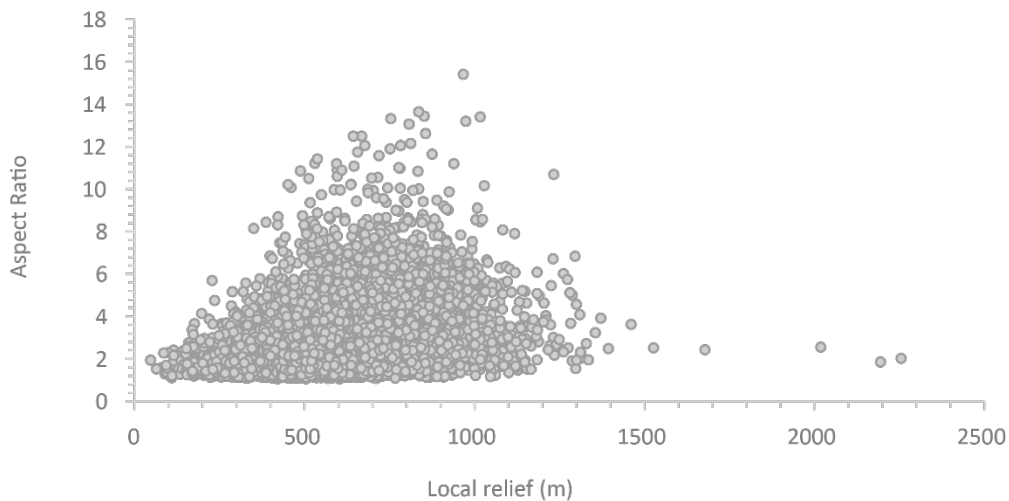


Figure 2.27. Correlation between local relief and AR across the entire ASM-inventory.

2.7.2.3 Landslide size

Overall, the ASM-inventory has a three-parameter inverse-gamma distribution scaling exponent of 1.79, which is within the typical range of 1.5 – 2.5 observed for other rainfall triggered landslide inventories in the literature (Guzzetti *et al.* 2002; Malamud *et al.* 2004a; Van Den Eeckhaut *et al.* 2007a; Borgomeo *et al.* 2014; Tanyaş

et al. 2019b). However, whilst falling within the expected range, this value is smaller than that observed for other rainfall triggered landslide events. For example, 9594 landslides triggered during the 1998 Hurricane Mitch (Guatemala) had an exponent of 2.4 (Malamud *et al.* 2004a), whilst an inventory of 217 rainfall triggered landslides in the Flemish Ardennes had an exponent of 2.3 (Van Den Eeckhaut *et al.* 2007a). The exponent of the ASM-inventory is also smaller than the exponent values obtained for the Gorkha coseismic inventory of Roback *et al.* (2018) and a monsoon-triggered inventory developed by Marc *et al.* (2019), both of which had exponents of 2.48 - 2.5.

The higher exponent value of the ASM-inventory is likely an artefact of inventory mapping technique and completeness. This ASM-inventory was mapped at a resolution of 15 – 30 m, with a minimum mapped landslide size of ~1,000 m² and a roll-over value of ~3,200 m². In comparison, the Guatemala inventory is considered to be substantially complete for landslides > 225 m², whilst the Ardennes landslides were mapped in the field at a higher scale of 1:10,000. Furthermore, the Gorkha coseismic inventory was mapped using imagery with < 1 m resolution, whilst the inventory developed by Marc *et al.* (2019) was developed using 5 m resolution RapidEye imagery. As such, the apparent observation that the ASM-inventory has a lower exponent (i.e. higher proportion of large landslides) could be because the lower resolution imagery used to develop this inventory has caused an under-sampling of the smallest landslides relative to other inventories.

Despite the possible under-sampling of the smallest landslides, the ASM-inventory allows an opportunity to quantify how topographical factors may be influencing landslide size. It has previously been posited that topography may set the upper limit on landslide size (Gallen *et al.* 2015), with lower local reliefs limiting the potential for large landslides (Van Den Eeckhaut *et al.* 2007a; Valagussa *et al.* 2019). Indeed, Medwedeff *et al.* (2020) find a positive correlation between landslide size and local relief, with average landslide size reflecting the distribution of hillslope dimensions across a landscape. However, in contrast, Valagussa *et al.* (2019) find that whilst relief may limit maximum landslide area, it is not a first order control on landslide size, with only the 2008 Wenchuan coseismic inventory showing a statistically significant

positive correlation between local relief and landslide size of the six coseismic inventories they studied. This highlights that the relationship between topography and landslide size is still uncertain. The ASM-inventory developed here can contribute to this discussion as it includes a significant number of landslides in the Sub, Lesser and Greater Himalaya, which have increasingly extreme topographies. If topography does impact landslide size, it is expected that average landslide sizes will increase, and power-law exponents decrease, from the Sub, to Lesser to Greater Himalaya. The three-parameter inverse-gamma power law exponent for the Sub Himalaya is 2.13 compared to 1.79 and 1.82 for the Lesser and Greater Himalaya. These results suggest that landslide size is proportionally greater in the more topographically extreme Greater and Lesser Himalaya, tentatively corroborating the observation that relief limits and controls landslide size. However, no statistically significant correlation is observed between landslide size and any single topographic metric (Figs. 2.28a – c). This finding supports Valagussa *et al.* (2019), who suggest that whilst local relief does have some influence, it does not impart a first-order control on landslide size.

There are several potential reasons why topography is not exhibiting a first order control on landslide size. One, is that landslide size is instead controlled by the magnitude of the triggering event. Medwedeff *et al.* (2020) and Valagussa *et al.* (2019) both find that for coseismic landslides, ground motion and distance to fault traces influences landslide size. For this ASM-inventory, the triggering event is monsoonal rainfall. As shown by Figure 2.5b, average precipitation in this region actually decreases from south to north as a consequence of the orographic nature of Nepal's climate. Furthermore, as shown by Figures. 2.28d - f, the log of landslide area is normally distributed with average, total and peak monsoonal rainfall, suggesting that the trigger event is not directly controlling landslide size. Two, is that as discussed in the following section, landslide size is instead influenced more strongly by lithology and rock strength.

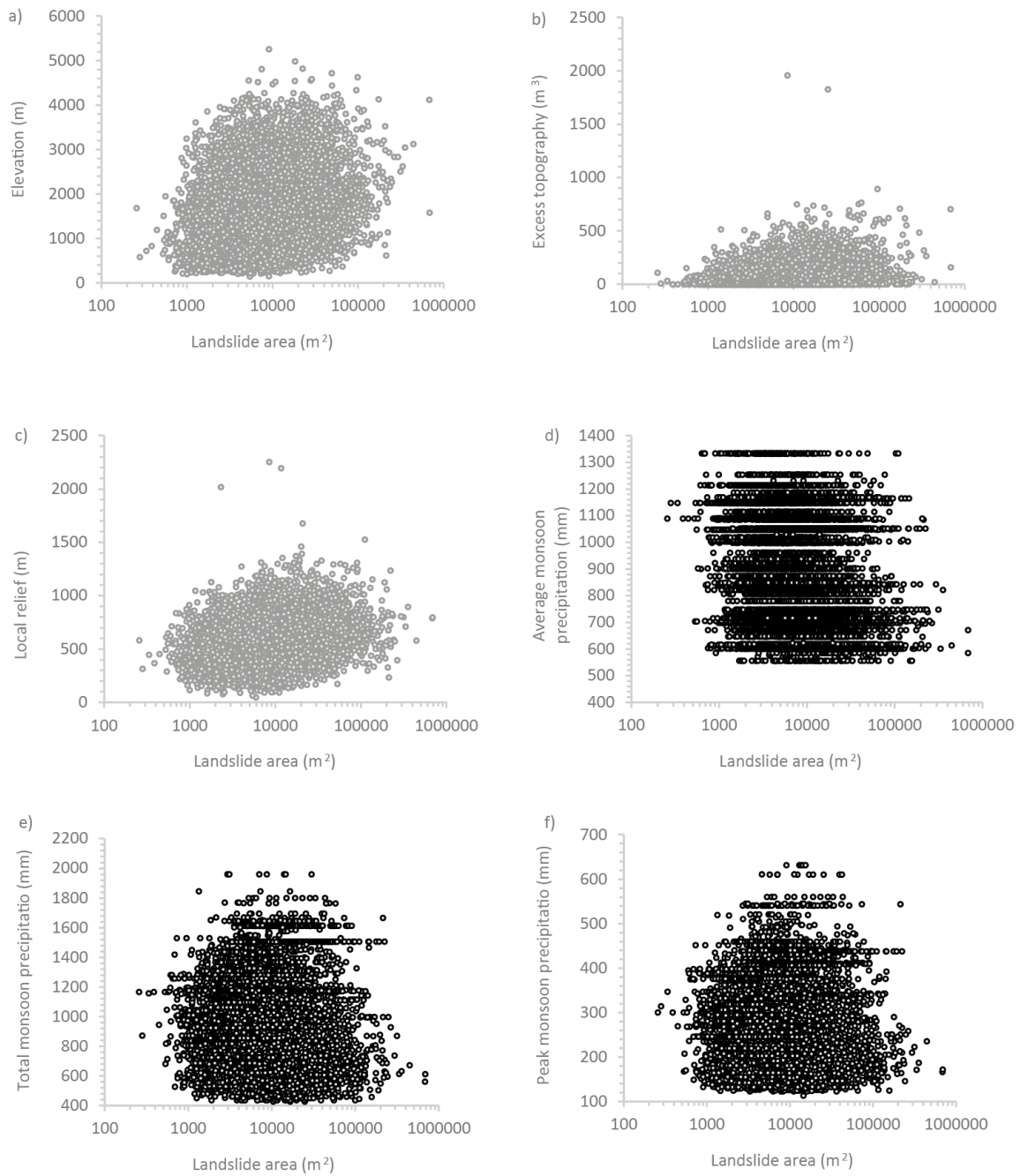


Figure 2.28. Correlation between the log of landslide area and a) elevation, b) excess topography, c) local relief, d) average total monsoon rainfall, e) annual total monsoonal rainfall, and f) annual peak monthly rainfall.

2.7.3 Influences of lithology on landslide distributions and morphology

Lithology is observed to have a strong influence on the spatial distributions of ASM-triggered landslides. Landslides are found to be less likely to have occurred than would be expected in regions with granite/gneisses and Quaternary sandstones/conglomerates given the amount of these rock types across the study region, but more likely than expected to have occurred in regions of schist and phyllite (Fig. 2.21a – c). These results are corroborated by Tanoli *et al.* (2017) who found that 45% of monsoon-triggered landslides in the Upper Bhoite Kosi occurred in phyllites, conglomerates and quartzites. These results are unsurprising given that less indurated sedimentary and lower-grade metamorphic rocks are most susceptible to failure relative to highly indurated igneous and metamorphic rocks (Keefer 2002). Less indurated rocks are typically more porous, thus allowing greater rates of infiltration and permeation. Similarly, structural features such as active and dormant faults allow increased infiltration of groundwater, which can lead to weakening through geochemical alteration (Warr & Cox 2001).

However, in contrast to the ASM-inventory, the Gorkha coseismic landslides were as likely to occur in higher-grade Proterozoic gneisses / granites as they were in lower-grade metamorphic rocks (Gnyawali & Adhikari 2017; Martha *et al.* 2017; Tanoli *et al.* 2017; Roback *et al.* 2018). One potential explanation for this is rock strength. The five main rock types to observe landsliding across Nepal are dolomites, granites/gneisses, phyllites, schists and sandstones. For each of these rock groups, estimates of Uniaxial Compressive Strength (UCS) are obtained from the literature (Bhasin *et al.* 1995; Bagde 2000; Samadhiya & Jain 2003; Bagde & Petroš 2005; Tamrakar *et al.* 2007; Tandon & Gupta 2015) (Table 2.8). Note that these UCS estimates were all from similar rock-types in the Himalaya, but not always from Nepal, and often for a small number of samples. This is an unavoidable limitation of the data availability in this region. These UCS values highlight that, as expected, the higher grade quartzites, gneisses and granites in the Himalaya typically have greater compressive strengths than the schists and sandstones. These rock types will thus require greater applied force to fail, thus explaining why these rock types observed

landsliding during the M_w 7.8 Gorkha earthquake, but do not during a typical monsoon season.

Rock type	Av. UCS (Mpa)	No. UCS Samples	UCS Source	Max area (m ²)	α	Rollover (m ²)
Dolomite	53	6	(Tandon et al., 2014)	131163	1.95	3390
Granite/gneiss	58	21	(Tandon et al., 2014)	680500	1.8	4130
Phyllite	46	11	(Samadhiya & Jain, 2003)	684783	1.67	3272
Sandstone	27	44	(Tamrakar et al., 2007)	212401	2.12	2280
Schist	28	6	(Bagde et al., 2000; Bhasin et al., 1995)	264918	2.04	3178

Table 2.8. Summary of rock type UCS and associated landslide size statistics.

The ASM-inventory and UCS data also allow an opportunity to quantify whether rock strength and lithology influence landslide size. Using the power-law size analysis methodology outlined in section 2.4.3, the three-parameter inverse-gamma distributions are fitted to the ASM-landslides that occur within each of the five main rock types (Fig. 2.29a – e). The UCS values for each rock type are then plotted against mean landslide area, the exponent of the power law, and the rollover of the power-law for the landslides in each rock group (Fig. 2.30a – c; Table 2.8). This shows that harder rock types have larger average landslide size (Fig. 2.30a), and that as rock strength increases the exponent of the inverse power law decreases (Fig. 2.30b), i.e., stronger rock types have a higher proportion of large area landslides. Furthermore, as shown by the position of the rollover (Fig. 2.30c), greater rock strength increases the area of the most frequently observed landslide size. These results provide good evidence to suggest that lithology exerts a direct control on landslide size

This result is corroborated by other studies in the literature. For example, Stark & Guzzetti (2009), Frattini & Crosta (2013), and Roda-Boluda *et al.* (2018) show that landslide size distributions are modulated by lithology and rock strength, with incoherent lithologies typically leading to shallower, smaller landslides, whilst cohesive lithologies lead to deeper, larger landslides. Furthermore, as observed here, Hurst *et al.* (2013) found that rock types with greater strength have landslides with lower exponent values, as these rock types observed a higher proportion of large landslides.

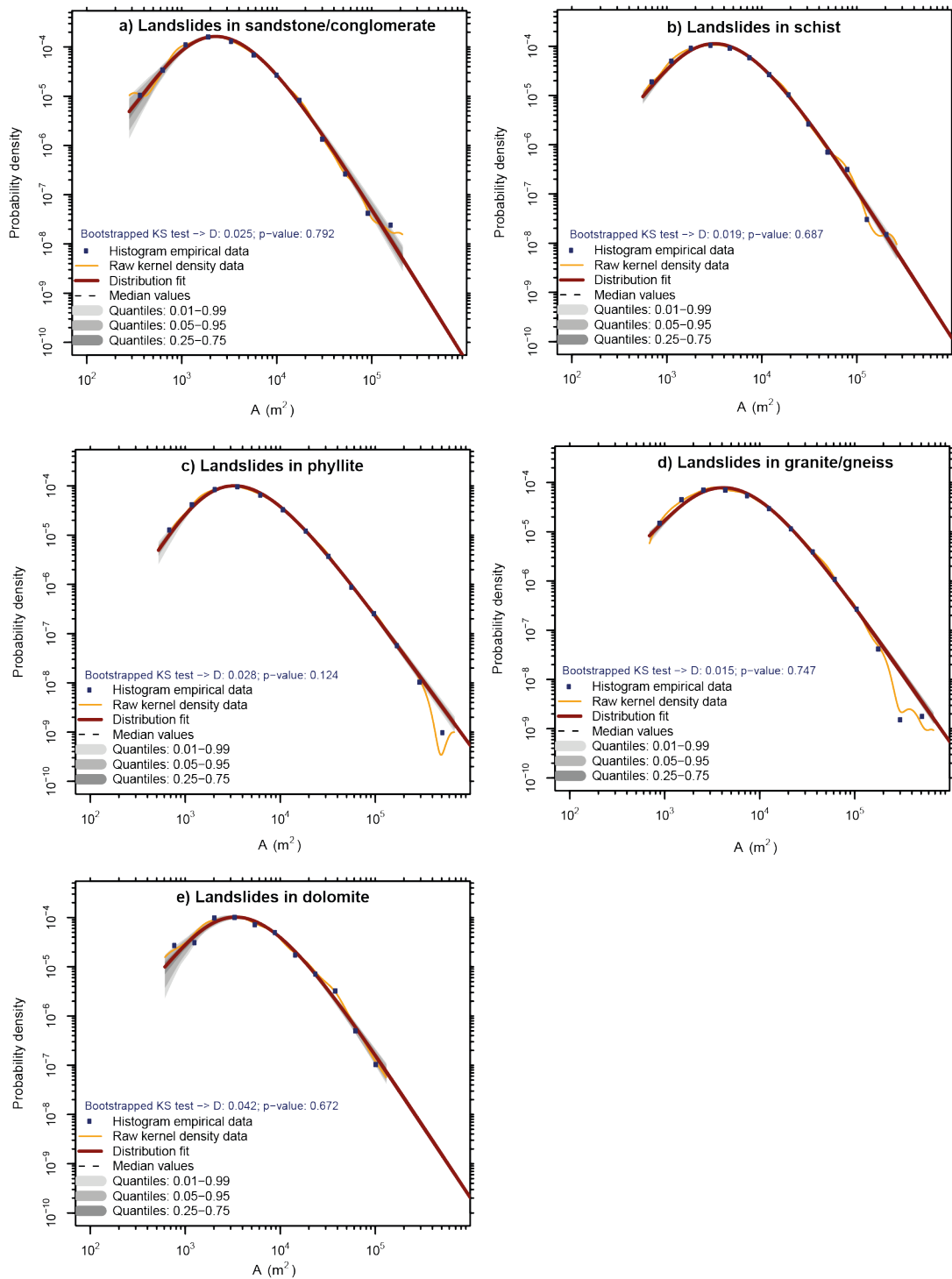


Figure 2.29. Three-parameter inverse-gamma distributions fitted to the probability density functions of landslide area for landslides that occurred within a) sandstone and conglomerate, b) schist, c) phyllite, d) granites and gneisses, and e) dolomites. Note that a p -value > 0.01 indicates that the three-parameter inverse-gamma distribution provide a good fit to the actual data, whilst the D -value gives the maximum distance between the actual data and the fitted distribution.

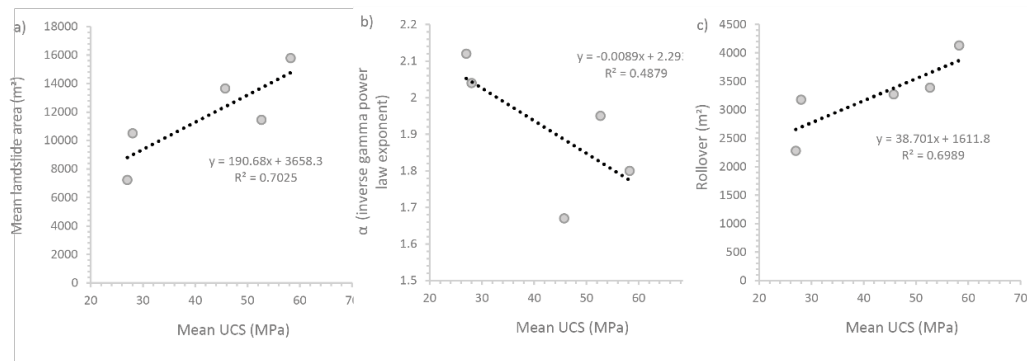


Figure 2.30. Correlations between rock Uniaxial Compressive Strength (UCS) and a) average landslide size, b) power-law exponent, and c) power-law rollover value.

2.7.4 Influences of distance to roads and land use

For distance to roads, the ASM-inventory landslides were slightly more likely to have occurred within 500 m of a road than would have been expected given the distributions of road distances across the study region (Fig. 2.19d – f). This result corroborates that of Tanoli *et al.* (2017) who observed that 49% of monsoon-triggered landslides in the Upper Bhote Kosi were within 800 m of a road. However, in the Upper Bhote Kosi, only 17% of Gorkha coseismic landslides were within 800 m of a road. As roads are typically constructed lower on hillslopes, this difference between monsoon-triggered and coseismic landslides is likely because coseismic events tend to occur at higher slope positions. The results for the ASM-inventory are also corroborated by McAdoo *et al.* (2018), who find that monsoon-triggered landslides in central Nepal are twice as likely in terrain with poorly constructed roads as would be expected in the absence of roads. This is because road undercutting leads to over-steepened hillslopes that are more prone to both shallow and deep-seated failures (Sidle & Ochiai 2006).

Compared to the land use distributions across the study region, the ASM-inventory landslides were more likely to occur than expected in irrigated and rain-fed cropland, but less likely than expected where snow/ice was permanent and in forested regions (Fig. 2.20d – f). Similarly, Tanoli *et al.* (2017) found that 50% of monsoon-triggered landslides in the Upper Bhote Kosi occurred in cultivated land and just 21% in forest. However, Tanoli *et al.* (2017) also describe how 44% of 2015 coseismic landslides in

the same region occurred in forest compared to just 23% in cultivated land. This is likely another reflection of the shifting topographic position of the coseismic landslides relative to the monsoon-triggered, with coseismic landslides occurring on higher hillslopes where there is less cultivated land and more natural forest. These results are likely explained by the fact that poorly managed drainage and cultivation systems can increase infiltration rates and reduce soil cohesion (Alexander 1992). Furthermore, where forest has been cleared for cultivation, the loss of deep-rooted vegetation can decrease slope stability as less water is removed via transpiration (Sidle & Bogaard 2016).

2.7.5 Landslide susceptibility

2.7.5.1 Regression coefficients and AUROC

For those factors selected at least 50% of the time by the LASSO, the assigned regression coefficients are consistent with the observations from the control factor analysis in section 2.6.4. Factors such as snow/ice, permafrost, elevation, profile curvature, aspect and forest have negative regression coefficients of varying magnitudes, suggesting that as the values (or presence, in the case of the categorical variables) of those factors increase, probability of landsliding decreases. However, it should be noted that the results pertaining to snow/ice and permafrost could be due to incomplete landslide mapping in snow-covered regions (see section 2.2.3.3.). Similarly, factors such as slope angle, local relief, quaternary sandstones/conglomerates, cropland, planform curvature and mean precipitation all had positive regression coefficients, suggesting that as the values (or presence) of these factors increase so does the probability of landsliding. However, potentially important predisposing factors such as near channel k_{sn} and distance to both rivers and roads, were very rarely selected as dominant controls on landslide occurrence by the LASSO. This highlights the importance of using such factor selection operators to reduce model complexity, as these factors are often, perhaps unnecessarily, included in landslide susceptibility studies. In this case, the low importance of distance to roads could be due to the temporal issues relating to the road data as outlined in section 2.3.2.7.

The self-validated and independently validated AUROC results ($AUC \approx 0.77$), confirm that the model is successful at estimating landslide occurrence, but how does it compare to other susceptibility models developed in the study region? Table 2.9 summarises the results of several other susceptibility models developed for this region. Across the various methods, prediction AUROC values are typically 0.58 – 0.90, with an average across Table 2.9 of 0.79. The ASM- inventory model developed here is thus slightly below the average. One explanation for this is study region size. The average study size of the models in Table 2.9 is $\sim 400 \text{ km}^2$, whereas the study region used here is $\sim 45,000 \text{ km}^2$. This is potentially a large source of error in the ASM-inventory model, because as described throughout the results and discussion section, significant variations in landslide characteristics and distribution are observed across the different tectonic units that make up the overall region. As such, the ASM-inventory model developed here is deriving regression coefficients that give the average response of landsliding to a given control factor across regions with a heterogeneous landslide response, whereas the models in Table 2.9 will be obtaining coefficients that are specific to their respective localities. This issue of spatial dependency is discussed further in the following section.

2.7.5.2 Data and methodological limitations

There are a number of limitations with the data and methodology used in this chapter to model susceptibility. First, is data availability and resolution. Nepal is a data-scarce country that lacks freely available high resolution ($< 30 \text{ m}$) topographical data, whilst data for factors such as land use, PFI and geology are only available at regional scales, often without significant field validation and only at specific time periods. For geological data, only regional bedrock information is available, with limited structural and lithological information. The lack of structural geology data is potentially problematic, as bedrock faulting, foliation and fracture spacing are known to influence slope stability and source material availability (Neely & DiBiase 2020; Verdian *et al.* 2020). This limitation is considered further in Chapter 3, where field investigations in two sub regions of the wider study region were undertaken to obtain detailed geological data and quantitatively assess the influences of geology on landslide occurrence.

Reference	Region size	Inventory type	Model type	Validation type	Prediction power
(Poudyal et al., 2010)	168 km ²	Monsoon (historical)	Frequency Ratio	AUC (with other data)	0.822
"	"	"	Artificial Neural Network	"	0.782
(Regmi et al., 2014a)	138 km ²	Monsoon (historical)	Frequency Ratio	AUC (67% train, 33% test)	0.754
"	"	"	Statistical Index	"	0.749
"	"	"	Weights of Evidence	"	0.746
(Devkota et al., 2013)	65 km ²	Monsoon (historical)	Index of Entropy	AUC (75% train, 25% test)	0.902
"	"	"	Logistic Regression	"	0.863
"	"	"	Certainty Actor	"	0.836
(Kayastha, 2012)	228 km ²	Monsoon (historical)	Fuzzy Logic	AUC	0.79
(Regmi et al., 2016)	121 km ²	Monsoon (historical)	Evidential Belief Function	AUC (80% train, 25% test)	0.864
(Regmi et al., 2014b)	71 km ²	Monsoon (historical)	Frequency Ratio	AUC (70% train, 30% test)	0.786
"	"	"	Weights of Evidence	"	0.796
(Kayastha et al., 2013)	562 km ²	Monsoon (historical)	Analystical Hierarchy Process	AUC	0.775
(Dahal, 2013)	3844 km ²	Monsoon (historical)	Logistic Regression	AUC (with other data)	0.82
(Acharya & Lee, 2018)	58 km ²	Monsoon (historical) + coseismic	Relative Frequency	AUC (70% train, 30% test)	0.581
(Tanoli et al., 2017)	404 km ²	Monsoon (historical)	Frequency Ratio	AUC	0.78

Table 2.9. Summary of published susceptibility models developed within the study region used for this thesis.

For land use and PFI, unfortunately there are no methods within the scope of this project that can be used to improve the data availability. As such, it is necessary to consider the impacts of this lower resolution data on the susceptibility results. For both the permanent snow/ice land use class and PFI, the regression coefficients magnitudes are large (> 0.5). Consequently, the low resolution of both of these datasets is leaving visible linear features within the susceptibility maps at the boundaries between class values. For example, in the Langtang sub region (Fig. 2.25c), there are multiple sharp changes in susceptibility that clearly do not correspond with topographically sensible changes in hillslope stability. These changes are found to directly correspond with the grid-cells of the land use and PFI inputs, highlighting that in the Greater Himalaya, regions that transition to snow/ice and/or PFI are being assigned geomorphologically unfeasible susceptibility changes that are actually artefacts of low data resolution.

Second, whilst the BLR approach used within this chapter is the most commonly applied approach to landslide susceptibility (Reichenbach *et al.* 2018), there remain several limitations and uncertainties with this approach. One, as with many others models across the literature (e.g. Youssef *et al.* 2016; Camilo *et al.* 2017; Lombardo & Mai 2018; Arabameri *et al.* 2019), the factors used within the BLR model are assumed to have a linear influence on landslide occurrence. In other words, a factor is assigned a single value, where a single positive value suggests that as that factor increases the likelihood of landslide occurrence increases, and vice versa. As shown by the AUROC, this approach does a good job at predicting landslide occurrence. However, as outlined throughout the results and discussion section, several of the most dominant factors in the regression model (e.g. elevation; Fig. 2.17a - c) do not exhibit a purely linear relationship with landslide occurrence, meaning that this linear assumption may not be optimal. Two, the results from this Chapter are obtained from analysis and modelling that was largely spatially and temporally independent. In other words, with the exception of the results pertaining to the different tectonic units, it did not consider how landslide characteristics and susceptibility varied through space and time. However, as outlined in detail in Chapter 1 (section 1.2), it is known that spatial heterogeneity can impact landslide occurrence, as can some transient, time-dependent processes such as landslide path dependency and earthquake preconditioning. As such, the following Chapters consider in more detail the issues of spatial and temporal heterogeneity. Chapter 3 will focus on the spatial heterogeneity of landslide characteristics and susceptibility in two distinctly different landscapes, Langtang Valley and the Arniko Highway. Chapter 4 will then consider temporal issues such as path dependency, and quantify whether temporal variations in landslide spatial distribution impact landslide susceptibility modelling. Finally, Chapter 5 will investigate how rates of landslide occurrence change through time, with a focus on quantifying the earthquake preconditioning process, before Chapter 6 discusses the wider implications of these issues for BLR-type susceptibility modelling.

2.7.6 Conclusions

Following the principles of landslides inventory mapping, Landsat imagery was used to develop a 30-year multi-seasonal monsoon-triggered landslide inventory containing 12,838 events across a ~45,000 km² region of central eastern Nepal. Analysis of this inventory according to landslide geometries, sizes, and spatial distributions, as well as an assessment of regional-scale landslide susceptibility, allowed the determination of the following key results:

1. Compared to the characteristics of the study region, monsoon-triggered landslides had high likelihoods of occurring at S/SE-facing aspects, slopes of 35 – 55°, excess topographies of 50 – 100 m³, convex curvature, elevations of < 2400 m, no permanent snow/ice/permafrost, local reliefs of 400 – 1000 m, between 100 – 400 m of channels, have a land use dominated by irrigated or rain-fed cropland, and have a bedrock geology dominated by lower grade metamorphic rocks such as schist and phyllite.
2. 14% of the landslides mapped here exhibit path dependence: on average these landslides are larger (though with a smaller maximum potential size), have lower roundness, and have higher ARs than spatially unassociated landslides. The temporal characteristics of path dependency are analysed and discussed further in Chapter 4.
3. Landslides in the Greater Himalaya and northern Lesser Himalaya have higher average ARs than the southern Lesser Himalaya and sub Himalaya, where runout is likely limited by local relief. High AR landslides are observed to have very different characteristics to lower AR landslides, with the former having larger average areas and occurring at higher elevations, higher local reliefs and further from channels.
4. Landslides in the Greater Himalaya have larger average areas than landslides elsewhere across the study region. This is likely due to the coincidence of extreme topography and harder bedrock in the Greater Himalaya, with rock strength observed to exhibit positive correlation with landslide areas, and negative correlation with the exponents of fitted three-parameter inverse-gamma distributions fitted to landslide size distributions.

5. A BLR model applied to the entire ASM-inventory produced a susceptibility model capable of predicting landslide occurrence across the region with AUROC values of ~ 0.77 . However, the limitations of this approach with respect to data availability, spatial dependency and temporal dependency are highlighted, and reference made to subsequent chapters where these issues will be investigated further.

Chapter 3 Spatial heterogeneity in landslide processes: insights from field data and BLR susceptibility modelling

Note, parts of this Chapter relating to the field observations in Langtang Valley have been published in the Quarterly Journal of Engineering Geology and Hydrogeology (Jones et al. 2020). The author copy of this publication can be found in Appendix C. The format of this chapter is not the same as the publication, with the Chapter having a different structure and further integrated analysis and discussion relating to subsequently conducted fieldwork along the Arniko Highway.

3.1 Introduction

The results from Chapter 2 were based solely on remotely sensed data. The main remote datasets used were Landsat imagery, which have a 15 – 30 m resolution, and the ALOS DEM, which has a 30 m resolution (see Chapter 2, sections 2.2.3 and 2.3.2). The relatively low resolutions of these data resulted in only broad classifications of landslide type, based solely on landslide geometries. Furthermore, whilst topographical data exist across the study region, detailed lithological and structural geology data are lacking. Consequently, detailed information on the landslide types across the study region and the impacts of lithology and structural geology on landslide occurrence remains uncertain. This latter point is important, as lithological and structural data are commonly used parameters for modelling landslide occurrence (e.g., Reichenbach et al., 2018), so it is important to assess how these controls may affect landslides within the study region. Similarly, as outlined in Chapter 1, section 1.4.3, understanding landslide type has important implications for interpreting landslide susceptibility models outputs and for how landslide

susceptibility models might inform subsequent landslide hazard management and mitigation.

Furthermore, the results from Chapter 2 included only limited consideration of how landslide characteristics, processes and susceptibility vary spatially. As discussed in Chapter 1 (section 1.2), it is known that landslide occurrence can be highly spatially heterogeneous. Indeed, the limited consideration of spatial heterogeneity in Chapter 2 (e.g. section 2.6.4) suggests that there are significant variations in landslide occurrence across the main tectonic units of the study region. This is unsurprising given that these tectonic units include both fluviially and glacially-dominated landscapes, which are known to be affected by different geomorphological processes and landforms (Mccoll 2012). However, as yet, the impacts of any potential spatial heterogeneity on landslide susceptibility modelling has not been considered.

As such, the overall aim of this chapter is to expand upon Chapter 2 by using additional field data from two sub-regions with distinctly different landscapes (Langtang Valley and the Arniko Highway) to investigate the spatial characteristics, types, processes, and BLR-based susceptibility of landslides in Nepal. The main objectives of this chapter are as follows:

- 1) To use additional field data (landslide observations, lithological descriptions, and structural data) collected from two sub-regions with distinctly different landscapes (Langtang Valley and the Arniko Highway; see section 3.2) to provide further insight into landslide characteristics, types, processes, and spatial distributions, with a focus on how these vary spatially. Specifically, this will involve using the field observations from each sub-region to qualitatively describe the landslide types and failure processes across both sub-regions, as well as investigating how lithology and structural geology are influencing landslide occurrence. Finally, combining the obtained information on landslide type with the susceptibility model outputs allows for discussion into how landslide type affects the applicability and interpretation of landslide susceptibility modelling and hazard management in Nepal.

- 2) To combine the field data from 1) with a comprehensive inventory of Gorkha earthquake coseismic landslides to assess how spatial heterogeneity in landslide

occurrence impacts BLR-type susceptibility models. Specifically, for each sub-region, landslide inventories are developed using a combination of field mapping and remote sensing from high resolution (1 – 5 m) GoogleEarth imagery. The BLR modelling techniques described in Chapter 2 (section 2.5) are then used to quantify how landslide occurrence in each sub-region relates to several landslide control factors, and to develop local-scale landslide susceptibility models for each region. The ability of each susceptibility model to forecast or hindcast the landslide data from the other region is then assessed using AUROC validation. Finally, a BLR coseismic landslide susceptibility model is developed for the wider study region using the Gorkha coseismic inventory. This regional-scale model is then used to hindcast the coseismic landslide occurrences in each of the two-sub regions, in order to assess how well regional-scale models can classify local landslide occurrence. This answers the questions raised in Chapter 1 (sections 1.2.1 and 1.3) pertaining to spatial heterogeneity, which are: how well can susceptibility models developed from one region be used to forecast/hindcast another? How well do regional-scale landslide susceptibility models forecast/hindcast local regions? And consequently, is it appropriate to undertake spatially disparate or regional scale susceptibility modelling without considering spatial heterogeneity?

3.2 Study region

This section will describe the locations, known geologies, and geomorphologies of the two study regions used in this chapter: Langtang Valley and the Arniko Highway.

3.2.1 Langtang Valley

Langtang Valley is located ~60 km north of Kathmandu near the Nepal – China border (Fig. 3.1a). It is a U-shaped valley that forms part of the Langtang river catchment. Langtang Valley is 46% glaciated (Immerzeel *et al.* 2012), and is strongly influenced by glacial, periglacial, and fluvial processes of erosion. Here, a 320 km² portion of the valley is investigated (Fig. 3.1b). Geomorphologically, the landforms found across the valley are diverse, with active glaciers, moraines, alluvial fans, braided rivers, landslides, rock avalanches, debris-flows and sediment-mantled slopes. Topographically, elevations across the valley range from 1400 – 7100 m, with

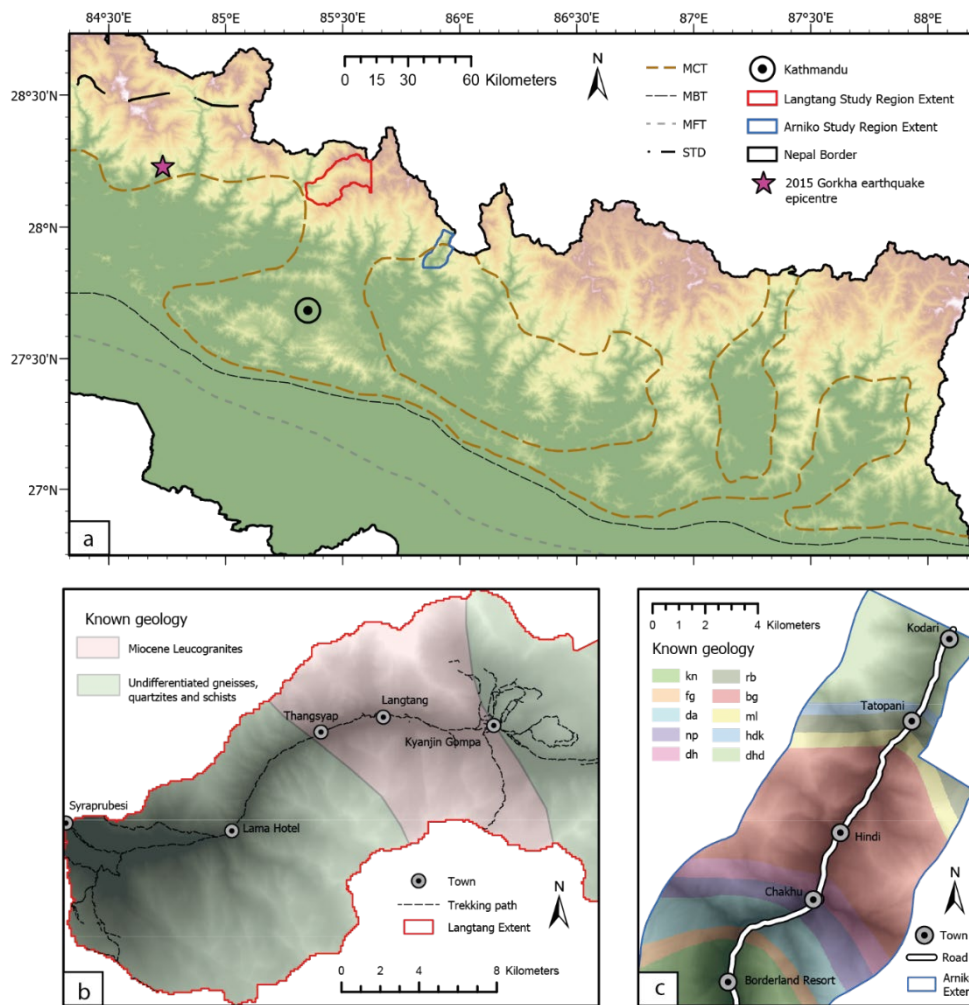


Figure 3.1. a) regional locations of Langtang Valley (red outline), the Arniko Highway (blue outline), Kathmandu, the Gorkha earthquake epicentre, the Main Central Thrust (MCT), Main Boundary Thrust (MBT), Main Frontal Thrust (MFT) and the South Tibetan Detachment (STD). b) The known geology, main towns, and trekking routes within Langtang. c) The known geology, main towns, and main road within the Arniko region. All geology data are from maps provided by the Nepal Government Department of Mines and Geology

an average hillslope angle of 33°. Approximately 80% of Langtang’s annual precipitation (~700 mm) occurs during the monsoon season (Lacroix 2016), and ~60% of the valley contains permafrost (Gruber 2012).

The valley lies within the Greater Himalayan Sequence, bounded by the Main Central Thrust (MCT) to the south and the South Tibetan Detachment (STD) to the north. The lithology of the valley is poorly constrained, mapped by the Nepal Department of Mines and Geology as simply “undifferentiated gneisses, migmatites,

quartzites and schists” (Fig. 3.1b). A band of Miocene leucogranites is also known to extend through the central-eastern portion of the valley (Inger & Harris 1993; Decelles *et al.* 2001) (Fig. 3.1b). There is no existing information on the discontinuity geometries of these units, barring two dip/dip-direction measurements recorded by the Nepal Department of Geology and Mines (Department of Mines and Geology 2021). Langtang Valley is also socioeconomically important for both the local populace and the wider country. It hosts a large National Park that is popular with trekkers, making tourism the main form of income alongside agriculture for the ~4500 people who live across the five main settlements in the valley (Lama Hotel, Bamboo, Thangsyap, Langtang and Kyanjin Gompa). In 2015, Gorkha coseismic landslides caused a significant humanitarian crisis across Langtang. In particular, the devastating ‘Langtang Avalanche’, a large debris fall composed of glacial ice, snow and rock, completely buried the village of Langtang, killing over 350 people (Kargel *et al.* 2016). The valley was completely closed to both locals and tourists for several months after the earthquake, but since mid-2016 has experienced significant reconstruction and is now once again open to tourism. However, as outlined by Jones *et al.* (2020), landslides continue to pose significant risks to the trekking infrastructure across the Valley.

3.2.2 Arniko Highway

The Arniko Highway stretches from Kathmandu to the Nepal-China border town of Kodari (Fig.3.1a). This thesis investigates a 110 km² portion of the northern part of the highway, located ~50 km north east of Kathmandu (Fig. 3.1a, c). The landscape here is dominated by steeply incised bedrock-limited rivers, bounded by river terraces and anthropogenic terraces developed for agriculture. Elevations extend from ~1000 – 3600 m, with an average hillslope angle of 33°. In contrast to Langtang, these lower elevations lack glaciation or permafrost cover, with the landscape instead dominated by fluvial erosion. As with most of Nepal, this region receives the majority of its rainfall during the monsoon months, with an annual average of 600 – 800 mm of rainfall.

Geologically, this region is intersected by the Main Central Thrust, with bedrock lithologies dominated by varying metamorphic grade phyllites, schists, dolomites and quartzites. The lithologies across the region are better defined than they are in Langtang, with ten formations classified by the Nepal Department of Geology and Mines (Fig. 3.1c). However, like Langtang, the region lacks comprehensive data on discontinuity geometries.

This region also has significant socioeconomic importance. Until recently, this highway was the main trade route between China and Nepal, thus providing a vital economic service for the entire country and supporting a number of towns along the highway (Fig. 3.1c). This region also attracts tourists, particularly for white water rafting, bungee jumping, and trekking.

3.3 Methods

This section describes the main methodologies used to collect field data and model the results. It should be noted that the susceptibility modelling methodologies used in this chapter are described in Chapter 2 (section 2.5), so will not be repeated in full here.

3.3.1 Field methodologies

The main aims of the fieldwork were to map, observe and collect data on variations in landslide characteristics, bedrock lithology and structural geology across each study region using the methodologies described in the following sections. Further details on field methodologies and observation can be found in Jones *et al.* (2020) (Appendix C).

3.3.1.1 Landslide mapping

In both study regions, observed landslides were mapped using the following approach. First, the locations of an observed landslide would be recorded using a GARMIN 78 series handheld GPS unit. For landslides that were physically accessible (i.e. they intersected a trekking path or road) the GPS coordinates were recorded as being 'on the landslide'. For landslides that were being viewed on the opposite side

of the valley the coordinates were recorded as being ‘opposite the landslide’ and the compass direction between the GPS location and the landslide was recorded.

In select cases that provided particularly good examples of landslide type or failure process, geomorphological sketches (e.g. Griffiths et al., 2015) of the landslides were constructed. The geomorphological sketches included the size and morphology of the landslides, including the source, runout and debris zones, as well as the morphology of the hillslope on which the landslide had occurred. Hillslope and landslide morphologies were obtained using field walkover surveys conducted using a TruPulse 360 laser rangefinder and handheld GPS unit. The geomorphological sketches also included other geomorphological features within the landscape such as rivers, terraces, relict channels, state of the terrain (e.g. hummocky, planar, etc.), level of vegetation and whether any human structures were present.

Once mapping had been completed in the field, the identified landslides were corroborated using high resolution satellite imagery (2017 Planet Team Rapid Eye imagery for Langtang, 2017 Google Earth Pro/CNES/Airbus imagery for Arniko). This was done because field mapping has inherent sampling bias introduced by the fact that the topography results in only being able to map landslides that are visible from the ground. The field observations and remote imagery were then used in tandem to delineate final polygons of each mapped landslide. In both cases, though mostly in the Arniko region, satellite imagery was also used to remotely map landslides that were unreachable in the field, to ensure that the landslide inventories for each region were sufficiently complete. As such, in both locations, the final inventories should be considered as combined field-remote sensing inventories. The final polygonal landslide inventories developed for Langtang and Arniko are provided in Data Files 3 and 4, which can be accessed [here](#) and [here](#).

3.3.1.2 Lithological mapping

Across both study regions, lithological descriptions were obtained from bedrock outcrops and landslide debris deposits where safely accessible. The lithologies were assessed according to identified mineralogy, measured mineral size, degree of foliation, degree of fracturing and texture. Where possible, rock shear strengths were

estimated. This was done using a ‘simple means’ test as outlined by Hack and Huisman (2002). This method allows an estimation of rock strength based on how a sample responds to applied pressure (Table 3.1). These tests are most accurate when conducted on intact bedrock. However, as this was not always possible, when applied to landslide debris it was ensured that the tested samples were as un-weathered as possible and at least 40 x 40 cm in size.

Intact rock strength	simple means' test (standard geological hammer of approx. 1 kg)
< 1.25 MPa	Crumbles in hand
1.25 - 5.0 MPa	Thin slabs break easily in hand
5.0 - 12.5 MPa	Thin slabs break by heavy hand pressure
12.5 - 50 MPa	Lumps broken by light hammer blows
50 - 100 MPa	Lumps broken by heavy hammer blows
100 - 200 MPa	Lumps only chip by heavy hammer blows
> 200 MPa	Rocks ring on hammer blows. Spaks fly

Table 3.1. Rock-strength estimate descriptions of Hack and Huisman (2002).

3.3.1.3 Structural mapping

Across both study regions the geometries (dip / dip-direction) of any visible structural discontinuities (mostly joints and faults) in bedrock outcrops were measured. Ideally, these measurements were taken directly from the outcrop. However, in some cases the bedrock was inaccessible, so in these cases discontinuity geometries were estimated from a distance using a compass clinometer.

3.3.1.4 Landslide susceptibility mapping

Using the same methodology as described in Chapter 2 (section 2.5), BLR models implemented alongside a LASSO were developed for both study regions. As with the analysis in Chapter 2, for each region, 50 balanced training subsets consisting of 70% of the landslide presences and an equal number of randomly selected absences were modelled. This allows for an appreciation of error and uncertainty, as well as returning results on LASSO percentage selection for each independent predisposing

factor considered. These models used most of same independent predisposing factor datasets as used in Chapter 2, however, in this case, average 30-year precipitation and distance to roads were not used. Average precipitation was omitted because the Arniko region is only encompassed by one rainfall grid-cell, and Langtang by only two cells, so there are insufficient data values in this factor for accurate regression. Distance to roads was omitted because it was found to be highly collinear with elevation. As such, the elevation results should be interpreted with consideration of distance to roads. Once the 50 models for each region had been developed, they were validated following the AUROC methods outlined in Chapter 2 (section 2.5.5) using 10-fold cross validation with 10 balanced testing subsets consisting of 30% of the landslide presences and an equal number of randomly selected absences. Finally, to assess how spatial heterogeneity in landslide control factors between the two regions impacts model predictive power, 10-fold AUROC cross-validation was used to assess how well each region's developed susceptibility models could forecast/hindcast the landslide occurrences in the other region.

3.4 Results

3.4.1 Lithological units

As outlined in section 3.2.1, the lithology of Langtang was previously defined only as “undifferentiated gneisses, migmatites, quartzites and schists”, with a known band of Miocene leucogranite (Inger & Harris 1993). Here, four main lithological units across the region are defined and described. Conversely, as outlined in section 3.2.2, the Arniko highway had 10 units already defined, most of which were combinations of phyllite, quartzite, schist, and dolomite. However, detailed lithological information on these rock types was unavailable, so more detailed descriptions of each type are now presented.

3.4.1.1 Langtang Unit 1

The first unit is a gneiss dominated by muscovite, biotite, and quartz, with subordinate plagioclase and garnet. This unit is medium to coarse grained, with an average crystal size of 0.3 – 3 cm. The minerals were generally quite platy (Fig. 3.2a), with elongated plagioclase orientated parallel to foliation (Fig. 3.2b) and in some

cases a strong mylonitic fabric (Fig. 3.2c), particularly in the outcrops nearest Syraprubesi (Fig. 3.2d). *In situ* strength tests conducted on both outcrops and loose debris suggest that this unit is hard (50 – 100 MPa).

3.4.1.2 Langtang Unit 2

The second unit is a gneiss dominated by muscovite, biotite, and quartz, with subordinate tourmaline (Fig. 3.3a). Like unit 1, this unit is medium to coarse grained, but with slightly larger average crystal sizes of 1 – 3 cm and only occasional evidence of migmatite facies (Fig. 3.3b). This unit had very occasional garnet (Fig. 3.3c), but this was far less pervasive than in unit 1. This unit had much higher proportions (60 – 70%) of muscovite and biotite compared to unit 1 (Fig. 3.3c), which, combined with the presence of tourmaline, possibly suggests an igneous protolith. In many cases, this unit had been intruded by leucogranites (Fig. 3.3b). Strength tests conducted on both outcrops and debris (Fig. 3.3d) suggest that this unit was very hard (100 – 250 MPa).

3.4.1.3 Langtang Unit 3

The third unit is the Miocene leucogranites. The leucogranite was coarse-grained, with a crystalline texture and minerals that were frequently 2 – 6 cm. This unit was dominated by quartz and plagioclase, and was often found with large minerals of muscovite, tourmaline, epidote and occasionally garnet (Fig. 3.4a - d). These observations are in agreement with Inger & Harris, (1993) who described two main groups of leucogranite in this region: a muscovite-biotite facies and a tourmaline – muscovite facies. This unit was often found intruded within unit 4 (Fig. 3.4e) and was commonly observed in the bedrock scars of landslides in the eastern portions of the valley (Fig. 3.4f). In terms of strength, this unit was measured as hard to very hard (50 – 250 MPa).

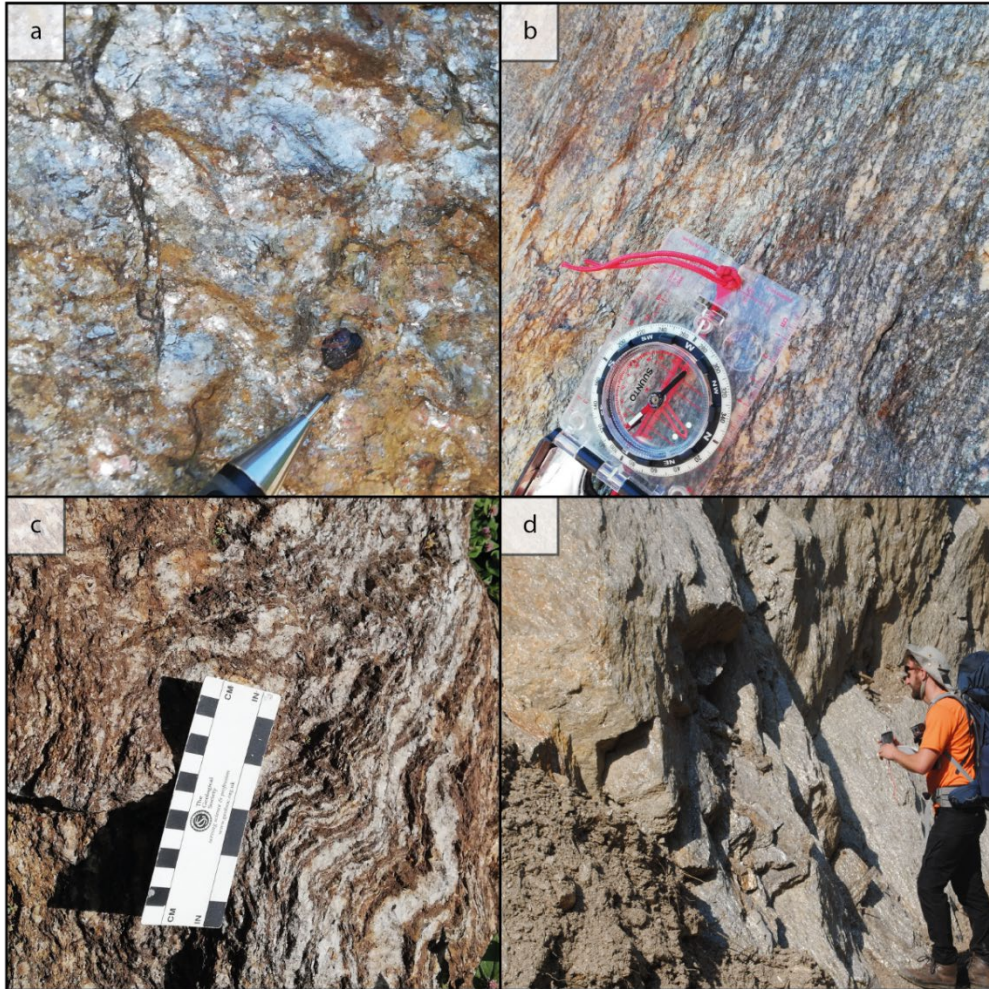


Figure 3.2. Photo panel depicting Langtang Unit 1. a) platy mineral texture and small garnet minerals. b) elongated plagioclase orientated parallel to foliation. c) mylonitic fabric. d) typical appearance of an outcrop.

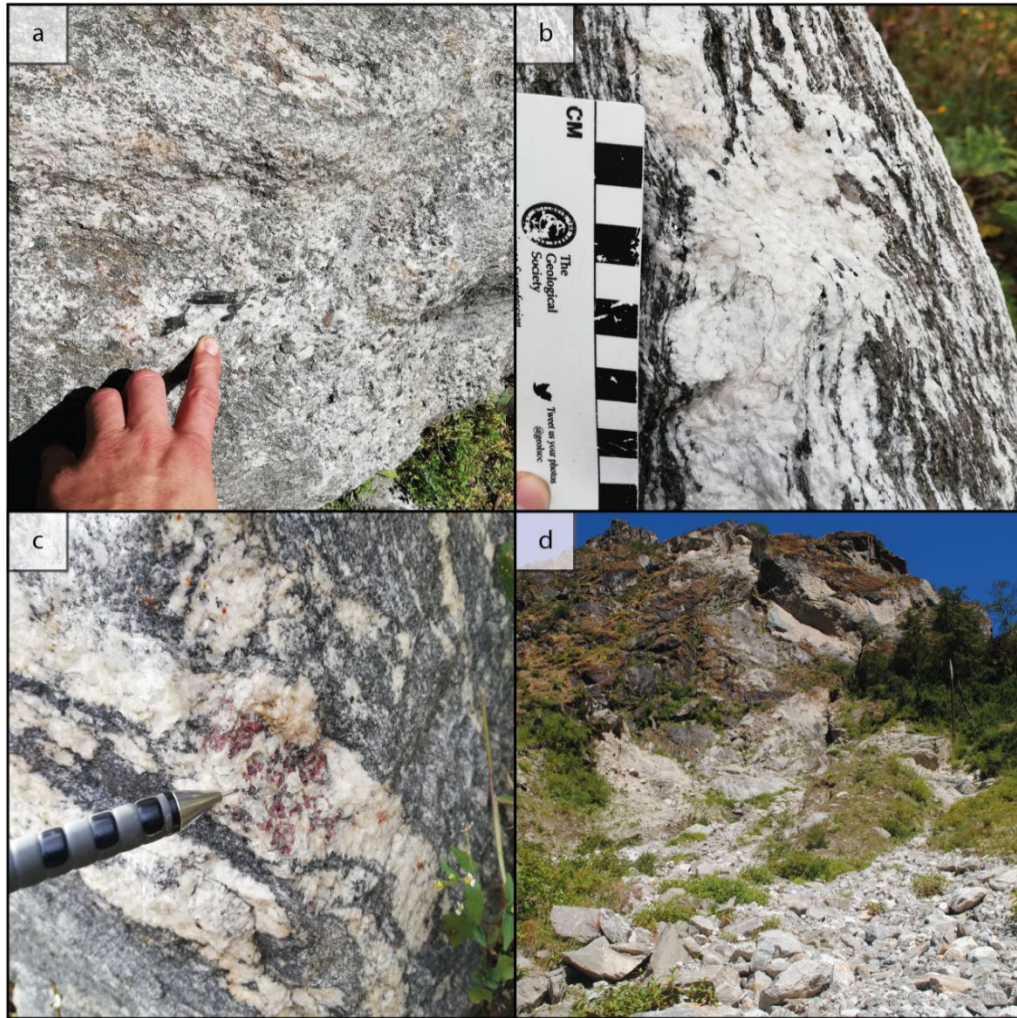


Figure 3.3. Photo panel depicting Langtang Unit 2. a) mineralogy dominated by muscovite, biotite, and quartz, with subordinate tourmaline. b) mylonitic fabric and leucogranite intrusions. c) high proportions of biotite and muscovite with occasional garnets within leucogranite intrusions. d) typical appearance of an outcrop / landslide scar.

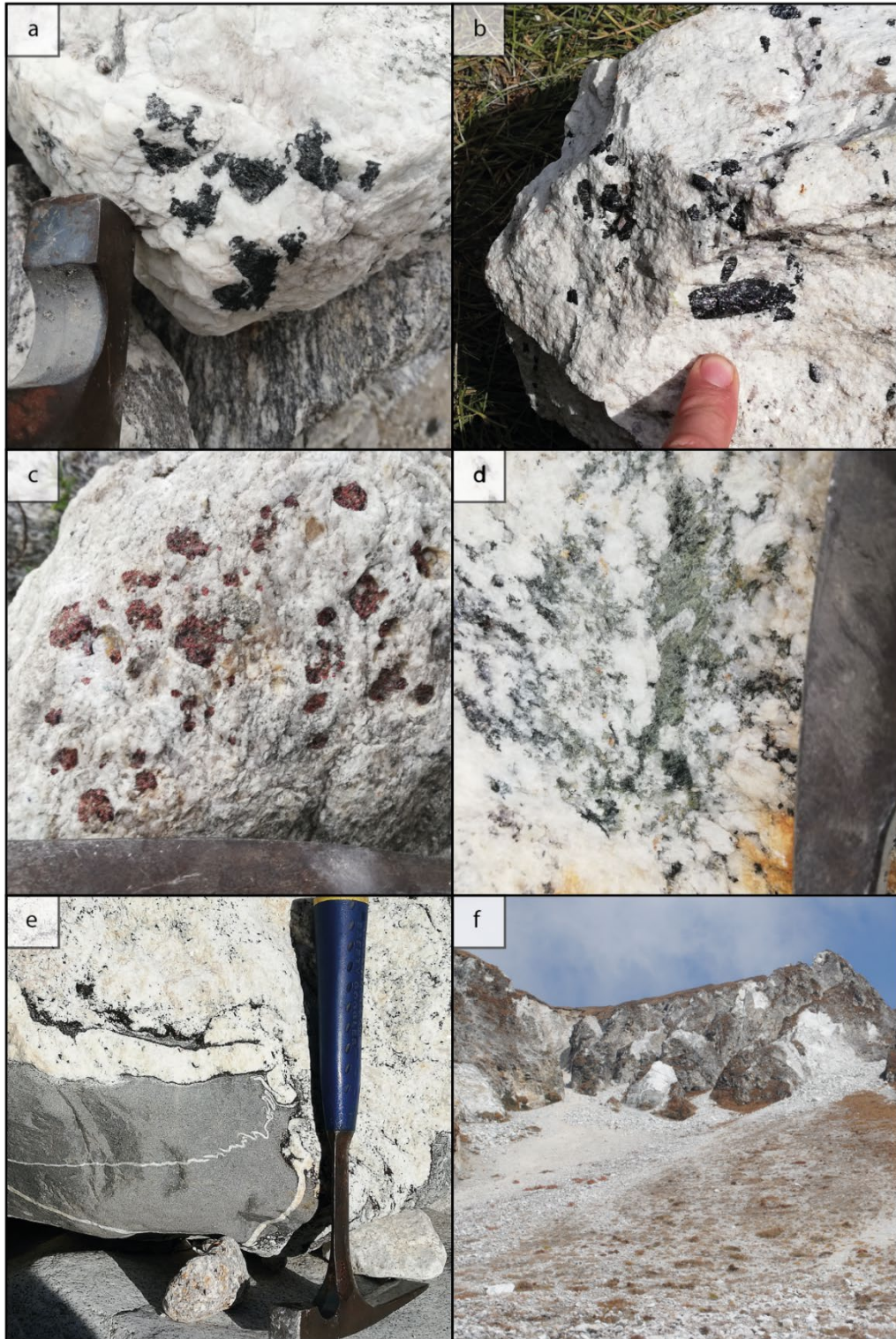


Figure 3.4. Photo panel depicting Langtang Unit 3. Leucogranites dominated by a) muscovite, b) tourmaline, c) garnet and d) epidote, were common. This unit was often found intruded into unit 4 (e) and in bedrock across the eastern portions of the valley (f).

3.4.1.4 Langtang Unit 4

The fourth unit in Langtang is a biotite, plagioclase, muscovite, quartz, semi-pelite schist. This unit was finer grained than the other units, with mineral sizes of 0.1 – 1 cm (Fig. 3.5a – c). It was dark to light grey in colour and was frequently observed in contact with leucogranite (Fig. 3.5b - c). Due to its fine-grained nature, it is hypothesised that this unit had a much more fine-grained protolith than units 1 and 2, possibly a mudstone. This unit was found to be very hard (100 – 250 MPa).

3.4.1.5 Arniko phyllite

The phyllites in the Arniko region were very fine-grained (0.1 – 0.5 cm) and very well foliated at the grain scale (Fig. 3.6a – d) They were typically composed of ~30-40% muscovite, which was often very platy, 30 – 40% plagioclase, ~10% biotite, ~30% quartz (Fig. 3.6a) and occasional small (< 0.5 cm) garnets. These phyllites were commonly intruded by quartz veins (Fig. 3.6c), which were often micro-folded. *In situ* strength tests suggest they had a shear strength of 5 – 100 MPa.

3.4.1.6 Arniko quartzite

The quartzites in the Arniko region were fine – to medium-grained (0.5 – 2 cm) with a crystalline structure composed of 60 – 75% quartz with subordinate biotite and plagioclase (Fig. 3.7a – b). *In situ* strength tests suggest they had a shear strength of 50 – 200 MPa.

3.4.1.7 Arniko schist

The schists in the Arniko region were very fine-grained (0.1 – 1 cm) and well foliated (sub cm spacing). They were typically composed of ~60% biotite and muscovite, 30% plagioclase and 10% quartz (Fig. 3.8a – b). The biotite crystals were typically < 0.5 cm in size, with platy muscovite's up to 1 cm in size. As with the phyllites, there were occasional < 1 cm sized garnets. *In situ* strength tests suggest they had a shear strength of 50 – 200 MPa.

3.4.1.8 Arniko dolomite

The dolomites in the Arniko region were very fine-grained (< 0.5 cm) and typically near 100% calcareous (Fig. 3.9a – d), though with occasional < 1 mm wide veins of

biotite and muscovite spaced at 5 – 10 cm (Fig. 3.9c). In situ strength tests suggest they had a shear strength of 100 – 200 MPa.

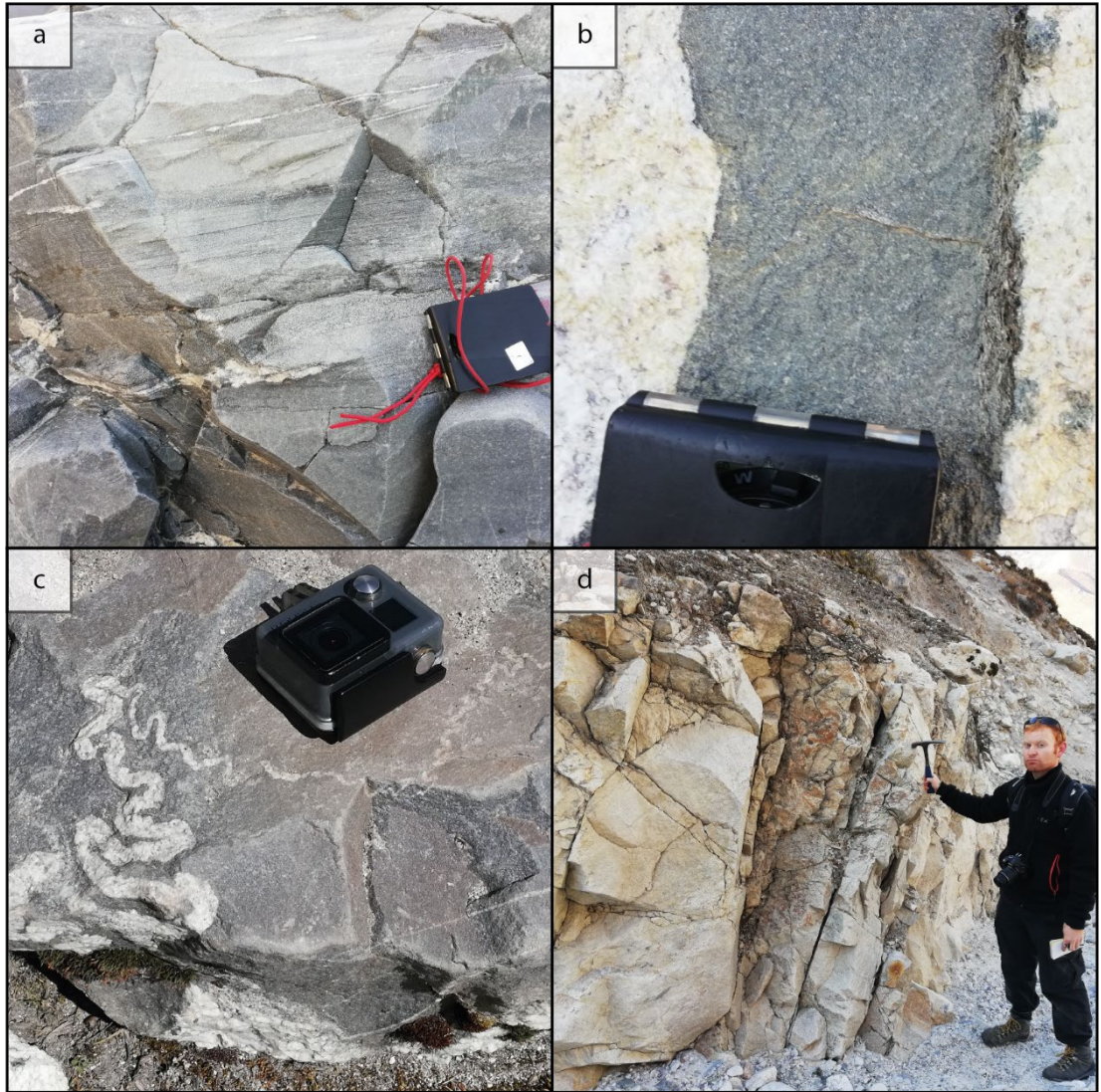


Figure 3.5. Photo panel depicting Langtang Unit 4. a – c) fine grained nature of this unit, b – c) leucogranite intrusions into this unit. d) typical appearance of an outcrop.

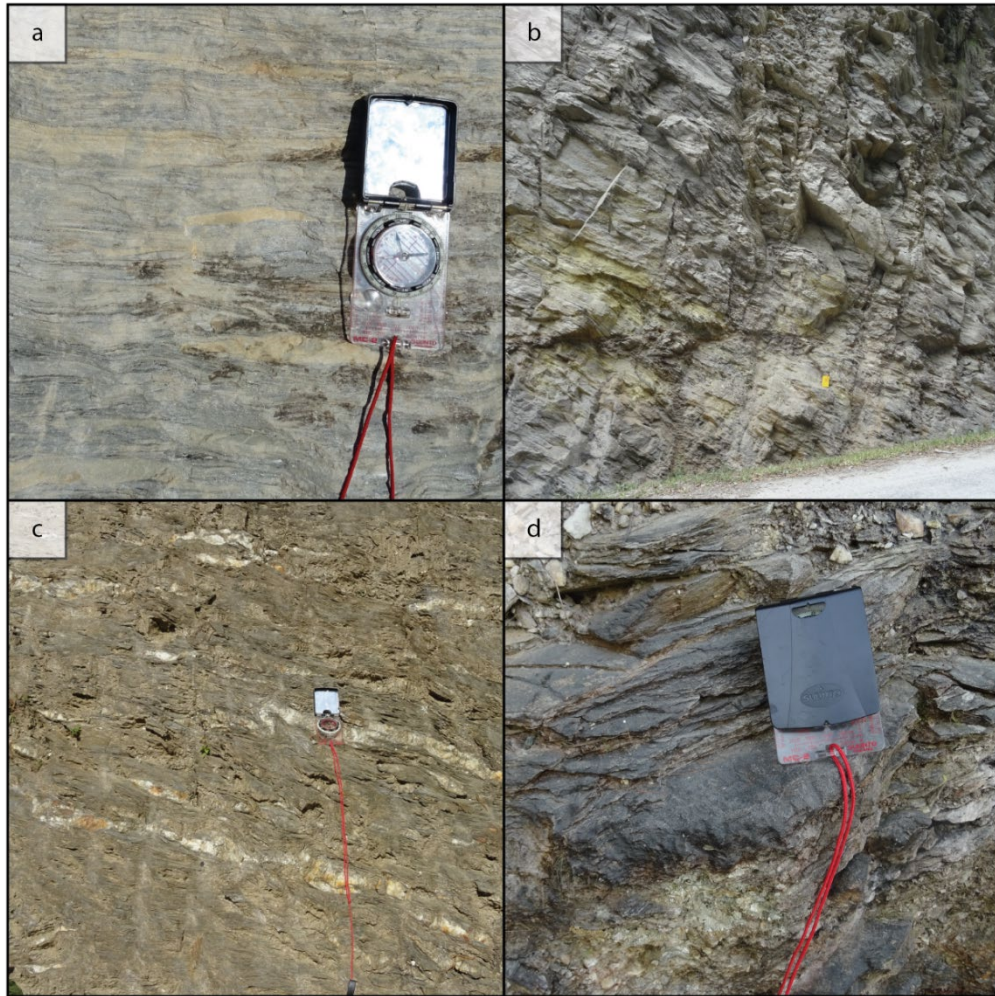


Figure 3.6. Photo panel depicting Arniko phyllite. a) muscovite-plagioclase rich mineralogy. b) typical outcrop. c) quartz vein intrusions. d) well foliated and fissile composition.

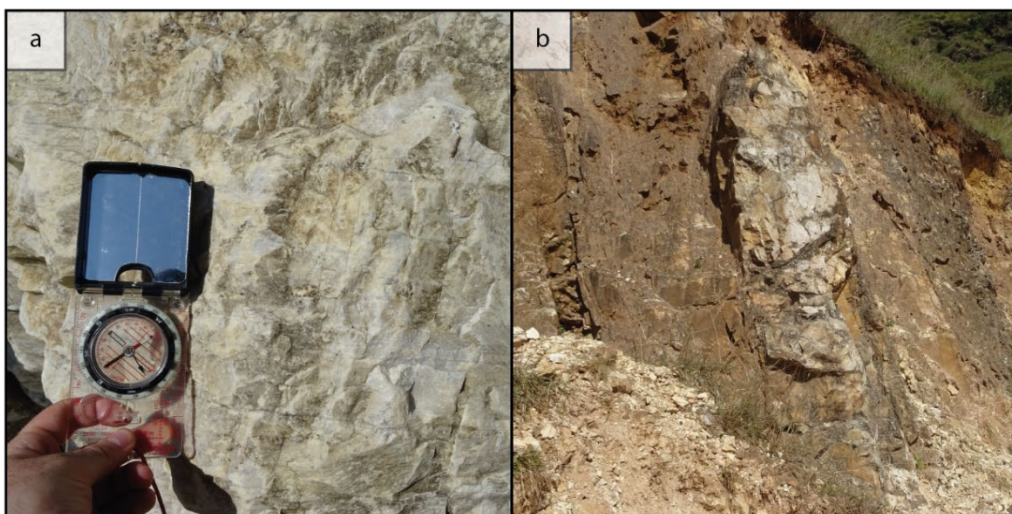


Figure 3.7. Photo panel depicting Arniko quartzite. a) crystalline, quartz rich composition. b) typical appearance of an outcrop.



Figure 3.8. Photo panel depicting Arniko schist. a – b) fine grained and well-banded biotite and muscovite rich mineralogy.



Figure 3.9. Photo panel depicting Arniko dolomite. a – c) fine grained calcareous mineralogy. c) biotite and muscovite veins. d) typical appearance of an outcrop.

3.4.2 Landslide inventory mapping

Figure 3.10a - b shows the landslide inventories developed for each region. As mentioned above, polygon shapefiles of these inventories are provided in Data Files 3 (Langtang) and 4 (Arniko), which can be accessed [here](#), and [here](#). There were 183 events mapped in the field within Langtang (Fig. 3.2a), of which 155 (85%) were identified as (likely coseismic) rockfalls or debris flows and 28 (15%) as monsoon/climate-triggered slumps/slides and relict alluvial fans. In the Arniko Region, 177 events were mapped within the field (Fig. 3.10b), of which 161 (91%) were identified as (likely coseismic) rockfalls and debris flows and 16 (9%) as monsoon/climate-triggered slumps/slides and relict alluvial fans. As described in Chapter 2, defining whether a given landslide was coseismic was based on a combination of geomorphic observations and local knowledge. The geomorphic observations included whether or not a landslide initiated at the hillslope toe or ridge (Densmore & Hovius 2000), whether there was any evidence of erosion at the hillslope toe, and whether the style of failure was dominated by falling or slumping/sliding. Local knowledge was obtained by speaking to members of nearby populations to see if they could provide any insight into when a given landslide happened. Furthermore, in the Arniko case, to ensure the inventory was comprehensive, the field-mapped landslides were combined with a further 304 coseismic landslides (mostly rockfalls and debris flows) mapped from high resolution (0.5 m) imagery in Google Earth.

For both regions, three-parameter inverse-gamma distributions were fitted to the probability density functions of landslide area (Fig. 3.11 a - b; see Chapter 2 [section 2.4.3] for the methodology for this analysis). Both regions have lower than expected three-parameter inverse-gamma distribution exponents of 0.9 in Arniko and 1.2 in Langtang, suggesting that in both regions proportionally larger landslides are contributing significantly to the overall distribution. However, despite having a larger exponent, the maximum and rollover (modal) areas for Langtang (809,000 m² and 2,400 m²) are higher than they are for Arniko (123,000 m², and 340 m²) (Table 3.2). It is notable that the three-parameter inverse-gamma distributions do not provide as good a fit to these data sets compared with the fit observed for the larger,

regional, data sets presented in Chapter 2. The most likely reason for this is differences in the inventories. As discussed in section 3.3.1.1, these inventories are largely based on field assessment, which biases the sampling towards larger failures that are easily visible, thus potentially explaining why proportionally larger landslides seem to be contributing more in both of these regions compared to the regional datasets. Furthermore, as mentioned in Chapter 2, sample size strongly limits the certainty of power-law fitting. The regional cases from Chapter 2 typically included at least several thousand landslides. Conversely, these inventories included only several hundred. As such, it is possible that the poor fit to the three-parameter inverse-gamma distribution in these cases results from sample biases and lower numbers of landslides in the inventory, rather than any physical process.

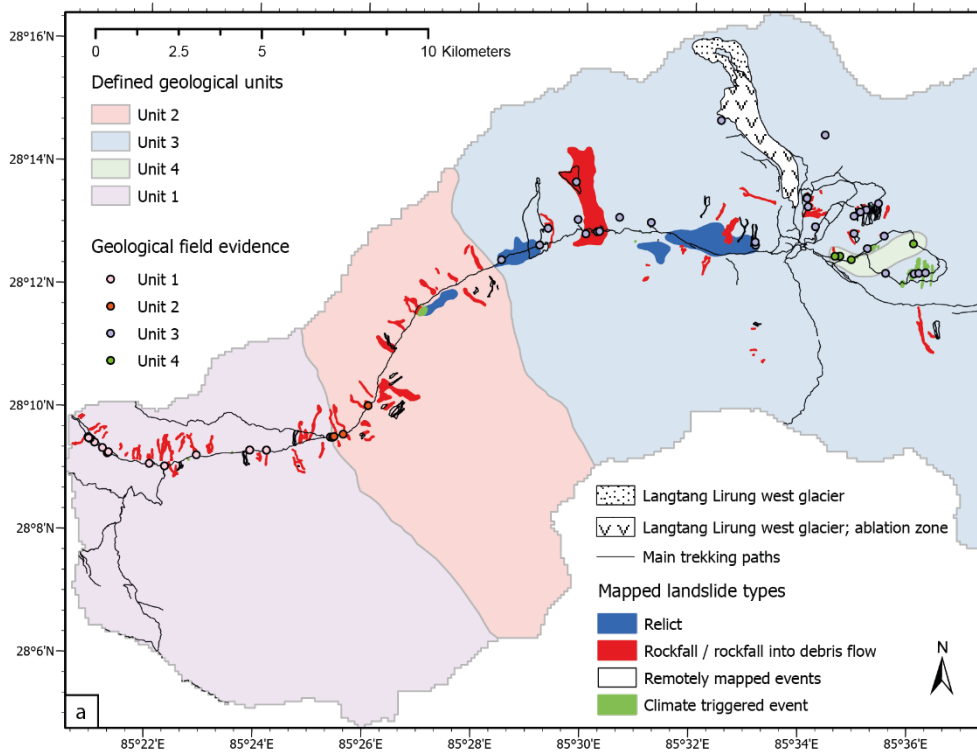


Figure 3.10. a) Summary of landslide and lithology collected in the field across Langtang and subsequently defined geological unit boundaries. The location of the main trekking paths and positions of the Langtang Lirung west glacier and ablation zones are also shown. b) (next page) Summary of field landslide and lithology data collected across the Arniko region.

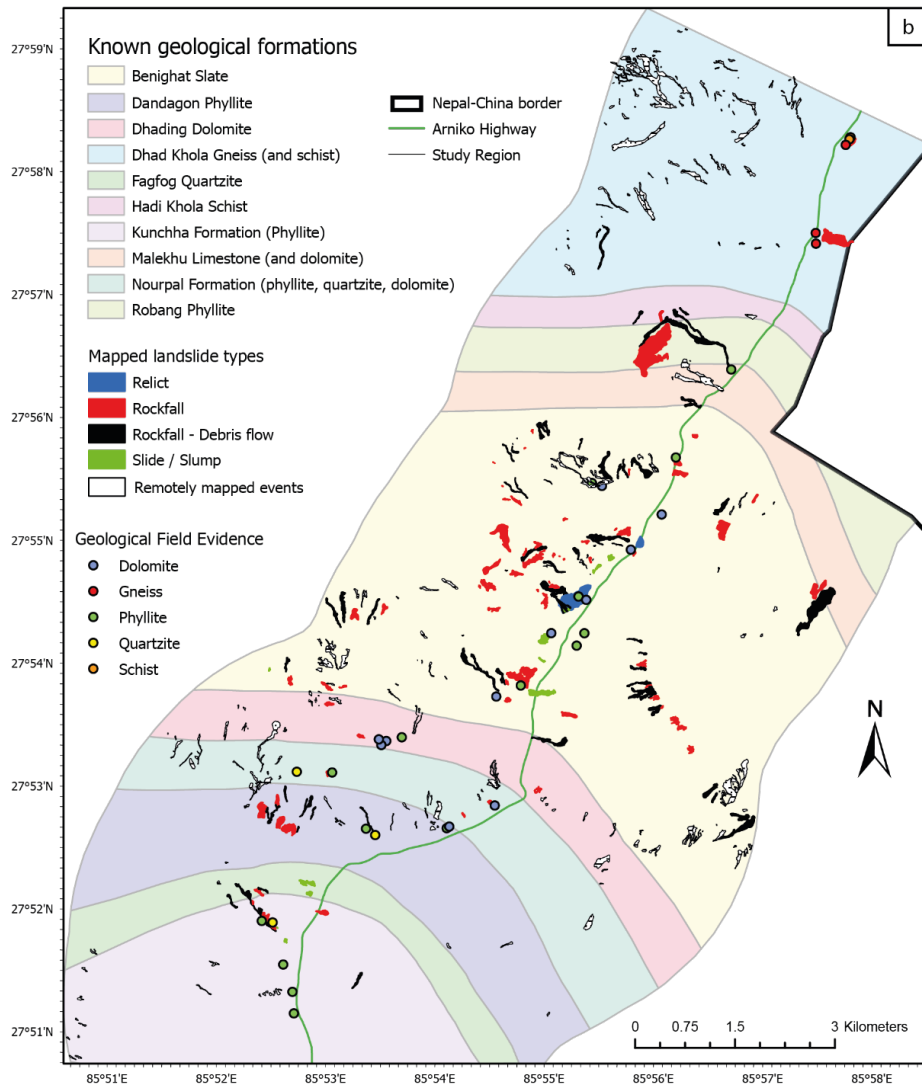


Figure 3.10 b) Summary of field landslide and lithology data collected across the Arniko region.

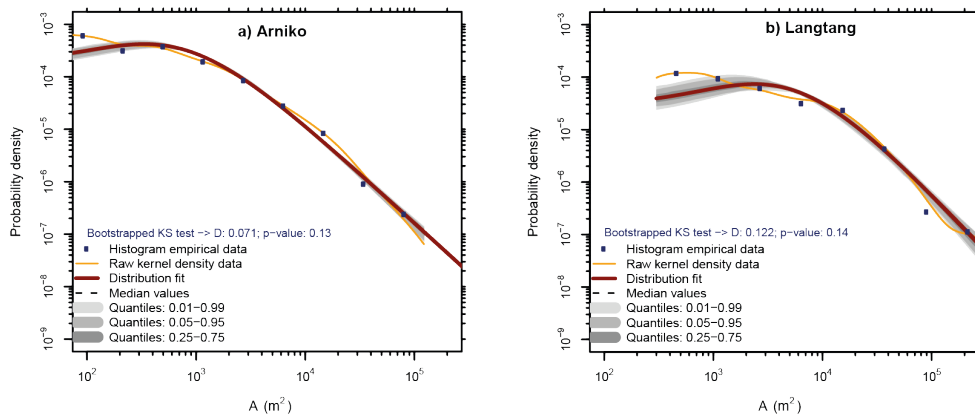


Figure 3.11. Three-parameter inverse-gamma distributions fitted to the probability density functions of landslide area for landslides in, a) Langtang, and b) Arniko. Following the approach of Marc et al. (2019), the two largest events were removed from the Langtang case

as they were > 2 times greater than the third largest event. Note that a p -value > 0.01 indicates that the three-parameter inverse-gamma distribution provide a good fit to the actual data, whilst the D -value gives the maximum distance between the actual data and the fitted distribution.

Region	Maximum area (m ²)	α	η	λ	Rollover (m ²)
Arniko	123345	0.9 +/- 0.075	16.14 +/- 1.56	33.64 +/- 2.75	336
Langtang*	809459	1.21 +/- 0.18	43.27 +/- 6.72	96.75 +/- 13.64	2370

with the two largest landslide events removed, both of which were more than 2 greater than the third largest

Table 3.2. Summary size statistics for the Langtang and Arniko field-remote sensing landslide inventories. *Note, in the Langtang case, the two largest events, both of which were >2* the size of the third largest, were removed from the analysis following the method of Marc *et al.* (2019), see Chapter 5 (section 5.2.2.1).

3.4.3 Qualitative descriptions of landslide types and processes

Field observations indicate that the three most common landslide types across both study regions are rockfalls, rotational slumps and slides, and debris flows. However, other landslide types and processes were also observed, including shallow translational slides, debris avalanches, and relict alluvial fans (inactive deposits of old landslide material). The following sections describe each of these types with reference to representative field photographs.

3.4.3.1 Rockfalls

Rockfalls were the most commonly observed landslide type in both study regions. Rockfalls can be described as an abrupt movement of mass that has become detached from a steep slope or cliff, usually along an existing discontinuity, under the force of gravity (Hung *et al.* 2014; Fig 1.3). The rockfalls mapped across Langtang and Arniko occurred on slopes of up to 75 - 80° (Fig. 3.12a – b), elevations of 1600 – 5100 m and across all mapped geological units. This demonstrates that this single type of failure occurred under a wide variety of geological and geomorphological conditions. Across both regions, rockfall occurrence aligned strongly to the bedrock

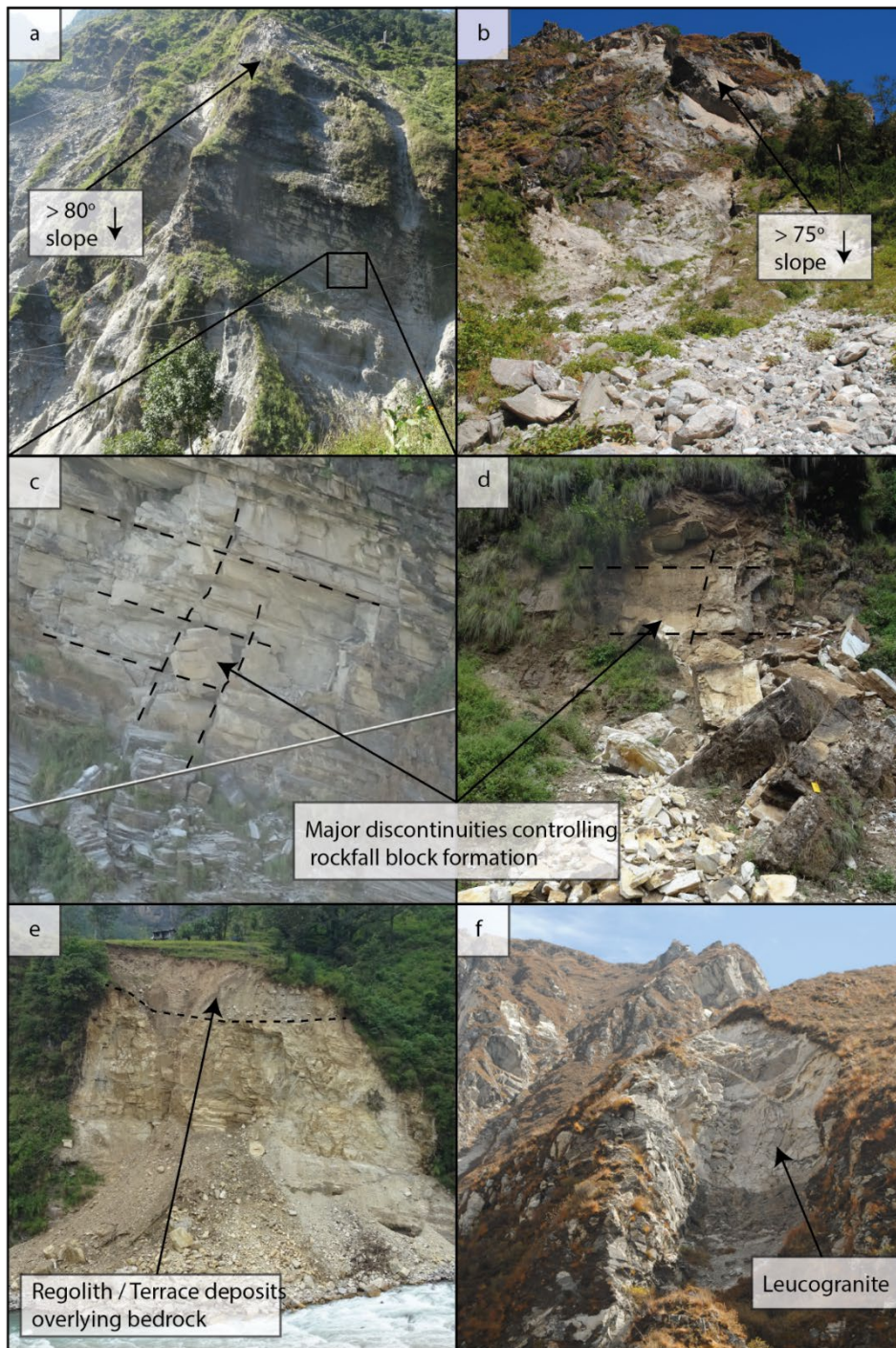


Figure 3.12. Photo panel depicting typical rockfalls observed across both regions. a – b) larger-scale rockfalls. c – d) control of bedrock discontinuity geometry on block development and failure. e) monsoon triggered rockfall beneath a terrace deposit. f) leucogranite intrusions into the bedrock of a rockfall scar.

discontinuity geometry, suggesting that this is a major control on overall rockfall debris size and runout / mobility (Fig. 3.12c – d). Furthermore, in Langtang it was common for bedrock, including bedrock exposed by landsliding, to coincide with intrusion by Miocene leucogranite (e.g. Fig. 3.4f and Fig. 3.12f). Finally, as the rockfalls in both regions tended to initiate near ridgelines or other major slope breaks (Fig. 3.12a – b), it is likely that the majority of these rockfalls are coseismic (Densmore & Hovius 2000; Meunier *et al.* 2008). Some monsoon-triggered rockfalls were also identified, with these failures occurring on steep (< 45 - 50°) portions of bedrock, but usually within a few hundred metres of the nearest stream network at the base of terrace deposits (Fig. 3.12e).

3.4.3.2 Rotational slides and slumps

A rotational slide or slump is a failure that has occurred along a surface that is curved concavely upwards with mass movement that is approximately rotational about an axis that is parallel to the ground surface (Hungri *et al.* 2014; Fig 1.3). In both regions, this type of failure was typically observed to occur within terrace deposits at the hillslope toe, often adjacent to river or stream channels (Fig. 3.13a- c). As such, these failures were interpreted as being either monsoon-triggered or triggered by over steepening of hillslopes due to river incision.

3.4.3.3 Shallow translational slides

Translational slides are failures that occur along a planar surface (Fig. 1.3). In both regions, this type of failure was relatively uncommon. In Langtang, the upper portions of the Tsergo Ri region observed several shallow translational slides (Fig. 3.14a). These were < 1 m in depth, but with lengths and widths of up to 500 m. These events largely occurred in regolith material, though did expose the bedrock in the upper portions of the hillslope. In Arniko, the few translational slides that were observed occurred near the toe of terrace deposits (Fig. 3.14b). These failures appeared to be triggered by undercutting of the terraces by the river channel.

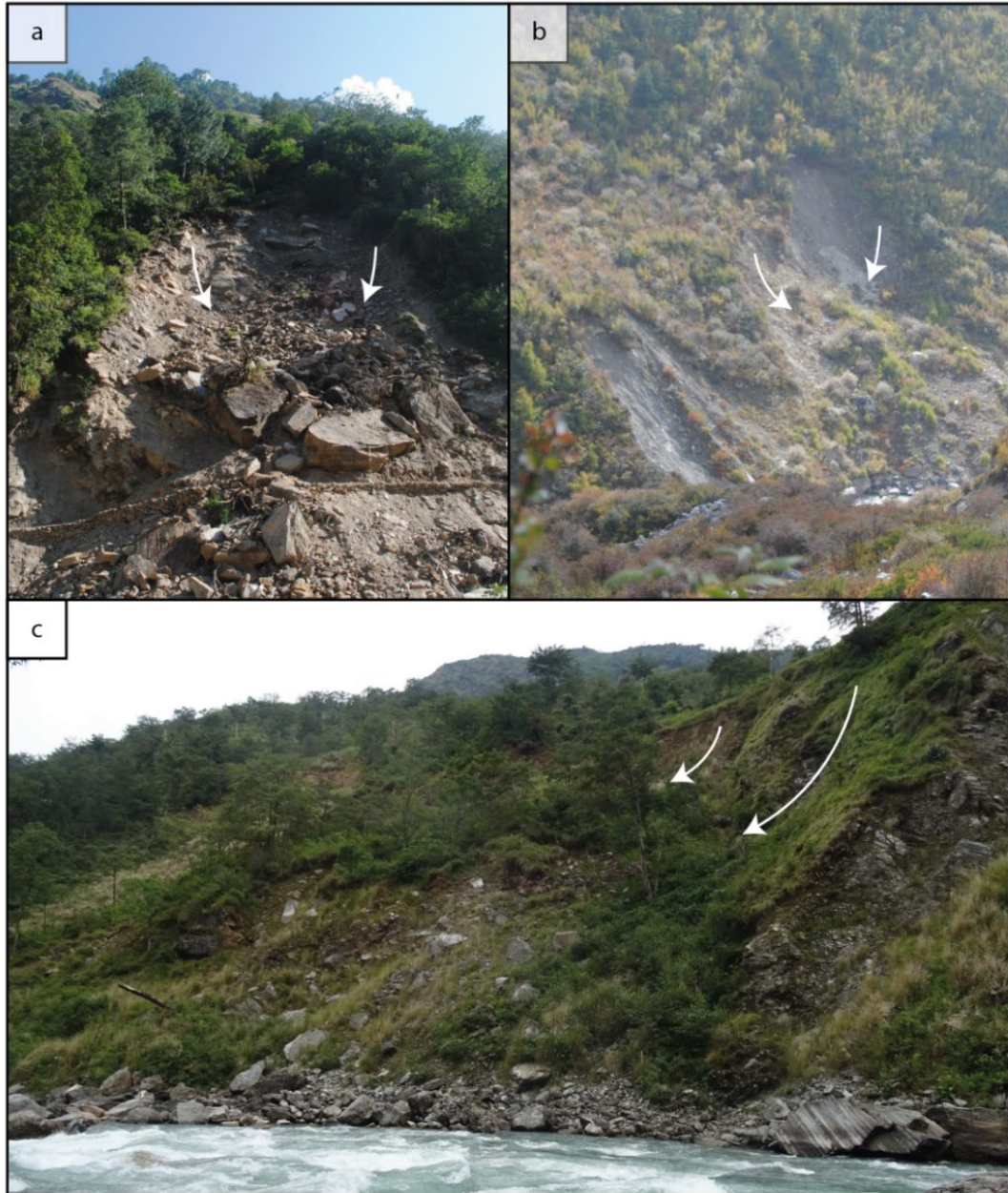


Figure 3.13. Photo panel depicting typical rotational slides and slumps in Langtang (a – b) and Arniko (c).

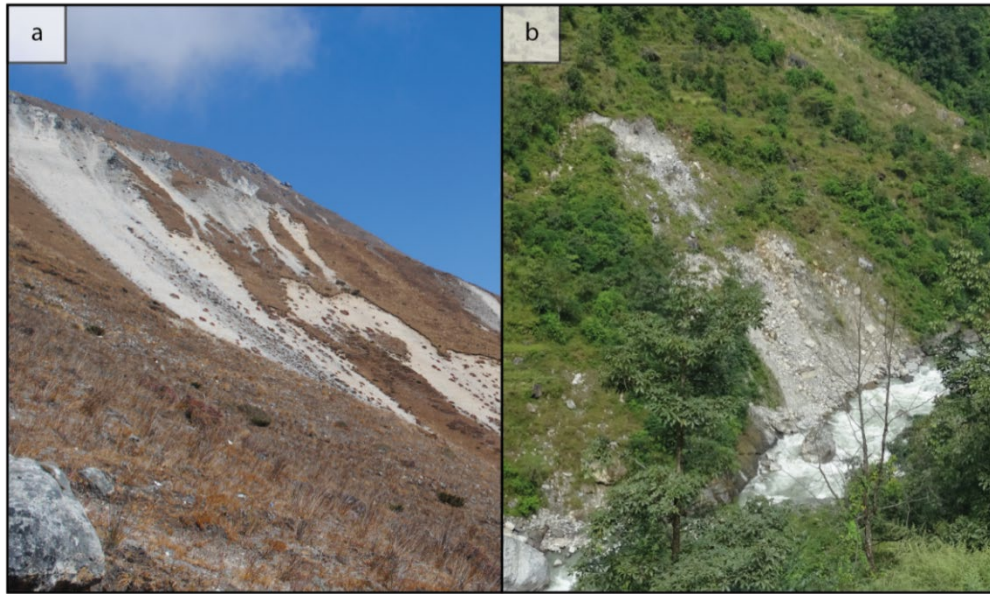


Figure 3.14. a) Shallow translational slides observed in the upper reaches of Langtang Valley. B) small translational failure at the toe of a hillside in the Arniko region.

3.4.3.4 Debris flows

A debris flow is defined as a very rapid to rapid mass-movement of saturated rock and other regolith material in a steep channel (Hung *et al.* 2014; Fig 1.3). These events were common across both Langtang and Arniko. Typically, the initial materials involved in these events were sourced from coseismic rockfalls on steep bedrock cliffs (Fig. 3.15a – c). These source rockfall events were often relatively small, reflecting that the fact that the majority of debris flow material usually originates from scouring and entrainment of the channel, rather than the initial source (Santi *et al.* 2008; Kang & Chan 2017). It was often observed that the material from several source zones amalgamated into a single debris flow channel (Fig. 3.15a – c). Furthermore, material from tributary instabilities or lower channel rockfalls would often add to the channelized volume (Fig. 3.15b). Channels were typically lined by debris levees and had widths and depths of 2 – 8 m (Fig. 3.15b – d) and 0.5 – 2 m, respectively. Owing to the steep nature of the topography in both regions, the debris flows often remained channelized until they intersected rivers at the floor of the main valley, though where slope angles decreased before then, channels commonly splayed into debris fans (Fig. 3.15c).

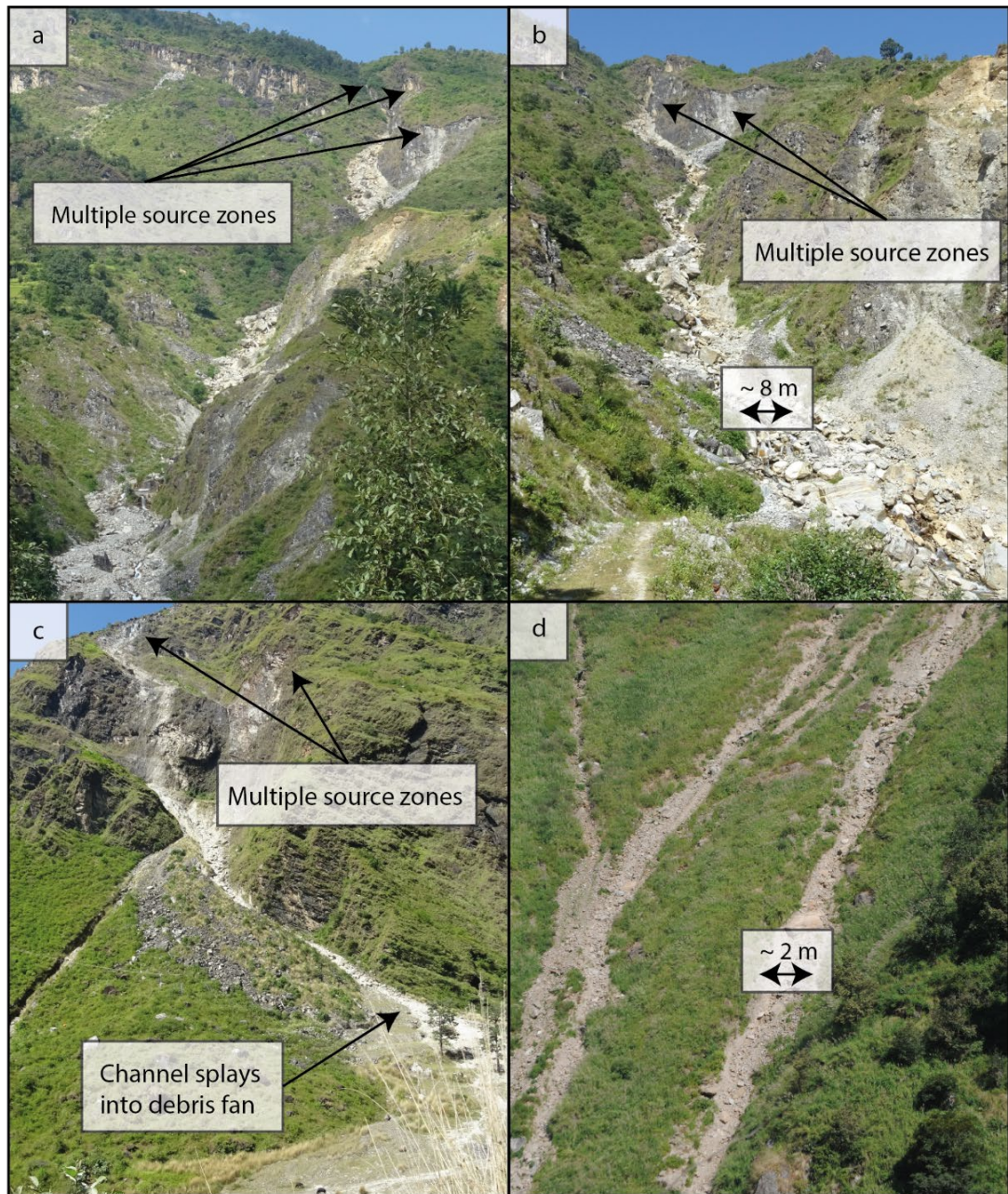


Figure 3.15. Photo panel depicting debris flows observed across both regions. a – c) large debris flows in Arniko with multiple source zones. d) debris flow levee channels observed in Langtang.

3.4.3.5 Debris avalanche (*Langtang Avalanche*)

A debris avalanche is defined as a very rapid to extremely rapid flow of material under gravity (Hung *et al.* 2014). The main difference between a debris avalanche and a rockfall is that the material in an avalanche has become hyper-concentrated, usually owing to the presence of water or snow, thus causing it to move like a single fluid rather than a series of discontinuous solids. Only one debris avalanche was observed across the study regions. This was the 'Langtang Avalanche', which was perhaps the most renowned coseismic landslide to have occurred during the 2015 Gorkha earthquake, having destroyed the village of Langtang with the loss of at least 170 lives (Nagai *et al.* 2017). This event was a complex compound occurrence that began when earthquake strong ground motion caused a portion of glacial material within an ice-carved hanging valley, as well as a portion of bedrock $\sim 500 \times 1000 \times 200$ m in size (Fig. 3.16a) to collapse (Nagai *et al.* 2017). The deposits from this event have been previously estimated through remote sensing techniques to have a depth of ~ 60 m, an area of $0.63\text{--}0.88$ km² and a volume of $5.51\text{--}9.66 \times 10^6$ m³ (Lacroix 2016; Nagai *et al.* 2017). Assessment of the debris deposits show that the failure mostly involved gneisses (Unit 2; see section 3.4.1.2) and leucogranites (Unit 3; see section 3.4.1.3).

The back-scar of this event is remarkably smooth, with striations caused by scouring of the bedrock by the material entrained in the avalanche and subsequent reworking by meltwater and precipitation. It is also evident that the back-scar is not planar, with clear breaks in slope in the lower third of the failure. It is unclear what caused these changes in slope, but they could be due to existing structural weaknesses in the bedrock, a reduction in power of the avalanche as it reached the valley floor, or a rotational component of bedrock failure. This event demonstrates that whilst debris avalanches occur less frequently than rockfalls, they have the potential for much greater destruction. Indeed, this event completely buried a ~ 500 m long section of the main trekking path, which has since been reinstated over the landslide deposits. Figure 3.16b shows the position of the new trekking path at the point where a river has incised through the deposits. The path here is highly precarious, with some sections <30 cm wide beneath a $>80^\circ$, 10 m high slope of loose deposits, which are

vulnerable to movement during a future trigger event. Furthermore, the path crosses over a narrow tunnel that has been created by the river (Fig. 3.16b - c). This portion of the deposits is unstable, and several boulders were witnessed falling from beneath the tunnel into the river.

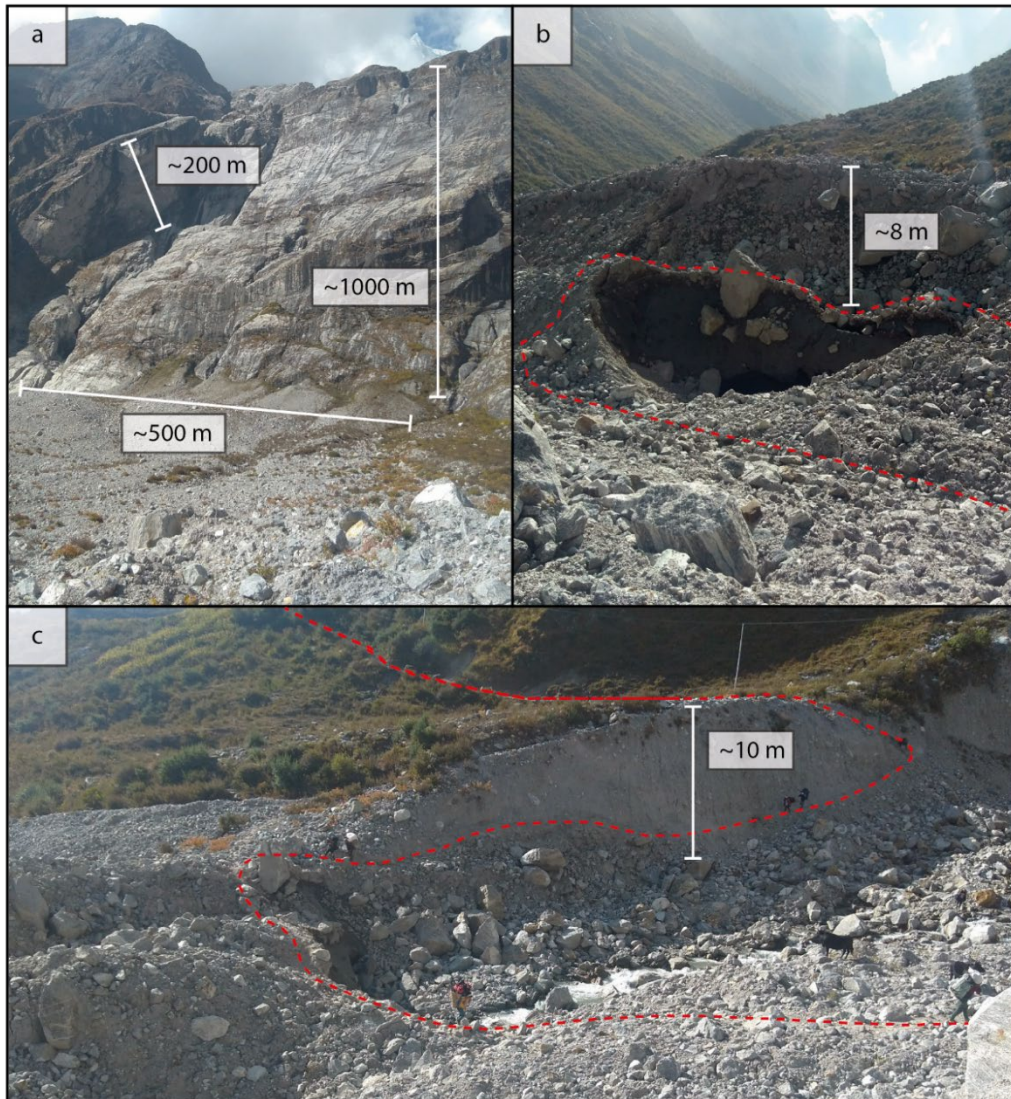


Figure 3.16 . a) The bedrock scar and deposition zone of the Langtang avalanche. b – c) the intersection between trekking paths and the avalanche debris in October 2018. Trekking path highlighted with red-dashed line.

3.4.3.6 Relict alluvial fans

The final type of landslide mapped across Langtang Valley was relict landslides. A relict landslide can be defined as a now-stable mass of past landslide debris. These were usually highly vegetated and mainly identifiable by their fan-like morphology

and evidence of highly weathered debris that has clearly been exposed for several years to decades (Fig. 3.17). The degree of vegetation and weathering of these features may reveal several stages of past failure, such as Fig. 3.17, which shows clear evidence of a recent debris levee channel that has incised through the main portion of the relict fan.

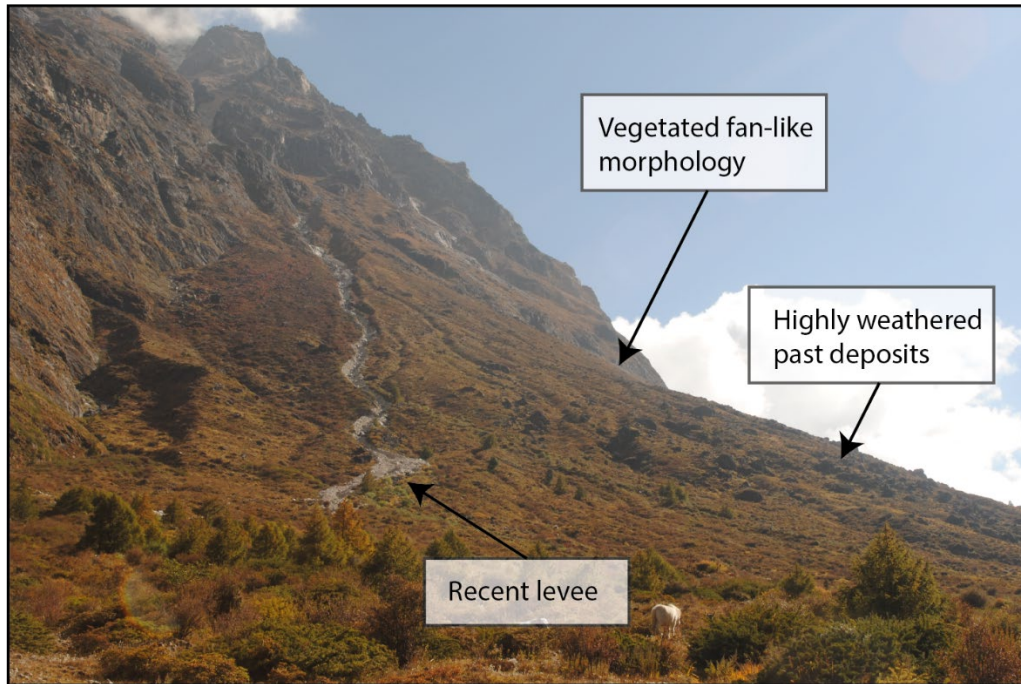


Figure 3.17. Relic alluvial fan incised by a more recent debris flow in Langtang Valley.

3.4.4 Structural data

A further component of the field mapping was constraining the dip and dip directions of foliation and faulting across both study regions to assess whether these show any correlation or controls on landslide occurrence. Across the Arniko Highway, 357 discontinuity measurements were recorded, of which 339 were of bedrock joint sets and 18 of faults (Fig. 3.18a). Three distinct joint sets can be identified. Set 1, which dip shallowly (average of 28°) towards the NE (Fig. 3.18b). Set 2, which dip more steeply (average of 65°) towards the SW (Fig. 3.18c), and set 3, which dip steeply (average of 71°) towards the SE (Fig. 3.18d). Of the measured faults, most dipped towards the W and SW, with average dip angles of 45° (Fig. 3.18e).

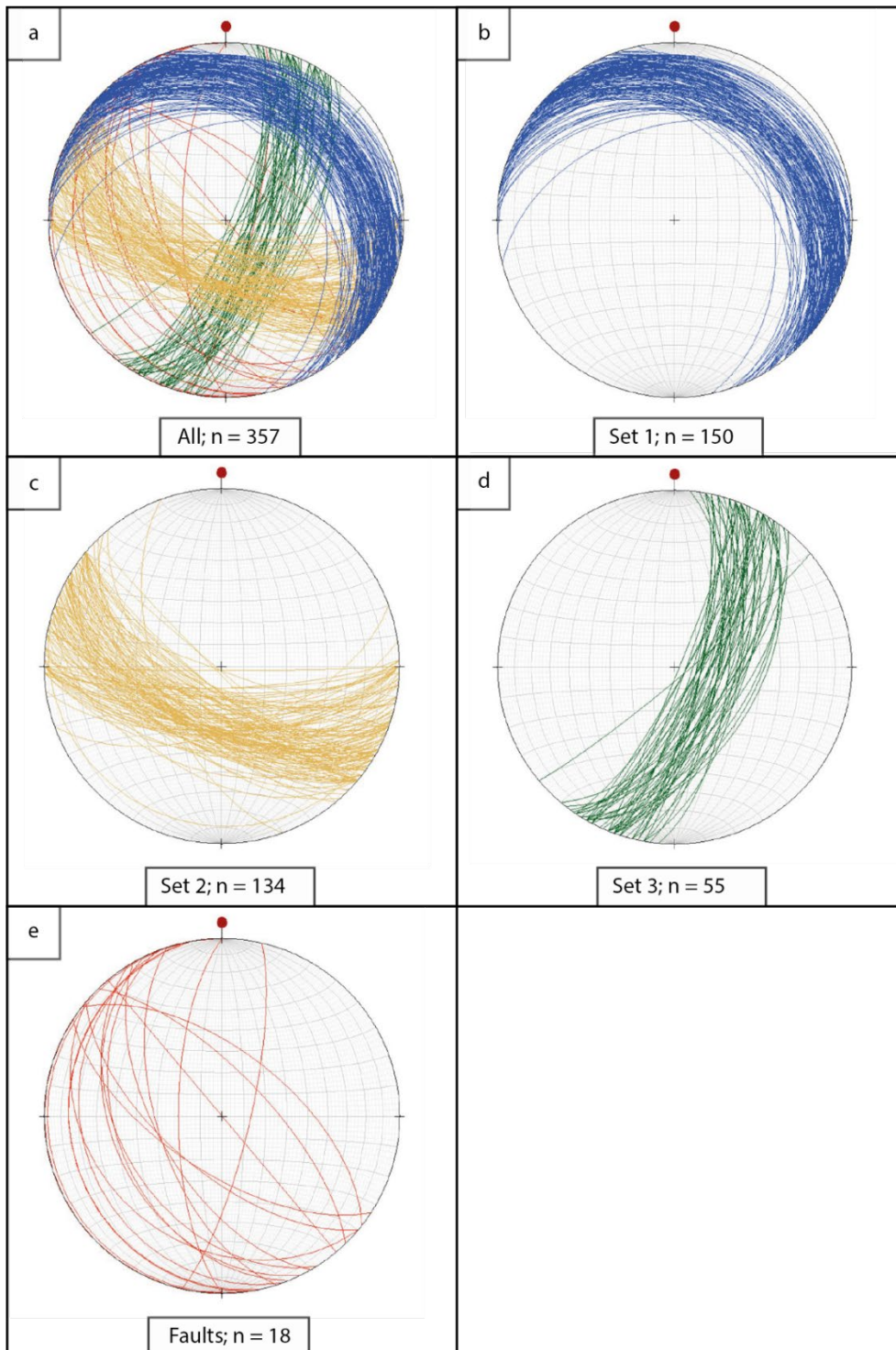


Figure 3.18. a) All discontinuity data collected in the Arniko region. b) Set 1 data. c) Set 2 data. d) Set 3 data. e) fault data.

Across Langtang, 170 discontinuity measurements were recorded, of which 141 were bedrock joint sets and 29 were faults (Fig. 3.19a). The joint sets across Langtang were harder to split into sets than in the Arniko region, with the vast majority of measurements falling within a main group that dipped between the NE to SE at an average dip angle of 40° (Fig. 3.19b). The remaining joints measured in Langtang dipped towards the WSW at an average angle of 43° (Fig. 3.19c). The faults measured in Langtang were mostly moderate angle (average dip of 56°) thrust faults that dipped towards the W and SW (Fig. 3.19d), which is similar to the majority of faults observed across the Arniko highway.

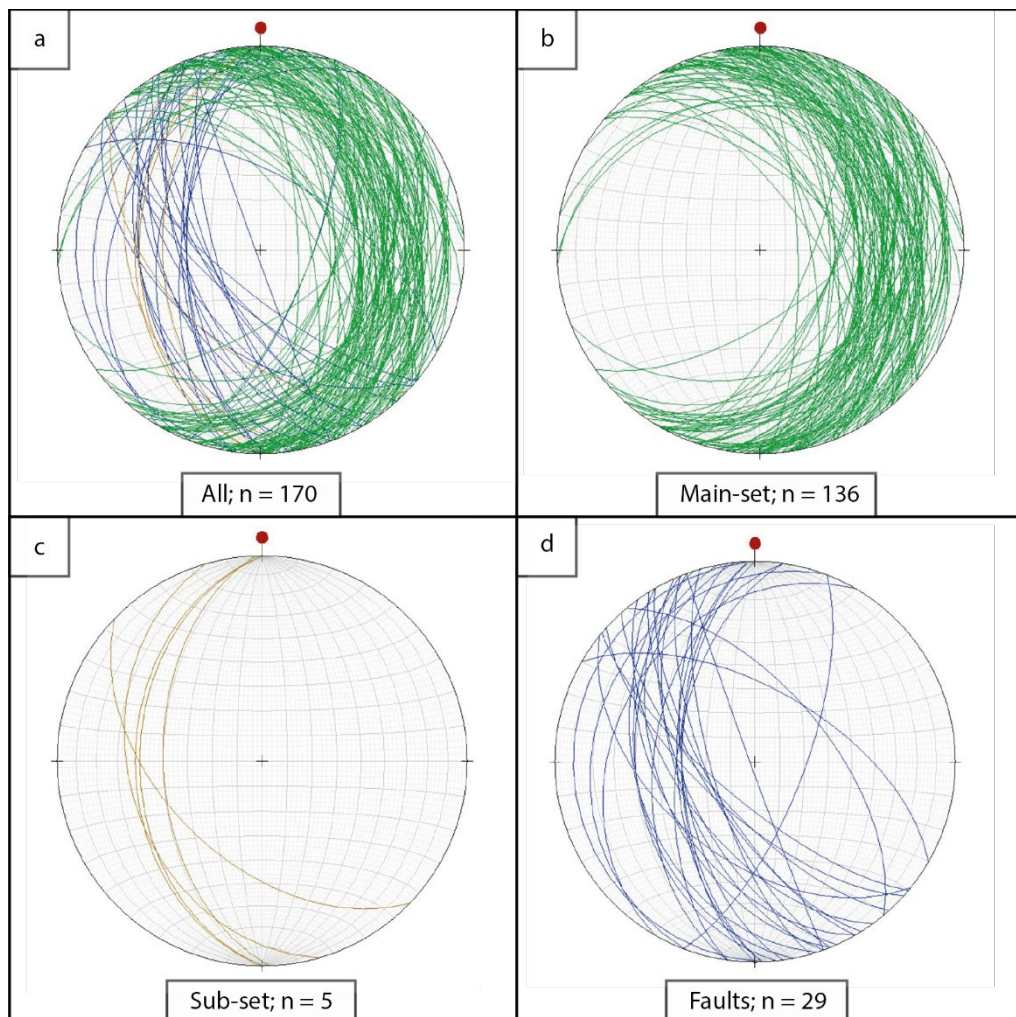


Figure 3.19. a) All discontinuity data collected in Langtang. b) Main set data. c) Sub-set data. d) fault data.

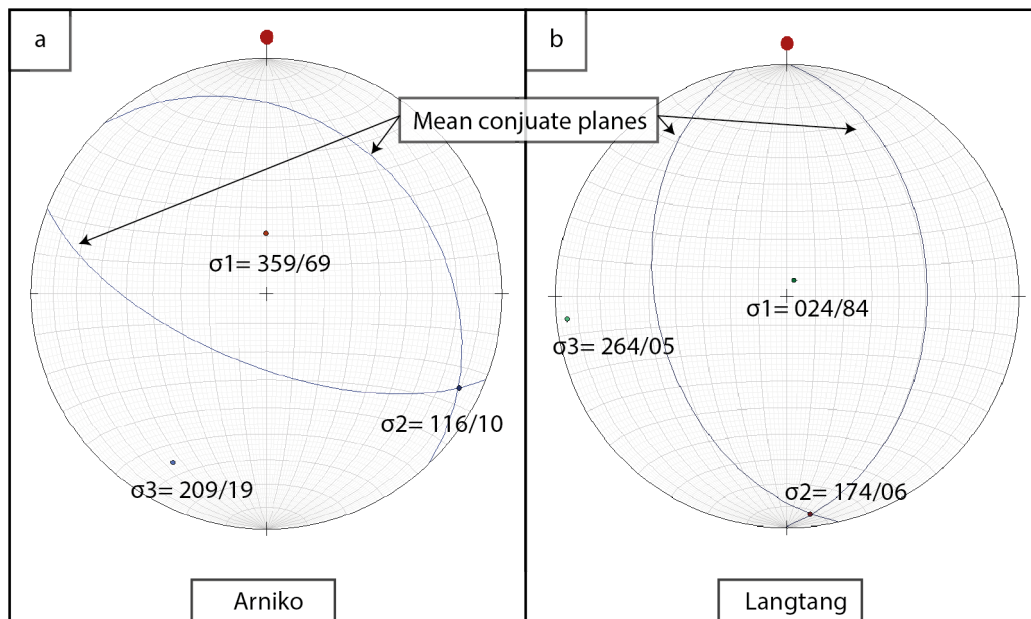


Figure 3.20. The mean conjugate planes and principal stress axes for a) Arniko and b) Langtang.

It is also noted that in both regions, two of the joint sets appear to form near-conjugate sets (joint sets 1 and 2 in Arniko, and the main and sub-sets in Langtang; Fig. 3.18b – c; Fig. 3.19b – c). On the assumption that these sets are indeed conjugate, the axis of the main tectonic stresses occurring in the region can be estimated based on the Coulomb criterion (Twiss & Moores 1992). This concept assumes that a pair of joints formed as a conjugate set in a co-axial stress regime, and that during compression, the rocks fail along conjugate planes that intersect along the intermediate stress axis, σ_2 , with the acute angle between them bisecting the principal stress axis, σ_1 (Gupta 2005). Information on the main tectonic stresses in each region is useful, as the intermediate stress axis has previously been found to correlate with landslide occurrence (Gupta 2005), thus potentially offering some explanation for why and how the mapped structural discontinuities may be influencing landslide occurrence (see section 3.5.1).

In this case, the average intersection angle between the two joints sets in each region is $\sim 90^\circ$, with a spread suggesting that it is possible the two sets in each case are conjugates. Therefore, the intermediate stress axis, σ_2 , in each region can be simply calculated from the intersection of the mean planes (Fig. 3.20a – b) of each set. The principal stress in the region is approximately N-S, so it can be assumed which of the

two 90° angles between the two joint sets relates to the principal stress axis, σ_1 , thus allowing all three stress axis to be defined. In Arniko, this results in $\sigma_1 = 359/69$, $\sigma_2 = 116/10$ and $\sigma_3 = 209/19$. Whilst in Langtang, it results in $\sigma_1 = 024/84$, $\sigma_2 = 174/06$ and $\sigma_3 = 264/05$. This suggests that the stress regime in Langtang is rotated approximately 25 – 55° clockwise relative to Arniko.

3.4.5 BLR analysis and susceptibility modelling

3.4.5.1 BLR coefficient and LASSO results

BLR landslide susceptibility models were developed for 50 balanced training sets per region. Despite these local study regions being smaller than the overall main region modelled in Chapter 2 (and later in Chapter 4), 50 balanced training / testing sets were still used, as these smaller regions still had hundreds of thousands of pixels and using multiple balanced model-runs allowed a comparable appreciation of uncertainty to the analysis in the other chapters. Figure 3.21a – p shows the mean regression coefficient and LASSO selection percentage results for each independent variable and study region. For most variables (slope, aspect, profile and planform curvature, cropland and near channel SSP; Figs. 3.21a – f), the two regions had regression coefficients within +/- 0.2 of each other and selection percentages of 80 – 100%. Likewise, whilst each region had separately defined geological units, in both regions' units with phyllites acted to make landsliding less likely (e.g. Unit 1 on Fig. 3.21g; the Robang and Dandagon phyllites on Fig. 3.21h); whilst granites and gneisses act to make landsliding more likely (e.g. Unit 3 on Fig. 3.21g; Dhad gneisses on Fig. 3.21g). However, for other factors there were some significant differences between the two regions. Specifically, the coefficients for elevation and local relief (Figs. 3.21i; 3.21k) were negative in Langtang but positive for Arniko, whilst distance to channels (Fig. 3.21l) was positive in Langtang yet negative in Arniko. The coefficients for excess topography were positive in both regions, but with a lower magnitude in Langtang, i.e., excess topography was a less dominant control factor in Langtang (Fig. 3.21j).

Other key differences between the two regions are that both near channel K_{sn} and the presence of shrubs/grassland made landslide more likely in Langtang but less likely

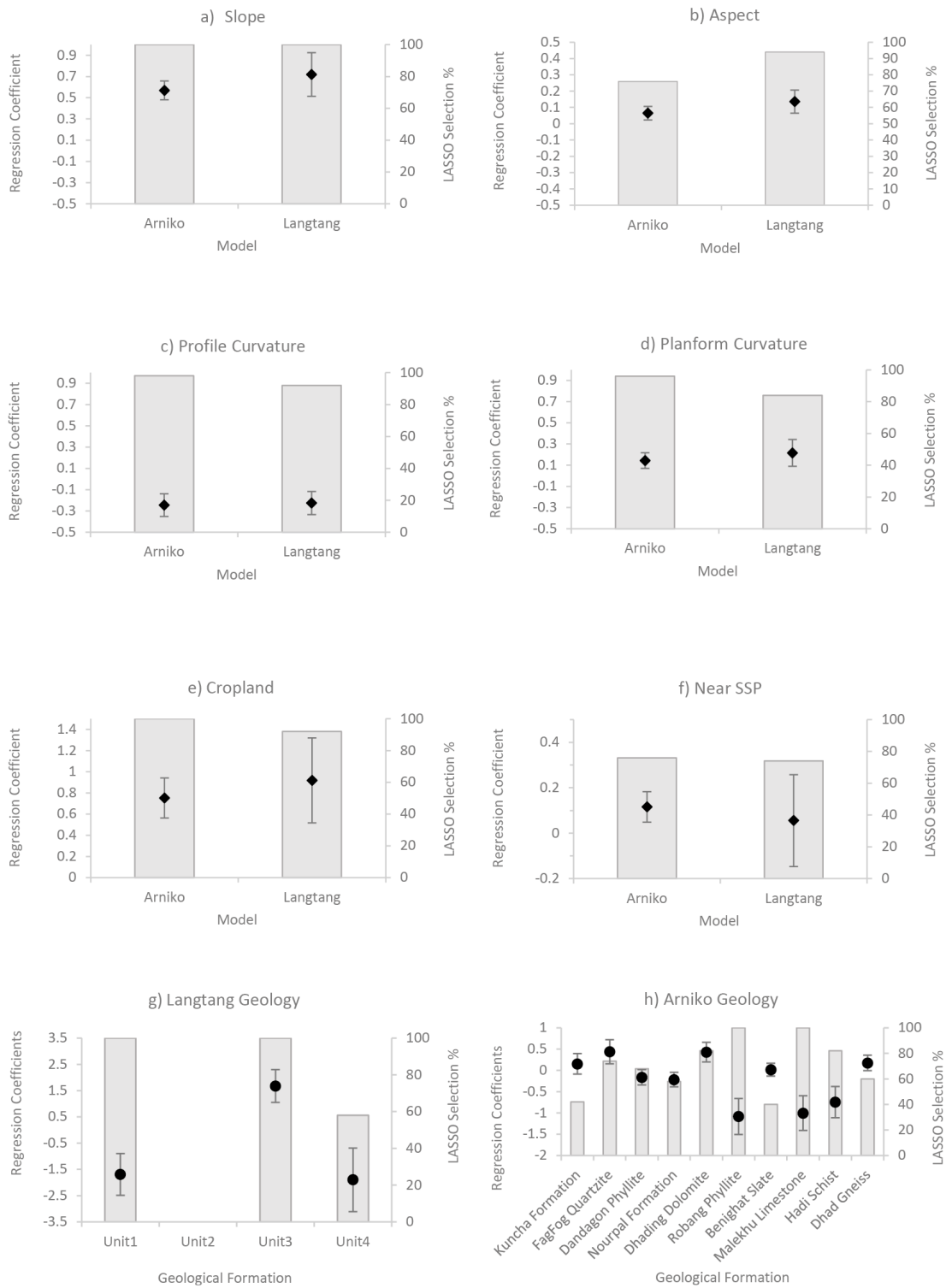


Figure 3.21. a – p) BLR coefficients and LASSO selection percentages for all independent predisposing factor variables included within the BLR modelling.

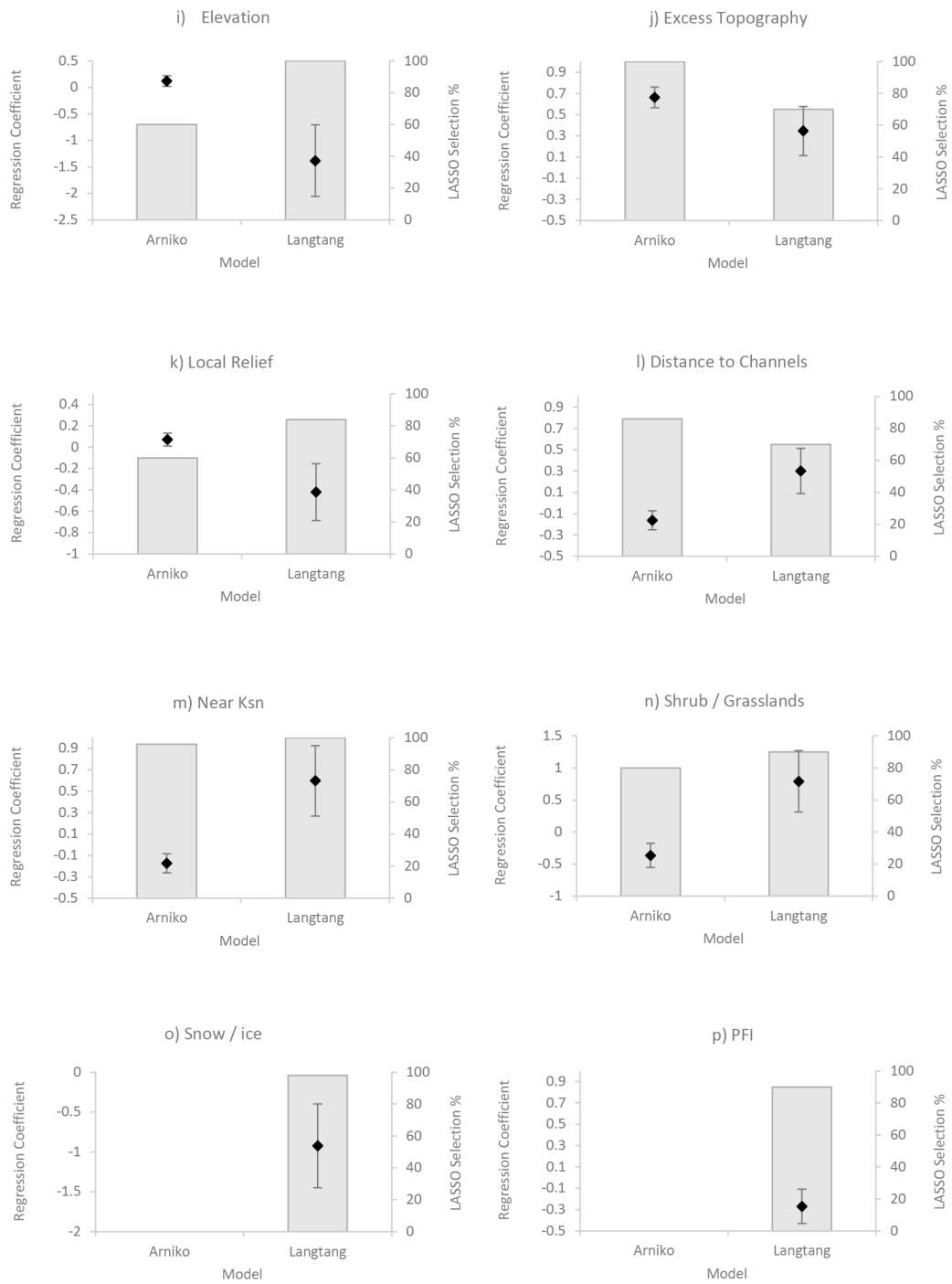


Figure 3.21 a – p) BLR coefficients and LASSO selection percentages for all independent predisposing factor variables included within the BLR modelling.

in Arniko (Figs. 3.21n). Finally, the presence of permanent snow/ice and permafrost index (Figs. 3.21o - p) are dominant factors in controlling landsliding in Langtang, but do not occur along the Arniko so have no influence there.

3.4.5.2 Susceptibility modelling and AUROC validation results

Figure 3.22a – b shows the final susceptibility maps developed for each region (using the same method as that outlined in Chapter 2, section 2.5.6) based on the average regression coefficients and intercept of the 50 developed models per region. Along the Arniko highway, the highest zones of landslide likelihood are located in the higher elevation, higher excess topography regions along the valley. Conversely, in Langtang, the highest zone of landslide likelihood is the lower, central, and western portions of the valley, with a sharp decrease in likelihood in the higher elevation and eastern portions of the Valley. However, it should be noted that in the Langtang case, the lower susceptibility values in the higher elevation areas could be an artefact of incomplete landslide mapping in snow-covered regions (see section 2.2.3.3).

Figure 3.23a – b shows the average AUROC success rates of the 50 models per region, i.e. the success of each model in classifying the 70% of landslide data used to train each model. The average AUROC value for Arniko was 0.8 (i.e. 80% success), whilst for Langtang it is 0.88 (88% success). Figures 3.23c – d show the AUROC results of the 10-fold independent validation for each region, where the models from each region were validated using the respective 30% of landslides assigned to each regions testing datasets. This shows that the Arniko models have an average predictive power of 0.78 (78%) whilst the Langtang models have an average predictive power of 0.82 (82%), both of which are very good results. It should be noted that the low resolution of the ROCs in Figure 3.23d is due to the low number of landslides (30% of the total 183 landslides mapped in Langtang) available for testing.

Finally, Figures 3.23e – f show the 10-fold cross validation AUROC results for how well the models from one region could hindcast the landslides in the other region. The Arniko models had an average success rate at predicting the Langtang training datasets of 0.66 (66%) (Fig. 3.23e), which is acceptable, but not good. Conversely, the Langtang models had an average success rate at predicting the Arniko landslide training datasets of just 0.58 (58%), with some models returning AUROC values < 0.5 (50%), which is a very poor result (Fig. 3.23f).

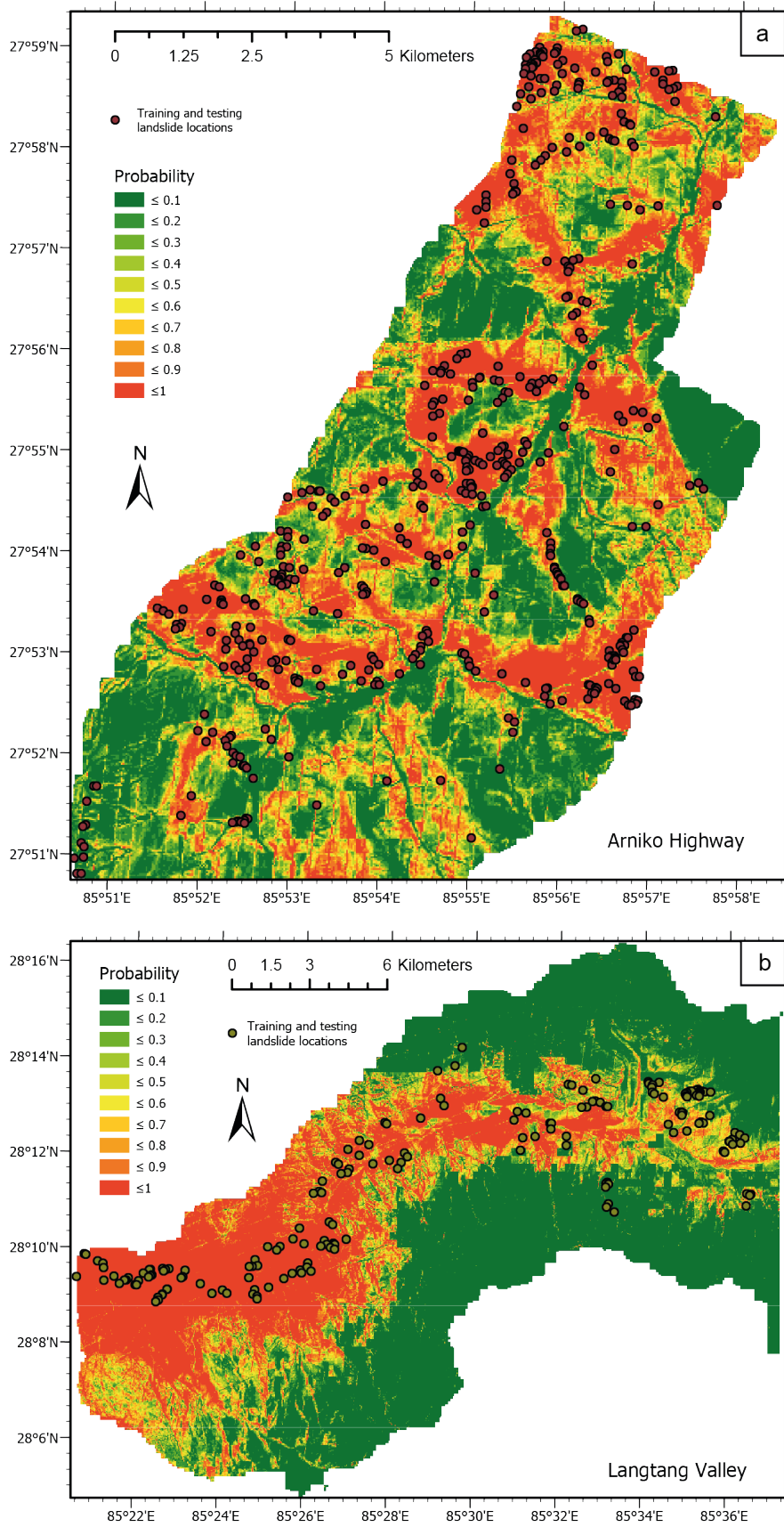


Figure 3.22. Final susceptibility maps developed from the average regression coefficients from the 50 models developed for, a) Arniko, and b) Langtang.

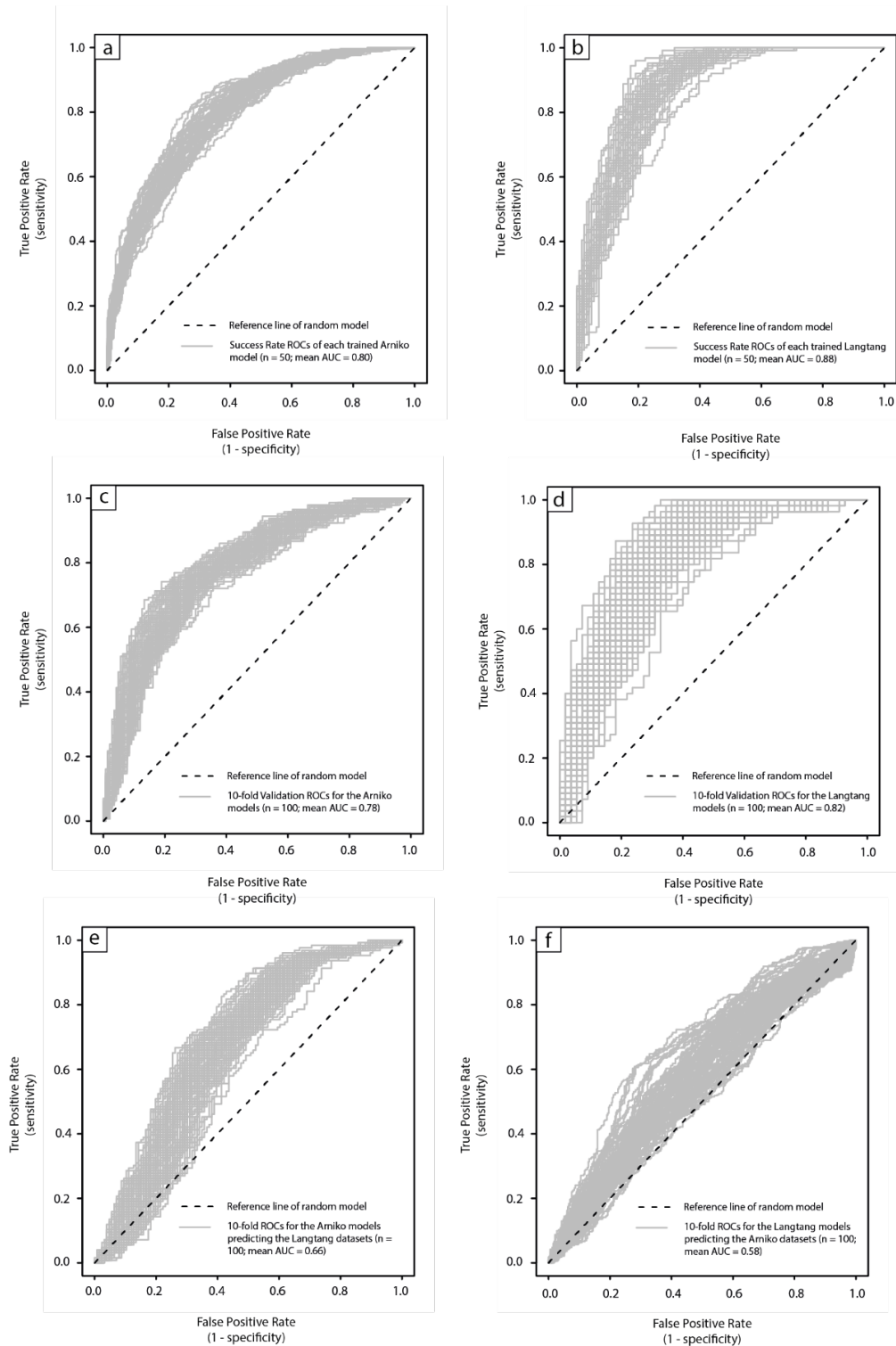


Figure 3.23. ROCs and AUC values for a) the self-validated (success rate) of the Arniko models. b) the self-validated (success rate) of the Langtang models. c) independent 10-fold validated success of the Arniko models. d) independent 10-fold validated success of the Langtang models. e) 10-fold validated success of using the Arniko models to hindcast the Langtang landslides. f) 10-fold validated success of using the Langtang models to hindcast the Arniko landslides.

3.5 Discussion

3.5.1 Insights from field data: impacts of leucogranite and bedrock discontinuities

The field observations highlight two particularly interesting potential landslide controlling processes (e.g. Figs. 3.4 / 3.12); one, the intrusion of leucogranite, and two, the development of discontinuities within bedrock. Here, it will be discussed in more detail how and why these processes may control landslide occurrence, including some further analysis on the relationship between discontinuities and landslides.

In terms of the influence of leucogranite intrusions, the regression modelling (Fig. 3.21g) quantitatively corroborates the field observations, demonstrating that Unit 3, which was the unit heavily intruded by leucogranite, is the most susceptible to landsliding across Langtang. In fact, the regression analysis shows that Unit 3 had the largest magnitude positive regression coefficient (1.7) of all independent variables (Fig. 3.21), suggesting that this was one of the most important controls on landsliding across the region. There are a number of reasons why leucogranite intrusions might be having such an effect. For example, Mordensky *et al.* (2018) describe how magmatic intrusions can control the mechanical and physical properties of their host-rock. Under near-surface conditions, the pressure exerted by intruding magma can generate compressional and tensile stresses that lead to the development of discontinuities within the host rock (Galland *et al.* 2003; Casey *et al.* 2006), a process that can be amplified by intrusion-related host-rock alteration (Watters & Delahaut 1995). The development of discontinuities is important, as discontinuities have long been known to be a first order control on rock-mass strength (Jaeger 1960), which facilitates bedrock movement and rotation (Hoek 1983). Furthermore, discontinuities can increase rock porosity and permeability (Sousa *et al.* 2005), thus allowing more fluid (precipitation, meltwater etc.) into the rock mass, increasing weight, pore pressures and thus the likelihood of slope failure. These processes were observed at Pinnacle Ridge, Mt. Ruapehu, New Zealand, where it was found that intrusion-related discontinuities reduced rock mass strength via

the development of joints and fractures, and that host-rock permeability was increased at a distance roughly proportional to 1 – 2 times the intrusion thickness (Mordensky *et al.* 2018). In Langtang, intrusions with thicknesses of several metres were observed (e.g. Fig. 3.4f) as well as portions of bedrock with significant discontinuity development (e.g. Fig. 3.24a - c). As such, the literature provides support for the idea that the high density of discontinuities and subsequent reductions in rock-mass strength caused by leucogranite intrusions are enhancing the likelihood of landslide occurrence in Langtang.

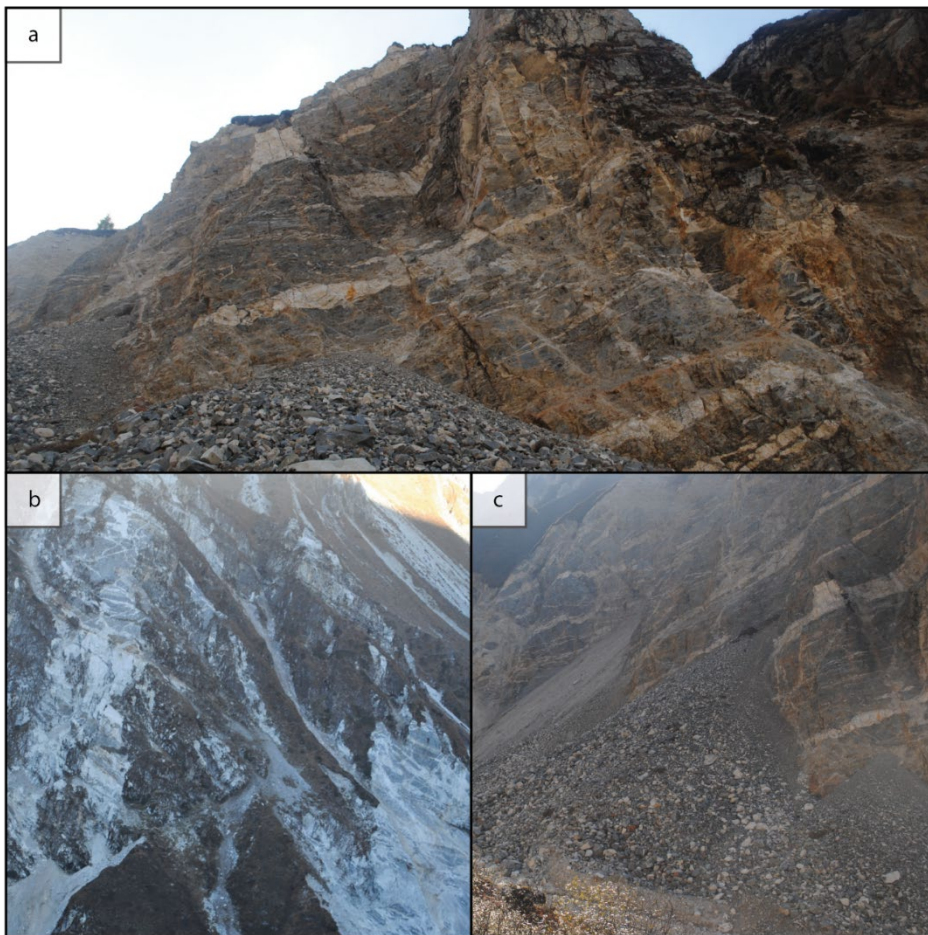


Figure 3.24. Photo panel depicting the extensive leucogranite intrusions observed within Langtang Valley. Photos taken during October 2018.

The following sections further discuss how discontinuities can control landslide occurrence. As highlighted in section 3.4.4, discontinuities were pervasive across both study regions, with three main joints sets identified in Arniko and two in Langtang, as well as a number of faults (Fig. 3.18 – 3.19). Bedrock discontinuities can have several influences on landslide occurrence. First, it was qualitatively observed that boulder production in the study region was controlled by the fracture spacing of major discontinuities (e.g. Figs. 3.4c - d). This highlights that talus deposits and sediment grain size are strongly sensitive to fracture spacing, particularly in regions dominated by bare bedrock on steep landscapes (Neely & DiBiase 2020; Verdian *et al.* 2020).

Second, planar discontinuities fundamentally act to degrade rock mass strength (Schultz 1995), with hillslope stability strongly related to the orientations and geometries of rock mass discontinuities (Park *et al.* 2016). Indeed, it has long been reported that landslide sliding surfaces are controlled by the geometric relationships between discontinuity planes and topography, with discontinuities that dip in the direction of the slope at a similar angle to the slope representing a high landslide risk, particularly for translational-type failures (e.g., Guzzetti *et al.*, 1996; Schuster, 1978). As such, in this case, if landslides are being controlled by discontinuities, it would be expected that the dip directions of major joint/fault sets are coincident with landslide aspect. Fig. 3.25 shows the aspect data for the landslides in each region, where Figs. 3.25a – b show the proportion of landslides that occurred at each aspect bin relative to the total distribution of the landscape in each bin, and Figs. 3.25c – d show rose diagrams of the overall aspect distributions of the landslides. These figures highlight that in the Arniko region, if picked at random from the inventory, a landslide had a higher percentage likelihood of having occurred on SE, S and SW facing slopes, whilst in Langtang they had a higher percentage likelihood of having occurred on SW and S facing slopes, despite the fact that the aspects of the hillslopes in both regions are approximately uniformly distributed. In Arniko, the dominant joint sets are oriented shallowly towards the NE (set 1; Fig. 3.18a - b) and more steeply towards the SW and SE (sets 2 and 3; Fig. 3.18a, c - d), whilst the faults are oriented steeply towards the W and SW. This suggests that in the Arniko region, the shallowly

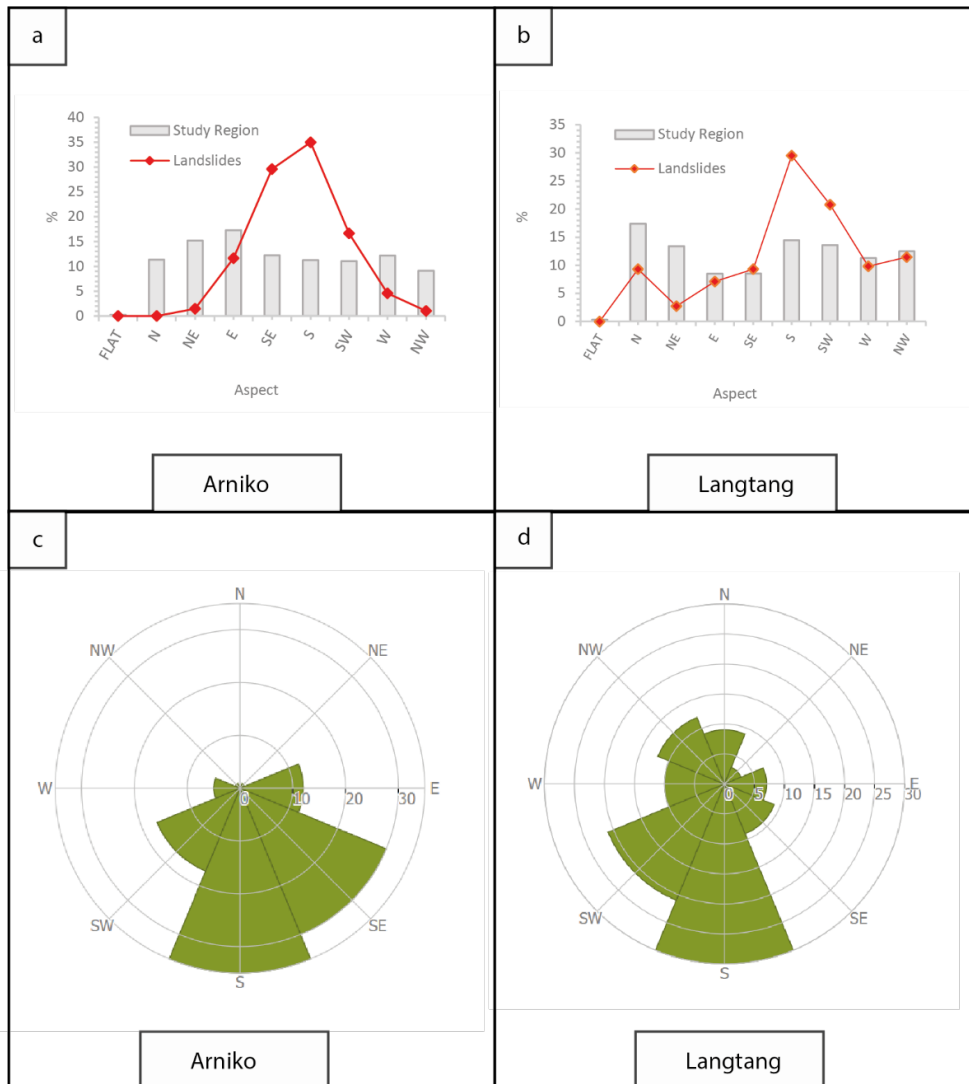


Figure 3.25. The proportion of landslides and the study regions within aspect bins for a) Arniko and b) Langtang. Rose diagrams of landslide aspect data for c) Arniko and d) Langtang.

dipping discontinuities are not significantly influencing landslide occurrence, but that the more steeply dipping SE, S and SW discontinuities do influence landslide occurrence. Likewise, in Langtang the dominant joints sets were orientated at moderate dip angles towards the NE – SE and WSW (Fig. 3.19a – b), with steeper angle faults oriented to the W and SW (Fig. 3.19d). Again, this suggests that the shallower NE-oriented discontinuities are imparting less control than those trending towards the S and SW at higher dip angles. These results corroborate the results of numerous other studies that have found a link between discontinuous and landsliding. For example, Brideau *et al.* (2009) outline several case studies, including

the pre-historic Aishihik river landslide (Yukon), the Hope Slide (British Columbia) and the Randa rockslide (Switzerland) that were all strongly influenced by discontinuity geometry. Likewise, Lee *et al.* (2002) found that the strike and dip of foliation, joint and fault geometries in the Janghung area of Korea strongly related to landsliding in the region, with gneiss foliation imparting a key control. More recently, Dini *et al.* (2020) undertook detailed kinematic analysis in Bhutan, finding that out of seven defined structural domains, five imparted a strong structural control on hillslope stability, with foliation geometry strongly influencing sliding mechanism. Overall, the results of this thesis and the aforementioned literature studies suggest that discontinuities are expected to correlate with landslide occurrence.

It is also interesting to consider landslide occurrence across the study areas in the context of the regional tectonic stress axes. As outlined in section 3.4.4, the principal stress axis in Arniko plunge towards the north (σ_1), the ESE (σ_2) and the SSW (σ_3). This suggests that it is σ_2 and σ_3 that relates most strongly to landslide occurrence. Similarly, in Langtang, the principal stress axes plunge almost vertically (σ_1), to the S (σ_2), and to the SW (σ_3), again suggesting that it is σ_2 and σ_3 that relate most strongly to landslide occurrence. This finding corroborates the results of Gupta, (2005) who found that landslides in the Satluj valley, Nepal, were aligned closely to σ_2 and σ_3 . Overall, these observations and semi-quantitative results suggest that discontinuity orientations are influencing landslide occurrence; although further, more detailed kinematic investigation into tectonic stress orientations would be required to confirm that the SE – SW prevalence of landsliding is not just a reflection of other processes relating to hillslope aspect (e.g., see Chapter 1 section 1.4.3.1 and Chapter 2 section 2.7.2.1).

3.5.2 Spatial heterogeneity in landslide controls

The results of the regression analysis highlight that there are significant differences between the controls on landsliding in each sub-region (Figs. 3.21i – p). Most notably, it is evident that in Langtang, increasing elevations make landslides significantly less likely, whereas in Arniko elevation has little influence on landslide

occurrence. Similarly, whilst increasing excess topography makes landslides more likely in both regions, the effect is more dominant in Arniko compared to Langtang (Fig. 3.21j). The clear differences in the trends with elevation and excess topography in the two regions raises the important question of why similarly triggered (predominantly coseismic) landslides in these two landscapes have such differing responses to topographical control factors. As seen in Fig. 3.21o - p, another major difference between Langtang and Arniko is the presence of permanent snow/ice and PFI. In Langtang, these factors have a dominant influence on landslide occurrence, but in Arniko they have no effect, as this region is too low (and thus temperatures too high) for permanent snow/ice and permafrost to exist. This suggests that the differences observed in the elevation and excess topography trends between the two regions may relate to glacial, paraglacial and/or periglacial processes.

A glacial environment can be defined as one where active glaciers and associated processes are present. Paraglacial and periglacial environments can be defined respectively as zones recently transitioned or still transitioning from glacial to non-glacial conditions, and non-glacial zones where frost processes are the dominant geomorphic process (Kääb *et al.* 2005). There is extensive literature on the linkages between climate change, glacial processes, paraglacial processes, periglacial processes and landsliding (e.g., Ballantyne 2002; Crozier 2010; Gariano & Guzzetti 2016; Mccoll 2012; Pánek 2019), with a general consensus that processes associated with glacial retreat and permafrost degradation will affect slope stability in high mountain regions (Seneviratne *et al.* 2012).

If glacier retreat has exerted a control on the predominantly coseismic landslides included in the Langtang inventory, then some coincidence between landslide occurrence and the elevations impacted by glacial retreat would be expected. In Langtang, the study region includes regions that experienced glacial retreat over the millennial scale to decadal scale. On the decadal scale, since 1979 it is estimated that the two main glaciers in the region, the Lirung and Kimjung glaciers, have retreated by 900 and 400 m, respectively (Rai *et al.* 2017). Based on recent GoogleEarth satellite imagery, the lowest part of the Lirung glacier (Fig. 3.2a) is currently located at an elevation of ~4,800 m, with a zone of recent ablation extending from elevations of

~4,800 – 4000 m (Fig. 3.2a). This suggests a rate of retreat that is broadly in agreement with that estimated by Rai *et al.* (2017). In terms of longer term glacial retreat, Shiraiwa & Watanabe (1991) divide the glacial history of Langtang into six stages. They propose that the two oldest stages (Lama and Gora Tabela) occurred in the early Last Glacial and Last Glacial Maximum (LGM), with glaciers extending to elevations of ~2,600 m and 3,200 m, respectively. However, the extent of the glacier in the Lama stage is disputed, with Heuberger & Ibetsberger (1998) arguing that glaciation was unlikely to have reached this extent based on the limits of other glaciers at this time (Barnard *et al.* 2006). However, regardless of the precise minimum extent of glaciation, there is consensus that glaciation reached an elevation of at least 3,200 m during the LGM. Using this information, Fig. 3.26a shows the percentage of landslides in the inventory that fall within 200 m elevation bins across the study region, and the estimated lower extents of glaciation during the LGM and the 1970s. This shows that after an initial increase in landsliding between 1400 – 1800 m, landsliding remains broadly static, with 2 – 7% of total landsliding occurring in each elevation bin between elevations of 1800 and ~3400 m. Then, from 3400 – 4600 m a sustained increase to 13% of total landsliding in the 4600 – 4800 elevation bin was observed, before a rapid decrease down to 0% landsliding in any elevation bins > 5000 m. The period of sustained increase coincides with the elevation range that observed deglaciation between the LGM and the 1970s. This (very) tentatively suggests that millennial scale glacial retreat and associated processes are having an influence on landslide occurrence in Langtang. This is feasible, as processes associated with glacial retreat such as the debuttrussing of rock slopes (e.g. Grämiger *et al.* 2017) and the release of lithospheric stresses during and after deglaciation (e.g. Pánek 2019) are known to influence hillslope stability over decadal to millennial timescales (Huggel *et al.* 2012; Ballantyne *et al.* 2014; Pánek *et al.* 2017; Böhme *et al.* 2019; Matsuoka 2001; Fischer *et al.* 2006; Cossart *et al.* 2008; Sauber & Ruppert 2008; Pánek *et al.* 2016; Liu *et al.* 2021).

The other process that can potentially provide explanation for the differences in landslide occurrence between Langtang and Arniko is permafrost degradation (Gruber & Haeberli 2007), where permafrost is defined as lithosphere material that

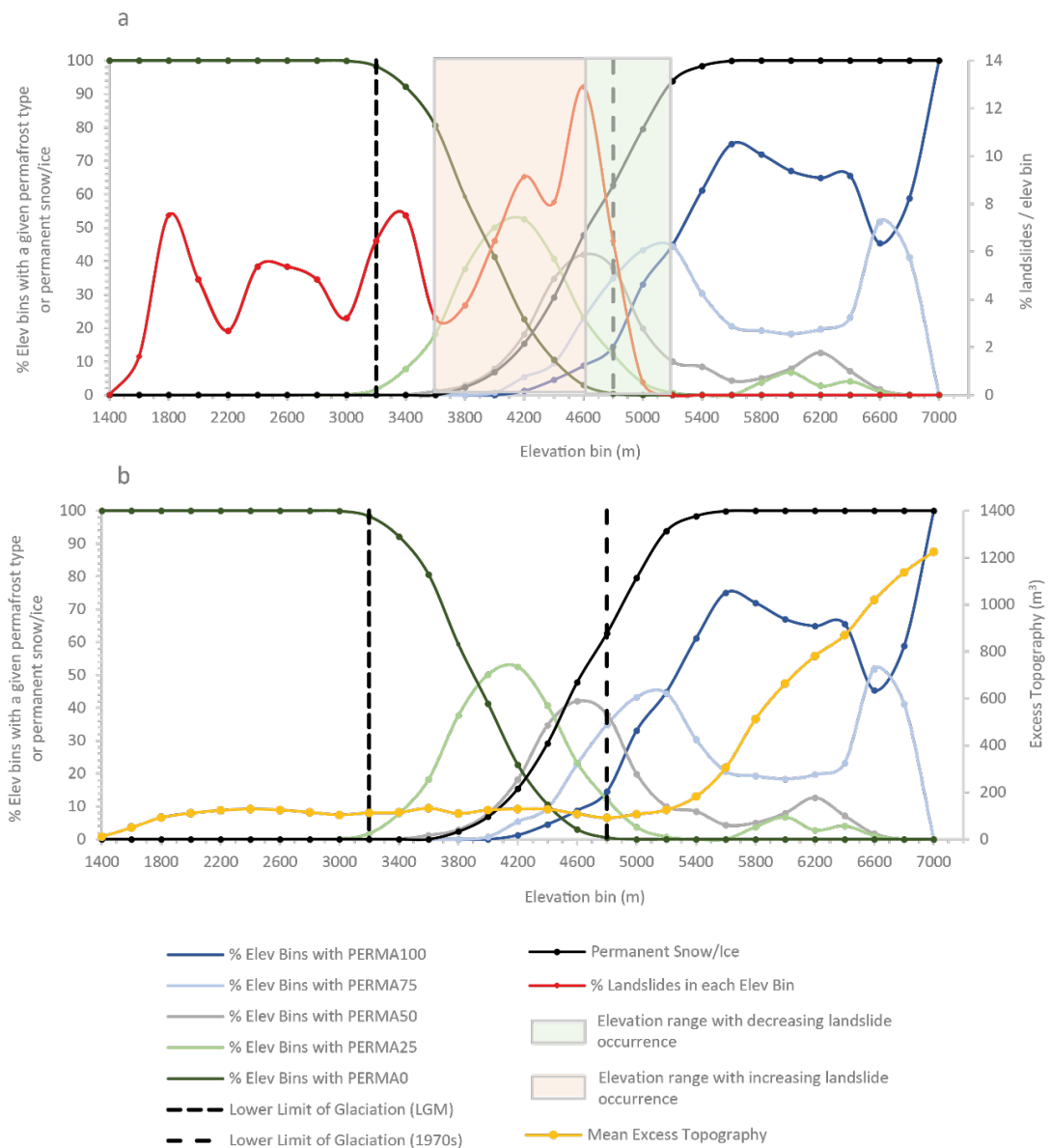


Figure 3.26. a) The percentage of landslides across each 200 m elevation bin across Langtang as well as the percentage of each elevation bin that is covered by different degrees of permanent snow/ice and permafrost, with permafrost defined by the Permafrost Index (PFI) of Gruber, (2012). PERMA100 = PFI of 1 – 0.75, PERMA75 = PFI of 0.5 – 0.75, PERMA25 = PFI of 0 – 0.25, and PERMA0 = no permafrost. This also shows the estimated lower limits of glaciation during the LGM and 1970s, as well as elevation ranges characterised by anomalous increases and decreases in landslide occurrence. b) the same permafrost, permanent snow/ice, and glacial extent data as in a), but with mean excess topography per elevation bin.

remains at or below 0°C for at least two consecutive years. If permafrost degradation is influencing landslide occurrence, then correlation between landslide occurrence, elevation, and permafrost would be expected across Langtang. Fig. 3.26a shows the percentage of landslides across each 200 m elevation bin across Langtang. It also shows the percentage of each elevation bin that is covered by different degrees of permafrost, as defined by the Permafrost Zonation Index of Gruber (2012) (see Chapter 2, section 2.3.2.5). This index defines permafrost with values between 0.01 and 1, where a value of 1 suggests that permafrost will be present under all conditions, whereas a value of 0.01 suggests that permafrost will only be present under ideal meteorological conditions. In Fig. 3.26a, PFI values are binned at 0.01 – 0.25, 0.25 – 0.5, 0.5 – 0.75 and 0.75 – 1. As seen in Fig. 3.26a, the period of sustained landslide increase occurs at elevations of ~3800 – 4600 m. This range is coincident with a marked decrease in cells impacted by no permafrost, but an increase in cells impacted by permafrost under only occasional meteorological conditions (lines PERMA025 AND PERMA50 on Fig. 3.26a). These PFI values are likely to represent zones of degrading permafrost, with pervasive freezing and melting. Furthermore, it is apparent that at 4,600 m, landslide occurrence begins to reduce rapidly. This elevation is coincident with an inflection point in the 0.25 – 0.5 PFI group, whereby at elevations greater than this, PFI values of 0.25 – 0.5 begin to decrease whilst PFI values > 0.5 continue to increase. By ~5200 m, the rate of landsliding falls to zero whilst the majority of ground at that elevation is predicted to have permafrost under all meteorological conditions. Furthermore, this decrease in landslide occurrence also corresponds with the elevations at which permanent snow and ice cover is almost total, which supports permafrost being pervasive at these elevations (Fig. 3.26a). This can also explain why excess topography is more dominant in Arniko than in Langtang, with Fig. 3.26b showing that the main increases in excess topography in Langtang occur where permafrost is extensive, and thus slope stability increased. These results strongly suggest that permafrost degradation is influencing landslide occurrence in Langtang. This is feasible, as there are several ways in which permafrost degradation can influence slope stability. One, is through the loss of ice-

bonded discontinuities, with shear box testing showing that permafrost degradation associated with temperature rise reduces the shear-strength of ice-bonded fractures and therefore reduces slope stability (Davies *et al.* 2001). Two, is via frost-cracking, which results from the freezing and thawing of water within rock. There are two theories as to how frost-cracking can impact slope stability. First, is through volumetric expansion, whereby if water fully saturates a discontinuity and then freezes, it expands by up to 9% (Matsuoka 1990), generating pressures of up to 207 MPa at -22 °C (Matsuoka & Murton 2008). This pressure would be sufficient to fracture most rock types; however, the conditions for these pressures to be generated are unlikely at most bedrock depths deeper than a few centimetres from the ground surface. Second, is through ice segregation, where fractures are developed through progressive micro-cracking associated with ice lens growth (Matsuoka & Murton 2008).

Furthermore, the Langtang observations corroborate numerous other examples where slope failures have been linked to permafrost degradation. For example, Huggel *et al.* (2012) describe how large rockfalls in Guttannen (Switzerland) and Monte Rosa (Italy) were likely related to permafrost degradation, whilst several studies have linked rockfalls in Norway to permafrost loss (e.g. Böhme *et al.* 2019; Hilger *et al.* 2018). Similarly, rockfalls and scree debris production in Canada, Japan, New Zealand and Utah have been shown to nucleate at narrow elevation ranges associated with zones of intense frost-cracking processes (Hales & Roering 2005; 2007). The presence of permafrost has also been shown to inhibit frost-cracking, with bedrock damage more extensive and at greater depths if permafrost is not present (Anderson *et al.* 2013).

Overall, these results relating to glacial retreat and permafrost strongly support the idea that these processes are controlling the observed landslide distributions in Langtang, with enhanced landsliding coincident with elevations impacted by glacial retreat and degrading or infrequently developing permafrost, and almost no landsliding at elevations above this where permafrost becomes pervasive. Furthermore, as outlined by Chauhan & Thakuri (2017) and Fukui *et al.* (2007), and confirmed by the permafrost data in Langtang (Gruber 2012), permafrost across the

central-eastern Himalaya is only pervasive above 5200 - 5400 m. The Arniko region does not exceed these elevations, and is therefore not expected to have any permafrost. Furthermore, the Arniko region is not believed to have experienced glaciation below ~4,200 m during the LGM (Williams 1983; Fort 1995), with field geomorphology confirming that there are no extensive glacial landforms within this portion of the Bhote Koshi basin (Higaki *et al.* 2000). This further supports the idea that permafrost degradation and glacial retreat can explain the elevation landslide control difference between Langtang and Arniko.

3.5.3 Impacts of spatial heterogeneity on landslide susceptibility modelling

The previous section highlights several ways in which landslide controls differ between the two distinct landscapes of Langtang and Arniko. But what are the impacts of this spatial heterogeneity on landslide susceptibility modelling?

The BLR analysis shows that susceptibility models developed locally for each region have success and prediction rates of 0.88 and 0.82 for Langtang, and 0.8 and 0.78 for Arniko (Fig. 3.23a – d). However, perhaps unsurprisingly, using the model developed in one locality to hindcast the landslides in the other locality leads to very poor prediction AUROC values of 0.58 when using the Langtang models to hindcast Arniko landslides, and 0.66 when using the Arniko models to hindcast Langtang landslides (Fig. 3.23e – f). This confirms that, as expected, it is unacceptable to use disparate susceptibility modelling, i.e., to use models developed from one region to forecast/hindcast landslide occurrence in another region with dissimilar geomorphic processes.

However, what is less obvious is the impact of heterogeneous processes on regional to global scale susceptibility models, which often include multiple geomorphic zones within a single developed model. Models at such scales, including the monsoon-triggered model presented in Chapter 2, are not uncommon (e.g. Lin *et al.* 2017; Sabatakakis *et al.* 2013; Stanley & Kirschbaum 2017; Thi Ngo *et al.* 2020). At such scales, typical BLR susceptibility approaches assume static and spatially homogenous relationships between landslide occurrence and regression coefficients (Yang *et al.* 2019b). In effect, this means that areas within a larger modelled region that are

similar to the average relationship should be well predicted, but areas with relationships that deviate significantly from the mean may be very poorly predicted, even if the overall model accuracy appears to be high.

To further investigate the impact of using regional scale modelling to forecast/hindcast local areas, a comprehensive dataset of 2015 Gorkha earthquake coseismic landslides (Roback *et al.* 2018) was used alongside the same independent predisposing factors as used for the modelling in this chapter, to model coseismic landslide susceptibility across the larger (45,000 km²) study region defined in Chapter 2. The regression coefficients and LASSO selection percentages obtained for the independent variables used in this model are shown in Appendix D. The model had success and hindcast rate AUROC values of 0.87, so a very good model (Fig. 3.27a – b). To see how well this model predicted the coseismic landslide data from smaller sub regions within its larger extent, it was validated using Roback coseismic landslide data from exclusively Langtang and Arniko respectively. This validation gave prediction AUROC values of 0.81 for Langtang and 0.73 for Arniko (Fig. 3.27c – d). These results are not bad, but are 6% (Langtang) and 15% (Arniko) worse than the AUROC values obtained for the overall region, and 7% (both Langtang and Arniko) worse than the success rate AUROC values obtained when those regions were modelled locally (Fig. 3.24a – d). This suggests that regional scale BLR modelling across heterogeneous geomorphic regions is suboptimal for local prediction and thus disaster management decision making on a local scale.

Overall, this regression modelling confirms that spatial heterogeneity does reduce the local accuracy of regional scale models, suggesting that regional scale BLR modelling without considering spatial heterogeneity is suboptimal. The wider implications of this, as well as some potential solutions, are discussed further in Chapter 6.

3.5.4 Impacts of landslide type on landslide susceptibility modelling and hazard management

As mentioned in Chapter 1, landslide types can have important implications for how landslide susceptibility models are interpreted and used. As such, the field-based

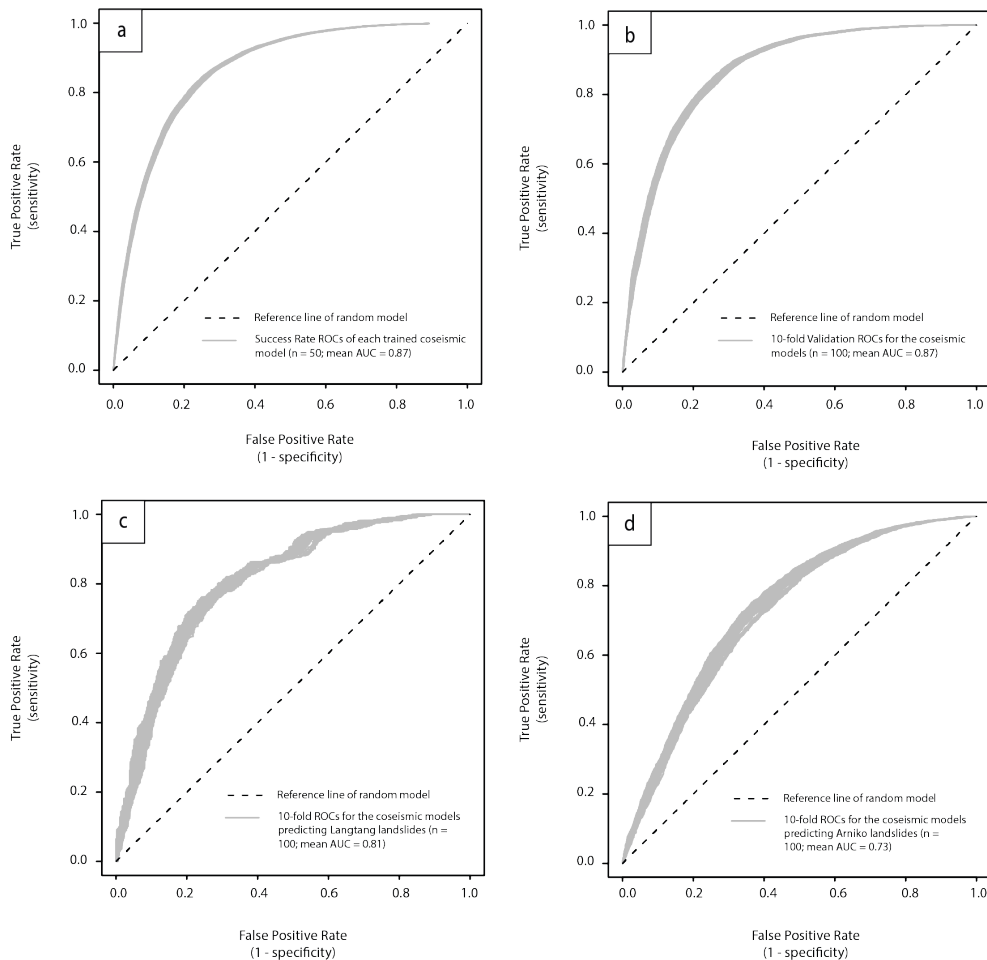


Figure 3.27. ROCs and AUC values for a) the self-validated (success rate) of the coseismic model. b) independent 10-fold validated success of the coseismic model. c – d) 10-fold validated success of using the coseismic model to hindcast the Langtang and Arniko data only.

landslide type descriptions presented in this chapter can provide some interesting insight and discussion into how landslide types impact susceptibility modelling and landslide hazard management.

Section 3.4.3 outlines that the three main landslide types observed in Langtang and Arniko are rockfalls, rotational slumps and slides, and debris flows, with rockfalls by far the most common. These observations show that these different landslide types typically occur in different locations within the landscape. For example, rockfalls tended to occur on steeper ($>75^\circ$) cliffs, with bedrock discontinuities controlling block size and formation. Conversely, rotational slumps/slides tended to occur within less steep terrace deposits, often at the hillslope toe in close proximity to river

channels, whilst debris flows often initiated as rockfalls before becoming saturated and having a runout that was controlled by the hillslope morphology. This suggests that the relationships between landsliding and predisposing factors defined by BLR models (e.g., the regression coefficients) may not be consistent across different landslide types, and that if landslide types were modelled in isolation the resulting regression coefficients may vary between types. Furthermore, it is well described in the engineering geology literature that different landslide types require different mitigation strategies (Popescu & Sasahara 2009). For example, coseismic rockfalls on steep bedrock cliffs are likely to be best mitigated by hard engineering strategies such as rock-nets, rock-bolts, bored piles, or rock-anchors, whilst rotational slumps/slides may be best mitigated by better drainage to remove water from concave hillslopes, or gabion/retaining walls at terrace toes (Waltham 2002). Conversely, debris flow events may be best managed via 'soft' engineering such as re-vegetating slopes to reduce runoff and flow potential, or through harder engineering strategies such as check dams (e.g. Chen *et al.* 2015).

This highlights that susceptibility models/maps produced here and elsewhere should always be combined with detailed field information on landslide type and process. In other words, landslide susceptibility maps should be used to preliminarily identify zones of high susceptibility, which can then inform where more detailed investigation into landslide type and process is needed before mitigation strategies are designed. Finally, further work that is considered beyond the scope of this thesis would be to conduct susceptibility modelling for each landslide type separately. This would allow identification of any spatial differences in susceptibility between landslide types and quantification of whether predisposing factor relationships differ between landslide types.

3.6 Conclusions

The main aims of this chapter were: One, to assess how field data can provide insight into landslide types and processes beyond that which could be observed remotely. Two, to quantify the differences in landslide occurrence between two distinct geomorphic regions to investigate the spatial heterogeneity of landslide occurrence

across the study region. Three, to assess the impacts of spatially heterogeneity on landslide susceptibility modelling.

The field observations showed that, in terms of landslide type, coseismic rockfalls and debris flows are most common across both regions. This is unsurprising given that both locations were badly impacted by the 2015 Gorkha earthquake (Tanoli *et al.* 2017; Roback *et al.* 2018; Jones *et al.* 2020). The field observations also suggest that leucogranite intrusions and discontinuity geometries strongly influence block development and slope stability.

The BLR modelling showed that there are significant differences between the landslide controls in Langtang and Arniko, with the former much more strongly controlled by elevation, the presence of permanent ice/snow, and permafrost, but less strongly controlled by excess topography. It is concluded that these differences are likely related to the glacial, paraglacial and periglacial processes that exist within Langtang, but not Arniko, specifically permafrost degradation, which is found to be coincident with elevation zones of heightened landslide activity. Finally, the BLR modelling highlights that the spatial heterogeneity between landslide processes observed in Langtang and Arniko does influence landslide susceptibility modelling, with local-scale models developed for the two sub-regions incapable of accurately predicting landslide occurrence in the other region, and regional scale models showing less accuracy at predicting landslides in Langtang and Arniko compared to the local scale models. This suggests that spatially disparate and regional scale BLR modelling that does not consider spatial heterogeneity is sub-optimal for landslide prediction, as will be discussed further in Chapter 6.

Chapter 4 Temporal variations in landslide processes and distributions: implications for landslide susceptibility modelling

Note, elements of this chapter have been published in two papers. First, the methodologies, results, and discussion pertaining to landslide path dependency have been published in Geomorphology (Roberts et al. 2021). This paper differs from this Chapter, as the paper integrates the relevant work presented in this chapter with separate analysis conducted by Plymouth MGeol student Storm Roberts. Second, the methodologies, results and discussion pertaining to how landslide distributions and susceptibility change through time have been published in the Journal of Geophysical Research – Earth Surface (Jones et al. 2021b). Again, the structure and format of this paper differs to this chapter, though the majority of the analysis, results and discussion are the same.

4.1 Introduction

As discussed in Chapters 1 and 2, there remains significant uncertainty over the temporal nature of landslide occurrence. For example, how is landslide occurrence impacted by transient processes such as path dependency? How stable are landslide spatial distributions through time, particularly in response to extreme events, and how do these issues impact typical landslide susceptibility modelling approaches? This chapter aims to answer these questions with four objectives.

First, is to use the ASM-inventory developed here and the methods of Samia *et al.* (2017) to quantify whether path dependency is occurring in the Nepal Himalaya. As outlined in Chapter 1 (section 1.2.2.1), path dependency describes how new landslides will be transiently more likely in locations impacted by past landslides. Chapter 2 quantifies how spatially associated landslides (those that overlap with a

previous landslide) have different geometries, sizes, and spatial distributions to spatially unassociated landslides (those that do not overlap with a previous landslide). However, an understanding of how spatially associated landslide characteristics differ from spatially unassociated landslides does not actually show whether past landslides are making future landslides more likely. As such, this Chapter will focus on quantifying whether path dependency is actually occurring, i.e., whether spatially associated landslides are occurring at a greater rate than would be expected if their occurrence was random.

Second, is to systematically investigate whether the spatial distributions of the landslides in the ASM-inventory vary through time, particularly in response to the 2015 Gorkha earthquake and other “extreme” events. Note that an “extreme” event is defined as any high magnitude landslide driver such as a storm, flood or earthquake that might cause landslide rates above that expected from a typical ASM-season (see Chapter 5). As outlined in Chapter 1 (section 1.2.2), it is typically assumed that landslide spatial distributions are static through time, and thus that time-independent susceptibility models developed using past landslide data are sufficient for future prediction (Aleotti & Chowdhury 1999). However, this assumption is rarely, if ever, quantified, largely due to the lack of published multi-temporal landslide inventories. The ASM-inventory developed here thus provides an excellent opportunity to assess the validity of the assumption that landslide spatial distributions are time-independent.

Third, is to quantify the impacts of any observed temporal variations in landslide spatial distributions on the predictive (or hindcasting) ability of BLR susceptibility models. As mentioned in the introduction, BLR approaches are the most commonly used landslide susceptibility modelling method (Reichenbach *et al.* 2018), so it is vital to understand and assess how this model type might be impacted by temporal variations in landslide occurrence, and therefore challenge the time-independent assumptions that this method often utilises.

Fourth, is to utilize the long record of landslide data in the ASM-inventory to investigate how the choice of landside data used to train a BLR susceptibility model

influences the model's predictive/hindcasting ability. As outlined in Chapter 2 (section 5.2.1), susceptibility models can be developed using a range of inventory types, from event or single-season inventories (e.g. Fiorucci *et al.* 2011; Roback *et al.* 2018) to longer historical or multi-event/season inventories (e.g. Jaiswal *et al.* 2011; Martha *et al.* 2012). As such, this objective will compare the hindcasting ability of susceptibility models developed using single ASM-season inventories that experienced an extreme event (e.g. an earthquake, storm, or flood) vs increasingly long pseudo-historical (multi-seasonal) inventories, to assess how inventory length impacts susceptibility model consistency and accuracy.

4.2 Data and methods

All of the analysis presented in this chapter uses the ASM-inventory of 12,383 landslides and associated predisposing factor datasets described in Chapter 2 (see Data Files 1 and 2, [here](#) and [here](#)). The following sections outline the methods used in this chapter that have not been described elsewhere.

4.2.1 Path dependency

The first objective of this chapter is to quantify whether path dependency is occurring in the Nepal Himalaya using three metrics introduced by Samia *et al.* (2017): the overlap index, unaffected area, and number of overlaps.

4.2.1.1 The overlap index

The overlap index quantifies the degree of overlap between landslides in two different inventory time slices according to equation 4.1 (Samia *et al.* 2017b).

$$\text{Overlap index}_{t-t+n} = \frac{AL_t \cap AL_{t+n}}{AL_t + AL_{t+n} - (AL_t \cap AL_{t+n})}$$

Equation 4.1. The overlap index.

Where, t is the average date of the first time slice, $t + n$ is the average date of the second time slice and \cap is the geometric intersection (overlapping area in m^2) between two time slices. Average dates were taken at the middle of each mapped monsoon period (June 15th). By plotting the overlap index values against the respective time intervals between time slices, the relationship between landslide overlap and time between landslides can be established. The overlap index was

calculated for every possible combination of time slices, as well as between each year and the 2015 Gorkha earthquake coseismic landslides of Roback *et al.* (2018). This gave 435 overlap index values.

4.2.1.2 Unaffected area

The unaffected area method compares the actual area of land unaffected by landsliding to the theoretical area of land that would be unaffected by landsliding if no overlapping of landslides occurred. The Actually Unaffected Area (AUA) is given by Equation 4.2 (Samia *et al.* 2017):

$$\text{Actually unaffected area}_t = (U_{i=1}^t AL_{Ti})/AS$$

Equation 4.2. Actually unaffected area (AUA).

Where, t is the time slice number (1988 = time slice 1, up to 2018 = time slice 30), AL_{Ti} is the total area of landsliding in time slice i, AS is the area of the study region, and U is the union of all landslides between time slice i =1 and time slice t. Accordingly, this metric calculates the total area of landsliding up to a given time slice, after accounting for overlaps, as a dimensionless fraction of the size of the study region.

Conversely, as shown in Equation 4.3 (Samia *et al.* 2017) the Theoretically Unaffected Area (TUA) does not account for overlaps:

$$\text{Theoretically unaffected area}_t = (\sum_{i=1}^t AL_{Ti})/AS$$

Equation 4.3. Theoretically unaffected area (TUA).

This metric calculates the total area of landsliding up to a given time slice, without accounting for overlaps (i.e., assuming all landslides are spatially unassociated), as a dimensionless fraction of the size of the study region. As such, if spatially associated landslides are occurring, when the AUA and TUA are plotted against one another through time, the AUA is expected to plot progressively lower than the TUA, with the distance between the two indicating the degree to which landslides are overlapping across the study region. These metrics were calculated at every time slice of the ASM-inventory i.e., calculated 30 times between 1988 and 2018 (the 29 ASM-inventory time slices plus the Gorkha earthquake coseismic time slice).

4.2.1.3 Number of overlaps

The number of overlaps method quantifies the relationship between number of landslide overlaps and total landslide area (Samia *et al.* 2017b). Specifically, this method calculates the actual area of landsliding at different degrees of overlap to the area of landsliding predicted to occur at different degrees of overlap by a random model. The actual number of overlaps in the ASM-inventory was calculated by first converting the landslide polygons in each time slice into rasters using the ArcGIS 'Feature to Raster' tool. These time slices were rasterised at the same resolution as the landslide mapping (i.e., 30 x 30 m cells). All landslide presence cells were given a value of 1, whilst landslide absence cells were given values of zero. Then, by summing all 29 time slice rasters across the ASM-inventory, the total number of landslide presence cells (and thus area of landsliding) at different degrees of overlap were calculated. The random model used a random number generator in Matlab to randomly assign the same number of landslide presence cells as existed in each time slice of the actual ASM-inventory to a grid with the same number of cells as the study region. The randomly assigned time slices were then summed to count the total number of landslide presence cells (and thus area of landsliding) at different degrees of overlap for the random model. The random model was run 50 times to get a mean number of overlaps. If landslides in the ASM-inventory are exhibiting path dependency, it would be expected that the actual data will show a greater area of landslides at higher degrees of overlap than is predicted by the random model. However, it should be noted that a limitation to this method is that the random clustering used by the MATLAB model does not consider the clustering of cells that exist in the real data. Consequently, the random model may underestimate the degree of overlapping relative to the actual data.

4.2.2 K-S and Chi-2 analysis

The second objective of this chapter is to assess how the spatial distributions of ASM-triggered landslides varies through time. This is achieved by using the Chi-2 and two-sample K-S (Kolmogorov-Smirnoff) tests to compare the distributions of landslides

with respect to several control factors across every mapped time slice of the ASM-inventory.

The two sample K-S test compares the similarity between two continuous samples, operating under the null hypothesis that the two samples being compared are similar. The null hypothesis can be rejected if the p-value of the K-S statistic, which measures the largest distance between the empirical cumulative distribution functions fitted to the continuous samples being compared (e.g. Fig. 4.1a), is lower than a given alpha (significance) value. Similarly, the Chi-2 test evaluates whether two categorical samples have similar underlying distributions, operating under the null-hypothesis that the two categorical samples have similar proportions of data in each category bin (e.g. a land use class or geological unit). The K-S and Chi-2 tests were applied as described below and in Fig. 4.1a to assess how the spatial distributions of the landslides in the ASM-inventory vary through time.

1) For every landslide in the ASM-inventory, the values of all continuous and categorical predisposing factors of interest were extracted at the highest elevation point (the assumed triggering location) of each landslide.

2) For the continuous predisposing factors, empirical Cumulative Distribution Functions (CDFs) were calculated for the landslides in every individual time slice, and for all of the time slices combined (the “all data” case). Similarly, for the categorical control factors, the proportion of landslides in each predisposing factor classification (e.g. individual geology or land use types) were calculated for the landslides in every individual time slice and for all of the time slices combined (the “all data” case).

3) For the continuous control factors, the K-S test was used to compare the CDFs of every time slice to, 1) the CDFs of every other time slice, and 2) the CDF of the “all data” case. With 29 time slices plus the “all data” case, this gave 435 unique test pairings ($30 \times 29 / 2$). Similarly, for the categorical control factors, the Chi-2 test was used to compare the proportions of landslides per bin of every time slice to the proportions of every other time slice plus the proportions of the “all data” case. Again, this gave 435 individual comparisons.

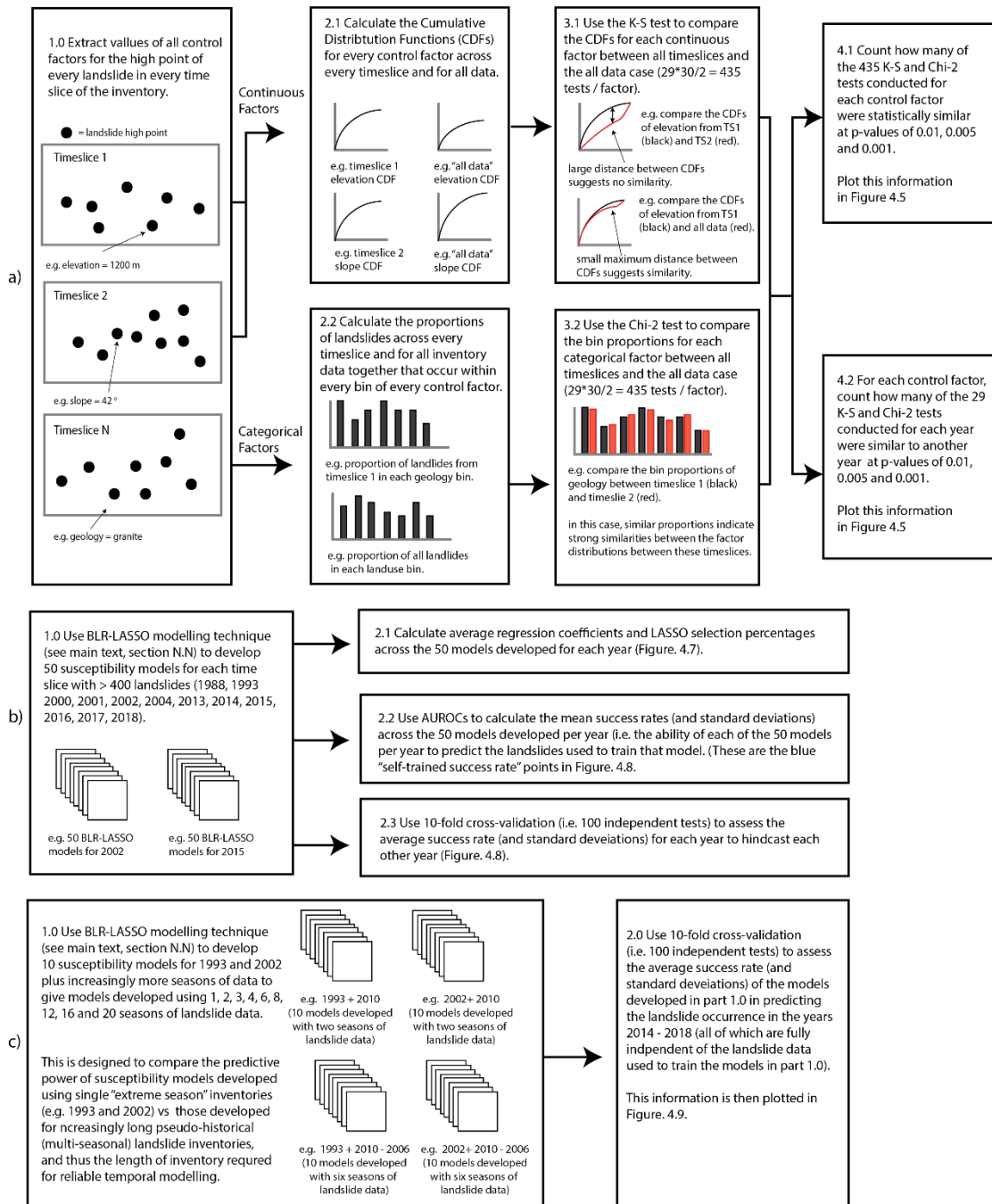


Figure 4.1. Workflow methodology for, a) comparing landslide distributions in different time slices using K-S and Chi-2 statistics. b) developing and validating landslide susceptibility models using the BLR-LASSO approach. c) developing and validating landslide susceptibility models using the BLR-LASSO approach for increasingly long pseudohistorical (multi-seasonal) landslide inventories.

4) For each continuous and categorical predisposing factor, the number of the 435 K-S or Chi-2 tests with p-values below significance (alpha) thresholds of 0.01, 0.005 and 0.001 were counted. From this, the overall percentage of time slices with statistically similar landslide distributions to another time slice or the “all data” case were obtained.

5) The results obtained from 4) give an overall appreciation of how similar the landslide distributions with respect to each predisposing factor are through time. However, this does not show where any dissimilarities are temporally concentrated. For example, if a given predisposing factor is found to be similar in only 50% of the 435 tests, it is not known whether this is because every year was only similar to 50% of the other years, or because 50% of the years were similar to no other years. This information is important for identifying where in time any dissimilarities actually occurred. So, for each predisposing factor, the number of the 29 K-S and Chi-2 tests conducted for each time slice that were similar to another time slice or the “all data” case were counted at significance thresholds of 0.01, 0.005, and 0.001.

4.2.3 BLR modelling

The K-S and Chi-2 tests allow quantification of the temporal variation in single landslide predisposing factor distributions, considered independently from any others. The third objective of this chapter is to assess how any temporal variations in landslide predisposing factor distributions impacts BLR susceptibility modelling. To do this, the BLR-LASSO method (e.g. Lombardo & Mai 2018) used in previous chapters; (see Chapter 2 section 2.5) is used to develop susceptibility models for 12 years (time slices) of the ASM-inventory. The 12 modelled years were 1988, 1993, 2000 – 2002, 2004, and 2013 – 2018, all of which observed > 400 landslides. The years that observed < 400 landslides were not modelled to ensure the robustness of the results (i.e., to ensure that any model differences could not be attributed to one year having a very small number of landslides).

Before running the models, the landslide and control factor data required further processing. First, the study region was divided into a 30 x 30 m grid of $\sim 5 \times 10^7$ cells. For each year, each grid-cell was assigned a value of one if it included a landslide

triggering point (landslide presence) and a value of zero if not (landslide absence). All control factor datasets were then resampled to this grid. Then, for each year, 50 balanced sub-datasets were extracted, where each subset included all control factor data associated with that year's landslide presence cells plus an equal number of randomly selected landslide absence cells. In total, this gave 600 balanced datasets across the 12 years to be modelled. Fifty model iterations were used as this was a good balance between computational efficiency and statistical robustness and in line with other landslide susceptibility studies, for example, work by Schlögel *et al.* (2018), uses 56 model iterations to assess slope unit based landslide susceptibility in the French Alps.

Each of these 600 datasets included information on landslide presence or absence, plus the associated values of 17 predisposing factors. Of these 17 factors, two were categorical (geology and land use) and the rest were continuous. To ensure the final regression coefficients calculated for each factor were objectively comparable, the continuous factors were rescaled using zero-mean unit variance (e.g. Lombardo & Mai 2018). Furthermore, with so many factors, it was possible that some would be collinear. This is potentially problematic, as significant collinearity between factors can introduce error and instability into regression models (Zuur *et al.* 2010). As such, before inputting the datasets into the glmnet model, collinearity between all factors in all 600 sub-datasets was tested using the Variance Inflation Factor (VIF) functions of Zuur *et al.* (2010). The VIF is a common measure of multi-collinearity in a set of regression variables that is equal to the ratio of the variance in a multi-variable model to the variance of a model that only includes a single independent variable. VIF's can be calculated for each individual variable, and a VIF > 5 suggests that the associated independent variable is highly collinear with at least one other variable in the model. Here, for each dataset, the VIF's for each independent control factor were calculated. Then, if any factors had VIFs > 5, the factor with the highest VIF was removed and the VIFs were recalculated for the remaining factors. This was repeated until all factors had VIFs < 5. In this case, the 'total rainfall' factor was found to be highly collinear with peak rainfall, average rainfall and elevation. Once total rainfall was removed, all other factors had VIFs of < 5. Finally, before running the glmnet model,

the two categorical factors were coerced into dummy variables (i.e. presence / absence for each sub-category).

The processed 50 balanced subsets for each of the 12 modelled years were then run through the glmnet model, where each model used the 10-fold cross-validated LASSO for factor selection. The resulting factor selections and associated regression coefficients were then averaged for each year based on all 50 models for that year. This allowed quantification of how each factors selection percentage and regression-coefficient varied through time across each of the 12 modelled years. This workflow is described graphically in Figure 4.1b.

4.2.4 AUROC model validation

The third objective of this chapter involves assessing how well the developed BLR susceptibility models for one year could forecast/hindcast the landslide data from other years. To assess how well one BLR model can forecast/hindcast another year's data, AUROC (Area Under Receiver Operator Curve) validation (see Chapter 2, section 2.5.5) was used to assess how well the 12 developed BLR models could forecast/hindcast the landslide distributions of each other mapped and modelled year (i.e. forecast/hindcast the landslide data from each of the other years; 1988, 1993, 2000 - 2004, 2013- 2018) (Fig. 4.1b). The Area Under the ROC (the AUROC value) indicates the degree to which a binary model correctly forecasted/hindcasted the observed classes, in this case landslide presences and absences. An AUROC value of one indicates that a model was 100% accurate, whilst an AUROC value of 0.5 is equivalent to the result of a random predictor with no classification capacity. A value < 0.5 indicates that a model is actively reciprocating the classification, i.e. in this case would be predicting landslide absences as presences and vice versa. Typically, models with AUROC values of 0.7 – 0.75 are considered good, whilst models with AUROC values of > 0.8 are considered very good (e.g. Marjanović, 2013; Vakhshoori & Zare, 2018). Here, 10-fold cross validation, whereby 100 AUROC tests between the models developed for a given year and random balanced landslide presence/absence datasets from another year, was used to calculate the average AUROC values and standard deviations for each year's ability to hindcast the landslide occurrence in each other

modelled year. If all 12 years had average AUROC values when hindcasting all other years of $> 0.7 - 0.75$, then it could be concluded that any temporal landslide control factor variation does not actually influence the overall predictive power of landslide susceptibility models developed on a given year. However, if some or all years were incapable of sufficiently hindcasting all or some other years, it would suggest that great care must be taken when developing and applying susceptibility models through time.

The fourth objective of this chapter is to assess whether BLR models developed with increasingly longer period pseudo-historical inventories have increasing hindcasting power relative to models developed from single years that observed extreme events. To do this, the following methodology (Fig. 4.1c) was used:

- 1) Take two single seasons of data (1993 and 2002) which when taken in isolation produced susceptibility models that were poor at hindcasting other years (see section 4.3.3; Fig. 4.8).
- 2) Systematically add additional seasons of landslide data to both the 1993 and 2002 datasets to create increasingly long pseudo-historical (multi-seasonal) datasets that include 2, 3, 4, 6, 8, 12, 16, and 20 seasons of landslide data. These inventories were developed by adding seasons from 2010 backwards. Thus, the “2-season” inventories were developed using data from 1993 + 2010 and 2002 + 2010, the “3-season” inventories from 1993 + 2010 + 2009 and 2002 + 2010 + 2009, etc.
- 3) Use the same methodology as described in section 4.2.3 to develop susceptibility models from each of the increasingly long pseudo-historical datasets.
- 4) Use 10-fold cross validated AUROC analysis as described above to assess how well each of these increasingly long multi-seasonal inventories could forecast the landslide occurrence in each individual year from 2014 – 2018.

4.3 Results

4.3.1 Path dependency

As described in the methods section, path dependency was investigated for the ASM-inventory using three metrics proposed by Samia *et al.* (2017): the overlap index, unaffected areas and number of overlaps.

4.3.1.1 *The overlap index*

From the overlap index analysis, it is apparent that there is a weak negative coincidence in the raw data between the amount of overlap between landslides in two time slices and the time period separating those time slices (Fig. 4.2a). As time increases between time slices, the overlap index decreases gradually from 0.01 – 0.02 at one year between time slices to 0 – 0.005 at 30 years between time slices (Fig. 4.2a). However, these observations are tentative, with significant variation in overlap index at different time intervals, and thus no conclusive R^2 values. Indeed, fig 4.2b shows the raw data from fig 4.2a displayed as boxplots, where each boxplot encompasses three years of time. This shows that the median index values remain stable between 0 and 12 years between time slices, before decreasing between 13 to 24 years between slices, and then rising slightly from 25 to 30 years between time slices. This suggests that whilst there is a slight decrease after 12 years, there is no conclusive evidence for a decay in landslide overlapping with time. Finally, it should be noted that the value at zero time is the point comparing the Gorkha earthquake time slice to the concurrent 2015 monsoon season time slice.

4.3.1.2 *Unaffected area*

For the unaffected area method, the actually unaffected area (AUA) gradually falls below the theoretically unaffected area (TUA) as time increases (Fig. 4.3). However, the divergence between the AUA and TUA is small, with a maximum difference of 3×10^{-4} . There is also a large perturbation in both the AUA and TUA that are coincident with cloud outburst storms in 1993 and 2002, and the Gorkha earthquake in 2015 (Fig. 4.3).

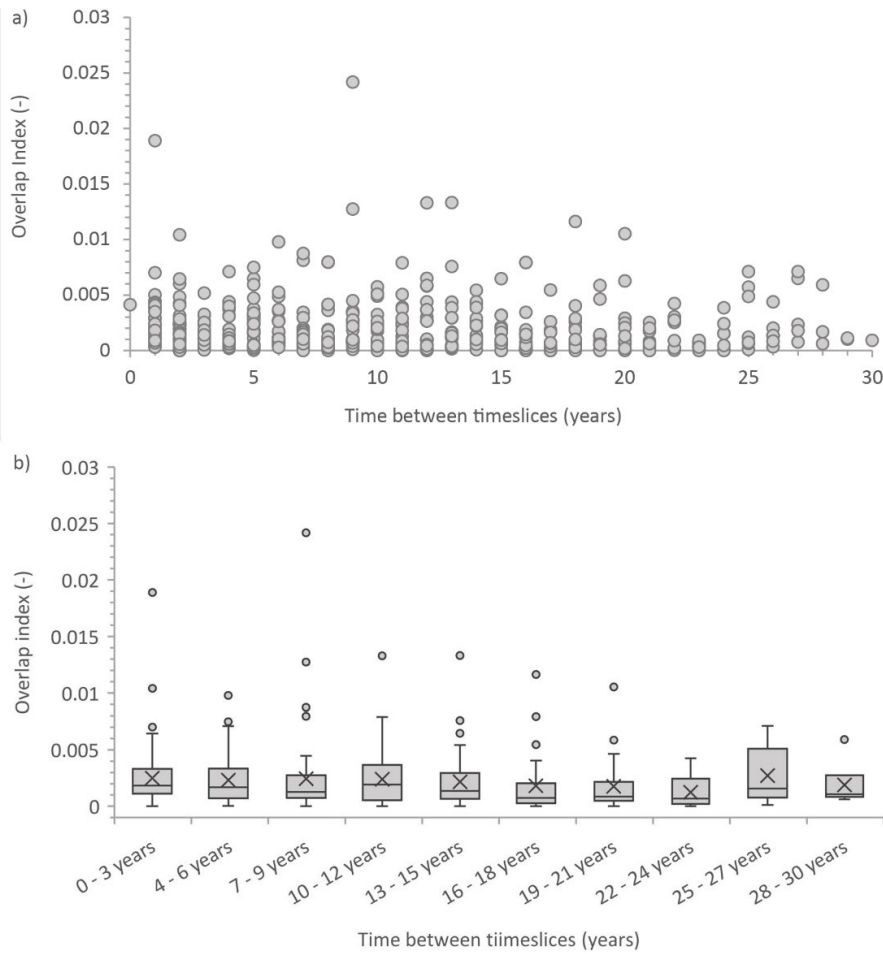


Figure 4.2. a) Raw Overlap Index vs time between time slices for the ASM-inventory. b) The same data as in a) but displayed as boxplots binned every three years.

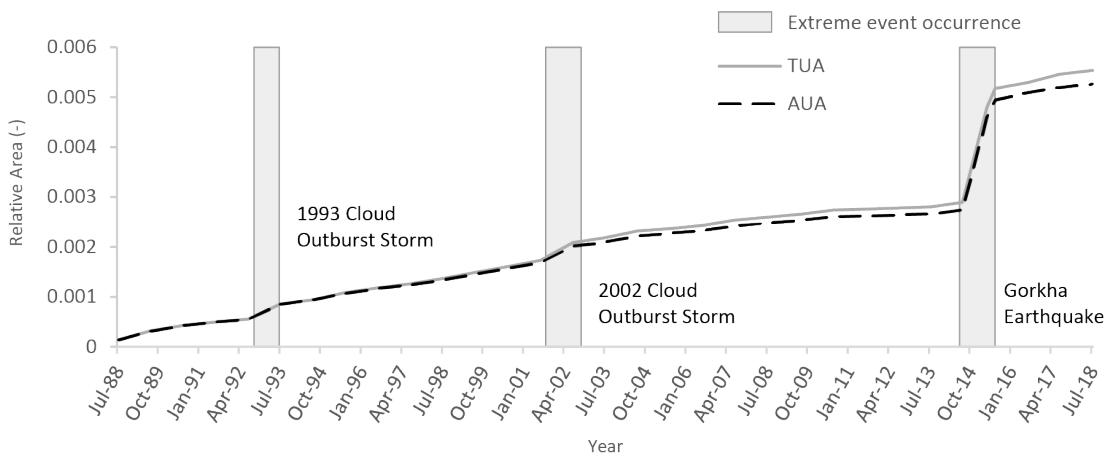


Figure 4.3. The Theoretically Unaffected Area (TUA) and Actually Unaffected Area (AUA) through time for the ASM-inventory and Roback et al. (2018) coseismic inventory.

4.3.1.3 Number of overlaps

For the number of overlaps, there is a greater area of landsliding at higher degrees of overlap than is expected based on the random model. The random model never observed more than three degrees of overlap, compared to five degrees of overlap in the actual data (Fig. 4.4).

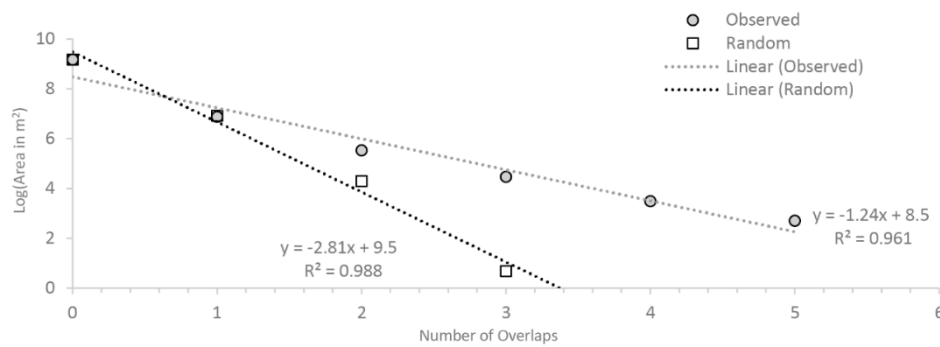


Figure 4.4. The area of landslides at different degrees of overlap for the ASM-inventory.

4.3.2 K-S and Chi-2 analysis

The K-S and Chi-2 analysis shows that there is significant variation between the landslide distributions at different predisposing factors in different years (Fig. 4.5). Of the 16 predisposing factor distributions compared across all years (435 tests), only four (profile curvature, near channel SSP, distance to channels and planform curvature; Fig. 4.5) had > 70% similarity across all tests. Factors commonly used to model landslide occurrence such as hillslope angle, aspect, relief, land use, elevation and geology had similar distributions in just 30 - 70% of all tests. The least similar factor distributions were average 30-year precipitation, peak monthly precipitation, and total monthly precipitation, which had maximum similarities across all tests of < 20%. However, these low values may be affected by the low (~ 30 km) spatial resolution of the PERSIANN-CDR data used to obtain these factor values.

The percentages quoted above are useful for obtaining an overall appreciation of predisposing factor distribution similarity; however, important information about where the dissimilarities are concentrated is hidden. For example, in the case of

slope, are the 30 - 44% of tests that showed no similarity to any other tests equally distributed across all 29 years? Or are they due to a small number of years that were totally dissimilar to every other year? To investigate this issue, for each predisposing factor the percentage of tests by year that were similar to another year were calculated (Fig. 4.6a – m). This analysis reveals that the dissimilarities in some factor distributions (geology, land use, distance to roads, near channel k_{sn} , aspect and elevation; Fig. 4.6a – f) are spread across multiple years. Conversely, the four factor distributions with the highest overall similarity between years (profile curvature, planform curvature, SSP and distance to channels; Fig. 4.6g - j) are relatively stable through time, with only minor dissimilarities in some years. Finally, some covariate distributions (slope, relief, excess topography; Fig. 4.6k – m) show a degree of stability across most years, but have a small number of years (notably 1993, 2002, 2015 and 2017) showing significant dissimilarity to all others.

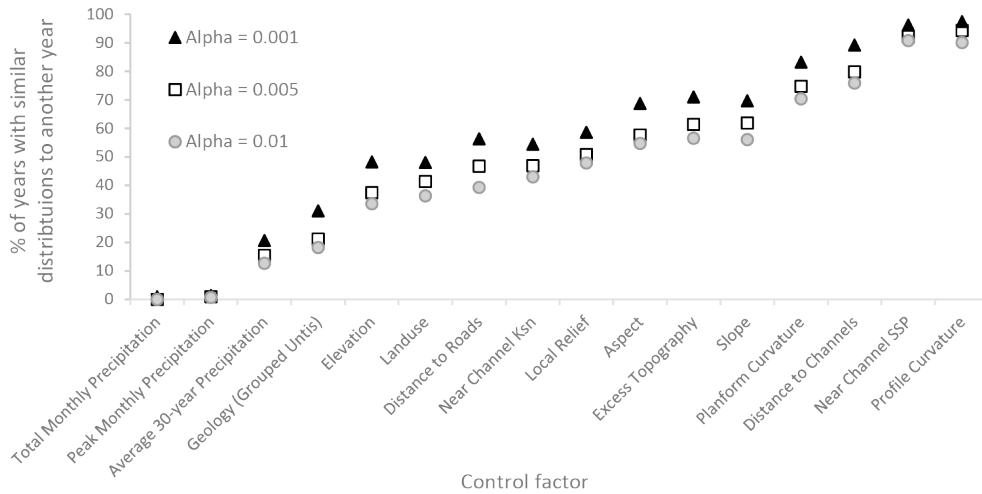


Figure 4.5. For each predisposing factor of interest, the percentage of the 435 K-S or Chi-2 tests that showed similarity between two years and different alpha significance values.

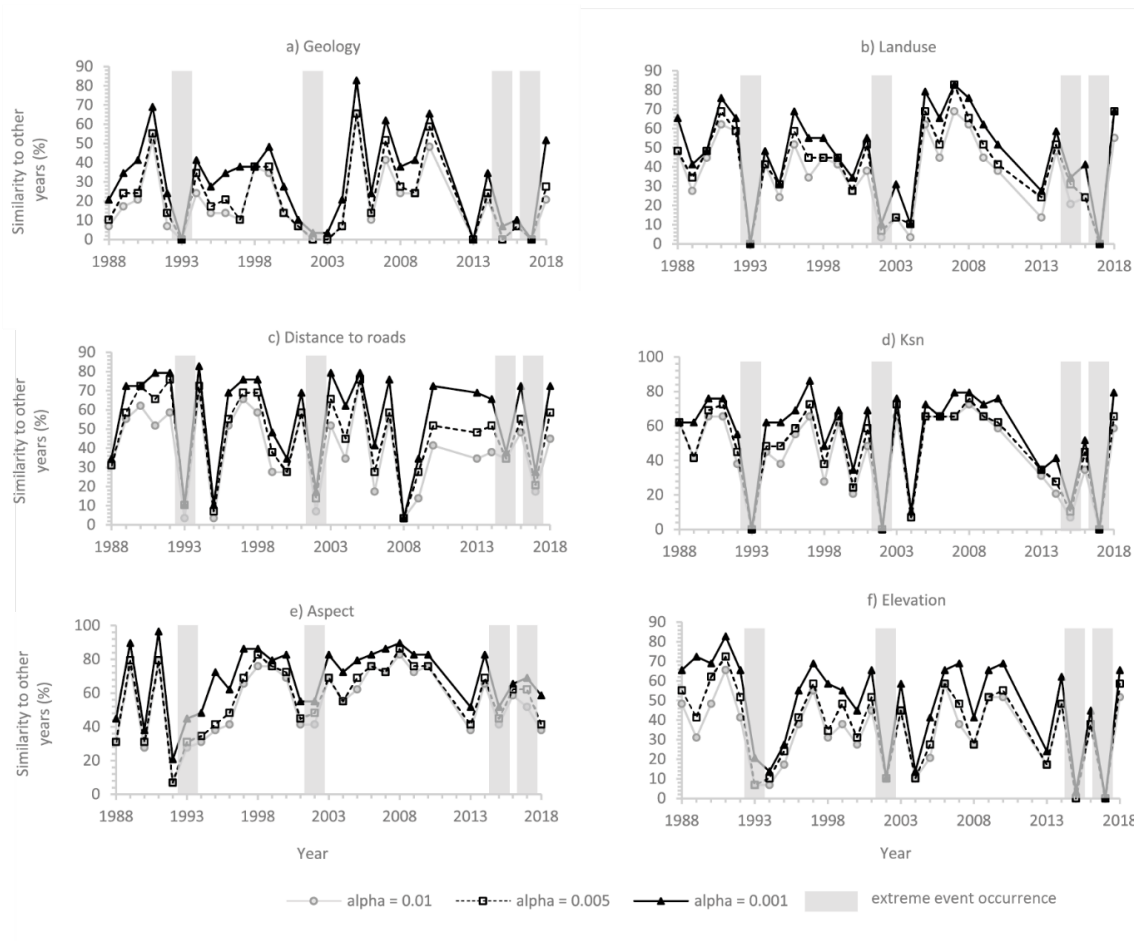


Figure 4.6. a – m) For each predisposing factor from Fig. 4.5 with > 20% overall similarity, the percentage of the 29 tests per year that showed similarity to at least one other year at different alpha significant values.

4.3.3 BLR modelling

The first outputs of the BLR modelling were the average regression coefficients and LASSO selection percentages obtained for each control factor across the 50 models ran for each of the 12 modelled years (Fig 4.7a – p). These outputs highlight that many of the predisposing factor coefficients and LASSO selection percentages change significantly through time. The most consistent continuous factors in terms of selection percentage were elevation, slope and PFI (Fig. 4.7a – c), which were

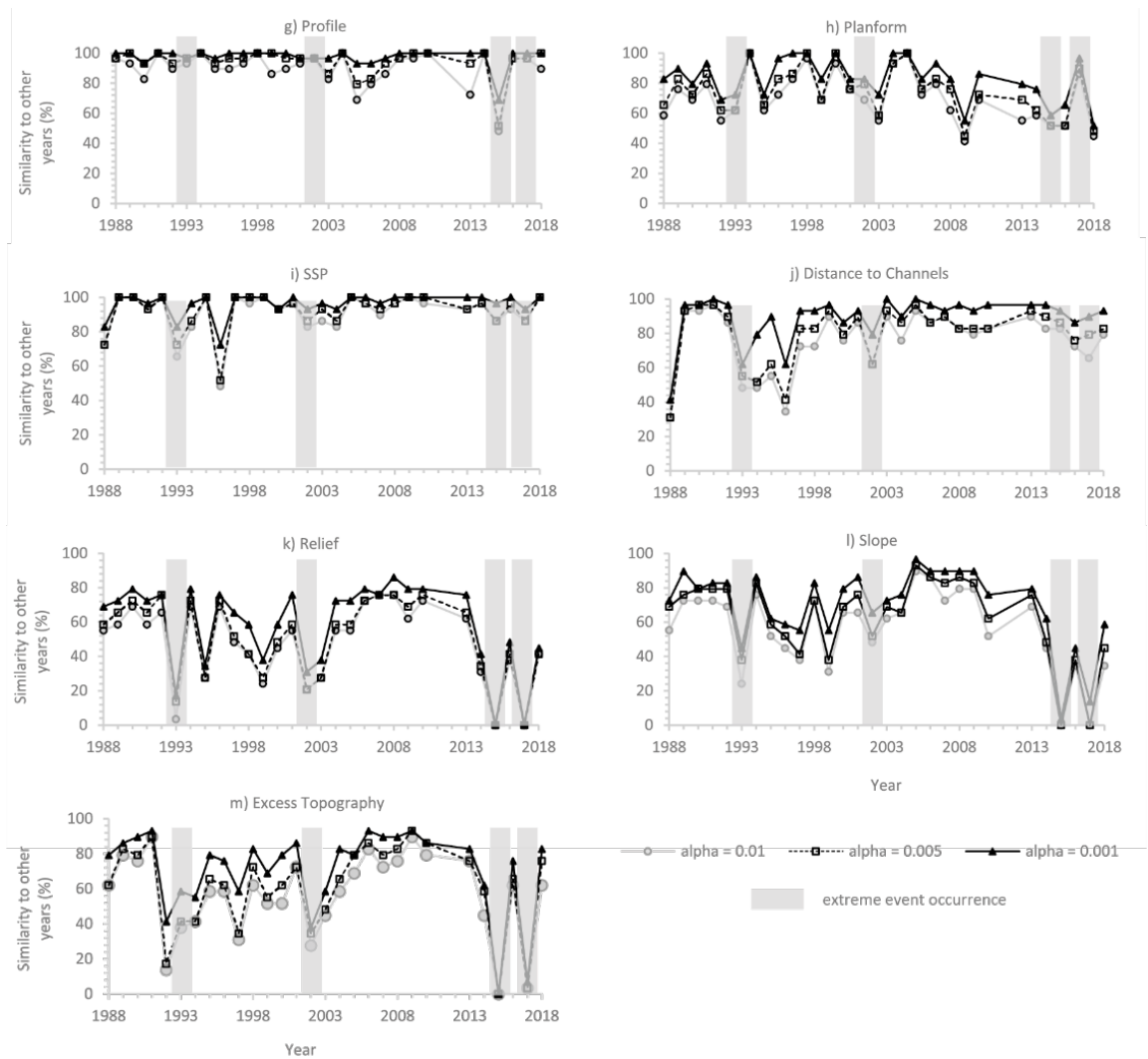


Figure 4.6 (cont.). a – m) For each predisposing factor from Fig. 4.5 with > 20% overall similarity, the percentage of the 29 tests per year that showed similarity to at least one other year at different alpha significant values.

selected in almost 100% of each year's 50 models. The regression coefficients for these factors were also stable in that they were always all positive (e.g. slope), suggesting that a factor was increasing the probability of landsliding, or negative (e.g. elevation and PFI), suggesting that a factor was decreasing the probability of landsliding. However, in the case of PFI, the 2015 regression coefficient was of notably greater magnitude than the other years, with a value close to -1.0, compared to values of -0.2 to -0.6 for most other years.

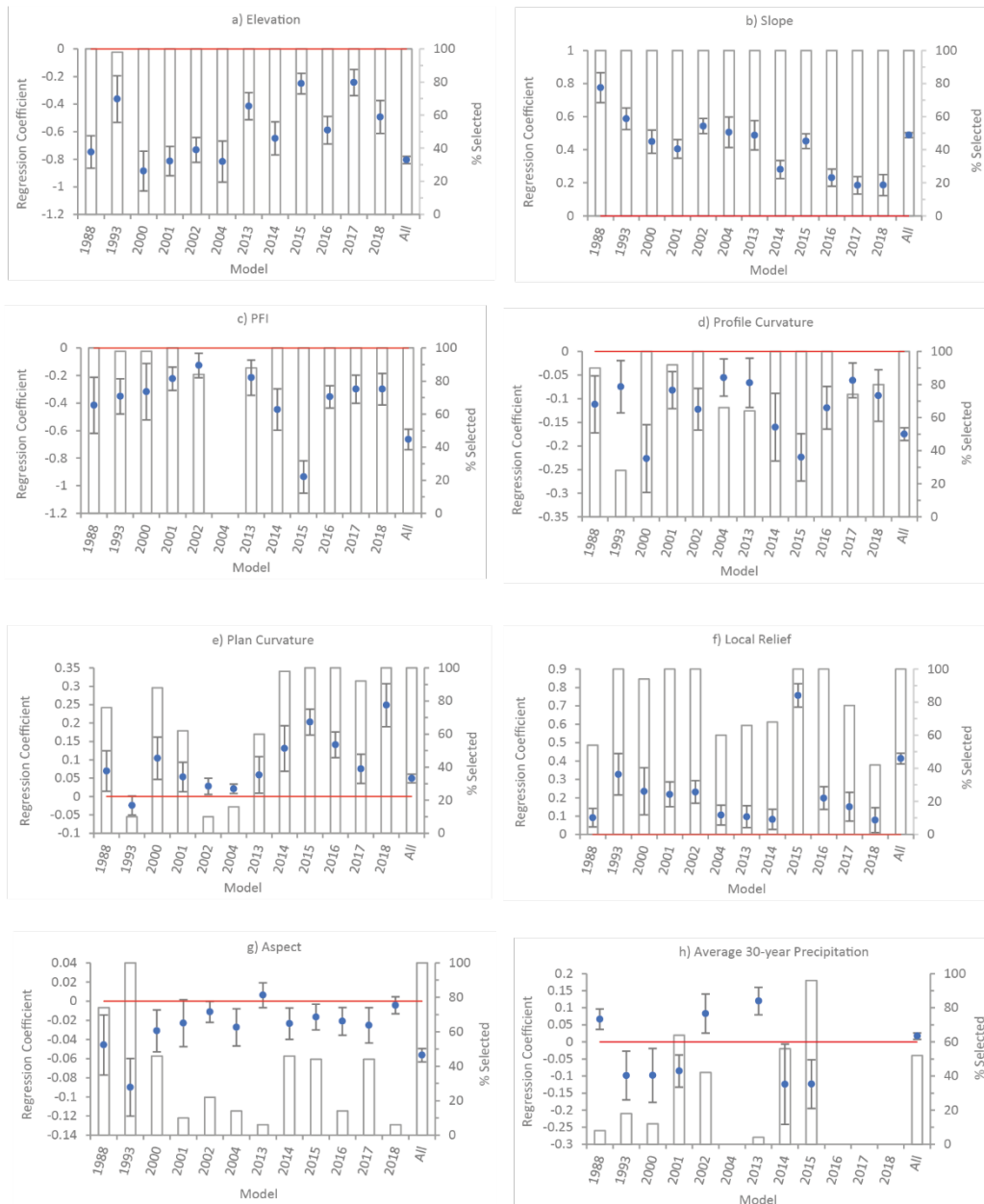


Figure 4.7. a – n) Results of Binary Logistic Regression (BLR) modelling for each predisposing factor. Blue circles show the average regression coefficient calculated from the 50-models run per year. Error bars show +/- 1 SD. Bars show the percentage of the 50 models run for each year in which that control factor was selected by the LASSO (Least Absolute Shrinkage and Selection Operator). Red line shows the 0-line of the regression coefficient axis. Positive coefficients indicate that a factor is making landslides more likely, whilst a negative coefficient indicates that a factor is making landslides less likely.

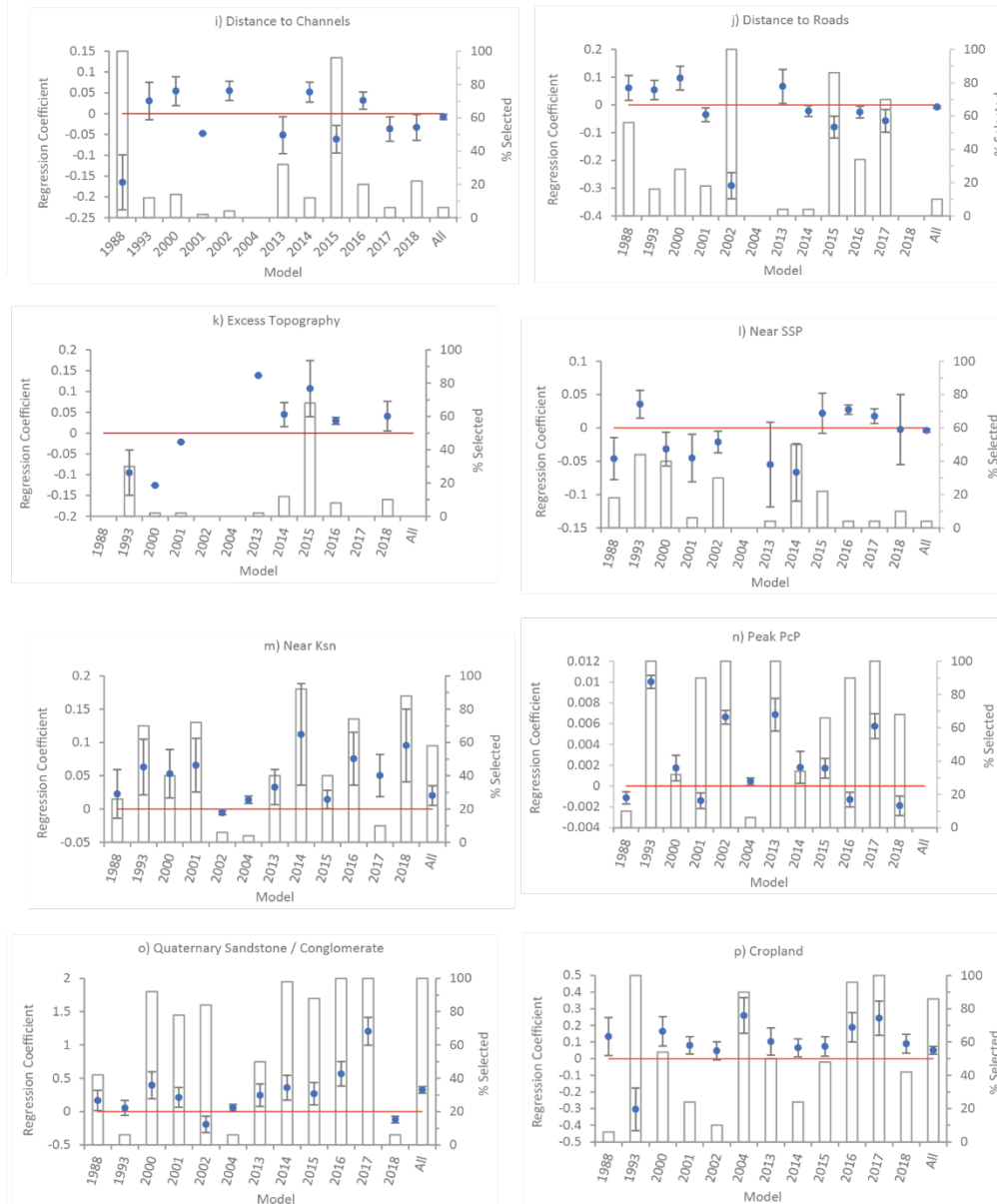


Figure 4.7. (cont.) a – n) Results of Binary Logistic Regression (BLR) modelling for each predisposing factor. Blue circles show the average regression coefficient calculated from the 50-models run per year. Error bars show ± 1 SD. Bars show the percentage of the 50 models run for each year in which that control factor was selected by the LASSO (Least Absolute Shrinkage and Selection Operator). Red line shows the 0-line of the regression coefficient axis. Positive coefficients indicate that a factor is making landslides more likely, whilst a negative coefficient indicates that a factor is making landslides less likely.

The next most consistent continuous factors in terms of selection percentage were profile curvature, planform curvature and local relief (Fig. 4.7d – f). Profile curvature was selected by > 80% of models for most years and had regression coefficients of -0.05 to -0.15 in all years but 2000 and 2015, which had slightly greater magnitude coefficients of \sim -0.25. Planform curvature was less consistently selected than profile curvature, particularly in the year's preceding 2014. The regression coefficients for planform curvature were also more variable, with 1993 having a negative coefficient (-0.05) whilst all other years were positive. Local relief was always selected by > 40% of models for a given year, with near 100% selection in 1993, 2000 – 2002 and 2015 – 2016. The regression coefficients for local relief were also highly stable through time, with most years having coefficients of 0.1 – 0.3. The exception to this was 2015, which had a significantly higher local relief coefficient of 0.8. All of the other continuous factors (Fig. 4.7g – n) were highly variable through time, in terms of both LASSO selection percentage and regression coefficients. The most notable observation from these factors is that excess topography (Fig. 4.7k), which had an almost 0% selection rate in most years, had selection rates of 30% and 70% in 1993 and 2015, respectively. However, despite 1993 and 2015 both having higher percentage excess topography selections than other years, their regression coefficients were of opposite sign, with 1993 having a value of -0.1, and 2015 a value of +0.1.

The two categorical factors also show significant variation through time in terms of LASSO selection percentage and regression coefficients. In terms of geology, the unit most consistently selected by the LASSO is Quaternary sandstone/conglomerate (Fig. 4.7o), which is selected at least 40% of the time in 8 of the 12 modelled years, and had regression coefficients that were positive for all years except 2002 and 2018. Most other units were rarely selected > 50% of the time for a given year, and had regression coefficients that fluctuate between being positive and negative (see Appendix Ea – h). In terms of land use, only cropland (Fig. 4.7p) was consistently selected by the LASSO, with five years having > 50% selection, and three years with > 40% selection. Furthermore, the regression coefficients for cropland are stable, with values of 0.05 – 0.3 for all years except 1993, which anomalously had a value of

- 0.3. Of the other land use variables (Appendix Ei - n), permanent snow/ice cover and forest were the next two most selected factors, with both having on average negative coefficients. For permanent snow/ice, as observed with PFI, 2015 differed from the other years in that it had a higher magnitude coefficient of -1.5 compared to > -0.5 in other years. Shrub/grassland, bare/sparse earth, water, and artificial land showed near-zero selection across all years.

4.3.4 AUROC validation

To assess how well each year could hindcast each other year, 10-fold cross-validation, whereby 100 independent AUROC tests between models from one year and data from another year, was used to obtain each reported AUROC value and associated error in Fig. 4.8. There is found to be significant variability in the hindcasting power of models trained on different years. The years 2000, 2001, 2002, 2004, 2013 and 2014 were all reasonably well hindcast by the models developed on other years relative to their self-validated AUROC success rates. For all of these years, the years least capable of hindcasting them were typically 1993, 2002, 2015, or 2017. The year 2015 was the hardest for the other years to forecast/hindcast relative to its self-validated AUROC success rate, with no year successfully forecasting or hindcasting it with $AUROC > 0.75$, and 2017 failing to hindcast it with $AUROC > 0.6$. The years 2016, 2017 and 2018 were mostly well forecast by other models relative to their self-validated AUROC values, though again, the 1993, 2002, 2015, 2017 and 2018 models were consistently the least capable of forecasting them. Overall, these results highlight that some years (1993 and 2015) were particularly hard to forecast/hindcast by the other models, and that models developed from some years (particularly 1993, 2002, 2015 and 2017) were consistently poor at forecasting/hindcasting other years.

Figures 4.9a - j shows the AUROC results of hindcasting the years 2014 - 2018 using susceptibility models developed using the years 2002 and 1993 alone (x-axis value of 1) plus increasingly more seasons of landslide data. In all but two cases, the AUROC values fit a positive logarithmic curve (R^2 values of 0.76 - 0.97), whereby the obtained AUROC values increase rapidly from using 1993 or 2002 alone to using 1993 and

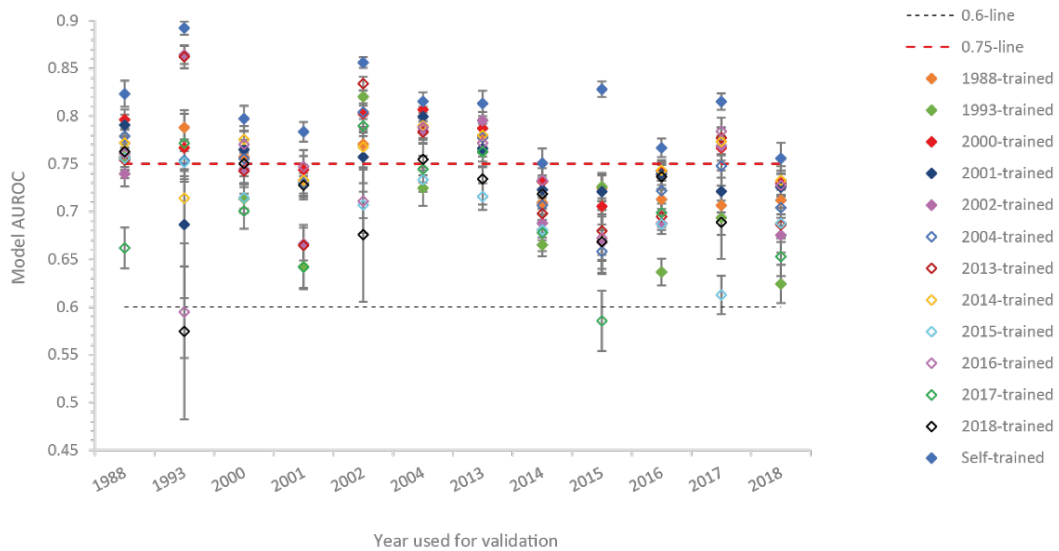


Figure 4.8. AUROC validation results quantifying how accurately the BLR susceptibility models trained on one year's landslide and control factor data could forecast/hindcast the landslide occurrences from another year. All results were obtained via 10-fold cross validation, whereby 10-models trained on one year were used to forecast/hindcast 10 random subsets of data from another year, thus giving 100 results per validation from which the averages and standard deviations on this plot were calculated.

2002 alongside 6 to 8 other seasons of data, with a stabilizing of the AUROC value when using more than ~8 seasons. This highlights that optimum susceptibility model prediction/hindcast accuracy can be attained when combining at least 6 – 8 seasons of landslide data. The main exception to this relates to hindcasting the 2017 season using the 2002 data plus other seasons (Fig. 4.9d). Here, the data fit a strong negative logarithmic curve ($R^2 = 0.91$), showing that adding more seasons of data to 2002 was reducing the hindcasting accuracy in this case. Finally, in the case where 1993 was used to hindcast 2015 (Fig. 4.9g), there is still a weak positive logarithmic correlation between number of seasons used and AUROC, but with more variance.

4.4 Discussion

4.4.1 Data limitations and assumptions

The results from the analysis in this chapter show that:

- 1) Landslides do exhibit path dependency.

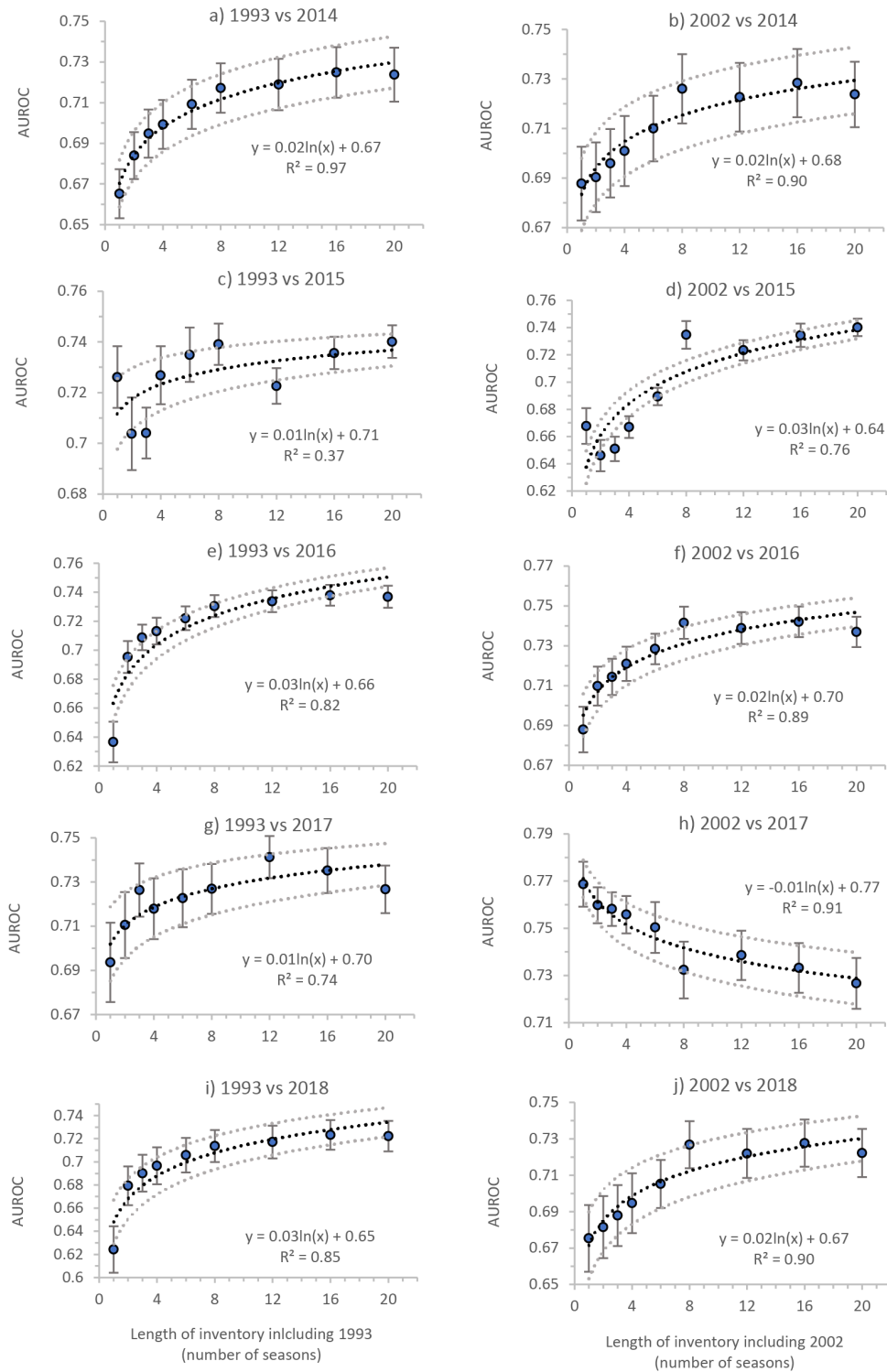


Figure 4.9. AUROC values obtained from predicting (or hindcasting) the landslide occurrence in the years 2014 – 2018 using models developed using 1993 and 2002 plus increasingly more seasons of landslide data (i.e. increasingly long pseudo-historical landslide inventories. Grey-dashed lines show +/- 1 standard error.

- 2) There is variation in landslide predisposing factor spatial distributions through time.
- 3) There is variation in landslide susceptibility modelling results and prediction/hindcast accuracy through time.
- 4) Susceptibility results improve when models are developed using several (at least 6 – 8) seasons of landslide data.

However, before discussing the implications and causes of these results in terms of physical processes, it is important to consider whether any of the observations could be due to limitations in the various predisposing factor datasets used. The main potential data limitation is that, as described in chapter 2 (section 2.3.2.7) some predisposing factor datasets, notably distance to major roads, PFI and land use, are considered as static factors in the K-S/Chi-2 and BLR modelling despite the fact that these factors may themselves vary through time. This is an unavoidable consequence of the data-scarce nature of the study region, but does raise the question of whether any of the observed temporal variance in the results is owing to this data limitation, rather than true physical processes. The following sections thus critically appraise the issues relating to the distance to road, PFI and land use data, highlighting these for the reader and outlining why it is not considered that they unduly impact the overall results.

In terms of distance to major roads, it is true that road locations will have changed throughout the 30-year period considered here, with road building initiatives increasing road density, particularly the density of small informal rural roads, across Nepal (McAdoo *et al.* 2018). However, as outlined in Chapter 2 (section 2.3.2.6), in the absence of available annual road data, the “distance to major roads” factor was based solely on the positions of large trunk, primary and secondary roads as they were in 2017. These larger roads were used exclusively as these types of infrastructure were more likely to have existed for the entirety of the mapped period. For example, construction of the Arniko highway trunk road began in 1961 (Murton 2017; Ao *et al.* 2020). However, it is still possible that some of the primary and secondary roads included in the dataset did not exist in the early part of the time period. As such, the

distance to roads metric can only be confidently considered as a topographic metric of “distance to road position in 2016”. This factor may not be geomorphologically useful, but the approach with the LASSO is designed to deal with this uncertainty. Indeed, very few models ever select distance to roads as an important factor. The main issue with the road data is thus how it is interpreted. In Figure 4.6c, the years 1993, 1995, 2002 and 2008 differ most significantly from all other years. Likewise, in Figure 4.7j, it is only 2002 that has both a high LASSO selection and significantly different regression coefficient to other years. These years can only be confidently interpreted as having different landslide positions relative to roads in 2016 compared to other years, meaning that these variations are not necessarily due to road occurrence, but rather any process that could shift landslide topographic distributions. This is an important distinction that requires acknowledgement when interpreting the results and discussion presented here, but it is not an issue that affects the validity of the overall conclusions of the chapter.

For the PFI data, to assess the impact of any temporal changes in permafrost on the results, it is first necessary to consider how much the limits of Himalaya permafrost have changed over the mapped period. It is estimated that the Lower Limit of permafrost extent (LLP) shifted no more than 100 - 300 m between 1973 and 1991, before remaining relatively stable until at least 2004 (Fukui *et al.* 2007). Furthermore, the current rate of change of permafrost is estimated to be $\sim 1.3 - 2.6$ m / year, with a maximum expected potential increase in LLP of 188 m between 2009 and 2039 (Chauhan & Thakuri, 2017). These studies show that whilst permafrost extent is likely changing in response to climate change, the rate of change is small relative to the 500 x 500 m resolution of the PFI data used here, with even the maximum expected changes below the resolution of the dataset. Furthermore, the permafrost data is an index which estimates the likelihood of permafrost based on climatic conditions, where a value of 1 suggests that permafrost will be present under all conditions whilst a value of 0.01 suggests that permafrost will be present under ideal meteorological conditions only. As a landslide was only classified as being in permafrost if it had a value of 1, the permafrost classifications should inherently account for any small annual changes in permafrost extent. Fig. 4.7c also shows that

PFI was consistently selected as an important factor by the LASSO, with all years but 2015 having very consistent regression coefficient values. There are two possible explanations for why 2015 differs. One, is that 2015 had very different permafrost conditions to that estimated by the PFI data used here, and if more accurate PFI data been used, then the 2015 perturbation would not be observed. Or two, as described in sections 4.3.3 and 4.4.3, it is due to a “true” shifting of the 2015 landslide distributions that made the negative relationship between PFI and landslide occurrence even stronger. Literature investigations reveal no evidence to support explanation 1. However, as described in Chapter 1 (section 1.2.2.2) and in Chapter 5, it is known that the 2015 monsoon-triggered landslides were impacted by earthquake preconditioning that shifted their locations relative to other years, supporting explanation 2. Therefore, it is possible that the PFI data do not fully account for temporal changes in permafrost extent and this should be considered by the reader when interpreting the results. However, as the PFI data used here are designed to account for meteorological change, and the only major observed change in PFI-related results occurred in 2015 following the Gorkha earthquake, it is considered a fair assumption that the results are not impacted by this data issue.

Over the past 30 years, land use in Nepal has changed, with a review by Paudel *et al.* (2016) showing that the main changes are increases in the area of cropland and urban land, and small decreases in forest and permanent snow/ice/glaciers. However, accurately quantifying land use change, particularly for the time period preceding high resolution satellites, is challenging, with different studies showing differing magnitudes and types of land use change through time (Paudel *et al.* 2016). Furthermore, there are no freely available annual land use products for the study region going back to the 1980s. As such, in this study, the ESA Glob-cover product is used, which as outlined in Chapter 2 (section 2.3.2.4), gives the land use classifications as they were in 2009 at a 300 x 300 m spatial resolution. This raises the question of whether any land use misclassifications resulting from the static use of 2009 land use data has impacted the results.

One of the most temporally dynamic land use products available is the MODIS dataset, which estimates global land cover between 2001 and 2018. As such, to assess

if the methodology used here has affected the results, the MODIS classifications for the landslide data from 2001 – 2018 are extracted. By grouping the MODIS classifications into the same broad categories as used for the ESA product, the number of landslides in each year from 2001 – 2018 that changed classifications relative to 2009 are counted. On average, less than 9% of landslides in the years 2001 – 2018 changed classification relative to 2009. Furthermore, the Chi-2 analysis for land use for the years 2001 – 2018 is repeated using the annual MODIS classification. If misclassification error in the approach used here is the cause of the variations observed in Fig. 4.6b, then the repeated Chi-2 analysis with temporally variable land use data would be expected to show a much higher level of stability. However, as shown in Figure 4.10, this is not the case, with significant variability between years, particularly in 2002, 2015, and 2017, as shown by the original analysis. This thus supports the assumption that the observed variability is dominantly caused by true physical processes, rather than data misclassification. Finally, as shown in Fig. 4.7p and Appendix Ei – n, most land use categories were rarely selected by the LASSO as being important. Furthermore, cropland, which was the most commonly picked, was still only picked consistently in four of the twelve modelled years. Fig. 4.7p also shows that the cropland results are very consistent between all years except 1993, where cropland is suddenly defined as making landslides less likely. Unfortunately, the MODIS data do not cover this period, however, there are two possibilities for why the 1993 results for cropland change. One, is that it is due to the use of stationary land use data, i.e. that the observed change in 1993 was caused by some sudden change in cropland distributions not classified by the data used here. Or two, that it is due to some other true physical process that shifted landslide distributions in that year to be less likely in croplands. Literature investigations reveal no evidence to support explanation one. Furthermore, if a sudden increase in cropland in 1993 caused the observed results, then this increase would have had to reverse by 2000, when the results return to as they were before 1993. Again, a literature investigation finds no evidence of such a change happening. The other explanation for the 1993 cropland result is that it is due to some physical process that dramatically shifted landslide distributions in that year. It is known that 1993 experienced an extreme

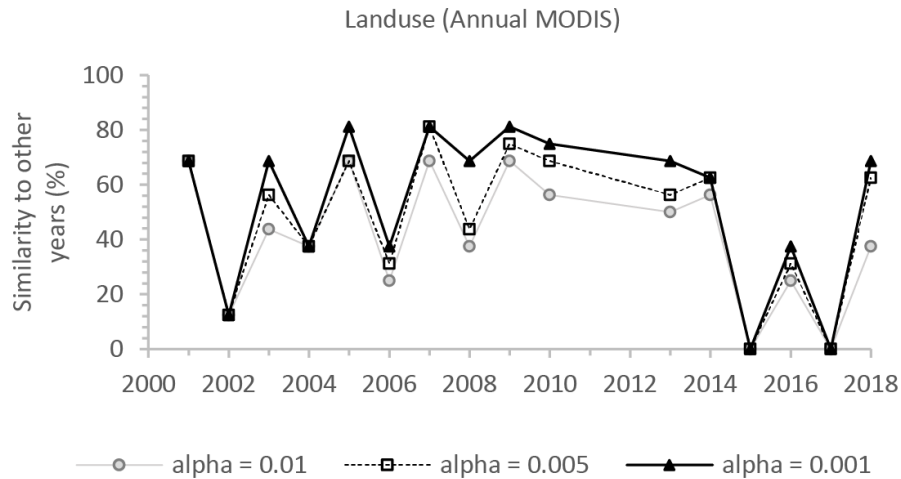


Figure 4.10. The percentage of the Chi-2 tests per year that showed similarity to at least one other year at different alpha values for the MODIS land use data.

cloud outburst event (e.g. Dhital 2003), which changed landslide distributions across most of the control factors investigated (Figs. 4.5 – 4.7). This supports the assumption that the observed change in 1993 is attributable to a physical process, rather than data misclassification. However, it is important to acknowledge this limitation and to consider it alongside subsequent discussions.

4.4.2 Landslide path dependency

The first objective of this chapter was to investigate whether landslides exhibit path dependency in the Nepal Himalaya by quantifying three path dependent metrics as used by Samia *et al.* (2017) (number of overlaps, overlap index and unaffected area) for the ASM-inventory. These metrics suggest strong evidence for path dependency in the region.

In terms of number of overlaps, there are larger areas of landsliding at higher degrees of overlap than is predicted by a random model (Fig. 4.4). This shows that new landslides overlap with earlier landslides to a greater extent than would be expected if the spatial distributions of landslides through time were random, which is indicative of path dependency. However, it should be noted that this result could be because the random model does not consider clustering of landslide cells. As such

future work should involve repeating this metric but with a more complex random-clustering model. However, this method and result still follow a similar trend to that found by Samia *et al.* (2017) in Collazzone, Italy, where the number of overlaps was greater than would be expected from a random model. However, whilst the general trend in Collazzone may be similar to Nepal, there are some subtle differences. Notably, the rate of decrease of landslide area with higher degrees of overlap in Collazzone is approximately half that observed in Nepal (-0.62 compared to -1.2), suggesting that the Collazzone region has the potential to generate greater degrees of overlap given enough time, but that Nepal has a greater area of overlap than expected at lower degrees of overlap. It is unclear whether this reflects physical processes that differ between the two regions, or is simply an artefact of the different inventory characteristics used between the two studies. For example, one explanation could be due to a difference in landside type and size between the two regions. In Italy, ancient deep-seated landslides are common (Cardinali *et al.* 2002) and included within the Samia *et al.* (2017) inventory. Conversely, this ASM-inventory for Nepal is dominated by shallow rockfalls and slides (see Chapter 3, section 3.4.3) that are pervasive across the Himalaya (Dahal *et al.* 2013), with deep-seated relict events not included. Deep seated landslides are generally larger than shallow movements because there is more material available to be mobilised (Zêzere *et al.* 2005), and as such could have greater potential for higher degrees of overlap with new landslides. Therefore, it is possible that if much older, large, deep seated landslides had been included in the ASM-inventory, then a similar rate of decreases to Collazzone would have been obtained for Nepal.

Whilst the number of overlap results confirm that the Nepal Himalaya observe more landslide overlap than expected if landslide occurrence was random, the overlap index and theoretical area analysis provide further quantification of the actual extent and characteristics of landslide overlap (and thus path dependency). The overlap index results tentatively support that path dependency occurs within the Himalaya, with a weak negative correlation between time between time slices and overlap index (Fig. 4.2). This trend suggests that the occurrence of spatially associated (i.e., overlapping) landslides relates to the time since earlier landsliding, with the

likelihood of a new landslide overlapping with an earlier landslide decreasing with time. However, it should be noted that this relationship is not statistically significant, with overlap index showing large variations, particularly at 5 – 15 years between time slices. Again, this result follows a similar trend to that found by Samia *et al.* (2017), who also observed a weak negative correlation between overlap index and time passed between time slices. However, the overlap index in the Collazzone region is at least a factor of 10 larger than in the region investigated here. As with the number of overlap results, this could be due to differences in landslide inventory type and size. Indeed, whilst more overlaps than expected given a random distribution were observed in this case, as the ASM-inventory only included recent shallow landslides, the overlaps between landslides were limited in their absolute potential area. Conversely, the first Samia *et al.* (2017) time slice was of large relict deep seated events, meaning that subsequent landslides had a high likelihood of occurring fully within these large early failures. Whilst the ASM-inventory and the Gorkha coseismic inventory did include some very large failures (e.g. the Langtang avalanche [Jones *et al.* 2020] and the Jure landslide [Regmi *et al.* 2017]) these occurred late in the time series, so there was less potential for subsequent large degrees of overlap.

Finally, the unaffected area results also suggest that path dependency is occurring across Nepal, with the AUA area diverging below the TUA over time (Fig. 4.3). In other words, the occurrence of overlapping landslides is reducing the actually affected area of landsliding, since if landslides never overlapped then the actually and theoretically unaffected areas would be the same. Again, this result follows the same general trend as that observed in Collazzone. However, it is notable that the relative area values are several orders of magnitude higher in Collazzone than they are in Nepal, with a larger observed divergence between the actually and theoretically unaffected areas. This discrepancy is again likely explained by the difference in study region size and landslide inventories of this study and that of Samia *et al.* (2017). The region studied by Samia *et al.* (2017) was relatively small ($\sim 78 \text{ km}^2$) and their analysis included very large relict deep seated events. Conversely, the study region here is $\sim 45,000 \text{ km}^2$ and the ASM-inventory only included recent small-scale landslides. Consequently, the landslide number densities per time slice in Collazzone ranged

from 0.21 – 8.88 N/km², whereas those in Nepal ranged from 0.003 – 0.54 N/km². As such, since this metric is proportional to study size, the lower densities of landsliding observed here explain why the relative area values in this case are so much lower. This also explains why the divergence between the actually and theoretically unaffected areas is less in this case, because even though there are more overlaps than expected (e.g. Fig. 4.4), as a proportion of the study region size the actual area affected by overlaps is low. Overall, these results suggest that path dependency is occurring in the Nepal Himalaya. However, it also shows that study region size and inventory type/resolution may affect the specific path dependency characteristics obtained (e.g. Roberts *et al.* 2021).

4.4.3 Landslide spatial distributions

The second objective of this chapter was to quantify whether landslide characteristics and spatial distributions varied through time. Overall, the K-S and Chi-2 results show that the landslide distributions for most control factors vary through time, with only profile and planform curvature, SSP and distance to channels having > 70% similarity across the 29 mapped years. Most concerningly, some of the control factors routinely used in landslide susceptibility models such as slope, elevation, geology, and land use showed some of the greatest temporal variations. Of these, slope was the only factor to have similar distributions in > 50% of years at all alpha values (0.01, 0.005 and 0.001), with geology having similar distributions in < 30% (Fig. 4.5).

These results highlight that significant temporal variations exist even for landslide distributions across the same region and trigger events (in this case rainfall). This result is similar to those of Kincey *et al.* (2021) who found significant changes in the characteristics and distributions of coseismic and monsoon-triggered landslides in Nepal across the period 2014 – 2018. But what causes these changes? It is apparent that in this thesis study, many of the most significant changes in landslide distributions occur in the years 1993, 2002, 2015 and 2017. All of these years were coincident with extreme events, with cloud outburst events in 1993 and 2002 (Dhital 2003; Paudel *et al.* 2003), severe flooding in 2017 (Gautam & Dong 2018; Thapa *et al.* 2020), and the Gorkha earthquake in 2015 (Roback *et al.* 2018). But can the nature

of these extreme events reasonably explain the observed changes in spatial distributions? To assess this hypothesis, the results from sections 4.3.2 and 4.3.3 for the seasons impacted by extreme events are considered in more detail alongside several new plots. These new plots show the proportions of landslides in each of the extreme years that occur across several key control factors (slope, local relief and excess topography), as well as the proportions of all other years and the study region across those control factors (Fig. 4.11a - c).

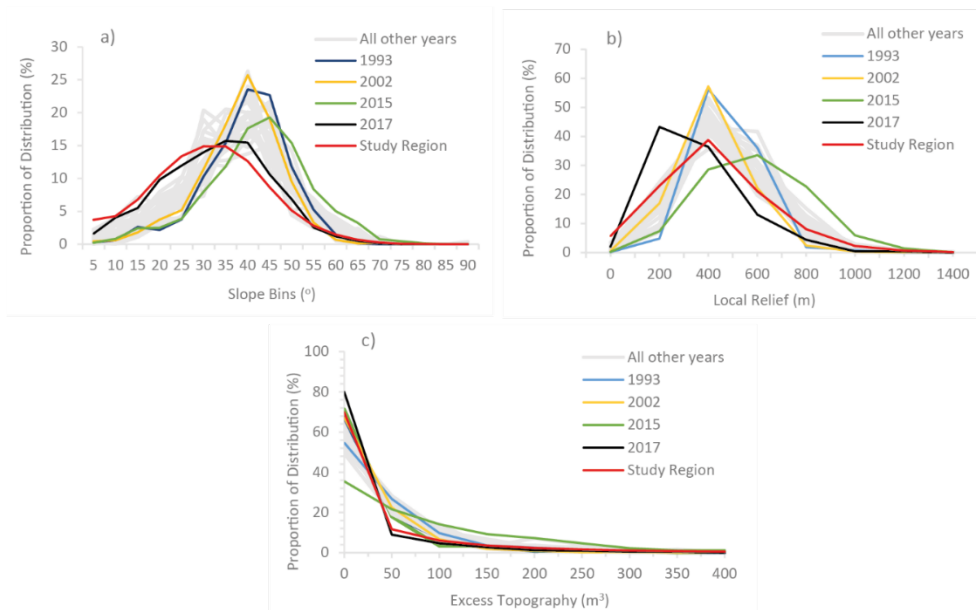


Figure 4.11. Proportion of the study region, all landslide data and landslide data per time slice that fall within given bins of a) slope, b) local relief and c) excess topography.

In the case of 1993, the atypically narrow distributions for slope and local relief (Fig. 4.11 a - b) show that landslide locations shifted to steeper than normal slopes of 35 – 55° and higher than normal reliefs of 300 – 750 m. This likely reflects the localized nature of rainfall across hillslopes in the Mahabharat Mountains that are dominated by these topographic characteristics (Lavé & Avouac 2001). In terms of excess topography, 1993 was one of the only years to have a negative (-0.1) regression coefficient (Fig. 4.7k), suggesting that landslides were more likely to have occurred in the absence of excess topography. This is geomorphologically sensible, as excess topography is likely to be expressed in the landscape as convex topography, yet it is

known that intense rainfall is more likely to accumulate and cause high pore-pressures in concave topography (Chang *et al.* 2007; Kayastha 2012). Landslides in 1993 also observed the largest selection percentage and regression coefficient for peak monthly rainfall (Fig. 4.7n), further highlighting the importance of intense rainfall in controlling the distributions observed in this year.

In the case of 2002, the distributions of landslides with slope were relatively average (Fig. 4.11a). However, the local relief distribution shifted to higher-than-average reliefs of 250 – 600 m (Fig. 4.11b), which, like for the 1993 event, is likely a consequence of the rainfall location, which occurred between the Siwalik Hills and the Mahabharat mountains where these reliefs dominate. Furthermore, landslides in 2002 closely followed the distribution of the study regions for excess topographies of up to 50 m, but also revealed that if picked at random, a landslide had a lower likelihood of having occurred at excess topographies of 50 – 100 m (Fig. 4.11c). Again, this is geomorphologically feasible, as it is expected that landslides triggered by intense rainfall will preferentially occur at lower slopes with concave topographies. However, as indicated by the regression modelling, this was a less-dominant characteristic of landslides in 2002 as it was for landslides in 1993. Interestingly, 2002 was also characterized with a more dominant than usual regression coefficient result for distance to roads (Fig. 4.7j), with a selection percentage of near 100% and a coefficient of -0.3 compared to near zero for all other years. This is likely because the 2002 cloud outburst storms occurred across the Kathmandu valley and adjacent regions that are some of the most densely populated and urbanized in Nepal. As this region has significant urbanization, the impact of roads on landsliding is more apparent relative to other years where landsliding was distributed more homogeneously across regions with and without significant urbanization. If picked at random, the 2002 landslides had a lower likelihood of having occurred in forested regions (Appendix Ei), which is expected as deep-rooted trees can increase slope material cohesion and reduce pore water pressures via transpiration (Sidle & Bogaard, 2016).

The regression modelling shows that, with the exception of excess topography, 1993 and 2002 had similar topographic and hydrological distributions across factors

including slope, relief, curvatures, peak rainfall, PFI, and elevation. However, these years had notably different distributions across geological and land use units (Fig. 4.6a – b; Appendix Ea – n). This likely reflects that the two outburst storms occurred over regions with slightly different land use and geologies. Indeed, the region impacted by the 1993 storm was composed predominantly of forest and shrub/grass overlying granite/gneisses and schists, whilst the 2002 storm impacted a similar region to 1993 as well as regions dominated by cropland and dolomite. This highlights that similar events can have very different impacts on regression modelling coefficients for spatially heterogeneous control factors, even if those events are partially coincident as in this case. As such, when modelling future landslide occurrence, unless the region to be predicted is entirely coincident with the region in which the training data were obtained, it is important to keep in mind that regression coefficients for spatially heterogeneous control factors may be sub-optimal.

In the case of 2017, which was impacted by severe flooding, the landslide slope distribution closely follows the slope configuration of the landscape (Fig. 4.11a), suggesting that, unusually, if picked at random, a landslide had neither a higher nor lower percentage likelihood of having occurred at any given slope range. In terms of local relief, 2017 was very different to all other years, showing that if picked at random, a landslide had a higher percentage likelihood of having occurred at reliefs of 0 - 400 m, but a lower percentage likelihood of having occurred at reliefs of 400 - 1000 m (Fig. 4.11b). This may be because landslides triggered in this monsoon season were more likely to have been influenced by undercutting of hillslopes due to turbulent flood waters and elevated flood water levels. This contrasts with other years where triggering occurred in regions with the typical combination of higher slopes and higher rainfall. The excess topography distribution for 2017 corroborates the observation that landslides in this year occurred lower on slopes, as it shows that if picked at random a landslide had a lower percentage likelihood of having occurred at higher excess topographies of 50 – 100 m (Fig. 4.11c). 2017 also saw the fourth highest regression coefficient for peak rainfall (Fig. 4.7n), highlighting that intense rainfall remained a key determinant in the distributions of 2017, even if more of the

landslides may have been triggered by floodwater. Furthermore, if picked at random, a landslide in 2017 had a lower percentage likelihood of having occurred in cropland (Fig. 4.7p), which is unsurprising given that poorly managed cultivation systems are known to increase infiltration rates and reduce soil cohesion (Alexander 1992), problems that would be exacerbated by intense rainfall and flooding.

In 2015, Fig. 4.11a - c, highlight that distributions of landslides with slope, local relief, and excess topography, were all significantly different to the average. Specifically, slope distributions shift from an average of 35 – 60° to 45 – 70°, relief distributions shift from an average of 250 – 800 m to 500 - 1200 m, and excess topography distributions shift from an average of 0 – 100 m³ to 50 – 300 m³. Furthermore, the “distance to channels” factor had a much higher (90%) selection percentage compared to most years, with a negative regression coefficient of -0.075. This suggests that in 2015, if picked at random, a landslide had a lower percentage likelihood of having occurred near channels. to the extent that this became an important factor for overall prediction of landslides in that year. These changes in topographic distributions are likely due to the topographic amplification of earthquake strong ground motion (e.g. Von Specht *et al.* 2019), which is often amplified near ridges and other topographic excesses (Meunier *et al.* 2008). The loading of hillslopes by ground motion has been observed via laboratory experiments to impact hillslope stability (Brain *et al.* 2017), with field observations following multiple earthquake events showing that rainfall triggered landslides following earthquakes occur at higher rates and in different topographic locations (Lin *et al.* 2006; Hovius *et al.* 2011; Marc *et al.* 2019). As such, the changing topographic distributions of monsoon triggered landslides observed here during 2015 are likely a consequence of the topographic damage signature of the Gorkha earthquake. It is also observed that the regression coefficients for PFI and snow/ice cover in 2015 had much greater negative magnitudes than in other years. This is likely because the 2015 earthquake occurred in the Greater Himalaya, so the damage signature of the earthquake was in a region with pervasive snow/ice and permafrost. Consequently, the negative influence of snow/ice and permafrost on rainfall triggered landslide occurrence was more apparent in 2015 than it is in a typical monsoon season, where

more landsliding occurs in the south where there is less pervasive snow/ice and permafrost. This highlights the importance of snow/ice cover and permafrost in preventing failures within landscapes. This is a salient point, as it is increasingly reported that snow/ice and permafrost cover within the Himalaya is reducing due to a warming climate (Gruber *et al.* 2017; Haeberli *et al.* 2017), thus representing a potential cause of increased future landslide activity. Overall, these results highlight that the transient topographic signature of earthquakes, as well as any large-scale time-dependent changes in permafrost distribution and snow/ice cover, should be considered in future landslide susceptibility modelling, highlighting the need to move towards susceptibility modelling methodologies that are more dynamic and time-dependent.

4.4.4 Impacts on landslide susceptibility modelling

The results from sections 4.3.1 and 4.4.2 clearly show that landslides in the Nepal Himalaya are impacted by path dependency. This raises the question of whether this process should be considered in landslide susceptibility models. As shown by Samia *et al.* (2018) path dependency has been shown to impact landslide susceptibility, with conventional logistic regression models developed with DEM-derived and path dependent variables providing good levels of prediction. Furthermore, characterisation of path dependency using space-time clustering is found to significantly improve the performance of conventional landslide susceptibility models whilst allowing the development of dynamic maps that change through time (Samia *et al.* 2020). However, until now, as quantification of path dependency in locations outside of Italy were lacking, it was unclear whether this process should be more universally included in conventional susceptibility models. However, the results from this chapter show that this process is widespread, suggesting that, as recommended by Samia *et al.* (2017, 2018, 2020), this process should be included in susceptibility modelling where possible. Unfortunately, due to time-constraints, exploring how path dependency impacts the susceptibility modelling conducted in Chapters 2, 3 and 4, is beyond the scope of this thesis. However, including path dependency in susceptibility modelling in Nepal is undoubtedly an important topic for future work.

The results and discussion in sections 4.3.2 and 4.4.3 highlight that landslide distributions vary significantly through time, particularly in years impacted by extreme events in 1993, 2002, 2015 and 2017. The third aim of this chapter was to quantify the impacts of this variation on the accuracy and hindcasting ability BLR susceptibility models. It is found that the monsoon-seasons impacted by extreme events (cloud outburst storms in 1993 and 2002, earthquake preconditioning in 2015, and floods in 2017) produced the worst performing susceptibility models, and were themselves the hardest seasons for other models to hindcast (Fig. 4.8). This suggests that the observed variations in individual landslide control factor distributions do have significant impacts on resulting susceptibility models. Consequently, as discussed in detail in Chapter 6, it can be concluded that BLR-based landslide susceptibility approaches may need to move away from time-independent modelling, which assumes landslide distributions are static, towards more dynamic or time-dependent modelling that can account for expected or unexpected temporal variations in landslide distributions, particularly following extreme events.

The final objective of this chapter was to assess the optimal length of landslide inventory required for accurate and reliable susceptibility modelling. As shown in Fig. 4.8 single season inventories from extreme years do not offer consistent and reliable prediction (or hindcasting) through time. However, as shown in Fig. 4.9a - j, as landslide data from an extreme season is combined with increasingly more seasons of data, model accuracy increases rapidly as the number of seasons increases from 2 – 6 years. This increase then begins to saturate as the number of seasons increases beyond 6 – 8 years. This result is similar to that of Ozturk *et al.* (2021), who found that the accuracy of a logistic regression based susceptibility model saturated after 0.01% of the study region had failed and was used to train the model. The reason for this saturation likely relates to the averaging of landslide distributions. If a single inventory was impacted by some process that makes the landslides within it have atypical distributions (e.g., as seen here, earthquake preconditioning shifting landslides to higher-than-normal excess topographies, or storms shifting landslides to higher slope angles but lower excess topographies) then a model developed from just that year will only be capable of predicting landslides with similarly atypical

landslide occurrences. However, if increasingly more “typical” landslide data are used to develop BLR susceptibility models alongside that extreme year, then the resulting model will shift towards being applicable to the average landslide distributions for that region. However, as shown by Fig. 4.9h, this only works when predicting a future year that is itself typical. When predicting a future year that is actually atypical (i.e. another extreme year), then it is possible that a model based on the longer-term average landslide distributions will not be the best model to forecast that year.

This highlights a fundamental problem in landslide susceptibility modelling, which is modelling blind of physical processes. This chapter shows that models developed using single “normal season” (i.e. those impacted by a known process such as typical monsoonal rainfall) can consistently hindcast other similarly “normal” seasons, but that models developed from seasons impacted by another processes such as extreme rainfall cannot unless combined with 6 – 8 seasons of other landslide data. Conversely, a model developed from a single season impacted by an extreme process might be well capable of predicting a similar extreme future season, in which case saturation with landslide data from normal seasons will makes a model worse. Therefore, accurate BLR susceptibility modelling requires that models developed from particular causal mechanisms are only used to forecast or hindcast that same mechanism. This finding is clearly pertinent to the Himalaya, but also has broader relevance to any region with multiple coincident landslide drivers. As such, future work should focus on investigating this problem in other tectonic and climatic regimes.

4.5 Conclusions

Overall, it is found that path dependency does influence landsliding in the Nepal Himalaya, with landslides in locations impacted by past landslides occurring at greater rates than would be expected if their distributions were random. It is also shown that the spatial distributions of monsoon-triggered landslides vary significantly through time, particularly in response to cloud outburst events in 1993 and 2002, flooding in 2017 and earthquake preconditioning following the 2015

Gorkha earthquake. Specifically, the topographic damage signature of Gorkha earthquake preconditioning shifted 2015 monsoon-triggered landslides to higher slopes ($45 - 70^\circ$), reliefs (500 – 1200 m) and excess topographies ($50 - 300 \text{ m}^3$). Cloud outburst events in 1993 and 2002 also shifted landslides to higher-than-average slopes ($35 - 55^\circ$ for 1993) and reliefs (250 – 600 m in 2002; 300 – 750 m in 1993), but, in contrast to earthquake preconditioning, regression modelling suggests a slight tendency for landslides triggered by extreme rainfall to cluster at lower excess topographies. Finally, flooding in 2017 shifted landslides to much lower-than-average reliefs ($< 400 \text{ m}$), slopes ($0 - 35^\circ$) and excess topographies ($50 - 100 \text{ m}^3$).

These variations are found to have significant impacts on BLR susceptibility modelling, with models trained on these extreme years unable to consistently forecast or hindcast the landslide occurrence in other years with sufficient accuracy. It is suggested here that one solution to this is to ensure that BLR susceptibility models are developed using historical or multi-seasonal landslide inventories with at least 6 – 8 separate years of landslide data. This should have the effect of averaging out any anomalous landslide distributions that may have occurred in periods impacted by extreme events, and thus provide more reliable prediction. Finally, regardless of the method used to deal with temporal variance, it is concluded that it is vital to ensure that susceptibility modelling is not undertaken “process blind”, with susceptibility models only used to forecast future landslide occurrences with similar causal mechanisms to the data used to train the model.

Chapter 5 Landslide rates associated with the Asia Summer Monsoon (ASM), extreme rainfall, and earthquake preconditioning

Note, the majority of the work presented in this Chapter has been published in Nature Communications (Jones et al. 2021a). However, due to the format style of Nature Communications, this chapter presents the work in a different structure to that used in the paper.

5.1 Introduction

As outlined in the previous chapters, understanding the spatiotemporal variations in landslide characteristics and distributions has important implications for landslide susceptibility. However, a robust assessment of landslide hazard also requires an understanding of landslide rates, i.e., how much landsliding is expected to occur in a particular region and time in response to a given magnitude trigger event.

In chapter 4, landslide distributions within each mapped monsoon period were found to change significantly when storms and large magnitude ($> M_w$ 6.0) earthquakes occurred within a monsoon season. This highlights that whilst the ASM-inventory predominantly includes landslides associated with monsoonal rainfall, in years where other trigger events or landslide-influencing processes occur concurrently with the monsoon season, the inventory will also include landslides associated with those triggers and processes. This reflects the fact that landsliding in the Himalaya is controlled by a diverse and varying set of processes and trigger events. Indeed, it is well described that background rates of landsliding in the Himalaya are driven by tectonic uplift and the Asia Summer Monsoon (ASM) (Bookhagen *et al.* 2005; Dahal & Hasegawa 2008; Andermann *et al.* 2012; Kirschbaum *et al.* 2015; Struck *et al.* 2015), with these background rates occasionally

perturbed by extreme events such as floods (Cook *et al.* 2018), extreme rainfall (Dhital 2003; Kirschbaum *et al.* 2020), and earthquakes (Roback *et al.* 2018; Marc *et al.* 2019).

As such, to fully understand the controls on landslide rates in Nepal, it is necessary to isolate and quantify the relative landslide-impacts of the ASM, extreme rainfall, and earthquakes. However, doing this remains challenging, as most studies only consider the landslide impacts of single trigger events (e.g. Dhital *et al.* 1993; Roback *et al.* 2018). Furthermore, even where studies have considered multiple trigger events (e.g. Marc *et al.* 2019), they have struggled to isolate the relative impacts of those trigger events due to the lack of an empirical relationship between ASM-strength and landsliding. This highlights that with current data availability, it is generally challenging to determine whether increased rates of landsliding in a given time period are due to increased monsoonal rainfall or some other process / trigger event. Such a problem is illustrated by the M_w 7.8 Gorkha earthquake. As well as triggering over 24,000 coseismic landslides (Martha *et al.* 2017; Roback *et al.* 2018), the Gorkha earthquake is considered to have subsequently caused elevated rates of monsoon-triggered landsliding in the 2015 monsoon season as a result of surface damage by seismically-induced strong ground motion (Marc *et al.* 2019), or ‘earthquake preconditioning’ (Marc *et al.* 2015; Parker *et al.* 2015). As outlined in Chapter 1 (sections 1.2 and 1.3), gaining a better understanding of earthquake preconditioning is a key objective of this thesis. However, it is currently impossible to fully constrain the timescale and magnitude of Gorkha earthquake preconditioning as without empirical relationships between ASM-strength and landslide volume, it is challenging to distinguish whether post-earthquake landsliding from 2016 onwards was actually perturbed above the rate expected given the ASM-strength (Marc *et al.* 2019). Therefore, until empirical relationships between ASM-strength and landslide volume are defined, our ability to quantify landslide perturbations in central-eastern Nepal due to storms and earthquake preconditioning is limited. This not only impedes efforts to fully quantify the characteristics and processes of earthquake preconditioning, but also makes it challenging to account for extreme events in forecasts of landslide rates and in landslide susceptibility models.

Consequently, the overall aim of this chapter is to isolate and quantify the impacts of the ASM, extreme rainfall, and earthquake preconditioning on landslide occurrence in Nepal. This is made possible because the ASM-inventory developed here is known to include the impacts of several processes and trigger events, and covers a temporal range sufficient for longer-term (~30-year) relationships between ASM-strength and landsliding to be defined. This chapter first defines empirical relationships between several proxies of ASM-strength and landslide rates across the study region. These empirical relationships are then used to derive ASM-strength normalised rates of landsliding across the entire 30-year mapped period. This normalised rate identifies any years that experienced landslide perturbations above that expected given the monsoon strength. By identifying extreme rainfall events (where an “extreme” event is defined by its Z-score anomaly, see section 5.2.3) and earthquake occurrence across the mapped time period, each perturbation is then attributed to either extreme rainfall or earthquake preconditioning. This then allows the timescales and magnitudes of landsliding caused by extreme rainfall and earthquake preconditioning to be quantified relative to the ASM. Finally, further analysis of landslide rates, Gorkha earthquake Peak Ground Accelerations (PGA), and topography are used to provide novel insights into the specific processes that are controlling earthquake preconditioning in this region.

5.2 Methods

5.2.1 Empirical relationships between ASM-strength and landsliding

5.2.1.1 Landslide volume derivations

To quantify an empirical relationship between the ASM and landsliding, two rates of landsliding are derived for each time slice of the ASM-inventory. It should be noted that this Chapter uses a slightly updated version of the ASM-inventory used in Chapters 2 – 4, which now has 12,920 landslides. These updates resulted from select re-checking of some portions of the inventory against the original imagery used to conduct the mapping to double check for missed landslides and/or erroneously amalgamated landslides. This resulted in a total of 82 landslides being added, of which one was added to 1988 and 2004, two to 2001, three to 2000 and 2002, four to

1998, five to 2018, seven to 1987, eight to 2016, nine to 2006, 2014 and 2017, and ten to 2013 and 2015. A shapefile of this updated version of the inventory is presented in Data File 5, which can be accessed [here](#): A point inventory that includes estimated scar areas and volumes of each landslide is also presented in Data File 6, which can be accessed [here](#): The two derived rates of landsliding are: 1) the absolute total volume of all mapped features, including new landslides, reactivations and remobilisations (“New + RR”); and 2) the total volume of new features only, with reactivations and remobilisations removed (“New Only”). Removing reactivations and remobilisations in the second case allows the isolation of new post-earthquake landsliding related to earthquake-induced landscape damage (i.e. earthquake preconditioning) from reactivations and remobilisations of coseismic and pre-existing landsliding. Both are significant for hazard assessment, however, considering them in isolation allows specific consideration of new, and thus particularly unpredictable, landsliding in the landscape. Volumes are used instead of just landslide number, as using only number would ignore the fact that larger landslides have bigger impacts on landscape evolution (as they involve movement of more material) and hazard (as they affect larger areas) than smaller landslides. As such, using just number of landslides would wrongly equate the impact of a very small landslide to a much larger one. Volumes are used instead of area because they give a more accurate estimate than area of how much material was involved in a given landslide.

For each measure, landslide volumes were calculated using the global area-volume scaling relationships of Larsen *et al.* (2010). However, as outlined in Chapter 2 (section 2.2.3), all mapped polygons in the ASM-inventory include combined scar, runout, and depositional zones. As landslide areas that include long runouts and large deposition zones can potentially cause overestimates in subsequent volume derivations, it is necessary to apply a correction for runout by estimating the area of just the scar zone of each landslide (Marc *et al.* 2019). This was done using the correction proposed by Marc *et al.* (2018), which is outlined in the following paragraphs.

First, the width of every landslide in the inventory was calculated from the total area of each mapped landslide polygon using equations 5.1 (Marc & Hovius 2015) and 5.2 (Marc *et al.* 2018). These equations use landslide polygon perimeters, areas, and the assumption that each feature can be approximated by an elliptical shape (Marc & Hovius 2015; Marc *et al.* 2018).

$$K = \frac{1}{2} \left(\frac{4}{9} \left(\frac{P}{\sqrt{\pi A}} + 1 \right)^2 - 2 + \sqrt{\left(\frac{4}{9} \left(\frac{P}{\sqrt{\pi A}} + 1 \right)^2 - 2 \right)^2 - 4} \right)$$

Equation 5.1. Derivation of 'K' constant required for estimating landslide widths.

$$W \approx \sqrt{\frac{4A}{\pi K}}$$

Equation 5.2. Estimation of landslide width using the 'K' constant.

Where, W is landslide width (m), P is landslide perimeter (m), A is landslide area (m²) and K is a constant derived from equation 5.1.

Second, assuming that landslide scars have an average aspect ratio of 1.5, as found by Domej *et al.* (2017) for a wide range of landslide sizes, scar areas can be calculated from equation 5.3:

$$A_s = 1.5W^2$$

Equation 5.3. Estimation of landslide scar areas.

where A_s is scar area (m²) and W is landslide width (m) calculated from equation 5.2.

Landslide volumes were then estimated for both total mapped polygon areas and the estimated scar areas using the scaling relationship of equation 5.4 (Larsen *et al.* 2010):

$$V = \alpha A^\gamma$$

Equation 5.4. Landslide area-volume relationship.

where V is volume (m³), A is area (m²) and α and γ are constant scaling parameters.

For scar areas, appropriate values of α and γ for shallow Himalaya landslides reported by Larsen *et al.* (2010) are: γ = 1.262 ± 0.009 and log₁₀α = -0.649 ± 0.021 for areas < 10,000 m² (i.e. scar areas assumed to be dominated by soil), and γ = 1.41 ± 0.02 and log₁₀α = -0.63 ± 0.06 for areas > 10,000 m² (i.e. scar areas assumed to be

dominated by bedrock). For total areas, the ‘all landslide’ parameters (Larsen *et al.* 2010) were used, where: $\gamma = 1.332 \pm 0.005$ and $\log_{10}\alpha = -0.836 \pm 0.015$. The total volumes for each of the four measures obtained for each year are shown in Table 5.1.

Year	No. mapped features	Total volume "new + RR" (m ³)	Total volume "new only" (m ³)	Scar volume "new + RR" (m ³)	Scar volume "New only" (m ³)	Satellite product used
1988	552	23842587	20327357	25329600	21316385	Landsat 4/5
1989	368	44606067	37795615	36977800	29307496	Landsat 4/5
1990	282	24798168	20356572	18248563	13367633	Landsat 4/5
1991	185	14664730	12655041	20171382	17717302	Landsat 4/5
1992	206	10757394	8060680	9882284	7721032	Landsat 4/5
1993	688	63706490	59524933	64963866	59052172	Landsat 4/5
1994	239	15881316	13668377	16828875	14655775	Landsat 4/5
1995	329	32881528	30801027	33287489	30403043	Landsat 4/5
1996	349	17878160	14024401	20811952	15219065	Landsat 4/5
1997	248	16196123	12896086	15801173	11798940	Landsat 4/5
1998	274	20637304	16252455	23724167	17550177	Landsat 4/5
1999	369	25149652	21853231	22080466	16885497	Landsat 4/5
2000	477	19763192	14557902	18940784	13471883	Landsat 7
2001	572	22742863	17444836	17995094	12919774	Landsat 7
2002	1337	66201168	52972260	57674509	42572127	Landsat 7
2003	297	19987080	16671775	17856598	14606480	Landsat 7
2004	564	22259342	18215714	20338658	16930196	Landsat 4/5
2005	149	9962131	8952169	7263236	5938146	Landsat 4/5
2006	206	14173187	12255139	13929565	10967058	Landsat 4/5
2007	211	22935697	18688172	27965378	21391510	Landsat 4/5
2008	216	12195684	10402270	9918266	8057466	Landsat 4/5
2009	175	11456406	9351355	9609328	6937638	Landsat 4/5
2010	310	14054953	10916087	13546765	10640480	Landsat 4/5
2013	433	9931421	8042592	7118385	4642711	Landsat 8
2014	507	20382998	18199991	25598549	24139158	Landsat 8
2015	1328	79809974	42454871	61102244	21285238	Landsat 8
2016	890	31772872	13029709	24516651	9213868	Landsat 8
2017	753	18691302	12983404	14089973	9062546	Landsat 8
2018	406	13507735	10991457	8200926	5270255	Landsat 8

Table 5.1. Summary volume statistics and satellite information for all mapped monsoon seasons within the ASM-inventory.

Finally, for each year in the inventory, all landslides were ranked from largest to smallest by scar volume. Following the approach of Marc *et al.* (2019), if the largest scar volume in any year was greater than twice as large as the second largest scar volume, then that event was removed from the subsequent analysis. These removed events can all be considered as anomalously large relative to the ASM-season in which they occurred. Removing them thus serves as a correction for the fact that the largest landslides often fail progressively over several monsoon seasons before failing catastrophically in a single monsoon season. Such events are not directly attributable

to the ASM-strength of the season in which they finally fail, and so can significantly bias the landslide rate in a given year. For example, the Jure landslide is widely considered to have occurred via progressive failure across multiple ASM-seasons (Yagi *et al.* 2020), so is not directly attributable to the 2014 season in which it failed catastrophically. The scar volume of this event accounted for 74% of the total scar volumes that occurred in 2014. As such, including this event in the subsequent analysis would make the 2014 season appear to be perturbed above the rate expected for the 2014 monsoon-season, even though this event did not fail as a direct result of the 2014 ASM-strength. In total, 12 events were removed from the analysis, one event in each of 1988, 1996, 2000, 2003, 2004, 2005, 2014 and 2017, and two events in both 2009 and 2015.

Finally, it should be noted that the use of landslide volumes has some potential limitations. One, as outlined above, landslide scar volume calculations involve several assumptions about landslide shape, notably that landslide scars have an average aspect ratio of 1.5. As outlined in section 2.7.2.2, the total landslide areas (e.g., areas including scar, runout, and deposition zones) had a wide range of aspect ratios, with a mean of 2.5. So, whilst there is some variation, it is not unreasonable to assume that the scar areas (where runouts are removed and thus aspect ratios are smaller) would have mean aspect ratios of approximately 1.5, particularly given that 89% of the total landslide areas have aspect ratios <4 before runouts are removed. However, the use of a fixed aspect ratios for landslides with known variations in length/width will remain an area of error and uncertainty, which is why an assumed 20% error is applied to the final normalisation results (see section 5.2.2.1). Two, is that the overall total volume estimates will be underestimates of the true total volumes as due to available imagery resolution, the inventories used here do not include the smallest landslides. However, this should not unduly affect the overall results presented in this chapter. As shown in section 5.2.2.2, each year has comparable area-frequency distributions. Assuming that these distributions would remain similar into the smaller area portion of the distributions, the numbers of smaller missed landslides relative to the number of larger landslides will be comparable in each year. As such, the effect of the missed smaller landslides should

not have affected any single year more than any other, and thus the overall normalisation results should be unaffected. This is however an issue that should be noted by the reader and considered throughout the subsequent discussions and results.,

5.2.1.2 Precipitation data: PERSIANN-CDR and APHRODITE

For the entire mapped region, each measure of landslide volume was correlated with proxies for ASM-strength derived from two rainfall products: PERSIANN-CDR (Ashouri *et al.* 2015; Sun *et al.* 2018) and APHRODITE (Yatagai *et al.* 2012). Before describing these proxies, the following paragraphs outline the key properties of both PERSIANN-CDR and APHRODITE, as well as the justifications for using them within this analysis.

As outlined in Chapter 2 (section 2.3.1.1), The PERSIANN Climate Data Record (CDR) has a spatial resolution of 0.25° by 0.25°, a temporal resolution of 3 hours, 6 hours, 1 day and 1 month, covers latitudes 60° S – 60° N, and covers 1983 – present (Ashouri *et al.* 2015). This record is developed by applying the PERSIANN algorithm on GridSat-B1 IR satellite data. The artificial neural network used to do this is trained using 6-hourly precipitation data from the National Centres for Environmental Prediction (NCEP) (Du 2021) and then adjusted using the Global Precipitation Climatology Project (GPCP) monthly gauge and satellite-based dataset (Ashouri *et al.* 2015). This product was selected as it is one of the few freely accessible precipitation products with a spatial resolution of at least 0.25° by 0.25° that spans the full required time period of 1988 – 2018 (Sun *et al.* 2018; see Table 2.4). Daily precipitation totals (mm) for May – September were obtained from the CHRS data portal (<https://chrsdata.eng.uci.edu/>) (Nguyen *et al.* 2019) for all PERSIANN-CDR grid tiles that were at least 50% within the study region. Standard GIS tools were then used to extract the various ASM-strength metrics used within this chapter.

PERSIANN-CDR is now a widely used product that has been well evaluated in the literature (e.g. Nguyen *et al.* (2020) and references therein). Indeed, PERSIANN-CDR was found to perform excellently when evaluated against 1400 ground-stations at capturing the spatial and temporal patterns of rainfall in the monsoon-regions of

eastern China (Miao *et al.* 2015), and outperformed the TMPA (TRMM Multi-satellite Precipitation Analysis) dataset in its ability to capture the overall characteristics of Hurricane Katrina (Nguyen *et al.* 2020). Furthermore, the PERSIANN-CDR product was found to have lower monthly mean variance when compared to other satellite derived products, showing particularly small variance with the GPCP1DD product (Huffman *et al.* 2001; Gehne *et al.* 2016). Similarly, despite being marginally outperformed by other products, the PERSIANN-CDR dataset was capable of capturing inter-annual monsoon precipitation in Pakistan, with high (0.8) R^2 values when compared to *in situ* data (Ullah *et al.* 2019). Nevertheless, it should be noted that the PERSIANN-CDR product has some limitations. First, as with all satellite derived products, it remains unclear how well orographic effects are captured (Adam *et al.* 2006). However, a benefit of the PERSIANN-CDR product is that it is designed specifically for use in longer-term (decadal) studies (Ashouri *et al.* 2015; Beck *et al.* 2017) and is considered one of the most temporally homogenous products. As such, unlike other satellite products whose methodologies could introduce temporal variance, any errors in the PERSIANN-CDR product introduced by orographic effects should be more systematic through time, and so not significantly bias the time-series. This is a key consideration for this Chapter, as the relative temporal impacts of rainfall on landsliding could be artificially skewed if a rainfall product changed its acquisition and data processing method mid-way through the time period. Second, PERSIANN-CDR is reported to have a tendency to under-predict values of extreme precipitation (Miao *et al.* 2015; Beck *et al.* 2017). As such, to ensure that any under prediction of rainfall by PERSIANN-CDR does not impact the normalisation, and to allow for a more robust consideration of daily extreme precipitation, the APHRODITE product (Yatagai *et al.* 2012) was also used within this Chapter.

APHRODITE (Asian Precipitation—Highly Resolved Observational Data Integration Towards Evaluation of water resources) has the same spatial resolution as PERSIANN-CDR (0.25° by 0.25°) across monsoon-Asia, with daily coverage across the study region for the period 1951 – 2015. The APHRODITE product is based on rain gauge data from 5,000–12,000 stations and is designed to optimise

representation of orographic precipitation patterns. The temporal coverage of APHRODITE has both advantages and disadvantages for this study. The main disadvantage is that it does not allow assessment of post-2015 earthquake preconditioning (which is major aim of this chapter and the reason for using the PERSIANN-CDR data to assess the entire time series). The main advantage of the temporal coverage is that with a 64-year time-series, a robust analysis of extreme rainfall and recurrence intervals can be undertaken (see section 5.2.3). The APHRODITE product is also considered to be one of the most accurate products over the Himalaya (Yatagai *et al.* 2012), making it a good product to corroborate the results of the full-time series normalisation undertaken with PERSIANN-CDR.

5.2.1.3 Proxies of ASM-strength

Four proxies of ASM-strength, for both PERSIANN-CDR and APHRODITE, were used to investigate the potential relationships between the ASM and each of the four metrics of landslide volume (total and scar volumes for the “New Only” rate and “New + RR” rate). These proxies were: total grid-averaged MJJAS (May – September) precipitation, total grid-averaged MJJAS precipitation > 25 mm (sum of all precipitation days from May to September with total rainfall values > 25 mm), total grid-averaged precipitation from 15th June – 30th September, and total grid-averaged precipitation > 25 mm for 15th June – 30th September (sum of all precipitation days within this time period with total rainfall values > 25 mm). These metrics were selected because they have been investigated in earlier studies (e.g. Marc *et al.* 2019; Muñoz-Torrero Manchado *et al.* 2021), with Muñoz-Torrero Manchado *et al.* (2021) showing that total monsoon-precipitation correlated well with the number of shallow landslides in far western Nepal. It should be noted that typical measures of monsoon strength such as the SASMI (Li & Zeng 2002) were avoided, as these are derived over extensive regional scales and so are unlikely to accurately capture local changes in monsoon conditions. Indeed, as shown in Appendix F, there is no strong relationship between SASMI and any metrics of landslide volume.

5.2.1.4 Correlations between landslide volume and ASM-strength proxies

Across the entire study region, for both the PERSIANN-CDR and APHRODITE products, the four proxies of ASM-strength (in mm / rainfall grid) were correlated with the four metrics of landslide volume (m^3/km^2) through time for the pre-2015 Gorkha earthquake years. The post-earthquake years as well as 1993 and 2002 were not included in this correlation as it was already known that these years were impacted by events other than the ASM, so these could not reasonably be used to define an empirical relationship between the ASM and landsliding. Finally, exponential equations (which were found to provide the best fit to the data) were fitted to each correlation and associated R^2 values obtained.

5.2.2 ASM-normalised rate

Following the methods of Marc *et al.* (2015), for each rainfall product, the best fit exponential equations from section 5.2.1.4 were used to derive ASM-strength normalised rates of landsliding across the entire mapped period (1988 – 2018) for each measure of landslide volume. The empirical equations were first used to calculate the predicted volumes of landsliding that would be expected in each year based on that years ASM-strength. Then, by taking the ratio of the actual mapped landslide volumes for each year to the predicted volumes, an ASM-normalised rate of landsliding for each year was obtained. Any years with normalised values significantly above +1 standard deviation from the normal (one) were thus identified as years with landsliding perturbations above that expected from the ASM-strength alone.

5.2.2.1 Error and uncertainty analysis

To define which years were considered “significantly” above +1 standard deviation of the normal, error and uncertainty analysis were undertaken. The errors in the normalised rates included the standard error in the best-fit exponential equations used to calculate the predicted landslide volumes, an assumed 20% standard deviation in the actual mapped landslide volumes (to account for erroneously mapped features, mapping error, error in scar volume calculations etc.) and the standard deviations reported for the Larsen *et al.* (2010) area-volume parameters.

Assuming that these errors are uncorrelated, they were combined using standard Gaussian propagation of error to obtain the uncertainties in each normalised value. If the lower-uncertainty bound of a given normalised value was above +1 standard deviation of the normal, then that value was considered “significantly” above the ASM-normal, and thus likely to be attributable to some other triggering process as well as the ASM.

Another area of uncertainty to be considered is the variable length of each mapped time-period. As outlined in Chapter 2 (section 2.2.3.1), each mapped time slice included a given year’s monsoon season (May – September) plus a varying number of non-monsoon months either side. The variation in the number of October – April months included in each time slice was an unavoidable consequence of the high levels of cloud cover across the Himalaya. However, as the time slices had varying lengths, both between time slices and within time slices (as several tiles were required to map the entire study region, and invariably these tiles had different acquisition dates and cloud cover), it is necessary to consider the effect of this on the results. The analysis of ASM-triggered and extreme rainfall triggered landsliding assumes that all landslides were triggered during a given time slice’s monsoon season. As these time slices include months outside of the monsoon period, it is possible that some of the mapped landslides did not actually occur during the monsoon. However, it is known that this region experiences little rainfall-triggered landsliding outside of the monsoon period (Petley *et al.* 2007; Stanley *et al.* 2020). Indeed, no correlation is found between the number of non-monsoon months within a time slice and the number of landslides mapped within that time slice (Fig. 5.1). Furthermore, no correlation is observed between the total rainfall in the non-monsoon months included in each time slice and the deviation of a time slice from the calculated normalisation values (Fig. 5.2). This suggests that, as expected, variable time slice length cannot explain the normalisation results. To further ensure that errors in mapping procedure do not affect the results, as outlined above, a 20% assumed error was applied to all mapped landslide areas.

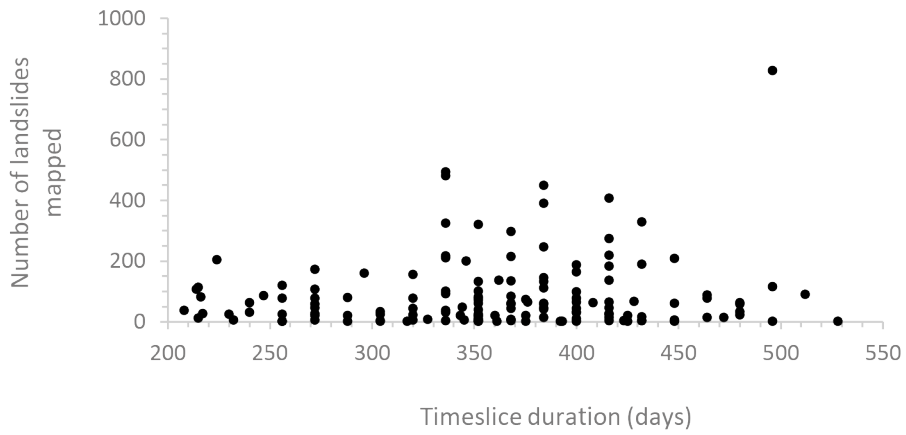


Figure 5.1. Correlation between time slice length (where variation is due to varying number of non-monsoon days between October and April) and number of mapped features.

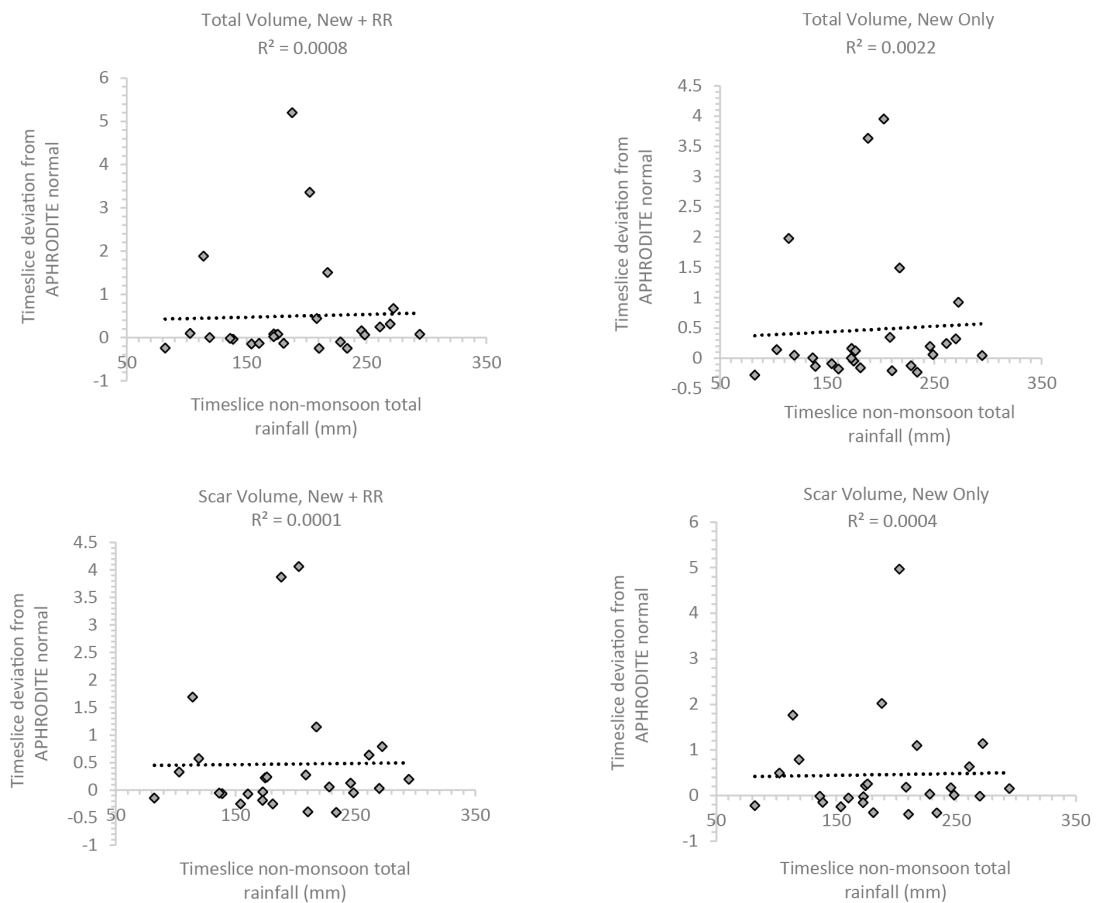


Figure 5.2. Relationship between total rainfall in the non-monsoon months included in each mapping interval and the deviations from the normal in the normalised rate (Figure 5.4b).

5.2.2.2 Size analysis

Before it could be assumed that a given perturbation was due to another triggering process, it was first necessary to confirm that each perturbation was not simply due to a small number of very large landslide events. As outlined in section 5.2.1.1, the largest landslides had already been removed. However, to further confirm that each perturbation could not be explained by a stochastic change in landslide size distributions, three-parameter inverse-gamma distributions were fitted to the probability density functions of landslide area for the following cases: all years, all pre-earthquake non-perturbed years, 1989, 1993, 1995, 2002, 2015, and the post-earthquake years. These distributions were fitted using the methods outlined in Chapter 2 (section 2.4.3).

5.2.3 Quantifying extreme rainfall

Following the size analysis (section 5.2.2.2), any years showing significant perturbation above the expected ASM-rate were assumed to be attributable to some other process or triggering event that occurred during that year. As stated in Chapter 4, it is known that cloud outburst storms occurred during the monsoon-seasons in 1993 and 2002. As such, it is necessary to investigate whether such events can explain any of the perturbations identified by the normalisation. This requires a quantitative definition for how extreme the 1993 and 2002 cloud outburst storms were. Once a quantitative definition for an “extreme” rainfall event is obtained, all extreme events that occurred between 1988 and 2018 can be identified and their relation to the normalised rate investigated.

To do this, the long (64 year; 1951 - 2015) APHRODITE time series of daily rainfall data is used to calculate Z-score anomalies for every monsoon-season (MJJAS) day across each of the 84 APHRODITE grids that encompass the study region, i.e., for each separate rainfall grid, the mean and standard deviations of all monsoon-season days from 1951 to 2015 were calculated, and from this the individual Z-scores for each day obtained. A Z-score is a simple measure that counts how many standard deviations a given measurement is above the mean. Z-scores were calculated using the multidimensional anomaly tools in ArcGIS-Pro.

Once the Z-scores for every monsoon-season day of every grid-cell across the study region had been obtained, the Z-scores for the 1993 and 2002 events were extracted. Then, the number of days within each monsoon season from 1988 to 2018 above the Z-score thresholds found for the 1993 and 2002 storms were counted across the whole study region, and correlated with the APHRODITE normalised rate of landsliding. Finally, by counting how many events of a given Z-score known to induce a perturbation occurred across the full 64-year time series, the return periods of landslide perturbing extreme rainfall events were estimated.

5.2.4 Quantifying earthquake preconditioning

Between 1988 and 2018, three large magnitude ($M_w > 6.0$) earthquakes in 1988, 2011 and 2015 occurred within the study region. As such, any identified perturbations to the ASM-normalised rate in the years during and following these earthquakes could be explained by a process known as earthquake preconditioning. As outlined in section 5.1 and Chapter 1 (section 1.2.2.2), earthquake preconditioning is the process by which ground motion induced landscape damage transiently increases landslides rates following an earthquake.

A key element of this thesis was to investigate and quantify the process of earthquake preconditioning in the Nepal Himalaya. The normalisation analysis already achieves this as it identifies whether the rates of new landsliding post-2015 were actually perturbed above the rate expected given the ASM-strength (i.e. whether preconditioning was occurring), quantifies the magnitudes of any earthquake preconditioning-induced landslide perturbations relative to the ASM (i.e. preconditioning magnitude), and defines how long after 2015 any perturbations remained (i.e. preconditioning timescales). However, whilst this study and others (e.g. Marc *et al.* 2015) have been able to quantitatively constrain the magnitudes and timescales of short-term earthquake preconditioning, the processes and mechanisms that cause it remain uncertain. It is generally accepted that short-term preconditioning occurs via near-surface earthquake damage that is rapidly exploited by subsequent rainfall as new failures, but what controls the spatial distributions of this damage remain largely speculative.

Here, the landslide volume data for the 2015 monsoon season are combined with USGS ground motion (USGS 2018c) data for the Gorkha earthquake, and topographic data for the study region to investigate how any excess landsliding in 2015 relates to Gorkha induced ground motion and the landscape topography. To do this, varying landsliding, PGA and topography across the entire study region had to be explicitly considered. As with the extreme rainfall analysis, this required a shift from regional scale analysis to a more localised, grid-scale, analysis. As such, the study region was divided into the same 84 APHRODITE grid-cells used for the extreme rainfall analysis. For each grid-cell, the maximum PGA observed during both the M_w 7.8 Gorkha earthquake main shock and 12/05/2015 M_w 6.3 aftershock were extracted and summed. For each grid-cell, the mean landsliding observed across all known unperturbed monsoon-seasons (i.e. all years except 1988, 1989, 1993, 1995, 2002 and 2015) was also calculated. Finally, the percentage change in 2015 monsoon-triggered landsliding for each grid relative to that grids mean was obtained. By only calculating each cell's average with the non-perturbed years, an approximation of average landsliding expected per grid in a monsoon season without extreme rainfall should be obtained. Therefore, as it is known that 2015 was not impacted by any extreme rainfall (see section 5.3.3), the percentage change in 2015 ASM-triggered landsliding for each grid should approximately reflect the "above average" or excess landsliding experienced in 2015 owing to the earthquake. The percentage change in 2015 ASM-triggered landslide rate is then plotted against the summed maximum PGA for all grids that experienced landsliding in 2015 and had < 10% snow cover.

Furthermore, as seismic ground motion is known to undergo amplification when travelling across ridgelines and other topographic excesses (Paolucci 2002; Nguyen & Gatmiri 2007; Wald & Allen 2007), earthquake preconditioning may be most likely where high PGA is coincident with high excess topography, where excess topography is defined as the volume of rock-mass above a landscape's threshold angle (Blöthe *et al.* 2015). To investigate this, the average excess topography of each grid-cell for five landscape threshold angles (25°, 30°, 35°, 40°, 45°) was calculated using the TopoToolBox (see Chapter 2 section 2.3.2.1). Then, for each grid-cell, each excess

topography measure was multiplied by the summed maximum 2015 PGA's (i.e. in each grid-cell, the maximum 2015 main shock PGA plus the maximum 2015 largest aftershock PGA all multiplied by the average excess topography). These weighted "PGA-Excess Topography" values were then plotted against each grid-cells percentage change in 2015 ASM-triggered landsliding.

5.3 Results and discussion

5.3.1 Empirical relationships between ASM-strength and landsliding

For both the PERSIANN-CDR and APHRODITE rainfall products, the four proxies of ASM-strength outlined in section 5.2.1.3 were correlated with the landslide volume measures outlined in section 5.2.1.1 for the pre-Gorkha years excluding 1993 and 2002. To identify outliers above the normal, in each case, exponential best-fit lines and associated standard deviations were calculated. Any years that fell above of one standard deviation of the best fit were then removed, and new best fit and standard deviations for the remaining years recalculated. This was repeated until all years were within one standard deviation of the best fit line. For the PERSIANN-CDR data, no years were above one standard deviation of the best fit, whilst for the APHRODITE product, the years 1989 and 1995 were initially above one standard deviation so were removed. Once these outliers had been removed from the correlations, the total MJJAS precipitation proxy provides the best fit in the PERSIANN-CDR case, whilst total MJJAS precipitation > 25 mm provides the best fit in the APHRODITE case (Fig. 5.3e – h) (For all other non-best fit correlations, see Appendices G, H, and I). As such, from this point forward, the term "ASM-strength" refers specifically to total MJJAS precipitation for PERSIANN, and total MJJAS > 25 mm for APHRODITE. Of the pre-Gorkha earthquake years included in the correlation between landsliding and ASM-strength, most show that landslide volume per unit area increases exponentially with total grid-averaged precipitation. Furthermore, when the years 1993, 2002, and post-2015 are included in these plots, it is evident that the volumes in these years are anomalously high for the observed ASM-strength relative to other years, as are 1989 and 1995 in the APHRODITE case.

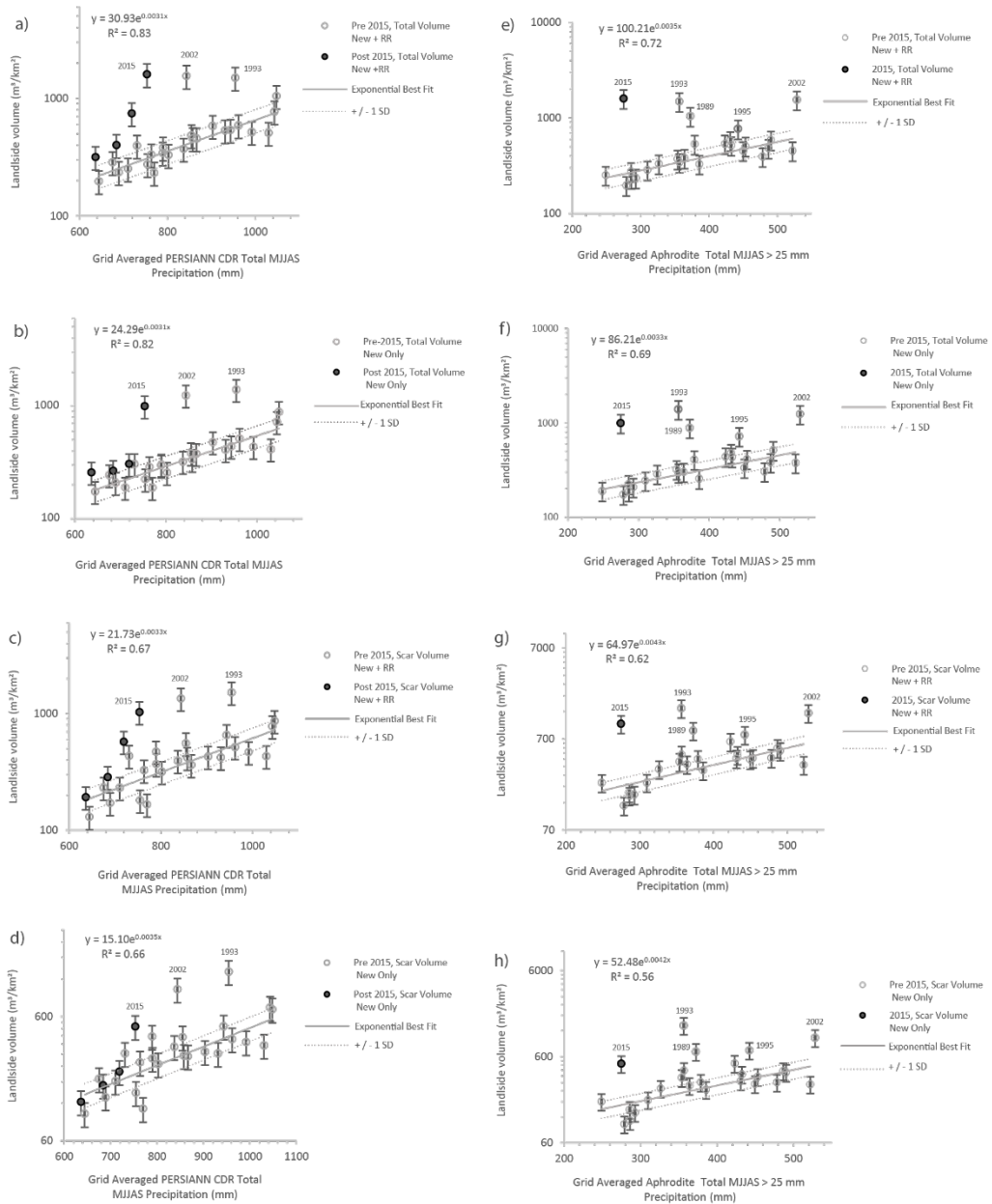


Figure 5.3. a – d) Empirical relationships between measures of landslide volume (m^3/km^2) and PERSIANN-CDR total MJJAS precipitation for a) total “New + RR” volume, b) total “New Only” volume, c) scar “New + RR” volume and d) scar “New Only” volume. e – h) Empirical relationships between measures of landslide volume (m^3/km^2) and APHRODITE total MJJAS precipitation > 25 mm for e) total “New + RR” volume, f) total “New Only” volume, g) scar “New + RR” volume and h) scar “New Only” volume.

With the anomalous years excluded, the R^2 values of the best fit equations are 0.69 – 0.83 for the PERSIANN-CDR data and 0.56 – 0.67 for the APHRODITE data.

5.3.2 ASM-strength normalisation

The best-fit empirical relationships between ASM-strength and landsliding (Fig. 5.3) were then used to derive ASM-strength-normalised rates of landsliding across the entire mapped period (1988 – 2018) for both the PERSIANN-CDR (Fig. 5.4a) and APHRODITE (Fig 5.4b) rainfall data.

These rates show that, for both rainfall products, most time slices fall within a narrow band of landsliding around the expected normalised value of one, with several years clearly perturbed above this rate. For the PERSIANN-CDR normalisation, there are perturbations above +1 SD of the normal in 1993, 2002, and post-2015 (Fig. 5.4a). Specifically, for the post-2015 perturbation, if coseismic reactivations and remobilisations are considered, then the years 2015 – 2016 are perturbed above the expected monsoons scaling, however, when considering only new landslides, only 2015 is perturbed. For the APHRODITE normalisation, the years 1989, 1993, 2002 and 2015 are perturbed above + 1 SD of the normal, with another possible perturbation in 1995 (Fig. 5.4b).

As the ASM-strength-normalised landslide rate accounts for variance in ASM-precipitation, the identified perturbations should be attributable to infrequent high-magnitude landslide drivers not accounted for by the metrics of ASM-strength. However, before this can be assumed, it is important to show that these perturbations are not due to stochastic variation in landsliding areas, i.e., to confirm that the perturbations are not simply caused by a small number of anomalously large landslide events. As outlined in the methods, this approach has already considered this by following the example of Marc *et al.* (2019), whereby before correlating landsliding with ASM-strength the largest landslides of each year were removed if their scar areas were greater than twice that of the second largest. This ensures that any large landslides that were affected by progressive failure across several monsoon seasons (e.g. the Jure landslide; Yagi *et al.* 2021), but failed catastrophically in one monsoon-season, are not incorrectly attributed to a single monsoon period.

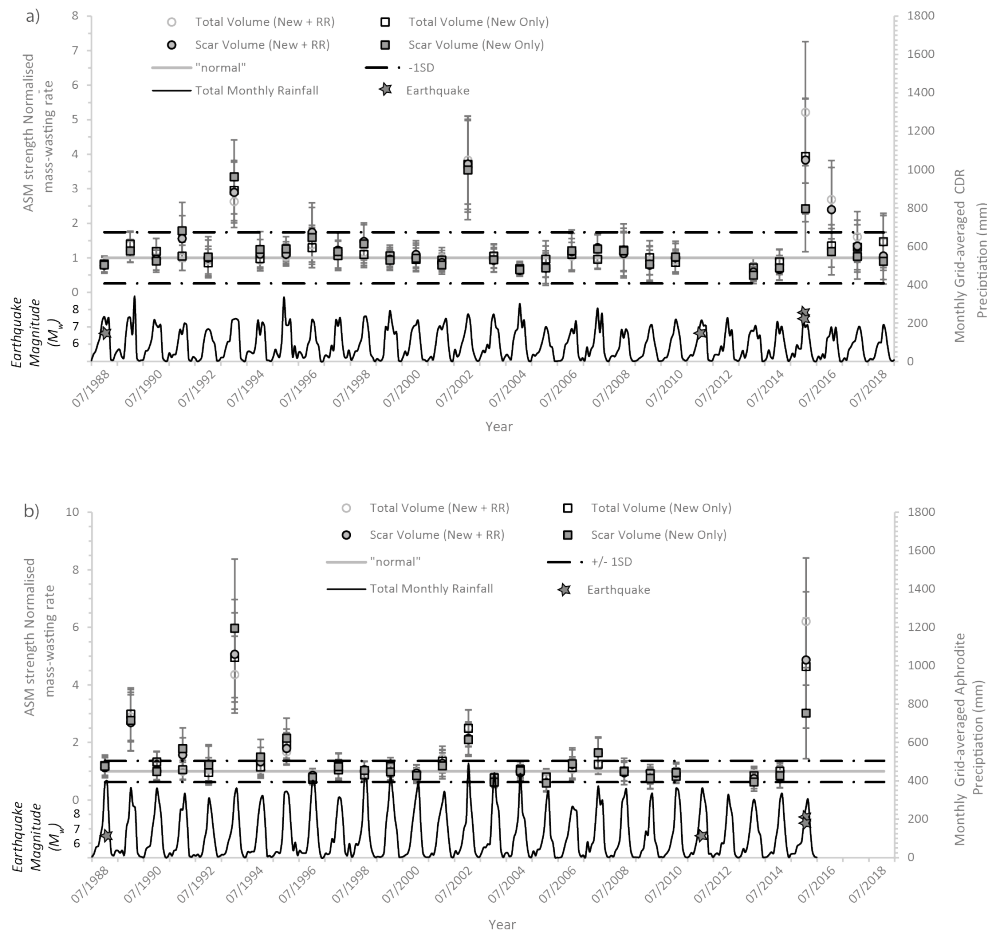


Figure 5.4. ASM strength-normalised rate of landsliding from 1988 - 2018 for a) the normalisation using PERSIANN-CDR data and total MJJAS precipitation, and b) the normalisation using APHRODITE data and total MJJAS precipitation > 25 mm. The occurrences of historical $M_w > 6.0$ earthquakes are shown, as are monthly grid-averaged PERSIANN-CDR (a) and APHRODITE (b) precipitation totals.

To further ensure that the perturbations are not explained by stochastic variation in landslide area, as outlined in section 5.2.2.2, three-parameter inverse-gamma distributions were fitted to the Probability Density Functions (PDFs) of landslide area for all years combined, all pre-2015 non perturbed years, 1989, 1993, 1995, 2002, 2015 and all post-2015 years (Fig. 5.5a – h). If the three-parameter inverse-gamma distributions fitted to each subset have similar scaling exponents (where a larger exponent indicates that larger landslides are contributing less to the overall inventory) and rollovers (which represents the size above which power law behaviour applies), then the observed perturbations being caused solely by statistical anomalies in landslide size can be ruled out.

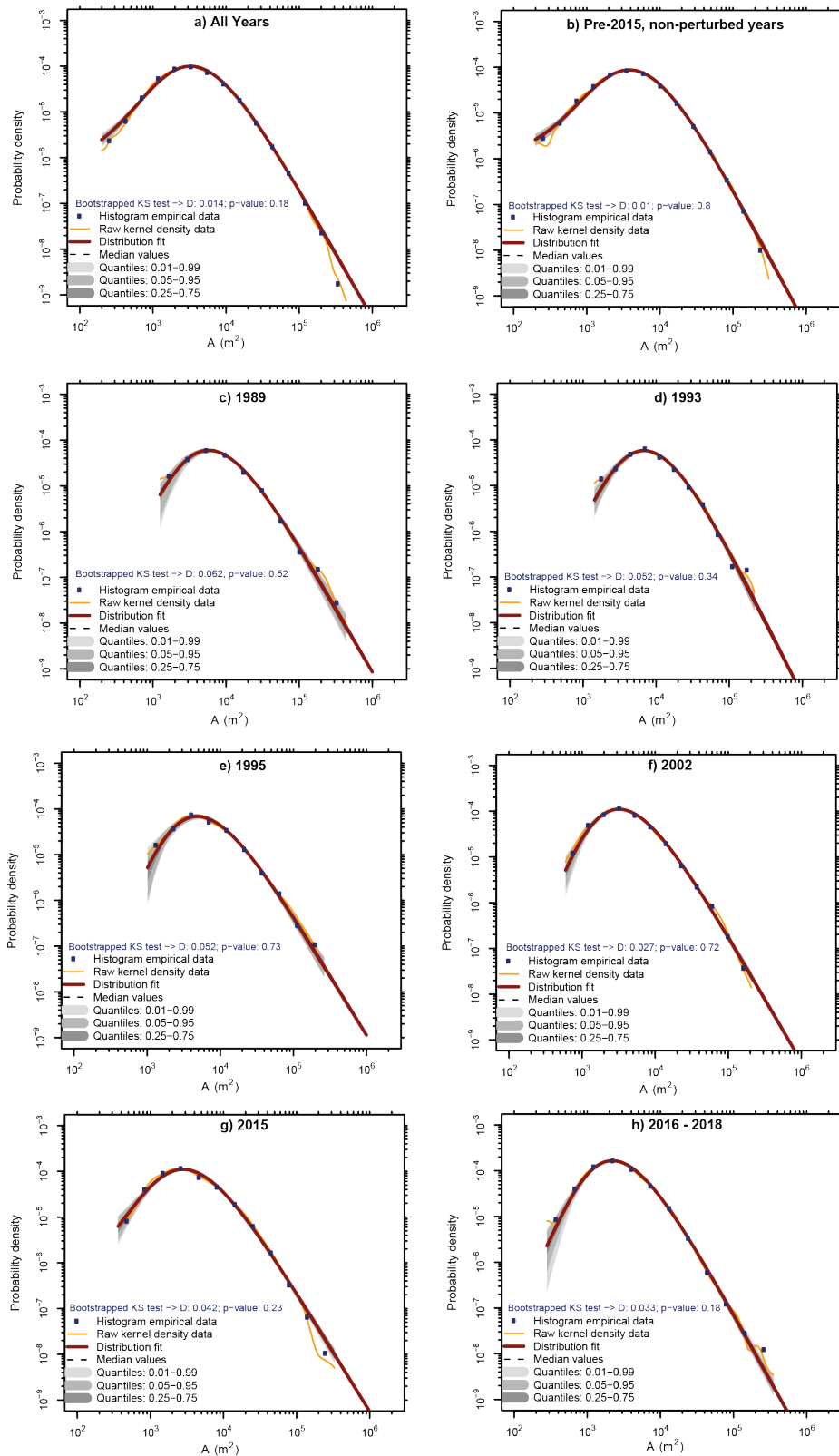


Figure 5.5. Three-parameter inverse-gamma distributions fitted to the probability density functions of landslide area for landslides that occurred in a) all years, b) the pre-2015 non-perturbed years, c) 1989, d) 1993, e) 1995, f) 2002, g) 2015, and h) post-2015).

Scaling exponents are found to fall within a narrow range of 1.8 – 2.2 for all subsets except 1995 and 2015, which had slightly lower exponents of 1.6. Similarly, the rollovers of most subsets fall within the range of 2000 – 6000 m², with the exception of 1989 and 1993, which had slightly higher rollovers of 6000 – 7000 m². Overall, as the scaling exponents of the fitted distributions are similar above comparable cut-offs, the area-frequency distributions can be described as scaled versions of one another, though with 2015 and 1995 having a slightly higher proportion of large area events. This suggests that the observed perturbations are not due solely to stochastic change in landsliding area-frequency distribution during that year, but instead are the result of physical processes increasing the frequency of all sizes of landslide.

5.3.3 Impacts of extreme rainfall

The ASM-strength normalised rates identify landsliding perturbations in 1993, 1995 and 2002 that are not coincident with earthquakes $> M_w$ 6.0 (Fig. 5.4a - b). These perturbations are 2.5 – 6 times higher than the ASM normal in 1993, and 2 – 3.5 times higher than the ASM normal in 2002. To investigate whether these perturbations could be explained by extreme rainfall, Z-score anomalies from the daily APHRODITE data were derived for every day and cell within the study region. If the years experiencing perturbations can be explained by extreme rainfall, it is expected that these years would have experienced higher than normal daily rainfall Z-scores.

To get an appreciation of the Z-score thresholds that can cause landslide perturbations, the Z-scores for the known perturbation-inducing outburst storms in 1993 and 2002 were extracted. The Z-scores for these events were found to be 12 - 13 in 1993 and 16 – 19 in 2002. To identify whether any other similar rainfall events can explain the other observed perturbations across the mapped time-period, the number of days within each monsoon season with Z-scores exceeding thresholds of 12, 14, and 16 were counted and correlated with the normalisation results from Figure 5.4b (Fig. 5.6).

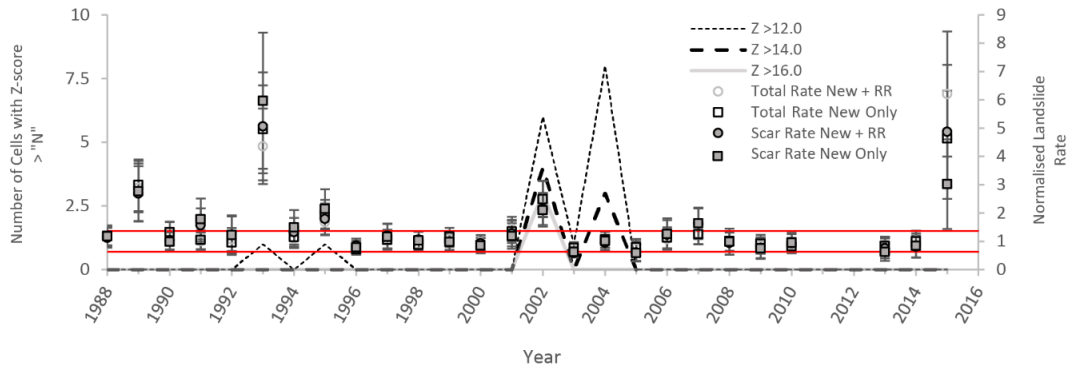


Figure 5.6. Number of daily cells per monsoon season that observed Z-score anomalies greater than 12, 14 and 16. For reference, the normalised rates and associated +/-1 SD (red lines) from Fig. 5.4b are also shown.

This shows that just two other years observed rainfall with Z-scores of > 12 , 1995, which also experienced a minor landsliding perturbation, and 2004, which did not. This tentatively suggests that a rainfall Z-score threshold of 12, relative to a grid-cells 1951 – 2015 long-term mean, is required to induce a significant landsliding perturbation above that expected from a typical monsoon season. The perturbations in 2015 and 1989 do not coincide with any anomalously high rainfall, with neither year observing any days with Z-scores > 10 , indicating that these perturbations are explained by another process (see section 5.3.4).

As highlighted above, the 2004 monsoon season had no landsliding perturbation, despite experiencing 8 cells across the study region with Z-scores > 12 and 3 cells with Z-scores > 14 . With the exception of 2002, which experienced Z-scores > 16 , 2004 observed the most extreme rainfall of any year. Given that all 8 of the cells experiencing extreme rainfall in 2004 occurred after June 15th, it is unlikely that the lack of landslide response can be attributed to incompletely saturated hillslopes (Gabet *et al.* 2004; Marc *et al.* 2019). However, there are three other potential explanations for why the 2004 rainfall did not induce a landslide response.

One possible explanation relates to the temporal distribution of the cells in 2004 that exhibited Z-scores > 12 . Of the 8 cells in 2004 that exhibited Z-scores > 12 , none were in the same cell on consecutive days. This is potentially important, as consecutive

high-intensity rainfall days will be more efficient at triggering landslides. If the lack of consecutive high Z-scores days can explain the lack of a significant landslide response in 2004, then it would be expected that 2002, 1995, and 1993 do experience consecutive high-Z-score days. However, in 2002, only cell 21 (see Fig. 5.7) experienced two consecutive days with Z-scores > 12, whilst no cells in 1993 or 1995 experienced consecutive days with Z-scores > 12. This suggests that a lack of consecutive high-intensity rainfall days cannot explain why 2004 lacked a landslide response relative to the other years that observed extreme rainfall.

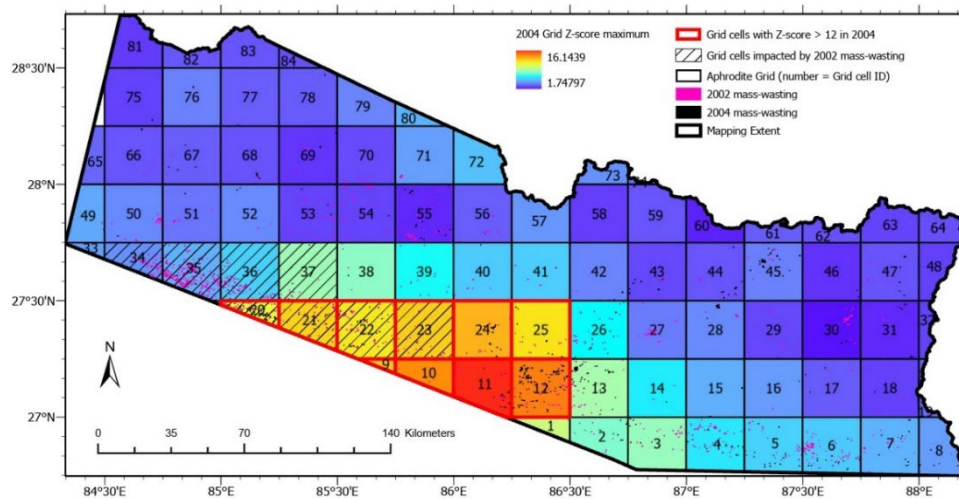


Figure 5.7. The locations and IDs of the 84 APHRODITE rainfall grid cells across the study region. Maximum Z-scores from the 2004 monsoon seasons are shown alongside the 2004 landsliding. Also shown is the extent of the 2002 extreme rainfall, the landsliding from 2002 and the extent of permafrost across the study region.

Two, is that the 2004 rainfall induced less landsliding because the landscape had yet to recover from the landslide perturbation in 2002. This concept of landscape recovery (e.g. Rathburn *et al.* 2018) is based on the idea that a major exhumation event will exhaust a landscape of soil material available to fail, and thus transiently limited future landsliding until the landscape has re-accumulated unstable regolith material. Fig 5.7 shows that the 2004 rainfall event was partially coincident with the 2002 event. This suggests that there is the potential for landscape recovery (or lack

of) to explain the subdued landslide response in 2004. The cells coincident with both the 2002 and 2004 events were cells 20, 21, 22 and 23. All four of these cells observed Z-scores of 11 – 13 in 2004, and Z-scores of 11 - 16 in 2002. Using the method outlined in section 5.2.4, the percentage change in 2002 and 2004 landsliding was obtained for all four of these cells (i.e. the landslide change relative to each cell's non-perturbed mean was obtained). In 2002, all four cells had percentage increases in landsliding of 233 – 2100%. In 2004, these cells also saw above average landsliding, with percentage increases of 20 – 435%, but with all cells having smaller increases than were observed in 2002. This can be compared to cells 9, 10, 11, 12 and 24, which were impacted by extreme rainfall in 2004, but not in 2002. These cells observed Z-scores in 2004 of 12 – 16, and had percentage changes in landsliding in 2004 of 220 – 700%. These are slightly higher increases in landsliding relative to the cells coincident with 2002, but are also higher Z-scores. As such, it remains inconclusive whether the 2002 event perturbed the landscape such that it had not recovered sufficiently to observe another perturbation in 2004. Furthermore, this concept of landscape recovery is contradicted by the observations shown both here and in other studies (e.g. Dadson *et al.* 2004; Hovius *et al.* 2011; Marc *et al.* 2015, 2019) for post-seismic landsliding, where landsliding actually increases immediately following a major exhumation event. As such, it seems unlikely that landscape recovery is playing a significant role in this case, though it is noted that this could be an interesting topic for more targeted future research.

Three, is inaccuracy and/or misallocation of the rainfall data. The APRHDOITE grid-cells are coarse (~30 km resolution), and the cells for the 2002 and 2004 events cross the boundary of the study region. Consequently, it is possible that the true rainfall amounts are inaccurate, i.e., that the high 2004 Z-scores are actually caused by rainfall located just outside of the study region, and thus that the observed landsliding actually occurred in response to less extreme local rainfall than is suggested by the larger-scale Z-score anomaly. In the absence of higher resolution long-time series data, it is challenging to quantify whether such inaccuracy exists, but it is an issue that should undoubtedly be considered when interpreting the results.

Overall, whilst it remains unclear exactly why 2004 did not observe a landslide response, this analysis does show that the perturbations in 1993, 1995 and 2002 all coincide with years that experienced rainfall Z-scores > 12 , suggesting that this is a threshold for which significant landsliding can be induced. As such, from both a hazard management and long-term erosional potential perspective, it would be useful to know the return periods of such events. From the ASM-normalisations (Figs 5.4a – b), two extreme rainfall-induced landslide anomalies occurred over a 30-year period, suggesting that across the entire study region, such landslide perturbations have return periods of ~ 15 years. Furthermore, based on the full 64-year time series of APHRODITE rainfall data, the return periods across the entire study region of rainfall events capable of causing these perturbations (Z scores > 12 and > 16) are found to be 5 – 30 years (15 and 2 events recorded over 64 years).

However, all of the result presented here pertaining to extreme rainfall should be interpreted cautiously, as whilst high Z-scores generally coincide with a landslide perturbation, the specific relationship between Z-score magnitude and landslide perturbation magnitude is inconsistent. For example, the 1993 landslide perturbation is the largest, but has smaller Z-scores than 2002 and 2004, the latter of which did cause a significant regional-scale landslide perturbation. The most likely explanation for this is inaccurate or misallocated rainfall values. As mentioned above, many of the rainfall cells impacted by the 1993, 2002, and 2004 events (e.g. cells 9, 10, 11, 20, 21; Fig 5.7) occurred across the boundary of our study region so it is possible that the true rainfall amounts are inaccurate. I.e., that the high 2004 Z-scores relative to the landslide response are actually caused by very high rainfall located just outside of the study region, or the lower 1993 Z-scores relative to the landslide response were due to anomalously low rainfall located just outside of the study region, which decreased the Z-score average for that cell. Another potential explanation is a sub-optimal quantification of the extreme. The daily Z-score approach is fairly simplistic and, as described above, does not consider consecutive vs distributed rainfall. Therefore, future work could consider a more detailed consideration of the extreme quantification (e.g. systematically looking at Z-scores across 2, 3, or 5 day bins) to assess whether the relationships found here between Z-

scores rainfall anomalies and landslide perturbations can be refined. Finally, another source of uncertainty is the disparity between the regional-scale normalisation used to identify major perturbations, and the localised nature of extreme rainfall. As highlighted above, even though the 2004 storm did not induce enough landsliding to produce a landslide perturbation significant at the regional scale (in contrast to 2002 and 1993), the local cells impacted by the 2004 storm did observe some significant (> 100%) increases in landsliding relative to those cell's averages in a non-perturbed year. As such, future work could attempt to repeat the normalisation approach used here at the regional scale for specific grid-cell(s) that experienced storms, and thus refine the relationships between extreme rainfall and landsliding.

5.3.4 Impacts of earthquake preconditioning

There are two main processes through which large magnitude ($> M_w$ 6.0) earthquakes can impact landsliding (Malamud *et al.* 2004b; Hovius *et al.* 2011; Francis *et al.* 2020). First, large magnitude earthquakes can trigger coseismic landslides that can be remobilised by subsequent rainfall or other exhumation events (Malamud *et al.* 2004b; Hovius *et al.* 2011; Dahlquist & West 2019). Second, earthquake strong ground motion can induce landscape damage that induces enhanced rates of new post-earthquake landsliding (Marc *et al.* 2015, 2019); a process termed earthquake preconditioning (Parker *et al.* 2015). Earthquake preconditioning has been observed following multiple earthquakes in different geomorphic settings. For example, the 1999 ChiChi earthquake in Taiwan caused a 2 – 5 year factor of 10 increase in subsequent typhoon triggered landsliding (Marc *et al.* 2015), whilst the 1929 Buller earthquake in New Zealand led to enhanced coseismic landsliding during the partially coincident 1968 Inangahua earthquake (Parker *et al.* 2015). Similarly, the 25th April 2015 M_w 7.8 Gorkha earthquake, which occurred just prior to the onset of the 2015 monsoon season, has previously been estimated to have caused a factor of 4 – 8 increase in new monsoon-triggered landsliding during the 2015 monsoon season (Marc *et al.* 2019). However, the full timescale of 2015 preconditioning remains unconstrained as, until now, it has not been possible to isolate the earthquake preconditioning impacts from the monsoon in 2016 – 2018. This is problematic, as the potential timescales of earthquake

preconditioning represents a major area of current uncertainty, a better understanding of which could inform landslide hazard modelling and management post-earthquake.

Here, the normalisation using the PERSIANN-CDR data (Fig. 5.4a) allows for the impacts of the 2015 earthquake and monsoon to be separated, providing further insight into the magnitude and timescales of the 2015 preconditioning. In 2015, the normalisations with both PERSIANN and APHRODITE corroborates previous results (Marc *et al.* 2019), showing that all measures of landsliding were perturbed above that expected given the monsoon strength, with “New + RR” landsliding (which comprises new landslides, reactivations, and remobilisations) perturbed by a factor of 3.8 – 6.2 and “New Only” landsliding (where reactivations and remobilisations are excluded) perturbed by a factor of 2.4 – 4.6 (Fig. 5.4a - b). In 2016, “New + RR” landsliding was still perturbed by a factor of 2.4 – 2.7, but the “New Only” rate was within +1SD of the normal (Fig. 5.4a). In 2017 and 2018, both “New + RR” and “New Only” rates were back within +/- SD of the normal (Fig. 5.4a).

These results provide important insight into the timescales of both the remobilisation of coseismic material and of earthquake preconditioning associated with the Gorkha earthquake. For earthquake preconditioning, enhanced rates of new landsliding are only observed in 2015, with new landsliding in 2016 back to within +1 SD of that expected given the monsoon forcing. This suggests that the Gorkha earthquake preconditioning lasted for only 5 – 14 months, i.e., up until the start of the 2016 monsoon season. This timescale is slightly shorter than the 2 – 5 year preconditioning period observed in Taiwan following the ChiChi earthquake (Marc *et al.* 2015), but similar to the observations of Dahlquist & West (2019) and Marc *et al.* (2019), who found that extra rainfall induced debris flows and landslides in Nepal following the Gorkha earthquake were anomalous in 2015 only. Furthermore, this time-scale matches the hydrogeological recovery period observed from geophysical investigations following large magnitude earthquakes (Marc *et al.* 2021), which could provide a mechanism to explain such a rapid recovery. This ~1 year timescale observation is also similar, though slightly shorter, to the timescale of recovery quantified by Kinsey *et al.* (2021), who found that when considering the occurrence

of new landslide activity only, the landscape returned to pre-Gorkha earthquake levels within just a few years. For the remobilisation of coseismic material, enhanced rates of landsliding when including remobilisations and reactivations continues into 2016, but not 2017, suggesting a recovery time of 17 – 24 months. This 1.5 – 2 year recovery time following the Gorkha earthquake is shorter than the 6 – 8 year time period over which anomalous fluvial sediment export, which likely includes both new and remobilise material, was observed following the 1999 ChiChi earthquake (Hovius *et al.* 2011). Similarly, the recovery measured here is shorter than that observed by Kincey *et al.* (2021) in Nepal following the Gorkha earthquake, who found that landslide activity remained more active than pre-earthquake levels into 2018. The difference between these timescales is likely because the ASM-landslide inventory used in this thesis only identifies large-scale remobilisations and reactivations, whereas measures of fluvial sediment export are much more sensitive to small scale changes that would not be visible at the resolution mapped here. Likewise, the high-resolution, more targeted mapping of Kincey *et al.* (2021) will have encapsulated much smaller-scale reactivations and remobilisations that are likely to have continued for a longer period post-earthquake. However, the observation in this thesis that remobilisation continued into 2016 does corroborate the results of Dahlquist and West (2019), who also observed substantial remobilisation of Gorkha coseismic material during the 2016 monsoon season. The APHRODITE-based normalisation also identifies a perturbation in 1989. The 1989 monsoon season was the first full monsoon season following an M_w 6.9 earthquake that occurred on 21/08/1988. In this case, both the earthquake preconditioning perturbation (“New Only” rate) and increase in reactivations and remobilisations (“New + RR” rate) are observed in 1989 only, suggesting a recovery period for these processes of no more than 13 – 20 months, i.e. similar to that observed for both Gorkha and ChiChi.

The normalisation analysis in this chapter provides insight into short-term Himalaya preconditioning of the type observed by Marc *et al.* (2015), and suggests that both the 1989 and 2015 monsoon seasons were impacted by short-term earthquake preconditioning. However, whilst this study and others have quantitatively

constrained the magnitudes and timescales of short-term earthquake preconditioning, the causative processes and mechanisms of this process remain uncertain. It has been proposed that short-term preconditioning occurs via earthquake damage that impacts both the mechanical and hydrogeological properties of the near surface (e.g. Marc *et al.* 2021) and is rapidly exploited by subsequent rainfall as new failures (Marc *et al.* 2015). However, what controls the spatial distributions of this damage remain speculative.

Here, as outlined in section 5.2.4, excess 2015 monsoon-triggered landsliding is combined with USGS ground motion data for the Gorkha earthquake and topographical data for the study region to examine how the excess landsliding observed in 2015 relates to Gorkha earthquake PGA and landscape topography. Fig. 5.8a shows the correlation between 2015 excess landsliding and summed maximum PGA for the 2015 main shock and largest aftershock, whilst Fig. 5.8e shows the same correlation but with the PGA values multiplied by excess topography above a threshold angle of 45°. Fig 5.9 shows the PGA of the Gorkha earthquake main shock, the epicentres of the main shock and largest aftershock, and the 2015 ASM-landsliding.

Interestingly, this shows that there is no correlation ($R^2 = 0.08$) between excess 2015 landsliding and PGA alone (Fig. 5.8a), but that the correlation becomes significant ($R^2 = 0.71$) when PGA is weighted by excess topography (Fig. 5.8e). It should be noted that this result was consistent across all excess topography thresholds (see Appendices Ja - d), but with a slight increase in R^2 as the threshold increased from 25 – 45°. This result was also consistent when only summing PGAs > 0.1 and 0.2 g, though with lower R^2 values (see Appendices La – b and Ma - b). These PGA values have been identified as thresholds which must be exceeded for landslides to be induced (Meunier *et al.* 2007), however, these results suggest that lower PGA values can still contribute to preconditioning, even if not directly triggering coseismic landslides. Overall, this analysis suggests that short-term earthquake preconditioning damage is concentrated where PGA and high excess topography are coincident. This is an important and novel result and could allow for more accurate prediction of where and how much landscape preconditioning should be expected

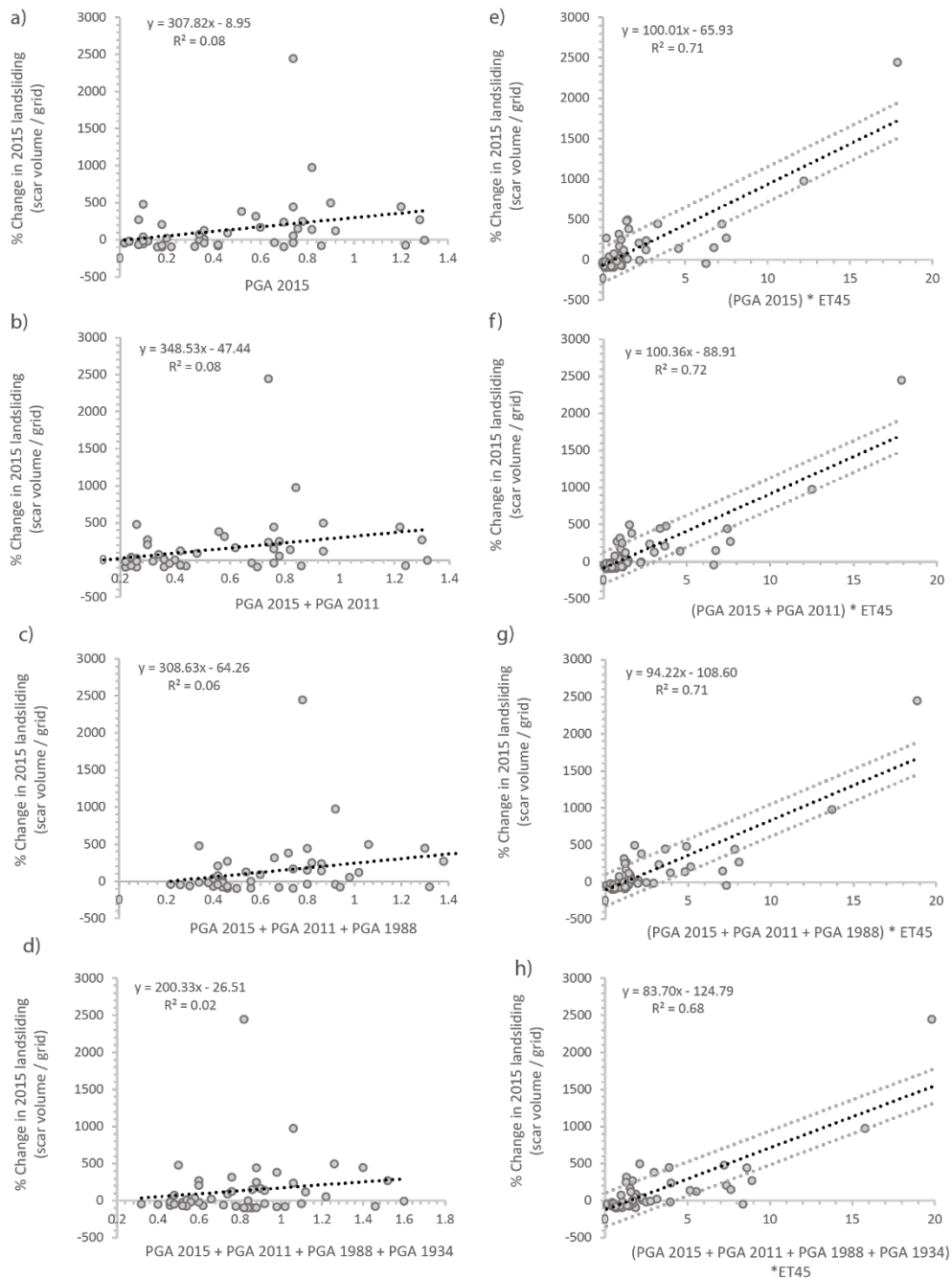


Figure 5.8. Correlations between maximum summed PGA and excess monsoon-triggered 2015 landsliding for a) PGA in the 2015 main shock and largest aftershock. b) the summed PGA from a) plus the PGA from 2011. c) the summed PGA from b) plus the PGA from 1988. d) the summed PGA from c) plus the PGA from 1934. e – f) show the same correlations as a – d) but this time with summed PGAs multiplied by excess topography above a threshold angle of 45°. The linear best-fits are shown with +/- 1 standard error in each case.

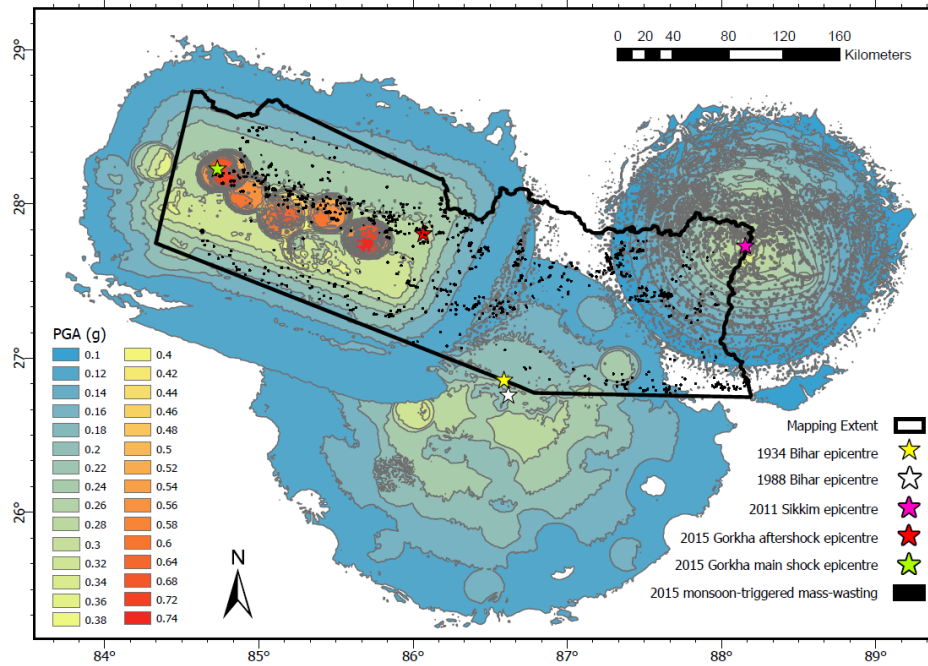


Figure 5.9. Map showing the 2015 ASM-landsliding and the epicentres of the 2015 Gorkha earthquake main shock, Gorkha earthquake largest aftershock, 2011 Sikkim earthquake, 1988 Bihar earthquake, and 1934 Bihar earthquake. The PGA distributions of the 2015 Gorkha earthquake main shock, the 2011 Sikkim earthquake, and the 1988 Bihar earthquake are also shown.

following a given magnitude earthquake. However, it should be noted that a similar relationship was not observed for the 1988 earthquake (see Appendix N). Reasons for this anomaly could be: 1) The 1988 earthquake had much lower PGAs than 2015 (a maximum of 0.28g in 1988 compared to >0.74g in 2015); 2) The region impacted by the 1988 event was to the south of our study region (see Fig. 5.9), where excess topography values are low, or 3) The 1989 perturbation was also contributed to by rainfall. Despite not having Z-scores as high as observed in 1993 or 2002, 1989 did observe higher Z-scores than 2015 (scores of 10, compared to 8). As described previously, reason 3 had already been discounted due to the relatively low Z-scores in 1989. However, it is possible that the impact of the earthquake caused a temporary reduction in the extreme rainfall required to induce a perturbation. This result is consistent with studies such as Shieh *et al.* (2009), Yu *et al.* (2014), and Zhou & Tang (2014) who show that reduced rainfall thresholds are required for landslide-

triggering following earthquakes. As such, it is tentatively suggested that the 1989 perturbation is due to a combination of both the earthquake and rainfall.

Whilst this analysis provides good insight into short-term earthquake preconditioning in the Himalaya, it does not consider any decadal scale preconditioning as was observed in New Zealand (Parker *et al.* 2015). Longer-term preconditioning is less frequently observed than the short-term, and could be caused by deeper bedrock damage that takes longer to be exploited by subsequent landsliding drivers. Such deep damage should be exploitable by rainfall, if less rapidly exploited than shallow damage would be, since rainfall is known to be capable of inducing deep-seated landslides (Marc *et al.* 2018, 2019). Furthermore, in New Zealand, it was observed that coseismic landslides associated with the 1968 M_w 7.1 Inangahua earthquake occurred at greater rates where the landscape was likely damaged by the earlier 1929 M_w 7.7 Buller earthquake. This suggests that lasting landscape damage due to the earlier event was compounded by the second event. Here in Nepal, it was investigated whether the 2015 monsoon-triggered perturbation was similarly affected by any long-term damage from early earthquakes that may have been compounded by the 2015 Gorkha earthquake. The study region is coincident with the rupture zones of several $> M_w$ 6.0 earthquakes over the past century (1934 M_w 8.0, 1988 M_w 6.9, 2011 M_w 6.9), so is well placed to investigate whether these earlier earthquakes had any impact on monsoon-triggered landsliding following the 2015 earthquake, and thus provide much needed insight into longer-term modes of preconditioning.

To test whether these earlier events contributed to the 2015 monsoon-triggered perturbation, the PGA-excess topography correlations are repeated, but this time cumulatively including the summed USGS-estimated PGA for 2011, 1988, and 1934 (USGS 2018b, a, d; see Fig 5.9 for the epicentres of all of these earthquake events, and the PGA for 2011 and 1988). These results, with PGA alone and PGA multiplied by excess topography at a threshold of 45° , are shown in Fig. 5.8b - h (for landslide correlations of these earthquake PGAs with other excess topographies, and at PGA thresholds > 0.1 and 0.2 , see Appendices J - M). If these events had a lasting legacy affect that significantly compounded the Gorkha earthquake damage, it is expected

inclusion of their PGAs would improve the fit observed between 2015 ASM-landsliding and PGA-excess topography.

However, the inclusion of 2011 PGA causes a non-significant change in the R^2 from 0.71 – 0.72 (Fig. 5.8b, f), whilst including the PGA from 1988 and 1934 actually worsens the fit (Fig. 5.8, c – d, g – h). There is thus no evidence to support that any of the past earthquakes had an impact on the distribution of the 2015 monsoon-triggered landsliding. There are several potential explanations for this. One, the time since these events is simply too long, and any damage caused by them has already been exploited. The 1934 event occurred 81 years before Gorkha, a period twice as long as the 39 years between the earthquakes in New Zealand. Two, the magnitudes of these events were too small to induce wide scale landscape damage. This explanation is less likely, as the results clearly show that the 2015 event induced damage, and the 1934 event was of a greater magnitude than 2015 (Sapkota *et al.* 2016). However, it is important here to note the distinction between earthquake magnitude and intensity, with the former being a measure of earthquake size, and the latter being a measure of the actual degree of shaking felt on the ground at a given place. As such, it is also important to consider how the earthquake intensities differed for these earthquake events, and whether this could explain why the earlier earthquakes did not impact the 2015 event. One common measure of earthquake intensity is the European Macroseismic Scale (EMS-98), which semi-quantitatively describes earthquake intensities across 12 levels based on observed impacts, where a value of 1 equates to shaking not felt and a value of 12 equals all structures destroyed. A series of papers by Martin & Szeliga (2010), Martin & Hough (2015) and Martin *et al.* (2015) estimate EMS-98 distributions for all four of the earthquakes of interest. These show that the maximum EMS-98 intensities in 1988 and 2011 were 8 and 7 respectively, with averages across the study region of 5 – 6 (Martin & Szeliga 2010; Martin & Hough 2015). In contrast, the 2015 Gorkha earthquake had maximum intensities of 9, with an average of 6 – 8 across the study region, whilst the 1934 earthquake had significant areas experiencing intensities of 9, with most of the study region observing intensities of 7 – 8 (Martin & Szeliga 2010; Martin *et al.* 2015). As such, as with the magnitudes, intensities alone cannot explain why the 1934 event

did not impact the landscape in 2015, as the 1934 event had more widespread high intensities than were observed in 2015. Three, these events were too far from the region impacted by Gorkha for any significant damage to overlap. This is the most likely explanation, as despite being of a magnitude that should be capable of inducing landscape damage, both the 1934 and 1988 events occurred in southern Nepal, with epicentral regions that did not significantly overlap with the main zones of ground motion that occurred in 2015.

5.4 Conclusions

In conclusion, by quantifying a previously unknown empirical relationship between ASM-strength and total landsliding, landslide perturbations 2 – 6.5 times higher than the ASM background caused by extreme rainfall events and the 2015 Gorkha earthquake landscape preconditioning have been isolated and investigated. Specifically, extreme (Z -score > 12) rainfall events with 5 – 30-year return periods are found to be capable of inducing 15-year return period landslide perturbations that are 2 – 6 times higher than the ASM background. However, it should be noted that due to possible rainfall data inaccuracy and misallocation, these results are somewhat uncertain, and future work should involve investigation into how the Z -score – landslide perturbation relationships can be refined (e.g., by considering consecutive days of rainfall, or by undertaking more local-scale normalisation analysis). The 2015 perturbation, which was 2.5 – 6 times higher than the ASM-background, is found to be controlled by short-term landscape preconditioning induced by the 2015 Gorkha earthquake, the signature of which is controlled by the combination of PGA and excess topography. This is a novel result that should allow for more accurate quantification and forecasting of expected increases in landsliding due to landscape preconditioning following large magnitude earthquakes. Finally, it is found that earlier large magnitude earthquakes in 1934, 1988 and 2011 have not compounded the 2015 preconditioning, suggesting that longer term preconditioning damage as observed in New Zealand was not a major driver of landsliding in this case.

Finally, the results and discussion presented in this Chapter have significant implications for landslide hazard. First, as highlighted by Kirschbaum *et al.* (2020), there remain large uncertainties in predicting how climate change may affect landsliding over the Himalaya. The results presented here contribute to reducing this uncertainty, as, when combined with possible ASM-strength scenarios under future climate change conditions (e.g. Douville *et al.* 2000; Hu *et al.* 2000; May 2002; Annamalai *et al.* 2007; Turner & Annamalai 2012), the empirical relationships between ASM-strength and landsliding can be used to provide quantitative assessments of expected changes in ASM-triggered landsliding across the Himalaya. Furthermore, if future climate change scenarios suggest an increase in the occurrence of the 5-year and 30-year return period extreme rainfall events observed here (Kripalani *et al.* 2007; Karki *et al.* 2017), then significant landsliding perturbations such as those in 1993 and 2002 could become more frequent, thus contributing increasingly to overall landsliding relative to other drivers. These results also have wider implications for landslide susceptibility modelling, which are discussed in detail in Chapter 6.

Chapter 6 Implications for BLR-type susceptibility modelling and overall conclusions

6.1 Summary of thesis main objectives and results

The aim of this thesis is to quantify the spatiotemporal characteristics, preconditioning and susceptibility of landslides in central-eastern Nepal. The objectives and results of this thesis, as presented in Chapters 2 – 5 are summarised below:

1) The first objective was to develop a new, multi-temporal, 30-year inventory of ASM-triggered landslides across central-eastern Nepal. This was completed, with a 30-year (29 time slice) multi-temporal inventory of 12,838 – 12,920 ASM-triggered landslides developed. As well as facilitating the analysis conducted in all subsequent chapters, this inventory has been made freely available, with the polygon inventory of 12,838 landslides (Data File 1) accessible [here](#), and the slightly updated inventory of 12,920 landslides (Data File 5) accessible [here](#). These inventories thus provide an important resource to geomorphologists, geohazards practitioners, and local stakeholders.

2) The second objective was to assess the overall (space and time independent) geometries, spatial associations, sizes, spatial distributions, and susceptibilities of the ASM-triggered landslides to provide insight into landslide processes in the Himalaya. This objective was also completed, with analysis of the ASM-inventory revealing several insights into the characteristics and processes of monsoon-triggered Himalaya landslides. Notably, 14% of the ASM-triggered landslides exhibit path-dependence, with these landslides being on average larger and more elongated than non-path dependent landslides. Furthermore, landslide runout is found to be limited by local relief, with higher Aspect Ratio (AR) landslides having larger average

sizes and occurring at higher elevations, higher local reliefs, and further from channels. Landslide size is also found to be on average largest in the Greater Himalaya. This is likely because landslide size is controlled by the coincidence of extreme topography and strong bedrock, with an observed positive correlation between rock strength and landslide area, and a negative correlation observed between rock strength and the scaling exponent of power laws fitted to the probability density functions of landslide area.

3) The third objective was to use additional field data from two sub-regions with distinctly different landscapes (Langtang Valley and the Arniko Highway) to provide insight into how landslide characteristics, types, processes, and distributions vary spatially. Specifically, the objective was to use this additional field data alongside an inventory of coseismic landslides to assess how spatial heterogeneity impacts BLR landslide susceptibility modelling. This objective was intended to answer specific questions such as: how well can susceptibility models developed from one region be used to forecast or hindcast another, how well do regional models forecast or hindcast local regions, and thus, is it appropriate to undertake regional scale susceptibility modelling without considering spatial heterogeneity?

This objective was successfully completed, with the regression modelling from Chapter 3 expanding the spatial heterogeneity observations from Chapter 2, showing that there were significant differences between the landslide controls in Langtang and Arniko. It is concluded that the differences in landslide occurrence and susceptibility between the two regions is largely due to glacial and periglacial processes such as permafrost degradation, which is coincident with heightened landslide activity in Langtang. The regression modelling from Chapter 3 also highlighted that the spatial heterogeneity between landslide controls observed in Langtang and Arniko does influence typical landslide susceptibility modelling approaches. Specifically, it was found that susceptibility models developed from one region are not necessarily sufficient for predicting another region, whilst regional scale models were less accurate at predicting the sub-region localities compared to the local-scale models. This suggests that it is sub-optimum to undertake regional scale modelling without considering spatial heterogeneity.

Furthermore, the field observations of landslide types (see Chapter 3) allowed for some preliminary discussion into how landslide type impacts the interpretation and use of susceptibility maps. Specifically, it is observed that different landslide types have different relationships with landslide predisposing factors and are typically mitigated using different strategies. As such, if a BLR susceptibility model is developed using a landslide inventory with multiple different landslide types, then the resulting regression coefficients will not be optimised for specific landslide types, but will instead be an average across all landslide types. Furthermore, such models will not necessarily indicate which landslide types are present in a given high susceptibility region, therefore inducing uncertainty into the most appropriate mitigation response. As such, it is concluded that susceptibility models/maps produced here and elsewhere should always be combined with detailed field information on landslide type and process. In other words, landslide susceptibility maps should be used to preliminarily identify zones of high susceptibility, which can then inform where more detailed investigation into landslide type and process is needed before mitigation strategies are designed. Finally, further work that is considered beyond the scope of this thesis would be to conduct susceptibility modelling by landslide type to assess the differences in zones of susceptibility and in the controls of predisposing factors.

4) The fourth set of objectives were to quantify how landslide processes and occurrence varies through time. Specifically, a) to investigate the characteristics of landslide path dependency; b) to assess whether ASM-triggered landslide spatial distribution vary through time, particularly in response to extreme events; c) to quantify the impacts of any observed temporal variation on the predictive (or hindcasting) power of BLR susceptibility modelling; and d), to investigate how the choice of landslide data used to train a model (i.e. event vs historical inventories) influences the accuracy and consistency of susceptibility modelling.

This set of objectives was successfully completed. It was found that path dependency does influence landsliding in the Nepal Himalaya, with landslides occurring in locations impacted by past landslides at greater rates than would be expected if their distributions were random. The spatial distributions of monsoon-triggered

landslides were found to vary significantly through time, particularly in response to cloud outburst storms in 1993 and 2002, flooding in 2017, and 2015 Gorkha earthquake preconditioning. These variations have significant impacts on BLR susceptibility modelling, with models trained on these extreme years unable to consistently forecast or hindcast the landslide occurrence in other years with sufficient accuracy. Using at least 6 – 8 year length historical inventories is found to make susceptibility models more consistently accurate when applied through time.

5) The fifth set of objectives were to investigate how the rates and drivers of landsliding in the Himalaya vary through time. Specifically, 1) to calculate an empirical relationship between ASM-strength and landsliding before using this to isolate and quantify the relative landslide impacts of the ASM, extreme rainfall and earthquake preconditioning; 2) to use this information to determine whether earthquake preconditioning is occurring in the Himalaya and, if so, to provide novel insight into its timescales, magnitudes and causes.

Again, these objectives were accomplished. Empirical relationships between ASM-strength and landsliding were defined, from which it was found that extreme rainfall events and earthquake preconditioning cause landslide perturbations 2 – 6.5 times higher than the ASM background rate. Specifically, 4-year and 30-year return period rainfall events are found to be capable of inducing landslide perturbations 2 – 6 times higher than the ASM background. Furthermore, the landscape takes time to recover from such perturbations, with extreme rainfall in 2004 not inducing a perturbation due to its coincidence with the perturbation in 2002. The 2015 perturbation, which was 2.5 – 6 times higher than the ASM-background, is found to be controlled by short-term landscape preconditioning induced by the 2015 Gorkha earthquake, the signature of which is controlled by the combination of PGA and excess topography.

6.2 Implications for BLR susceptibility modelling

The final objective of this thesis is to discuss the implications of the above results on the applicability and accuracy of BLR susceptibility models. As outlined in the introduction and throughout this thesis, BLR methods are the most commonly used in the literature for assessing landslide susceptibility. As such, it is particularly

important to assess and challenge commonly held assumptions associated with this methodology, and to discuss ways in which the application of this methodology could be improved. As such, the following section first uses the results of chapters 2 – 5 to outline the main limitations of typical BLR susceptibility modelling approaches. Then, the results of this thesis and the wider literature are used to discuss potential solutions to these limitations, before an overall framework is proposed for achieving best practice when conducting regression-based susceptibility modelling.

6.2.1 Limitations: spatial and temporal heterogeneity

As outlined in section 6.1, the results from Chapters 2 and 3 highlight that there is significant variation in landslide occurrence between tectonic units in Nepal, largely associated with spatially varying processes relating to geology, topography and climatic factors (e.g. local relief / geology controlling landslide runout and size [see Chapter 2, sections 2.7.2 and 2.7.3], and permafrost and deglaciation controlling landscape susceptibility to landsliding [see Chapter 3, section 3.5.2]). This spatial heterogeneity is observed to have a clear impact on typical BLR susceptibility approaches, with models from one locality unable to hindcast another locality, and regional scale models being sub-optimal for local hindcasting (see Chapter 3, sections 3.4.5 and 3.5.3).

Similarly, Chapters 4 and 5 highlight that there is significant temporal heterogeneity in landslide processes and occurrence, particularly associated with landslide path dependency (see Chapter 2 section 2.7.1, and Chapter 4 sections 4.3.1 and 4.4.2), extreme event occurrence (see Chapter 4, section 4.4.3), and earthquake preconditioning (see Chapter 5, sections 5.2.4 and 5.3.4). This also has a clear impact on typical BLR susceptibility approaches, with models trained on single years of data unable to consistently and reliably forecast or hindcast other years.

Typically, spatial and temporal heterogeneity in landslide susceptibility modelling is considered independently. For example, studies by Chalkias *et al.* (2020) and Yang *et al.* (2019) only consider spatial heterogeneity in landslide susceptibility, whilst studies by Meusburger & Alewell (2009) and Knevels *et al.* (2020) only consider temporal issues. However, the observations made across this thesis highlight that

modelling limitations relating to both spatial and temporal heterogeneity in landslide occurrence are actually caused by the same problem: process blind modelling.

In the case of spatially varying landslide-affecting processes, problems arise when attempting to apply BLR models developed from one region, with one set of processes, to another region with a different set of processes. For example, in the case of Langtang Valley and the Arniko Highway, one region was impacted by processes relating to permafrost and deglaciation, and the other was not. Consequently, the BLR models developed for Arniko were essentially blind to the periglacial processes, and the models developed for Langtang were blind to the specific fluvial processes occurring in Arniko. Consequently, the two models were incapable of accurately predicting the other region. Likewise, the coseismic BLR model developed at the regional scale, which essentially calculated an average response across the entire study region, was blind to any atypical, location-specific processes such as permafrost degradation/deglaciation. Consequently, this model could not hindcast landslide occurrence in local regions with as much accuracy as was obtained by models developed at the local scale. Similarly, in the case of temporal variability, the results from Chapter 4 show that extreme events (storms, floods and earthquake preconditioning) can trigger landslides with transiently atypical landslide distributions that leads to the development of BLR models that cannot accurately forecast or hindcast time periods with different landslide distributions. Overall, this highlights that if you are blind to the occurrence of any spatially or temporally varying process, or are aware of these but have been unable to account for them, then using space-time independent regression-based models to forecast another year's landslide occurrence may be inappropriate.

6.2.2 Potential solutions

So what are the solutions to the problem of spatial and temporal heterogeneity affecting space-time independent BLR modelling? Based on the results from this thesis and the wider literature, it is suggested that there are five possible solutions that are outlined and discussed below.

1) The simplest solution would be to only use space-time independent BLR modelling if you are confident that the landslides used to develop a susceptibility model are affected by the same processes as any landslides aimed to be predicted by that model. In other words, you are aware of any potential spatially / temporally varying processes (i.e. no longer process blind) and apply developed susceptibility models accordingly.

For example, this could involve only conducting basic BLR susceptibility modelling at a local scale, where there is high confidence that landslide processes are spatially homogenous. Such a local-scale approach can also be used to develop regional scale models, by simply subdividing a larger region into geomorphologically coherent zones, and developing models for each zone separately. This approach is not uncommon, for example, Bălteanu *et al.* (2020) developed a national scale landslide susceptibility map for Romania by using expert knowledge to partition the country into several local-scale homogenous units that were each modelled separately. Likewise, Günther *et al.* (2014) developed a pan-European landslide susceptibility model by subdividing the region into seven climate-physiographic zones that could each be considered separately. This approach can also be used through time. For example, as shown in Chapter 4, by only applying a storm-impacted year to another storm-impacted year, or a confirmed “normal monsoon” year to another “normal monsoon” year. In essence, this solution is to only develop and apply basic BLR susceptibility models between regions / time where you are certain there will be no process-change between the landslides used to develop a model, and the landslides aiming to be predicted by the model.

2) Another solution would be to always ensure that any potential spatially or temporally heterogeneous landslide processes are investigated, and where necessary quantitatively characterised as independent control factor variables to be included within a BLR model.

For example, Knevels *et al.* (2020) use temporally varying meteorological and land use variables within a binary Generalised Additive Model (GAM) for assessing rainfall triggered landslide susceptibility in Austria. Likewise, studies by Pisano *et al.*

(2017), Reichenbach *et al.* (2014), Schmaltz *et al.* (2017) and Torizin *et al.* (2018) also use temporally varying land use as a variable within landslide susceptibility assessment. More recently, this approach has been used by of Samia *et al.* (2020, 2018), who robustly quantify landslide path dependency before using this information to develop logistic regression models that include independent variables that characterise the path dependency process. They do this using a variety of metrics, which includes characterising path dependency using regionally calibrated time-decay equations (Samia *et al.* 2018) and Ripley's space-time K function (Samia *et al.* 2020). Irrespective of the method and scale used to quantify and include path dependency, inclusion of this process as an independent variable within a regression model was found to outperform conventional time-space independent regression-based susceptibility models.

In theory, the approach taken by Samia *et al.* (2020, 2018) could be replicated for any known spatially or temporally heterogeneous process that influences landslide occurrence. However, this of course requires that any such spatial/temporal processes are known (i.e. you are not blind to them), and that they can be characterised into a meaningful independent variable that can be included in a BLR model. In this context, many of the results of this thesis take on a new significance. For example, this thesis extends the work of Samia *et al.* by showing that path dependency is a process occurring in the Nepal Himalaya, and thus that we should not be "blind to" this process when it comes to susceptibility modelling. Furthermore, the results from across Chapters 3, 4 and 5 show that there are multiple other landslide-affecting processes that vary through space and time, from permafrost degradation, to extreme event occurrence to earthquake preconditioning. Not only does this work ensure we are not blind to the occurrence of these processes, but, in some cases, it provides novel insight into how these processes could be considered as independent variables within a BLR model. For example, the results and analysis pertaining to the causes of earthquake preconditioning led to the novel result that earthquake preconditioning occurs where Peak Ground Accelerations (PGAs) are coincident with high excess topographies. Likewise, the observations from Chapter 3 show that the interplays

between PFI, elevation, time, and deglaciation relate to landslide occurrence, whilst the results from Chapter 5 highlight empirical relationships between rainfall (monsoonal and storm) and rates of landslide occurrence. In all of these cases, the results from this thesis provide a starting point from which these spatially and temporally varying processes can be characterised, and thus facilitate investigation into whether the inclusion of these processes as independent variables can improve the applicability and accuracy of BLR-type susceptibility models. However, identifying and characterising spatially and temporally heterogeneous processes often requires significant amounts of available landslide data, particularly multi-temporal data. For example, path dependency in Italy required ~60 years of landslide data to observe and fully quantify (e.g. Samia *et al.* 2017a, 2017b). Likewise, in this thesis, earthquake preconditioning was only quantifiable as the 30-year ASM inventory allowed the development of empirical relationships between ASM-strength and landsliding, which earlier studies with shorter time series of data were unable to do (e.g. Marc *et al.* 2019). Consequently, it is necessary to consider further solutions to this problem for cases where fully quantifying spatially and temporally varying processes is not possible.

3) The third potential solution to this problem is to always use multiple inventories for the development of space-time independent BLR models. In the literature, it is very common for BLR models to be developed using landslide inventories developed from only a single event, region or time period (e.g. Griffiths *et al.* 2002; Kumar *et al.* 2008; Prakash *et al.* 2013; Sifa *et al.* 2020; Xu *et al.* 2013). However, as shown by the results in Chapter 4, issues of temporal heterogeneity were improved when at least 6 – 8 years of landslide data were used to develop a BLR model, even when those models were still process blind (i.e. models from a year impacted by one process were used to model years impacted by other processes). This solution is corroborated by other studies. For example, Ozturk *et al.* (2021) find that the AUROC success of BLR models increases as the number of time periods of landslide data increase, whilst Knevels *et al.* (2020) also advocate the use of landslide data from combined events for better prediction. Similarly, Kritikos *et al.*, (2015) found that for the spatial

application of fuzzy logic methods, using two inventories from different locations allowed accurate modelling of landslides in a third location.

The likely reason for this approach working is that using several time periods or regions of landslide data saturates out the influence of any anomalous or atypical landslides associated with some transient spatial or temporal process. However, as described previously, this averaging of landslide occurrence can be a problem in itself, as it can cause local regions / specific time slices to be poorly predicted if those do not conform to the average. For example, one case from Chapter 4 showed that the BLR models developed using more data were actually increasingly less able to forecast landsliding in 2017. As such, this approach should be used with the vital caveat that all endeavour must be made to identify potentially landslide-affecting processes, and that this approach should ideally only be used to forecast or hindcast similar regions or times periods (i.e. as describe in solution 1). Finally, another potential issue with this approach is that it still requires several years / periods of landslide data. So, despite likely requiring less data than solution 2, its use may be restricted in data-scarce locations.

4) The above solutions all retain the fundamental use of binary regression-based space-time independent susceptibility models. As outlined in Chapter 1, this model type was the focus of this thesis as it remains the most commonly applied method used in the literature. However, the results from this thesis suggest that typical BLR type models may be insufficient for modelling spatial and temporal heterogeneity, and thus that it is necessary to move to other (still regression-based) approaches that allow modelling to be space and/or time dependent. This suggestion follows a growing number of similar recommendations in the literature (e.g. Gorsevski *et al.*, 2006; Lombardo *et al.*, 2020; Meusburger & Alewell, 2009; Ozturk *et al.*, 2021). As such, the following sections outline some key examples of regression-based susceptibility modelling techniques that are spatially or temporally dependent.

4.1) Spatially Weighted Regression (SWR)

Spatially Weighted Regression (SWR) introduces spatial dependency by weighting the regression coefficients of each independent variable based on geographical

location (Wheeler & Páez 2010). Such weighting techniques have been used with some success in the landslide literature. For example, Chalkias *et al.* (2020) use locally weighted logistic regression models to calibrate a global landslide susceptibility model, whilst Feuillet *et al.* (2014) use weighted regression modelling to show that paraglacial landslide controls vary significantly through space, and thus that weightings are important for modelling over heterogeneous or global regions. Similarly, Yang *et al.* (2019) develop a factor selection and weighting process called “GeoDetector” that selects and weights independent landslide control factors based on the assumption that the spatial distributions between the independent variable and the dependent variable should be similar from pixel to slope unit scale. They then combine these weights with a typical logistic regression approach to develop final susceptibility models, finding that the spatially weighted models perform better than the non-weighted models (AUROC value of 0.93 compared to 0.79). Likewise, Erener & Düzgün (2012) apply geographically weighted regression techniques in Norway, finding that the spatially dependent regression models outperform typical spatially independent models.

4.2) Spatial and temporal latency

An increasingly common approach to dealing with spatial and temporal heterogeneity in landslide susceptibility is the exploitation of model error, deviation and latency. One of the earliest examples of this is a study by Meusburger & Alewell (2009), who use the deviation in susceptibility between maps developed from two time periods to better forecast a third, future, time period. Specifically, they develop two space-time independent regression-based susceptibility models for landslides in the Central Swiss Alps in the years 1959 and 2000. These models are found to have good accuracy when predicting landslides from the same respective years, but cannot sufficiently forecast landslides that occurred in 2004. However, by subtracting the 2000 susceptibility map from the 1959 susceptibility map, they obtained a susceptibility deviation map that was capable of predicting the 2004 landslides with > 85% accuracy. It is hypothesised that the success of this approach was because the deviations between the maps in 1959 and 2000 captured dynamic changes relating to land use that were not explicitly included in either model alone (Meusburger &

Alewell 2009). In other words, this provides a method for characterising potentially unknown temporally varying processes in the absence of detailed information about those specific processes. It is therefore not unreasonable to question whether this approach could also be used to better capture the temporal effects of processes such as path dependency and earthquake preconditioning, though further work on this concept is required.

More recently, a series of papers by Lombardo *et al.* (2020, 2018a, 2018b) have comprehensively assessed how model latency can be exploited to develop space and time dependent susceptibility models. Conceptually, this approach aims to incorporate the effects of both observed covariates (e.g. elevation, slope etc.) and unobserved or unavailable processes, where the latter are quantified from the deviations in landslide susceptibility (or intensity) not explained by the observed covariates (Lombardo *et al.* 2020). This is achieved using a Log-Gaussian Cox Process (LGCP) model. The mathematics behind this model are complex, and will not be described in full here (see Lombardo *et al.* (2019) for details). Essentially, this model uses a “doubly” stochastic process, whereby landslide intensity (counts of landslides per mapping unit) is described using a Poisson component and a Gaussian component on the log-scale, which includes both fixed effects (known covariates) and latent random effects (unknown processes that are correlated in space and time).

This approach has been used successfully on several occasions to obtain increased accuracy susceptibility models in cases where spatial and temporal information is lacking. For example, Lombardo *et al.* (2018a) use the LGCP model to assess landslide susceptibility following the Wenchuan and Lushan earthquakes in China. They develop three models, one with only known covariates, one with only a latent spatial effect, and one with both known covariates and the latent spatial effect. The best performing model was the one that included both the latent spatial effect and known covariates. In effect, the latent spatial component was found to capture local effects such as topographic amplification, which had not been possible to incorporate as known covariates. This latent effect was also considered to be capturing the legacy effect of previous earthquakes (Lombardo *et al.* 2018a), and whilst this process was not considered a major landslide control in this case, it highlights that this approach

should be capable of modelling processes such as earthquake preconditioning. Similarly, Lombardo *et al.* (2018) used the same approach to model rainfall-triggered debris flows in Sicily, Italy. As with the earthquake case, they found that the models that included latent spatial effects were most accurate, with the latent effect able to capture the otherwise unknown local conditions of the triggering storm events. Again, this suggests that this approach could be used effectively to deal with some of the problems observed in this thesis. Notably, to better capture landsliding triggered by cloud outburst storms, which as described in Chapter 4, were difficult for typical landslide susceptibility approaches to predict.

Finally, whilst the two above examples focus on latent spatial effects, Lombardo *et al.* (2020) also combine both spatial and temporal effects to better forecast landslides in Collazzone, Italy. Specifically, they develop five models, two with only fixed covariates, one with fixed plus spatial latent effects, one with fixed plus temporal latent effects, and one with fixed plus spatially and temporal latent effects. As with the previous examples, the models with latent effects had the best performance (initial AUROC success of 0.91 – 0.93 compared to 0.77 – 0.79), with the model including both spatial and temporal latency providing important insights into spatial and temporal processes (Lombardo *et al.* 2020). Indeed, this approach proves capable of accounting for both spatially and temporally heterogeneous processes, even in the absence of any information about these processes, thus representing a significant potential improvement on typical binary based regression approaches.

However, there are some problems with this approach that potentially limit its applicability. First, the mathematics behind this method is significantly more complex than that required for basic BLR-based susceptibility modelling. Indeed, the LGCP approach not only requires an understanding of Poisson/Gaussian statistics, but also requires the user to define various priors and hyper-parameters that govern the expected distributions of input variables and the smoothness and variation in the latent effects. As well as requiring expert understanding to avoid unrealistic or unstable model results, it also requires that the model uses a Bayesian framework for setting these priors. This approach does this using an R package called INLA (Integrated Nested Laplace Approximation), which leads to the second problem,

which is computing requirements. This more complex Bayesian approach is fundamentally more computationally demanding than methods that do not include random effects. Indeed, with approximately 5000 observations, the INLA process alone requires at least 1 GB of RAM and can take up to six hours to run (Lombardo *et al.* 2020). However, this requirement increases significantly as the number of observations increases, with larger regions or events with tens of thousands of landslides easily requiring >16 GB of RAM, tens of hours of time, and thus dedicated research computers (Lombardo *et al.* 2020). The third problem is that as with potential solutions 2) and 3), this approach requires significant landslide data through both space and time. The example of Lombardo *et al.* (2020) used over 5000 landslides across >800 defined slope units and six defined time intervals that span over 60 years. Indeed, Lombardo *et al.* (2020) suggest that the lack of accurate and detailed multi-temporal landslide inventories is actually a bigger problem for applying this method more widely than issues of computational requirements. In this context, the importance of the ASM-inventory produced in for this thesis is clear, as it offers potential for this approach to be applied across Nepal in the future. Overall, despite, these drawbacks, it is clear that by capturing latent spatial and temporal effects, this approach can incorporate spatial and temporal processes that the model would otherwise be blind to. Thus, this model takes a major step towards solving the problem of unknown or unquantifiable spatial/temporal heterogeneity.

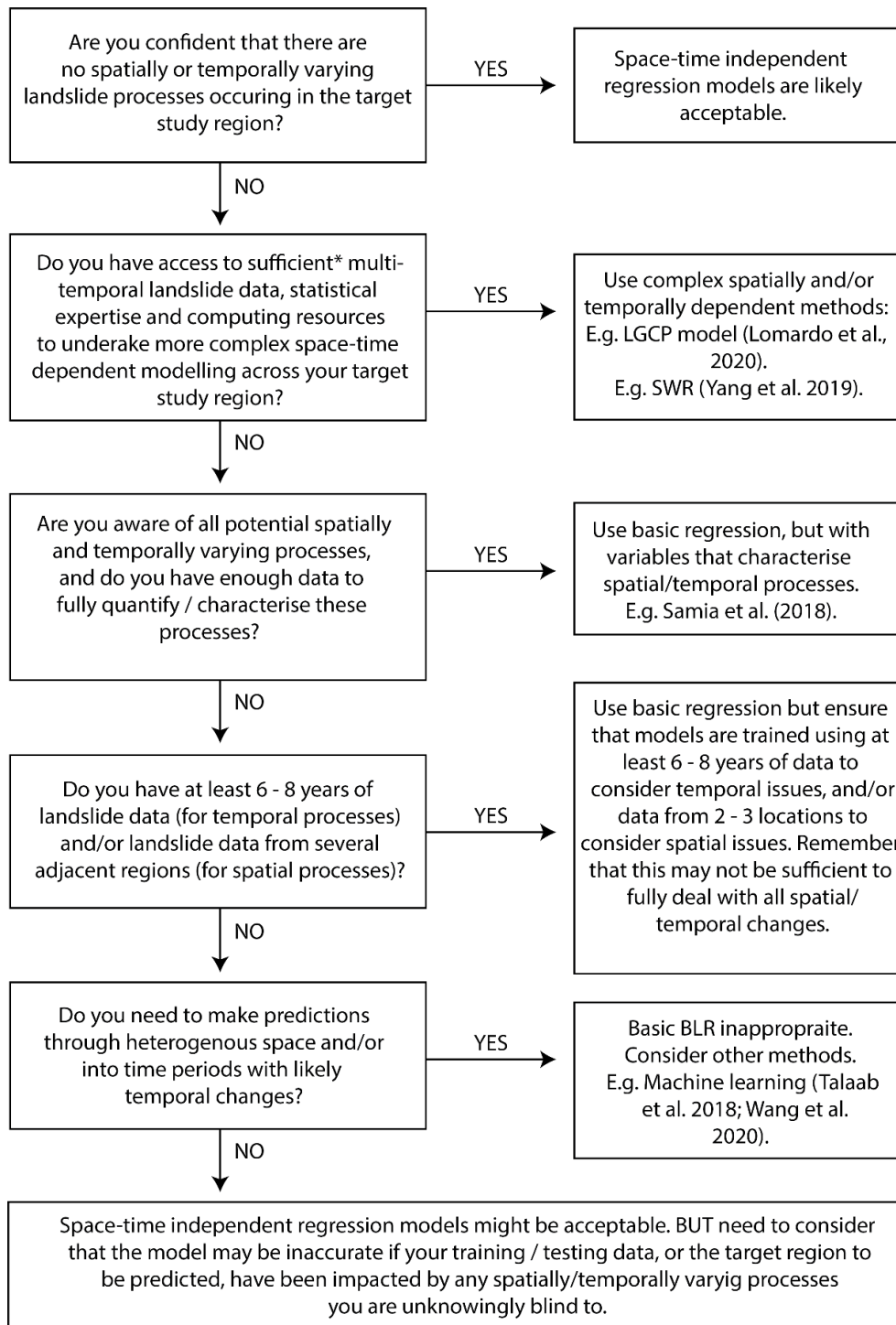
5) Finally, whilst the focus of this thesis, and of all the above solutions, has been on “classical statistics” (i.e. regression based susceptibility modelling), it is important to note that issues with spatial and temporal variability in landslide susceptibility could be solved using other modelling approaches, specifically, machine learning techniques. A detailed appraisal of machine learning applications is considered beyond the scope of this thesis; however, the following section outlines a few examples of how machine learning has been used to deal with issues of spatial heterogeneity. One, is the example of Taalab *et al.* (2018), who show that random forest models are capable of high accuracy classification across a large heterogeneous region of Piedmont, Italy, without needing to do multiple susceptibility assessments for different localities within that region. Two, is the example of machine learning

processes that can allow spatial weighting and clustering techniques to be combined. Indeed, Wang *et al.* (2020) use a tool called GeoSom to combine spatial weighting and clustering techniques to classify landslides clusters, and use these clusters as input in a machine learning ensemble (which included Support Vector Machine (SVM), Artificial Neural Networks (ANN) and Gradient Boosted Decision Trees (GBDT) machine learning methods). This approach was found to solve the problem of spatial heterogeneity, with the removal of the spatial clustering element causing model performance to drop significantly.

6.2.3 Proposed framework for optimum susceptibility modelling

The above section outlines several potential solutions to the issues of spatial and temporal heterogeneity. However, these remain limited in their usefulness unless it is clear when it is appropriate to use each solution. As such, a decision-making framework that considers spatial and temporal heterogeneity is proposed to aid in the selection of the most appropriate and attainable methodology for optimum susceptibility modelling. This framework is predominantly designed to be used by scientists and hazard assessors who need to conduct landslide susceptibility assessments in dynamic mountainous regions, though could also be of use to general landslide hazard and risk practitioners such as governments and local stakeholders.

This framework is outlined in Figure 6.1, and will not be repeated ad-verbatim here. This framework is essentially a decision tree that guides the user to the most appropriate methodology depending on landslide data availability and resource capacity. This framework assumes that if landslide-affected spatially and temporally heterogeneous processes are likely to be occurring, then typical space-time independent BLR modelling is inappropriate. It then assumes that space-time dependent methods (e.g. Lombardo *et al.* 2018a/b, 2020) are the optimum approach, but that if this is not possible (e.g. due to lack of resources / capacity), then depending on landslide data availability one of the other solutions presented in this thesis should be used instead. If neither space-time dependent modelling nor the other solutions presented are possible, then it recommends not using classical statistics, but instead investigating other methodologies (e.g. machine learning).



*"Sufficient" will be region specific, but is likely to require several thousand landslides over at least 6 time slices, expertise (or the capability to gain expertise) in Bayesian statistics, and, for study regions with tens of thousands of landslides, dedicated computing hardware.

Figure 6.1. Proposed decision-making framework for selecting the optimum susceptibility modelling method given your landslide data availability and resource capabilities.

As noted above, it is hoped that this framework will be a useful resource for geohazards managers, local stakeholders and scientists who are required to assess landslide susceptibility in dynamic mountainous regions that are likely to be impacted by spatially and/or temporally varying landslide-impacting processes. As well as helping to ensure that landslide susceptibility models are as accurate and robust as possible, this should have wider implications for landslide hazard management. This is because many mitigation strategies such as early warning systems (EWSs), land use planning and hazard zonation rely fundamentally on having accurate susceptibility models (Reichenbach *et al.* 2018) . Indeed, this could be particularly useful for EWSs, most of which currently do not consider transient events that could alter landslide initiation thresholds (Guzzetti *et al.* 2020), and have direct impacts on population vulnerability and risk (Thiebes & Glade 2019).

6.2.4 Implications for Nepal

As outlined in Chapter 1, a key motivation of this work, and a key reason for selecting the Himalayas as the study region, is that Nepal is a country in clear need of improved landslide hazard management. Consequently, it is important to consider the implications of the work presented in this thesis for landslide risk mitigation across Nepal. Section 1.4.3.4 describes the current state of landslide risk management practice in Nepal. This highlights several ways in which the results and discussion presented in this thesis could have important implications.

First, it is apparent that the relevant hazard management stakeholders in Nepal (e.g., the Nepal Department of Geology and Mines) do not currently have access to good quality landslide susceptibility maps. As such, the local and regional scale susceptibility maps presented throughout this thesis (most of which have good to very good, 75 – 80%, accuracies) provide an important potential resource. Furthermore, the BLR methodology descriptions (section 2.5) combined with the susceptibility modelling framework (section 6.2.3) provide a low-resource, low-technical capacity approach for developing further landslide susceptibility models across the country. Second, as described by Kinney *et al.* (2021) and Owen *et al.* (2021), landslide hazard in Nepal has been described as ‘too static’ and not properly

considering the evolving nature of landslide hazard. As such, the insight provided throughout this thesis into the spatially and temporally varying nature of landslide characteristics, distributions and susceptibility provide future hazard managers with important information about how to account for the evolving nature of landslide hazard. For example, the finding that earthquake preconditioning induced monsoon-triggered landslides are controlled by PGA and excess topography should allow for more accurate forecasting of post-earthquake landslide hazard. Third, it was seemingly apparent (e.g., through in-country visits) that relevant hazard management stakeholders in Nepal had little readily available landslide inventory information. This thesis provides an immediate solution to this problem, with the ASM-inventory of over 12,000 landslides made fully and freely available.

6.2.5 Wider implications and considerations

A fundamental component of this thesis was challenging the assumptions of time/space independency that are implicit in many typical BLR modelling approaches. As outlined in the previous sections, this issue has clear implications for landslide hazard and mitigation. However, it also has potential implications for other related disciplines that also use BLR techniques to model and understand physical processes and relationships between response and predictor variables. For example, forest and tropical wildfire occurrence is commonly modelled and forecasted using logistic regression-based techniques (e.g., Milanović *et al.* 2020; Sharma *et al.* 2020; Eslami *et al.* 2021; Heydari *et al.* 2021). Similarly, BLR techniques have been used for purposes such as modelling lahar development and debulking (Jones *et al.* 2017; Teran 2021), alluvial fan deposition (Lucà & Robustelli 2020), flood susceptibility (Al-Juaidi *et al.* 2018; Hidayat Jati *et al.* 2019; Chowdhuri *et al.* 2020; Pham *et al.* 2020), and dam instability (Shan *et al.* 2020). All of these examples share the same fundamental principles as those relating to landslide susceptibility, i.e., that the relationships between the physical process being modelled (be it wildfire locations, lahar occurrence, flood susceptibility etc.) and relevant predictor variables may vary spatially and temporally, so this must be accounted for to ensure accurate and reliable model outputs. As such, the general recommendations of this thesis (i.e., to ensure that spatially and temporally varying processes are quantitatively

characterised as independent variables within BLR models or to use more complex space-time dependent modelling techniques) are potentially relevant to any discipline that uses BLR modelling or forecasting.

Another important wider consideration to stem from this work is whether having no landslide susceptibility models/maps is better or worse than having models with large limitations and uncertainties (e.g., due to issues surrounding unquantified or unknown spatial/temporal dependency). Instinct may be to assume a mantra of “something is better than nothing”. However, in reality, this is unlikely to be the case. Susceptibility maps are commonly used for important purposes such as hazard zonation and early warning systems. As such, inaccurate landslide susceptibility maps could lead to ineffective, inappropriate, or insufficient hazard management strategies being implemented. Not only will this waste resources, but it could also present a danger to life and development. For example, if regions incorrectly classified as low susceptibility are subsequently built on, then human and infrastructure vulnerability could be increased. This is a potentially large problem, both for local populations and stakeholders who may be affected and for the scientists responsible for developing such maps. For example, following the 2009 L’Aquila earthquake, Italy, several earth scientists, and officials were actually prosecuted for allegedly providing inaccurate, incomplete, or contradictory statements about likely future seismic hazard. This highlights that it is vital for scientists to ensure that all the information they provide is accurate, with any limitations, assumptions and uncertainties fully and clearly described to any end-users. In this context it is therefore likely that a highly uncertain or limited susceptibility model may be worse than no model. This highlights the importance of studies such as this which seeks to assess and reduce the uncertainties and limitations of commonly used susceptibility methodologies.

6.3 Final conclusions

In conclusion, this thesis has met its main aim of investigating the characteristics, preconditioning and susceptibility of landslides in Nepal. Comprehensive analysis of

a newly developed monsoon-triggered landslide inventory reveals key results such as:

- Landslide occurrence in the Himalaya is influenced by spatially and temporally varying processes such as permafrost degradation, path dependency and earthquake preconditioning.
- Earthquake preconditioning is highly transient and controlled by the coincidence of PGA and excess topography.
- Landslide occurrence is impacted by extreme events such as cloud outburst storms and floods, which cause significant transient shifts in landslide spatial distributions.
- These spatial and temporal processes have significant impacts on the accuracy and applicability of typical time and space independent regression-based landslide susceptibility models, with models developed from single localities and time slices unable to provide consistently accurate prediction of other localities or time slices.
- Regression-based susceptibility models developed with 6 – 8 years of landslide data are consistently accurate and reliable, offering a potential solution to this problem.

The issues surrounding accounting for spatial and temporal heterogeneity within landslide susceptibility assessments are largely due to process blind susceptibility modelling, whereby typical space-time independent models are “blind to” (i.e. fail to account for) spatially and temporally varying processes. Further analysis and a wider review of the literature suggest there are several potential approaches that can be used to reduce problem of process blind susceptibility modelling. These include:

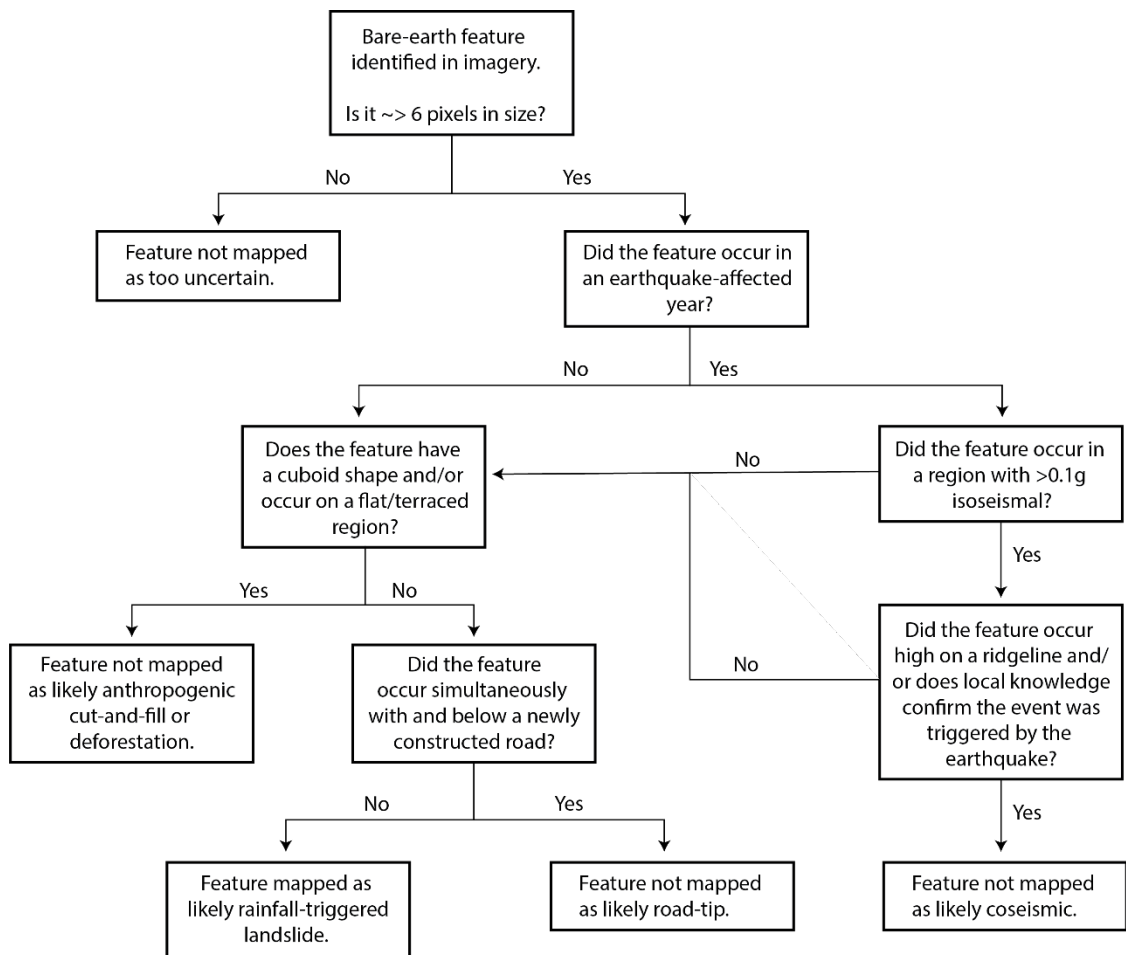
1. Ensuring that likely spatially and temporally varying processes are quantitatively characterised as independent variables within a typical susceptibility model (i.e. ensuring you do not model process blind).
2. Using at least 6 – 8 years of landslide data from a given region and trigger event to train a susceptibility model.

3. Using more complex space-time dependent modelling techniques (e.g., the LGCP approach of Lombardo 2020), that account for unknown processes (i.e., for process blind modelling) by exploiting model latency.

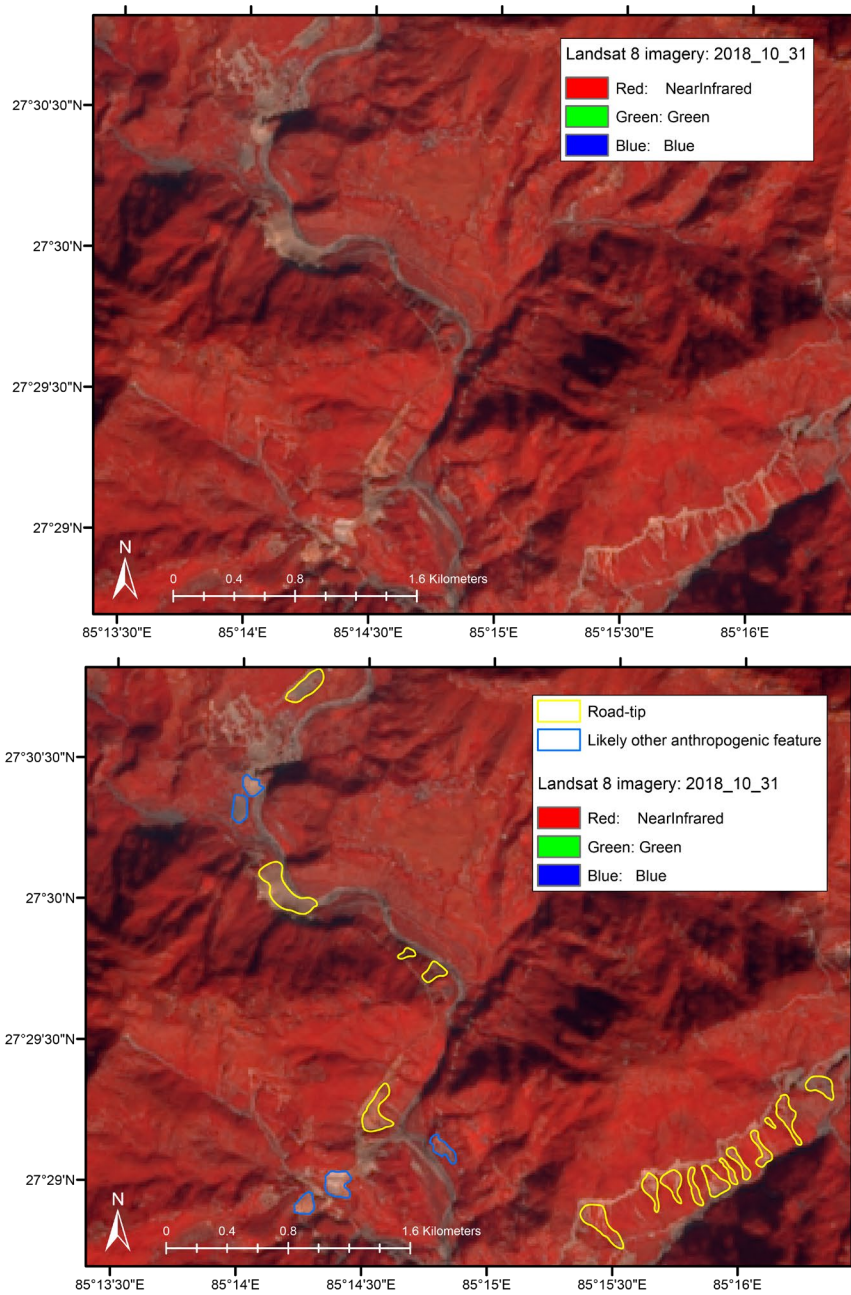
These solutions are then included in a proposed decision-making framework to aid geohazards managers and other stakeholders in using the optimum approach to conducting landslide susceptibility in regions impacted by spatially and temporally varying landslide processes given the available data and resources. Within the context of these solutions, some of the results and outputs of this thesis take on significant importance. For example, the novel results here that earthquake preconditioning is controlled by peak ground acceleration and excess topography can provide a basis for which to include earthquake preconditioning as a variable in susceptibility models. Furthermore, all of the proposed solutions require large multi-temporal landslide datasets, of which few are currently freely and publicly available. As such, the multi-temporal ASM-triggered inventory produced and published here will be a valuable resource to aid future investigations into landslide susceptibility. Overall, the results and outputs of this thesis have provided novel insights into the spatial and temporal processes affecting landslide susceptibility in the Nepal Himalaya, facilitating future advances in landslide susceptibility, hazard, and risk across dynamic mountainous regions.

Appendices

Appendix A. Decision tree outlining process for deciding whether a bare earth feature visible in satellite imagery should be mapped as a rainfall-triggered landslide.



Appendix B. Examples of road tip and other anthropogenic features often visible in the Landsat imagery,



Appendix B. Example false colour RGB pre- and post-monsoon season Landsat satellite imagery used to map landslides. a) pre-imagery. b) post-imagery.

Appendix C. Author version of paper published in the Quarterly Journal of Engineering Geology and Hydrogeology.

1 **Coseismic and monsoon-triggered landslide impacts on remote trekking infrastructure,**
2 **Langtang Valley, Nepal**

3
4 J. N. Jones^{1,2*}, M. Stokes², S. J. Boulton², G. L. Bennett¹ & M. R. Z. Whitworth³

5
6 ¹ School of Environmental Sciences, University of East Anglia, Norwich Research Park, Norwich, NR4 7TJ

7 ² School of Geography, Earth and Environmental Sciences, University of Plymouth, Drake's Circus, Plymouth,
8 PL4 8AA

9 ³ AECOM, East Wing Plumer House, Tailyour Road, Plymouth, PL6 5DH

10 *Corresponding author (email: joshua.jones@plymouth.ac.uk / Joshua.N.Jones@uea.ac.uk)

11 J.N.J: <https://orcid.org/0000-0002-8992-1572>

12 M.S: <https://orcid.org/0000-0003-3788-4615>

13 S.J.B: <https://orcid.org/0000-0002-8251-0025>

14 G.L.B: <https://orcid.org/0000-0002-4812-8180>

15 M.R.Z.W: <https://orcid.org/0000-0003-1837-3385>

16
17
18 Short title: Landslide impacts in Langtang, Nepal

19
20 **Abstract:** In 2015, the M_w 7.9 Gorkha earthquake struck Nepal, triggering thousands of landslides
21 across the central and eastern Himalayas. These landslides had many adverse effects, including causing
22 widespread damage to low-grade transport routes (e.g. tracks, footpaths) in rural regions that depend on
23 tourism for survival. Langtang Valley is a glacial/periglacial landscape located 60 km north of
24 Kathmandu. It is one of the most popular trekking regions in Nepal and has been severely affected by
25 Gorkha earthquake-triggered and monsoon-triggered landsliding. Here, qualitative and quantitative
26 observations from fieldwork and remote sensing are used to describe the materials and geomorphology
27 of the landslides across Langtang Valley, and to quantify the extent to which coseismic and monsoon-
28 triggered landslides have impacted upon Langtang's trekking infrastructure. The dominant bedrock

29 materials involved within Langtang landslides are found to be a range of gneisses and intruded
30 leucogranites. In total, 64 landslides are found to have intersected trekking paths across Langtang, with
31 coseismic and monsoon-triggered landslides impacting ~ 3 km and 0.8 km of path respectively. It is
32 observed that the practice of re-constructing paths through unstable landslide deposits is leaving the
33 trekking infrastructure across Langtang increasingly vulnerable to future failure.

34

35 Earthquakes have long been recognised as a primary trigger of landslides (Keefer 1984), with the
36 potential to initiate thousands of slope failures over relatively small regions (e.g. Harp & Jibson 1996;
37 Xu *et al.* 2014). Such coseismic landslides can typically be distinguished from monsoon-triggered
38 landslides by their tendency to occur at ridgelines or other major breaks in slope (Densmore & Hovius
39 2000). On 25th April, 2015, the M_w 7.9 Gorkha earthquake triggered over 24,000 slope failures across
40 central-eastern Nepal (Roback *et al.* 2018). The characteristics and distributions of these landslides
41 have been variably documented by previous, largely remote-sensing dominated, studies. For example,
42 Roback *et al.* (2018) find that the distributions of these landslides are best predicted by the overlap of
43 high Peak Ground Acceleration (PGA) and steep slopes, whilst Kargel *et al.* (2016) suggest that these
44 landslides are most densely distributed where PGA was greater than 0.6 g. Similarly, statistical analysis
45 by Martha *et al.* (2017) suggests that slope and geology are the dominant controls on landsliding, which
46 they propose, in agreement with Collins & Jibson (2016), is owing to the fact that steeper slopes have
47 more exposed bedrock with less vegetation cover. Martha *et al.* (2017) also show that 64% of coseismic
48 landslides occurred on the northern, down-thrown block of the fault, supporting the observations of
49 Kargel *et al.*, (2016).

50

51 The economic and social impacts of the Gorkha earthquake have also been reported. The Centre for
52 Disaster Management and Risk Reduction (CEDIM, 2015) estimates that the earthquake caused damage
53 to, or destruction of, 550,000 buildings, deaths of 9,000 people, and economic losses of ~\$10 bn.
54 Furthermore, the landslides associated with this event caused at least 500 deaths and over 2% of the
55 total economic losses attributed to the earthquake. Following this event, landslide research in Nepal has

56 been focused on conducting national and regional scale landslide susceptibility analysis (e.g. Shrestha
57 & Kang 2017; Roback *et al.* 2018), as well as landslide analysis of the districts surrounding Kathmandu
58 and the major road infrastructures linking Nepal and China (e.g. Xu *et al.* 2017; Acharya & Lee 2019).
59 However, less research has been conducted into landslide hazard in and around Nepal's most popular
60 trekking regions, despite the fact that rural tourism makes up over 5% of Nepal's economy (CEDIM,
61 2015). Between 1993 and 2014, Nepal received an annual average of 89,500 trekking tourists, but in
62 2015 received just 9,000, and in 2016 and 2017 still received some 20,000 less than the pre-earthquake
63 average (Ghimire *et al.* 2018). Part of the problem is that Nepal's trekking infrastructure is remotely
64 located and dominated by low-grade paths, which, as this feature will demonstrate, are severely
65 impacted by coseismic and monsoon-triggered landsliding.

66

67 The aim of this feature is to use qualitative and quantitative observations to examine the interaction
68 between landslides and trekking infrastructure in Langtang Valley, one of Nepal's most popular
69 trekking regions, located 60 km north of Kathmandu, and 70 km east of the Gorkha earthquake epicentre
70 (Fig. 1). In October 2018 field terrain evaluation was conducted to assess the composition and
71 characteristics of coseismic and monsoon-triggered landslides across the valley. We firstly describe the
72 geologic materials involved in the Langtang landslides, followed by geometric analysis to quantify the
73 total length of Valley, and total length of trekking paths, that have been impacted by landslides. We
74 then describe the morphologies and characteristics of some specific landslides that have contributed to
75 this impact, before briefly considering the impact that landslides are having on the future vulnerability
76 of trekking paths across Langtang Valley.

77

78 **Methodology**

79

80 Field data collection occurred along the main trekking routes in Langtang Valley between Syraprubesi
81 and Kyanjin Gompa, a total distance of approximately 50 km (Fig. 2). An inventory including both
82 coseismic and monsoon-triggered landslides was developed using a GARMIN 78 hand-held GPS unit

83 and a TruPulse laser range finder. Monsoon-triggered and coseismic landslides were differentiated
84 using their relative hillslope position and morphology. For example, monsoon-triggered failures are
85 typically smaller than coseismic failures, occur on monthly rather than decadal timescales, and tend to
86 initiate near the hillslope toe (Densmore & Hovius 2000). These field data were validated post-
87 fieldwork through time series interrogation of RapidEye 5 m spatial resolution satellite imagery
88 (PlanetTeam 2017), which was also used to validate whether landslides were coseismic or pre- / post-
89 seismic in nature.

90

91 Geological mapping allowed an assessment of the materials involved in different slope failures.
92 Lithological descriptions targeted landslide debris and backscar bedrock areas (where safe to access),
93 documenting their mineralogy, texture, and discontinuity type and configuration. *In situ* shear strength
94 testing was conducted using a ‘simple means’ approach that involves estimating intact rock shear
95 strength based on the response of a rock to applied pressure from rock hammer blows and/or hand
96 crumbling (Hack and Huisman, 2002). For example, a sample that crumbles in hand would be assigned
97 a strength of < 1.25 MPa, whilst a sample that only chipped after several heavy hammer blows would
98 be assigned a strength of 100 – 200 MPa. This method should ideally be conducted on intact bedrock,
99 however, since field access was often restricted to landslide debris, this was not always possible. As
100 such, where measurements were taken on landslide debris, we ensured that target samples were un-
101 weathered, and at least 40 x 40 cm in size. This method has been shown to give a more representative
102 estimate of rock strength than more elaborate testing (Hack and Huisman, 2002), and is the method
103 used in the British Standard for geotechnical investigations (BS EN ISO 14689:208).

104 Geological assessments also documented non-land slipped outcrops for strength comparison. Locations
105 of lithological analysis are shown in Fig. 2. These locations informed the geological map compilation
106 (Fig. 2), where the outcrop pattern is interpreted using topographic contours. Other mapping involved
107 using GPS and remote sensing to delineate pre- and post-earthquake path locations.

108

109 Once the above data were collated, it was possible to quantify the total length of valley impacted by
110 differently triggered landslides. This was estimated by fitting minimum bounding-area rectangles to all
111 landslides in our inventory, except those mapped as dormant events with no known trigger, using the
112 ArcGIS Minimum Bounding Geometry tool. This tool fits a minimum bounding rectangle that fully
113 encloses each landslide polygon. As the runout direction, and thus resulting rectangle length, of each
114 landslide is approximately perpendicular to the Valley strike, summing the rectangle widths gives an
115 estimate of the total valley length impacted. Furthermore, by using the ArcGIS intersect tool to
116 calculate the total length of intersection between our landslide polygons and a shapefile of the main
117 paths across the valley, it was possible to estimate the total length of paths impacted by both coseismic
118 and monsoon-triggered landslides.

119

120 **Geological observations**

121

122 Langtang Valley sits within the Greater Himalayan Sequence, structurally bounded by the Main Central
123 Thrust (MCT) to the south and the South Tibetan Detachment (STD) to the north. Regional scale (1:
124 250,000) geological maps held by the Nepal Department of Mines and Geology indicate that the
125 bedrock geology of the central-eastern Himalayas is dominated by gneisses, migmatites, quartzites
126 schists, and pervasive Miocene leucogranite intrusions. However, these maps lack detailed lithological
127 information on Langtang Valley, with simple generalization as 'Undifferentiated gneisses'. Thus, our
128 fieldwork allowed a more detailed, qualitative and quantitative assessment of the materials involved in
129 the Langtang landslides, previously lacking in published materials.

130

131 Four lithological units were identified within landslides across the valley. The first unit, termed here as
132 the Syraprubesi Formation, is a gneiss dominated by muscovite, biotite and quartz, with subordinate
133 components of plagioclase and garnet (e.g. Fig. 3a). This unit is medium- to coarse-grained, with
134 average grain size of 0.3 – 3 cm. The minerals were generally platy, with elongated plagioclase
135 orientated parallel to foliation and a strong mylonitic fabric. *In-situ* strength tests indicate that this unit

136 is hard (50 – 100 MPa). The second unit, the Bamboo Formation, is a gneiss dominated by muscovite,
137 biotite and quartz, with subordinate components of tourmaline (e.g. Fig. 3b). This unit was very similar
138 to unit one, but with a larger average grain size of 1 – 3 cm, and with the addition of tourmaline. Unit
139 two had a much higher proportion (60 – 70 %) of quartz and biotite compared to unit one, but maintained
140 the mylonitic fabric. Strength tests suggest that unit two is very hard (100 – 250 MPa). Unit three,
141 named the Langtang Formation, is a coarse-grained (2 – 6 cm) leucogranite, dominated by muscovite,
142 tourmaline, epidote, and occasionally garnet (e.g. fig. 4a). Unit three was commonly found intruded
143 into units two and four, and has a strength of 50 – 250 MPa. This unit was often observed in the source
144 zones of earthquake triggered rockfalls (e.g. fig. 4b). We hypothesize that the discontinuities induced
145 by the intruded leucogranite dykes and sills have reduced the shear strength of the bedrock, making
146 failures in regions with this unit more likely. Unit four, termed here the Lower Tsergo Ri Formation, is
147 a biotite, plagioclase, muscovite, quartz, semi-pelite schist (e.g. fig 4c). This unit was finer grained than
148 the other units (average grainsize 0.25 – 1 cm) and had an estimated strength of 100 – 250 MPa. This
149 unit was dark to light grey in colour and was frequently observed to be in contact with leucogranite.

150

151 **Landslide observations**

152

153 In total, our field-based landslide inventory contains 154 coseismic landslides, which were classified
154 using the BGS definitions and typologies (British Geological Survey, 2019) as being 58% falls, 27%
155 slides and 15% flows. A further 29 monsoon-triggered and inactive/dormant landslides that occurred
156 pre- or post-earthquake were also mapped (Fig. 2). In terms of total area, 46% of the mapped landslides
157 were $< 1.0 \times 10^4 \text{ m}^2$, 48% were $1.0 \times 10^4 - 1.0 \times 10^5 \text{ m}^2$, and 6% were greater than $1.0 \times 10^5 \text{ m}^2$, with the
158 largest event being the Langtang Avalanche, which had a total mapped area of approximately 1.86×10^6
159 m^2 . Our landslide inventory is one of several that covers the region. For example, the remotely-sensed
160 Gorkha earthquake-triggered landslide inventories of Kargel *et al.* (2016), Lacroix (2016), Martha *et*
161 *al.* (2017) and Roback *et al.* (2018) all cover Langtang Valley, and identify comparable numbers of
162 landslides across the main trunk of the valley. Minor differences between these inventories and ours are

163 likely caused by the varying spatial resolution of satellite sources used, and the fact that we only mapped
164 landslides visible from the main trekking routes and so did not include those triggered along tributary
165 valleys. A further difference is that our inventory is field-based, and thus represents the locations and
166 extents of landsliding three years since the earthquake occurred, unlike the previous inventories which
167 represent the immediate post-earthquake landslide distribution.

168

169 An aim of this paper was to quantify the impact of landslides in terms of length of valley affected and
170 length of paths affected using the GIS methodology outlined in the methods section. Coseismic
171 landslides are found to have impacted 14 km of the valley, whilst monsoon-triggered landslides
172 impacted just 1.5 km. In total, 64 of the 183 landslides in our inventory were found to have intersected
173 trekking paths, with coseismic landslides impacting ~ 3 km of path, and monsoon-triggered landslides
174 impacting ~ 0.8 km of path. The following sections describe the geomorphology and characteristics of
175 key examples of the landslides that contributed to this impact.

176

177 *The Langtang Avalanche*

178

179 The Langtang Avalanche is perhaps the most renowned coseismic landslide to have occurred during the
180 Gorkha earthquake, having entirely destroyed the village of Langtang with the loss of at least 300 lives.
181 This event was a complex compound occurrence that began when earthquake strong ground motion
182 caused a portion of glacial material within an ice-carved hanging valley, as well as a portion of bedrock
183 approximately 500 x 1000 m in size (Fig. 5a), to collapse (Nagai *et al.* 2017). The deposits from this
184 event have been previously estimated through remote sensing techniques to have a depth of ~60 m, an
185 area of 0.63 – 0.88 km², and a volume of 5.51 – 9.66 x10⁶ m³ (Lacroix 2016; Nagai *et al.* 2017). Pertinent
186 to this study is the interaction between the landslide deposits and trekking paths. This event completely
187 buried a ~ 500 m long section of the main trekking path, which has since been reinstated over the
188 landslide deposits. The material within the deposits is mostly gneisses (unit 2) and leucogranites (unit
189 3). Fig. 5b shows the position of the new trekking path at the point where a river has incised through

190 the deposits. The path here is highly precarious, with some sections < 30 cm wide beneath a > 80 °, 10
191 m high slope of loose deposits, which are vulnerable to movement during a future trigger event.
192 Furthermore, the path crosses over a narrow tunnel that has been created by the river (Fig. 5c). This
193 portion of the deposits is unstable, and several boulders were witnessed falling from beneath the tunnel
194 into the river. This demonstrates that the Langtang Avalanche is continuing to impact the safety and
195 vulnerability of Langtang's trekking paths more than three years since the initial failure occurred.

196

197 *Debris slides*

198

199 Whilst the Langtang Avalanche has undoubtedly had the greatest single impact on trekking
200 infrastructure, the cumulative impacts of smaller, but more widespread, coseismic failures cannot be
201 understated. For example, coseismic debris slides were pervasive along the lower, western portion of
202 the valley. Fig. 6 shows a debris slide that initiated near the ridgeline of a > 55° hillslope covered by
203 grassland in the lower slopes and trees and larger shrubs in the upper slopes. The bedrock geology of
204 the scar of this failure is dominated by the gneisses of unit 1. However, as the failure is shallow (< 0.5
205 m), and has mostly disturbed the unconsolidated regolith material overlying the bedrock, it is defined
206 as a debris slide rather than a rockslide. In terms of impact on trekking infrastructure, the localised
207 runout of this failure resulted in only a small volume of material intersecting the path. However, more
208 concerningly, it was observed that this debris slide came close to damaging several electricity pylons.
209 These pylons connect to the new hydropower station near Kyanjin Gompa, and are a vital component
210 of Langtang's energy infrastructure.

211

212 *Unconstrained rockfalls*

213

214 Unconstrained rockfalls were frequently observed to bury the main trekking route. Fig. 7a shows an
215 example of such an event. The material in the deposits confirm that this failure occurred within the
216 bedrock itself, which was composed of the unit 1 gneisses. The material from this failure buried a 30 m

217 long segment of the trekking path, reportedly killing 30 people. This landslide demonstrates that even
218 relatively small-scale events have the potential to cause loss of life when hazard overlaps with
219 vulnerability. Since the initial failure, a new trekking path has been re-dug through the deposits, with
220 no attempt at any mitigation against potential monsoonal reactivation of debris material. As such, this
221 section of the path should be considered at high-risk of being damaged or blocked by reactivated
222 landslide material in the future. Fig. 7b shows a debris fan from a combined rock/debris fall and a
223 rock/debris flow. The source zones for the flow and the fall appear to be at major $> 55^\circ$ and $> 65^\circ$
224 breaks in slope. The path of the flow appears to have been controlled by the existing hillslope
225 morphology, with a knoll splitting the flow into two channels just before the main rockfall debris fan.
226 The flow travelled for ~ 200 m before joining the main debris fan, whilst the debris from the main
227 rockfall travelled ~ 100 m. This failure totally buried a ~ 40 m section of the trekking path, and is reported
228 to have killed 20 people. Similar to the previous examples, the position of the new trekking path now
229 lies on top of the landslide deposits, with no measures aimed at moderating future instability. As such,
230 this section of the path is again considered to be at high risk of being blocked, or otherwise impacted,
231 by future reactivation of landside debris.

232

233 *Monsoon-triggered landsliding*

234

235 As well as coseismic landslides, monsoon-triggered landslides were frequently observed across the
236 valley, and care must be taken when distinguishing between these different triggering mechanisms. Fig.
237 8 shows a typical monsoon-triggered translational debris slide that has occurred on a forested, $> 45^\circ$
238 hillslope. This slide has a height of ~ 30 m, and completely destroyed an ~ 45 m wide section of the path
239 below, which has since been re-built. The sides of the new path have been supported with small, < 0.5
240 m high walls of unconsolidated debris material. The debris material remaining above the new path is
241 highly unstable, with several (> 10 m wide) blocks balancing within the deposits. This material will be
242 highly susceptible to movement during subsequent monsoon-seasons, and as such remains at-risk of
243 impacting the trekking path further.

244

245 **Conclusions**

246

247 Geometric analyses of our field data show that coseismic and monsoon-triggered landslides have
248 intersected over 3.8 km of trekking path, resulting in significant loss of life and damage. Furthermore,
249 our observations of the morphology and characteristics of these landslides demonstrate that the response
250 to this damage has been to simply re-dig new, unstable paths through the landslide deposits, with no
251 attempt at mitigation against future movement. This is a labour intensive, but low-cost practice which
252 has the advantage of allowing the trekking paths to be re-opened quickly after a landslide. However,
253 such an approach has had the major disadvantage of leaving the trekking paths highly susceptible to
254 blockage or damage by future monsoon- or seismic-triggered reactivations of material, resulting in an
255 increased risk of subsequent fatalities or damage across Langtang.

256

257 *This work was supported by the University of Plymouth and the Natural Environment Research Council*
258 *through a CASE-funded PhD studentship from the EnvEast Doctoral Training Partnership*
259 *[NE/L002582/1] and CASE partner AECOM; as well as through a 2018 Geological Society Elspeth*
260 *Matthews Research Grant. Timothy Webster is thanked for assistance in the field. We thank the*
261 *comments of an anonymous reviewers and that of the editors that have improved this feature.*

262

263 **References**

264

265 Acharya, T.D. & Lee, D.H. 2019. Landslide Susceptibility Mapping using Relative Frequency and Predictor Rate along Araniko Highway.
266 *KSCE Journal of Civil Engineering*, **23**, 763–776, <https://doi.org/10.1007/s12205-018-0156-x>.

267 British Geological Survey. 2019. How does the BGS classify
268 landslides?https://www.bgs.ac.uk/landslides/how_does_bgs_classify_landslides.html.

269 British Standards Institution. 2018. *Geotechnical Investigation and Testing: Identification, Description and Classification of Rock (ISO*
270 *14689:2018)*.

271 *Center for Disaster Management and Risk Reduction Technology CEDIM Forensic Disaster Analysis Group, CATDAT and Earthquake-*
272 *Report.Com, Nepal Earthquakes-Report #3. 2015.*

- 273 Collins, B.D. & Jibson, R.W. 2016. *Assessment of Existing and Potential Landslide Hazards Resulting from the April 25, 2015 Gorkha, Nepal*
274 *Earthquake Sequence, USGS Open-File Report 1142.*
- 275 Densmore, A.L. & Hovius, N. 2000. Topographic fingerprints of bedrock landslides. *Geology*, **28**, 371–374, [https://doi.org/10.1130/0091-](https://doi.org/10.1130/0091-7613(2000)28<371:TFOBL>2.0.CO)
276 [7613\(2000\)28<371:TFOBL>2.0.CO](https://doi.org/10.1130/0091-7613(2000)28<371:TFOBL>2.0.CO).
- 277 Ghimire, D.R., Ghimire, S., Ghimire, N., Janwali, D., Koirala, D. & Poudel, P. 2018. *Nepal Tourism Statistics 2017, Government of Nepal*
278 *Ministry of Culture, Tourism & Civil Aviation, Planning & Evaluation Division, Research & Statistical Section.* Singha Durbar,
279 Kathmandu.
- 280 Hack, R. & Huisman, M. 2002. *Engineering Geology for Developing Countries-Proceedings of 9 Th Congress of the International Association*
281 *for Engineering Geology and the Environment.*
- 282 Harp, E.L. & Jibson, R.W. 1996. Landslides Triggered by the 1994 Northridge, California, Earthquake. *Bulletin of the Seismological Society*
283 *of America*, **86**, 319–332.
- 284 Kargel, J.S., Leonard, G.J., et al. 2016. Geomorphic and geologic controls of geohazards induced by Nepal's 2015 Gorkha earthquake. *Science*
285 *(New York, N.Y.)*, **351**, aac8353, <https://doi.org/10.1126/science.aac8353>.
- 286 Keefer, D.K. 1984. Landslides caused by earthquakes. *Geological Society of America Bulletin*, **95**, 406–421.
- 287 Lacroix, P. 2016. Landslides triggered by the Gorkha earthquake in the Langtang valley, volumes and initiation processes. *Earth, Planets and*
288 *Space*, **68**, 46, <https://doi.org/10.1186/s40623-016-0423-3>.
- 289 Martha, T.R., Roy, P., Mazumdar, R., Govindharaj, K.B. & Kumar, K.V. 2017. Spatial characteristics of landslides triggered by the 2015 Mw
290 7.8 (Gorkha) and Mw 7.3 (Dolakha) earthquakes in Nepal. *Landslides*, **14**, 697–704, <https://doi.org/10.1007/s10346-016-0763-x>.
- 291 Nagai, H., Watanabe, M., Tomii, N., Tadono, T. & Suzuki, S. 2017. Multiple remote-sensing assessment of the catastrophic collapse in
292 Langtang Valley induced by the 2015 Gorkha earthquake. *Hazards Earth Syst. Sci*, **17**, 1907–1921, [https://doi.org/10.5194/nhess-17-](https://doi.org/10.5194/nhess-17-1907-2017)
293 [1907-2017](https://doi.org/10.5194/nhess-17-1907-2017).
- 294 PlanetTeam. 2017. Planet Application Program Interface: In Space for Life on Earth. *San Francisco, CA*<https://api.planet.com>.
- 295 Roback, K., Clark, M.K., et al. 2018. The size, distribution, and mobility of landslides caused by the 2015 Mw7.8 Gorkha earthquake, Nepal.
296 *Geomorphology*, **301**, 121–138, <https://doi.org/10.1016/J.GEOMORPH.2017.01.030>.
- 297 Shrestha, S. & Kang, T.-S. 2017. Assessment of seismically-induced landslide susceptibility after the 2015 Gorkha earthquake, Nepal. *Bulletin*
298 *of Engineering Geology and the Environment*, 1–14, <https://doi.org/10.1007/s10064-017-1191-4>.
- 299 Xu, C., Xu, X., Yao, X. & Dai, F. 2014. Three (nearly) complete inventories of landslides triggered by the May 12, 2008 Wenchuan Mw 7.9
300 earthquake of China and their spatial distribution statistical analysis. *Landslides*, **11**, 441–461, [https://doi.org/10.1007/s10346-013-](https://doi.org/10.1007/s10346-013-0404-6)
301 [0404-6](https://doi.org/10.1007/s10346-013-0404-6).
- 302 Xu, C., Tian, Y., Zhou, B., Ran, H. & Lyu, G. 2017. Landslide damage along Araniko highway and Pasang Lhamu highway and regional
303 assessment of landslide hazard related to the Gorkha, Nepal earthquake of 25 April 2015. *Geoenvironmental Disasters*, **4**, 14,

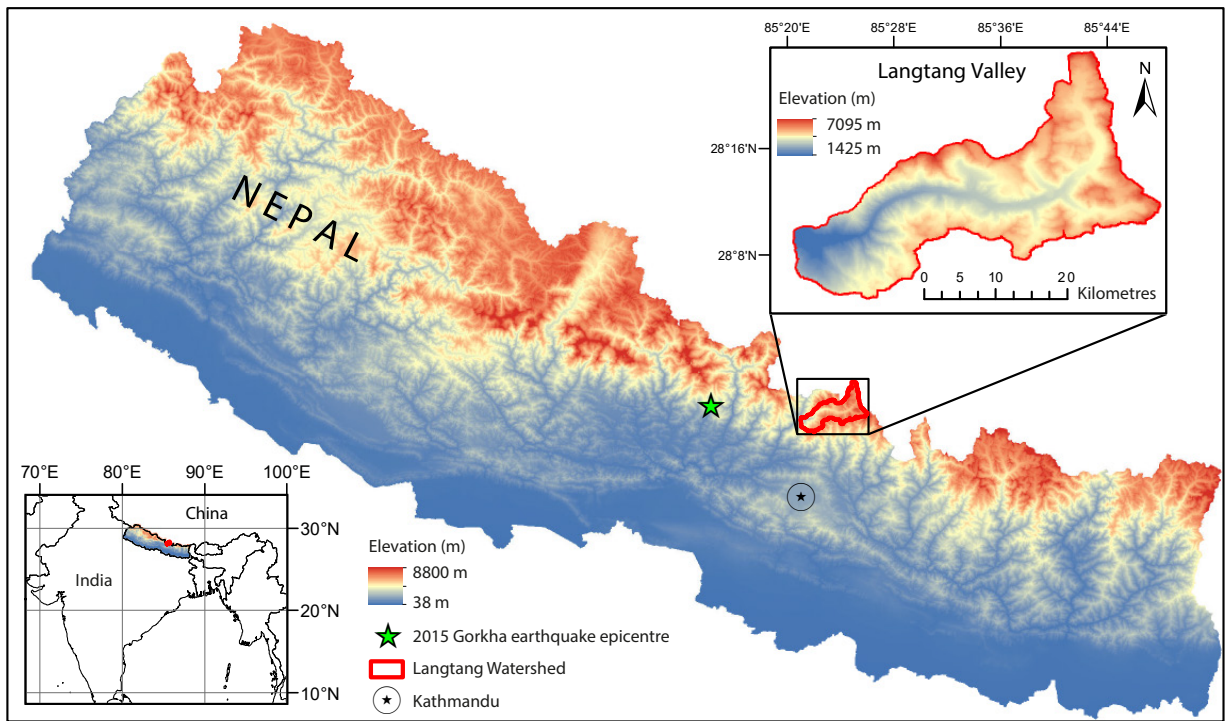


Fig. 1. Overview location map of Nepal and the Langtang Valley watershed.

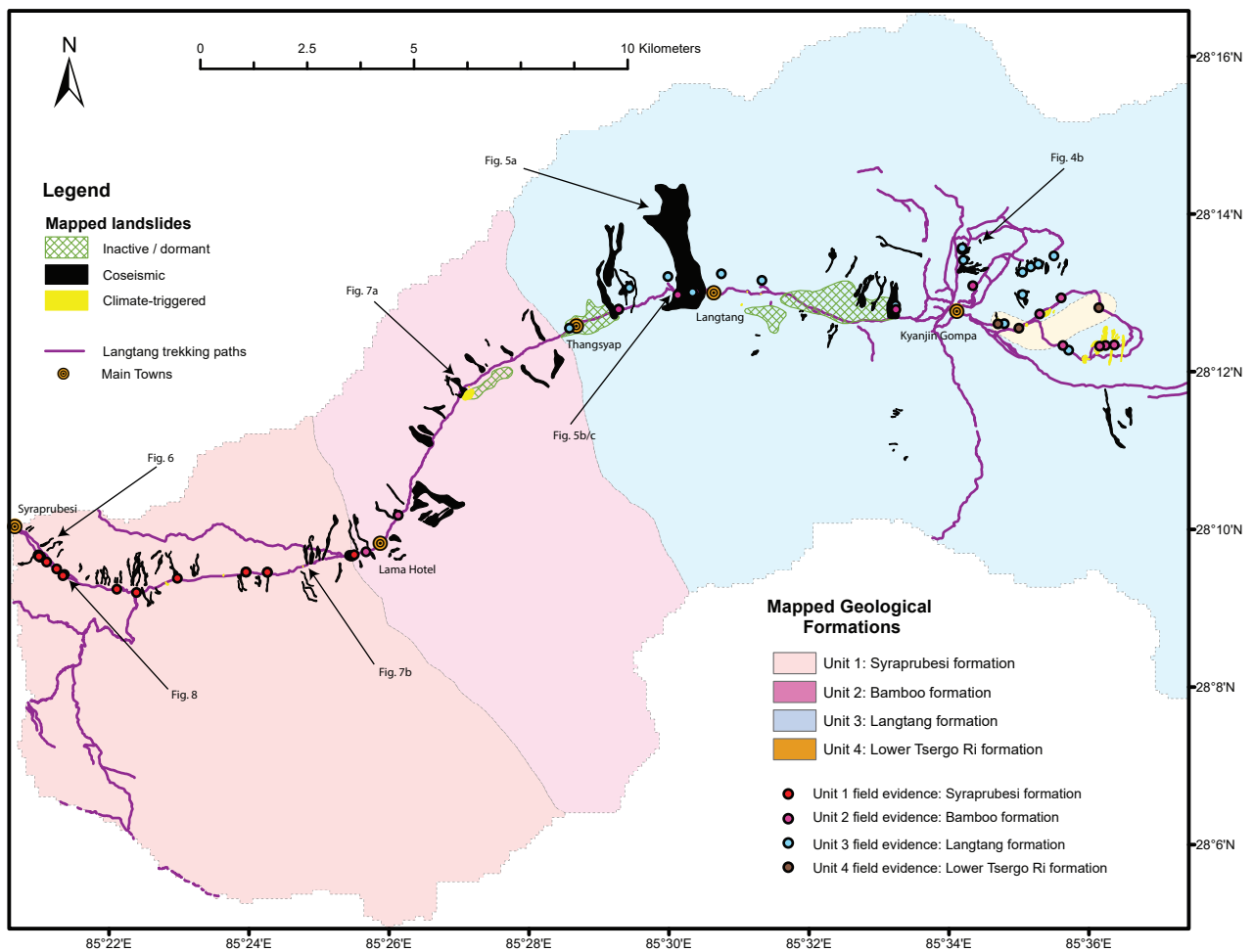


Fig. 2. Map of the lower portion of Langtang Valley that was the focus of the fieldwork. The main geological unit observations and estimated extents, towns, trekking routes and mapped landslides are displayed. The locations of the landslides in figures 4-8 are also highlighted.

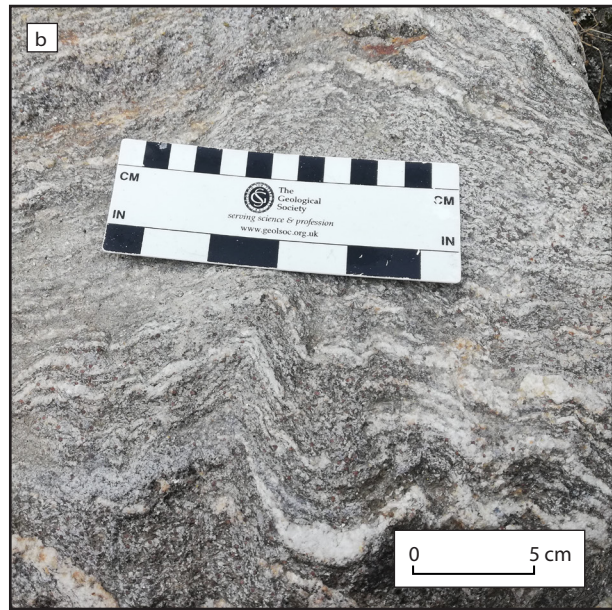
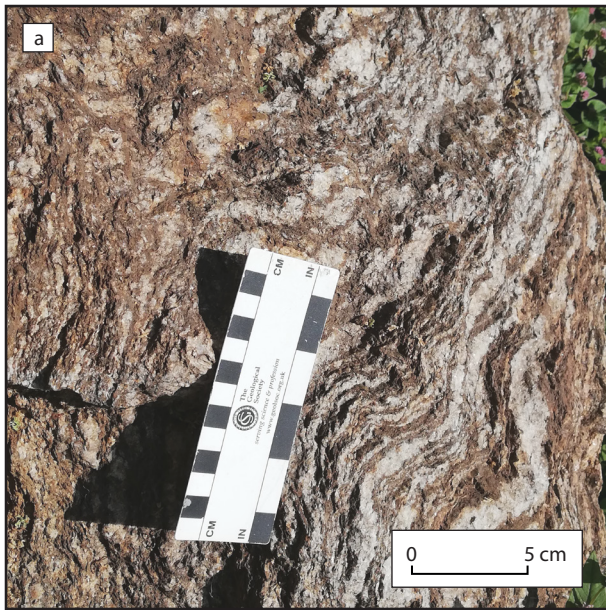


Fig. 3. (a) Example material of unit 1, a muscovite, biotite, plagioclase, quartz, garnet gneiss, termed here as the Syrarubesi Formation. Note the strong mylonitic fabric. **(b)** Example material of unit 2, a muscovite, biotite, plagioclase, quartz, tourmaline gneiss, termed here as the Bamboo Formation. Again, note the strong mylonitic fabric, and the dominance of quartz and biotite.

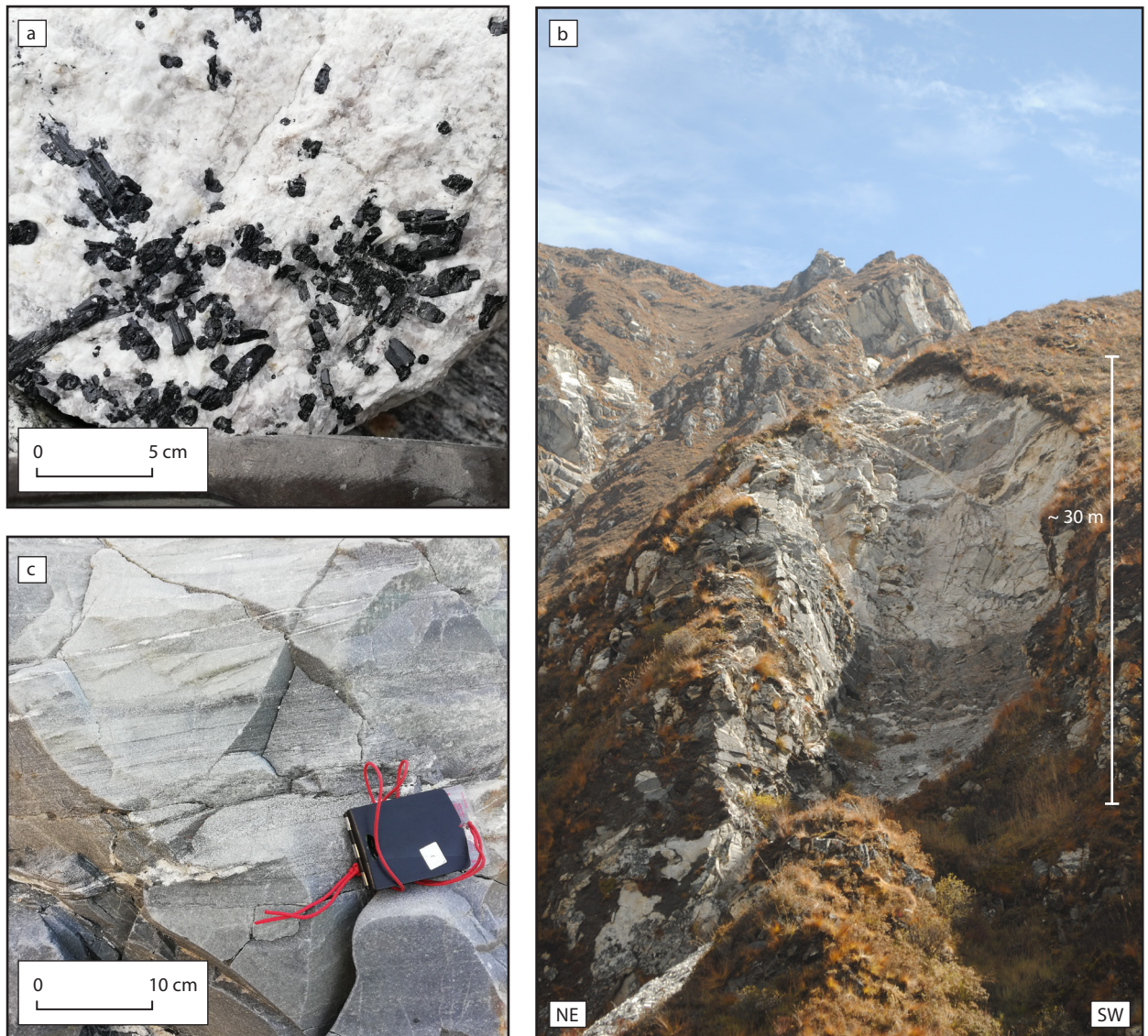


Fig. 4. (a) Example material of unit 3, a leucogranite with large, 1 – 5 cm, crystals of tourmaline, termed here as the Langtang formation. (b) A typical rockfall found in the eastern, higher elevation portions of Langtang Valley, with large intrusions of leucogranite within the bedrock of the scar. (c) Example material of unit 4, a finer grained, 0.25 – 1 cm, biotite, plagioclase, muscovite, quartz, semi-pelite schist, termed here as the Lower Tsergo Ri Formation.

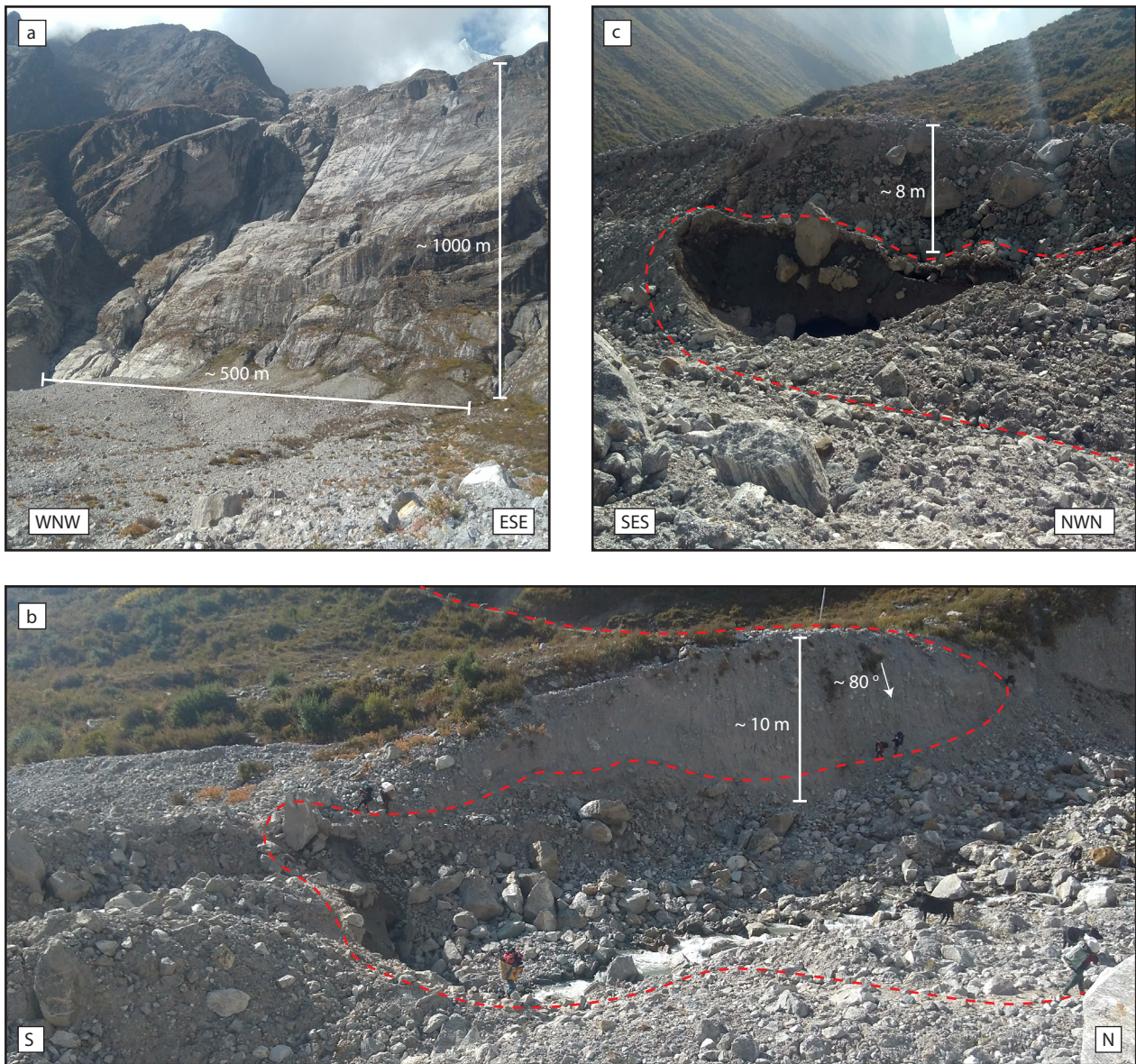


Fig. 5. (a) Front view of the Langtang Avalanche. Note the clear striations on the relatively smooth back-scar and change in slope of the back-scar which is indicative of a rotational element of movement. (b) A section of the Langtang Avalanche deposits that have been incised by a river. The precarious location of the new trekking route is shown by the red-dashed line. (c) A tunnel incised underneath the landslide deposits by a river. Red line indicates the current position of the trekking path over the top of the tunnel.



Fig. 6. Debris slide located ~4 km east of Syraprubesi. Red-dashed line indicates the main trekking path that has been impacted by the failure. The yellow boxes indicate the position of electricity / telegraph poles.

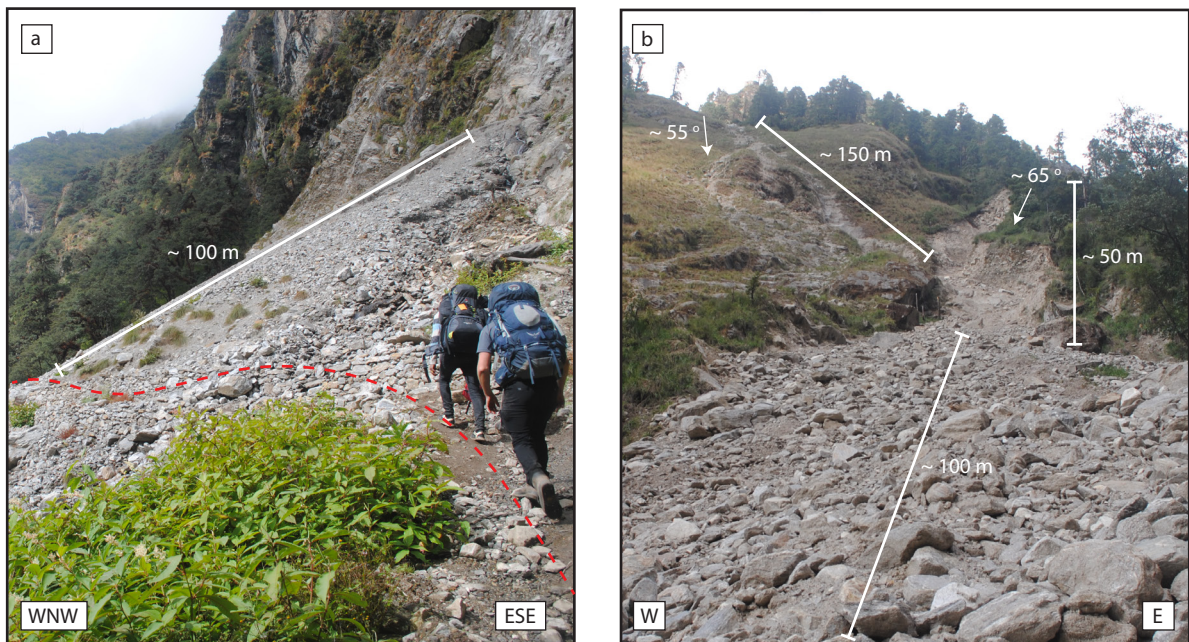


Fig. 7. (a) Debris fan of an unconstrained rockfall located ~ 4 km west of Thangsyap, which has intersected the trekking path (red-dashed line) below. (b) Debris fan of material from a debris flow and rock/debris fall that also intersected the trekking path (from where this photo was taken).

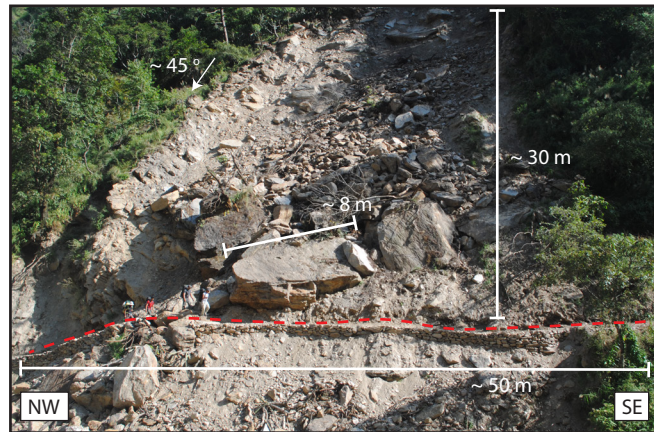


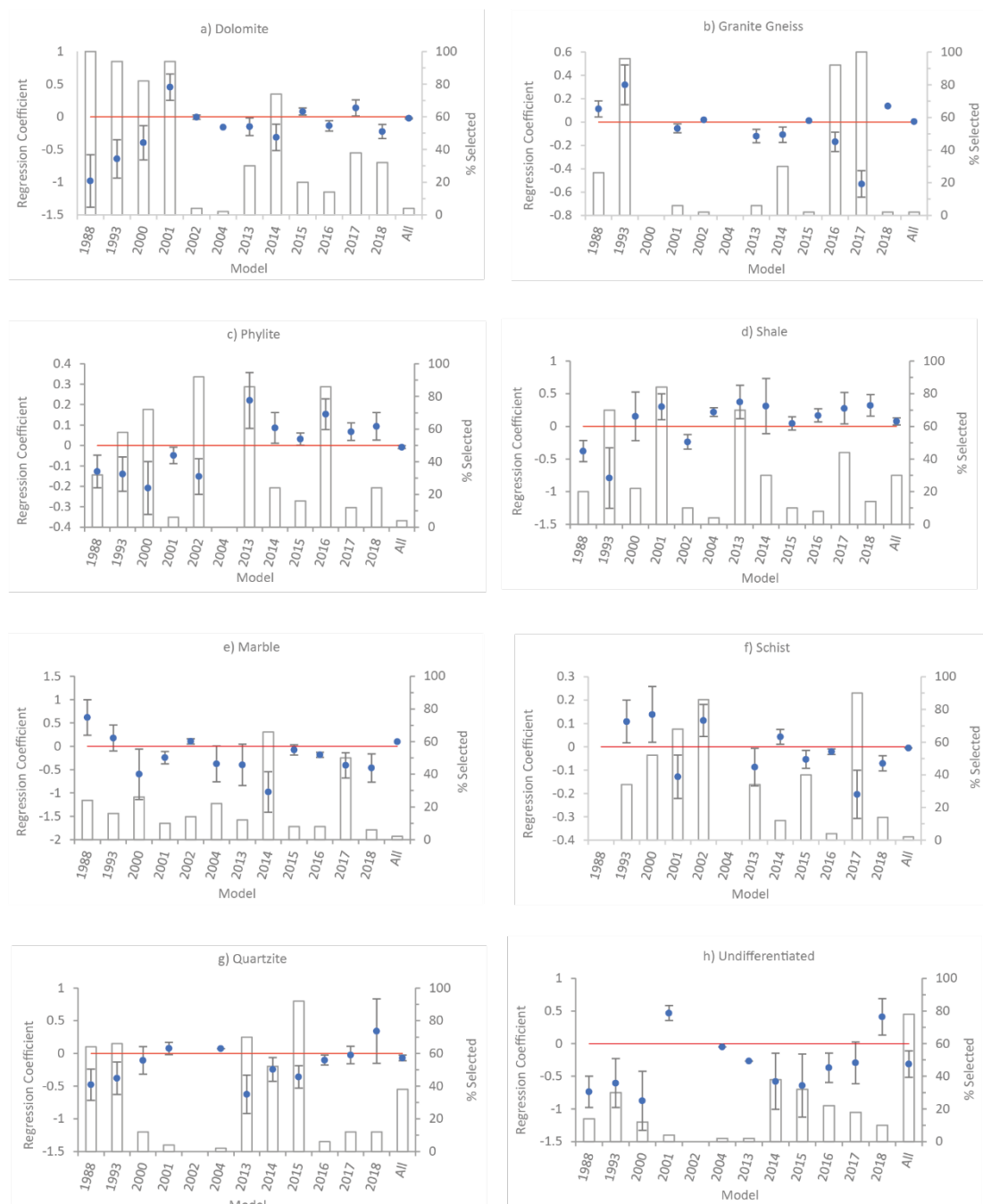
Fig. 8. Monsoon-triggered translational slide located 2 km east of Syraprubesi. A new trekking path (red-dashed line) has been constructed through the deposits, yet many large unstable boulders remain above the path.

Appendix D. Regional coseismic model regression coefficients and LASSO selection percentages.

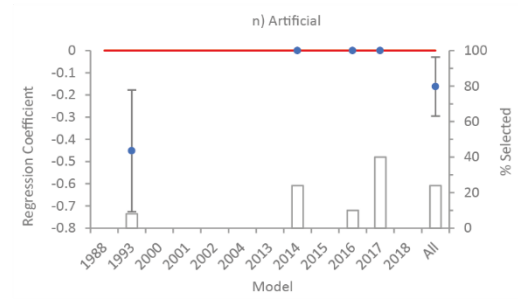
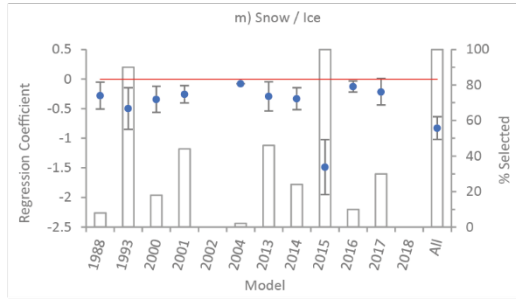
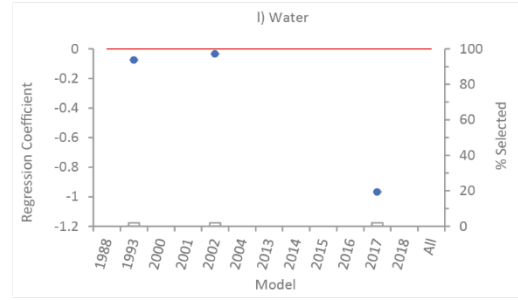
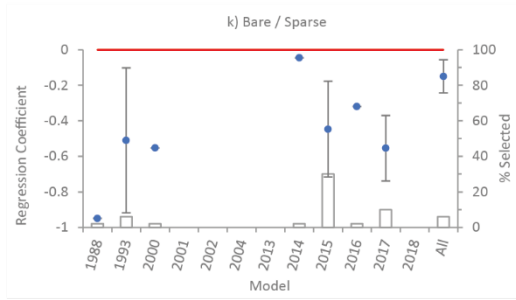
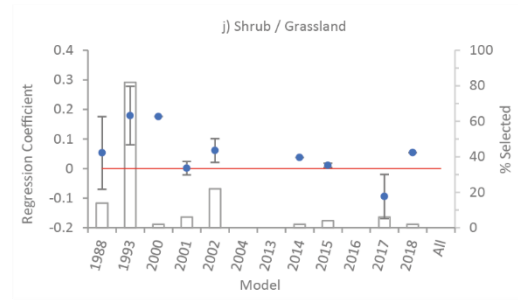
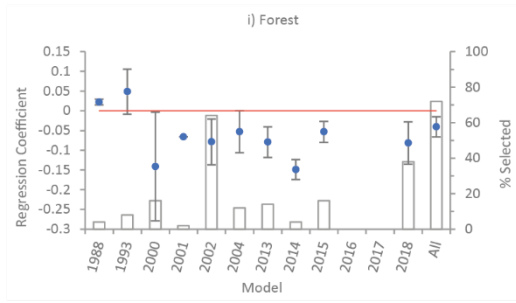
Factor	% times selected by LASSO	Mean regression coefficient	SD of regression coefficient
(Intercept)	100	1.4041	0.0647
Aspect	100	0.0157	0.0057
Distance to channels	100	-0.3797	0.0143
Elevation	100	-0.2797	0.0237
Excess topography	100	-0.0396	0.0171
Local Relief	100	0.4108	0.0225
Near channel k_{sn}	98	0.2059	0.0475
Near channel SSP	98	0.1044	0.0248
PFI	16	-1.1801	0.0107
Planform curvature	98	-0.0248	0.0126
Profile curvature	100	0.1084	0.0126
Slope	100	1.0796	0.0184
Dolomite	100	0.6125	0.0617
Granite / gneiss	70	0.0168	0.0248
Phyllite	100	-0.2548	0.0319
Quaternary sandstone / conglomerate	42	-3.4338	0.0685
Marble	64	-1.7376	0.1022
Schist	78	-1.4996	0.0366
Quartzite	100	0.2453	0.0675
Shale	100	0.1325	0.0714
Undifferentiated lithology	72	-1.4207	0.3154
Cropland	4	-0.0072	0.0071
Forest	100	0.0954	0.0208
Shrub / grassland	92	-0.0521	0.0244
Bare / sparse earth	100	-0.7780	0.2344
Water	28	-1.0645	0.5336
Permanent snow/ice	100	-0.4211	0.0756
Artificial	60	-0.6410	0.4261

Appendix D. The LASSO selection percentages and mean regression coefficients obtained for each control factor variable of the 50 developed regional coseismic models.

Appendix E. Land use and geology regression coefficients and LASSO selection percentages for the 12 BLR models developed in Chapter 4.

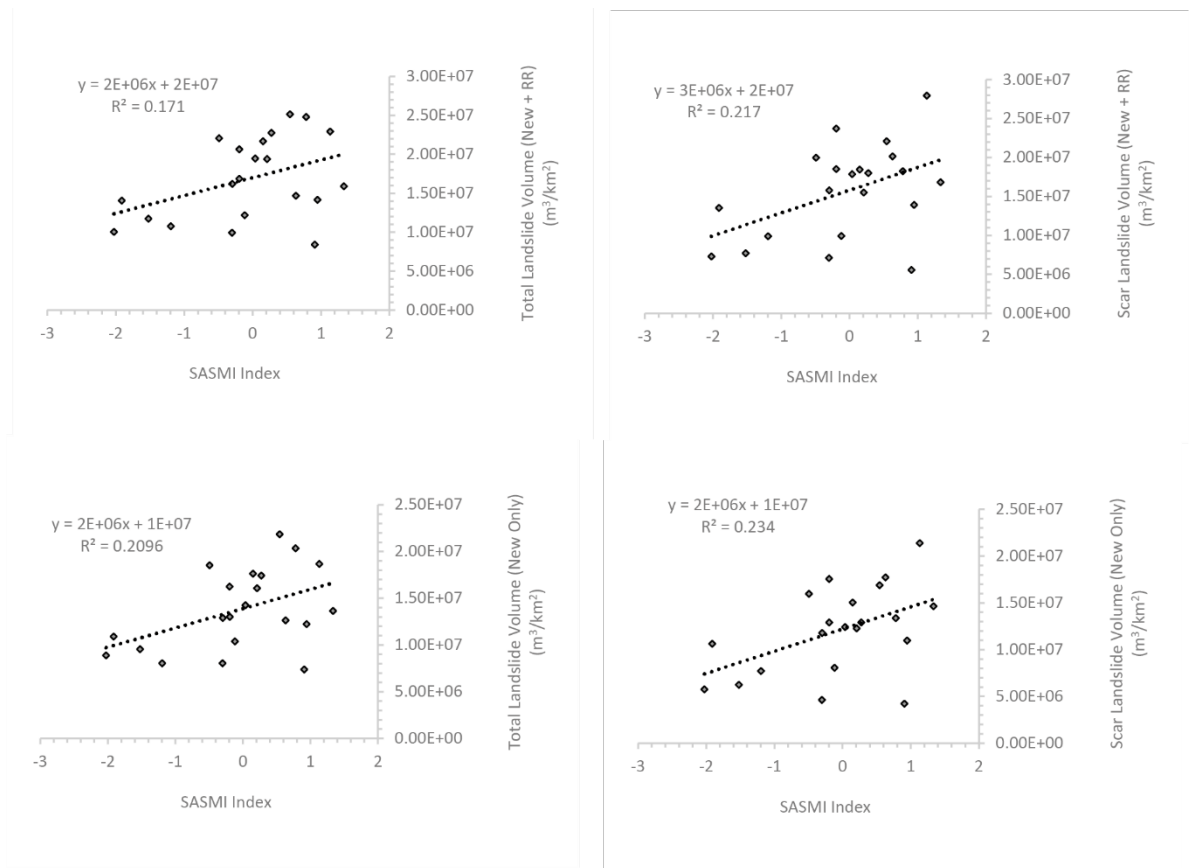


Appendix E. a – n) Results of multi-temporal Binary Logistic Regression (BLR) modelling for land use and geology. Blue circles show the average regression coefficient calculated from the 50-models run per year. Error bars show ± 1 SD. Bars show the percentage of the 50 models run for each year in which that control factor was selected by the LASSO (Least Absolute Shrinkage and Selection Operator). Red line shows the 0-line of the regression coefficient axis.



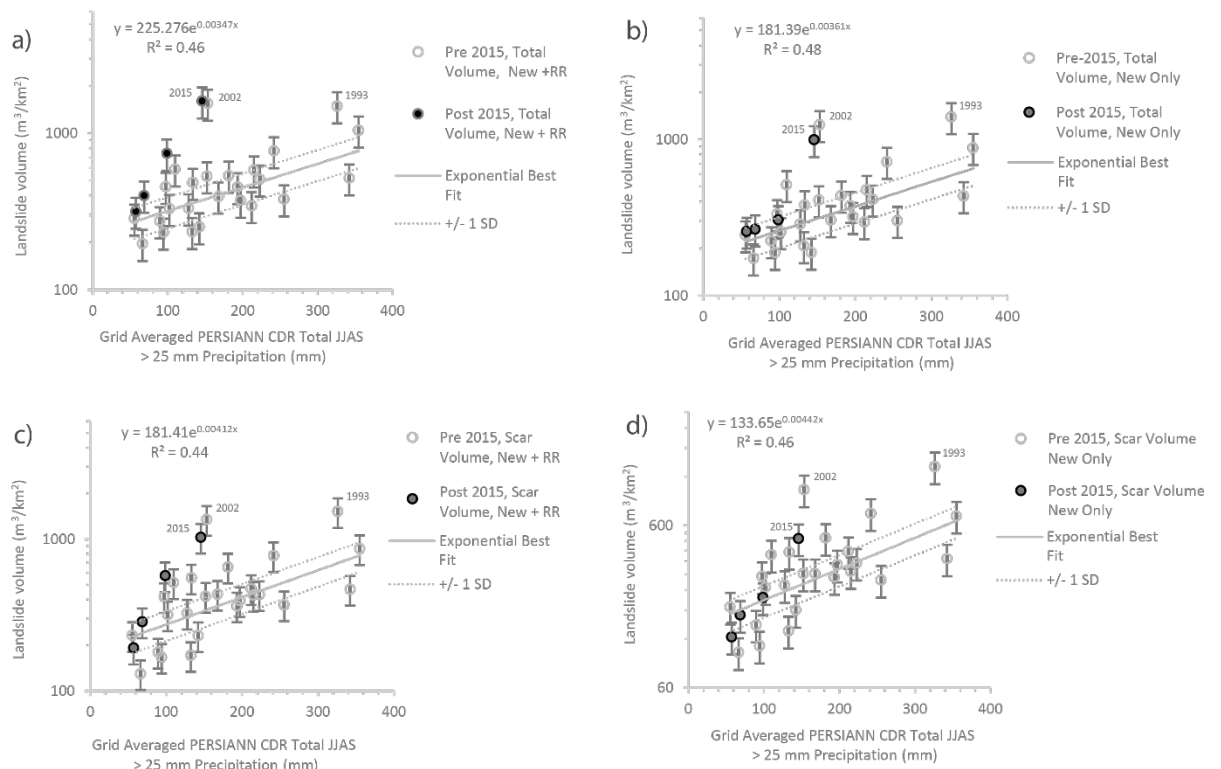
Appendix E (cont.). a – n) Results of multi-temporal Binary Logistic Regression (BLR) modelling for land use and geology. Blue circles show the average regression coefficient calculated from the 50-models run per year. Error bars show ± 1 SD. Bars show the percentage of the 50 models run for each year in which that control factor was selected by the LASSO (Least Absolute Shrinkage and Selection Operator). Red line shows the 0-line of the regression coefficient axis.

Appendix F. Correlations between SASMI and landslide volume.

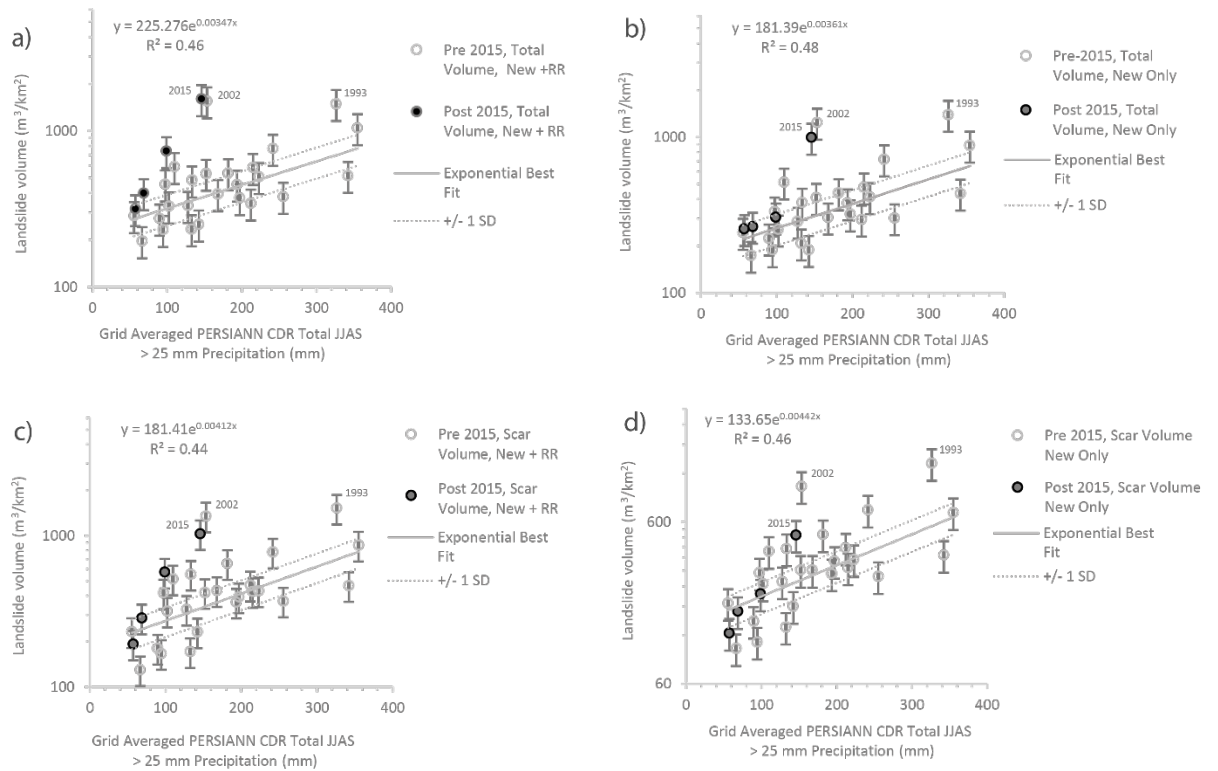


Appendix F. Correlations between the SASMI measure of Asia summer monsoon strength and the four measures of volumetric landslide rate used in Chapter 5.

Appendix G. Non-best-fit correlations between proxies of ASM-strength and landslide volume.

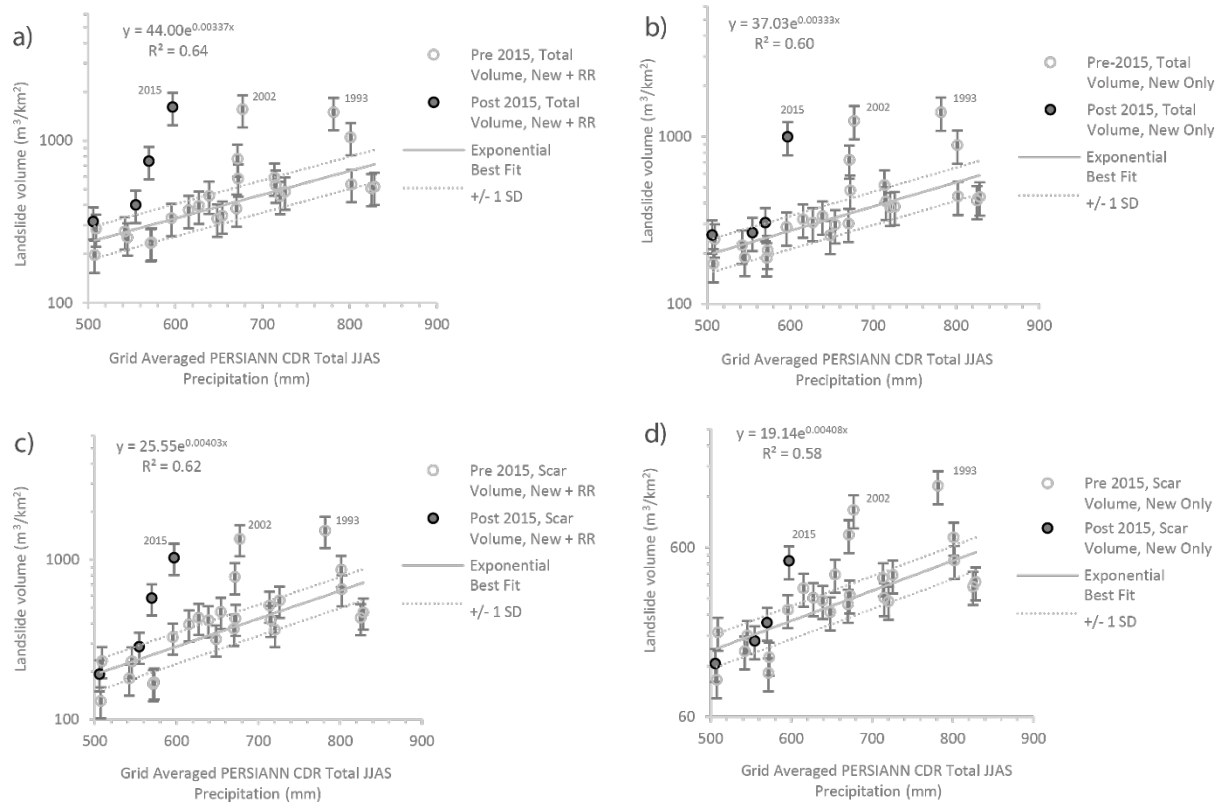


Appendix G. a – d) Empirical relationships between measures of landslide volume (m^3/km^2) and PERSIANN-CDR total MJJAS precipitation > 25 mm for a) total “New + RR” volume, b) total “New Only” volume, c) scar “New + RR” volume and d) scar “New Only” volume. Where, in all cases “New + RR” refers to the combined volumes of both new failures and reactivations/remobilisations and “New Only” refers to just the volumes of new failures, with reactivations and remobilisations excluded. The exponential best fits shown on these graphs apply to the non-anomalous pre-2015 points only, with all anomalous points labelled individually. The post-2015 points are also shown for reference, as are the ± 1 standard errors on the fit equations.

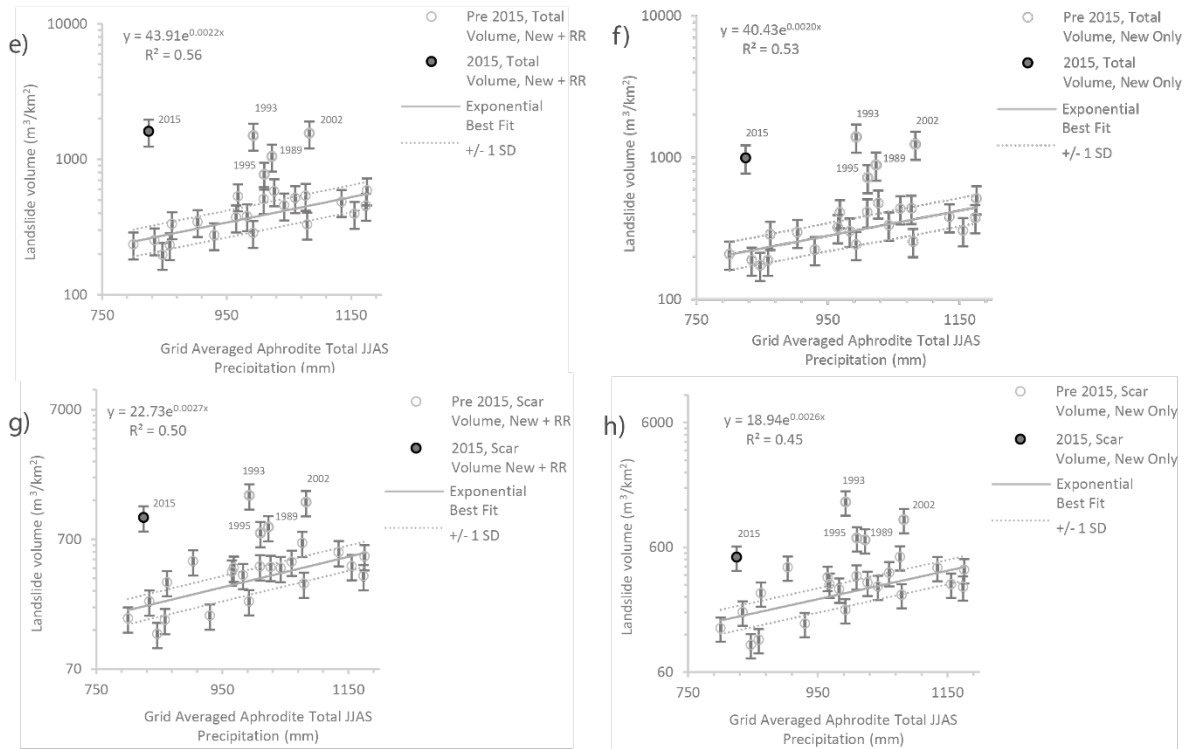


Appendix G (cont.) e – h) Empirical relationships between measures of landslide volume (m^3/km^2) and APHRODITE total 15th June - Sept precipitation > 25 mm for e) total “New + RR” volume, f) total “New Only” volume, g) scar “New + RR” volume and h) scar “New Only” volume. Where, in all cases “New + RR” refers to the combined volumes of both new failures and reactivations/remobilisations and “New Only” refers to just the volumes of new failures, with reactivations and remobilisations excluded. The exponential best fits shown on these graphs apply to the non-anomalous pre-2015 points only, with all anomalous points labelled individually. The post-2015 points are also shown for reference, as are the +/- 1 standard errors on the fit equations.

Appendix H. Non-best-fit correlations between proxies of ASM-strength and landslide volume.

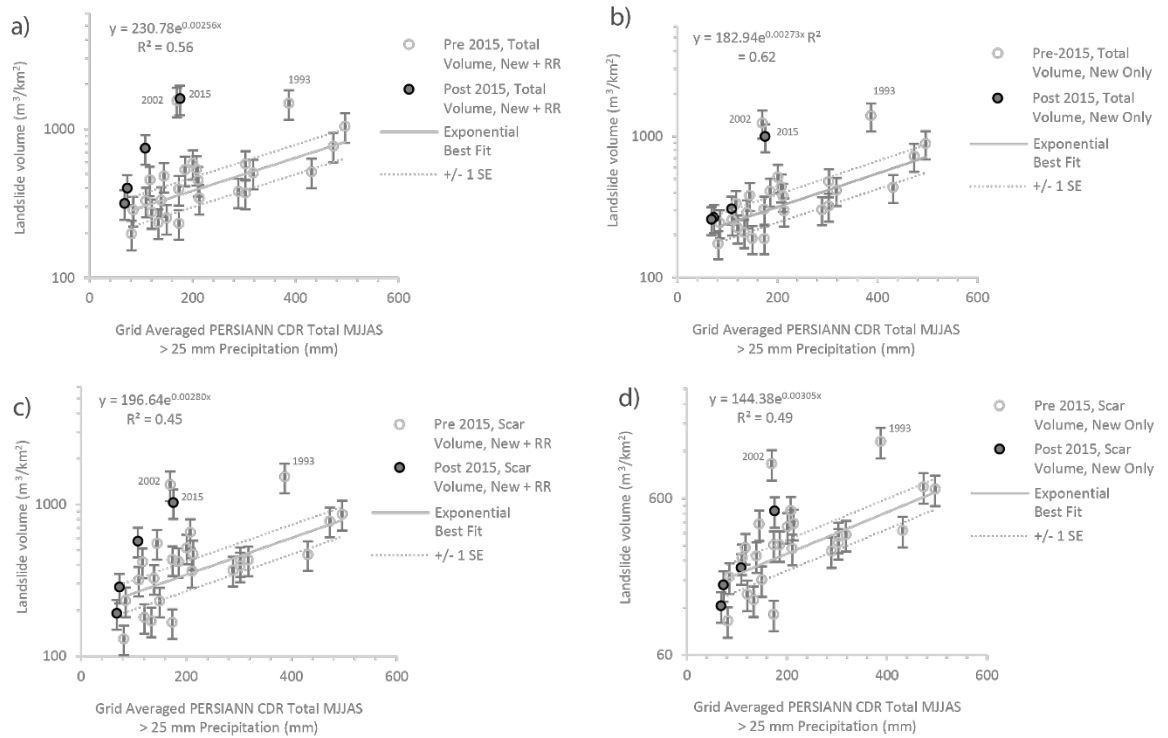


Appendix H. a – d) Empirical relationships between measures of landslide volume (m^3/km^2) and PERSIANN-CDR total 15th June - September precipitation for a) total “New + RR” volume, b) total “New Only” volume, c) scar “New + RR” volume and d) scar “New Only” volume. Where, in all cases “New + RR” refers to the combined volumes of both new failures and reactivations/remobilisations and “New Only” refers to just the volumes of new failures, with reactivations and remobilisations excluded. The exponential best fits shown on these graphs apply to the non-anomalous pre-2015 points only, with all anomalous points labelled individually. The post-2015 points are also shown for reference, as are the +/- 1 standard errors on the fit equations.

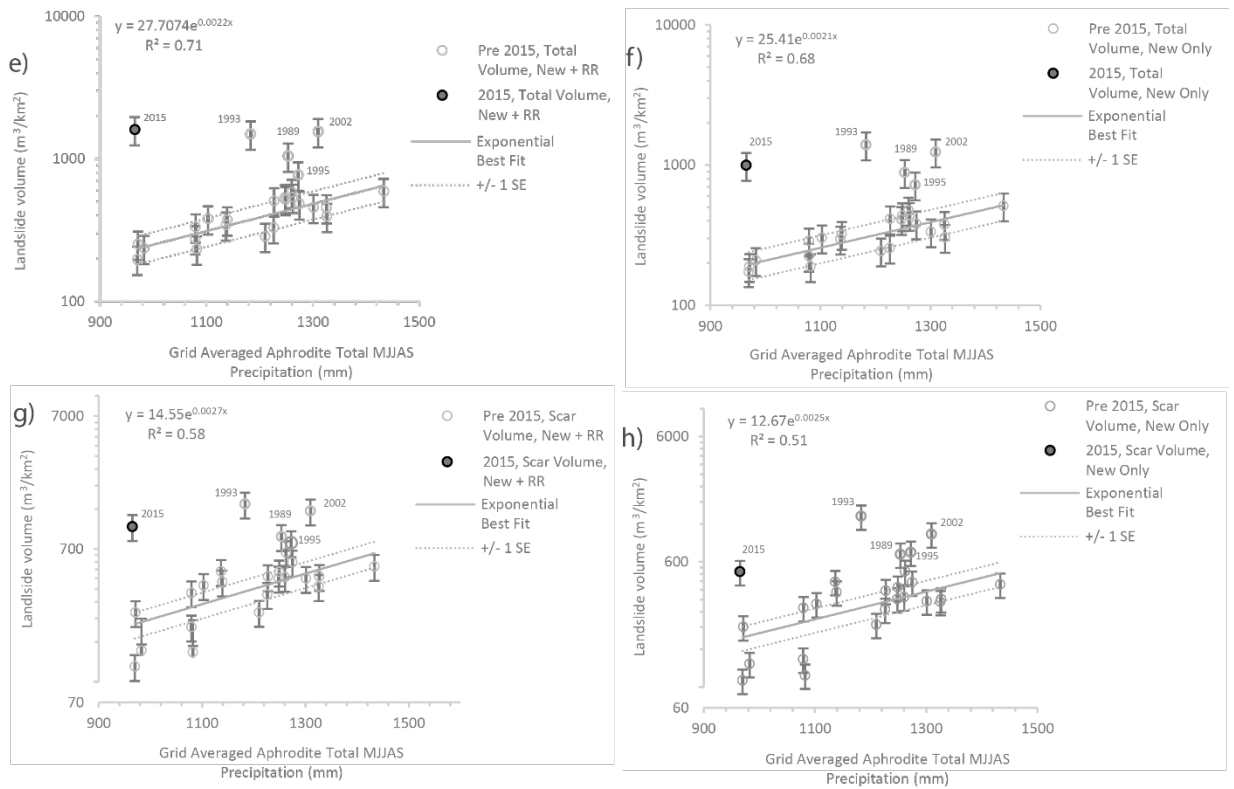


Appendix H (cont.) e – h) Empirical relationships between measures of landslide volume (m^3/km^2) and APHRODITE total 15th June – September precipitation for e) total “New + RR” volume, f) total “New Only” volume, g) scar “New + RR” volume and h) scar “New Only” volume. Where, in all cases “New + RR” refers to the combined volumes of both new failures and reactivations/remobilisations and “New Only” refers to just the volumes of new failures, with reactivations and remobilisations excluded. The exponential best fits shown on these graphs apply to the non-anomalous pre-2015 points only, with all anomalous points labelled individually. The post-2015 points are also shown for reference, as are the ± 1 standard errors on the fit equations.

Appendix I. Non-best-fit correlations between proxies of ASM-strength and landslide volume.

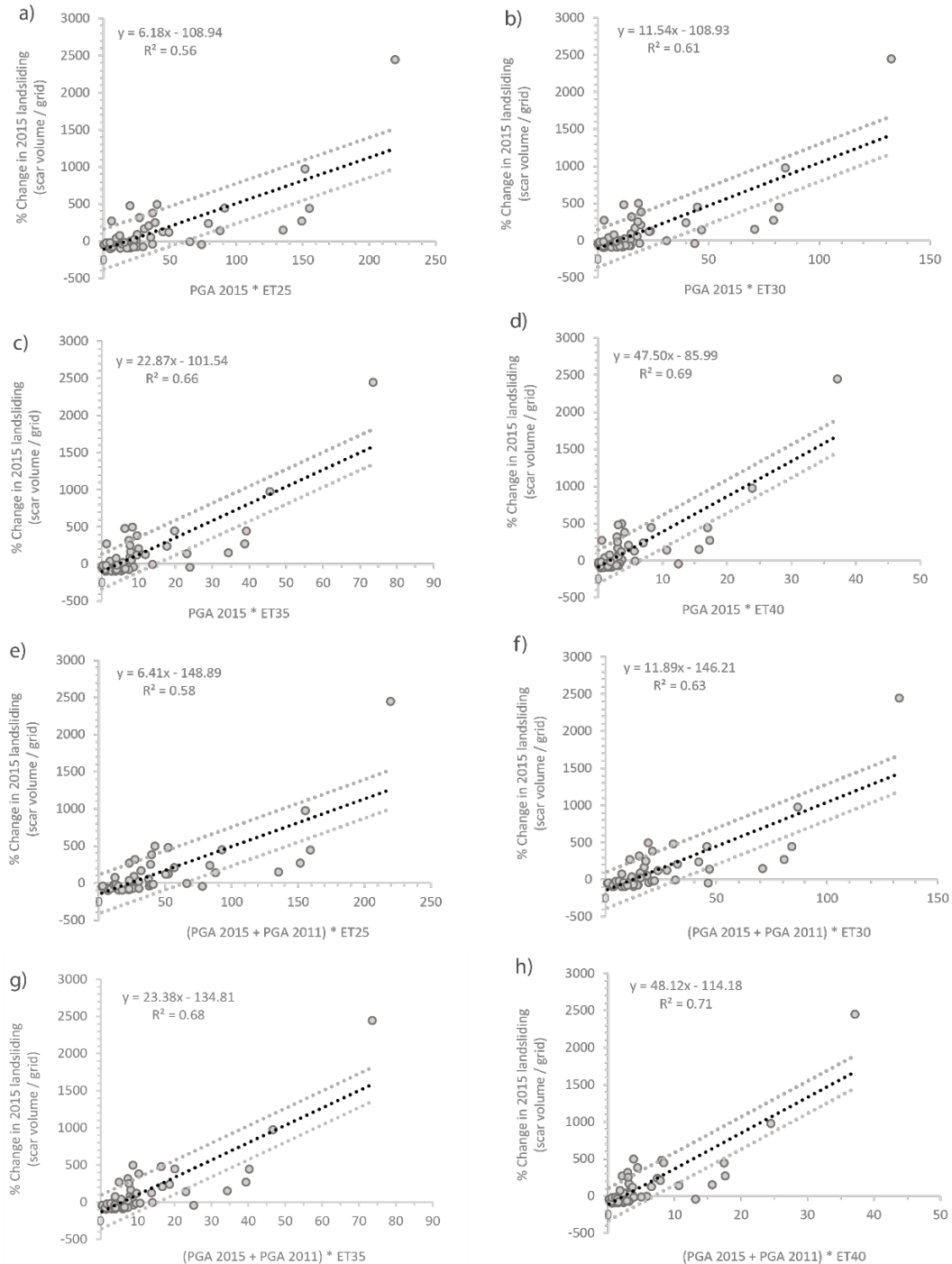


Appendix I a – d) Empirical relationships between measures of landslide volume (m^3/km^2) and PERSIANN-CDR total MJJAS > 25 mm precipitation for a) total “New + RR” volume, b) total “New Only” volume, c) scar “New + RR” volume and d) scar “New Only” volume. Where, in all cases “New + RR” refers to the combined volumes of both new failures and reactivations/remobilisations and “New Only” refers to just the volumes of new failures, with reactivations and remobilisations excluded. The exponential best fits shown on these graphs apply to the non-anomalous pre-2015 points only, with all anomalous points labelled individually. The post-2015 points are also shown for reference, as are the +/- 1 standard errors on the fit equations.



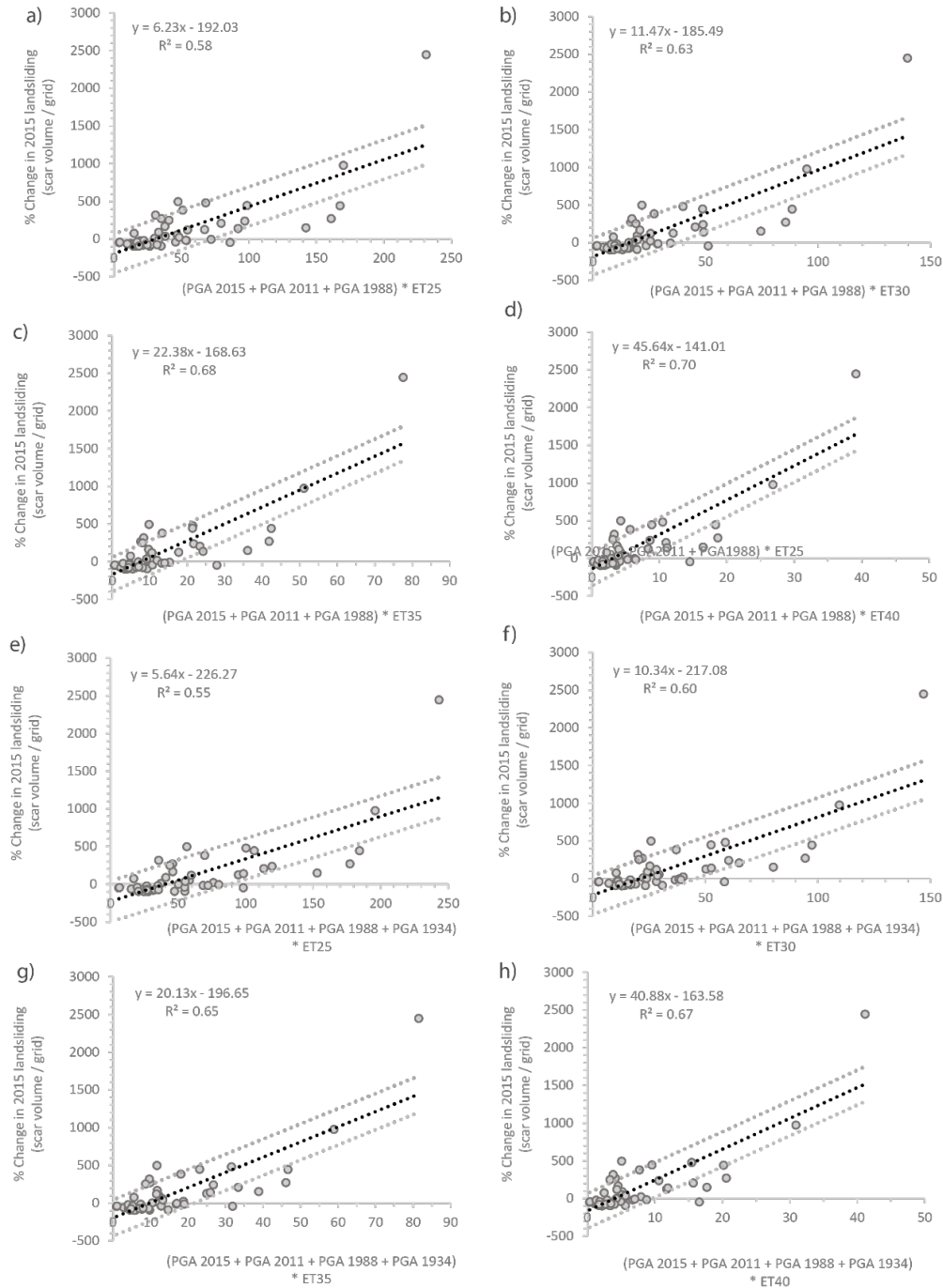
Appendix I (cont.) e – h) Empirical relationships between measures of landsliding volume (m^3/km^2) and APHRODITE total MJJAS precipitation for e) total “New + RR” volume, f) total “New Only” volume, g) scar “New + RR” volume and h) scar “New Only” volume. Where, in all cases “New + RR” refers to the combined volumes of both new failures and reactivations/remobilisations and “New Only” refers to just the volumes of new failures, with reactivations and remobilisations excluded. The exponential best fits shown on these graphs apply to the non-anomalous pre-2015 points only, with all anomalous points labelled individually. The post-2015 points are also shown for reference, as are the +/- 1 standard errors on the fit equations.

Appendix J. Correlations between 2015 percentage change in landsliding and ‘PGA-excess topography’ at excess topography thresholds of 25°, 30°, 35° and 40°.



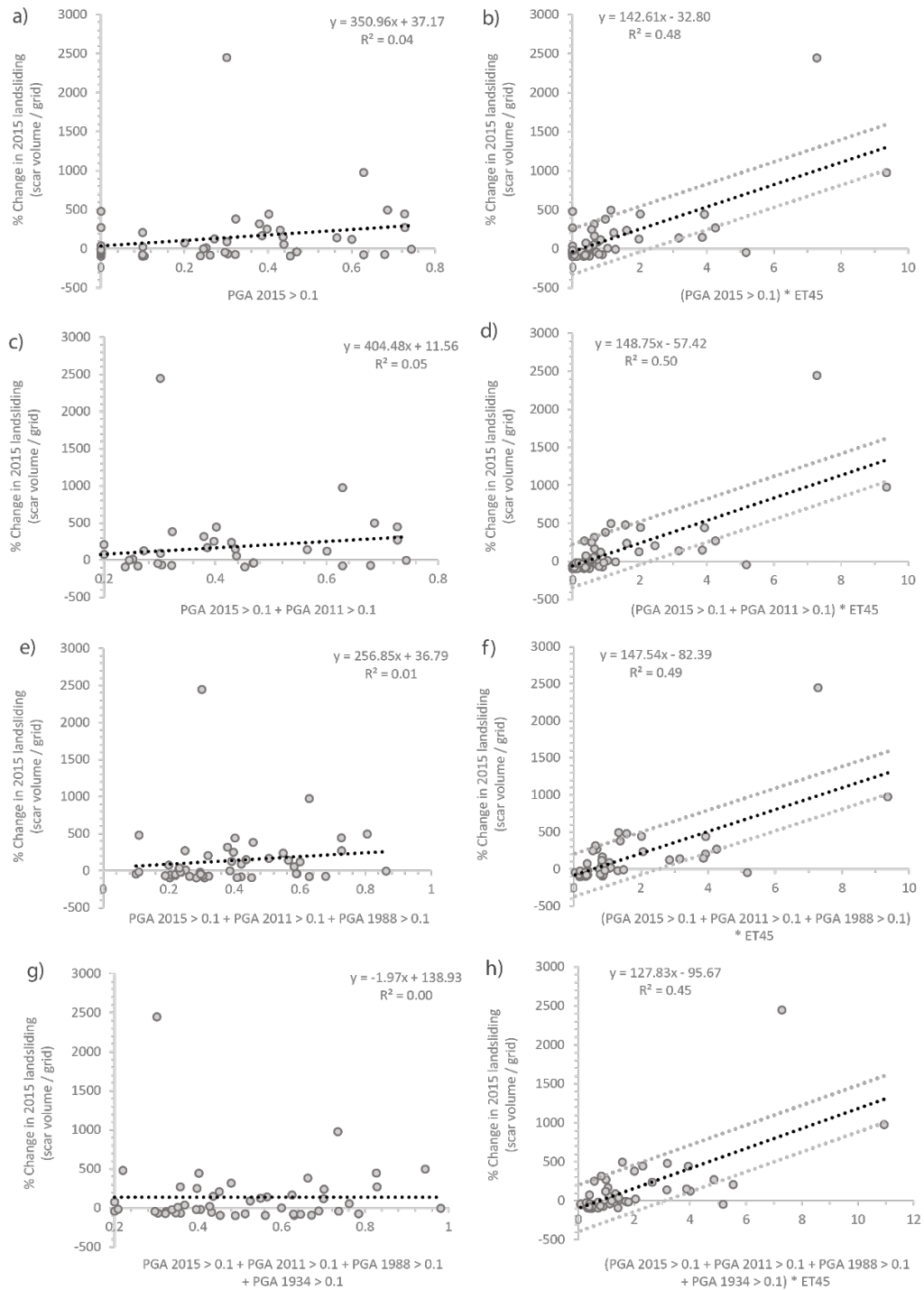
Appendix J Correlations between excess monsoon-triggered landsliding in 2015 and maximum summed PGA in the 2015 main shock and largest aftershock multiplied by excess topography above a threshold angles of a) 25o, b) 30o, c) 35o and d) 40o. e – h) Correlations as in a – d) but with the PGA from the 2011 earthquake included in the summed PGA. The linear best-fits are shown with +/- 1 standard error in each case.

Appendix K. Correlations between 2015 percentage change in landsliding and ‘PGA-excess topography’ at excess topography thresholds of 25°, 30°, 35° and 40°.



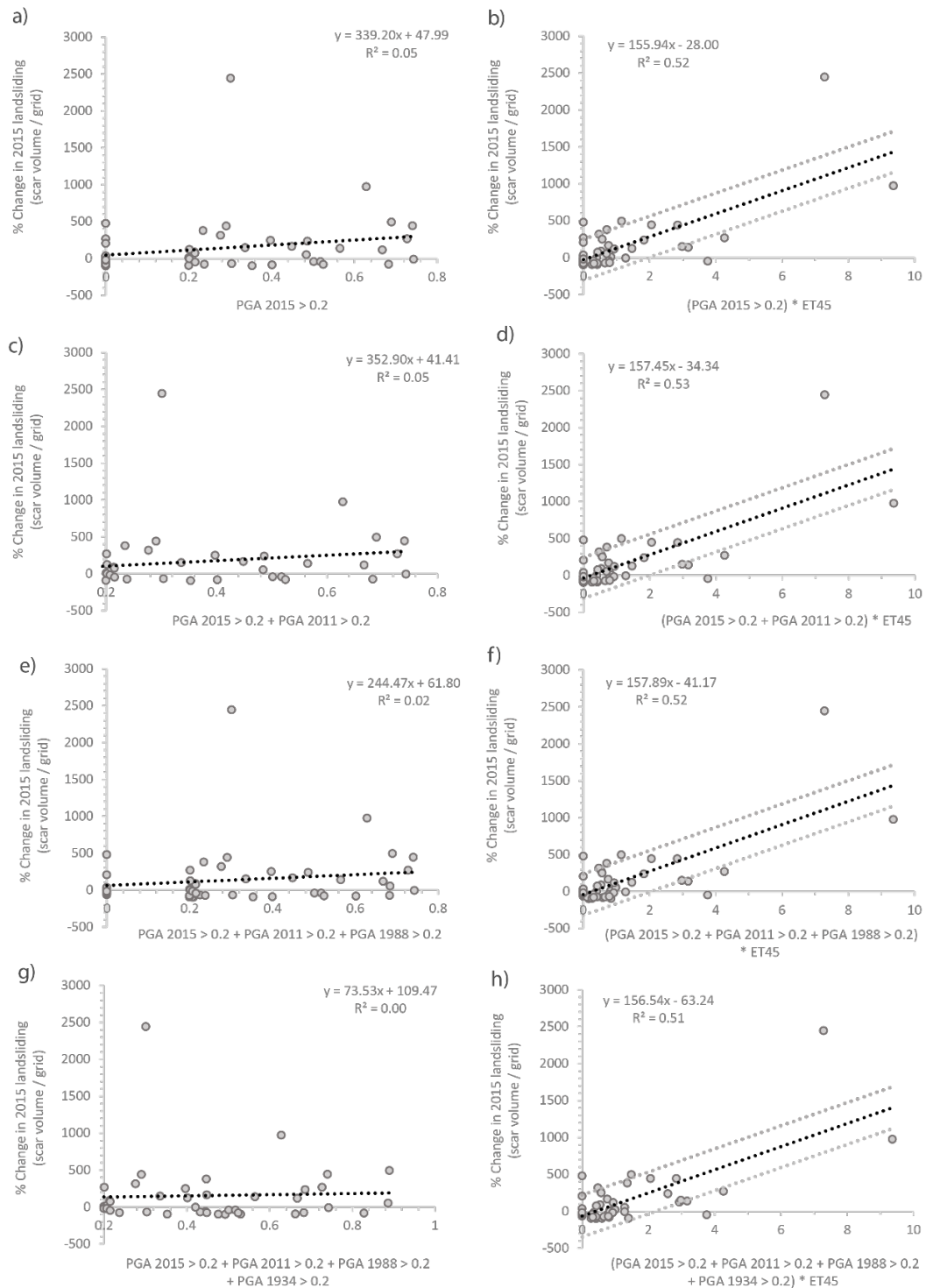
Appendix K. Correlations between excess monsoon-triggered landsliding in 2015 and maximum summed PGA in the 2015 main shock, 2015 largest aftershock, 2011 earthquake and 1988 earthquake multiplied by excess topography above a threshold angles of a) 25°, b) 30°, c) 35° and d) 40°. e – h) Correlations as in a – d) but with the PGA from the 1934 earthquake included in the summed PGA. The linear best-fits are shown with +/- 1 standard error in each case.

Appendix L. Correlations between 2015 percentage change in landsliding and ‘PGA-excess topography’ at PGA thresholds of > 0.1g.



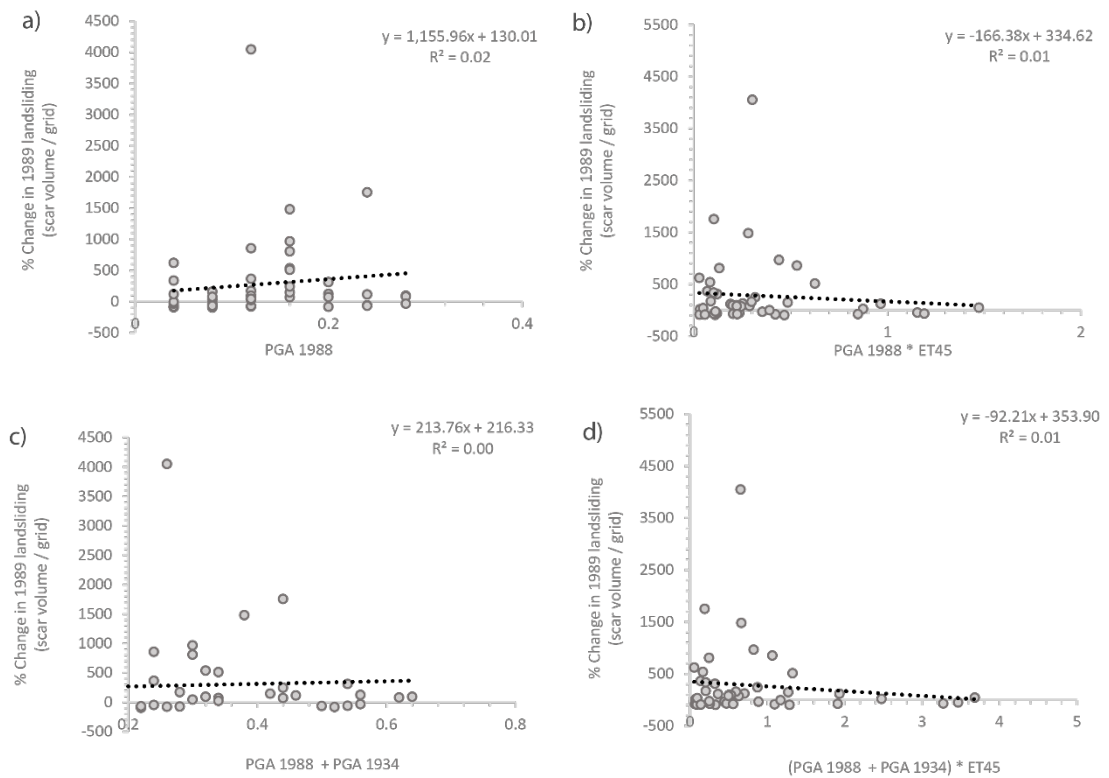
Appendix L. Correlations between excess monsoon-triggered landsliding in 2015 and summed PGA > 0.1 g in a) the 2015 main aftershock and largest aftershock, b) as a) but plus the 2011 PGA > 0.1 g, c) as b) but plus the 1988 PGA > 0.1 g, and d) as in c) but plus the 1934 PGA > 0.1 g. e – h) the same correlations in a – d) but with PGA multiplied by excess topography above a threshold angle of 45°.

Appendix M. Correlations between 2015 percentage change in landsliding and ‘PGA-excess topography’ at PGA thresholds of > 0.2g.



Appendix M. Correlations between excess monsoon-triggered landslides in 2015 and summed PGA > 0.2 g in a) the 2015 main aftershock and largest aftershock, b) as in a) but plus the 2011 PGA > 0.2 g, c) as in b) but plus the 1988 PGA > 0.2 g, and d) as in c) but plus the 1934 PGA > 0.2 g. e – h) the same correlations in a – d) but with PGA multiplied by excess topography above a threshold angle of 45°.

Appendix N. Correlations between 1989 percentage change in landsliding and ‘PGA-excess topography’ at an excess topography threshold of 45°.



Appendix N. Correlations between excess monsoon-triggered landsliding in 1989 and summed PGA in a) the 1988 earthquake, b) the 1988 earthquake multiplied by excess topography above a threshold angle of 45°, c) the 1988 ad 1934 earthquake, d) the 1988 and 1934 earthquakes multiplied by excess topography above a threshold angle of 45°.

References

- Adam, J.C., Clark, E.A., Lettenmaier, D.P. & Wood, E.F. 2006. Correction of global precipitation products for orographic effects. *Journal of Climate*, **19**, 15–38, <https://doi.org/10.1175/JCLI3604.1>.
- Adhikari, S. & Adhikary, D.K. 2019. *An Account of Nepal Disasters and Economic Fallout, Project Research and Management Associates, HAL-01995386*.
- Adition, A., Kubota, T. & Shinohara, Y. 2018. Comparison of GIS-based landslide susceptibility models using frequency ratio, logistic regression, and artificial neural network in a tertiary region of Ambon, Indonesia. *Geomorphology*, **318**, 101–111, <https://doi.org/10.1016/J.GEOMORPH.2018.06.006>.
- Al-Juaidi, A.E.M., Nassar, A.M. & Al-Juaidi, O.E.M. 2018. Evaluation of flood susceptibility mapping using logistic regression and GIS conditioning factors. *Arabian Journal of Geosciences*, **11**, 1–10, <https://doi.org/10.1007/S12517-018-4095-0/FIGURES/7>.
- Aleotti, P. & Chowdhury, R. 1999. Landslide hazard assessment: summary review and new perspectives. *Bulletin of Engineering Geology and the Environment*, **58**, 21–44, <https://doi.org/10.1007/s100640050066>.
- Alexander, D. 1992. On the causes of landslides: Human activities, perception, and natural processes. *Environmental Geology and Water Sciences*, **20**, 165–179, <https://doi.org/10.1007/BF01706160>.
- Alexandridis, T.K., Cherif, I., Kalogeropoulos, C., Monachou, S., Eskridge, K. & Silleos, N. 2013. Rapid error assessment for quantitative estimations from Landsat 7 gap-filled images. *Remote Sensing Letters*, **4**, 920–928, <https://doi.org/10.1080/2150704X.2013.815380>.
- Alford, D. 1992. Hydrological aspects of the Himalayan region. *ICIMOD Occasional paper No. 18*.
- Alvioli, M., Marchesini, I., Reichenbach, P., Rossi, M., Ardizzone, F., Fiorucci, F. &

- Guzzetti, F. 2016. Automatic delineation of geomorphological slope units with r.slopeunits v1.0 and their optimization for landslide susceptibility modeling. *Geosci. Model Dev*, **9**, 3975–3991, <https://doi.org/10.5194/gmd-9-3975-2016>.
- Amato, G., Eisank, C., Castro-Camilo, D. & Lombardo, L. 2019. Accounting for covariate distributions in slope-unit-based landslide susceptibility models. A case study in the alpine environment. *Engineering Geology*, **260**, 105237, <https://doi.org/10.1016/j.enggeo.2019.105237>.
- Andermann, C., Crave, A., Gloaguen, R., Davy, P. & Bonnet, S. 2012. Connecting source and transport: Suspended sediments in the Nepal Himalayas. *Earth and Planetary Science Letters*, **351–352**, 158–170, <https://doi.org/10.1016/j.epsl.2012.06.059>.
- Anderson, R.S., Anderson, S.P. & Tucker, G.E. 2013. Rock damage and regolith transport by frost: an example of climate modulation of the geomorphology of the critical zone. *Earth Surface Processes and Landforms*, **38**, 299–316, <https://doi.org/10.1002/esp.3330>.
- Annamalai, H., Hamilton, K. & Sperber, K.R. 2007. The South Asian summer monsoon and its relationship with ENSO in the IPCC AR4 simulations. *Journal of Climate*, **20**, 1071–1092, <https://doi.org/10.1175/JCLI4035.1>.
- Ao, M., Zhang, L., Dong, Y., Su, L., Shi, X., Balz, T. & Liao, M. 2020. Characterizing the evolution life cycle of the Sunkoshi landslide in Nepal with multi-source SAR data. *Scientific Reports*, **10**, 17988, <https://doi.org/10.1038/s41598-020-75002-y>.
- Arabameri, A., Pradhan, B., Rezaei, K., Sohrabi, M. & Kalantari, Z. 2019. GIS-based landslide susceptibility mapping using numerical risk factor bivariate model and its ensemble with linear multivariate regression and boosted regression tree algorithms. *Journal of Mountain Science*, **16**, 595–618, <https://doi.org/10.1007/s11629-018-5168-y>.
- Ashouri, H., Hsu, K.-L., et al. 2015. PERSIANN-CDR: Daily Precipitation Climate Data Record from Multisatellite Observations for Hydrological and Climate

- Studies. *Bulletin of the American Meteorological Society*, **96**, 69–83, <https://doi.org/10.1175/BAMS-D-13-00068.1>.
- Avouac, J.-P. 2003. Mountain building, erosion, and the seismic cycle in the Nepal Himalaya. *Advances in geophysics*, **46**, 1–80.
- Baeza, C. & Corominas, J. 2001. Assessment of shallow landslide susceptibility by means of multivariate statistical techniques. *Earth Surface Processes and Landforms*, **26**, 1251–1263, <https://doi.org/10.1002/esp.263>.
- Bagde, M.N. 2000. An investigation into strength and porous properties of metamorphic rocks in the Himalayas: A case study. *Geotechnical and Geological Engineering*, **18**, 209–219, <https://doi.org/10.1023/A:1026518616345>.
- Bagde, M.N. & Petroš, V. 2005. Fatigue properties of intact sandstone samples subjected to dynamic uniaxial cyclical loading. *International Journal of Rock Mechanics and Mining Sciences*, **42**, 237–250, <https://doi.org/10.1016/J.IJRMMS.2004.08.008>.
- Bagde, M.N. & Petroš, V. 2009. Fatigue and dynamic energy behaviour of rock subjected to cyclical loading. *International Journal of Rock Mechanics and Mining Sciences*, **46**, 200–209, <https://doi.org/10.1016/j.ijrmms.2008.05.002>.
- Bai, S., Wang, J., Thiebes, B., Cheng, C. & Yang, Y. 2014. Analysis of the relationship of landslide occurrence with rainfall: a case study of Wudu County, China. *Arabian Journal of Geosciences*, **7**, 1277–1285, <https://doi.org/10.1007/s12517-013-0939-9>.
- Ballantyne, C.K. 2002. Paraglacial geomorphology. *Quaternary Science Reviews*, **21**, 1935–2017, [https://doi.org/10.1016/S0277-3791\(02\)00005-7](https://doi.org/10.1016/S0277-3791(02)00005-7).
- Ballantyne, C.K., Sandeman, G.F., Stone, J.O. & Wilson, P. 2014. Rock-slope failure following Late Pleistocene deglaciation on tectonically stable mountainous terrain. *Quaternary Science Reviews*, **86**, 144–157, <https://doi.org/10.1016/j.quascirev.2013.12.021>.
- Bălteanu, D., Micu, M., et al. 2020. National-scale landslide susceptibility map of

- Romania in a European methodological framework. *Geomorphology*, **371**, 107432, <https://doi.org/10.1016/j.geomorph.2020.107432>.
- Barnard, P.L., Owen, L.A., Finkel, R.C. & Asahi, K. 2006. Landscape response to deglaciation in a high relief, monsoon-influenced alpine environment, Langtang Himal, Nepal. *Quaternary Science Reviews*, **25**, 2162–2176, <https://doi.org/10.1016/J.QUASCIREV.2006.02.002>.
- Beck, H.E., Vergopolan, N., et al. 2017. Global-scale evaluation of 22 precipitation datasets using gauge observations and hydrological modeling. *Hydrology and Earth System Sciences*, **21**, 6201–6217, <https://doi.org/10.5194/hess-21-6201-2017>.
- Bennett, G.L., Miller, S.R., Roering, J.J. & Schmidt, D.A. 2016. Landslides, threshold slopes, and the survival of relict terrain in the wake of the Mendocino Triple Junction. *Geology*, **44**, 363–366, <https://doi.org/10.1130/G37530.1>.
- Bhasin, R., Barton, N., Grimstad, E. & Chryssanthakis, P. 1995. Engineering geological characterization of low strength anisotropic rocks in the Himalayan region for assessment of tunnel support. *Engineering Geology*, **40**, 169–193, [https://doi.org/10.1016/0013-7952\(95\)00055-0](https://doi.org/10.1016/0013-7952(95)00055-0).
- Blöthe, J.H., Korup, O. & Schwanghart, W. 2015. Large landslides lie low: Excess topography in the Himalaya-Karakoram ranges. *Geology*, **43**, 523–526, <https://doi.org/10.1130/G36527.1>.
- Böhme, M., Hermanns, R.L., Gosse, J., Hilger, P., Eiken, T., Lauknes, T.R. & Dehls, J.F. 2019. Comparison of monitoring data with paleo-slip rates: Cosmogenic nuclide dating detects acceleration of a rockslide. *Geology*, **47**, 339–342, <https://doi.org/10.1130/G45684.1>.
- Bontemps, S., Defourny, P., Van Bogaert, E., Arino, O., Kalogirou, V. & Ramos Perez, J. 2011. *GLOBCOVER 2009 Products Description and Validation Report*.
- Bookhagen, B., Thiede, R.C. & Strecker, M.R. 2005. Abnormal monsoon years and their control on erosion and sediment flux in the high, arid northwest

- Himalaya. *Earth and Planetary Science Letters*, **231**, 131–146, <https://doi.org/10.1016/j.epsl.2004.11.014>.
- Borgomeo, E., Hebditch, K. V., Whittaker, A.C. & Lonergan, L. 2014. Characterising the spatial distribution, frequency and geomorphic controls on landslide occurrence, Molise, Italy. *Geomorphology*, **226**, 148–161, <https://doi.org/10.1016/j.geomorph.2014.08.004>.
- Brain, M.J., Rosser, N.J. & Tunstall, N. 2017. The control of earthquake sequences on hillslope stability. *Geophysical Research Letters*, **44**, 865–872, <https://doi.org/10.1002/2016GL071879>.
- Brenning, A. 2005. Spatial prediction models for landslide hazards: review, comparison and evaluation. *Nat. Hazards Earth Syst. Sci.*, **5**, 853–862, <https://doi.org/10.1029/2005-5-853>.
- Brideau, M.A., Yan, M. & Stead, D. 2009. The role of tectonic damage and brittle rock fracture in the development of large rock slope failures. *Geomorphology*, **103**, 30–49, <https://doi.org/10.1016/j.geomorph.2008.04.010>.
- Brown, J., Ferrians, O.J., Heginbottom, J.A. & Melnikov, E.S. 1997. Circum-Arctic map of permafrost and ground-ice conditions. *Circum-Pacific Map Series*, U.S.G.S.
- Brune, J.N. 2001. Shattered Rock and Precarious Rock Evidence for Strong Asymmetry in Ground Motions during Thrust Faulting. *Bulletin of the Seismological Society of America*, **91**, 441–447, <https://doi.org/10.1785/0120000118>.
- Bueechi, E., Klimeš, J., Frey, H., Huggel, C., Strozzi, T. & Cochachin, A. 2019. Regional-scale landslide susceptibility modelling in the Cordillera Blanca, Peru—a comparison of different approaches. *Landslides*, **16**, 395–407, <https://doi.org/10.1007/s10346-018-1090-1>.
- Burbank, D.W., Bookhagen, B., Gabet, E.J. & Putkonen, J. 2012. Modern climate and erosion in the Himalaya. *Comptes Rendus - Geoscience*, **344**, 610–626, <https://doi.org/10.1016/j.crte.2012.10.010>.

- Burg, J.P. & Chen, G.M. 1984. Tectonics and structural zonation of southern Tibet, China. *Nature*, **311**, 219–223, <https://doi.org/10.1038/311219a0>.
- Caine, N. & Mool, P.K. 1982. Landslides in the Kolpu Khola drainage, middle mountains, Nepal. *Mountain Research and Development*, 157–173.
- Caldas de Castro, M. & Singer, B.H. 2006. Controlling the false discovery rate: A new application to account for multiple and dependent tests in local statistics of spatial association. *Geographical Analysis*, **38**, 180–208, <https://doi.org/10.1111/j.0016-7363.2006.00682.x>.
- Camilo, D.C., Lombardo, L., Mai, P.M., Dou, J. & Huser, R. 2017. Handling high predictor dimensionality in slope-unit-based landslide susceptibility models through LASSO-penalized Generalized Linear Model. *Environmental Modelling and Software*, **97**, 145–156, <https://doi.org/10.1016/j.envsoft.2017.08.003>.
- Cardinali, M., Reichenbach, P., et al. 2002. A geomorphological approach to the estimation of landslide hazards and risks in Umbria, Central Italy. *Natural Hazards and Earth System Sciences*, **2**, 57–72, <https://doi.org/10.5194/nhess-2-57-2002>.
- Carrara, A., Catalano, E., Sorriso-Valvo, M., Reali, C. & Osso, I. 1978. Digital terrain analysis for land evaluation. *Geologia Applicata e Idrogeologia*, **13**, 69–127.
- Carrara, A., Crosta, G. & Frattini, P. 2008. Comparing models of debris-flow susceptibility in the alpine environment. *Geomorphology*, **94**, 353–378, <https://doi.org/10.1016/j.geomorph.2006.10.033>.
- Cascini, L. 2008. Applicability of landslide susceptibility and hazard zoning at different scales. *Engineering Geology*, **102**, 164–177, <https://doi.org/10.1016/j.enggeo.2008.03.016>.
- Casey, M., Ebinger, C.J., Keir, D., Gloaguen, R. & Mohamed, F. 2006. Strain accommodation in transitional rifts: extension by magma intrusion and faulting in Ethiopian rift magmatic segments. *Geological Society Special Publication*, **259**, 143–163, <https://doi.org/10.1144/GSL.SP.2006.259.01.13>.

- Catlos, E.J., Harrison, T.M., Kohn, M.J., Grove, M., Ryerson, F.J., Manning, C.E. & Upreti, B.N. 2001. Geochronologic and thermobarometric constraints on the evolution of the Main Central Thrust, central Nepal Himalaya. *Journal of Geophysical Research: Solid Earth*, **106**, 16177–16204, <https://doi.org/10.1029/2000JB900375>.
- Chalise, S.R. & Khanal, N.R. 2001. Rainfall and related natural disasters in Nepal. *Landslide hazards, mitigation to the Hindukush-Himalayas. ICIMOD, Kathmandu*, 63–70.
- Chalkias, C., Kalogirou, S. & Ferentinou, M. 2014. Landslide susceptibility, Peloponnese Peninsula in South Greece. *Journal of Maps*, **10**, 211–222, <https://doi.org/10.1080/17445647.2014.884022>.
- Chalkias, C., Polykretis, C., Karymbalis, E., Soldati, M., Ghinoi, A. & Ferentinou, M. 2020. Exploring spatial non-stationarity in the relationships between landslide susceptibility and conditioning factors: a local modeling approach using geographically weighted regression. *Bulletin of Engineering Geology and the Environment*, **79**, 2799–2814, <https://doi.org/10.1007/s10064-020-01733-x>.
- Chang, K.-T., Chiang, S.-H. & Hsu, M.-L. 2007. Modeling typhoon- and earthquake-induced landslides in a mountainous watershed using logistic regression. *Geomorphology*, **89**, 335–347, <https://doi.org/10.1016/J.GEOMORPH.2006.12.011>.
- Chauhan, R. & Thakuri, S. 2017. Periglacial environment in Nepal Himalaya: Present contexts and future prospects. *Nepal Journal of Environmental Science*, **5**, 35–40, <https://doi.org/10.3126/njes.v5i0.22713>.
- Chen, H. & Hawkins, A.B. 2009. Relationship between earthquake disturbance, tropical rainstorms and debris movement: an overview from Taiwan. *Bulletin of Engineering Geology and the Environment*, **68**, 161–186, <https://doi.org/10.1007/s10064-009-0209-y>.
- Chen, X., Cui, P., You, Y., Chen, J. & Li, D. 2015. Engineering measures for debris flow hazard mitigation in the Wenchuan earthquake area. *Engineering*

Geology, **194**, 73–85, <https://doi.org/10.1016/J.ENGCEO.2014.10.002>.

Chowdhuri, I., Pal, S.C. & Chakraborty, R. 2020. Flood susceptibility mapping by ensemble evidential belief function and binomial logistic regression model on river basin of eastern India. *Advances in Space Research*, **65**, 1466–1489, <https://doi.org/10.1016/J.ASR.2019.12.003>.

Clarke, B.A. & Burbank, D.W. 2011. Quantifying bedrock-fracture patterns within the shallow subsurface: Implications for rock mass strength, bedrock landslides, and erodibility. *Journal of Geophysical Research*, **116**, F04009, <https://doi.org/10.1029/2011JF001987>.

Coleman, M.E. 1998. U-Pb constraints on Oligocene-Miocene deformation and anatexis within the central Himalaya, Marsyandi Valley, Nepal. *American Journal of Science*, **298**, 553–571.

Collins, B.D. & Jibson, R.W. 2015. *Assessment of Existing and Potential Landslide Hazards Resulting from the April 25, 2015 Gorkha, Nepal Earthquake Sequence, USGS Open-File Report 1142*.

Conforti, M., Robustelli, G., et al. 2012. Application and validation of bivariate GIS-based landslide susceptibility assessment for the Vittravo river catchment (Calabria, south Italy). **61**, 127–141, <https://doi.org/10.1007/s11069-011-9781-0>.

Cook, K.L., Andermann, C., Gimbert, F., Adhikari, B.R. & Hovius, N. 2018. Glacial lake outburst floods as drivers of fluvial erosion in the Himalaya. *Science*, **362**, 53–57, <https://doi.org/10.1126/science.aat4981>.

Cossart, E., Braucher, R., Fort, M., Bourlès, D.L. & Carcaillet, J. 2008. Slope instability in relation to glacial debuttreasing in alpine areas (Upper Durance catchment, southeastern France): Evidence from field data and ¹⁰Be cosmic ray exposure ages. *Geomorphology*, **95**, 3–26, <https://doi.org/10.1016/j.geomorph.2006.12.022>.

Costanzo, D., Rotigliano, E., Irigaray, C., Jiménez-Perálvarez, J.D. & Chacón, J. 2012. Factors selection in landslide susceptibility modelling on large scale following

- the gis matrix method: application to the river Beiro basin (Spain). *Hazards Earth Syst. Sci*, **12**, 327–340, <https://doi.org/10.5194/nhess-12-327-2012>.
- Craddock, W.H., Burbank, D.W., Bookhagen, B., Gabet, E.J., Burbank, D.W., Bookhagen, B. & Gabet, E.J. 2007. Bedrock channel geometry along an orographic rainfall gradient in the upper Marsyandi River valley in central Nepal. *J. Geophys. Res*, **112**, 3007, <https://doi.org/10.1029/2006JF000589>.
- Crozier, M.J. 2010. Deciphering the effect of climate change on landslide activity: A review. *Geomorphology*, **124**, 260–267, <https://doi.org/10.1016/j.geomorph.2010.04.009>.
- Dadson, S.J., Hovius, N., et al. 2004. Earthquake-triggered increase in sediment delivery from an active mountain belt. *Geology*, **32**, 733–736, <https://doi.org/10.1130/G20639.1>.
- Dahal, R.K. & Hasegawa, S. 2008. Representative rainfall thresholds for landslides in the Nepal Himalaya. *Geomorphology*, **100**, 429–443, <https://doi.org/10.1016/J.GEOMORPH.2008.01.014>.
- Dahal, R.K., Hasegawa, S., Yamanaka, M. & Nishino, K. 2006. Rainfall triggered flow-like landslides: understanding from southern hills of Kathmandu, Nepal and northern Shikoku, Japan. *Proc 10th Int Congr of IAEG, The Geological Society of London, IAEG2006 Paper*, 1–14.
- Dahal, R.K., Bhandary, N.P., Timilsina, M., Yatabe, R. & Hasegawa, S. 2013. Earthquake-Induced Landslides in the Roadside Slopes of East Nepal After Recent September 18, 2011 Earthquake. *In: Earthquake-Induced Landslides*. Berlin, Heidelberg, Springer Berlin Heidelberg, 149–157., https://doi.org/10.1007/978-3-642-32238-9_16.
- Dahlquist, M.P. & West, A.J. 2019. Initiation and Runout of Post-Seismic Debris Flows: Insights From the 2015 Gorkha Earthquake. *Geophysical Research Letters*, **46**, 9658–9668, <https://doi.org/10.1029/2019GL083548>.
- Dai, F.C., Xu, C., Yao, X., Xu, L., Tu, X.B. & Gong, Q.M. 2011. Spatial distribution of landslides triggered by the 2008 Ms 8.0 Wenchuan earthquake, China. *Journal*

of Asian Earth Sciences, **40**, 883–895,
<https://doi.org/10.1016/J.JSEAES.2010.04.010>.

Davies, M.C.R., Hamza, O. & Harris, C. 2001. The Effect of Rise in Mean Annual Temperature on the Stability of Rock Slopes Containing Ice-Filled Discontinuities. *PROCESSES Permafrost Periglac. Process*, **12**, 137–144,
<https://doi.org/10.1002/ppp>.

Decelles, P.G., Robinson, D.M., Quade, J., Ojha, T.P., Garzzone, C.N., Copeland, P. & Upreti, B.N. 2001. Stratigraphy, structure, and tectonic evolution of the Himalayan fold-thrust belt in Western Nepal. *Tectonics*, **20**, 487–509,
<https://doi.org/10.1029/2000TC001226>.

DeCelles, P.G., Gehrels, G.E., Quade, J. & Ojha, T.P. 1998. Eocene-early Miocene foreland basin development and the history of Himalayan thrusting, western and central Nepal. *Tectonics*, **17**, 741–765,
<https://doi.org/10.1029/98TC02598>.

DeCelles, P.G., Gehrels, G.E., Quade, J., LaReau, B. & Spurlin, M. 2000. Tectonic implications of U-Pb zircon ages of the himalayan orogenic belt in nepal. *Science (New York, N.Y.)*, **288**, 497–499,
<https://doi.org/10.1126/SCIENCE.288.5465.497>.

Defourny, P., Schouten P B P, F.L., et al. 2009. *Accuracy Assessment of a 300 m Global Land Cover Map: The GlobCover Experience CIRAD-Guyane-Université Laval*.

Densmore, A.L. & Hovius, N. 2000. Topographic fingerprints of bedrock landslides. *Geology*, **28**, 371–374,
[https://doi.org/10.1130/0091-7613\(2000\)28<371:TFOBL>2.0.CO](https://doi.org/10.1130/0091-7613(2000)28<371:TFOBL>2.0.CO).

Department of Mines and Geology. 2021. Department of Mines and Geology, General Geology <https://www.dmgnepal.gov.np/general-geology>.

Dhital, M.R. 2003. Causes and consequences of the 1993 debris flows and landslides in the Kulekhani watershed, central Nepal. *In: Rickenmann, D. & Chen, C. L. (eds) Proc. 3rd Intl. Conf. Debris-Flow Hazards Mitigation: Mechanics,*

Prediction and Assessment. Millpress, Rotterdam, 931–942.

- Dhital, M.R., Khanal, N. & Thapa, K.B. 1993. The role of extreme weather events, mass movements, and land use changes in increasing natural hazards: a report of the causes of the recent damages incurred in South-central Nepal during 19-20 July 1993.
- Dini, B., Aaron, J., Manconi, A., De Palezieux, L., Leith, K. & Loew, S. 2020. Regional-Scale Investigation of Preconditioning Factors of Rock Slope Instabilities in NW Bhutan. *Journal of Geophysical Research: Earth Surface*, **125**, <https://doi.org/10.1029/2019JF005404>.
- Domej, G., Bourdeau, C., Lenti, L., Martino, S. & Piuta, K. 2017. Mean landslide geometries inferred from a global database of earthquake- and non-earthquake-triggered landslides. *Italian Journal of Engineering Geology and Environment*, **2**, 87–107, <https://doi.org/10.4408/IJEGE.2017-02.O-05>.
- Douville, H., Royer, J.-F., Polcher, J., Cox, P., Gedney, N., Stephenson, D.B. & Valdes, P.J. 2000. Impact of CO₂ Doubling on the Asian Summer Monsoon. *Journal of the Meteorological Society of Japan. Ser. II*, **78**, 421–439, https://doi.org/10.2151/jmsj1965.78.4_421.
- Du, J. 2021. GCIPEOP Surface: Precipitation NCEP/EMC 4KM Gridded Data (GRIB) Stage IV Data. Version 1.0. UCAR/NCAR - Earth Observing Laboratory. <https://doi.org/10.5065/D6PG1QDD>.
- Duman, T.Y., Çan, T., Emre, Ö., Keçer, M., Doğan, A., Ateş, Ş. & Durmaz, S. 2005. Landslide inventory of northwestern Anatolia, Turkey. *Engineering Geology*, **77**, 99–114, <https://doi.org/10.1016/J.ENGGEOL.2004.08.005>.
- Dunning, S.A., Massey, C.I. & Rosser, N.J. 2009. Structural and geomorphological features of landslides in the Bhutan Himalaya derived from Terrestrial Laser Scanning. *Geomorphology*, **103**, 17–29, <https://doi.org/10.1016/j.geomorph.2008.04.013>.
- Elliott, J.R., Jolivet, R., González, P.J., Avouac, J.-P., Hollingsworth, J., Searle, M.P. & Stevens, V.L. 2016. Himalayan megathrust geometry and relation to

- topography revealed by the Gorkha earthquake. *Nature Geoscience*, **9**, 174–180, <https://doi.org/10.1038/ngeo2623>.
- Erener, A. & Düzgün, H.S.B. 2010. Improvement of statistical landslide susceptibility mapping by using spatial and global regression methods in the case of More and Romsdal (Norway). *Landslides*, **7**, 55–68, <https://doi.org/10.1007/s10346-009-0188-x>.
- Erener, A. & Düzgün, H.S.B. 2012. Landslide susceptibility assessment: What are the effects of mapping unit and mapping method? *Environmental Earth Sciences*, **66**, 859–877, <https://doi.org/10.1007/s12665-011-1297-0>.
- Eslami, R., Azarnoush, M., Kialashki, A. & Kazemzadeh, F. 2021. GIS-BASED FOREST FIRE SUSCEPTIBILITY ASSESSMENT BY RANDOM FOREST, ARTIFICIAL NEURAL NETWORK AND LOGISTIC REGRESSION METHODS. *Source: Journal of Tropical Forest Science*, **33**, 173–184, <https://doi.org/10.2307/27007565>.
- Fell, R., Corominas, J., Bonnard, C., Cascini, L., Leroi, E. & Savage, W.Z. 2008. Guidelines for landslide susceptibility, hazard and risk zoning for land-use planning on behalf of the JTC-1 Joint Technical Committee on Landslides and Engineered Slopes. *Engineering Geology*, **102**, 99–111, <https://doi.org/10.1016/j.enggeo.2008.03.014>.
- Feuillet, T., Coquin, J., Mercier, D., Cossart, E., Decaulne, A., Jónsson, H.P. & Sæmundsson, Þorsteinn. 2014. Focusing on the spatial non-stationarity of landslide predisposing factors in northern Iceland. *Progress in Physical Geography: Earth and Environment*, **38**, 354–377, <https://doi.org/10.1177/0309133314528944>.
- Fiorucci, F., Cardinali, M., et al. 2011. Seasonal landslide mapping and estimation of landslide mobilization rates using aerial and satellite images. *Geomorphology*, **129**, 59–70, <https://doi.org/10.1016/j.geomorph.2011.01.013>.
- Fischer, L., Kääh, A., Huggel, C. & Noetzli, J. 2006. Geology, glacier retreat and permafrost degradation as controlling factors of slope instabilities in a high-

- mountain rock wall: the Monte Rosa east face. *Natural Hazards and Earth System Sciences*, **6**, 761–772, <https://doi.org/10.5194/nhess-6-761-2006>.
- Fischer, L., Purves, R.S., Huggel, C., Noetzli, J. & Haeberli, W. 2012. On the influence of topographic, geological and cryospheric factors on rock avalanches and rockfalls in high-mountain areas. *Natural Hazards and Earth System Sciences*, **12**, 241–254, <https://doi.org/10.5194/nhess-12-241-2012>.
- Fort, M. 1995. The Himalayan glaciation: myth and reality. *Journal of Nepal Geological Society*, **11**, 257–272.
- Francis, O.R., Hales, T.C., Hobley, D.E.J., Fan, X., Horton, A.J., Scaringi, G. & Huang, R. 2020. The impact of earthquakes on orogen-scale exhumation. *Earth Surface Dynamics*, **8**, 579–593, <https://doi.org/10.5194/esurf-8-579-2020>.
- Frank, W., Grasemann, B., Guntli, P. & Miller, C. 1995. Geological map of the Kishtwar-Chamba-Kulu region (NW Himalayas, India). *Jahrbuch der Geologischen Bundesanstalt*, **138**, 299–308.
- Frattini, P. & Crosta, G.B. 2013. The role of material properties and landscape morphology on landslide size distributions. *Earth and Planetary Science Letters*, **361**, 310–319, <https://doi.org/10.1016/j.epsl.2012.10.029>.
- French, H., Heginbottom, J., Johnston, G., Ladanyi, B., Sego, D. & van Everdingen, R. 1988. *Glossary of Permafrost and Related Ground-Ice Terms*. Ottawa.
- Friedman, J., Hastie, T. & Tibshirani, R. 2010. Regularization paths for generalized linear models via coordinate descent. *Journal of Statistical Software*, **33**, 1–22, <https://doi.org/10.18637/jss.v033.i01>.
- Froude, M.J. & Petley, D.N. 2018. Global fatal landslide occurrence from 2004 to 2016. *Natural Hazards and Earth System Sciences*, **18**, 2161–2181, <https://doi.org/10.5194/nhess-18-2161-2018>.
- Fukui, K., Fujii, Y., Ageta, Y. & Asahi, K. 2007. Changes in the lower limit of mountain permafrost between 1973 and 2004 in the Khumbu Himal, the Nepal Himalayas. *Global and Planetary Change*, **55**, 251–256, <https://doi.org/10.1016/j.gloplacha.2006.06.002>.

- Gabet, E.J., Burbank, D.W., Putkonen, J.K., Pratt-Sitaula, B.A. & Ojha, T. 2004. Rainfall thresholds for landsliding in the Himalayas of Nepal. *Geomorphology*, **63**, 131–143, <https://doi.org/10.1016/j.geomorph.2004.03.011>.
- Gaire, S., Delgado, R.C. & González, P.A. 2015. Disaster risk profile and existing legal framework of Nepal: floods and landslides. *Risk Management and Healthcare Policy*, **8**, 139, <https://doi.org/10.2147/RMHP.S90238>.
- Galland, O., de Bremond d'Ars, J., Cobbold, P.R. & Hallot, E. 2003. Physical models of magmatic intrusion during thrusting. *Terra Nova*, **15**, 405–409, <https://doi.org/10.1046/j.1365-3121.2003.00512.x>.
- Gallart, F. & Clotet, N. 1988. Some aspects of the geomorphic processes triggered by an extreme rainfall event: the November 1982 flood in the Eastern Pyrenees. *Catena supplement*, **13**, 79–95.
- Gallen, S.F., Clark, M.K. & Godt, J.W. 2015. Coseismic landslides reveal near-surface rock strength in a high-relief, tectonically active setting. *Geology*, **43**, 11–14, <https://doi.org/10.1130/G36080.1>.
- Gariano, S.L. & Guzzetti, F. 2016. Landslides in a changing climate. *Earth-Science Reviews*, **162**, <https://doi.org/10.1016/j.earscirev.2016.08.011>.
- Gautam, D. & Dong, Y. 2018. Multi-hazard vulnerability of structures and lifelines due to the 2015 Gorkha earthquake and 2017 central Nepal flash flood. *Journal of Building Engineering*, **17**, 196–201, <https://doi.org/10.1016/j.jobbe.2018.02.016>.
- Gehne, M., Hamill, T.M., Kiladis, G.N. & Trenberth, K.E. 2016. Comparison of global precipitation estimates across a range of temporal and spatial scales. *Journal of Climate*, **29**, 7773–7795, <https://doi.org/10.1175/JCLI-D-15-0618.1>.
- Glade, T. 2003. Landslide occurrence as a response to land use change: a review of evidence from New Zealand. *CATENA*, **51**, 297–314, [https://doi.org/10.1016/S0341-8162\(02\)00170-4](https://doi.org/10.1016/S0341-8162(02)00170-4).
- Gnyawali, K.R. & Adhikari, B.R. 2017. Spatial Relations of Earthquake Induced Landslides Triggered by 2015 Gorkha Earthquake Mw = 7.8. *In: Advancing*

- Culture of Living with Landslides*. Springer International Publishing, 85–93.,
https://doi.org/10.1007/978-3-319-53485-5_10.
- Godin, L., Parrish, R.R., Brown, R.L. & Hodges, K. V. 2001. Crustal thickening leading to exhumation of the Himalayan Metamorphic core of central Nepal: Insight from U-Pb Geochronology and $^{40}\text{Ar}/^{39}\text{Ar}$ Thermochronology. *Tectonics*, **20**, 729–747, <https://doi.org/10.1029/2000TC001204>.
- Goetz, J.N., Guthrie, R.H. & Brenning, A. 2011. Integrating physical and empirical landslide susceptibility models using generalized additive models. *Geomorphology*, **129**, 376–386, <https://doi.org/10.1016/j.geomorph.2011.03.001>.
- Gorsevski, P. V., Gessler, P.E., Boll, J., Elliot, W.J. & Foltz, R.B. 2006. Spatially and temporally distributed modeling of landslide susceptibility. *Geomorphology*, **80**, 178–198, <https://doi.org/10.1016/j.geomorph.2006.02.011>.
- Grämiger, L.M., Moore, J.R., Gischig, V.S., Ivy-Ochs, S. & Loew, S. 2017. Beyond debuitressing: Mechanics of paraglacial rock slope damage during repeat glacial cycles. *Journal of Geophysical Research: Earth Surface*, **122**, 1004–1036, <https://doi.org/10.1002/2016JF003967>.
- Griffiths, J.S., Mather, A.E. & Hart, A.B. 2002. Landslide susceptibility in the Río Aguas catchment, SE Spain. *Quarterly Journal of Engineering Geology and Hydrogeology*, **35**, 9–17, <https://doi.org/10.1144/qjegh.35.1.9>.
- Griffiths, J.S., Mather, A.E. & Stokes, M. 2015. Mapping landslides at different scales. *Quarterly Journal of Engineering Geology and Hydrogeology*, **48**, 29–40, <https://doi.org/10.1144/qjegh2014-038>.
- Gruber, S. 2012. Derivation and analysis of a high-resolution estimate of global permafrost zonation. *The Cryosphere*, **6**, 221–233, <https://doi.org/10.5194/tc-6-221-2012>.
- Gruber, S. & Haerberli, W. 2007. Permafrost in steep bedrock slopes and its temperature-related destabilization following climate change. *Journal of Geophysical Research*, **112**, F02S18, <https://doi.org/10.1029/2006JF000547>.

- Gruber, S., Hoelzle, M. & Haeberli, W. 2004. Permafrost thaw and destabilization of Alpine rock walls in the hot summer of 2003. *Geophysical Research Letters*, **31**, n/a-n/a, <https://doi.org/10.1029/2004GL020051>.
- Gruber, S., Fleiner, R., et al. 2017. Review article: Inferring permafrost and permafrost thaw in the mountains of the Hindu Kush Himalaya region. *Cryosphere*, **11**, 81–99, <https://doi.org/10.5194/tc-11-81-2017>.
- Günther, A., Van Den Eeckhaut, M., Malet, J.P., Reichenbach, P. & Hervás, J. 2014. Climate-physiographically differentiated Pan-European landslide susceptibility assessment using spatial multi-criteria evaluation and transnational landslide information. *Geomorphology*, **224**, 69–85, <https://doi.org/10.1016/j.geomorph.2014.07.011>.
- Gupta, V. 2005. The relationship between tectonic stresses, joint patterns and landslides. *Journal of Nepal Geological Society*, **31**, 51–58, <https://doi.org/10.3126/jngs.v31i0.260>.
- Guzzetti, F., Cardinali, M. & Reichenbach, P. 1996. The influence of structural setting and lithology on landslide type and pattern. *Environmental and Engineering Geoscience*, **2**, 531–555, <https://doi.org/10.2113/gseegeosci.ii.4.531>.
- Guzzetti, F., Malamud, B.D., Turcotte, D.L. & Reichenbach, P. 2002. Power-law correlations of landslide areas in central Italy. *Earth and Planetary Science Letters*, **195**, 169–183, [https://doi.org/10.1016/S0012-821X\(01\)00589-1](https://doi.org/10.1016/S0012-821X(01)00589-1).
- Guzzetti, F., Reichenbach, P., Cardinali, M., Galli, M. & Ardizzone, F. 2005. Probabilistic landslide hazard assessment at the basin scale. *Geomorphology*, **72**, 272–299, <https://doi.org/10.1016/j.geomorph.2005.06.002>.
- Guzzetti, F., Reichenbach, P., Ardizzone, F., Cardinali, M. & Galli, M. 2006. Estimating the quality of landslide susceptibility models. *Geomorphology*, **81**, 166–184, <https://doi.org/10.1016/J.GEOMORPH.2006.04.007>.
- Guzzetti, F., Mondini, A.C., Cardinali, M., Fiorucci, F., Santangelo, M. & Chang, K.-T. 2012. Landslide inventory maps: New tools for an old problem. *Earth-Science Reviews*, **112**, 42–66,

<https://doi.org/10.1016/J.EARSCIREV.2012.02.001>.

Guzzetti, F., Gariano, S.L., Peruccacci, S., Brunetti, M.T., Marchesini, I., Rossi, M. & Melillo, M. 2020. Geographical landslide early warning systems. *Earth-Science Reviews*, **200**, 102973, <https://doi.org/10.1016/j.earscirev.2019.102973>.

Hack, R. & Huisman, M. 2002. *Engineering Geology for Developing Countries-Proceedings of 9 Th Congress of the International Association for Engineering Geology and the Environment*.

Haeberli, W., Schaub, Y. & Huggel, C. 2017. Increasing risks related to landslides from degrading permafrost into new lakes in de-glaciating mountain ranges. *Geomorphology*, **293**, 405–417, <https://doi.org/10.1016/j.geomorph.2016.02.009>.

Hales, T.C. & Roering, J.J. 2005. Climate-controlled variations in scree production, Southern Alps, New Zealand. *Geology*, **33**, 701, <https://doi.org/10.1130/G21528.1>.

Hales, T.C. & Roering, J.J. 2007. Climatic controls on frost cracking and implications for the evolution of bedrock landscapes. *Journal of Geophysical Research: Earth Surface*, **112**, <https://doi.org/10.1029/2006JF000616>.

Hasegawa, S., Dahal, R.K., Yamanaka, M., Bhandary, N.P., Yatabe, R. & Inagaki, H. 2009. Causes of large-scale landslides in the Lesser Himalaya of central Nepal. *Environmental Geology*, **57**, 1423–1434, <https://doi.org/10.1007/s00254-008-1420-z>.

Hastie, T. & Qian, J. 2014. Glmnet Vignette https://web.stanford.edu/~hastie/glmnet/glmnet_alpha.html.

Heginbottom, J.A. & Dubreuil, M.A. 1993. A new permafrost and ground ice map for the National Atlas of Canada. *In: Proceedings of the Sixth International Conference on Permafrost*. 255–260.

Heuberger, H. & Ibetsberger, I. 1998. Problems of Holocene glacier advances in Langtang, central Nepal. *In: Proceedings of the International Conference on Ecohydrology of High Mountain Areas-Kathmandu*. 459–464.

- Heydari, M., Attar Roshan, S., Jaferyan, E. & Abiyat, M. 2021. Modeling and Zoning of Fire Prone Areas in Zagros Forests Using Geographic Information System Based on Logistic Regression. *Journal of Geography and Environmental Hazards*, **10**, 43–58, <https://doi.org/10.22067/GEOEH.2021.68903.1019>.
- Hidayat Jati, M.I., Suroso & Santoso, P.B. 2019. Prediction of flood areas using the logistic regression method (case study of the provinces Banten, DKI Jakarta, and West Java). *Journal of Physics: Conference Series*, **1367**, 012087, <https://doi.org/10.1088/1742-6596/1367/1/012087>.
- Higaki, D., Yagi, H., Asahi, K. & Miyake, N. 2000. Landslides on the late Quaternary deposits in the Bhote Koshi area, central Nepal Aerial watching of landslides in Japan View project. *Journal of Nepal Geological Society*, 505–512.
- Hilger, P., Hermanns, R.L., Gosse, J.C., Jacobs, B., Etzelmüller, B. & Krautblatter, M. 2018. Multiple rock-slope failures from Mannen in Romsdal Valley, western Norway, revealed from Quaternary geological mapping and ¹⁰Be exposure dating. *The Holocene*, **28**, 1841–1854, <https://doi.org/10.1177/0959683618798165>.
- Hodges, K. V., Parrish, R.R. & Searle, M.P. 1996. Tectonic evolution of the central Annapurna Range, Nepalese Himalayas. *Tectonics*, **15**, 1264–1291, <https://doi.org/10.1029/96TC01791>.
- Hoek, E. 1983. Strength of jointed rock masses. *Géotechnique*, **33**, 187–223, <https://doi.org/10.1680/geot.1983.33.3.187>.
- Hovius, N., Meunier, P., et al. 2011. Prolonged seismically induced erosion and the mass balance of a large earthquake. *Earth and Planetary Science Letters*, **304**, 347–355, <https://doi.org/10.1016/j.epsl.2011.02.005>.
- Hu, Z.-Z., Latif, M., Roeckner, E. & Bengtsson, L. 2000. Intensified Asian Summer Monsoon and its variability in a coupled model forced by increasing greenhouse gas concentrations. *Geophysical Research Letters*, **27**, 2681–2684, <https://doi.org/10.1029/2000GL011550>.
- Huffman, G.J., Adler, R.F., et al. 2001. Global precipitation at one-degree daily

- resolution from multisatellite observations. *Journal of Hydrometeorology*, **2**, 36–50, [https://doi.org/10.1175/1525-7541\(2001\)002<0036:GPAODD>2.0.CO;2](https://doi.org/10.1175/1525-7541(2001)002<0036:GPAODD>2.0.CO;2).
- Huggel, C., Clague, J.J. & Korup, O. 2012. Is climate change responsible for changing landslide activity in high mountains? *Earth Surface Processes and Landforms*, **37**, 77–91, <https://doi.org/10.1002/esp.2223>.
- Humanitarian Data Exchange. 2020. Humanitarian OpenStreetMap Team (HOT)<https://data.humdata.org/organization/hot>.
- Hungr, O., Leroueil, S. & Picarelli, L. 2014. The Varnes classification of landslide types, an update. *Landslides*, **11**, 167–194, <https://doi.org/10.1007/s10346-013-0436-y>.
- Hurst, M.D., Ellis, M.A., Royse, K.R., Lee, K.A. & Freeborough, K. 2013. Controls on the magnitude-frequency scaling of an inventory of secular landslides. *Earth Surface Dynamics*, **1**, 67–78, <https://doi.org/10.5194/esurf-1-67-2013>.
- Immerzeel, W.W., van Beek, L.P.H., Konz, M., Shrestha, A.B. & Bierkens, M.F.P. 2012. Hydrological response to climate change in a glacierized catchment in the Himalayas. *Climatic Change*, **110**, 721–736, <https://doi.org/10.1007/s10584-011-0143-4>.
- Inger, S. & Harris, N. 1993. Geochemical Constraints on Leucogranite Magmatism in the Langtang Valley, Nepal Himalaya. *Journal of Petrology*, **34**, 345–368, <https://doi.org/10.1093/petrology/34.2.345>.
- Jaeger, J.C. 1960. Shear Failure of Anisotropic Rocks. *Geological Magazine*, **97**, 65–72, <https://doi.org/10.1017/S0016756800061100>.
- Jaiswal, P., van Westen, C.J. & Jetten, V. 2011. Quantitative assessment of landslide hazard along transportation lines using historical records. *Landslides*, **8**, 279–291, <https://doi.org/10.1007/s10346-011-0252-1>.
- Jones, J.N., Stokes, M., Boulton, S.J., Bennett, G.L. & Whitworth, M.R.Z. 2020. Coseismic and monsoon-triggered landslide impacts on remote trekking infrastructure, Langtang Valley, Nepal. *Quarterly Journal of Engineering*

Geology and Hydrogeology, **53**, 159–166, <https://doi.org/10.1144/qjegh2019-048>.

Jones, J.N., Boulton, S.J., Stokes, M., Bennett, G.L. & Whitworth, M.R.Z. 2021a. 30-year record of Himalaya mass-wasting reveals landscape perturbations by extreme events. *Nature Communications* 2021 12:1, **12**, 1–15, <https://doi.org/10.1038/s41467-021-26964-8>.

Jones, J.N., Boulton, S.J., Bennett, G.L., Stokes, M. & Whitworth, M.R.Z. 2021b. Temporal Variations in Landslide Distributions Following Extreme Events: Implications for Landslide Susceptibility Modeling. *Journal of Geophysical Research: Earth Surface*, **126**, e2021JF006067, <https://doi.org/10.1029/2021JF006067>.

Jones, R., Manville, V., Peakall, J., Froude, M.J. & Odbert, H.M. 2017. Real-time prediction of rain-triggered lahars: Incorporating seasonality and catchment recovery. *Natural Hazards and Earth System Sciences*, **17**, 2301–2312, <https://doi.org/10.5194/NHESS-17-2301-2017>.

Kääb, A., Huggel, C., et al. 2005. Remote sensing of glacier- and permafrost-related hazards in high mountains: an overview. *Natural Hazards and Earth System Sciences*, **5**, 527–554, <https://doi.org/10.5194/nhess-5-527-2005>.

Kang, C. & Chan, D. 2017. Modeling of Entrainment in Debris Flow Analysis for Dry Granular Material. *International Journal of Geomechanics*, **17**, 04017087, [https://doi.org/10.1061/\(ASCE\)GM.1943-5622.0000981](https://doi.org/10.1061/(ASCE)GM.1943-5622.0000981).

Kargel, J.S., Leonard, G.J., et al. 2016. Geomorphic and geologic controls of geohazards induced by Nepal's 2015 Gorkha earthquake. *Science (New York, N.Y.)*, **351**, aac8353, <https://doi.org/10.1126/science.aac8353>.

Karki, R., Hasson, S. ul, Schickhoff, U., Scholten, T. & Böhner, J. 2017. Rising Precipitation Extremes across Nepal. *Climate*, **5**, 4, <https://doi.org/10.3390/cli5010004>.

Kayastha, P. 2012. Application of fuzzy logic approach for landslide susceptibility mapping in Garuwa sub-basin, East Nepal. *Frontiers of Earth Science*, **6**, 420–

432, <https://doi.org/10.1007/s11707-012-0337-8>.

Keefer, D.K. 2002. Investigating Landslides Caused by Earthquakes – A Historical Review. *Surveys in Geophysics*, **23**, 473–510, <https://doi.org/10.1023/A:1021274710840>.

Kellogg, K.S. 2001. Tectonic controls on a large landslide complex: Williams Fork Mountains near Dillon, Colorado. *Geomorphology*, **41**, 355–368, [https://doi.org/10.1016/S0169-555X\(01\)00067-8](https://doi.org/10.1016/S0169-555X(01)00067-8).

Khanal, N.R. & Watanabe, T. 2005. Landslide and debris flow hazards induced by heavy precipitation in Nepal. *In: Proceedings of Himalaya International Symposium on Landslide Hazard in Orogenic Zone from the Himalaya to Island Arc in Asia*. 111–118.

Kidd, C. 2001. Satellite rainfall climatology: a review. *International Journal of Climatology*, **21**, 1041–1066, <https://doi.org/10.1002/joc.635>.

Kidd, C., Becker, A., et al. 2017. So, How Much of the Earth's Surface Is Covered by Rain Gauges? *Bulletin of the American Meteorological Society*, **98**, 69–78, <https://doi.org/10.1175/BAMS-D-14-00283.1>.

Kincey, M.E., Rosser, N.J., et al. 2021. Evolution of Coseismic and Post-seismic Landsliding After the 2015 M_w 7.8 Gorkha Earthquake, Nepal. *Journal of Geophysical Research: Earth Surface*, **126**, e2020JF005803, <https://doi.org/10.1029/2020JF005803>.

Kirby, E. & Whipple, K. 2001. Quantifying differential rock-uplift rates via stream profile analysis. *Geology*, **29**, 415, [https://doi.org/10.1130/0091-7613\(2001\)029<0415:QDRURV>2.0.CO;2](https://doi.org/10.1130/0091-7613(2001)029<0415:QDRURV>2.0.CO;2).

Kirchner, J.W., Finkel, R.C., Riebe, C.S., Granger, D.E., Clayton, J.L., King, J.G. & Megahan, W.F. 2001. Mountain erosion over 10 yr, 10 k.y., and 10 m.y. time scales. *Geology*, **29**, 591–594, [https://doi.org/10.1130/0091-7613\(2001\)029<0591:MEOYKY>2.0.CO;2](https://doi.org/10.1130/0091-7613(2001)029<0591:MEOYKY>2.0.CO;2).

Kirschbaum, D., Stanley, T. & Zhou, Y. 2015. Spatial and temporal analysis of a global landslide catalog. *Geomorphology*, **249**, 4–15,

<https://doi.org/10.1016/j.geomorph.2015.03.016>.

Kirschbaum, D., Kapnick, S.B., Stanley, T. & Pascale, S. 2020. Changes in Extreme Precipitation and Landslides Over High Mountain Asia. *Geophysical Research Letters*, **47**, <https://doi.org/10.1029/2019GL085347>.

Kirschbaum, D.B., Adler, R., Hong, Y., Hill, S. & Lerner-Lam, A. 2010. A global landslide catalog for hazard applications: method, results, and limitations. *Natural Hazards*, **52**, 561–575, <https://doi.org/10.1007/s11069-009-9401-4>.

Klose, M., Maurischat, P. & Damm, B. 2016. Landslide impacts in Germany: A historical and socioeconomic perspective. *Landslides*, **13**, 183–199, <https://doi.org/10.1007/s10346-015-0643-9>.

Knevels, R., Petschko, H., Proske, H., Leopold, P., Maraun, D. & Brenning, A. 2020. Event-based landslide modeling in the styrian basin, Austria: Accounting for time-varying rainfall and land cover. *Geosciences (Switzerland)*, **10**, 217, <https://doi.org/10.3390/geosciences10060217>.

Korup, O. 2004. Landslide-induced river channel avulsions in mountain catchments of southwest New Zealand. *Geomorphology*, **63**, 57–80, <https://doi.org/10.1016/J.GEOMORPH.2004.03.005>.

Korup, O., Clague, J.J., Hermanns, R.L., Hewitt, K., Strom, A.L. & Weidinger, J.T. 2007. Giant landslides, topography, and erosion. *Earth and Planetary Science Letters*, **261**, 578–589, <https://doi.org/10.1016/J.EPSL.2007.07.025>.

Kripalani, R.H., Oh, J.H., Kulkarni, A., Sabade, S.S. & Chaudhari, H.S. 2007. South Asian summer monsoon precipitation variability: Coupled climate model simulations and projections under IPCC AR4. *Theoretical and Applied Climatology*, **90**, 133–159, <https://doi.org/10.1007/s00704-006-0282-0>.

Kritikos, T., Robinson, T.R. & Davies, T.R.H. 2015. Regional coseismic landslide hazard assessment without historical landslide inventories: A new approach. *Journal of Geophysical Research: Earth Surface*, **120**, 711–729, <https://doi.org/10.1002/2014JF003224>.

Kumar, R., Ae, D., et al. 2008. GIS-based weights-of-evidence modelling of rainfall-

- induced landslides in small catchments for landslide susceptibility mapping. *Environmental Geology*, **54**, 311–324, <https://doi.org/10.1007/s00254-007-0818-3>.
- Lacroix, P. 2016. Landslides triggered by the Gorkha earthquake in the Langtang valley, volumes and initiation processes. *Earth, Planets and Space*, **68**, 46, <https://doi.org/10.1186/s40623-016-0423-3>.
- Larsen, I.J. & Montgomery, D.R. 2012. Landslide erosion coupled to tectonics and river incision. *Nature Geoscience*, **5**, 468–473, <https://doi.org/10.1038/ngeo1479>.
- Larsen, I.J., Montgomery, D.R. & Korup, O. 2010. Landslide erosion controlled by hillslope material. *Nature Geoscience*, **3**, 247–251, <https://doi.org/10.1038/NGEO776>.
- Lavé, J. & Avouac, J.P. 2001. Fluvial incision and tectonic uplift across the Himalayas of central Nepal. *Journal of Geophysical Research: Solid Earth*, **106**, 26561–26591, <https://doi.org/10.1029/2001JB000359>.
- Lee, C.-T., Huang, C.-C., Lee, J.-F., Pan, K.-L., Lin, M.-L. & Dong, J.-J. 2008. Statistical approach to storm event - induced landslides susceptibility. *Nat . Hazards Earth Syst. Sci*, **8**, 941–960, <https://doi.org/10.5194/nhess-8-941-2008>.
- Lee, S., Chwae, U. & Min, K. 2002. Landslide susceptibility mapping by correlation between topography and geological structure: The Janghung area, Korea. *Geomorphology*, **46**, 149–162, [https://doi.org/10.1016/S0169-555X\(02\)00057-0](https://doi.org/10.1016/S0169-555X(02)00057-0).
- Leech, M.L., Singh, S., Jain, A.K., Klemperer, S.L. & Manickavasagam, R.M. 2005. The onset of India–Asia continental collision: Early, steep subduction required by the timing of UHP metamorphism in the western Himalaya. *Earth and Planetary Science Letters*, **234**, 83–97, <https://doi.org/10.1016/j.epsl.2005.02.038>.
- LeFort, P. 1975. Himalayas: The collided range. Present knowledge of the continental arc. *Amer. J. Sci.*, **275**, 1–44.

- Li, J. & Zeng, Q. 2002. A unified monsoon index. *Geophysical Research Letters*, **29**, 115–1, <https://doi.org/10.1029/2001GL013874>.
- Lin, C.W., Liu, S.H., Lee, S.Y. & Liu, C.C. 2006. Impacts of the Chi-Chi earthquake on subsequent rainfall-induced landslides in central Taiwan. *Engineering Geology*, **86**, 87–101, <https://doi.org/10.1016/j.enggeo.2006.02.010>.
- Lin, G.-W., Chen, H., Chen, Y.-H. & Horng, M.-J. 2008. Influence of typhoons and earthquakes on rainfall-induced landslides and suspended sediments discharge. *Engineering Geology*, **97**, 32–41, <https://doi.org/10.1016/J.ENGCEO.2007.12.001>.
- Lin, L., Lin, Q. & Wang, Y. 2017. Landslide susceptibility mapping on a global scale using the method of logistic regression. *Natural Hazards and Earth System Sciences*, **17**, 1411–1424, <https://doi.org/10.5194/nhess-17-1411-2017>.
- Liu, G. & Einsele, G. 1999. Jurassic sedimentary facies and paleogeography of the former Indian passive margin in southern Tibet. *SPECIAL PAPERS-GEOLOGICAL SOCIETY OF AMERICA*, 75–108.
- Liu, J., Wu, Y. & Gao, X. 2021. Increase in occurrence of large glacier-related landslides in the high mountains of Asia. *Scientific Reports*, **11**, 1635, <https://doi.org/10.1038/s41598-021-81212-9>.
- Lombardo, L. & Mai, P.M. 2018. Presenting logistic regression-based landslide susceptibility results. *Engineering Geology*, **244**, 14–24, <https://doi.org/10.1016/j.enggeo.2018.07.019>.
- Lombardo, L., Bakka, H., Tanyas, H., van Westen, C., Mai, P.M. & Huser, R. 2018a. Geostatistical modeling to capture seismic-shaking patterns from earthquake-induced landslides.
- Lombardo, L., Opitz, T. & Huser, R. 2018b. Point process-based modeling of multiple debris flow landslides using INLA: an application to the 2009 Messina disaster. *Stochastic Environmental Research and Risk Assessment*, **32**, 2179–2198, <https://doi.org/10.1007/s00477-018-1518-0>.
- Lombardo, L., Opitz, T. & Huser, R. 2019. Numerical Recipes for Landslide Spatial

- Prediction Using R-INLA. *Spatial Modeling in GIS and R for Earth and Environmental Sciences*, 55–83, <https://doi.org/10.1016/b978-0-12-815226-3.00003-x>.
- Lombardo, L., Opitz, T., Ardizzone, F., Guzzetti, F. & Huser, R. 2020. Space-time landslide predictive modelling. *Earth-Science Reviews*, **209**, 103318, <https://doi.org/10.1016/j.earscirev.2020.103318>.
- Loye, A., Jaboyedoff, M. & Pedrazzini, A. 2009. Identification of potential rockfall source areas at a regional scale using a DEM-based geomorphometric analysis. *Natural Hazards and Earth System Sciences*, **9**, 1643–1653, <https://doi.org/10.5194/nhess-9-1643-2009>.
- Lucà, F. & Robustelli, G. 2020. Comparison of logistic regression and neural network models in assessing geomorphic control on alluvial fan depositional processes (Calabria, southern Italy). *Environmental Earth Sciences*, **79**, 1–18, <https://doi.org/10.1007/S12665-019-8775-1/FIGURES/8>.
- MacFarlane, A.M., HODGES, K. V. & LUX, D. 1992. A structural analysis of the Main Central Thrust zone, Langtang National Park, central Nepal Himalaya. *Geological Society of America Bulletin*, **104**, 1389–1402, [https://doi.org/10.1130/0016-7606\(1992\)104<1389:ASAOTM>2.3.CO;2](https://doi.org/10.1130/0016-7606(1992)104<1389:ASAOTM>2.3.CO;2).
- Malamud, B.D., Turcotte, D.L., Guzzetti, F. & Reichenbach, P. 2004a. Landslide inventories and their statistical properties. *Earth Surf. Process. Landforms Process. Landforms*, **29**, 687–711, <https://doi.org/10.1002/esp.1064>.
- Malamud, B.D., Turcotte, D.L., Guzzetti, F. & Reichenbach, P. 2004b. Landslides, earthquakes, and erosion. *Earth and Planetary Science Letters*, **229**, 45–59, <https://doi.org/10.1016/j.epsl.2004.10.018>.
- Marc, O. & Hovius, N. 2015. Amalgamation in landslide maps: effects and automatic detection. *Natural Hazards and Earth System Sciences*, **15**, 723–733, <https://doi.org/10.5194/nhess-15-723-2015>.
- Marc, O., Hovius, N., Meunier, P., Uchida, T. & Hayashi, S. 2015. Transient changes of landslide rates after earthquakes. *Geology*, **43**, 883–886,

<https://doi.org/10.1130/G36961.1>.

- Marc, O., Stumpf, A., Malet, J.-P., Gosset, M., Uchida, T. & Chiang, S.-H. 2018. Initial insights from a global database of rainfall-induced landslide inventories: the weak influence of slope and strong influence of total storm rainfall. *Earth Surface Dynamics*, **6**, 903–922, <https://doi.org/10.5194/esurf-6-903-2018>.
- Marc, O., Behling, R., Andermann, C., Turowski, J.M., Illien, L., Roessner, S. & Hovius, N. 2019. Long-term erosion of the Nepal Himalayas by bedrock landsliding: the role of monsoons, earthquakes and giant landslides. *Earth Surface Dynamics*, **7**, 107–128, <https://doi.org/10.5194/esurf-7-107-2019>.
- Marc, O., Sens-Schönfelder, C., et al. 2021. Toward Using Seismic Interferometry to Quantify Landscape Mechanical Variations after Earthquakes. *Bulletin of the Seismological Society of America*, **111**, 1631–1649, <https://doi.org/10.1785/0120200264>.
- Marjanović, M. 2013. Comparing the performance of different landslide susceptibility models in ROC space. *In: Landslide Science and Practice: Landslide Inventory and Susceptibility and Hazard Zoning*. Springer Science and Business Media Deutschland GmbH, 579–584., https://doi.org/10.1007/978-3-642-31325-7_76.
- Martha, T.R., Kerle, N., van Westen, C.J., Jetten, V. & Vinod Kumar, K. 2012. Object-oriented analysis of multi-temporal panchromatic images for creation of historical landslide inventories. *ISPRS Journal of Photogrammetry and Remote Sensing*, **67**, 105–119, <https://doi.org/10.1016/j.isprsjprs.2011.11.004>.
- Martha, T.R., Roy, P., Mazumdar, R., Govindharaj, K.B. & Kumar, K.V. 2017. Spatial characteristics of landslides triggered by the 2015 Mw 7.8 (Gorkha) and Mw 7.3 (Dolakha) earthquakes in Nepal. *Landslides*, **14**, 697–704, <https://doi.org/10.1007/s10346-016-0763-x>.
- Martin, S. & Szeliga, W. 2010. A Catalog of Felt Intensity Data for 570 Earthquakes in India from 1636 to 2009. *Bulletin of the Seismological Society of America*, **100**, 562–569, <https://doi.org/10.1785/0120080328>.

- Martin, S.S. & Hough, S.E. 2015. The 21 May 2014 Mw 5.9 Bay of Bengal Earthquake: Macroseismic Data Suggest a High-Stress-Drop Event. *Seismological Research Letters*, **86**, 369–377, <https://doi.org/10.1785/0220140155>.
- Martin, S.S., Hough, S.E. & Hung, C. 2015. Ground Motions from the 2015 M_w 7.8 Gorkha, Nepal, Earthquake Constrained by a Detailed Assessment of Macroseismic Data. *Seismological Research Letters*, **86**, 1524–1532, <https://doi.org/10.1785/0220150138>.
- Matsuoka, N. 1990. Mechanisms of rock breakdown by frost action: An experimental approach. *Cold Regions Science and Technology*, **17**, 253–270, [https://doi.org/10.1016/S0165-232X\(05\)80005-9](https://doi.org/10.1016/S0165-232X(05)80005-9).
- Matsuoka, N. 2001. Direct observation of frost wedging in alpine bedrock. *Earth Surface Processes and Landforms*, **26**, 601–614, <https://doi.org/10.1002/esp.208>.
- Matsuoka, N. & Murton, J. 2008. Frost weathering: Recent advances and future directions. *Permafrost and Periglacial Processes*, **19**, 195–210, <https://doi.org/10.1002/ppp.620>.
- May, W. 2002. Simulated changes of the Indian summer monsoon under enhanced greenhouse gas conditions in a global time-slice experiment. *Geophysical Research Letters*, **29**, 1118, <https://doi.org/10.1029/2001GL013808>.
- McAdoo, B.G., Quak, M., Gnyawali, K.R., Adhikari, B.R., Devkota, S., Rajbhandari, P.L. & Sudmeier-Rieux, K. 2018. Roads and landslides in Nepal: how development affects environmental risk. *Hazards Earth Syst. Sci*, **18**, 3203–3210, <https://doi.org/10.5194/nhess-18-3203-2018>.
- Mccoll, S.T. 2012. Paraglacial rock-slope stability. *Geomorphology*, **153–154**, 1–16, <https://doi.org/10.1016/j.geomorph.2012.02.015>.
- McFadden, L.D., Eppes, M.C., Gillespie, A.R. & Hallet, B. 2005. Physical weathering in arid landscapes due to diurnal variation in the direction of solar heating. *Geological Society of America Bulletin*, **117**, 161, <https://doi.org/10.1130/B25508.1>.

- Medwedeff, W.G., Clark, M.K., Zekkos, D. & West, A.J. 2020. Characteristic landslide distributions: An investigation of landscape controls on landslide size. *Earth and Planetary Science Letters*, **539**, 116203, <https://doi.org/10.1016/j.epsl.2020.116203>.
- Meunier, P., Hovius, N. & Haines, A.J. 2007. Regional patterns of earthquake-triggered landslides and their relation to ground motion. *Geophysical Research Letters*, **34**, L20408, <https://doi.org/10.1029/2007GL031337>.
- Meunier, P., Hovius, N. & Haines, J.A. 2008. Topographic site effects and the location of earthquake induced landslides. *Earth and Planetary Science Letters*, **275**, 221–232, <https://doi.org/10.1016/j.epsl.2008.07.020>.
- Meusburger, K. & Alewell, C. 2009a. *Natural Hazards and Earth System Sciences On the Influence of Temporal Change on the Validity of Landslide Susceptibility Maps*.
- Meusburger, K. & Alewell, C. 2009b. On the influence of temporal change on the validity of landslide susceptibility maps. *Natural Hazards and Earth System Science*, **9**, 1495–1507, <https://doi.org/10.5194/nhess-9-1495-2009>.
- Miao, C., Ashouri, H., Hsu, K.-L., Sorooshian, S. & Duan, Q. 2015. Evaluation of the PERSIANN-CDR Daily Rainfall Estimates in Capturing the Behavior of Extreme Precipitation Events over China. *Journal of Hydrometeorology*, **16**, 1387–1396, <https://doi.org/10.1175/JHM-D-14-0174.1>.
- Michelson, D.B. 2004. Systematic correction of precipitation gauge observations using analyzed meteorological variables. *Journal of Hydrology*, **290**, 161–177, <https://doi.org/10.1016/J.JHYDROL.2003.10.005>.
- Milanović, S., Milanović, S.D., Marković, N., Pamučar, D., Gigović, L. & Kostić, P. 2020. Forest Fire Probability Mapping in Eastern Serbia: Logistic Regression versus Random Forest Method. *Forests 2021*, Vol. 12, Page 5, **12**, 5, <https://doi.org/10.3390/F12010005>.
- Mitchell, T., Carter, T., Jones, P., Hulme, M. & New, M. 2003. *A Comprehensive Set of High-Resolution Grids of Monthly Climate for Europe and the Globe*

European Climate Energy Mixes View Project.

- Molnar, P. & England, P. 1990. Late Cenozoic uplift of mountain ranges and global climate change: Chicken or egg? *Nature*, **346**, 29–34, <https://doi.org/10.1038/346029a0>.
- Mordensky, S.P., Villeneuve, M.C., Farquharson, J.I., Kennedy, B.M., Heap, M.J. & Gravley, D.M. 2018. Rock mass properties and edifice strength data from Pinnacle Ridge, Mt. Ruapehu, New Zealand. *Journal of Volcanology and Geothermal Research*, **367**, 46–62, <https://doi.org/10.1016/j.jvolgeores.2018.09.012>.
- Mukul, M., Jade, S., Ansari, K. & Matin, A. 2014. Seismotectonic implications of strike-slip earthquakes in the Darjiling-Sikkim Himalaya. *Current Science*, **106**.
- Müller, M.F. & Thompson, S.E. 2013. Bias adjustment of satellite rainfall data through stochastic modeling: Methods development and application to Nepal. *Advances in Water Resources*, **60**, 121–134, <https://doi.org/10.1016/J.ADVWATRES.2013.08.004>.
- Munich RE. 2021. Record hurricane season and major wildfires – The natural disaster figures for 2020 | Munich Re <https://www.munichre.com/en/company/media-relations/media-information-and-corporate-news/media-information/2021/2020-natural-disasters-balance.html>.
- Muñoz-Torrero Manchado, A., Allen, S., Ballesteros-Cánovas, J.A., Dhakal, A., Dhital, M.R. & Stoffel, M. 2021. Three decades of landslide activity in western Nepal: new insights into trends and climate drivers. *Landslides*, <https://doi.org/10.1007/s10346-021-01632-6>.
- Murton, G. 2017. Bordering Spaces, Practising Borders: Fences, Roads and Reorientations across a Nepal–China Borderland. *South Asia: Journal of South Asian Studies*, **40**, 239–255, <https://doi.org/10.1080/00856401.2017.1292616>.
- Nagai, H., Watanabe, M., Tomii, N., Tadono, T. & Suzuki, S. 2017. Multiple remote-

- sensing assessment of the catastrophic collapse in Langtang Valley induced by the 2015 Gorkha earthquake. *Hazards Earth Syst. Sci.*, **17**, 1907–1921, <https://doi.org/10.5194/nhess-17-1907-2017>.
- Najman, Y., Appel, E., et al. 2010. Timing of India-Asia collision: Geological, biostratigraphic, and palaeomagnetic constraints. *Journal of Geophysical Research: Solid Earth*, **115**, 1–18, <https://doi.org/10.1029/2010JB007673>.
- Nara, Y., Morimoto, K., Yoneda, T., Hiroyoshi, N. & Kaneko, K. 2011. Effects of humidity and temperature on subcritical crack growth in sandstone. *International Journal of Solids and Structures*, **48**, 1130–1140, <https://doi.org/10.1016/J.IJSOLSTR.2010.12.019>.
- Neely, A.B. & DiBiase, R.A. 2020. Drainage Area, Bedrock Fracture Spacing, and Weathering Controls on Landscape-Scale Patterns in Surface Sediment Grain Size. *Journal of Geophysical Research: Earth Surface*, **125**, <https://doi.org/10.1029/2020jf005560>.
- Newmark, N.M. 1965. Effects of earthquakes on dams and embankments. *Geotechnique*, **15**, 139–160.
- Nguyen, P., Shearer, E.J., et al. 2019. The CHRS data portal, an easily accessible public repository for PERSIANN global satellite precipitation data. *Scientific Data*, **6**, <https://doi.org/10.1038/sdata.2018.296>.
- Nguyen, P., Ashouri, H., Ombadi, M., Hayatbini, N., Hsu, K.L. & Sorooshian, S. 2020. PERSIANN-CDR for hydrology and hydro-climatic applications. *In: Advances in Global Change Research*. Springer, 993–1012., https://doi.org/10.1007/978-3-030-35798-6_26.
- Nguyen, K. Van & Gatmiri, B. 2007. Evaluation of seismic ground motion induced by topographic irregularity. *Soil Dynamics and Earthquake Engineering*, **27**, 183–188, <https://doi.org/10.1016/j.soildyn.2006.06.005>.
- Ohlmacher, G.C. 2007. Plan curvature and landslide probability in regions dominated by earth flows and earth slides. *Engineering Geology*, **91**, 117–134, <https://doi.org/10.1016/J.ENGGEOL.2007.01.005>.

- Oven, K., Rana, S., Basayal, G.K., Rosser, N. & Kincey, M. 2021. Policies and institutions for disaster risk management in Nepal: A review. *In: Hutt, M., Liechty, M. & Lotter, Stefanie (eds) *Epicentre to Aftermath: Rebuilding and Remembering in the Wake of Nepal's Earthquakes*. Cambridge University Press, 151–450.*
- Ozturk, U., Pittore, M., Behling, R., Roessner, S., Andreani, L. & Korup, O. 2021. How robust are landslide susceptibility estimates? *Landslides*, **18**, 681–695, <https://doi.org/10.1007/s10346-020-01485-5>.
- Palau, R.M., Hürlimann, M., Berenguer, M. & Sempere-Torres, D. 2020. Influence of the mapping unit for regional landslide early warning systems: comparison between pixels and polygons in Catalonia (NE Spain). *Landslides*, <https://doi.org/10.1007/s10346-020-01425-3>.
- Pánek, T. 2019. Landslides and Quaternary climate changes—The state of the art. *Earth-Science Reviews*, **196**, 102871, <https://doi.org/10.1016/j.earscirev.2019.05.015>.
- Pánek, T., Engel, Z., Mentlík, P., Braucher, R., Břežný, M., Škarpich, V. & Zondervan, A. 2016. Cosmogenic age constraints on post-LGM catastrophic rock slope failures in the Tatra Mountains (Western Carpathians). *Catena*, **138**, 52–67, <https://doi.org/10.1016/j.catena.2015.11.005>.
- Pánek, T., Mentlík, P., Engel, Z., Braucher, R. & Zondervan, A. 2017. Late Quaternary sackungen in the highest mountains of the Carpathians. *Quaternary Science Reviews*, **159**, 47–62, <https://doi.org/10.1016/j.quascirev.2017.01.008>.
- Paolucci, R. 2002. Amplification of earthquake ground motion by steep topographic irregularities. *Earthquake Engineering & Structural Dynamics*, **31**, 1831–1853, <https://doi.org/10.1002/eqe.192>.
- Parise, M. & Jibson, R.W. 2000. A seismic landslide susceptibility rating of geologic units based on analysis of characteristics of landslides triggered by the 17 January, 1994 Northridge, California earthquake. *Engineering Geology*, **58**, 251–270, [https://doi.org/10.1016/S0013-7952\(00\)00038-7](https://doi.org/10.1016/S0013-7952(00)00038-7).

- Park, H.J., Lee, J.H., Kim, K.M. & Um, J.G. 2016. Assessment of rock slope stability using GIS-based probabilistic kinematic analysis. *Engineering Geology*, **203**, 56–69, <https://doi.org/10.1016/j.enggeo.2015.08.021>.
- Park, H.J., Jang, J.Y. & Lee, J.H. 2019. Assessment of rainfall-induced landslide susceptibility at the regional scale using a physically based model and fuzzy-based Monte Carlo simulation. *Landslides*, **16**, 695–713, <https://doi.org/10.1007/s10346-018-01125-z>.
- Parker, R.N., Hancox, G.T., Petley, D.N., Massey, C.I., Densmore, A.L. & Rosser, N.J. 2015. Spatial distributions of earthquake-induced landslides and hillslope preconditioning in the northwest South Island, New Zealand. *Earth Surf. Dynam*, **3**, 501–525, <https://doi.org/10.5194/esurf-3-501-2015>.
- Parker, R.N., Rosser, N.J. & Hales, T.C. 2017. Spatial prediction of earthquake-induced landslide probability. *Natural Hazards and Earth System Sciences*, under review, <https://doi.org/10.5194/nhess-2017-193>.
- Parrish, R.R. & Hodges, V. 1996. Isotopic constraints on the age and provenance of the Lesser and Greater Himalayan sequences, Nepalese Himalaya. *Geological Society of America Bulletin*, **108**, 904–911, [https://doi.org/10.1130/0016-7606\(1996\)108<0904:ICOTAA>2.3.CO;2](https://doi.org/10.1130/0016-7606(1996)108<0904:ICOTAA>2.3.CO;2).
- Paudel, B., Zhang, Y. li, Li, S. cheng, Liu, L. shan, Wu, X. & Khanal, N.R. 2016. Review of studies on land use and land cover change in Nepal. *Journal of Mountain Science*, **13**, 643–660, <https://doi.org/10.1007/s11629-015-3604-9>.
- Paudel, P.P., Omura, H., Kubota, T. & Morita, K. 2003. Landslide damage and disaster management system in Nepal. *Disaster Prevention and Management: An International Journal*, **12**, 413–419, <https://doi.org/10.1108/09653560310507235>.
- Petley, D. 2012. Global patterns of loss of life from landslides. *Geology*, **40**, 927–930, <https://doi.org/10.1130/G33217.1>.
- Petley, D.N., Higuchi, T., Petley, D.J., Bulmer, M.H. & Carey, J. 2005. Development of progressive landslide failure in cohesive materials. *Geology*, **33**, 201,

<https://doi.org/10.1130/G21147.1>.

- Petley, D.N., Rosser, A.N.J., et al. 2007. Trends in landslide occurrence in Nepal. *Nat Hazards*, **43**, 23–44, <https://doi.org/10.1007/s11069-006-9100-3>.
- Pham, B.T., Phong, T. Van, et al. 2020. A Comparative Study of Kernel Logistic Regression, Radial Basis Function Classifier, Multinomial Naïve Bayes, and Logistic Model Tree for Flash Flood Susceptibility Mapping. *Water* 2020, Vol. 12, Page 239, **12**, 239, <https://doi.org/10.3390/W12010239>.
- Pisano, L., Zumpano, V., Malek, Roskopf, C.M. & Parise, M. 2017. Variations in the susceptibility to landslides, as a consequence of land cover changes: A look to the past, and another towards the future. *Science of the Total Environment*, **601–602**, 1147–1159, <https://doi.org/10.1016/j.scitotenv.2017.05.231>.
- Popescu, M.E. & Sasahara, K. 2009. Engineering Measures for Landslide Disaster Mitigation. In: *Landslides – Disaster Risk Reduction*. Berlin, Heidelberg, Springer Berlin Heidelberg, 609–631., https://doi.org/10.1007/978-3-540-69970-5_32.
- Pourghasemi, H.R., Teimoori Yansari, Z., Panagos, P. & Pradhan, B. 2018. Analysis and evaluation of landslide susceptibility: a review on articles published during 2005–2016 (periods of 2005–2012 and 2013–2016). *Arabian Journal of Geosciences*, **11**, 1–12, <https://doi.org/10.1007/s12517-018-3531-5>.
- Pradhan, B. 2010. Landslide susceptibility mapping of a catchment area using frequency ratio, fuzzy logic and multivariate logistic regression approaches. *Journal of the Indian Society of Remote Sensing*, **38**, 301–320, <https://doi.org/10.1007/s12524-010-0020-z>.
- Prakash, N., Ranjan, B., et al. 2013. Rainfall event-based landslide susceptibility zonation mapping. **69**, 365–388, <https://doi.org/10.1007/s11069-013-0715-x>.
- Rabby, Y.W. & Li, Y. 2019. An integrated approach to map landslides in Chittagong Hilly Areas, Bangladesh, using Google Earth and field mapping. *Landslides*, **16**, 633–645, <https://doi.org/10.1007/s10346-018-1107-9>.
- Rahaman, W., Singh, S.K., Sinha, R. & Tandon, S.K. 2009. Climate control on erosion

- distribution over the Himalaya during the past ~ 100 ka. *Geology*, **37**, 559–562, <https://doi.org/10.1130/G25425A.1>.
- Rai, S.M., Upreti, B.N., Dhakal, S., Bhattarai, T.N., Adhikari, B.R., Bajracharya, S.R. & Yoshida, M. 2017. Climate Change Impact on Glacier Retreat and Local Community in the Langtang Valley, Central Nepal. *Journal of Development Innovations*, **1**, 45–59.
- Rathburn, S.L., Shahverdian, S.M. & Ryan, S.E. 2018. Post-disturbance sediment recovery: Implications for watershed resilience. *Geomorphology*, **305**, 61–75, <https://doi.org/10.1016/j.geomorph.2017.08.039>.
- Rech, J.A., Reeves, R.W. & Hendricks, D.M. 2001. The influence of slope aspect on soil weathering processes in the Springerville volcanic field, Arizona. *CATENA*, **43**, 49–62, [https://doi.org/10.1016/S0341-8162\(00\)00118-1](https://doi.org/10.1016/S0341-8162(00)00118-1).
- Regmi, A.D., Devkota, K.C., Yoshida, K., Pradhan, B., Pourghasemi, H.R., Kumamoto, T. & Akgun, A. 2014. Application of frequency ratio, statistical index, and weights-of-evidence models and their comparison in landslide susceptibility mapping in Central Nepal Himalaya. *Arabian Journal of Geosciences*, **7**, 725–742, <https://doi.org/10.1007/s12517-012-0807-z>.
- Regmi, A.D., Peng, C. & Dhital, M.R. 2017. Distribution Characteristics of Mass Movements in the Upper Bhote Koshi Watershed Before and After the Gorkha Earthquake and Their Susceptibility Evaluation. *In: Advancing Culture of Living with Landslides*. Cham, Springer International Publishing, 847–857., https://doi.org/10.1007/978-3-319-53498-5_97.
- Reichenbach, P., Busca, • C, Mondini, • A C & Rossi, • M. 2014. The Influence of Land Use Change on Landslide Susceptibility Zonation: The Briga Catchment Test Site (Messina, Italy). *Environmental Management*, **54**, 1372–1384, <https://doi.org/10.1007/s00267-014-0357-0>.
- Reichenbach, P., Rossi, M., Malamud, B.D., Mihir, M. & Guzzetti, F. 2018. A review of statistically-based landslide susceptibility models. *Earth-Science Reviews*, **180**, 60–91, <https://doi.org/10.1016/J.EARSCIREV.2018.03.001>.

- Roback, K., Clark, M.K., et al. 2018. The size, distribution, and mobility of landslides caused by the 2015 Mw7.8 Gorkha earthquake, Nepal. *Geomorphology*, **301**, 121–138, <https://doi.org/10.1016/J.GEOMORPH.2017.01.030>.
- Roberts, S., Jones, J.N. & Boulton, S.J. 2021. Characteristics of landslide path dependency revealed through multiple resolution landslide inventories in the Nepal Himalaya. *Geomorphology*, **390**, 107868, <https://doi.org/10.1016/J.GEOMORPH.2021.107868>.
- Robinson, D.M., DeCelles, P.G., Patchett, P.J. & Garzzone, C.N. 2001. The kinematic evolution of the Nepalese Himalaya interpreted from Nd isotopes. *Earth and Planetary Science Letters*, **192**, 507–521, [https://doi.org/10.1016/S0012-821X\(01\)00451-4](https://doi.org/10.1016/S0012-821X(01)00451-4).
- Roda-Boluda, D.C., D'Arcy, M., McDonald, J. & Whittaker, A.C. 2018. Lithological controls on hillslope sediment supply: insights from landslide activity and grain size distributions. *Earth Surface Processes and Landforms*, **43**, 956–977, <https://doi.org/10.1002/esp.4281>.
- Roering, J.J., Kirchner, J.W. & Dietrich, W.E. 1999. Evidence for nonlinear, diffusive sediment transport on hillslopes and implications for landscape morphology. *Water Resources Research*, **35**, 853–870, <https://doi.org/10.1029/1998WR900090>.
- Romer, C. & Ferentinou, M. 2016. Shallow landslide susceptibility assessment in a semiarid environment - A Quaternary catchment of KwaZulu-Natal, South Africa. *Engineering Geology*, **201**, 29–44, <https://doi.org/10.1016/j.enggeo.2015.12.013>.
- Rossi, M. & Malamud, B.D. 2014. *LAMPRE, Prototype SW for Determination of Landslide Statistics from Inventory Maps*.
- Royden, L.H. & Burchfiel, B.C. 1987. Thin-skinned N-S extension within the convergent Himalayan region: gravitational collapse of a Miocene topographic front. *Geological Society, London, Special Publications*, **28**, 611–619, <https://doi.org/10.1144/GSL.SP.1987.028.01.40>.

- Rudolph, B., Becker, A., Schneider, U., Meyer-Christoffer, A. & Ziese, M. 2011. *New GPCP Full Data Reanalysis Version 5 Provides High-Quality Gridded Monthly Precipitation Data ERA_CLIM2 View Project Reference Publication on the Deliverables of the Global Precipitation Climatology Centre View Project.*
- Sabatakakis, N., Koukis, G., Vassiliades, E. & Lainas, S. 2013. Landslide susceptibility zonation in Greece. *Natural Hazards*, <https://doi.org/10.1007/s11069-012-0381-4>.
- Samadhiya, N.K. & Jain, P.K. 2003. Strength Behaviour of Phyllites Under Triaxial Stress Condition. *Journal of Rock Mechanics and Tunnelling Tech.*, **9**.
- Samia, J., Temme, A., Bregt, A., Wallinga, J., Guzzetti, F., Ardizzone, F. & Rossi, M. 2017a. Characterization and quantification of path dependency in landslide susceptibility ARTICLE INFO Keywords: Time-variant susceptibility Path dependency Follow-up landslides Multi-temporal landslide inventory Landslide geometry, <https://doi.org/10.1016/j.geomorph.2017.04.039>.
- Samia, J., Temme, A., Bregt, A., Wallinga, J., Guzzetti, F., Ardizzone, F. & Rossi, M. 2017b. Do landslides follow landslides? Insights in path dependency from a multi-temporal landslide inventory. *Landslides*, **14**, 547–558, <https://doi.org/10.1007/s10346-016-0739-x>.
- Samia, J., Temme, A., et al. 2018. Implementing landslide path dependency in landslide susceptibility modelling. **15**, 2129–2144, <https://doi.org/10.1007/s10346-018-1024-y>.
- Samia, J., Temme, A., Bregt, A., Wallinga, J., Guzzetti, F. & Ardizzone, F. 2020. Dynamic path-dependent landslide susceptibility modelling. *Natural Hazards and Earth System Sciences*, **20**, 271–285, <https://doi.org/10.5194/nhess-20-271-2020>.
- Santangelo, M., Cardinali, M., Rossi, M., Mondini, A.C. & Guzzetti, F. 2010. Remote landslide mapping using a laser rangefinder binocular and GPS. *Hazards Earth Syst. Sci*, **10**, 2539–2546, <https://doi.org/10.5194/nhess-10-2539-2010>.
- Santi, P.M., deWolfe, V.G., Higgins, J.D., Cannon, S.H. & Gartner, J.E. 2008. Sources

- of debris flow material in burned areas. *Geomorphology*, **96**, 310–321, <https://doi.org/10.1016/j.geomorph.2007.02.022>.
- Sapkota, S.N., Bollinger, L. & Perrier, F. 2016. Fatality rates of the M w ~8.2, 1934, Bihar–Nepal earthquake and comparison with the April 2015 Gorkha earthquake. *Earth, Planets and Space*, **68**, 40, <https://doi.org/10.1186/s40623-016-0416-2>.
- Sassa, K. & Canuti, P. (eds). 2009. *Landslides – Disaster Risk Reduction*. Berlin, Heidelberg, Springer Berlin Heidelberg, <https://doi.org/10.1007/978-3-540-69970-5>.
- Sauber, J.M. & Ruppert, N.A. 2008. Rapid Ice Mass Loss: Does It Have an Influence on Earthquake Occurrence in Southern Alaska? *In: Active Tectonics and Seismic Potential of Alaska*. Wiley Blackwell, 369–384., <https://doi.org/10.1029/179GM21>.
- Schelling, D. & Arita, K. 1991. Thrust tectonics, crustal shortening, and the structure of the far-eastern Nepal Himalaya. *Tectonics*, **10**, 851–862, <https://doi.org/10.1029/91TC01011>.
- Schiermeier, Q. 2003. Alpine thaw breaks ice over permafrost's role. *Nature*, **424**, 712–712, <https://doi.org/10.1038/424712a>.
- Schlögel, R., Marchesini, I., Alvioli, M., Reichenbach, P., Rossi, M. & Malet, J.P. 2018. Optimizing landslide susceptibility zonation: Effects of DEM spatial resolution and slope unit delineation on logistic regression models. *Geomorphology*, **301**, 10–20, <https://doi.org/10.1016/J.GEOMORPH.2017.10.018>.
- Schmaltz, E.M., Steger, S. & Glade, T. 2017. The influence of forest cover on landslide occurrence explored with spatio-temporal information. *Geomorphology*, **290**, 250–264, <https://doi.org/10.1016/j.geomorph.2017.04.024>.
- Schultz, R.A. 1995. Limits on strength and deformation properties of jointed basaltic rock masses. *Rock Mechanics and Rock Engineering*, **28**, 1–15, <https://doi.org/10.1007/BF01024770>.
- Schuster, R.L. 1978. Introduction to landslides: analysis and control. *Transportation*

Research Board Special Report.

- Schwanghart, W. & Scherler, D. 2014. Short Communication: TopoToolbox 2 – MATLAB-based software for topographic analysis and modeling in Earth surface sciences. *Earth Surf. Dynam*, **2**, 1–7, <https://doi.org/10.5194/esurf-2-1-2014>.
- Searle, M.P., Parrish, R.R., Hodges, K.V., Hurford, A., Ayres, M.W. & Whitehouse, M.J. 1997. Shisha Pangma Leucogranite, South Tibetan Himalaya: Field Relations, Geochemistry, Age, Origin, and Emplacement. *The Journal of Geology*, **105**, 295–318, <https://doi.org/10.1086/515924>.
- Seneviratne, S.I., Nicholls, N., et al. 2012. Changes in climate extremes and their impacts on the natural physical environment. *In: Managing the Risks of Extreme Events and Disasters to Advance Climate Change Adaptation: Special Report of the Intergovernmental Panel on Climate Change*. Cambridge University Press, 109–230., <https://doi.org/10.1017/CBO9781139177245.006>.
- Shan, Y., Chen, S. & Zhong, Q. 2020. Rapid prediction of landslide dam stability using the logistic regression method. *Landslides*, **17**, 2931–2956, <https://doi.org/10.1007/S10346-020-01414-6/FIGURES/9>.
- Sharma, R., Rani, S. & Memon, I. 2020. A smart approach for fire prediction under uncertain conditions using machine learning. *Multimedia Tools and Applications*, **79**, 28155–28168, <https://doi.org/10.1007/S11042-020-09347-X/TABLES/8>.
- Shieh, C.L., Chen, Y.S., Tsai, Y.J. & Wu, J.H. 2009. Variability in rainfall threshold for debris flow after the Chi-Chi earthquake in central Taiwan, China. *International Journal of Sediment Research*, **24**, 177–188, [https://doi.org/10.1016/S1001-6279\(09\)60025-1](https://doi.org/10.1016/S1001-6279(09)60025-1).
- Shiraiwa, T. & Watanabe, T. 1991. Late Quaternary glacial fluctuations in the Langtang Valley, Nepal Himalaya, reconstructed by relative dating methods. *Arctic & Alpine Research*, **23**, 404–416, <https://doi.org/10.2307/1551682>.
- Shrestha, B.B. & Nakagawa, H. 2016. Hazard assessment of the formation and failure

- of the Sunkoshi landslide dam in Nepal. *Natural Hazards*, **82**, 2029–2049, <https://doi.org/10.1007/s11069-016-2283-3>.
- Shrestha, B.R. 2019. An Assessment of Disaster Loss and Damage in Nepal. *The Geographic Base*, **6**, 42–51, <https://doi.org/10.3126/tgb.v6i0.26166>.
- Shroder, J.F. & Bishop, M.P. 1998. Mass movement in the Himalaya: new insights and research directions. *Geomorphology*, **26**, 13–35, [https://doi.org/10.1016/S0169-555X\(98\)00049-X](https://doi.org/10.1016/S0169-555X(98)00049-X).
- Sidle, R.C. & Bogaard, T.A. 2016. Dynamic earth system and ecological controls of rainfall-initiated landslides. *Earth-Science Reviews*, **159**, 275–291, <https://doi.org/10.1016/J.EARSCIREV.2016.05.013>.
- Sidle, R.C. & Ochiai, H. 2006. *Landslides: Processes, Prediction and Land Use*. American Geophysical Union.
- Sifa, S.F., Mahmud, T., Tarin, M.A. & Haque, D.M.E. 2020. Event-based landslide susceptibility mapping using weights of evidence (WoE) and modified frequency ratio (MFR) model: a case study of Rangamati district in Bangladesh. *Geology, Ecology, and Landscapes*, **4**, 222–235, <https://doi.org/10.1080/24749508.2019.1619222>.
- Sousa, L.M.O., Suárez del Río, L.M., Calleja, L., Ruiz de Argandoña, V.G. & Rodríguez Rey, A. 2005. Influence of microfractures and porosity on the physico-mechanical properties and weathering of ornamental granites. *Engineering Geology*, **77**, 153–168, <https://doi.org/10.1016/j.enggeo.2004.10.001>.
- Stanley, T. & Kirschbaum, D.B. 2017. A heuristic approach to global landslide susceptibility mapping. *Natural Hazards*, **87**, 145–164, <https://doi.org/10.1007/s11069-017-2757-y>.
- Stanley, T., Kirschbaum, D.B., Pascale, S. & Kapnick, S. 2020. Extreme precipitation in the Himalayan landslide hotspot. *In: Advances in Global Change Research*. Springer, 1087–1111., https://doi.org/10.1007/978-3-030-35798-6_31.
- Stark, C.P. & Guzzetti, F. 2009. Landslide rupture and the probability distribution of

- mobilized debris volumes. *Journal of Geophysical Research: Earth Surface*, **114**, <https://doi.org/10.1029/2008JF001008>.
- Stark, C.P. & Hovius, N. 2001. The characterization of landslide size distributions. *Geophysical Research Letters*, **28**, 1091–1094, <https://doi.org/10.1029/2000GL008527>.
- Strangeways, I. 2006. *Precipitation: Theory, Measurement and Distribution*. Cambridge University Press.
- Struck, M., Andermann, C., et al. 2015. Monsoonal hillslope processes determine grain size-specific suspended sediment fluxes in a trans-Himalayan river. *Geophysical Research Letters*, **42**, 2302–2308, <https://doi.org/10.1002/2015GL063360>.
- Sun, Q., Miao, C., Duan, Q., Ashouri, H., Sorooshian, S. & Hsu, K.-L. 2018. A Review of Global Precipitation Data Sets: Data Sources, Estimation, and Intercomparisons. *Reviews of Geophysics*, **56**, 79–107, <https://doi.org/10.1002/2017RG000574>.
- Syvitski, J.P.M. & Kettner, A. 2011. Sediment flux and the anthropocene. *Philosophical Transactions of the Royal Society A: Mathematical, Physical and Engineering Sciences*, **369**, 957–975, <https://doi.org/10.1098/rsta.2010.0329>.
- Taalab, K., Cheng, T. & Zhang, Y. 2018. Mapping landslide susceptibility and types using Random Forest. *Big Earth Data*, **2**, 159–178, <https://doi.org/10.1080/20964471.2018.1472392>.
- Takagi, H., Arita, K., Sawaguchi, T., Kobayashi, K. & Awaji, D. 2003. Kinematic history of the Main Central Thrust zone in the Langtang area, Nepal. *Tectonophysics*, **366**, 151–163, [https://doi.org/10.1016/S0040-1951\(03\)00052-0](https://doi.org/10.1016/S0040-1951(03)00052-0).
- Tamrakar, N.K., Yokota, S. & Shrestha, S. Das. 2007. Relationships among mechanical, physical and petrographic properties of Siwalik sandstones, Central Nepal Sub-Himalayas. *Engineering Geology*, **90**, 105–123, <https://doi.org/10.1016/j.enggeo.2006.10.005>.

- Tan, W.P. 1996. Basic theory and study situation of rainstorm debris flow forecast in China. *Journal of Soil and Water Conservation*, **2**, 88–95.
- Tandon, R.S. & Gupta, V. 2015. Estimation of strength characteristics of different Himalayan rocks from Schmidt hammer rebound, point load index, and compressional wave velocity. *Bulletin of Engineering Geology and the Environment*, **74**, 521–533, <https://doi.org/10.1007/s10064-014-0629-1>.
- Tang, C., Jiang, Z. & Li, W. 2015. Seismic Landslide Evolution and Debris Flow Development: A Case Study in the Hongchun Catchment, Wenchuan Area of China. *In: Engineering Geology for Society and Territory - Volume 2*. Cham, Springer International Publishing, 445–449., https://doi.org/10.1007/978-3-319-09057-3_72.
- Tanoli, J.I., Ningsheng, C., Regmi, A.D. & Jun, L. 2017. Spatial distribution analysis and susceptibility mapping of landslides triggered before and after Mw7.8 Gorkha earthquake along Upper Bhote Koshi, Nepal. *Arabian Journal of Geosciences*, **10**, 277, <https://doi.org/10.1007/s12517-017-3026-9>.
- Tanyaş, H., Westen, C.J., Allstadt, K.E. & Jibson, R.W. 2019. Factors controlling landslide frequency–area distributions. *Earth Surface Processes and Landforms*, **44**, 900–917, <https://doi.org/10.1002/esp.4543>.
- Taylor, F.E., Malamud, B.D., Witt, A. & Guzzetti, F. 2018. Landslide shape, ellipticity and length-to-width ratios. *Earth Surface Processes and Landforms*, <https://doi.org/10.1002/esp.4479>.
- Temme, A., Guzzetti, F., Samia, J. & Mirus, B.B. 2020. The future of landslides' past—a framework for assessing consecutive landsliding systems. *Landslides*, **17**, 1519–1528, <https://doi.org/10.1007/s10346-020-01405-7>.
- Teran, S. 2021. *A Probabilistic Analysis of Lahar Bulking and Debulking in Channelized Proximal Volcanic Settings - ProQuest*. The University of Texas at San Antonio.
- Thapa, P.B. & Dhital, M.R. 2000. Landslide and debris flows of 19--21 July 1993 in the Agra Khola watershed of central Nepal. *Jour. Nepal Geol. Soc*, **21**, 5–20.

- Thapa, S., Shrestha, A., Lamichhane, S., Adhikari, R. & Gautam, D. 2020. Catchment-scale flood hazard mapping and flood vulnerability analysis of residential buildings: The case of Khando River in eastern Nepal. *Journal of Hydrology: Regional Studies*, **30**, 100704, <https://doi.org/10.1016/j.ejrh.2020.100704>.
- Thi Ngo, P.T., Panahi, M., Khosravi, K., Ghorbanzadeh, O., Karimnejad, N., Cerda, A. & Lee, S. 2020. Evaluation of deep learning algorithms for national scale landslide susceptibility mapping of Iran. *Geoscience Frontiers*, <https://doi.org/10.1016/j.gsf.2020.06.013>.
- Thiebes, B. & Glade, T. 2019. Landslide Early Warning Systems—fundamental concepts and innovative applications. *In: Landslides and Engineered Slopes. Experience, Theory and Practice*. CRC Press, 1903–1911., <https://doi.org/10.1201/9781315375007-227>.
- Tian, Y., Xu, C., Chen, J., Zhou, Q. & Shen, L. 2017. Geometrical characteristics of earthquake-induced landslides and correlations with control factors: a case study of the 2013 Minxian, Gansu, China, Mw 5.9 event. *Landslides*, **14**, 1915–1927, <https://doi.org/10.1007/s10346-017-0835-6>.
- Tian, Y., Owen, L.A., Xu, C., Shen, L., Zhou, Q. & Figueiredo, P.M. 2020. Geomorphometry and Statistical Analyses of Landslides Triggered by the 2015 Mw 7.8 Gorkha Earthquake and the Mw 7.3 Aftershock, Nepal. *Frontiers in Earth Science*, **8**, 407, <https://doi.org/10.3389/feart.2020.572449>.
- Tibaldi, A., Ferrari, L. & Pasquarè, G. 1995. Landslides triggered by earthquakes and their relations with faults and mountain slope geometry: an example from Ecuador. *Geomorphology*, **11**, 215–226, [https://doi.org/10.1016/0169-555X\(94\)00060-5](https://doi.org/10.1016/0169-555X(94)00060-5).
- Tiwari, B., Ajmera, B. & Dhital, S. 2017. Characteristics of moderate- to large-scale landslides triggered by the M w 7.8 2015 Gorkha earthquake and its aftershocks. *Landslides*, **14**, 1297–1318, <https://doi.org/10.1007/s10346-016-0789-0>.
- Torizin, J., Wang, L. chao, et al. 2018. Statistical landslide susceptibility assessment in a dynamic environment: A case study for Lanzhou City, Gansu Province,

- NW China. *Journal of Mountain Science*, **15**, 1299–1318, <https://doi.org/10.1007/s11629-017-4717-0>.
- Trigila, A., Frattini, P., et al. 2013. Landslide susceptibility mapping at national scale: The Italian case study. *In: Landslide Science and Practice: Landslide Inventory and Susceptibility and Hazard Zoning*. Springer Berlin Heidelberg, 287–295., https://doi.org/10.1007/978-3-642-31325-7_38.
- Turner, A.G. & Annamalai, H. 2012. Climate change and the South Asian summer monsoon. *Nature Climate Change*, **2**, 587–595, <https://doi.org/10.1038/nclimate1495>.
- Twiss, R.J. & Moores, E.M. 1992. *Structural Geology*. San Francisco, W. H. Freeman & Co, <https://doi.org/10.1002/gj.3350290408>.
- Ullah, W., Wang, G., Ali, G., Tawia Hagan, D., Bhatti, A. & Lou, D. 2019. Comparing Multiple Precipitation Products against In-Situ Observations over Different Climate Regions of Pakistan. *Remote Sensing*, **11**, 628, <https://doi.org/10.3390/rs11060628>.
- Upreti, B.N. 1999. An overview of the stratigraphy and tectonics of the Nepal Himalaya. *Journal of Asian Earth Sciences*, **17**, 577–606, [https://doi.org/10.1016/S1367-9120\(99\)00047-4](https://doi.org/10.1016/S1367-9120(99)00047-4).
- Upreti, B.N. & Dhital, M.R. 1996. Landslide studies and management in Nepal. *International Centre for Integrated Mountain Development (ICIMOD)*.
- USGS. 2004a. Landslide Types and Processes. **Fact Sheet**, <https://pubs.usgs.gov/fs/2004/3072/pdf/fs2004-3072>.
- USGS. 2004b. Landslide Types and Processes. *Fact Sheet 2004-3072*, 1–4.
- USGS. 2018a. M 6.9 Nepal-India Border Region, 1988. *Earthquake Hazards Program* <https://earthquake.usgs.gov/earthquakes/eventpage/usp0003k6t#executive>.
- USGS. 2018b. M 6.9 Sikkim, India, 2011. *Earthquake Hazards Program* <https://earthquake.usgs.gov/earthquakes/eventpage/usp000j88b#executive>.

- USGS. 2018c. M 7.8, 36 km E of Khudi, Nepal, 2015. *Earthquake Hazards Program*<https://earthquake.usgs.gov/earthquakes/eventpage/us20002926#executive>.
- USGS. 2018d. M 8.0 - Nepal-India border region, 1934-01-15<https://earthquake.usgs.gov/earthquakes/eventpage/iscgem904745/executive>.
- Vakhshoori, V. & Zare, M. 2018. Is the ROC curve a reliable tool to compare the validity of landslide susceptibility maps? *Geomatics, Natural Hazards and Risk*, **9**, 249–266, <https://doi.org/10.1080/19475705.2018.1424043>.
- Valagussa, A., Marc, O., Frattini, P. & Crosta, G.B. 2019. Seismic and geological controls on earthquake-induced landslide size. *Earth and Planetary Science Letters*, **506**, 268–281, <https://doi.org/10.1016/j.epsl.2018.11.005>.
- Van Den Eeckhaut, M., Poesen, J., Govers, G., Verstraeten, G. & Demoulin, A. 2007a. Characteristics of the size distribution of recent and historical landslides in a populated hilly region. *Earth and Planetary Science Letters*, **256**, 588–603, <https://doi.org/10.1016/j.epsl.2007.01.040>.
- Van Den Eeckhaut, M., Poesen, J., et al. 2007b. Use of LIDAR-derived images for mapping old landslides under forest. *Earth Surface Processes and Landforms*, **32**, 754–769, <https://doi.org/10.1002/esp.1417>.
- Van Der Geest, K. & Schindler, M. 2016. Brief communication: Loss and damage from a catastrophic landslide in Nepal. *Hazards Earth Syst. Sci*, **16**, 2347–2350, <https://doi.org/10.5194/nhess-16-2347-2016>.
- van Westen, C.J., Castellanos, E. & Kuriakose, S.L. 2008. Spatial data for landslide susceptibility, hazard, and vulnerability assessment: An overview. *Engineering Geology*, **102**, 112–131, <https://doi.org/10.1016/j.enggeo.2008.03.010>.
- Van Westen, C.J., Seijmonsbergen, A.C. & Mantovani, F. 1999. Comparing landslide hazard maps. *In: Natural Hazards*. Springer Netherlands, 137–158., <https://doi.org/10.1023/a:1008036810401>.
- Vannay, J.-C., Grasemann, B., Rahn, M., Frank, W., Carter, A., Baudraz, V. & Cosca,

- M. 2004. Miocene to Holocene exhumation of metamorphic crustal wedges in the NW Himalaya: Evidence for tectonic extrusion coupled to fluvial erosion. *Tectonics*, **23**, n/a-n/a, <https://doi.org/10.1029/2002TC001429>.
- Varnes, D.J. 1958. Landslide Types and Processes. *Landslides and engineering practice*, **24**, 20–47.
- Verdian, J., Sklar, L., Riebe, C. & Moore, J. 2020. Sediment size on talus slopes correlates with fracture spacing on bedrock cliffs: Implications for predicting initial sediment size distributions on hillslopes. *Earth Surface Dynamics Discussions*, 1–23, <https://doi.org/10.5194/esurf-2020-54>.
- Von Specht, S., Ozturk, U., Veh, G., Cotton, F. & Korup, O. 2019. Effects of finite source rupture on landslide triggering: The 2016 Mw 7.1 Kumamoto earthquake. *Solid Earth*, **10**, 463–486, <https://doi.org/10.5194/se-10-463-2019>.
- Wald, D.J. & Allen, T.I. 2007. Topographic slope as a proxy for seismic site conditions and amplification. *Bulletin of the Seismological Society of America*, **97**, 1379–1395, <https://doi.org/10.1785/0120060267>.
- Waltham, A.C. 2002. Foundations of engineering geology. *Foundations of engineering geology*, <https://doi.org/10.1201/9781482267785/FOUNDATIONS-ENGINEERING-GEOLOGY-TONY-WALTHAM>.
- Wang, H.J., Xiao, T., Li, X.Y., Zhang, L.L. & Zhang, L.M. 2019. A novel physically-based model for updating landslide susceptibility. *Engineering Geology*, **251**, 71–80, <https://doi.org/10.1016/j.enggeo.2019.02.004>.
- Wang, Y., Feng, L., Li, S., Ren, F. & Du, Q. 2020. A hybrid model considering spatial heterogeneity for landslide susceptibility mapping in Zhejiang Province, China. *Catena*, **188**, 104425, <https://doi.org/10.1016/j.catena.2019.104425>.
- Warr, L.N. & Cox, S. 2001. Clay mineral transformations and weakening mechanisms along the Alpine Fault, New Zealand. *Geological Society, London, Special Publications*, **186**, 85–101, <https://doi.org/10.1144/GSL.SP.2001.186.01.06>.

- Watkinson, I.M. & Hall, R. 2019. Impact of communal irrigation on the 2018 Palu earthquake-triggered landslides. *Nature Geoscience*, **12**, 940–945, <https://doi.org/10.1038/s41561-019-0448-x>.
- Watters, R.J. & Delahaut, W.D. 1995. Effect of argillic alteration on rock mass stability. *In: GSA Reviews in Engineering Geology*. Geological Society of America, 139–150., <https://doi.org/10.1130/REG10-p139>.
- Wegmann, M., Gudmundsson, G.H. & Haeberli, W. 1998. Permafrost changes in rock walls and the retreat of alpine glaciers: a thermal modelling approach. *Permafrost and Periglacial Processes*, **9**, 23–33, [https://doi.org/10.1002/\(SICI\)1099-1530\(199801/03\)9:1<23::AID-PPP274>3.0.CO;2-Y](https://doi.org/10.1002/(SICI)1099-1530(199801/03)9:1<23::AID-PPP274>3.0.CO;2-Y).
- Wesnousky, S.G., Kumar, S., Mohindra, R. & Thakur, V.C. 1999. Uplift and convergence along the Himalayan Frontal Thrust of India. *Tectonics*, **18**, 967–976, <https://doi.org/10.1029/1999TC900026>.
- Wheeler, D.C. & Páez, A. 2010. Geographically Weighted Regression. *In: Handbook of Applied Spatial Analysis*. Springer Berlin Heidelberg, 461–486., https://doi.org/10.1007/978-3-642-03647-7_22.
- Wieczorek, G.F. 1996. Landslide triggering mechanisms. *Landslides: Investigation and mitigation*, **247**, 76–90.
- Williams, S. Van. 1983. Present and Former Equilibrium-Line Altitudes Near Mount Everest. *Arctic and Alpine Research*, **15**, 201–211, <https://doi.org/10.1080/00040851.1983.12004344>.
- Woodcock, C.E., Allen, R., et al. 2008. Free access to Landsat imagery. *Science (New York, N.Y.)*, **320**, 1011, <https://doi.org/10.1126/science.320.5879.1011a>.
- Xu, C., Xu, X., et al. 2013. Application of an incomplete landslide inventory, logistic regression model and its validation for landslide susceptibility mapping related to the May 12, 2008 Wenchuan earthquake of China. *Natural Hazards*, **68**, 883–900, <https://doi.org/10.1007/s11069-013-0661-7>.
- Yagi, H., Sato, G., Higaki, D., Yamamoto, M. & Yamasaki, T. 2009. Distribution and

- characteristics of landslides induced by the Iwate–Miyagi Nairiku Earthquake in 2008 in Tohoku District, Northeast Japan. *Landslides*, **6**, 335–344, <https://doi.org/10.1007/s10346-009-0182-3>.
- Yagi, H., Sato, G., Sato, H.P., Higaki, D., Dangol, V. & Amatya, S.C. 2020. Slope Deformation caused Jure Landslide 2014 Along Sun Koshi in Lesser Nepal Himalaya and Effect of Gorkha Earthquake 2015. *In: Workshop on World Landslide Forum WLF 2020: Understanding and Reducing Landslide Disaster Risk*. Springer, Cham, 65–72., https://doi.org/10.1007/978-3-030-60319-9_5.
- Yang, J., Song, C., Yang, Y., Xu, C., Guo, F. & Xie, L. 2019a. New method for landslide susceptibility mapping supported by spatial logistic regression and GeoDetector: A case study of Duwen Highway Basin, Sichuan Province, China. *Geomorphology*, **324**, 62–71, <https://doi.org/10.1016/j.geomorph.2018.09.019>.
- Yang, Y., Yang, J., Xu, C., Xu, C. & Song, C. 2019b. Local-scale landslide susceptibility mapping using the B-GeoSVC model. *Landslides*, **16**, 1301–1312, <https://doi.org/10.1007/s10346-019-01174-y>.
- Yatagai, A., Kamiguchi, K., Arakawa, O., Hamada, A., Yasutomi, N. & Kitoh, A. 2012. Aphrodite constructing a long-term daily gridded precipitation dataset for Asia based on a dense network of rain gauges. *Bulletin of the American Meteorological Society*, **93**, 1401–1415, <https://doi.org/10.1175/BAMS-D-11-00122.1>.
- Yin, A. 2006. Cenozoic tectonic evolution of the Himalayan orogen as constrained by along-strike variation of structural geometry, exhumation history, and foreland sedimentation. *Earth-Science Reviews*, **76**, 1–131, <https://doi.org/10.1016/j.earscirev.2005.05.004>.
- Yin, A. & Harrison, T.M. 2000. Geological Evolution of the Himalayan-Tibetan Orogen. *Annual Reviews of Earth and Planetary Sciences*, **28**, 211–280, <https://doi.org/10.1080/01947641003598252>.
- Youssef, A.M., Pourghasemi, H.R., Pourtaghi, Z.S. & Al-Katheeri, M.M. 2016. Landslide susceptibility mapping using random forest, boosted regression tree,

- classification and regression tree, and general linear models and comparison of their performance at Wadi Tayyah Basin, Asir Region, Saudi Arabia. *Landslides*, **13**, 839–856, <https://doi.org/10.1007/s10346-015-0614-1>.
- Yu, B., Wu, Y. & Chu, S. 2014. Preliminary study of the effect of earthquakes on the rainfall threshold of debris flows. *Engineering Geology*, **182**, 130–135, <https://doi.org/10.1016/j.enggeo.2014.04.007>.
- Zêzere, J.L., Trigo, R.M. & Trigo, I.F. 2005. Shallow and deep landslides induced by rainfall in the Lisbon region (Portugal): Assessment of relationships with the North Atlantic Oscillation. *Natural Hazards and Earth System Science*, **5**, 331–344, <https://doi.org/10.5194/nhess-5-331-2005>.
- Zhang, M. & Liu, J. 2010. Controlling factors of loess landslides in western China. *Environmental Earth Sciences*, **59**, 1671–1680, <https://doi.org/10.1007/s12665-009-0149-7>.
- Zhang, S. & Zhang, L.M. 2017. Impact of the 2008 Wenchuan earthquake in China on subsequent long-term debris flow activities in the epicentral area. *Geomorphology*, **276**, 86–103, <https://doi.org/10.1016/J.GEOMORPH.2016.10.009>.
- Zhou, W. & Tang, C. 2014. Rainfall thresholds for debris flow initiation in the Wenchuan earthquake-stricken area, southwestern China. *Landslides*, **11**, 877–887, <https://doi.org/10.1007/s10346-013-0421-5>.
- Zuur, A.F., Ieno, E.N. & Elphick, C.S. 2010. A protocol for data exploration to avoid common statistical problems. *Methods in Ecology and Evolution*, **1**, 3–14, <https://doi.org/10.1111/j.2041-210x.2009.00001.x>.